

Structural Integrity 27

Series Editors: José A. F. O. Correia · Abílio M. P. De Jesus

José António Fonseca de Oliveira Correia  
Satyabrata Choudhury  
Subhrajit Dutta *Editors*

# Advances in Structural Mechanics and Applications


Proceedings of ASMA-2021 (Volume 3)

# Structural Integrity

Volume 27

## Series Editors

José A. F. O. Correia , Faculty of Engineering, University of Porto, Porto, Portugal

Abílio M. P. De Jesus , Faculty of Engineering, University of Porto, Porto, Portugal

## Advisory Editors

Majid Reza Ayatollahi, School of Mechanical Engineering, Iran University of Science and Technology, Tehran, Iran

Filippo Berto, Department of Mechanical and Industrial Engineering, Faculty of Engineering, Norwegian University of Science and Technology, Trondheim, Norway

Alfonso Fernández-Canteli, Faculty of Engineering, University of Oviedo, Gijón, Spain

Matthew Hebdon, Virginia State University, Virginia Tech, Blacksburg, VA, USA

Andrei Kotousov, School of Mechanical Engineering, University of Adelaide, Adelaide, SA, Australia


Grzegorz Lesiuk, Faculty of Mechanical Engineering, Wrocław University of Science and Technology, Wrocław, Poland

Yukitaka Murakami, Faculty of Engineering, Kyushu University, Higashiku, Fukuoka, Japan

Hermes Carvalho, Department of Structural Engineering, Federal University of Minas Gerais, Belo Horizonte, Minas Gerais, Brazil

Shun-Peng Zhu, School of Mechatronics Engineering, University of Electronic Science and Technology of China, Chengdu, Sichuan, China

Stéphane Bordas, University of Luxembourg, ESCH-SUR-ALZETTE, Luxembourg

Nicholas Fantuzzi , DICAM Department, University of Bologna, BOLOGNA, Bologna, Italy

Luca Susmel, Civil Engineering, University of Sheffield, Sheffield, UK

Subhrajit Dutta, Department of Civil Engineering, National Institute Of Technology Silchar, Silchar, Assam, India

Pavlo Maruschak, Ternopil IP National Technical University, Ruska, Ukraine

Elena Fedorova, Siberian Federal University, Krasnoyarsk, Russia



The *Structural Integrity* book series is a high level academic and professional series publishing research on all areas of Structural Integrity. It promotes and expedites the dissemination of new research results and tutorial views in the structural integrity field.

The Series publishes research monographs, professional books, handbooks, edited volumes and textbooks with worldwide distribution to engineers, researchers, educators, professionals and libraries.

Topics of interested include but are not limited to:

- Structural integrity
- Structural durability
- Degradation and conservation of materials and structures
- Dynamic and seismic structural analysis
- Fatigue and fracture of materials and structures
- Risk analysis and safety of materials and structural mechanics
- Fracture Mechanics
- Damage mechanics
- Analytical and numerical simulation of materials and structures
- Computational mechanics
- Structural design methodology
- Experimental methods applied to structural integrity
- Multiaxial fatigue and complex loading effects of materials and structures
- Fatigue corrosion analysis
- Scale effects in the fatigue analysis of materials and structures
- Fatigue structural integrity
- Structural integrity in railway and highway systems
- Sustainable structural design
- Structural loads characterization
- Structural health monitoring
- Adhesives connections integrity
- Rock and soil structural integrity.

**\*\* Indexing: The books of this series are submitted to Web of Science, Scopus, Google Scholar and Springerlink \*\***

**This series is managed by team members of the ESIS/TC12 technical committee.**

Springer and the Series Editors welcome book ideas from authors. Potential authors who wish to submit a book proposal should contact Dr. Mayra Castro, Senior Editor, Springer (Heidelberg), e-mail: [mayra.castro@springer.com](mailto:mayra.castro@springer.com)

More information about this series at <https://link.springer.com/bookseries/15775>


José António Fonseca de Oliveira Correia ·  
Satyabrata Choudhury · Subhrajit Dutta  
Editors

# Advances in Structural Mechanics and Applications

Proceedings of ASMA-2021 (Volume 3)

 Springer

*Editors*

José António Fonseca de Oliveira Correia   
Faculty of Engineering  
University of Porto  
Porto, Portugal

Satyabrata Choudhury  
Department of Civil Engineering  
National Institute of Technology Silchar  
Silchar, India

Subhrajit Dutta  
Department of Civil Engineering  
National Institute of Technology Silchar  
Silchar, Assam, India

ISSN 2522-560X

ISSN 2522-5618 (electronic)

Structural Integrity

ISBN 978-3-031-04792-3

ISBN 978-3-031-04793-0 (eBook)

<https://doi.org/10.1007/978-3-031-04793-0>

© The Editor(s) (if applicable) and The Author(s), under exclusive license  
to Springer Nature Switzerland AG 2022

This work is subject to copyright. All rights are solely and exclusively licensed by the Publisher, whether the whole or part of the material is concerned, specifically the rights of translation, reprinting, reuse of illustrations, recitation, broadcasting, reproduction on microfilms or in any other physical way, and transmission or information storage and retrieval, electronic adaptation, computer software, or by similar or dissimilar methodology now known or hereafter developed.

The use of general descriptive names, registered names, trademarks, service marks, etc. in this publication does not imply, even in the absence of a specific statement, that such names are exempt from the relevant protective laws and regulations and therefore free for general use.

The publisher, the authors and the editors are safe to assume that the advice and information in this book are believed to be true and accurate at the date of publication. Neither the publisher nor the authors or the editors give a warranty, expressed or implied, with respect to the material contained herein or for any errors or omissions that may have been made. The publisher remains neutral with regard to jurisdictional claims in published maps and institutional affiliations.

This Springer imprint is published by the registered company Springer Nature Switzerland AG  
The registered company address is: Gewerbestrasse 11, 6330 Cham, Switzerland

# Contents

<b>Application of Mechanics to Concrete Material Science for Structures</b> .....	1
Bishwajit Bhattacharjee	
<b>Investigation of Seismic Design Parameters in Irregular Reinforced Concrete Buildings with Masonry Infills</b> .....	7
Mangeshkumar R. Shendkar, Denise-Penelope N. Kontoni, Sasankasekhar Mandal, and Pabitra Ranjan Maiti	
<b>Railway Bridge Model Calibration Using the Search Group Algorithm</b> .....	26
Thiago Fernandes	
<b>Aftershock Seismic Capacity Assessment of Concrete Bridge Piers Considering Post-mainshock Strength Degradation</b> .....	43
Borislav Todorov and A. H. M. Muntasir Billah	
<b>Seismic Analysis of Carbon Fiber Reinforced Polymer Cable Structure Using ETABS</b> .....	62
Vaibhav Patel and Hanumant Magarpatil	
<b>Analysis of Accidental Collision of Blue Whale with Submerged Floating Tunnel</b> .....	79
Sahil Rana, M. Abdul Akbar, Rachit Sharma, and Ankush Thakur	
<b>Structural Audit of Mutha River Bridge Using Displacement Sensors</b> .....	88
Husain Anandwala and Hanamant Magarpatil	
<b>Analysis and Cost Comparison of Framed Structure Using Different Building Materials</b> .....	102
Jinka Lakshmi Narayana, Gutti Nikhil Vamsi, Boddu Venkata Sai Prakash, and P. Bhuvaneshwari	

<b>Study of Simply Supported Skew Composite Bridge Decks Under IRC Loading</b> .....	118
J. Jane Regita and A. Sofi	
<b>Structural Assessment of Composite Concrete Members for Waterproofing and Thermal Insulation</b> .....	138
Hanamant Magarpatil, Ankita Thorat, and Vedang Patil	
<b>Use of Polyvinyl Acetate and Glass Fiber for Improving Expansive Soil</b> .....	153
Vijay Kumar, R. P. Tiwari, and Deepak Kumar	
<b>Effect of Terrain Category, Aspect Ratio and Number of Storeys on the Shear Lag Phenomenon in RCC Framed Tube Structures</b> .....	163
Sapna Kumari, Ashish Singh, and Sasankasekhar Mandal	
<b>Flexural and Torsional Moment of Clamped RC Curved Beam: A Parametric Study</b> .....	177
Abhishek Kumar, Anjani Kumar Shukla, and P. R. Maiti	
<b>Effect of Infill Walls on Seismic Behaviour of Buildings: A Review</b> .....	187
Azeel P. Kassim and Satyabrata Choudhury	
<b>Seismic Base Isolation of 7 Storey RC Structure Using Single Friction Pendulum System</b> .....	200
Sumbul Iqbal and Nazrul Islam	
<b>A Vision-Based Data-Analytics Tool for Crack Characterization in Reinforced Concrete Structures</b> .....	210
Sandeep Das, Subhrajit Dutta, Dibyendu Adak, and Shubhankar Majumdar	
<b>Response of Two-Way RCC Slab with Unconventionally Placed Reinforcements Under Contact Blast Loading</b> .....	219
Qurat ul Ain, Mehtab Alam, and S. M. Anas	
<b>Response Mitigation of Structure Using Tuned Liquid Column Ball Damper: A Review</b> .....	239
Shulanki Pal, Bijan Kumar Roy, and Satyabrata Choudhury	
<b>Numerical Analysis of One-Way Flexural Strength of Voided Slab</b> .....	250
N. Nareshnayak and B. N. Rao	
<b>Influence of Hot Air Exposure on CFRP Shear Strengthened RC T-Beams</b> .....	257
Franklin F. R. Frederick, U. K. Sharma, and V. K. Gupta	
<b>Mathematical Models for Seismic Analysis of Elevated Water Tanks: A Review</b> .....	272
Kangkana K. Baruah and Satyabrata Choudhury	

**Seismic Vulnerability Assessment Methods: A Review** . . . . . 282  
 N. Sarma Roy and Satyabrata Choudhury

**Advancement in Direct Displacement-Based Design: A Review** . . . . . 301  
 Manish Pal and Satyabrata Choudhury

**Study on High Strength Concrete with Hybrid Combination of Steel and Polypropylene Fibers** . . . . . 325  
 G. Prasanna and A. Sumathi

**Response of T-shaped Tall Building Under Wind Load** . . . . . 336  
 P. G. Priyadarsh and Neelam Rani

**Source Localization in a Framed Structure for Effective Damage Detection Using Acoustic Emission Technique** . . . . . 344  
 Anupam Kumar Biswas, Alope Kumar Datta, Pijush Topdar, and Sanjay Sengupta

**Study on Evaluation of Angle Connection for Transmission Towers** . . . . . 353  
 Vinay Kumar Singh and Abhishek Kumar Gautam

**Performance-Based Seismic Design on Bridge Piers: A Review** . . . . . 364  
 Gaddam Sudheer and Satyabrata Choudhury

**Vibration and Stability Characteristics of the Laminated Composite Plates (LCPs) for Various Delamination Positions** . . . . . 373  
 H. S. Rakshith, L. Ravi Kumar, D. L. Prabhakara, and T. Rajanna

**Strengthening of Distressed Reinforced Concrete Structural Member by Use of FRP Composites: A Review** . . . . . 390  
 Nitesh Kumar and H. K. Sharma

**Performance-Based Seismic Design: A Review** . . . . . 404  
 Shruti Chaudhary and Satyabrata Choudhury

**Evaluation of Role of Hybrid Damping System in Seismic Assessment** . . . . . 416  
 Ankita Thorat and Hanamant Magarpatil

**Author Index** . . . . . 429



# Application of Mechanics to Concrete Material Science for Structures

Bishwajit Bhattacharjee<sup>(✉)</sup>

Civil Engineering Department, Indian Institute of Technology Delhi,  
New Delhi 110016, India  
bishwa@civil.iitd.ac.in

**Abstract.** Concrete is the most popular construction material in the world because of its mold-ability, reasonably adequate mechanical characteristics and durability. However, application of mechanics to concrete material science had made slow progress because of the heterogeneity of the constituent and their near natural state. Complexity involved in modelling the concrete composite for various performances had added to this slow progress. However, in recent times steps towards application of mechanistic approach to concrete performance is initiated and this paper elaborates some of these steps.

**Keywords:** Concrete · Rheology · Material fracture · Strength durability · Fluid ingress · Moisture flow

## 1 Introduction

Concrete material science is about 100 years old with Duff A Abrams postulating strength vs water to cement ratio (W/C) relationship (Abrams 1919). Similarly slump cone and the slump test were also proposed by the same researcher. These and similar other useful relationship used in design of concrete structures are empirical in nature. For example, elastic modulus used in structural design of the concrete structures is of the form  $E = k(f_c)^n$  and is not according to the law of mechanics, rather empirical. Where  $E$  is elastic modulus and  $f_c$  stands for cube/cylinder strength ‘ $n$ ’ is an empirical exponent.

However, structural designers need such properties for design and hence their utility is justified. The understanding of concrete material science had advanced over the last century parallel with the development of material itself. Application of fundamental principles of physical sciences, particularly some branches of mechanics to concrete material science, namely, application of concepts of rheology to plastic concrete, fracture concepts to measured strength, concepts of flow through porous media in the context of durability and material degradation are some examples. These applications of fundamental principles of physical sciences can, not only provide bases of generalization of relationship between decision variables related to constituent material ingredients of concrete and concrete material performance, but would also enhance the reliability of performance prediction enabling more trustworthy material system design. At present, being purely empirical, ‘ $k$ ’ and ‘ $n$ ’ mentioned earlier in the context of elastic modulus; ‘ $E$ ’, varies from code to code i.e., practice to practice. There



are infinite numbers of strength to W/C curves and similarly methods of prediction of workability/mold-ability also vary from practice to practice.

The purpose of this article is to illustrate some of the baby step attempts made in the past to infuse some concepts of mechanics in to concrete material science, escaping from the clutch of shear empiricism that largely prevails in concrete material science and practice. Three aspects are mainly looked in to, the rheology of plastic concrete, strength and microstructure through fracture mechanics concept and moisture and chloride ingress through concepts of transport through porous media.

## 2 Workability and Rheology

Plastic concrete is known to be recognized as Bingham fluid characterized by rheological properties namely; yield shear stress ( $\tau_0$ ) and plastic viscosity ( $\mu$ ). Workability is the effort required to compact/consolidate concrete in the mold under a normal stress due to self-weight. Relatively drier concrete tend to support itself via arching action with an angle of repose. The compaction is generally attained through vibratory action with agitation pressure greater than the normal stress. However, the bandwidth of the effort required varies widely depending upon type of concrete being compacted. At the one end is the roller compacted concrete (RCC) requiring extremely high quantum effort and at the other end is the self-compacting concrete (SCC) that needs no effort at all as shown in (Fig. 1). Thus empirical workability performance indicators vary from concrete to concrete. Modified Ve-be test is adopted for RCC and slump test is most popular for normal concrete, while more than one test, including slump flow test are used for SCC. A measure of compacting effort based on fundamentals of mechanics can serve single handedly to all concretes. This compacting effort mentioned above is the work required for compaction and can be expressed in term of yield shear stress at no load ( $\tau_0$ ) and plastic viscosity ( $\mu$ ) as given in Eq. 1.

$$W = \frac{(\tau_0 + \mu[\sigma + \dot{\gamma}])\gamma_y}{2\eta} \quad (1)$$

The terms  $\sigma$  represents normal stress acting horizontal surface perpendicular to direction of flow,  $\eta$  represents an efficiency factor less than equal to 1,  $\gamma_y$  represents maximum designated shear strain and  $\dot{\gamma}$  represents shear strain rate. The ‘ $\eta$ ’ depends on compaction method and is 1 for SCC with least value for RCC. Viscometers are typically used for determination of rheological properties of paste, mortar and concrete. Banfill (2003) presented a review on rheology of cement and concrete and provided the reported ranges of yield shear stress at no load ( $\tau_0$ ) and plastic viscosity ( $\mu$ ) of cement paste, grout flowing concrete, self-compacting concrete and normal concrete etc. There are attempts to obtain these parameters from simpler tests (Laskar 2008; Ajay and Girish 2015; Ferraris et al. 2017; Subramanian 2019). Thus, the first baby step in this context is already made. Next challenge would be to relate these rheological parameters to properties of constituent materials of concrete and their proportion in the composition through appropriate micro-modelling.

### 3 Strength and Fracture at Pore Scale

Strength is accepted as mainly being governed by W/C ratio at macro level. At micro level however, it is demonstrated that W/C controls both porosity and pore size distribution. Pores are voids or holes in the solid system, which induce stress concentration around their boundary resulting in fracture and crack propagation when rate of strain energy supplied is more than the rate of surface energy required for creation of new surfaces as a function of equivalent pore radius, on the basis of Griffith's fracture concept. The resulting semi empirical equation takes the following form expressed in Eq. 2 for OPC paste (Kondraivebdhan and Bhattacharjee 2010; Kondraivebdhan and Bhattacharjee 2014).

$$f_c = Kc\alpha \frac{(1-P)}{\sqrt{r_{0.5}}} \quad (2)$$

K is constant,  $f_c$  is the compressive strength, c is the cement content in paste, and  $\alpha$  is degree of hydration, P is the porosity and  $r_{0.5}$  is the mean/median distribution radius of the pore in pore size distribution. For concrete the equation obtained is given in Eq. 3, (Kumar and Bhattacharjee 2003).

$$f_c = kc\gamma_{ca}\gamma_a\gamma_e\gamma_T \frac{(1-P)}{\sqrt{r_{0.5}}} \quad (3)$$

The k is the empirical constant,  $\gamma$  represents correction factors corresponding to subscript ca, a, e and T representing coarse aggregate, age, exposure and temperature conditions respectively. The general mechanistic form of the equation is given in Eq. 4, and the above equations are derived from the general equation by introducing other terms through empirical approach.

$$\sigma_t = \sqrt{\frac{2E_0T_0}{\pi}} \frac{(1-P)}{\sqrt{r_{0.5}}} \quad (4)$$

The  $E_0$  and  $T_0$  are equivalent elastic tension modulus of pore free solid and  $\sigma_t$  critical tensile stress for fracture to propagate from a pore. The uniaxial compressive strength  $f_c$  is a function of  $\sigma_t$ . Since one is dealing with pores at micro level, formation of plastic zone at the tip is not considered which is valid for notch or damage induced cracks. Surface energy is considered instead of fracture energy. The pore size distribution curve has been expressed through following general form given in Eq. 5, (Patil and Bhattacharjee 2008).

$$V = \frac{Pr_{0.5}^d}{r^d + r_{0.5}^d} \quad (5)$$

The V is the pore volume corresponding to pore radius r and the porosity P,  $r_{0.5}$  etc. have been related to W/C ratio or W/(C + F) where F is the fly ash content

(Kondraivebdhan and Bhattacharjee 2013).  $E_0$  depends on aggregate elastic modulus and modulus of elasticity of product of cement hydration and un-hydrated cement. Similarly,  $T_0$  depends on surface of aggregate and hydration product etc. Relationship between  $f_c$  and  $\sigma_t$  from mechanistic point of view needs research attention. At the nano-level, nano-indentation technique can provide experimental values of  $E$  values of phases of hardened concrete and molecular dynamics also allow for computational model.

## 4 Flow Through Porous Media and Durability

Durability of structure is its capability to maintain a minimum performance level over a specified period of time when exposed to service environment Hence durability is quantified in terms of time. Since the current design practice involve designing structure element wise, durability of concrete structural elements are expressed in terms service life i.e., in time dimension, usually in years. Service life is defined as the time when the element debilities to a serviceability limit, e.g., appearance of first visible crack etc. Thus durability design is the design of the concrete element (RCC or PSC) for specified service life generally expressed in years.

Concrete elements in general are manmade systems and are produced at the expense of energy; hence are likely to deteriorate with time because of degradation of material, leading to decline in their performance. The degradation of material is generally caused by chemical action of harmful agents that can ingress from exposure environment of the concrete. These agents are fluids, and either directly penetrates in to concrete or more commonly penetrates in solution phase with water as solvent. The chemical actions of such agents usually produce expansive products leading to internal tensile stresses within concrete followed by disruption and cracking. In some cases the chemical action may lead to leaching and consequent increase in porosity and further ingress and leaching leading to weakening of the structure itself. The most common medium that acts as solvent and allow ingress of harmful agents is water; besides most reactions also takes place in solution phase with water as solvent.

Durability design therefore necessitates modelling of moisture flow through concrete for appropriate boundary condition given by exposure. Concrete being a porous medium, concepts of mechanics of flow through porous media can be appropriately adopted for durability design of concrete. In general driving force for the flow of harmful fluid or agent may be concentration gradient, hydraulic suction, pressure head, advection etc. Corresponding fluxes may be superimposed assuming linearity and general equations can be developed through Fick's law, Richard's equation etc. The Richard's equation is given below in Eq. 6 and

$$\frac{\partial \theta}{\partial x} = \frac{\partial}{\partial x} \left[ D(\theta) \frac{\partial \theta}{\partial x} \right] \quad (6)$$

$D$  is Hydraulic diffusivity of concrete and  $\theta$  is relative moisture content. Similarly the equation for chloride ingress in partially saturated concrete is given in Eq. 7. Solving these equations for appropriate boundary condition can lead to service life estimation for given concrete and cover depth for known exposure environment.

$$\frac{\partial}{\partial x} \left[ D(C_{Cl}) \frac{\partial C_{Cl}}{\partial x} \right] + C_{Cl} \frac{\partial}{\partial x} \left[ D(\theta_{sl}) \frac{\partial \theta_{sl}}{\partial x} \right] = \gamma \frac{\partial C_{Cl}}{\partial x} \quad (7)$$

$D_{Cl}$  is Chloride diffusion coefficient of concrete and  $\theta_{sl}$  is degree of solution saturation,  $C_{Cl}$  is the free chloride concentration and  $\gamma$  is chloride binding coefficient. However, there are plenty of uncertainty regarding determination of material coefficient and experimental validation (Nagesh and Bhattacharjee 1998; Sarkar and Bhattacharjee 2014).

## 5 Conclusions

It is illustrated through discussions in this paper that, mechanics in general can penetrate in to concrete material science for generalization, material design otherwise is largely empirical at present.

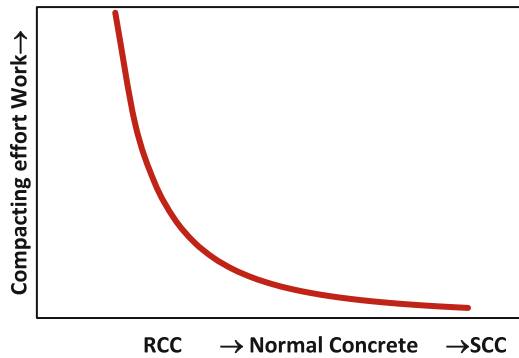


Fig. 1. Compacting effort work against type of concrete.

## References

- Abrams, D.A.: Design of Concrete Mixtures, Bulletin I, Structural Materials Research Laboratory, Lewis Institute Chicago (1919)
- Ajay, N., Girish, S.: A scientific approach for determining the workability of concrete. In: Proceedings Recent Development in Infrastructural Development-2015, Bangalore, 6 pp (2015)
- Banfill, P.F.G.: Rheology of fresh cement and concrete-a review. In: Proceedings of 11th International Cement Chemistry Congress, Durban, May, 14 pp (2003)
- Ferraris, C.F., et al.: Role of rheology in achieving successful concrete performance. In: Concrete International, ACI, vol. 39, no. 6, June, pp. 43–51 (2017)
- Kondraivebdhan, B., Bhattacharjee, B.: Effect of age and water-cement ratio on size dispersion of pores in ordinary portland cement paste. *ACI Mater. J.* **107**(2), 147–154 (2010)
- Kondraivebdhan, B., Bhattacharjee, B.: PSD modification of OPC paste through inclusion of fly ash and sand. *Mag. Concr. Res.* **65**(11), 673–684 (2013)

- Kondraivebdhan, B., Bhattacharjee, B.: Prediction of strength, permeability and hydraulic diffusivity of OPC paste. *ACI Mater. J.* **111**(6), 172–178 (2014)
- Kumar, R., Bhattacharjee, B.: Porosity, pore size distribution and in situ strength of concrete. *Cem. Concr. Res.* **33**(1), 155–164 (2003)
- Laskar, A.I.: Study of rheological behavior of high-performance concrete. Ph.D. thesis, Indian Institute of Technology Guwahati, Guwahati, March, 203 pp (2008)
- Nagesh, M., Bhattacharjee, B.: Modelling of chloride diffusion in concrete and determination of diffusion coefficients. *ACI Mater. J.* **95**(2), 113–120 (1998)
- Patil, S.G., Bhattacharjee, B.: Size and volume relationship of pore for construction materials. *J. Mater. Civil Eng.* **20**(6), 410–418 (2008)
- Sarkar, K., Bhattacharjee, B.: Moisture distribution in concrete subjected to rain induced wetting-drying. *Comput. Concr.* **14**(6), 635–656 (2014)
- Subramanian, N.: *Building Materials, Testing and Sustainability*, 788 pp. Oxford University Press, New Delhi (2019)



# Investigation of Seismic Design Parameters in Irregular Reinforced Concrete Buildings with Masonry Infills

Mangeshkumar R. Shendkar<sup>1</sup>(✉), Denise-Penelope N. Kontoni<sup>2,3</sup>(✉),  
Sasankasekhar Mandal<sup>1</sup>, and Pabitra Ranjan Maiti<sup>1</sup>

<sup>1</sup> Department of Civil Engineering, Indian Institute of Technology (IIT-BHU),  
Varanasi 221005, India

{mraj कुमार. shendkar. rs. civ18, smandal. civ,  
pramaiti. civ}@iitbhu. ac. in

<sup>2</sup> Department of Civil Engineering, University of the Peloponnese,  
26334 Patras, Greece  
kontoni@uop. gr

<sup>3</sup> School of Science and Technology, Hellenic Open University,  
26335 Patras, Greece  
kontoni. denise@ac. eap. gr

**Abstract.** In this study, four different building models, namely eight, five and three storey (Part-A and Part-B) reinforced concrete (RC) buildings, have been seismically evaluated with and without masonry infills. The four different building models considered herein are: model I (G+7), model II (G+4 Open ground storey), model III (G+2 Part-A), and model IV (G+2 Part-B). The pushover analysis has been carried out in the SeismoStruct software. Masonry walls have been modeled as double strut nonlinear cyclic model. The current seismic design provision includes the nonlinearity present in a structure through the response reduction factor ( $R$ ). The  $R$ -factor is the design tool that shows the level of inelasticity in the structures. The ductility reduction factor and over-strength factors were calculated from the pushover analysis, and ultimately the response reduction factor has been evaluated for each model and compared with the value given by the IS 1893 - Part 1 (2016) code of the Bureau of Indian Standards (BIS). The results demonstrate that when infill walls are considered in the RC buildings, the average  $R$  factor is higher than its value in bare frames. However, the average  $R$ -values of bare frames are lesser than the corresponding values recommended in the IS 1893 - Part 1 (2016). As well, the response reduction factor decreases as the height of the structure increases.

**Keywords:** Reinforced concrete building · Nonlinear static pushover analysis · Response reduction factor · Overstrength factor · Ductility · Infill walls

## 1 Introduction

In most of the constructions, presently, the structures are being built in RC frames with masonry infills. Masonry infills are one of the most affected components during earthquakes (Gautam et al. 2016; Gautam and Chaulagain 2016). These reinforced

concrete structures are more admired all over the world. The presence of the infill walls increases the lateral stiffness considerably. Due to the change in stiffness and mass of the structural system, the dynamic characteristics change as well. In several moderate earthquakes, RC buildings with infills have shown good seismic performance. In the recent era, the seismic load acts on the structure are mostly higher than the considered design load. Many of the seismic design codes give the guideline for nonlinearity in structure by using the response reduction factor. The R factor is also identified as a “response modification factor” or “behavior factor” in other country codes. In earthquake phenomena, the structures are generally designed by using the linear static method to resist the dynamic load; the response reduction factor plays an important role in reducing the elastic behavior to the inelastic behavior of the structure.

From the existing literature, the R-value increases when masonry infills are considered in the frames, so the R-value is sensitive to the material and geometrical configuration of the structures. The R-factor considerably decreases as the opening in masonry infills as well as the seismic zone increases. As well, the R-factor reduces as the height of the structure increases. The “Miranda and Bertero relationship” (Miranda and Bertero 1994) is the most realistic approach for the calculation of the R-factor as compared to other methods (Shendkar and Pradeep Kumar 2018a, b; Chaulagain et al. 2014; Maheri and Akbari 2003; Goud and Pradeep Kumar 2014; Motiani et al. 2018; Nishanth et al. 2017; Zahid et al. 2013; Shendkar et al. 2020a, b, c; Mandal and Shendkar 2020; Shendkar et al. 2021a, b, c). Alguhane et al. (2015) presented a study on the response modification factor of a 5-storey RC infilled building at Madinah city, and different models have been studied for the evaluation of the response modification factor. That study indicated that the R-factor increases due to the presence of infill, but the bare frame does not satisfy the requirement of the response modification factor as per the SBC 301 code. Maheri and Akbari (2003) evaluated the R-factor of RC buildings for steel X-braced and knee-braced systems, and the pushover analysis was carried out in Drain 2DX software. These authors analyzed three models, namely, four, eight, and twelve storeys buildings. Their results indicated that the evaluated response reduction factor is higher in the X-braced frame and knee braced frame as compared to the unbraced moment resisting frame. Uang (1991) worked on establishing the response reduction factor (R) and displacement amplification factors ( $C_d$ ) for building seismic provisions. In that study, the author derived the expression for response reduction factor and displacement amplification factor used in NEHRP provisions. Both these factors depend on the structural overstrength factor and ductility factor. As per that author’s study, it is very difficult to predict the values of R and  $C_d$  for most building systems. In the NEHRP provision, the  $R/C_d$  ratio is also recommended, and it is totally dependent on the structural ductility factor only. The results indicate that the R factor is the function of overstrength and ductility factors. The values of R and  $C_d$  recommended by NEHRP are not consistent with various structural systems. Mapari and Ghugal (2018) studied the seismic performance of multi-storied RC SMRF (Special moment-resisting frame) and OMRF (Ordinary moment-resisting frame) buildings. In that study, the response reduction factor was evaluated using the FEMA P695 methodology. The nonlinear static pushover analysis was carried out by using the SAP2000 software. The different 16 space frames were studied as SMRF, OMRF with 4, 6, 8 and 10 storeys are considered out of that some frames are infilled and remaining



are bare frames. These authors concluded that the evaluated R factors of infilled frames are higher than the value recommended by the IS 1893 (2002). The stiffness of the frame was enhanced by introducing the infill in the frame. The ductility of SMRF frames is higher than the OMRF frames. Elnashai and Mwafy (2002) worked on the overstrength and force reduction factor of multi-storied reinforced concrete buildings. In that study, twelve reinforced concrete buildings were assessed. These buildings were designed as per the guidelines of the EC8 code. Building height variation, different moment-resisting systems, vertical irregularity, etc., were considered for the detailed study. The “finite element method” based program ADAPTIC was used to carry out nonlinear static as well as dynamic analysis. From the detailed study, the authors concluded that the ultimate capacity of structure based on a triangular load pattern is on the conservative side. These authors proposed the direct relationship between the lateral capacity and the design seismic force. It is suggested to utilize an additional measure of response as termed the inherent overstrength factor. Smyrou et al. (2011) described the implementation of the four-node panel element for masonry infills in the SeismoStruct program. Shendkar et al. (2021a, b, c) developed the new material strain limit approach for the seismic assessment of reinforced concrete buildings. Also, Shendkar et al. (2021a, b, c) evaluated the seismic risk assessment of the Koyna-Warna region through the EDRI method.

The other country codes and guidelines give the values of the R factor for different structures. However, in IS 1893 (2016), the code does not give any particular clarification on different issues like structural and geometrical configuration, irregularities, etc. Thus, the primary focus of the present study is to investigate the seismic design parameters of different irregular reinforced concrete buildings.

## 2 Response Reduction Factor

The response reduction factor is one of the major parts of seismic design parameters, which is used to reduce elastic response spectra to inelastic response spectra. The response reduction factor is also named as response modification factor and behavior factor. The IS 1893 - Part 1 (2016) code of the Bureau of Indian Standards (BIS) gives the two R-values, i.e., 3 and 5, for ordinary moment resisting frame (OMRF) and special moment resisting frame (SMRF), respectively. From the review of existing literature, it can be seen that the response reduction factor depends upon three parameters: ductility, overstrength, and redundancy. Generally, the parameters related to the R factor can be mathematically expressed as:

$$R = R_d \times R_O \times R_R \quad (1)$$

where R is the Response reduction factor,  $R_d$  is the ductility reduction factor,  $R_O$  is the overstrength factor, and  $R_R$  is the redundancy.

But according to the Indian seismic code IS 1893 - Part 1 (2016), the response reduction factor can be presented as shown in Eq. 2 (Chaulagain et al. 2014; Shendkar et al. 2020a, b, c; Mandal and Shendkar 2020). Figure 1 also shows this relation (Chaulagain et al. 2014).

$$2R = R_d \times R_O \tag{2}$$

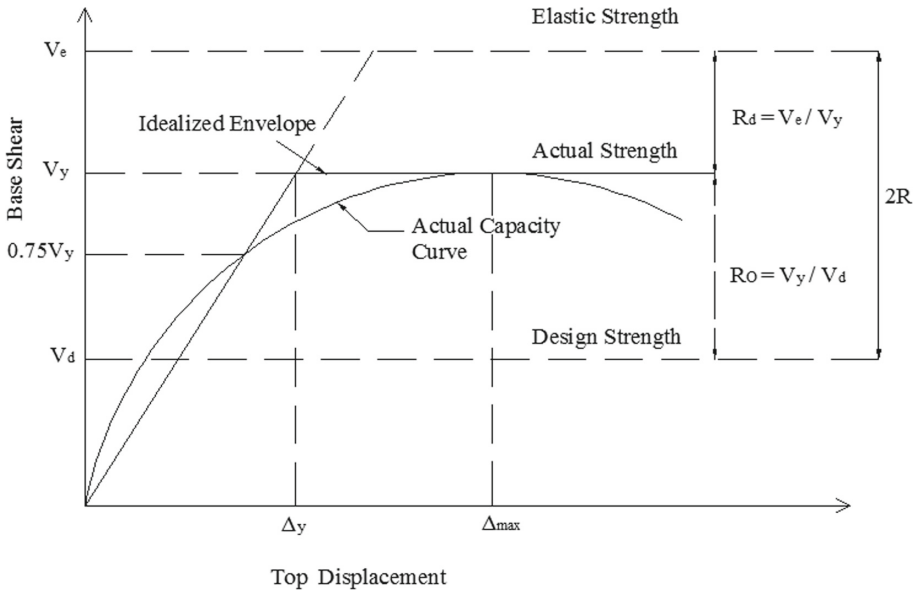


**Fig. 1.** Relation between response reduction factor, over-strength and ductility reduction factor.

According to the ATC-19 (1995), the response reduction factor ( $R$ ) is simply evaluated by the product of the ductility reduction factor, the over-strength factor and the redundancy (Eq. 1). Herein the ductility reduction factor was calculated based on the expressions of Newmark and Hall (1982), and the ductility has been calculated based on the reduced stiffness method (Park 1988), as shown in Fig. 2. The ductility is the ratio of maximum displacement to yield displacement. The maximum displacement is corresponding the peak base shear. In this study, the design base shear ( $V_d$ ) is obtained for each model as per the IS 1893 - Part 1 (2016) code. The overstrength factor  $R_O$  is the ratio of the ideal yield base shear ( $V_y$ ) to the design base shear ( $V_d$ ). In this study, the redundancy  $R_R$  is included in the overstrength factor  $R_O$ .

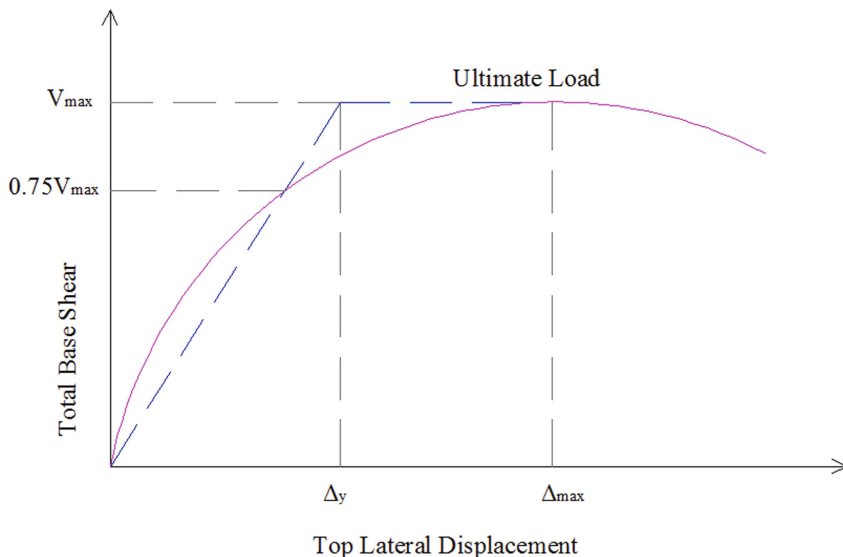


**Fig. 2.** Reduced stiffness method.

### Sample Calculation of the Overstrength Factor ( $R_O$ )

As per Fig. 1, the overstrength factor is the ratio of actual strength, i.e., the capacity of the pushover curve to the design strength.

$$R_O = V_y/V_d \quad (3)$$

For the G+2 Part-A building:

The design base shear is 978.77 kN calculated as per the IS 1893 - Part1 (2016) code.

The actual capacity of the bare frame in the long direction is 2350.29 kN.

The actual capacity of the bare frame in the short direction is 2737.45 kN.

The actual capacity of the RC infilled frame in the long direction is 6288.28 kN.

The actual capacity of the RC infilled frame in the short direction is 7731.24 kN.

Thus,

The overstrength factor ( $R_O$ ) for the bare frame in the long direction is 2.40.

The overstrength factor ( $R_O$ ) for the bare frame in the short direction is 2.79.

The overstrength factor ( $R_O$ ) for the RC infilled frame in the long direction is 6.42.

The overstrength factor ( $R_O$ ) for the RC infilled frame in the short direction is 7.89.

## 3 Model Description

For this study, eight-storey, five-storey and three-storey (Part-A and Part-B) reinforced concrete buildings are considered. These buildings are considered in seismic zone IV according to the Indian code IS 1893 - Part 1 (2016) and designed as per the current construction practices in India. The buildings are modeled using the SeismoStruct software. Figure 3 shows the plan of buildings, and all the dimensions are in m. All the plans are irregular in nature, and the structural details of the buildings are illustrated in Table 1. Figure 4 shows the model of the buildings.

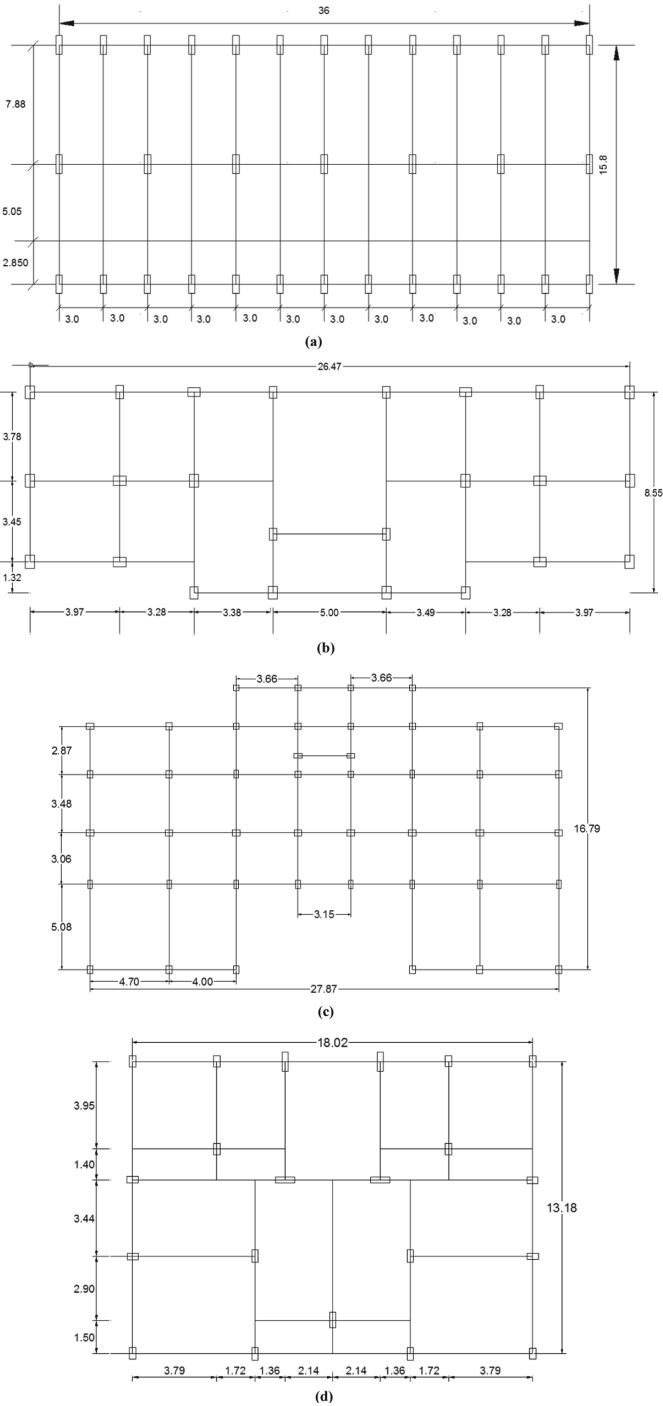


**Fig. 3.** Plan of the four buildings: (a) G+7 building, (b) G+2 Part-A building, (c) G+2 Part-B building, (d) G+4 building. (Dimensions in m).

**Table 1.** Structural details of buildings

Model system	G+7	G+2 Part-A	G+2 Part-B	G+4 (Open Ground Storey building)
Floor height	3 m	3.15 m	3.5 m	2.88 m
Dimensions of the building	Longer dimension is 36 m, Shorter dimension is 15.8 m	Longer dimension is 26.47 m, Shorter dimension is 8.55 m	Longer dimension is 27.87 m, Shorter dimension is 16.79 m	Longer dimension is 18.02 m, Shorter dimension is 13.18 m
Infill wall	External wall 230mm, and internal wall 150 mm	External wall 230mm, and internal wall 150 mm	External wall 230mm, and internal wall 150 mm	External wall 230mm, and internal wall 150 mm
Compressive strength of masonry ( $f_m$ )	6 MPa	6 MPa	6 MPa	6 MPa
Modulus of elasticity of infill	3300 MPa	3300 MPa	3300 MPa	3300 MPa
Type of soil	Medium soil	Medium soil	Medium soil	Medium soil
Size of column	450 mm × 1230 mm 430 mm × 1230 mm	530 × 370 mm, 550 × 400 mm, 560 × 350 mm, 610 × 400 mm, 570 × 330 mm, 530 × 450 mm, 500 × 350 mm	270 × 480 mm, 350 × 450 mm, 350 × 350 mm	290 × 500 mm, 270 × 700 mm, 270 × 870 mm, 270 × 570 mm
Size of beam	MB: 350 × 740mm, SB: 350 × 600 mm	250 × 300 mm	250 × 350 mm	270 × 450 mm
Depth of slab	150 mm	220 mm	200 mm	200 mm
Material	M 25 grade concrete, and Fe 415 reinforcement	M 25 grade concrete, and Fe 415 reinforcement	M 25 grade concrete, and Fe 415 reinforcement	M 25 grade concrete, and Fe 415 reinforcement
Damping	5%	5%	5%	5%
Importance factor	1.5	1	1	1
Response reduction factor	5	5	5	5

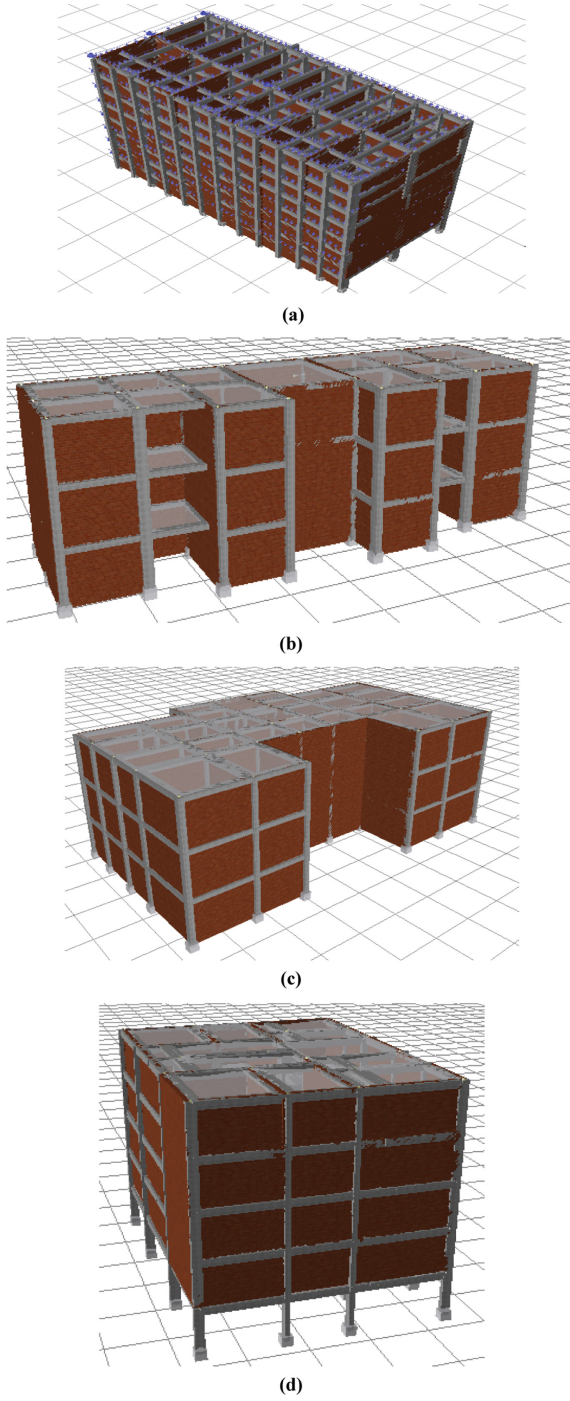


**Fig. 4.** Model of the four buildings: (a) Model of G+7 building, (b) Model of G+2 Part-A building, (c) Model of G+2 Part-B building, (d) Model of G+4 building.

### 3.1 Material Parameters

#### 3.1.1 Concrete Model

This model is a uniaxial nonlinear constant confinement model. The confinement effects provided by the lateral transverse reinforcement are incorporated as suggested by Mander et al. (1988a, b).

#### 3.1.2 Steel Model

This is a uniaxial steel model initially programmed by Yassin (1994) based on the stress-strain relationship proposed by Menegotto and Pinto (1973). Isotropic hardening is considered in this model.

#### 3.1.3 Inelastic Infill Panel Element (Infill)

The infill panel element is represented by four axial struts and two shear springs, as shown in Fig. 5 and this four-node panel masonry element was developed by Crisafulli (1997). It accounts the separate shear and compressive behavior of masonry and adequately represents the hysteretic response. This model is also known as “double strut nonlinear cyclic model”.

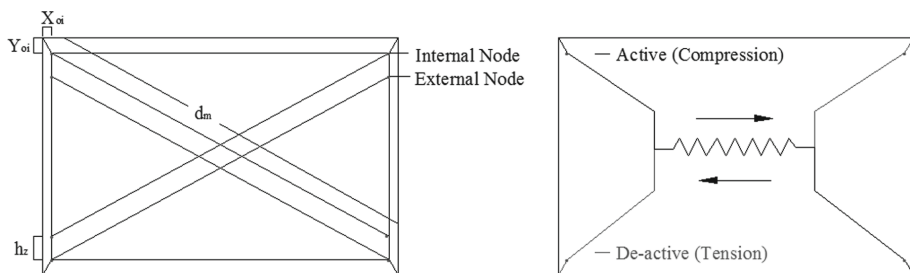


Fig. 5. Inelastic infill panel element.

Here,  $X_{oi}$  and  $Y_{oi}$  represent horizontal and vertical offsets, respectively,  $d_m$  is the diagonal strut length, and  $h_z$  is the equivalent contact length.

#### Sample Calculation of Equivalent Parameters of Infill Wall for the Eight Storey Building

For bay length = 3m, storey height = 3m and thickness of infill = 230 mm,

Infill panel net length =  $3 - 0.45 = 2.55$ m, Infill panel net height =  $3 - 0.74 = 2.26$  m.

Diagonal length ( $d_{inf}$ ) = 3.42 m.

Calculation of Equivalent width of strut:

$$\lambda_h = h^4 \sqrt{\frac{E_{inf} t \sin 2\theta}{4E_c I_c h_{inf}}} = 1.80 \quad (\text{Dimensionless parameter}) \quad (4)$$

$$Z = \frac{\pi}{2\lambda_h} \times h \quad (5)$$



$$h_z = \frac{Z}{3h_{inf}} \times 100 = 29.08\% \quad (6)$$

$$\text{Width of strut} = 0.175 d_{inf} (\lambda_h)^{-0.4} = 473.10 \text{ mm} \quad (7)$$

Area of strut for infill =  $b_w \times t = 108813.55 \text{ mm}^2$

Horizontal offset ( $X_{oi}$ ) =  $\frac{0.215}{3} \times 100 = 7.16\%$

Vertical offset ( $Y_{oi}$ ) =  $\frac{0.37}{3} \times 100 = 12.33\%$

Similarly, the parameters of the infill walls were calculated for the other models. Using those respective parameters, the 3-D analysis has been carried out for four different cases, viz., model I (G+7), model II (G+4 Open ground storey), model III (G+2 Part-A), and model IV (G+2 Part-B). The column-beam dimensions and detailing are described in Table 2 and Table 3, respectively.

**Table 2.** Column dimensions and detailing

Model of building	Size (mm)	Main reinforcement	Shear reinforcement
G+7	All columns	4 of $\emptyset$ 25 mm at corners and 8 of $\emptyset$ 25 mm parallel to the weak axis of the column	$\emptyset$ 8 mm @ 250 mm c/c
G+2 Part-A	All columns	4 of $\emptyset$ 20 mm at corners and 2 of $\emptyset$ 20 mm parallel to the weak axis of the column	$\emptyset$ 8 mm @ 300 mm c/c
G+2 Part-B	All columns	4 of $\emptyset$ 20 mm at corners	$\emptyset$ 8 mm @ 300 mm c/c
G+4	All columns	4 of $\emptyset$ 20 mm at corners	$\emptyset$ 8 mm @ 250 mm c/c

**Table 3.** Beam dimensions and detailing

Model of building	Size (mm)	Main reinforcement	Shear reinforcement
G+7	350 × 740 350 × 600	3 of $\emptyset$ 20 mm at top and bottom	$\emptyset$ 8 mm @ 250 mm c/c
G+2 Part-A	250 × 300	2 of $\emptyset$ 20 mm at top and bottom	$\emptyset$ 8 mm @ 300 mm c/c
G+2 Part-B	250 × 350	2 of $\emptyset$ 20 mm at top and bottom	$\emptyset$ 8 mm @ 300 mm c/c
G+4	270 × 450	2 of $\emptyset$ 20 mm at top and bottom	$\emptyset$ 8 mm @ 250 mm c/c

## 4 Results and Discussion

### 4.1 Pushover Curves

Pushover is a nonlinear static analysis where a structure is subjected to gravity load and a monotonic lateral load. In this study, four-node panel element infill model is used for numerical simulation of frames. The various parameters namely, strength, ductility, R-factor, etc. are computed from the pushover curves. Using these pushover curves, one can get the capacity of the whole structure. From Fig. 6, it is concluded that the RC infilled frames have maximum capacity base shear as compared to the bare frames due to incorporation of masonry infills which play an important role in the seismically active zones.

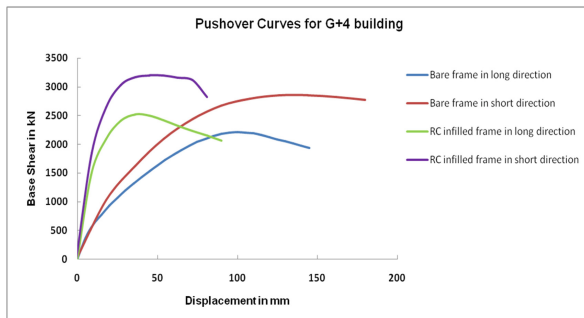
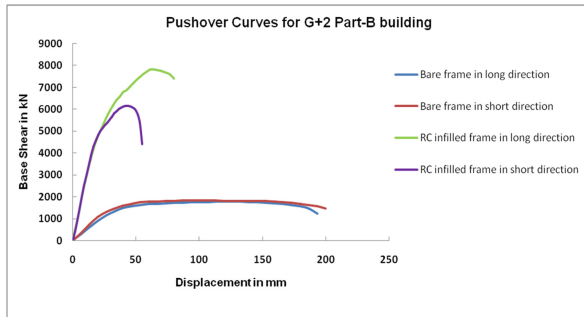
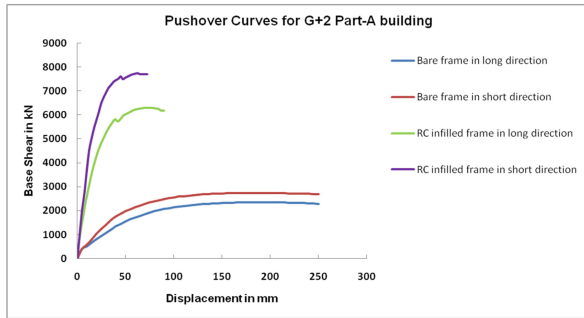
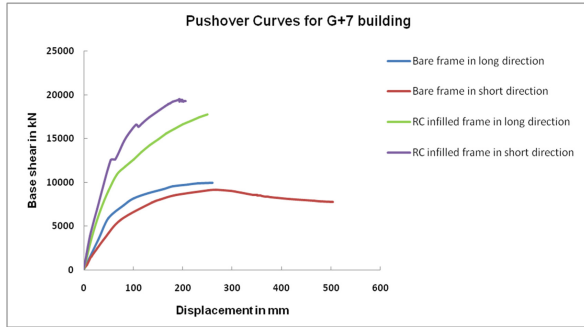


**Fig. 6.** Comparison of Pushover Curves for: (a) G+7 building, (b) G+2 Part-A building, (c) G+2 Part-B building, (d) G+4 building.

### 4.2 Base Shear

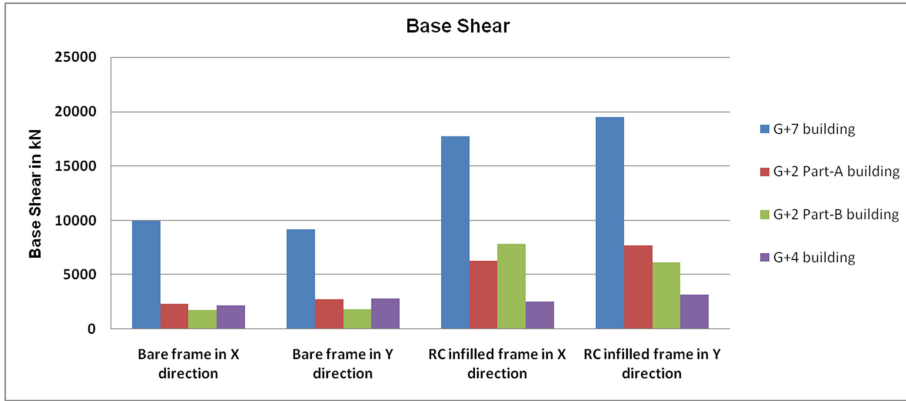


Fig. 7. Comparison of base shear.

As per Fig. 7, the base shear is lowest in the bare frame as compared to RC infilled frames. Base shear increases significantly in RC infilled frames when infills are incorporated in the bare frames. In the case of G+4 open ground storey building, nearly 26.80% base shear increases for RC infilled frame in the short Y direction as compared to RC infilled frame in the long X direction and averagely (average value in long X and short Y direction) 12.79% base shear increases in RC infilled frame as compared to the bare frame which is comparatively less as compared to other buildings because of soft storey building. In the case of G+7, G+2 Part-A, and G+2 Part-B building, base shear increases averagely (average value in long X and short Y direction) by 94.67%, 175.55% and 287.82% respectively in RC infilled frame as compared to the bare frame.

### 4.3 Ductility

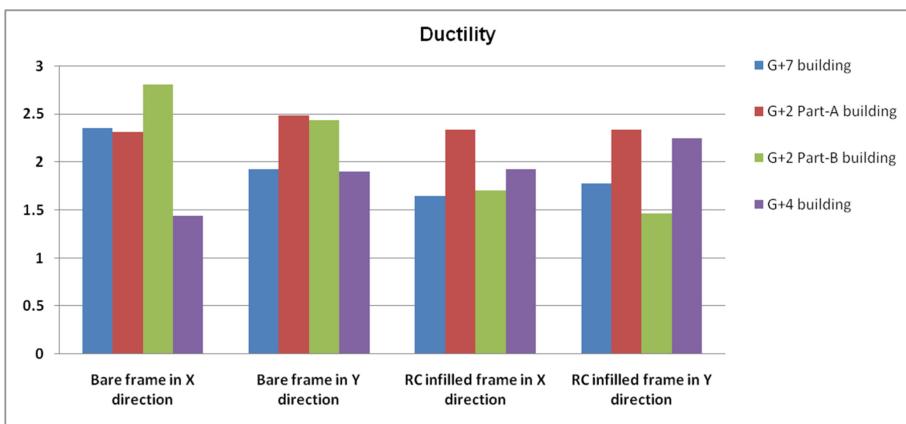


Fig. 8. Comparison of ductility.

As per Fig. 8, the ductility obtained is higher in bare frames as compared to RC infilled frames. In the case of G+7, G+2 Part-A and G+2 Part-B, the ductility increases averagely (average value in long X and short Y direction) by 25.14%, 2.56% and 64.77% respectively in the bare frame as compared to RC infilled frame. In the case of G+4 building the ductility increases averagely by 25.14% in RC infilled frame as compared to bare frame due to soft storey effect.

#### 4.4 Ductility Reduction Factor

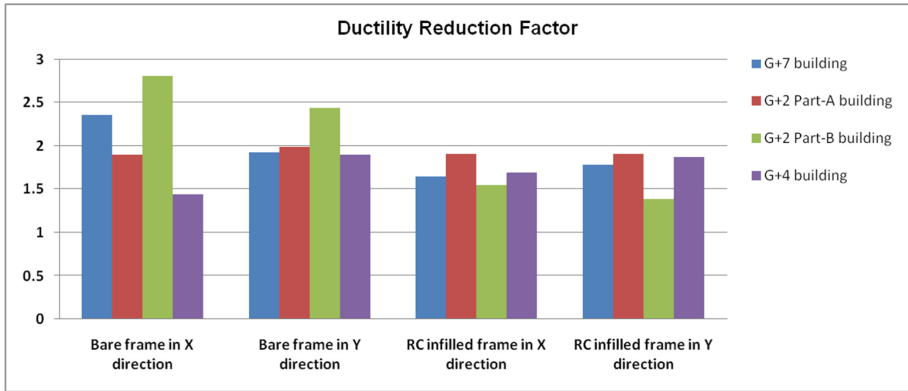


Fig. 9. Comparison of ductility reduction factor.

The ductility reduction factor is evaluated based on the “Newmark and Hall” theory. As per Fig. 9, in the case of G+7, G+2 Part-A and G+2 Part-B, the ductility reduction factor increases averagely (average value in long X and short Y direction) by 25.14%, 1.83% and 78.23%, respectively in the bare frame as compared to RC infilled frame. As per Fig. 9, in the case of the G+4 building, the ductility reduction factor increases averagely by 6.58% in RC infilled frame as compared to bare frame due to the soft storey effect.

### 4.5 Overstrength Factor

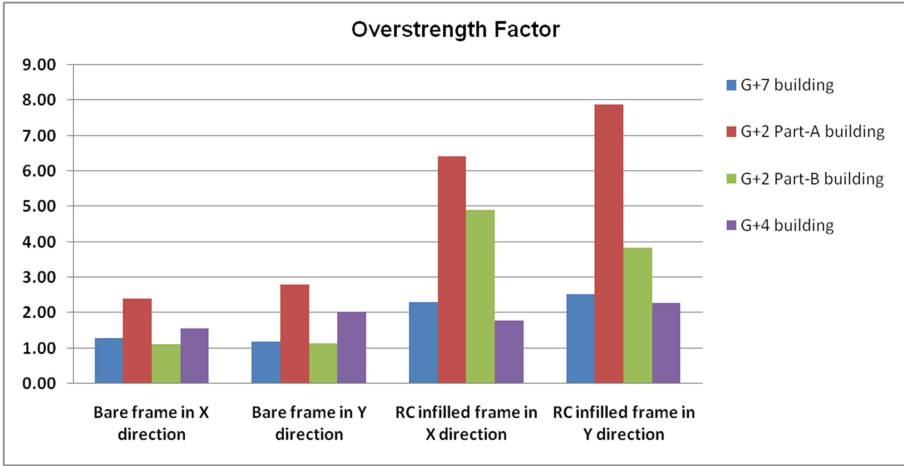


Fig. 10. Comparison of overstrength factor.

As per Fig. 10, the overstrength factor is higher in RC infilled frames as compared to bare frames. In the case of G+7, G+2 Part-A, G+2 Part-B and G+4 building, the overstrength factor increases averagely (average value in long X and short Y direction) by 94.35%, 175.72%, 289.33% and 12.77% respectively in RC infilled frame as compared to bare frame due to presence of masonry infills.

### 4.6 Response Reduction Factor

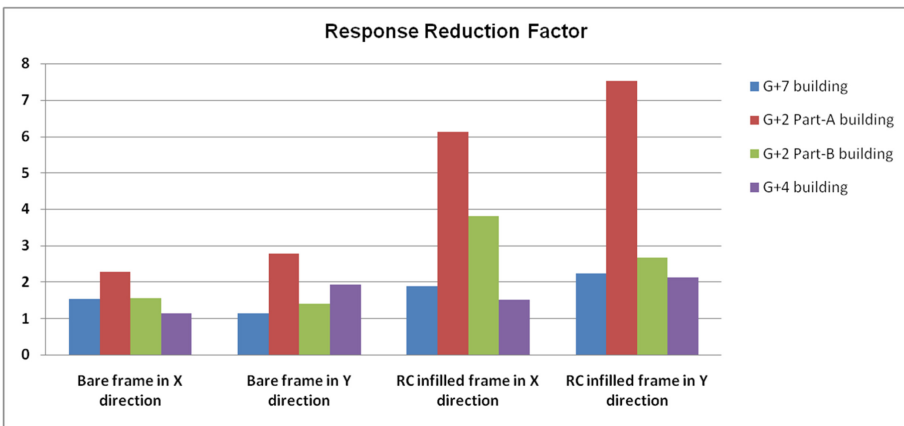


Fig. 11. Comparison of response reduction factor.

The response reduction factor is evaluated based on Eq. 2. As per Fig. 11, the Response reduction factors are higher in RC infilled frames as compared to bare frames. In the case of G+7, G+2 Part-A, G+2 Part-B and G+4 building, the R-factor increases averagely (average value in long X and short Y direction) by 55.26%, 170.49%, 120.06% and 19.01% respectively in RC infilled frame as compared to the bare frame.

According to existing research, the R-factor is higher by 54.83% in RC infilled frames as compared to bare frames (Shendkar and Pradeep Kumar 2018a, b). Notably, the results obtained by Alguhane et al. (2015) indicate that the R-factor of the bare frame is lesser than the specified Saudi code value by 18.4% (R-factor is 2.5 in the Saudi Building Code SBC 301). However, the R-factor increased by 82% with including infills in the frame system.

#### 4.7 Suggested Modifications in the IS 1893 - Part 1 (2016)

We would like to suggest the following regarding R-factor in the IS 1893 (2016) code of the Bureau of Indian Standards (BIS).

1. The response reduction factor is a sensitive seismic design parameter that shows the level of inelasticity in structure. Currently, there are two values of R given in IS 1893 (2016) regarding moment frame systems, i.e.,  $R = 3$  for OMRF and  $R = 5$  for SMRF case. In the present study, we have taken all models under SMRF case with different plan and height. As per the results of this study, the R value depends on the material, geometrical and structural configuration of structure, so we cannot give single value of R for all structures.
2. As per our opinion, the R-value changes as per the height of the building, plan configuration, etc., so the average R-value should be given separately for low-rise, mid-rise, and high-rise structures with the contribution of infill walls.
3. Along with the R factor, the overstrength factor should be given separately in the code for respective frames.

#### 4.8 Damage Index

The damage analysis is a very important parameter for the application in the seismic assessment and rehabilitation of existing buildings. The damage state of a building is identified by using qualitative indicators such as none, minor, repairable, severe, and failure. The damage index (DI) of the whole frame can be calculated as follows:

$$DI = 1 - (K_{final}/K_{initial})$$

where  $K_{initial}$  is the initial slope of the pushover curve and  $K_{final}$  is the effective slope of the pushover curve where the building is subjected to after the earthquake. The relationship between the damage states and damage index is shown in Table 4 (Ghobarah et al. 1999).

**Table 4.** Damage index for different damage states

Damage state	Damage index
Minor	0.0–0.15
Moderate	0.15–0.3
Severe	0.3–0.8
Collapse	> 0.8

As per Table 4, the damage states of the buildings are shown in Table 5.

**Table 5.** Evaluated damage index of different buildings

Damage state	Damage index	Condition
G+7	0.713	Severe
G+2 Part-A	0.135	Minor
G+2 Part-B	0.168	Moderate
G+4	0.165	Moderate

Table 5 shows the damage index of the different buildings. In the present study, G+7 building is in severe condition, G+2 Part-A is in minor condition, G+2 Part-B and G+4 buildings are in moderate condition as per the response-based damage assessment study of structures.

## 5 Conclusions

After the interpretation of analytical results and comparison of values, the conclusions drawn from this study are as summarized below:

The base shear values are larger in RC infilled frames as compared to bare frames. Ductility and ductility reduction factor are higher in bare frames compared to RC infilled frames because there is no infill in the frame. And in the case of the G+4 building, the ductility and ductility reduction factor are higher in RC infilled frame as compared to bare frame due to the soft storey effect. The over-strength factor and the response reduction factor are significantly influenced by the incorporation of infills in the RC frame. The response reduction factor  $R$  of the RC infilled frame is higher than the bare frame in all presented cases.

The computed  $R$  values for bare frames obtained by nonlinear static pushover analysis of all buildings are less than the value suggested in the IS 1893 - Part 1 (2016) code. The evaluated average  $R$  values are less than the values recommended by the IS 1893 - Part 1 (2016) code after the incorporation of infills in the frames due to the presence of different irregularities and the unsymmetrical plans in the G+4 open ground storey building, G+7 building and G+2 Part-B building. As per this study, the average value of  $R$  decreases as the height of the building increases due to a decrease in the stiffness of the building. The G+2 (Part-A) and G+2 (Part-B) buildings are having 3



storeys with different plan configurations. The average value of  $R$  is more in the G+2 (Part-A) as compared to the G+2 (Part-B) building due to less irregularity present in the structure. According to the present study, the response reduction factor ( $R$ ) is a sensitive seismic design parameter that depends on the material, structural and geometrical configuration, and the irregularity in the structure.

## References

- Alguhane, T.M., Khalil, A.H., Fayed, M.N., Ismail, A.M.: Seismic assessment of old existing RC Buildings with masonry infill in Madinah as per ASCE. *Int. J. Comput. Syst. Eng.* **9**(1), 52–63 (2015). <https://doi.org/10.5281/zenodo.1099078>
- ATC-19: Structural response modification factors, ATC-19 Report; Applied Technology Council (ATC): Redwood City, California, USA (1995)
- Chaulagain, H., Rodrigues, H., Spacone, E., Guragain, R., Mallik, R., Varum, H.: Response reduction factor of irregular RC buildings in Kathmandu valley. *Earthq. Eng. Eng. Vib.* **13**(3), 455–470 (2014). <https://doi.org/10.1007/s11803-014-0255-8>
- Crisafulli, F.J.: Seismic behaviour of reinforced concrete structures with masonry infills. Ph.D. thesis, University of Canterbury, New Zealand (1997). <https://doi.org/10.26021/1979>
- Elnashai, A.S., Mwafy, A.M.: Overstrength and force reduction factors of multistorey reinforced-concrete buildings. *Struct. Des. Tall Build.* **11**(5), 329–351 (2002). <https://doi.org/10.1002/tal.204>
- Gautam, D., Rodrigues, H., Bhetwal, K.K., Neupane, P., Sanada, Y.: Common structural and construction deficiencies of Nepalese buildings. *Innov. Infrastruct. Solut.* **1**(1), 1–18 (2016). <https://doi.org/10.1007/s41062-016-0001-3>
- Gautam, D., Chaulagain, H.: Structural performance and associated lessons to be learned from world earthquakes in Nepal after 25 April 2015 (MW 7.8) Gorkha earthquake. *Eng. Fail. Anal.* **68**, 222–243 (2016). <https://doi.org/10.1016/j.engfailanal.2016.06.002>
- Goud, S.S., Pradeep Kumar, R.: Rationalizing response reduction factor  $R$  for better Performance of reinforced concrete framed buildings. In: *Proceedings of the National Conference on Recent Research Advances in Civil Engineering (RRACE-2014)*, Tamilnadu, India (2014)
- Ghobarah, A., Abou-Elfath, H., Biddah, A.: Response-based damage assessment of structures. *Earthq. Eng. Struct. Dyn.* **28**, 79–104 (1999). [https://doi.org/10.1002/\(SICI\)1096-9845\(199901\)28:1%3C79::AID-EQE805%3E3.0.CO;2-J](https://doi.org/10.1002/(SICI)1096-9845(199901)28:1%3C79::AID-EQE805%3E3.0.CO;2-J)
- IS 1893: Criteria for earthquake resistant design of structures - Part 1 general provisions and buildings, Sixth Revision; Bureau of Indian Standards (BIS): New Delhi, India (2016)
- IS 1893: Criteria for earthquake resistant design of structures - Part 1 general provisions and buildings, Fifth Revision; Bureau of Indian Standards (BIS): New Delhi, India (2002)
- Miranda, E., Bertero, V.: Evaluation of strength reduction factors for earthquake-resistant design. *Earthq. Spectra* **10**(2), 357–379 (1994). <https://doi.org/10.1193/1.1585778>
- Maheri, M.R., Akbari, R.: Seismic behaviour factor,  $R$ , for steel X-braced and knee-braced RC buildings. *Eng. Struct.* **25**(12), 1505–1513 (2003). [https://doi.org/10.1016/S0141-0296\(03\)00117-2](https://doi.org/10.1016/S0141-0296(03)00117-2)
- Mander, J.B., Priestley, M.J.N., Park, R.: Theoretical stress-strain model for confined concrete. *J. Struct. Eng. (ASCE)* **114**(8), 1804–1826 (1988). [https://doi.org/10.1061/\(ASCE\)0733-9445\(1988\)114:8\(1804\)](https://doi.org/10.1061/(ASCE)0733-9445(1988)114:8(1804))
- Mander, J.B., Priestley, M.J.N., Park, R.: Observed stress-strain behavior of confined concrete. *J. Struct. Eng. (ASCE)* **114**(8), 1827–1849 (1988). [https://doi.org/10.1061/\(ASCE\)0733-9445\(1988\)114:8\(1827\)](https://doi.org/10.1061/(ASCE)0733-9445(1988)114:8(1827))

- Mandal, S., Shendkar, M.R.: Evaluation of response reduction factor of RC-infilled frames. In: Proceedings of the 17th World Conference on Earthquake Engineering (17WCEE), Sendai, Japan, 13–18 September 2020, pp. 1–12 (2020)
- Mapari, A.K., Ghugal, Y.M.: Seismic performance of multi-storey RC SMRF and OMRF buildings. *J. Struct. Eng.* **44**(6), 663–672 (2018)
- Menegotto, M., Pinto, P.E.: Method of analysis for cyclically loaded R.C. plane frames including changes in geometry and non-elastic behavior of elements under combined normal force and bending. In: Proceedings of the ISBE Symposium on the Resistance and Ultimate Deformability of Structures Acted on by Well Defined Repeated Loads, International Association for Bridge and Structural Engineering (IABSE), Lisbon, Portugal, pp. 15–22 (1973)
- Motiani, R., Kunal, J.R., Gahrana, S., Nambiar, A., Desai, M.: Evaluation of response reduction factor by pushover analysis. *Int. J. Struct. Eng.* **9**(2), 116–129 (2018). <https://doi.org/10.1504/IJSTRUCTE.2018.092999>
- Newmark, N.M., Hall, W.J.: *Earthquake Spectra and Design*. Earthquake Engineering Research Institute: Berkeley, California (1982)
- Nishanth, M., Visuvasam, J., Simon, J., Packiaraj, J.S.: Assessment of seismic response reduction factor for moment-resisting RC frames. *IOP Conf. Ser. Mater. Sci. Eng.* **263**(3), 1–11 (2017). <https://doi.org/10.1088/1757-899X/263/3/032034>
- Park, R.: Ductility evaluation from laboratory and analytical testing. In: Proceedings of the 9th World Conference on Earthquake Engineering, University of Tokyo, Japan, vol. 8, pp. 605–616 (1988)
- SeismoStruct: SeismoStruct - A computer program for static and dynamic nonlinear analysis of framed structures, Seismosoft Ltd., Pavia, Italy (2020). <https://seismosoft.com/>. Accessed 10 Oct 2020
- Shendkar, M., Pradeep Kumar, R.: Response reduction factor of RC framed structures with semi-interlocked masonry and unreinforced masonry infill. *Indian Concr. Inst. (ICI) J.* **2018**, 24–28 (2018a)
- Shendkar, M., Mandal, S., Pradeep Kumar, R., Maiti, P.R.: Response reduction factor of RC-infilled frames by using different methods. *Indian Concr. Inst. (ICI) J.* **2020**, 14–23 (2020a)
- Shendkar, M.R., Mandal, S., Pradeep Kumar, R.: Effect of lintel beam on response reduction factor of RC-infilled frames. *Curr. Sci.* **118**(7), 1077–1086 (2020b). <https://doi.org/10.18520/cs/v118/i7/1077-1086>
- Shendkar, M.R., Pradeep Kumar, R., Maiti, P.R.: Effect of aspect ratio on response reduction factor of RC framed structures with semi-interlocked masonry and unreinforced masonry infill. *Indian Concr. J.* **94**(12), 7–16 (2020c)
- Shendkar, M.R., Kontoni, D.-P.N., Mandal, S., Maiti, P.R., Gautam, D.: Effect of lintel beam on seismic response of reinforced concrete buildings with semi-Interlocked and unreinforced Brick Masonry Infills. *Infrastructures* **6**(1), 1–18 (2021a). Article 6. <https://doi.org/10.3390/infrastructures6010006>
- Shendkar, M., Pradeep Kumar, R.: Influence of opening in infill on R factor of RC infilled frame structures. *Indian Concr. Inst. (ICI) J.* **2018**, 1–6 (2018b)
- Shendkar, M.R., Kontoni, D.-P.N., Mandal, S., Maiti, P.R., Tavasoli, O.: Seismic evaluation and retrofit of reinforced concrete buildings with masonry infills based on material strain limit approach. *Shock Vib.* **2021**, 1–15 (2021b). <https://doi.org/10.1155/2021/5536409>
- Shendkar, M.R., Pradeep Kumar, R., Mandal, S., Maiti, P.R., Kontoni, D.-P.N.: Seismic risk assessment of reinforced concrete buildings in Koyna-Warna region through EDRI method. *Innov. Infrastruct. Solut.* **6**(3), 1–25 (2021). <https://doi.org/10.1007/s41062-021-00505-0>

- Smyrou, E., Blandon, C., Antoniou, S., Pinho, R., Crisafulli, F.: Implementation and verification of a masonry panel model for nonlinear dynamic analysis of in-filled RC frames. *Bull. Earthq. Eng.* **9**, 1519–1534 (2011). <https://doi.org/10.1007/s10518-011-9262-6>
- Uang, C.M.: Establishing R and Cd factors for building seismic provisions. *J. Struct. Eng. ASCE* **117**(1), 19–28 (1991). [https://doi.org/10.1061/\(ASCE\)0733-9445\(1991\)117:1\(19\)](https://doi.org/10.1061/(ASCE)0733-9445(1991)117:1(19))
- Yassin, M.H.M.: Nonlinear analysis of prestressed concrete structures under monotonic and cyclic loads. Ph.D. thesis, University of California, Berkeley, USA (1994)
- Zahid, M., Robert, D., Shahrin, F.: An evaluation of overstrength factor of seismic designed low rise RC buildings. *Procedia Eng.* **53**, 48–51 (2013). <https://doi.org/10.1016/j.proeng.2013.02.008>



# Railway Bridge Model Calibration Using the Search Group Algorithm

Thiago Fernandes<sup>(✉)</sup>

Federal University of Santa Catarina, Florianópolis, Brazil  
tfernandes@alunos.utfpr.edu.br

**Abstract.** In structural engineering, there are many cases where design data is insufficient or even nonexistent. Thus, there is a demand to assess the structural integrity of these constructions, usually depending on experimental field data. Given the limited design information, inverse approach can be an efficient tool in estimating the parameters of interest via structural optimization. In this work, it is proposed to estimate unknown design variables by means of the calibration of numerical models using experimental modal data. A real railway bridge structure is studied. Three numerical models of the railway bridge are studied in order to estimate four parameters of interest: stiffness of the supports, modulus of elasticity of concrete, modulus of elasticity of ballast and ballast density. For the efficiency of the calibration of numerical models via optimization, the robustness of the algorithm is essential. For this purpose, Search Group Algorithm (SGA) is employed to update the unknown model parameters. Finally, it is presented that in the creation of numerical models to assess real structures, one must be very sparing in order not to make a problem overly complex and, as result of, high computational cost. Further, simpler numerical models may be effective, both in relation to their computational, as well as obtaining accurate responses with error quantification in relation to the real problem.

**Keywords:** Finite element model updating · Structural optimization · Search Group Algorithm · Railway bridges

## 1 Introduction

Structural safety has gained attention in the field of engineering, peculiarly for structures such as bridges and viaducts, so that development of computers and mathematical tools was fundamental to overcome several imbroglios in structural analysis.

In the approach of structures with complex behavior, the use of numerical models based on Finite Element (FE) methods allows to simulate a real structure and evaluate its effects. The process of development a FE model can involve many simplifications related to geometry, discretization, boundary conditions and mechanical properties of the material that may cause errors (Ribeiro et al. 2012).

In these cases, the use of experimental data such as dynamic measurements are important to validate the numerical model as reported by Ren et al. (2004). Thus, the process of calibrating numerical models via optimization aims to match the numerical and experimental responses and to estimate the parameters of interest. The updated

numerical model can be used with confidence in structural analysis, to predict of dynamic responses under new operating speed or under new load scenarios, or for damage identification, proceeding from Structural Health Monitoring (SHM). The application of the SHM in railway bridges can be found in Kolakowski et al. (2011), Vagnoli et al. (2018) and Meixedo et al. (2021).

In the context of methods for model updating, the solution can be done by probabilistic inferences. In this case, the algorithm course the search space of the parameters of interest, that is, the bounds of design variables known a priori and, evaluates the discrepancy between the numerical and the experimental responses through the penalty function, called objective function or cost function. This process is iterative and it is repeated in order to reduce the difference between the answers to search the global optimal solution of the problem. The global optimum characterizes the solution of the problem and the identification of the parameters of interest. Several methods are presented in the literature to solve optimization problems. These includes gradient-based methods (Belegundu and Arora 1985); surface response methods (Roux et al. 1998); heuristic methods (Zanakis and Evans 1981), generally based on inspirations from nature; or in the combination of the methods mentioned (Lagaros et al. 2002).

Ribeiro et al. (2012) updated a numerical model of a railway bridge based on vibrational responses through the genetic algorithm (GA). The authors explain that GA has some advantages such as the ability to handle with a large number of parameters of interest and constrains, not dependent on a starting point for design variables, capability to deal with discrete variables and the ability to find the global optimum of the function. However, a low convergence rate compared to methods based on gradient is reported to be its main drawback. Furthermore, in the literature there are several hybrid methods that combine different optimization algorithms in order to improve the search for optimal solution. Papadrakakis et al. (2001) proposed the combination of gradient-based methods with evolutionary algorithms to solve optimization problems for structures under static and seismic loading. Kaveh and Talatahar (2008) implemented an algorithm based on the combination of the particle swarm with the ant colony algorithm for the optimization of trusses. In the context of hybrid methods for structural optimization of bridges, Jung and Kim (2013) applied a hybrid algorithm with the combination of the GA and the modified Nelder-Mead algorithm for updating a numerical model of a simply supported bridge. The objective function of the problem included displacement and modal responses. Deng and Cai (2009) proposed a combination genetic algorithm and the surface response technique to handle with FE model updating using static and modal responses. A hypothetic example of simply supported beam was performed and this method was also applied to a numerical model of a real bridge.

The Search Group Algorithm is a metaheuristic optimization algorithm, i.e. must have to able to find a reasonable solution related exploration and exploitation. Exploration, or global phase, is the capability of the algorithm to search promising regions in all design domain. Exploitation, also referred to as local phase, is the ability of the algorithm to refine the search only in these promising regions, as reported by Gonçalves et al. (2015). In this context, SGA have recognized advantages such as the high convergence rate compared to methods based on gradient and nature inspired algorithm, not dependent on a starting point for design variables, ability to manage a

huge number of design variables and constraints, which includes the possibility to handle with discrete and continuous variables, and capability to find the global minimum in functions that have several local minimum (Gonçalves et al. 2015). On the other hand, the input parameters of the SGA may vary depending on the characteristics of the problems to be solved which can make it exhausting and to be its main drawback.

This paper reports the numerical model calibration of a filler-beam railway bridge based on experimental vibrational responses. Three numerical models developed by Silva (2010) is detailed in order to estimate four parameters of interest: stiffness of the supports, modulus of elasticity of concrete, modulus of elasticity of ballast and ballast density. The calibration of the numerical models involves an optimization process using the SGA algorithm. This iterative process evaluates the objective function in order to reduce the difference between the numerical and experimental natural frequency responses of the bridge under study.

As far as the authors' knows, this is the first work aiming at numerical model calibration of railway bridge using the Search Group Algorithm. This may be related to the method being recent in the literature.

## 2 Structural Optimization

The optimization methods are, in general, numerical techniques for identifying parameters of interest. These techniques start from a starting point of the project and are carried out in small steps in order to improve the value of the objective function. The search is completed when a certain number of iterations is reached, when there is no progress in improving the objective function without the violation some of the constraints, or in some methods, when the convergence of the problem becomes very slow (Haftka and Gürdal 1992). Briefly, the general formulation of an optimization problem is given by:

$$\begin{aligned} & \text{minimize} && f(x) \\ & \text{subject to} && g_j(x) \geq 0, \quad j = 1, \dots, n_g \end{aligned} \quad (1)$$

where  $x$  is a vector of design variables with components  $x_i, i = 1, \dots, n$ ;  $f(x)$  denotes the objective function,  $g_j(x)$  are the inequality constraints and  $h_k(x)$  are the equality constrains.

### 2.1 Optimization Algorithms

The correct choice of the optimization algorithm is crucial for the identification of the variables of a given problem. In the literature, there is a diversity of algorithms to solve structural optimization problems. To name just a few, response surface techniques, methods based on gradient approximations (sequential programming, Quasi-Newton, augmented Lagrangian, etc.); heuristic and metaheuristic methods, generally inspired

by observations of nature (genetic algorithm, ant colony algorithm, particle swarm, etc.); in hybrid methods, based on the combination of optimization algorithms (Ribeiro et al. 2012).

Gradient-based algorithms depend on first and/or second order derivative calculations. These methods are usually built to converge to local minimum and guarantee the optimal global solution as long as it is proved that the objective function and constraints are convex in their design domains. If the convexity of an optimization problem is proven, it is guaranteed that there is only one minimum and that this is the global minimum (Carlson 2015). However, the gradient-based algorithms have some disadvantages such as the difficulty in identifying optimal global solutions, as they are very dependent on the starting point, and the difficulty of operating with non-differentiable functions.

Ren and Chen (2010) evaluated the application of the surface response method in the update of the bridge numerical model and describes that this is a mathematical tool to achieve the optimal solution of objective functions and constraints based on functional evaluations at the points in the design domain. Furthermore, the author reported that this technique may involve some strategies such as experimental procedures, statistical and probabilistic inferences that allow the analyst to make an efficient empirical exploration of the structure under study.

Regarding heuristic optimization methods, the algorithms have the characteristic of not depending on the gradient information of the objective function neither the gradient of the constraints. This occurs because heuristics use only the value of the objective function at certain points, which makes it possible to treat problems with discrete domains. However, for continuous domains, in general heuristics present a significantly slower convergence than gradient-based methods, as reported by Carlson (2015). A problem of worse convergence is translated into a higher computational cost in search for the optimal solution.

## 2.2 Search Group Algorithm

The heuristic method used in this work for the calibration of models is the Search Group Algorithm (SGA), and defines how the particles move in the domain due to a provoked disturbance. In this format, to generate the new position of each individual, it is added the current position to a defined constant disturbance and a random variable. Initially, for a high value it disturbs to be reduced until the local phase.

The first step of the method is to generate a random population  $\mathbf{P}$ , as shown in Fig. 1a, where each dot characterizes an individual of the initial population at the two-dimensional design domain. After to generate a population, each individual is evaluated by the objective function, as shown in Fig. 1b, which the biggest points represent the best objective functions. In sequence, there is a greater chance of selecting individuals with the best objective function. As illustrate in Fig. 2, the search group  $\mathbf{R}$  is created by selecting  $n_g$  individuals for  $\mathbf{P}$ , which, being disturbed, generates a number of new points through the disturbance  $\alpha$ , which in turn is controlled during the iterations. In order to increase the ability of the algorithm to explore the design domain, a given

number of individuals of the search group  $\mathbf{R}$  is mutated at each iteration. The basic idea of the mutation is exploring new regions of the search design domain. Figure 2(b) shows the search group of Fig. 2(a) after mutation, which a mutated individual represented by the green circle replaced a member of the search group. The better the value of the objective function, the more points are created, and this process is repeated, characterizing the exploration or global search, which is also controlled by parameter  $\alpha$ . Figure 3a and b illustrates of one of the first iterations of the algorithm. With each iteration, the value of  $\alpha$  decreases, and in this way, the individuals generated by a given search group member tends to remain in its neighborhood so that in the local phase it becomes more refined, as it is shown in Fig. 4a and b. The Fig. 4b illustrates the families generated by each one of the five search group members of Fig. 4a.

As mentioned above, the algorithm is composed by the global and local phases. In the first  $i_{global}^{max}$  iterations, named the global phase or exploration, the algorithm aims to explore the most of the design domain. When the number of the iteration is higher than  $i_{global}^{max}$ , the algorithm goes to the local phase and tend to exploit the promising regions. This step is performed by the best  $n_g$  individuals among all the families that form a new search group. More details about the SGA may be found in Gonçalves et al. (2015).

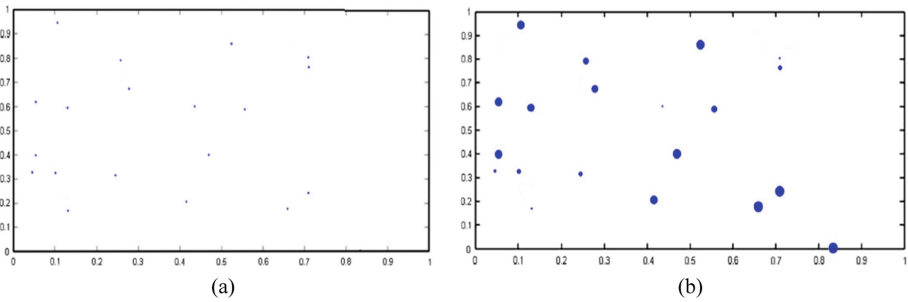


Fig. 1. Evaluation of the objective function of the initial population (Gonçalves et al. 2015).

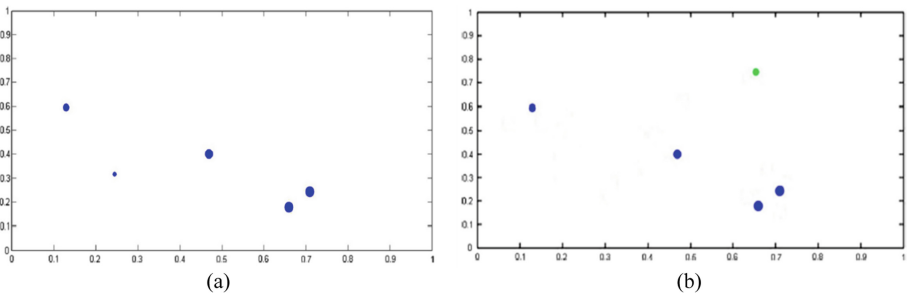
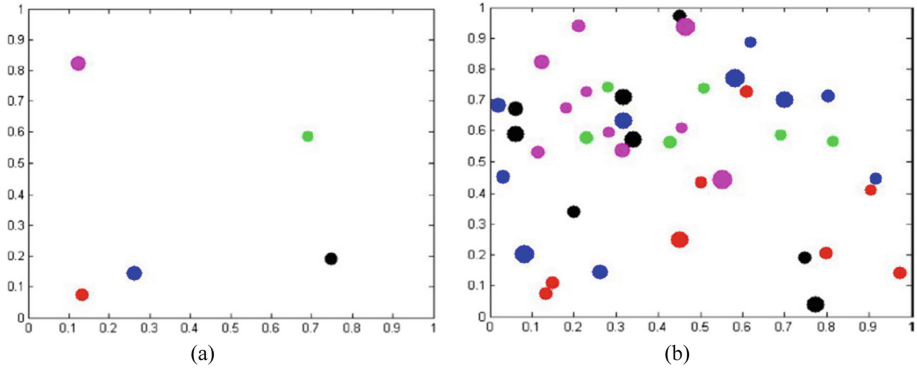
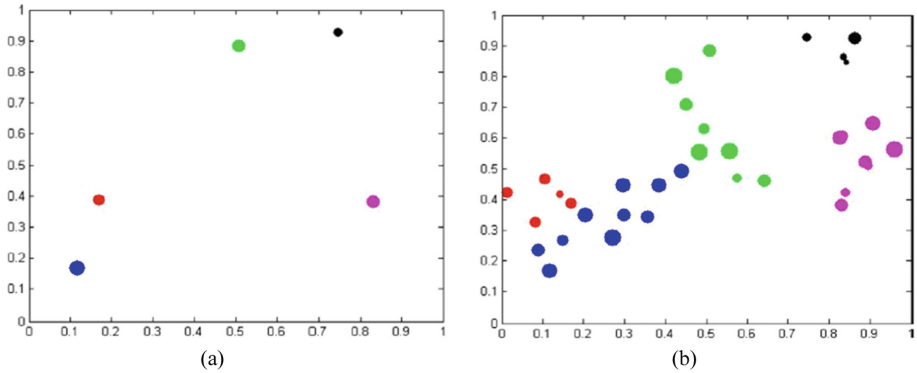


Fig. 2. Mutation of the initial search group of the initial population (Gonçalves et al. 2015).





**Fig. 3.** Families generation of the search group member in the first iteration (Gonçalves et al. 2015).



**Fig. 4.** Families generation of the search group member in a latter iteration (Gonçalves et al. 2015).

### 3 Canelas Railway Bridge

Canelas Bridge is selected for this study. The structure is part of the Portuguese railway line, near Aveiro, and has a total length of 72 m between the axes of supports. This structure consists of 6 simply supported spans, each 12 m long, Fig. 5. It is a composite steel-concrete of the type *filler beam*, composed of two half independent concrete slab decks, each supporting a railway track. Both slab decks are 6.2 m wide, with 4.5 m of 0.7 m thick slab with nine HE500B metal beams spaced 0.475 m apart. The ends of the slabs are composed of consoles 1.7 m wide and linearly variable in thickness between 0.3 and 0.7 m. The bridge deck is also equipped with a ballast guard consisting of a beam 0.60 m high and 0.3 m wide, located between the concrete slab and the side console. Ballast, sleepers and rails are placed on the board. The ballast guard causes the ballast structure to be confined to the board. All spans of the board are fixed on one side (side where the train is going) and mobile on the other side (side where the train is

going), made of neoprene involving stainless steel sheets and supported under each HE500B profile, totaling 9 support devices. In this work, the span called P5-E2 is studied, i.e., the gap closest to the landfill towards Porto. The longitudinal view and the respective cross section of this bridge are illustrated in Fig. 6. The main reason for choosing this type of bridge is due to the fact that the structural system of concrete is the most used in railway bridges in Brazil.



**Fig. 5.** General view of the Canelas railway bridge (Rocha et al. 2016).

### 3.1 Past Research

The Canelas bridge has been the target of experimental and numerical studies by some researchers. Presented in 2004, Rodrigues' doctoral thesis (Rodrigues 2005) was supported by the Portuguese laboratory LNEC and addressed the suitability of the Canelas railway bridge to increase the maximum operating speed of alpha-commuter trains from 140 km/h to 220 km/h. The study involved conducting in situ tests to assess the dynamic characteristics of the structure and the dynamic effects of rail traffic. The first vertical vibration mode and the first torsional mode of the bridge sections were identified.

Silva (2010) studied the dynamic behavior of the Canelas bridge using numerical models developed in ANSYS and coupled in Matlab for solving dynamic equilibrium equations. The dynamic analysis under moving loads corresponding to several trains that operate on the Canelas bridge, was applied and compared with results from major static analysis. Three finite element models of the bridge were developed, from the simplest to the most complete model. Based on the experimental responses of the first vibrational modes of structure, studied by Rodrigues (2005), numerical models were updated in relation to the parameters: elasticity module of the concrete, ballast elasticity module, ballast density and stiffness of supports. For this update, a sensitivity analysis of the parameters was used.

Rocha et al. (2016) published some studies on the dynamic behavior of the Canelas bridge were carried out by means of probabilistic approaches. The analysis of the

sensitivity of the bridge dynamic responses as a function of its structural parameters was considered, as well as the effect of rail irregularities. For such simulations, the Monte Carlo Method was applied. Thereby, Rocha demonstrated that the inertia of the cross section of the deck, the height of the ballast layer, the concrete elasticity module and the vertical stiffness of the supports were the parameters that most altered the bridge's response.

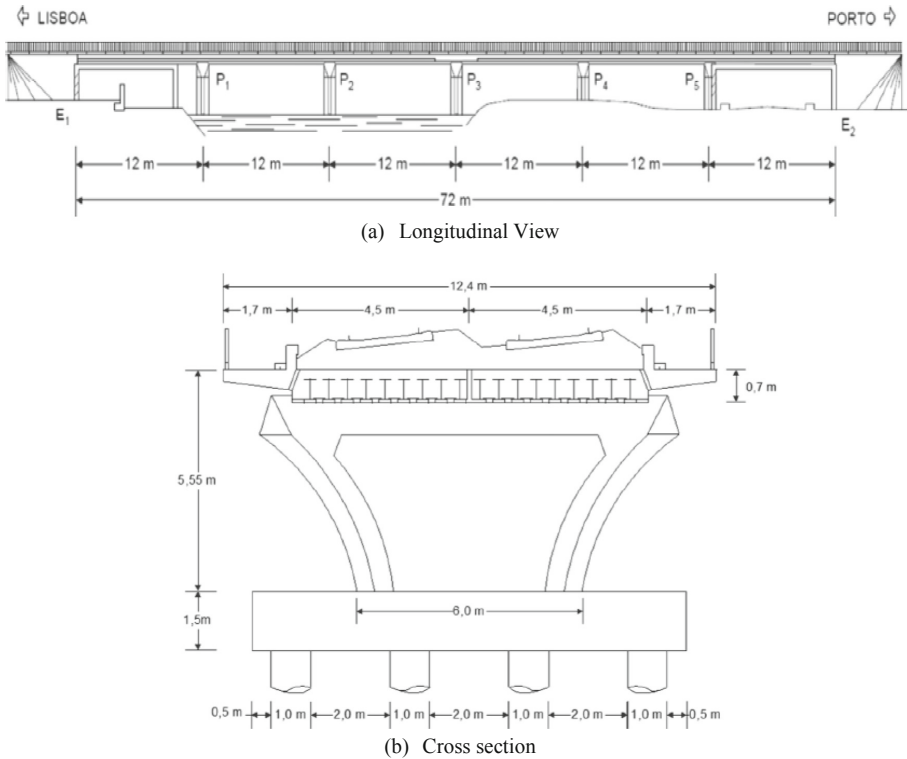


**Fig. 6.** Canelas railway bridge (Rocha et al. 2015).

### 3.2 Numerical Models

The numerical models of the bridge are developed by the Finite Element Method. Considering that this study basically focuses on the evaluation of the P5-E2 section, the representation of the entire length of the bridge and track becomes unviable due to the high computational cost of the numerical model. Thus, a simplification of the model with the inclusion of only the section under study and the continuity of the track in the adjacent section can guarantee an adequate model and with a significant gain in processing time. Thus, three numerical models developed by Silva (2010) are studied and presented in the following sections. A simpler numerical model, denominated C1, with only one half-span, where the track is represented by an equivalent distributed load on

the slab. A second, more complete than C1, the half-board model with two successive spans and an extension of the road to take into account the continuity effect is called C2. Finally, a more complete C3 numerical model, but with higher computational cost, is represented by two successive spans and an extension of the track, as in the model C2, plus the duplication of the half board, through the axis of symmetry of the structure represented by the longitudinal axis. In the three numerical models performed, the pillars and the bridge embankment were not considered. In view of the analyzes to be carried out, the ANSYS 16.0 software is used in the APDL language for modeling.

Subsequently, numerical models are calibrated by updating four properties of the bridge that are considered most relevant for possible changes in their dynamic behavior in modal terms: the stiffness of the supports, the modulus of elasticity of the concrete, the modulus of elasticity ballast and ballast density. Table 1 shows the variables of interest and their respective bounds, studied by Silva (2010).

Regarding computational modeling, shell elements (SHELL63) were used to simulate the concrete of the slab, console and ballast guard. The beam elements (BEAM44) were considered to represent the steel profiles of the slab and rails. Solid elements (SOLID45) were used to simulate ballast, sleepers and pads. In addition to these elements, rigid beam elements (MPC184) were introduced to connect the ballast to the slab, mass elements (MASS21) to simulate the guardrails and, finally, spring elements (COMBIN14) for elastic supports. The arrangement of the finite elements is given in relation to the center of gravity of the elements that make up the bridge structure, in the same way that the supports are located in the center of rotation.

**Table 1.** Variables considered in updating the models

Variables	Description	Unit	Bounds
$K_v$	Vertical Stiffness of the supports	MN/m	117–547
$E_c$	Modulus of the Young of the concrete	GPa	32–37
$E_l$	Modulus of the Young of the ballast	MPa	120–200
$\rho_o$	Ballast density	kg/m <sup>3</sup>	1800–2700

### 3.2.1 Numerical Model C1

The numerical model C1, the simplest model of the span under study, represents the half board P5-E2 without the inclusion of track elements. In this case, the mass of the track; composed of ballast, sleepers and rails; it is simulated by means of a uniformly distributed load on the shell elements of the slab, that is, it is considered as the dead load in which the stiffness of the track does not influence the model's responses. The structure was discretized into 3335 elements and 2759 nodes. At Fig. 7 shows the numerical model C1 with its adaptive elements.

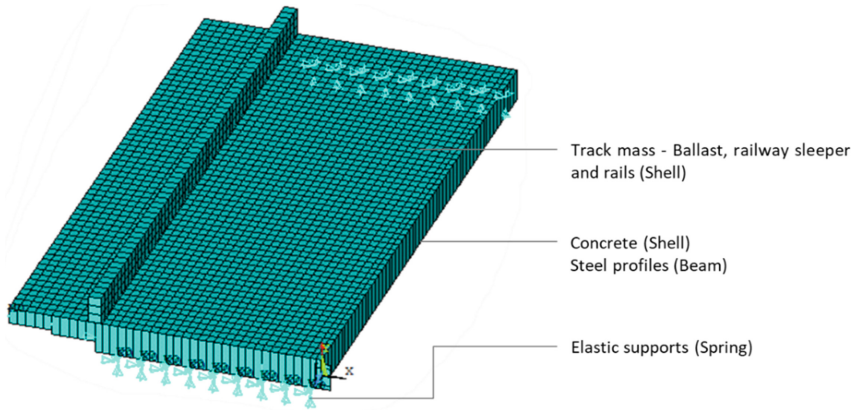


Fig. 7. Numerical model C1.

### 3.2.2 Numerical Model C2

In the numerical model C2, half slab is simulated with two successive spans, the span under study and the next span, and an extension of the road to simulate its continuity over the landfill. In this model, the elements of the track are considered, which implies the influence not only of the mass, but also of the stiffness of these elements in the simulated responses. The slab structure has no connection between the gaps, given by a 6 cm joint, this connection being made by the elements of the track. The model was discretized into 23709 elements and 29150 nodes. Figure 8 shows the numerical model C2 with its different elements.

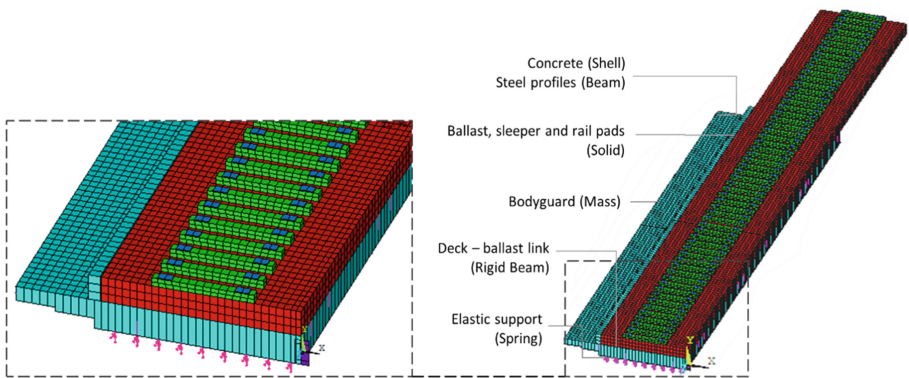


Fig. 8. Numerical model C2.

### 3.2.3 Numerical Model C3

The numerical model C3 is the most complete of the three, representing two half slabs and two successive gaps, in addition to the extension of the road over the embankment. As in the C2 model, the connection between the four-half slabs takes place via the

track, with no structural connection between the concrete trays. Likewise, the track elements also influence the stiffness of the structure. The model was discretized into 47860 elements and 58300 nodes. Figure 9 shows the numerical model C3 with its respective structural elements. A more detailed study of the numerical model of the Canelas bridge can be seen in Silva (2010).

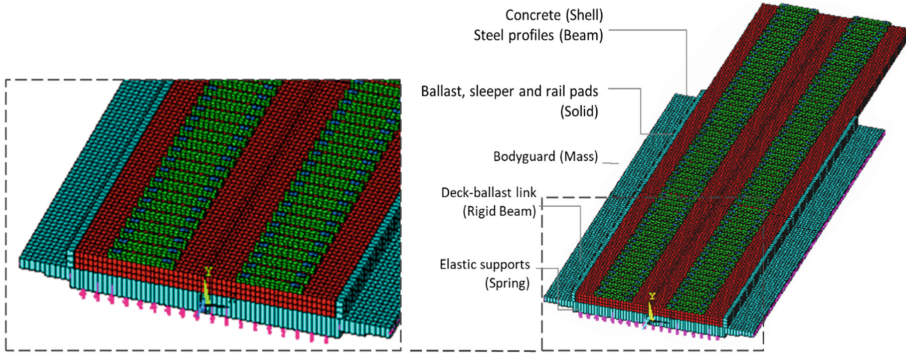


Fig. 9. Numerical model C3.

#### 4 Numerical Model Calibration

In this section, the optimal values of the properties of the bridge are estimated using numerical models, in order to adjust the values of the natural frequencies obtained previously in experimental tests developed by Rodrigues (2005). The experimental values of the natural frequencies are shown in Table 2.

Table 2. Experimental natural frequencies (Rodrigues 2005)

1 <sup>st</sup> vertical bending mode (Hz)	1 <sup>st</sup> torsional mode (Hz)
8.60	15.60

The numerical frequencies are fitted by minimizing the objective function, aiming to approximate the values of the experimental natural frequencies and, thus, to identify the respective values of the parameters of interest. The objective function is given by Eq. (2):

$$f_{obj} = \sqrt{\left(\frac{f_1^{exp} - f_1^{num}}{f_1^{exp}}\right)^2 + \left(\frac{f_2^{exp} - f_2^{num}}{f_2^{exp}}\right)^2} \quad (2)$$

where  $f_1^{exp}$  and  $f_2^{exp}$  are the values of the experimental natural frequency of the first vertical bending mode and the first torsional mode, respectively, and  $f_1^{num}$  and  $f_2^{num}$  are the corresponding natural frequencies of the numerical model to be calibrated.

Figure 10 shows a flowchart that resumes the optimization loop of numerical model calibration through the SGA. This process involves combining two software packages:

ANSYS® and MATLAB®. Note that the closer to zero the objective function is, the smaller the error of the numerical response in relation to the experimental response.

In the numerical model C1, as described in the previous chapter, the elements of the track are not included, in such a way that the load of these elements on the board is simulated by means of a distributed load. In this way, three parameters of interest are estimated: the stiffness of the supports, the concrete elasticity module and the ballast density. Table 3 shows the value of the numerical frequencies of the model C1. The calibration of this model, due to its lower computational cost, was performed with a high number of population and iterations, represented by 100 individuals and 200 iterations. Table 4 presents the estimated values of the parameters of interest for the model C1. In minimizing the objective function for this model, despite the high number of population and iterations, the natural numerical frequencies not converges to a value very close to the experimental natural frequencies, having an error in the order of 0.0283.

Aiming to reduce the difference between the values of the numerical and experimental frequencies, the bounds of the parameters of interest, shown in Table 1, are expanded. In this case, the violation of the limits of the parameters of interest characterizes an error between the actual information of the bridge and the numerical model under study.

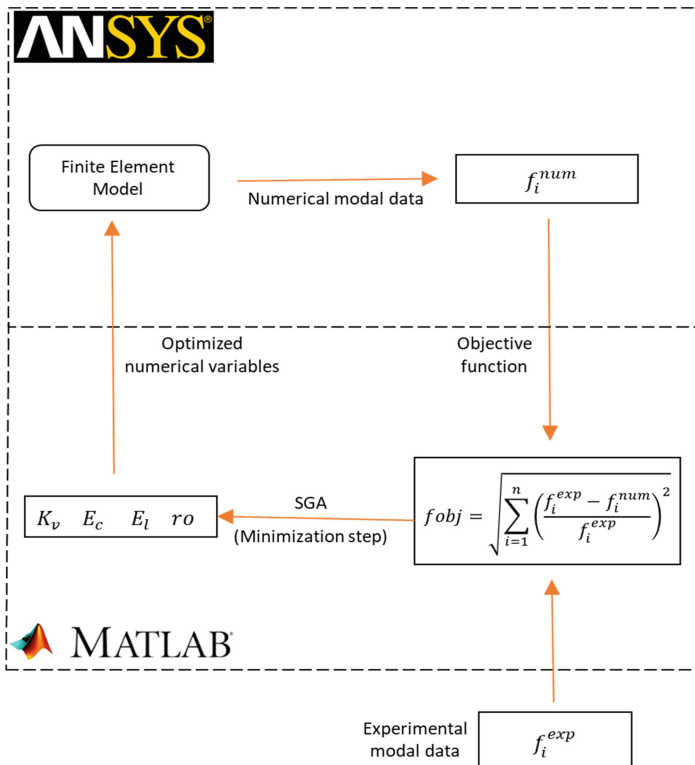


Fig. 10. Flowchart for numerical model calibration through the structural optimization.



**Table 3.** Numerical frequencies for model C1

Vibrational modes	Experimental value (Hz)	Numerical value (Hz)
1 <sup>st</sup> vertical bending	8.60	8.36
1 <sup>st</sup> torsional	15.60	15.67

**Table 4.** Updated variables for numerical model C1

Variables (output)	Unit	Estimated value
Vertical Stiffness of the supports	MN/m	344.1
Modulus of the Young of the concrete	GPa	37.0
Ballast density	kg/m <sup>3</sup>	1800

In Table 5, the final values of the update of the numerical model C1 are presented and in Fig. 11, the first vertical bending vibration mode and the first torsional mode of the C1 model are illustrated. Due to the higher computational cost of the C2 model, the model updating was performed with a relatively low number of evaluations of the objective function, represented by 50 individuals and 20 iterations.

**Table 5.** Updated variables for numerical model C1 after the expanded bounds

Variables (output)	Unit	Estimated value
Vertical Stiffness of the supports	MN/m	309.6
Modulus of the Young of the concrete	GPa	38.8
Ballast density	kg/m <sup>3</sup>	1556

In minimizing the objective function for the numerical model C2, the numerical natural frequencies converges to a value of the experimental natural frequencies. The convergence, in this case, although the model is more expensive compared to the C1 model, was given for a low number of population and iterations. This makes the model C2 more accurate in obtaining the parameters of interest. In Fig. 12, the first vertical bending vibration mode and the first torsional mode of the C2 model are illustrated, respectively.

In the numerical model C3, the most complete model of the three, the characteristics of the structure and its materials are kept as close as possible to reality. In this way, four parameters of interest are estimated: the stiffness of the supports, the concrete elasticity module, the ballast elasticity module and the ballast density. The optimization of the C3 numerical model was performed with a population of 100 individuals and 50 iterations.

In minimizing the objective function for the numerical model C3, as well as in the model C2, the natural numerical frequencies converges to a value of the experimental natural frequencies. This also makes the C3 model more accurate in obtaining the parameters of interest. On the other hand, this model has a very high computational cost. In Fig. 13 are illustrated the first vertical bending vibration mode and the first torsional mode of the C3, respectively. It is important to note that in the configuration of the vibration modes of the C3 model, the first torsional mode is visually similar to a



vertical flexion vibration mode. This is due to the geometrical complexity of the structure, which implies a difficulty in characterizing the modes it represents, already in its first modes of global vibration. However, in this work, it was decided to use the natural frequency value in a numeric of the first torsional mode, given its coherence in response compared to the experimental response. In addition, Silva (2010) more accurately evaluated the modal responses of the C3 model and characterized it this mode. Table 6 presents the values of the parameters of interest of the updated numerical models. Thus, it can be inferred that for numerical model C1 the disregard of the track stiffness implied a significant increase in the concrete's elasticity module and a sudden reduction in the ballast density, considered as dead load, since the natural frequency is directly proportional to the stiffness and inversely proportional to the mass. Analogously to the C3 model, the significant increase in natural frequencies in relation to the C2 model may be directly linked to the inclusion of the second half board, which implies an increase in the stiffness of the modeled structure.

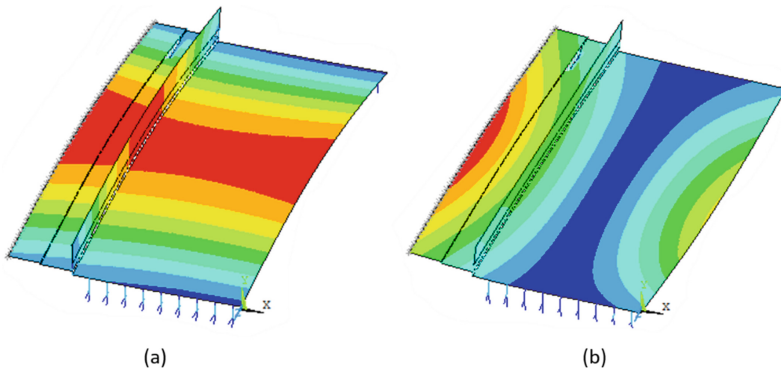


**Fig. 11.** Vibration modes of C1: (a) First vertical bending mode and (b) First torsional mode.

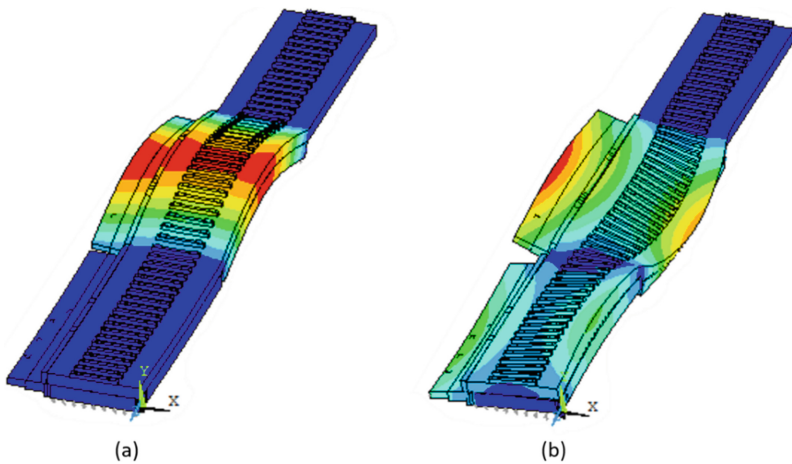


**Fig. 12.** Vibration modes of C2: (a) First vertical bending mode and (b) First torsional mode.

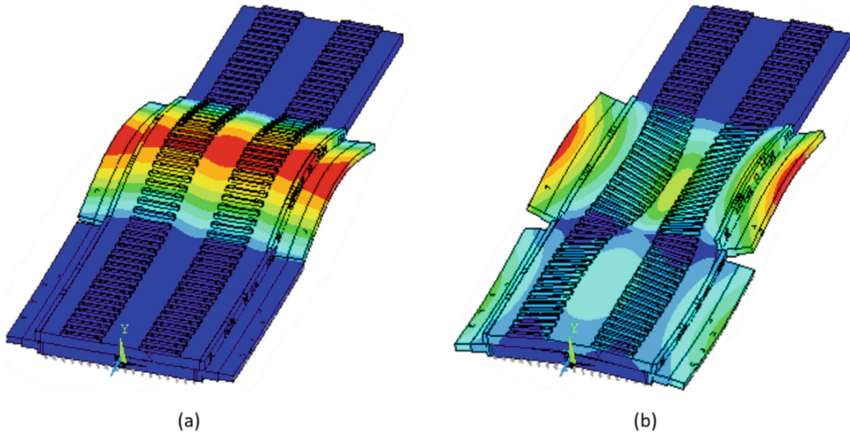


**Fig. 13.** Vibration modes of C3: (a) First vertical bending mode and (b) First torsional mode.

**Table 6.** Variable values of the optimized models

Variable	Unit	Bounds of the design	C1	C2	C3
$K_v$	MN/m	117–547	309.6	486.5	335
$E_c$	GPa	32–37	38.8	33.5	32.7
$E_l$	MPa	120–200	–	130	162.5
$\rho_o$	kg/m <sup>3</sup>	1800–2700	1556	2571	2636

## 5 Conclusion

This work aims to estimate unknown design variables in structures from previously known responses. A real example of a short-span railway bridge is selected for this study and three numerical models are updated using the SGA optimization algorithm based on modal responses obtained in the field.

The simplest numerical model of the bridge, called C1, with the lowest computational cost, did not show a good convergence in minimizing the objective function within the lower and upper bounds of the parameters of interest, featuring a priori a numerical model with a grade of errors. Models C2 and C3, which are more complete and have a higher computational cost, presented numerical values of natural frequencies that converges to experimental values within the limits of the design variables.

Models C2 and C3 presented values of the parameters of interest that were closest to each other when compared to model C1. This is due to the influence of the track on the stiffness of the models. For the C1 model, due to the non-inclusion of the stiffness of the track elements, this showed a sharp drop in the value of the dead load that represents the ballast, in this case, the ballast density parameter.

Therefore, in the process to make numerical models to evaluate real structures, one must be very sparing in order not to make an exaggeratedly complex problem and, as a consequence, of high computational cost. Simpler numerical models can be efficient,

both in relation to its computational cost, and in obtaining accurate answers with the quantification of their errors in relation to the real problem.

Future research consists to estimate the total uncertainty regarding updated parameters and the errors between numerical models. Hence, reliable bounds for such uncertainties can be predicted. In addition, own error parameters can be included as quantities to be updated in the process.

## References

- Belegundu, A.D., Arora, J.S.: A study of mathematical programming methods for structural optimization. Part I: theory. *Int. J. Numerical Methods Eng.* **21**(9), 1583–1599 (1985). Article first published online: 21 June 2005. <https://doi.org/10.1002/nme.1620210904>
- Deng, L., Cai, C.S.: Bridge model updating using response surface method and genetic algorithm. *J. Bridge Eng.* **15**(5), 553–564 (2009). Article first published online: 27 Nov 2009. [https://doi.org/10.1061/\(ASCE\)BE.1943-5592.0000092](https://doi.org/10.1061/(ASCE)BE.1943-5592.0000092)
- Carlson, A.G.: Desenvolvimento de um novo operador de algoritmos metaheurísticos baseado na minimização da rigidez aplicado à otimização de estruturas treliçadas (Master's thesis), Federal University of Santa Catarina, Brazil (2015). <https://repositorio.ufsc.br/handle/123456789/169546>
- Gonçalves, M.S., Lopez, R.H., Miguel, L.F.F.: Search group algorithm: a new metaheuristic method for the optimization of truss structures. *Comput. Struct.* **153**, 165–184 (2015). Article first published online: 29 March 2015. <https://doi.org/10.1016/j.compstruc.2015.03.003>
- Haftka, R.T., Gürdal, Z.: *Elements of Structural Optimization*, vol. 11. Kluwer Academic Publishers, Dordrecht (1992)
- Priestley, M.J.N., Calvi, G.M., Kowalsky, M.J.: *Displacement-Based Seismic Design of Structures*. IUUSS Press, Pavia (2007)
- Jung, D.S., Kim, C.Y.: Finite element model updating on small-scale bridge model using the hybrid genetic algorithm. *Struct. Infrastruct. Eng.* **9**(5), 481–495 (2013). Article first published online: 07 Apr 2011. <https://doi.org/10.1080/15732479.2011.564635>
- Kaveh, A., Talatahar, S.: (2008), A hybrid particle swarm and ant colony optimization for design of truss structures. *Asian J. Civil Eng. (Build. Hous.)* **9**(4), 329–348 (2008)
- Kołakowski, P., Szelążek, J., Sekuła, K., Świercz, A., Mizerski, K., Gutkiewicz, P.: Structural health monitoring of a railway truss bridge using vibration-based and ultrasonic methods. *Smart Mater. Struct.* **20**(3), 1–10 (2011). Article first online published: 14 Feb 2011. <https://doi.org/10.1088/0964-1726/20/3/035016>
- Lagaros, N.D., Papadrakakis, M., Kokossalakis, G.: Structural optimization using evolutionary algorithms. *Comput. Struct.* **80**(7–8), 571–589 (2002). [https://doi.org/10.1016/S0045-7949\(02\)00027-5](https://doi.org/10.1016/S0045-7949(02)00027-5)
- Meixedo, A., Ribeiro, D., Santos, J., Calçada, R., Todd, M.: Progressive numerical model validation of a bowstring-arch railway bridge based on a structural health monitoring system. *J. Civil Struct. Health Monit.* **11**, 421–449 (2021). Article first published online: 06 Feb 2021. <https://doi.org/10.1007/s13349-020-00461-w>
- Papadrakakis, M., Lagaros, N.D., Tsompanakis, Y., Plevris, V.: Large scale structural optimization: computational methods and optimization algorithms. *Arch. Comput. Methods Eng.* **8**(3), 239–301 (2001)
- Ren, W.X., Chen, H.B.: Finite element model updating in structural dynamics by using the response surface method. *Eng. Struct.* **32**(8), 2455–2465 (2010). Article first published online: 04 May 2010. <https://doi.org/10.1016/j.engstruct.2010.04.019>

- Ren, W.X., Zhao, T., Harik, I.E.: Experimental and analytical modal analysis of steel arch bridge. *J. Struct. Eng.* **130**(7), 1022–1031 (2004). Article first published online: 15 June 2004. [https://doi.org/10.1061/\(ASCE\)0733-9445\(2004\)130:7\(1022\)](https://doi.org/10.1061/(ASCE)0733-9445(2004)130:7(1022))
- Ribeiro, D., Caçada, R., Delgado, R., Brehm, M., Zabel, V.: Finite element model updating of a bowstring-arch railway bridge based on experimental modal parameters. *Eng. Struct.* **40**, 413–435 (2012). Article first published online: 05 April 2012. <https://doi.org/10.1016/j.engstruct.2012.03.013>
- Rocha, J.M., Henriques, A.A., Caçada, R., Rönquist, A.: Efficient methodology for the probabilistic safety assessment of high-speed railway bridges. *Eng. Struct.* **101**(15), 138–149 (2015). Article first published online: 29 July 2015. <https://doi.org/10.1016/j.engstruct.2015.07.020>
- Rocha, J.M., Henriques, A.A., Caçada, R.: Probabilistic assessment of the train running safety on a short-span high-speed railway bridge. *Struct. Infrastruct. Eng.* **12**(1), 78–92 (2016). Article first published online: 02 Jan 2015. <https://doi.org/10.1080/15732479.2014.995106>
- Rodrigues, J.M.V.B.L.: Identificação modal estocástica: métodos de análise e aplicações em estruturas de engenharia civil (Doctoral thesis), Faculty of Engineering of the University of Porto, Portugal (2005). <https://repositorio-aberto.up.pt/handle/10216/11964>
- Roux, W.J., Stander, N., Haftka, R.T.: Response surface approximations for structural optimization. *Int. J. Numer. Methods Eng.* **42**(3), 517–534 (1998). Article first published online: 04 Dec 1998. [https://doi.org/10.1002/\(SICI\)1097-0207\(19980615\)42:3<517::AID-NME370>3.0.CO;2-L](https://doi.org/10.1002/(SICI)1097-0207(19980615)42:3<517::AID-NME370>3.0.CO;2-L)
- Silva, L.D.C.F.M.D.: Comportamento dinâmico de uma ponte ferroviária de pequeno vão para tráfego de alta velocidade (Master's thesis), Faculty of Engineering of the University of Porto, Portugal (2010). <https://repositorio-aberto.up.pt/handle/10216/61199>
- Vagnoli, M., Remenyte-Priscott, R., Andrews, J.: Railway bridge structural health monitoring and fault detection: state-of-the-art methods and future challenges. *Struct. Health Monit.* **17**(4), 971–1007 (2018). Article first published online: 24 Aug 2017. <https://doi.org/10.1177/1475921717721137>
- Zanakis, S.H., Evans, J.R.: Heuristic “optimization”: why, when, and how to use it. *Interfaces* **11**(5), 84–91 (1981). Article first published online: 01 Oct 1981. <https://doi.org/10.1287/inte.11.5.84>



# Aftershock Seismic Capacity Assessment of Concrete Bridge Piers Considering Post-mainshock Strength Degradation

Borislav Todorov and A. H. M. Muntasir Billah<sup>(✉)</sup>

Department of Civil Engineering, Lakehead University, Thunder Bay, Canada  
{btodorov, muntasir.billah}@lakeheadu.ca

**Abstract.** Bridge infrastructure serves as part of the backbone to the transportation industry, playing an often-overlooked role in the economy until service is disrupted. The sophistication of seismic design practices continues to improve and holds an expanding stake in maximizing service life of bridges in the research and engineering community alike. Mainshock-Aftershock earthquake sequences present another design challenge, as aftershocks typically occur within a time period where repairs to the initial damage incurred during the mainshock are not able to be realized. The objective of this study is to investigate the effect of mainshock strength degradation on the post-aftershock seismic capacity in terms lateral load carrying capacity and post-earthquake functionality. In this study, a parameterized set of circular bridge pier columns are designed according to the performance-based design guidelines present in the current edition of the Canadian Highway Bridge Design Code for a major-route bridge located in Vancouver, BC. Using nonlinear finite element model with a strain-based strength degradation scheme, the bridge piers are analyzed under a suite of as-recorded mainshock-aftershock ground motion records representing different hazard levels. The outcome of this study will aid in understanding the role of performance-based design on the post-aftershock seismic performance and functionality of bridge piers.

**Keywords:** Performance-based design · Mainshock-aftershock · Bridge pier

## 1 Introduction

Bridge piers are one of the most critical components in the bridge system that dictate the overall performance of bridges during seismic events. In reinforced concrete bridges, much of the energy imparted to the bridge structure by ground acceleration is dissipated by the deterioration of the bridge pier columns, where concrete cracking and spalling, plastic hinge formation, and reinforcement yielding and buckling mechanisms dissipate energy. Current seismic design guidelines which are implemented in North America allow all but the highest importance lifeline bridges to undergo large inelastic deformations so long as load carrying capacity is maintained and collapse does not occur. The Canadian Highway Bridge Design Code (CSA S6-19) has implemented performance-based design (PBD) as a requirement for seismic design of more important or irregular bridges. Bridges designed to PBD guidelines must demonstrate that they meet explicitly

outlined performance criteria such as damage limits and service levels. This means explicit performance objectives are defined and have to be demonstrated, in contrast to traditional codes where performance objectives are implicit. While the Canadian Highway Bridge Design Code (CHBDC) has implemented PBD as a requirement for the seismic design of lifeline and major route bridges, the nature of PBD techniques translate to a design process that is not universally compatible for all scenarios and hazards. Therefore, there is great benefit to be realized in the development of PBD guidelines for mainshock-aftershock seismic sequences for scenarios in which the chance to assess and repair a bridge is not possible following a recent mainshock.

All seismic activity presents a risk for the damage to a bridge or its components, where a subsequent repair or retrofit may be unlikely to restore the full capacity of the intact bridge. Moreover, mainshock-aftershock (MS-AS) events, present little to no time to mobilize repair to the already damaged structure, which presents a compounding risk to the fragility of bridges. Typically, sequences which involve multiple dependent earthquakes are defined in terms of components of foreshocks, mainshock, and aftershocks based on their relative intensity. As a multiple earthquake sequence occurs, the current earthquake with the largest intensity is termed the mainshock, with the preceding excitations being denoted foreshocks, and the following labelled aftershocks.

Past studies were cognizant of the potential for increased vulnerability that aftershocks pose, however were not able to apply real MS-AS records. Instead, a common technique of reiterating the original mainshock record was employed, termed back-to-back application of mainshocks. Luco et al. (2004) contributed some of the first analytical research for demonstrating the increased vulnerability of structures subjected to MS-AS sequences, where the residual capacity of a 3-storey steel moment resisting frame (SMRF) building was used as a case study. Shin and Kim (2017) explored the effects of frequency content of aftershock ground motions on reinforced concrete bridge pier responses. Using three column experimental results from literature, finite element models were modelled using Open Sees and validated based on the resulting force-displacement outputs from cyclic loading analysis. The seismic response under dynamic loading of the columns was explored to demonstrate the importance of properly selected ground motion sequences. Liang et al. (2020) investigated the time-varying seismic fragility of offshore bridges under MS-AS sequence. They considered time-dependent material properties of bridge components due to aging and deterioration and analyzed the bridge based on time-varying seismic action in the entire life cycle. They concluded that with increasing bridge material deterioration, the vulnerability increases under MS-AS sequential ground motions.

An overarching goal of this research is to study and assess the seismic performance of concrete bridge piers in order to aid in the development of performance limits for bridge piers under sequential seismic events. This study analytically explored a parameterized set of 20 reinforced concrete bridge piers which share several geometrical and material properties with typical bridge bents that support many Canadian bridges. Of those piers, half are designed using current PBD guidelines provided in the 2019 edition of the CHBDC, whereas the remaining half are designed with insufficient transverse reinforcement commonly found in the bridges designed pre-2000. To support this study, a nonlinear fiber-based modelling approach with a proposed material strength degradation scheme is developed using the Open Sees finite element analysis software. A multiple

conditional mean spectra (CMS) approach is used to select a suite of 50 mainshock-aftershock ground motion records for the selected site in Vancouver, British Columbia, which consist of crustal, in-slab, and interface earthquakes that commonly occur in areas near the Cascadia Subduction zone. Nonlinear time history analysis is performed for mainshock-only and mainshock-aftershock excitations, and static pushover analysis is also performed in lateral and axial directions for the intact columns, as well as in their respective post-MS and post-AS damaged states. Using the resulting data, this study assessed the fragility of the bridge piers subjected to mainshock-only and mainshock-aftershock earthquakes. Probabilistic seismic demand models (PSDMs) are derived for the columns designed using current PBD guidelines (PBD-compliant) to evaluate whether the current PBD criteria is sufficient for resisting aftershock effects. Additional PSDMs are generated for the columns with inadequate transverse reinforcement (PBD-deficient) to assess aftershock vulnerability of older bridges. The developed fragility curves indicate an increased fragility of all bridge piers for all damage levels.

## 2 Design of Archetype Bridge Piers

The performance of circular bridge pier prototypes representative of those commonly found in highway bridges throughout Canada have been detailed in this section. The bridge piers are assumed to be part of a multi-span major route bridge located in Vancouver, British Columbia, soil class-D and have been designed following the performance-based seismic design requirements as outlined in the 2019 edition of the CHBDC (CSA S6-19). Figure 1 shows the response spectra corresponding to different return periods in soil class-D. Performance levels for three different categories of bridges, such as Lifeline, Major Route, and Other are defined in S6-19. Since the bridge piers are part of a major route bridge, they must satisfy the performance requirements for the service and damage levels for 475- and 2475-year return period earthquakes. In the context of performance-based design, performance criteria are defined in terms of material strain (concrete and longitudinal reinforcement strain).

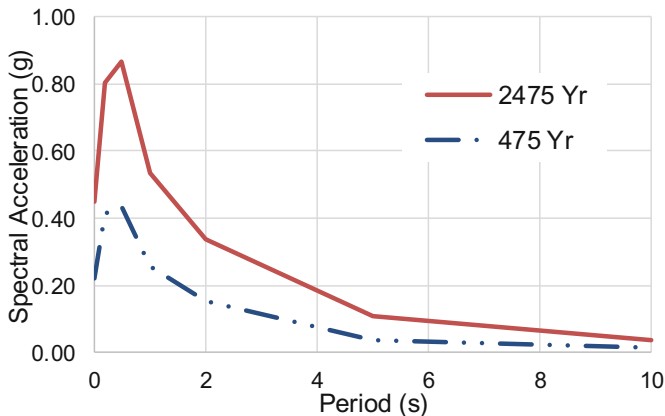


Fig. 1. Response spectrum of bridge site location in Vancouver BC, soil class-D.

Additional limits on displacement or damage to bridge components such as main structural members, connections, bearings, joints, restrainers, and foundations are also specified by the CHBDC; however, the focus of this study is the bridge pier only, whose performance criteria have been defined in Table 1, where the fiber section steel ( $\epsilon_s$ ) and concrete ( $\epsilon_c$ ) material strains are observed.

**Table 1.** Performance criteria for reinforced concrete bridges (CSA-S6-19)

Damage level	Material observed	Performance criteria
Minimal	Concrete	$\epsilon_c \leq 0.006$
	Reinforcing steel	$\epsilon_s \leq 0.010$
Repairable	Reinforcing steel	$\epsilon_s \leq 0.025$
Extensive	Concrete	Core concrete not permitted to exceed 80% of ultimate strain
	Reinforcing steel	$\epsilon_s \leq 0.050$
Probable replacement	Concrete	Core crushing not permitted to occur
	Reinforcing steel	$\epsilon_s \leq 0.075$

The column test matrix which makes up the analytical experiments of this research consists of 20 columns. The first 10 columns, denoted as C1 through C10 are designed using the current PBD requirements. In the preliminary design of these columns, diameter, aspect ratios, axial load ratios, and concrete compressive strength are defined to represent a large range of typical configurations. Furthermore, an iterative design procedure is implemented where the steel detailing is the design variable. Inelastic static pushover analysis (SPO) is performed where steel and concrete material strains are collected, and the longitudinal reinforcement ratio are incrementally adjusted until the bridge pier meets the performance criteria for minimal and extensive damage levels. Figure 2 illustrates the capacity curve for the first column which was designed in this study. The two shaded areas represent the minimal and extensive limits, and as can be seen in the figure, all performance limits occur at larger displacement values which demonstrates a PBD-compliant design. Although aging bridge piers would also have reduced longitudinal reinforcement and lower grade rebars, these parameters have been maintained to compare the effects of transverse reinforcement detailing only.



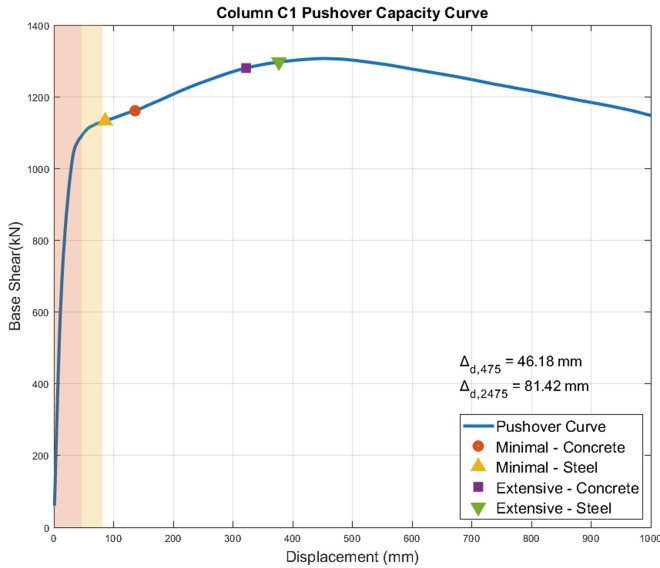


**Fig. 2.** Column C1 static pushover capacity curve.

### 3 Analytical Model Development and Validation

The seismic performance of the studied bridge piers is realized through the use of a 2D fiber based finite element modelling approach using Open Sees (Mazzoni et al. 2006). Reinforced concrete behavior is modeled using the ‘concrete07’ material model, which is based on an implementation of the original Chang and Mander concrete model (1994) with simplified unloading and reloading branches. Reinforcing steel is modeled using the ‘steel02’ material provided by Open Sees which uses the Menegotto-Pinto steel constitutive model (1973) which was later extended by Filippou et al. (1983) to include isotropic strain hardening. Furthermore, an Open Sees material wrapper object, ‘fatigue’ has been merged with the steel02 model to include low-cycle fatigue based on Miner’s rule linear strain accumulation which is implemented using a rain flow cycle counting algorithm. The fatigue material has the additional option to define maximum and minimum strain limits which have also been enabled and defined at  $\epsilon_s = 0.10$  to model longitudinal bar rupture.

The fiber sections are aggregated into a single material section, which is then used to model the pier in the finite element model space using a beam-column element (BCE). In this research, a modified force-based BCE is used through the command ‘beamWithHinges’ (BWH). Not only is the BWH element shown to provide more accurate moment curvature response (Scott and Fenves 2006), but there is an advantage to specifying different material section properties at the plastic hinge (PH) locations and the interior, as is the case for increased transverse reinforcement in the PH region.

Plastic hinge length  $L_p$  is calculated based on the equation determined by Paulay and Priestley (1992) which is approximated as:

$$L_p = 0.08L + 0.022d_b f_y \quad (1)$$

where  $L$  is the length of the pier in mm,  $d_b$  represents the longitudinal bar diameter, and  $f_y$  is the yield strength of the rebar in MPa.

The developed nonlinear model exists in abstract space until its performance can be deemed accurate in simulating real world conditions. Fortunately, many research efforts from 1980–2000 focused on the performance of real bridge pier columns and have made their hysteretic responses available for validation efforts. One such study by Lehman and Moehle (2000) explored the performance of five concrete bridge columns with varying amounts of longitudinal steel and aspect ratios subjected to reversed cyclic loading. Column 415 has been selected to be modeled with the same material and geometric properties in order to validate the proposed Open Sees model. The comparison of the hysteretic response of Column 415 from the experiment and finite element model are shown in Fig. 3. From Fig. 3, it can be seen that the developed Open Sees model achieves good agreement with the recorded experimental data. The developed model captures reinforced concrete hysteresis well during low displacement, and reasonably well during high energy dissipation cycles.

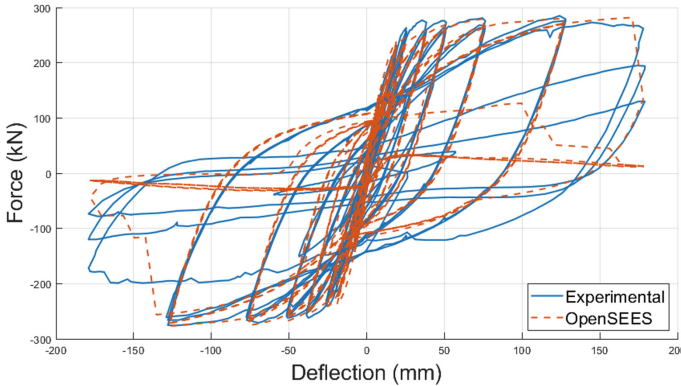


**Fig. 3.** Open Sees model column cyclic response compared to column 415 (Lehman and Moehle 2000).

### 3.1 Strain-Based Strength Degradation Scheme

Strength and stiffness deterioration of materials is more difficult to capture in Open Sees. Typically, material pinching effects are applied using one of several implementations of the Ibarra-Medina-Krawinkler Deterioration Model (2005). There are several studies which have used this model; however, it is necessary to calibrate all parameters for each configuration, which would pose a challenge for a large column test matrix. Instead, a simplified strain-based strength modification scheme is applied to the fiber

elements located in the plastic hinge region of the bridge pier at post-mainshock and post-aftershock column states. Recent studies which have evaluated the residual seismic capacity of post-earthquake RC column members in structures, have also assigned reduction factors which are associated with various damage levels. Ludovico et al. (2013) assembled and explored a database of cyclic tests of 23 flexure or flexure-shear failure dominated rectangular RC columns with deformed rebars, and 13 with smooth bars. Using the experimental data, modification factors for strength, stiffness, and residual drift were proposed for modifying the plastic hinges of RC columns which have exceeded elastic limits. Similarly, Chiu et al. (2019) performed experimental analysis of 6 column specimens, in which flexure, flexure-shear, and shear failure modes were observed and used to calibrate a residual seismic capacity model for which strength, stiffness, and energy dissipation are modified. The viability of the method was demonstrated by performing a post-earthquake assessment of a school building which was damaged during an earthquake in Taiwan.

Similarly, a reduction factor scheme is developed and suggested in this study for the sectional strength modification of concrete and reinforcing steel fibers in the bridge pier's plastic hinge region. Longitudinal steel damage levels have been proposed at five key strain damage levels as obtained from the appropriate literature and summarized in Table 2. The initial damage state implemented for steel corresponding to  $\varepsilon_s = 0.002$  is defined based on the commonly used 0.2% yield offset strain. Goodnight et al. (2015) performed large scale experiments of 30 bridge pier columns, where a high-fidelity 3D optical position measurement system to record column strain data was implemented. A statistical analysis of the obtained results during experimental testing correlated longitudinal rebar strain corresponding to 1 mm and 2 mm crack widths as  $\varepsilon_s = 0.010$  and  $\varepsilon_s = 0.020$ , respectively. Furthermore, Goodnight et al. (2016) developed empirical formulations for bar buckling which were compared against the existing drift-based methods proposed by Berry and Eberhard (2003) and strain-based methods by Feng et al. (2015). Using the combined datasets from Goodnight et al. (2015) and Berry and Eberhard (2003) study, a modified approach for predicting bar buckling limit states was developed, and shown to produce more accurate peak tensile strain estimates when predicting bar buckling. Tensile strain corresponding to bar buckling is calculated as:

$$\varepsilon_{bb} = 0.03 + 700\rho_s \frac{f_{yh}}{E_s} - 0.1 \frac{P}{f'_c A_g} \quad (2)$$

where  $\rho_s$  is the transverse volumetric steel ratio,  $f_{yh}$  is the yield strain of transverse steel,  $E_s$  is the corresponding transverse steel modulus of elasticity, and  $P/f'_c A_g$  is the axial load ratio.

Concrete material damage states have been proposed at four strain levels as shown in Table 2. The initial damage state implemented for concrete corresponding to  $\varepsilon_c = 0.004$  is defined based on the serviceability concrete compression strain (Kowalsky 2000). Damage level II  $\varepsilon_c = 0.006$  is adopted by S6-19 for minimal damage performance as the strain corresponds to the onset of cover concrete spalling (Priestley et al. 1996). Furthermore, concrete core crushing strain is approximated at  $\varepsilon_c = 0.015$ , and

ultimate concrete compressive strain is approximated using the following formula (Priestley et al. 1996)

$$\epsilon_{cu} = 0.004 + 1.4\rho_s f_{yh} \epsilon_{su} / f'_c \tag{3}$$

where  $\rho_s$  is the transverse volumetric steel ratio,  $f_{yh}$  is the yield strain of transverse steel,  $\epsilon_{su}$  is the ultimate steel tensile strain, and  $f'_c$  is the concrete compressive strength.

Regression functions are proposed for the strength reduction parameters which are applied to the concrete and reinforcing steel fibers located in the plastic hinge region of the bridge pier. Figure 4 represents the 3<sup>rd</sup> order polynomial line fitted to the damage level strains. Floating point values based on maximum concrete compressive and rebar tensile strains which are obtained from MS-only and MS+AS analysis are determined and applied to the material strength properties. Concrete compressive strength,  $f'_c$  is multiplied by the reduction factor, and both confined and unconfined material properties are recalculated based on the reduced strength. Similarly, reinforcing steel  $f_y$ , is also multiplied by the steel reduction factor. It should be mentioned that material reduction parameters are applied to the intact properties only, i.e. 75% and 60% reduction factors determined for post-MS and post-AS states, respectively are exclusively applied to the intact material properties and do not “compound” for a total reduction of 45%.

**Table 2.** Suggested reinforcing steel and concrete reduction factors

Steel reinforcement				Concrete			
Damage level	Performance criteria (rebar strain)	Damage state	Reduction factor	Damage level	Performance criteria (concrete strain)	Damage state	Reduction factor
0	No Damage	DS-0	1	0	No Damage	DS-0	1
I	0.002	DS-1	0.8	I	0.004	DS-1	0.75
II	0.01	DS-2	0.6	II	0.006	DS-2	0.5
III	0.02	DS-3	0.4	III	0.015	DS-3	0.25
IV	$\epsilon_{bb}$	DS-4	0.2	IV	$\epsilon_{cu}$	DS-4	0
V	0.1	DS-5	0				

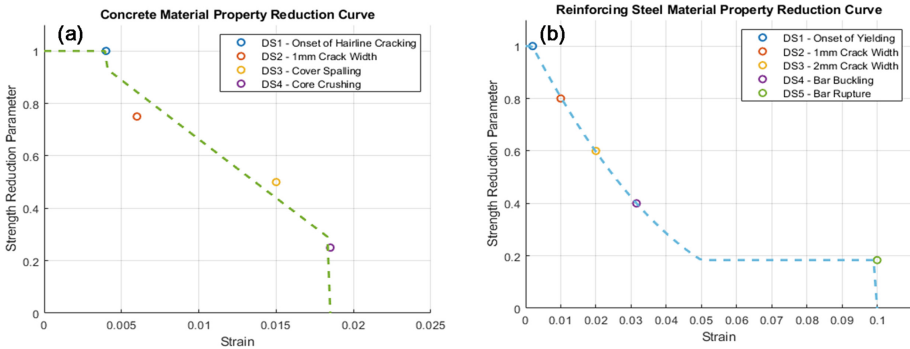


**Fig. 4.** Property reduction curve (a) concrete and (b) reinforcing steel.

To further illustrate the effect of the material property reduction values, the individual uniaxial material models have been plotted again in Fig. 5, for the intact and two reduced strength states. The different behaviour of the material reductions can be noticed in the figure, where the concrete strength reduction is applied to the compressive strength,  $f_c'$  and the remaining properties have been recalculated, resulting in the compressive envelope being shortened while the tensile strength remains relatively unchanged. In the case of the steel material, the reduction parameter is applied to the modulus of elasticity,  $E_s$  which results in an envelope which is shifted and produces lower peak compressive and tensile strengths.

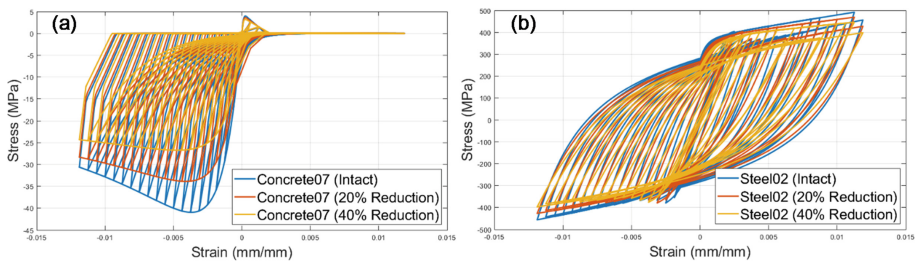


**Fig. 5.** Effect of strength reduction for (a) Concrete07 and (b) Steel02 uniaxial materials.

## 4 Ground Motion Suite

Mainshock-Aftershock ground motion records are selected for assessing the seismic performance of the bridge pier of a multi-span highway bridge in Vancouver, British Columbia. Each ground motion consists of a mainshock and aftershock(s), such that the effects due to mainshock-aftershock sequences rather than conventional mainshock-only records, can be investigated using the selected records. The record selection procedure is based on the multiple conditional mean spectra (CMS) (Baker 2011; Atkinson and Goda 2011), where separate target response spectra are developed for earthquakes having distinct record characteristics. For the seismicity in Vancouver, consideration of shallow crustal, deep in-slab, and mega-thrust Cascadia subduction events is important because they have very different event and ground motion characteristics due to different source and path effects. The multiple CMS-based record selection can take into account such physical characteristics and their relative contributions to overall seismic hazard. To define the CMS for different earthquake types, regional seismic hazard information on dominant scenarios is required. This information is obtained from detailed probabilistic seismic hazard analysis (PSHA) for typical sites in Vancouver (Atkinson and Goda 2011).

The multiple CMS-based record selection is carried out by following the same procedures described in Tesfamariam et al. (2015) and Tesfamariam and Goda (2017). The target CMS are developed for crustal, interface, and in-slab earthquakes, based on full PSHA results. The site of interest is downtown Vancouver, and its surface soil is classified as site class D. The PSHA is conducted based on the updated regional

seismic hazard model by Atkinson and Goda (2011). Figure 6 shows the uniform hazard spectrum (UHS) for return period of 475-year and 2475-year return periods, respectively. Seismic deaggregation is based on spectral acceleration at 1.0 s. To develop CMS for different earthquake types, mean record characteristics for individual earthquake types are obtained from the PSHA results.

The record database is built from an extended dataset of real mainshock-aftershock sequences; it has been developed by combing the NGA database (Goda and Taylor 2012) with the updated version of the KKiKSK database (Tesfamariam and Goda 2017). The number of available mainshock-aftershock sequences is 606; among them, there are 197 crustal earthquakes, 340 interface earthquakes, and 69 inslab earthquakes. The interface events are from the 2003 Tokachi-oki earthquake and the 2011 Tohoku earthquake which have similar event characteristics as the expected Cascadia subduction earthquake. Using the target CMS, a set of ground motion records are selected by comparing response spectra of candidate records with the target spectra. The total number of MS-AS records is set to 50 with an even distribution of earthquake type representation selected to include crustal, interface, and inslab earthquakes. Since MS-AS records are multicomponent ground motions, the response spectra are defined as the geometric mean of the two horizontal components and the target CMS is computed for the MS portion of the MS-AS sequences. The vibration period range for the spectral matching is considered from  $0.5 T_1$  to  $2.0 T_1$ , which is inclusive of the major vibration periods of the bridge piers studied. Furthermore, the response spectra of the selected records and the target CMS are similar for the crustal and interface records; for inslab records, the selected records contain richer short-period spectral content than the target spectra. Given the availability of ground motion records and the size of ground motion records (i.e., 16–17 for each earthquake type), matching of the candidate response spectra with the target is deemed to be adequate.

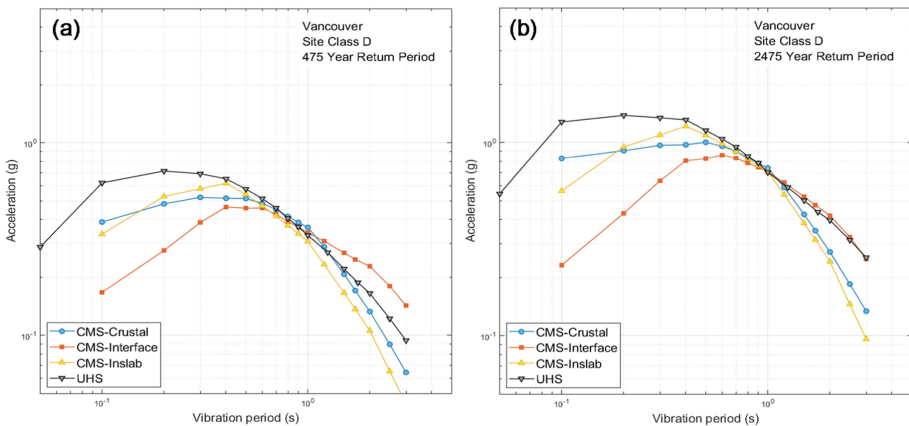


**Fig. 6.** Uniform hazard spectrum and conditional mean spectra for crustal, interface, and inslab events in Vancouver (site class D) (a) return period of 475 years and (b) return period of 2475 years.

## 5 Static Pushover and Nonlinear Time History Analyses

After generating the finite element models, the piers are subjected to a static analysis where the superstructure mass is gradually applied to the top of the column. A static pushover analysis in both orthogonal directions (i.e. lateral and axial) is performed for each intact column following gravity loading to establish intact pier capacity prior to any earthquake loading. Eigenvalue analysis is performed for the first mode of the column and a 5% Rayleigh damping is applied. The first nonlinear time history analysis is performed, in which the MS-only component of the selected ground motion is analyzed using the Newmark average acceleration method integrator. Material reduction factors are calculated based on the outputted strains and are applied for the following post-MS pushovers to determine residual capacities. Subsequently, a second time history analysis is performed using the post-MS damaged model, where the aftershock component of the records is analyzed. A final strength modification factor is determined for the post-AS damage state, and residual lateral and axial capacities are again determined. Though the data generated here is an intermediate step in preparation for the following sections, it is clear that the consideration of aftershocks increases the susceptibility to further damage accumulation in bridge components, as observed from the decrease in median residual capacity when comparing post-MS and post-AS damage states. The data generated using the NLTHA in this section are further processed in the subsequent section and used as the basis of the fragility analysis of the bridge piers.

## 6 Fragility Assessment of Bridge Piers Subjected to Mainshock-Aftershock Sequence

### 6.1 Characterization of Damage States

Fragility function requires the description of damage states (DS) which reflect the element and system level damage quantitatively and qualitatively. An important step in generating fragility curves is to define a qualitative or quantitative measure of various stages of damage known as damage states (DS). Past researchers have considered different forms of EDPs to measure the DS of bridge piers such as Park and Ang damage index (Park and Ang 1985), bridge pier capacity demand ratio (Hwang et al. 2000), drift limits (Dutta and Mander 1999), displacement ductility (Billah et al. 2013), curvature ductility (Padgett and DesRoches 2009), maximum drift (Billah and Alam 2018), and residual drift (Billah and Alam 2018). Some researchers considered material strain-based damage states (Mackie and Stojadinović 2005) and maximum drift corresponding to different seismic performance criteria as DS (Billah and Alam 2016; Todorov and Billah 2021) for fragility assessment of bridge piers.

A common approach to defining damage states in the seismic vulnerability assessment of engineering structures (Billah and Alam 2016; Todorov and Billah 2021) is accomplished using the damage levels provided in HAZUS-MH (2011). However, in order to provide a basis for comparison with existing CHBDC PBD guidelines, the established damage levels for major route bridges are used instead; namely, minimal

and extensive damage states. Limit state capacities are derived based on the drifts obtained from static pushover analysis of the bridge piers corresponding to the performance levels defined in CHBDC (Table 1). Typically, DSs are linked to each bridge piers' capacity which are characterized by the two parameters median,  $S_C$  and dispersion,  $\beta_c$ , respectively. These two parameters are considered to follow a lognormal distribution. However, all the limit state capacities obtained from pushover analyses are associated with uncertainties that are described using a lognormal standard deviation or dispersion ( $\beta_c$ ). The values of lognormal standard deviation or dispersion ( $\beta_c$ ) have been obtained following the procedure described in Nielson (2005). Table 3 presents the limit state capacities for the bridge piers in terms of median and dispersion values.

**Table 3.** Limit states for PBD-compliant bridge pier fragility assessment

PBD-compliant bridge pier					PBD-deficient bridge pier				
Column ID	Minimal damage		Extensive damage		Column ID	Minimal damage		Extensive damage	
	$S_c$	$\beta_c$	$S_c$	$\beta_c$		$S_c$	$\beta_c$	$S_c$	$\beta_c$
Column C1	1.15	0.59	4.29	0.64	Column C11	1.16	0.59	3.51	0.64
Column C2	1.56	0.59	5.87	0.64	Column C12	1.59	0.59	4.74	0.64
Column C3	1.91	0.59	7.32	0.64	Column C13	1.95	0.59	5.79	0.64
Column C4	1.2	0.59	4.33	0.64	Column C14	1.23	0.59	2.76	0.64
Column C5	1.63	0.59	5.92	0.64	Column C15	1.68	0.59	3.73	0.64
Column C6	2.01	0.59	7.36	0.64	Column C16	2.07	0.59	4.52	0.64
Column C7	1.23	0.59	4.12	0.64	Column C17	1.27	0.59	2.87	0.64
Column C8	1.68	0.59	5.62	0.64	Column C18	1.73	0.59	3.89	0.64
Column C9	2.06	0.59	6.93	0.64	Column C19	2.13	0.59	4.72	0.64
Column C10	1.67	0.59	5.29	0.64	Column C20	1.7	0.59	3.31	0.64

## 6.2 Probabilistic Seismic Demand Model

For bridges subjected to aftershocks following an initial mainshock, the probability of additional damage to the already affected structure can be expected to increase. Probabilistic seismic demand models (PSDM) provide the basis for fragility curve development, where the conditional probability of damage state exceedance under a given ground motion intensity is expressed. The PSDM establishes a correlation between the engineering demand parameters (EDP) and the ground intensity measures (IMs). In this research, the component level models are used to generate the analytical fragility functions using nonlinear time history analyses of models C1 to C10 and C11 to C20, respectively. Two of the most common approaches for PSDM are the scaling approach (Zhang and Huo 2009) and the cloud approach (Billah et al. 2013). In the scaling approach, ground motion data is scaled to determined intensity levels, via incremental dynamic analysis (IDA) which is performed for each increment. In contrast, the cloud approach neglects any scaling, and instead performs nonlinear time history analysis (NLTHA) using the as-recorded motions to develop the PSDM.



In this research, the cloud method is utilized due to the quality and availability of the as-recorded mainshock-aftershock records which have been gathered specifically to represent the seismic hazards typically present in Vancouver, British Columbia. In the selected PSDM approach, regression analysis is performed to obtain the mean and standard deviation for the minimum and extensive damage states based on the power-law function (Cornell et al. 2002) which provides a logarithmic correlation between the EDP and selected IM in the form of:

$$EDP = a(IM)^b \quad (4)$$

The above equation can be expressed in the transformed space, where the parameter  $b$  is the slope and parameter  $\ln(a)$  is the vertical intercept, such that  $a$  and  $b$  can be estimated through regression analysis of the response data provided through the NLTHA. The transformed equation is expressed as:

$$\ln(EDP) = \ln(a) + b \times \ln(IM) \quad (5)$$

In order to supplement additional data for the cloud approach where the peak ground acceleration (PGA) exceeds the maximum unscaled PGA of the selected ground motion records, additional entries are extrapolated using the above equation. In the development of the PSDMs, the suite of parameterized bridge piers is subjected to the aforementioned MS-AS ground motion suite, with peak column drift demands recorded. The logarithmic standard deviation (dispersion) of the drift demand,  $\beta_{EDP|IM}$  conditioned upon the IM is estimated using the following equation (Baker and Cornell 2006):

$$\beta_{EDP|IM} \cong \sqrt{\frac{\sum_{i=1}^N (\ln(EDP) - \ln(a \times IM^b))^2}{N - 2}} \quad (6)$$

where  $N$  is the total number of EDP|IM data entries. The fragility curves for the different damage levels considered can be developed using the intensity measure and engineering demand parameters using Eq. (7) (Nielson 2005).

$$P[DS|IM] = \Phi \left[ \frac{\ln(IM) - \ln(IM_n)}{\beta_{comp}} \right] \quad (7)$$

$$\text{where, } \ln(IM_n) = \frac{\ln(S_c) - \ln(a)}{b} \quad (8)$$

In which,  $\Phi(\cdot)$  is the standard normal cumulative distribution function,  $IM_n$  is the median value of the intensity measure,  $S_c$  is the median value for the damage states of

the bridge pier, and  $a$  and  $b$  are the regression coefficients of the PSDM. Lastly, the dispersion component is calculated using Eq. (9) (Nielson 2005).

$$\beta_{comp} = \frac{\sqrt{\beta_{EDPIM}^2 + \beta_c^2}}{b} \quad (9)$$

where  $\beta_c$  is the dispersion value for the damage states of the bridge pier.

### 6.3 Development of Fragility Curves

The formulated PSDM is used to derive the fragility curves which help express the effect of aftershock consideration on the seismic demand imposed on the studied bridge piers. Because of the efficiency, practicality, sufficiency, and hazard computability of PGA, many researchers (Billah et al. 2013; Padgett et al. 2008) have suggested PGA as the optimal intensity measure for fragility assessment of bridges and bridge piers. Accordingly, for the purpose of this study, and to maintain consistency with the CHBDC, PGA is selected as the optimal IM for this study. Furthermore, the PGA intensity measure is distinguished for both mainshock-only and mainshock-aftershock fragility analyses. An appropriate EDP selection is a function of the structural system and desired performance objectives. In this study, maximum drift (MD) of the bridge pier, which represents different performance-based limit states as per CHBDC, is considered as the EDP.

Nonlinear time history analyses which were carried out for each of the bridge piers for both MS-only and MS-AS earthquake records are used to determine the maximum drift of the piers. The resulting maximum drift and peak ground acceleration pairs are incorporated into a PSDM which establishes a linear regression of the pair in the log-transformed space for each of the ground motions considered. Figure 7 shows the PSDMs for columns C1 and C11 for MS-only and MS-AS ground motions, where the equation for the linear regression line as well as the corresponding  $R^2$  value are also shown. The corresponding  $R^2$  values of the PSDMs show a weak correlation, which is in part due to the generally low number of EDP-IM pairs considered. It is commonplace to simply use more ground motions or to perform multiple NLTHAs with scaling such as incremental dynamic analysis (IDA) in order to generate more points for this approach, however, due to the large number of columns considered in this study, a trade-off was made in PSDM correlation strength.

Using the formulation shown in Eq. (7) combined with the seismic demand and capacity models described in the preceding sections, fragility curves for the PBD-compliant and PBD-deficient bridge piers are generated. These curves provide the basis for comparing the effect of aftershocks as well as the bridge pier transverse reinforcement configurations on bridge pier vulnerability. Since it is not worthwhile to compare the fragilities of each bridge pier individually, median fragility curves are developed for the PBD-compliant and PBD-deficient bridge piers to facilitate a meaningful comparison. The median fragility curves developed for the PBD-compliant bridge piers (C1–C10) are displayed in Fig. 8a, and fragility curves developed for columns C11–C20 which are representative of columns with inadequate transverse

reinforcement are shown in Fig. 8b. Comparison between the MS-only and MS-AS fragility curves in Fig. 8 confirm the conclusions which other research has found where an increased seismic vulnerability of structures subjected to aftershock effects is observed. Moreover, the vertical offset between the MS-only and MS-AS curves for the minimal damage level demonstrate a large increase in the probability of damage occurrence which is especially high at lower ground motion intensities, and later converging at higher intensities. A dissimilar effect is observed for the extensive damage level, where low intensities pose similar levels of risk, and a divergence is observed when the ground motion intensity increases.

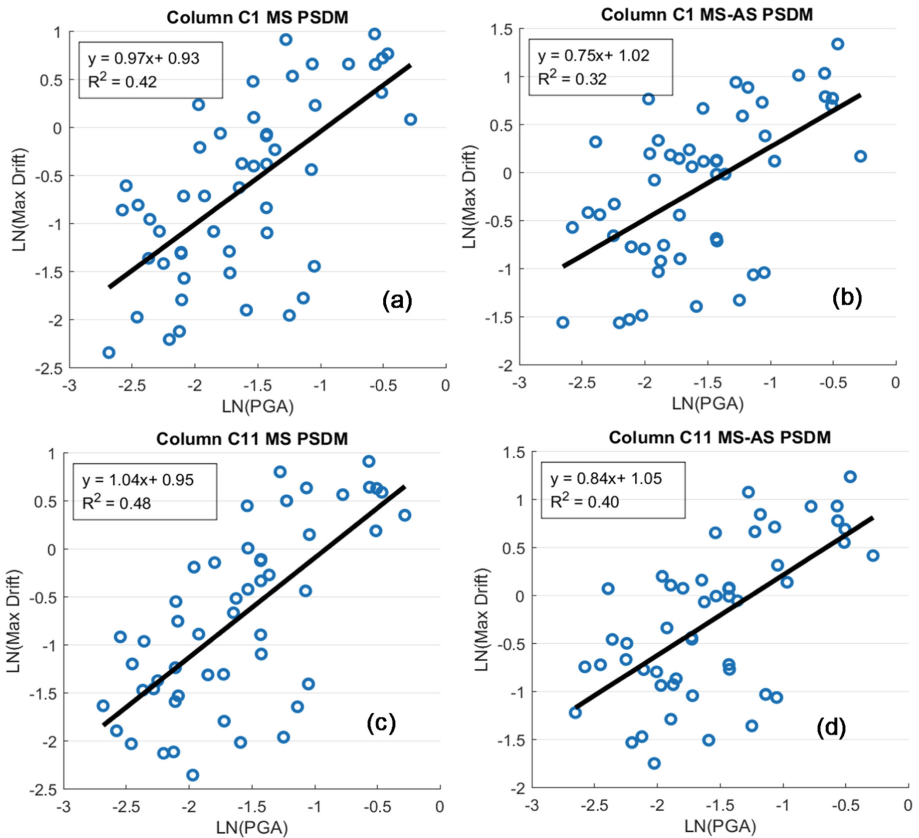


**Fig. 7.** PSDMs for different bridge piers subjected to: (a) column C1 subjected to MS-only ground motion, (b) column C1 subjected to MS-AS ground motion, (c) column C11 subjected to MS-only ground motion, (d) column C11 subjected to MS-AS ground motion.

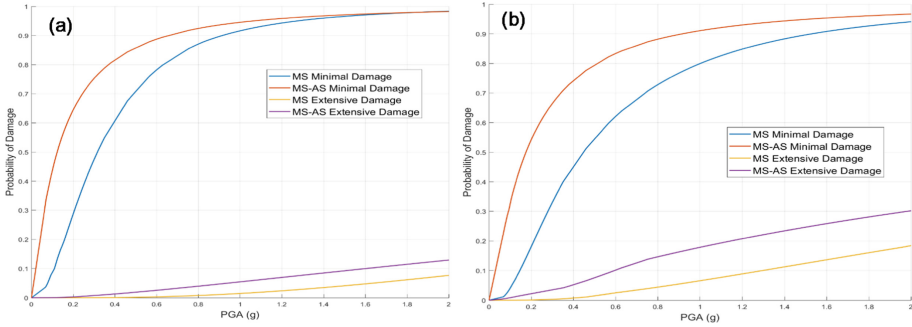


**Fig. 8.** Median fragility curves for (a) PBD-compliant bridge piers and (b) PBD-deficient bridge piers subjected to mainshock-only and mainshock-aftershock sequences.

Table 4 summarizes the median probability of exceeding minimal and extensive damage states for the PBD-compliant and PBD-deficient bridge piers at peak ground acceleration of 0.20 g and 0.37 g corresponding to the design PGA for the 475- and 2475-year return period earthquake, respectively. For the PBD-compliant piers, a 35.7% increase in the median probability of exceedance is observed for minimal damage levels when aftershock effects are considered. On the other hand, the probability of exceedance for extensive damage levels does not increase much when subjected to aftershock. Overall, the increased seismic demand that aftershocks present for the extensive damage level is fairly insignificant, whereas the minimal damage criteria show a larger variance in the two curves. This suggests that the PBD-compliant columns are fairly well designed for aftershock effects in the case of extensive damage levels, and are relatively under-designed in the case of minimal damage levels.

**Table 4.** Probability of exceeding different damage states at design PGAs

Damage state	Probability of exceedance (%)	
	PBD-compliant	PBD-deficient
MS-Minimal	28.77	18.10
MS-AS Minimal	64.47	54.22
MS-Extensive	0.07	0.60
MS-AS Extensive	1.18	4.59

Moreover, in the case of fragility curves for the PBD-deficient columns shown in Fig. 8b, the same effect of increased seismic demand is present for aftershock effects. For the PBD-deficient piers, a 36.1% increase in the median probability of exceedance is observed for minimal damage levels in Table 4. This increase is very similar to the PBD-compliant piers; however, the overall risk of exceedance is approximately 10% lower. This suggests a lower seismic demand as compared to the PBD-compliant piers which is contrary to what is expected, and warrants further investigation. For extensive damage levels, there is a much greater risk of exceedance as compared to the

PBD-compliant columns. Despite a 4% increase in aftershock vulnerability being observed at the design PGA, the fragility curves in Fig. 5.3 demonstrate a much greater seismic vulnerability at higher intensities as compared to the PBD-compliant. Overall, the increased seismic demand that aftershocks present for bridge piers with insufficient transverse reinforcement is telling of a much greater seismic risk. This suggests that there is a need for retrofitting strategies for much of the aging infrastructure where exposure to aftershocks is a possibility.

Furthermore, the large variation in fragility between the minimal and extensive damage levels is to be expected, but leaves more information to be desired. A design strategy that defines two performance criteria at extreme ends of damage levels leaves the opportunity for improvement of current practices. What's more, is that the 2014 edition of the CHBDC considered an optional repairable damage state corresponding to 975-year return period earthquakes for major route bridges which has since been removed in the 2019 edition. Developing MS-AS performance limit states for the three damage levels would make for better performance criteria which would better capture the seismic risk of bridges, but could also lead to more resilient designs.

## 7 Conclusions

In order to address the growing interest in developing a generation of bridge infrastructure that is more resilient to seismic hazards, a greater understanding needs to be developed for hazard interactions such as mainshock-aftershock sequences. Current bridge design practices employed in Canada and outlined in the Canadian Highway Bridge Design Code recognize the presence of aftershock effects but do not provide any explicit guidelines to practicing engineers. In order to help bridge this knowledge gap, this thesis focused on analytically examining a wide range of reinforced concrete bridge piers which represent a variety of configurations found in Canadian bridges. Fragility assessment of the selected bridge piers is performed where the effects of aftershocks are examined. A comparative analysis of the aftershock effects on the fragility of piers designed to current performance-based design standards as well as piers with insufficient transverse reinforcement has been carried out using the existing CHBDC performance criteria. Based on the results of the fragility assessment study, the following conclusions have been derived:

- The developed PSDMs which incorporated aftershock effects demonstrated an increased fragility for all bridge piers examined, for all damage levels considered.
- Bridge piers designed using current PBD guidelines were at an insignificant risk of exceeding extensive damage levels following mainshock-only and mainshock-aftershock excitations.
- Aftershock effects accounted for increases of 35% and greater for both PBD-compliant and PBD-deficient bridge piers' probability of exceeding minimal damage levels.

**Acknowledgement.** The financial contribution of the Natural Sciences and Engineering Research Council of Canada (NSERC) through the Discovery Grant Program is gratefully acknowledged.

## References

- Atkinson, G.M., Goda, K.: Effects of seismicity models and new ground-motion prediction equations on seismic hazard assessment for four Canadian cities. *Bull. Seismol. Soc. Am.* **101**(1), 176–189 (2011)
- Baker, J.W.: Conditional mean spectrum: tool for ground-motion selection. *J. Struct. Eng.* **137**(3), 322–331 (2011)
- Baker, J.W., Cornell, C.A.: Correlation of response spectral values for multicomponent ground motions. *Bull. Seismol. Soc. Am.* **96**, 215–227 (2006)
- Berry, M., Eberhard, M.O.: Performance Models for Flexural Damage in Reinforced Concrete Columns. 162. Pacific Earthquake Engineering Research Center (2003)
- Billah, A.H.M.M., Alam, M.S., Bhuiyan, M.A.R.: Fragility analysis of retrofitted multicolumn bridge bent subjected to near-fault and far-field ground motion. *J. Bridg. Eng.* **18**(10), 992–1004 (2013)
- Billah, A., Alam, M.: Performance based seismic design of concrete bridge pier reinforced with shape memory alloy-part 1: development of performance-based damage states. *ASCE J. Struct. Eng.* **142**(12), 1–11 (2016)
- Billah, A.H.M.M., Alam, M.S.: Probabilistic seismic risk assessment of concrete bridge piers reinforced with different types of shape memory alloys. *Eng. Struct.* **162**, 97–108 (2018)
- CSA: Canadian Highway Bridge Design Code S6-19. National Research Council of Canada (2019)
- Chang, G.A., Mander, J.B.: Seismic Energy Based Fatigue Damage Analysis of Bridge Columns: Part 1 - Evaluation of Seismic Capacity. 244 (1994)
- Chiu, C.-K., Sung, H.-F., Chi, K.-N., Hsiao, F.-P.: Experimental quantification on the residual seismic capacity of damaged RC column members. *Int. J. Concr. Struct. Mater.* **13**(1), 1–22 (2019). <https://doi.org/10.1186/s40069-019-0338-z>
- Cornell, C.A., Jalayer, F., Hamburger, R.O., Foutch, D.A.: Probabilistic basis for 2000 SAC federal emergency management agency steel moment frame guidelines. *J. Struct. Eng.* **128**(4), 526–533 (2002)
- Di Ludovico, M., Polese, M., Gaetani d’Aragona, M., Prota, A., Manfredi, G.: A proposal for plastic hinges modification factors for damaged RC columns. *Eng. Struct.* **51**, 99–112 (2013)
- Dutta, A., Mander, J.B.: Seismic fragility analysis of highway bridges. Tokyo, Japan, pp. 311–325 (1999)
- Feng, Y., Kowalsky, M.J., Nau, J.M.: Finite-element method to predict reinforcing bar buckling in RC structures. *J. Struct. Eng.* **141**(5), 04014147 (2015)
- Filippou, F.C., Popov, E.P., Bertero, V.V.: Effects of bond deterioration on hysteretic behavior of reinforced concrete joints. Earthquake Engineering Research Center, University of California Berkeley (1983)
- Goodnight, J.C., Feng, Y., Kowalsky, M.J., Nau, J.M.: The effects of load history and design variables on performance limit states of circular bridge columns (2015)
- Goodnight, J.C., Kowalsky, M.J., Nau, J.M.: Strain limit states for circular RC bridge columns. *Earthq. Spectra* **32**(3), 1627–1652 (2016)
- Goda, K., Taylor, C.A.: Effects of aftershocks on peak ductility demand due to strong ground motion records from shallow crustal earthquakes. *Earthq. Eng. Struct. Dyn.* **41**, 2311–2330 (2012)
- Hazus, M.: Multi-hazard loss estimation methodology: earthquake model hazus-MH MR5. Washington, D.C. (2011)
- Hwang, H., Jernigan, J.B., Lin, Y.-W.: Evaluation of seismic damage to memphis bridges and highway systems. *J. Bridg. Eng.* **5**(4), 322–330 (2000)
- Ibarra, L.F., Krawinkler, H.: Global collapse of frame structures under seismic excitations. Pacific Earthquake Engineering Research Center Berkeley, CA (2005)

- Kowalsky, M.J.: Deformation limit states for circular reinforced concrete bridge columns. *J. Struct. Eng.* **126**(8), 869–878 (2000)
- Liang, Y., Yan, J.L., Cheng, Z.Q., Chen, P., Ren, C.: Time-varying seismic fragility analysis of offshore bridges with continuous rigid-frame girder under main aftershock sequences. *J. Bridg. Eng.* **25**(8), 04020055 (2020)
- Lehman, D.E., Moehle, J.P.: Seismic performance of well-confined concrete bridge columns. PEER 1998/01 (2000)
- Luco, N., Bazzurro, P., Cornell, C.A.: Dynamic Versus Static Computation of the Residual Capacity of a Mainshock-Damaged Building to Withstand an Aftershock. Vancouver, BC, Canada, 15 (2004)
- Mackie, K.R., Stojadinović, B.: Fragility basis for California highway overpass bridge seismic decision making. Pacific Earthquake Engineering Research Center, College of Engineering (2005)
- Mazzoni, S., McKenna, F., Scott, M., Fenves, G.L.: OpenSees Command Language Manual (2006)
- Menegotto, M., Pinto, P.E.: Method of analysis for cyclically loaded RC plane frames including changes in geometry and non-elastic behavior of elements under combined normal force and bending. In: Proceedings of IABSE Symposium on Resistance and Ultimate Deformability of Structures Acted on by Well Defined Repeated Loads, pp. 15–22 (1973)
- Nielson, B.G.: Analytical Fragility Curves for Highway Bridges in Moderate Seismic Zones. Georgia Institute of Technology (2005)
- Padgett, J.E., DesRoches, R.: Retrofitted bridge fragility analysis for typical classes of multispan bridges. *Earthqu. Spectra* **25**(1), 117–141 (2009)
- Padgett, J.E., Nielson, B.G., DesRoches, R.: Selection of optimal intensity measures in probabilistic seismic demand models of highway bridge portfolios. *Earthq. Eng. Struct. Dyn.* **37**(5), 711–725 (2008)
- Park, Y., Ang, A.H.-S.: Mechanistic seismic damage model for reinforced concrete. *J. Struct. Eng.* **111**(4), 722–739 (1985)
- Paulay, T., Priestley, M.J.N.: *Seismic Design of Reinforced Concrete and Masonry Buildings*. Wiley, New York (1992)
- Priestley, M.N., Seible, F., Calvi, G.M.: *Seismic Design and Retrofit of Bridges*. Wiley, Hoboken (1996)
- Scott, M.H., Fenves, G.L.: Plastic hinge integration methods for force-based beam-column elements. *J. Struct. Eng.* **132**(2), 244–252 (2006)
- Shin, M., Kim, B.: Effects of frequency contents of aftershock ground motions on reinforced concrete (RC) bridge columns. *Soil Dyn. Earthq. Eng.* **97**, 48–59 (2017)
- Tesfamariam, S., Goda, K.: Energy-based seismic risk evaluation of tall reinforced concrete building in Vancouver, BC, Canada, under Mw9 megathrust subduction earthquakes and aftershocks. *Front. Built Environ.* **3**, 29 (2017)
- Tesfamariam, S., Goda, K., Mondal, G.: Seismic vulnerability of reinforced concrete frame with unreinforced masonry infill due to main shock-aftershock earthquake sequences. *Earthq. Spectra* **31**(3), 1427–1449 (2015)
- Todorov, B., Billah, A.H.M.M.: Seismic fragility and damage assessment of reinforced concrete bridge pier under long-duration, near-fault, and far-field ground motions. *Structures* **31**, 671–685 (2021)
- Zhang, J., Huo, Y.: Evaluating effectiveness and optimum design of isolation devices for highway bridges using the fragility function method. *Eng. Struct.* **31**(8), 1648–1660 (2009)



# Seismic Analysis of Carbon Fiber Reinforced Polymer Cable Structure Using ETABS

Vaibhav Patel<sup>(✉)</sup> and Hanumant Magarpatil

School of Civil Engineering, Dr. Vishwanath Karad MIT World Peace University, Pune, India

vaibhavpatel221998@gmail.com,  
hanumant.magarpatil@mitwpu.edu.in

**Abstract.** The Indian subcontinent does have a record of tragic seismic events. The Indian plate, which continues slamming into the Asian plate, is really the cause of the high frequency and intensity of earthquakes, with Northeast India being the most at hazardous location. Structures may not resist earthquakes completely, so the objective is to perform better during seismic action. Consequently, Carbon fiber reinforced polymer (CFRP) cables are introduced that can make building safer from the devastating seismic forces. CFRP cables have a high strength-to-weight ratio, are lightweight, and have no corrosion or fatigue issues. In order to resist ground motion during an earthquake event, a new method has been introduced using CFRP cables. Hundreds of CFRP cables were inserted from the rooftop to the ground, on the outer side of the building. In the present work, a comparative study of a midrise G+11 RCC building using Carbon fiber reinforced polymer (CFRP) Cable against X-bracing system. Various earthquake analyses were carried to compare the structures for higher magnitude ground motions. This study shows that CFRP cables have a better dynamic performance and can be used to achieve higher strength and efficiency of the structure.

**Keywords:** CFRP cables · X-bracing system · Cable structure · Seismic analysis · Structural performance

## 1 Introduction

A cable structure is a structure that uses a cable or a set of cables as the visible and main load bearing structural element. When looking back at the history of cable constructions, it is clear that advancements in cable materials have had a significant impact on their growth. Because of the existence of high-strength steel cables, long span cable systems, such as suspension bridges, can be installed. It also allows for the development of modern cable systems with new materials and shapes, such as cable roofs and cable facades.

Carbon Fiber Reinforced Polymer (CFRP) is a material made of nonmetallic composites composed of fibers of carbon reinforced with polymer resin. CFRP includes greater strength, fatigue behavior, corrosion resistance and also light weight. Therefore, CFRP has a big future as a cable and as a replacement for steel cables in cable systems,



which will help it develop in this time frame. A comparative study is done on a mid-rise building which is being proposed by X-Bracing and Carbon Fiber Reinforced Polymer cables for different seismic parameters. Severe earthquake damages the structure with major fatal and economical losses in earthquake prone areas. Therefore response spectrum analysis and time history analysis is done on ordinary rigid frame structure, X-Bracing and the structure with CFRP cables under major earthquake loads.

## 2 Literature Review

CABKOMA Strand Rod was created by Komatsu Seiten Fabric Laboratory in Japan, a new thermoplastic carbon fiber composite. It is light weighted and has higher strength than steel rod. Its first application was designed by Kengo Kuma for use on the façade of three story Komatsu Seiten's head office building. For the project the rods were inserted from the roof top to the ground around the outer side of the building. It is currently used as exhibition, workspace and research facility. And it showed that it demonstrably improved behavior of the building under lateral forces. This results in an airy, organic façade that has a fabric-like aesthetic while still offering the strength to resist ground motion during an earthquake event.

Eshelman presented a study which shows that strand rods provide greater strength with less weight. And also high performance fiber reinforced cementitious composite was tested in order to compare it with the strand rods in which Composite panels add durability and ductility to beam-to-column and beam-to-shear wall connections, in order to strengthen the structure. It was seen that both methods were ease to use, cost effective and have minimal interruption (Eshelman 2019).

Mochida and Imoto developed a carbon fiber reinforced thermoplastic strand rod. Test like cavity ratio test and fiber content, alkali resistance test, tensile strength test, temperature dependency test, weather resistance test etc. were performed on strand rods. It shows that it has a very high strength and can be used in seismic retrofit of the entire building (Mochida et al. 2019).

In this research, Carbon Fiber Reinforced Polymer (CFRP) cable is used as a replacement of the CABKOMA strand rod to make the structure strong enough to resist ground motion using same method.

Liu et al. presents an overview of the use of CFRP cables in cable constructions with a historical review, the state of the art and perspectives for the future. Properties of carbon fibers, the mechanical properties and the structural shapes of CFRP cables are discussed which are included in the paper (Liu et al. 2015).

## 3 Structure Modelling

The ETABS software was used to model and analyze G+11 OMRF RCC frames in order to do a Response spectrum and Time history analysis for the building's seismic performance. Frames are designed optimally as per guidelines of I.S 456:2000, I. S:1893:2000 (Part 1) and I.S 875:1987. The building has a rectangular shaped plan with dimensions 8.6 m \* 28 m with a floor height of 3m situated in seismic zone V in

India on the medium soil type. Three structural models are built to carry analysis on earthquake loads. (i) Rigid frame (ii) Structure with steel X-Bracing frame (iii) Structure with CFRP cables attached around the building.

Structure general information and preliminary design considerations are tabulated in Tables below.

**Table 1.** General parameters of the structure

Sr. no.	Contents	Description
1	Structure type	RCC (OMRF)
2	Number of story	G+11
3	Materials	Concrete (M35) Steel Reinforcement (Fe500)
4	Specific weight of RCC	25 KN/m <sup>3</sup>

**Table 2.** Dimension values of structure

Model	Rigid	X-bracing	CFRP cables
Beam	450 × 300 mm	450 × 300 mm	450 × 300 mm
Column	300 × 450 mm	300 × 450 mm	300 × 450 mm
Slab	150 mm	150 mm	150 mm
Height of each floor	3 m	3 m	3 m
Total height of structure	36.2 m	36.2 m	36.2 m

All the three structure were modelled with the general parameters and dimension values of the structure shown in Table 1 and Table 2.

### 3.1 Rigid Structure

Structure is modelled with a shear wall with the above configurations of the building as mentioned in Table1 and Table 2 (Figs. 1 and 2).

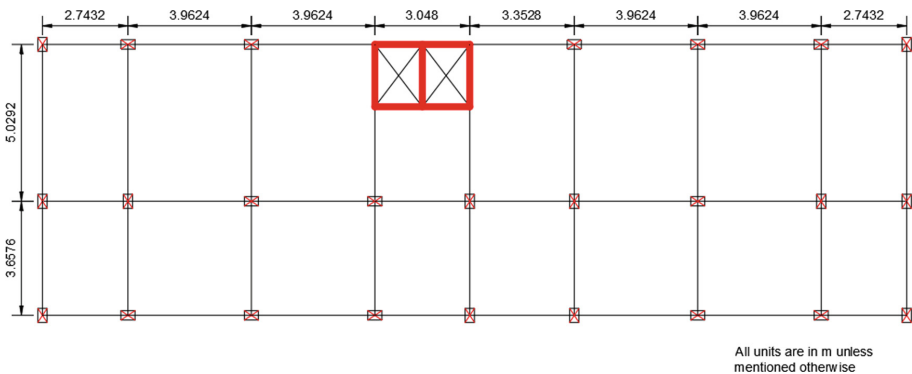


**Fig. 1.** Plan for Rigid body and X-Bracing.

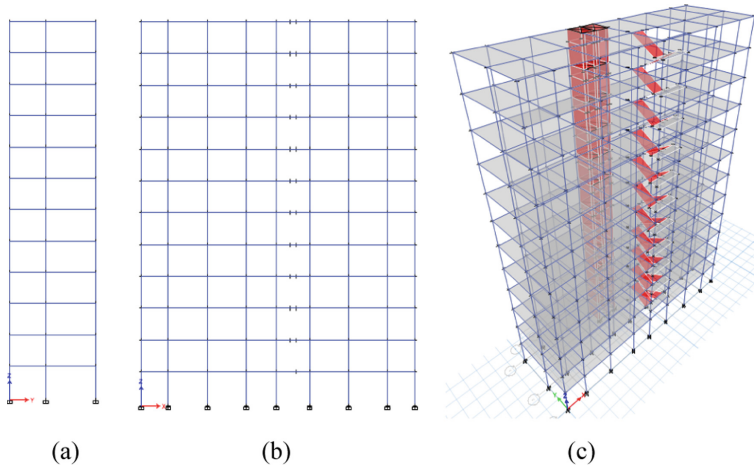


**Fig. 2.** (a) (b) Elevation and (c) 3D model of rigid frame.

### 3.2 Braced Structure

For braced structure Indian Standard Medium Weight Beam is used for steel bracing in the structure which is ISMB 175 in order to build diagonal steel X-bracing system in X-direction of the building on both the sides (Fig. 3).

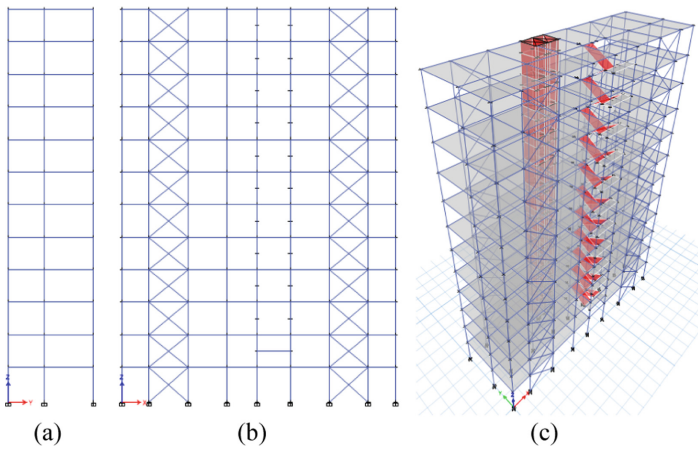


**Fig. 3.** (a) (b) Elevation and (c) 3D model of braced frame.

### 3.3 CFRP Cabled Structure

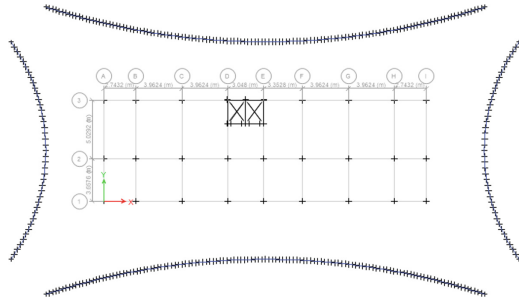


Fig. 4. Plan for CFRP cabled model.

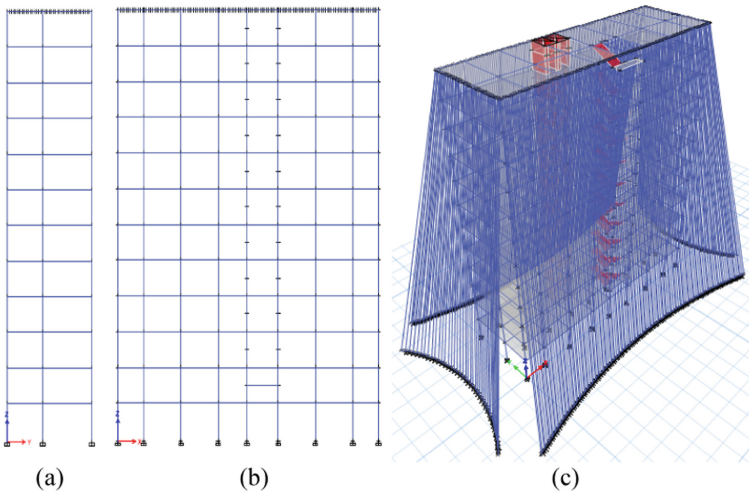


Fig. 5. (a) (b) Elevation and (c) 3D model model of CFRP cabled frame.

For CFRP cabled structure, cables were inserted from the roof top to the ground around the exterior of the building. Around 340 cables are attached around the building. The diameter of the cable is 40 mm and around 4.5 m spacing is provided to pass a truck or vehicle easily into the building (Figs. 4 and 5).

Table 3. Comparing the properties of CFRP cable to steel cable

Material	Steel rod	CFRP cable
$\rho$ – Density ( $\text{kg/m}^3$ )	7850	1500
$\sigma_u$ – Tensile strength (Gpa)	1.5	2.1
$E$ – Modulus of elasticity (Gpa)	160	137
$\sigma_u/(\rho g)$ – Breaking length (km)	23	205

As shown in Table 3, the density and elastic modulus of the steel rod is higher than the CFRP cable while CFRP cable has much higher tensile strength than steel rods. Breaking length is an excellent parameter for demonstrating CFRP cable's high strength and light weight. It is described as the greatest length of a hanging rod which can sustain its very own weight and may be computed using the formula  $\sigma_u/(g)$ , wherein  $g$  is the standard gravity value of  $9.8 \text{ m/s}^2$ . As shown in the table, CFRP cable breaking lengths are much better than steel rod breaking lengths.

## 4 Structural Analysis

The analysis can be performed on the structures or structural material behavior and on the basis of external action. By using IS 1893-2002, earthquake loads and load combinations on the structure is considered for analysis.

Three methods are used to see the Performance of each structure.

- a. Equivalent static method
- b. Response spectrum method
- c. Time history analysis

Equivalent static method depends upon the fundamental period of structure defined by IS Code 1893:2002. Loads given in Table 4 is considered for carrying out the analysis.

**Table 4.** Loading parameters

Sr. no	Contents	Description
1	Impose load	2–3 KN/m <sup>2</sup>
2	Importance factor	1
3	Seismic zone	V
4	Zone factor	0.36
5	Response reduction factor	3

Response spectrum analysis is a linear dynamic method used for determining a structure's maximum response when subjected to ground motion. It defines the base acceleration applied to each mode based on its period. It is carried out using IS: 1893 (Part 1)-2002 (Figs. 6, 7, 8 and Table 5).

**Table 5.** Details of earthquake time histories considered in study

Sr. no	Earthquake details	Recording station name	Epicentral distance (R) in kms
1	Chamoli Earthquake, Uttarakhand, India; 29 <sup>th</sup> March 1999; N20E component	IITR, Gopeshwar	17.3 (NF)
2	Bishop Round valley; United States; 23 <sup>rd</sup> November, 1984; NS component	McGee Creek surface	21.93 (FF)
3	N. Palm Springs; United States; 8 <sup>th</sup> July, 1986; N162E component	Lake Matthews Dike Toe	79.23 (FF)

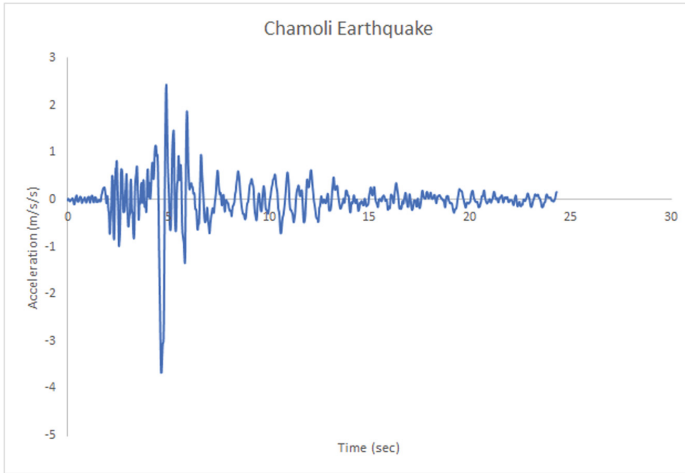


**Fig. 6.** Timeline of Chamoli earthquake.

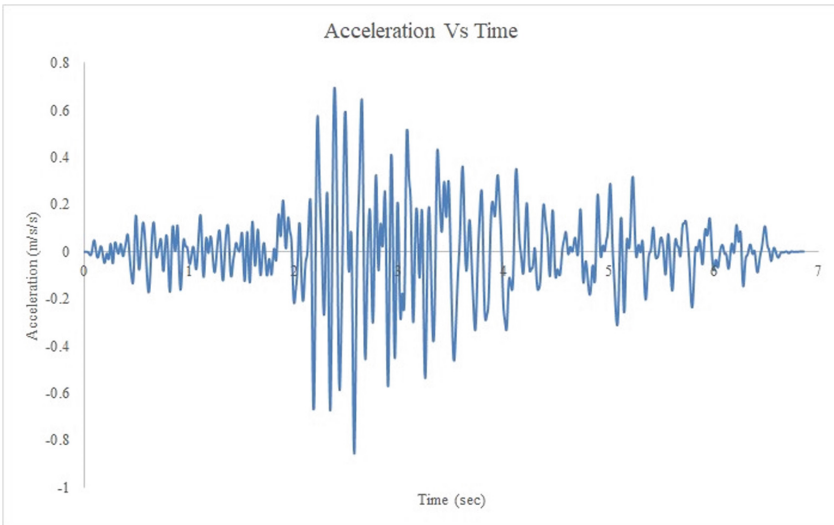


**Fig. 7.** Timeline of Bishop round valley earthquake.

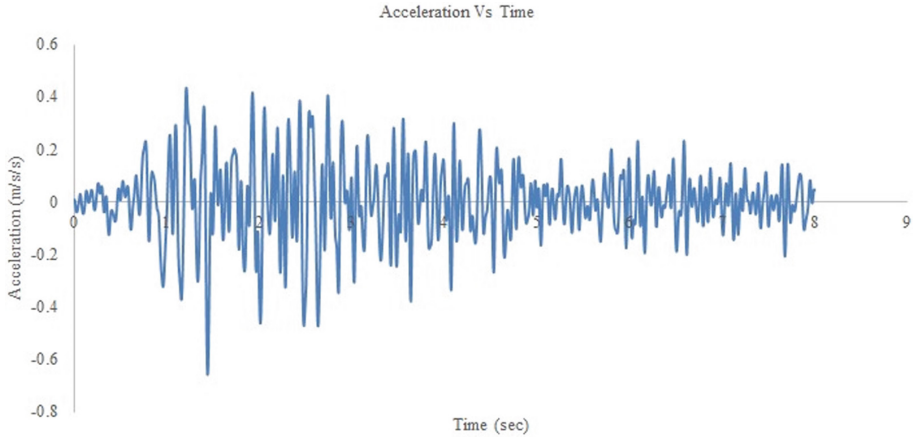


**Fig. 8.** Timeline of N.palm springs earthquake.

Time history analysis is a non-linear dynamic method under the loading which may differ according to specified time function. In this analysis Chamoli earthquake 1999, Bishop round valley earthquake 1984 and N. Palm springs earthquake is taken into consideration.

## 5 Results and Discussion

All the three models were analyzed under Equivalent static method, response spectrum method and time history analysis and are compared with story displacement in both X-direction and Y-direction.

### 5.1 Equivalent Static Method

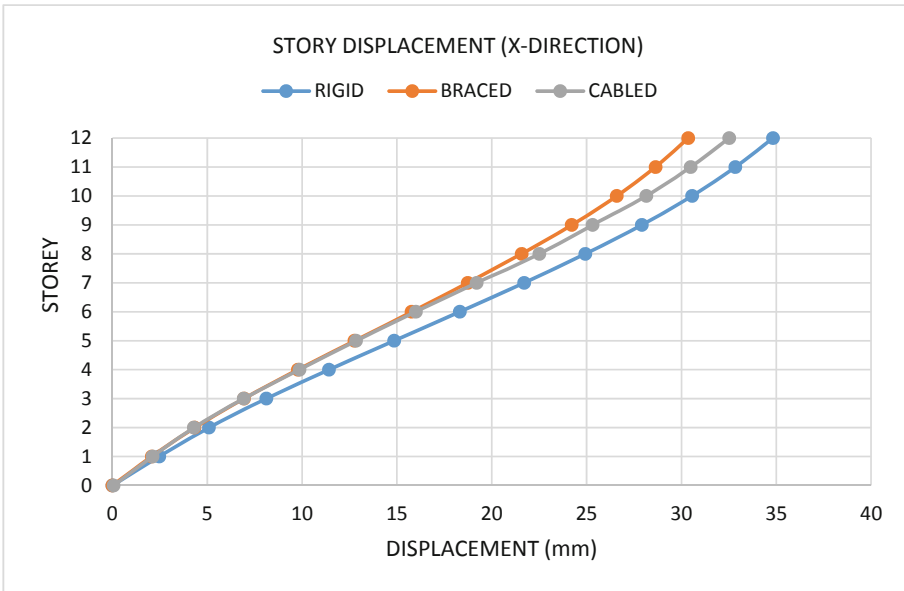


Fig. 9. Comparison of Story displacement in X-direction for Equivalent static method.

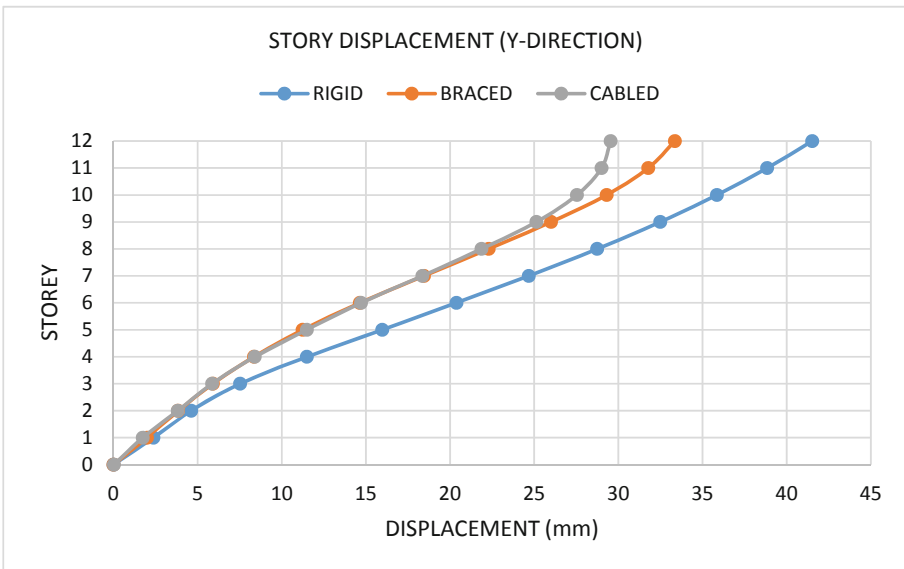


Fig. 10. Comparison of Story displacement in Y-direction for Equivalent static method.

As shown in Fig. 9 and Fig. 10 both braced and cabled structure shows better results than normal rigid structure. Cabled structure performed 28.8% better than rigid structure and 11.45% better than braced structure in Y-direction. But in X-direction braced



structure performed 6.6% better than the cabled structure whereas, cabled structure shows 6.6% decrease in deflection than the rigid structure.

### 5.2 Response Spectrum Analysis

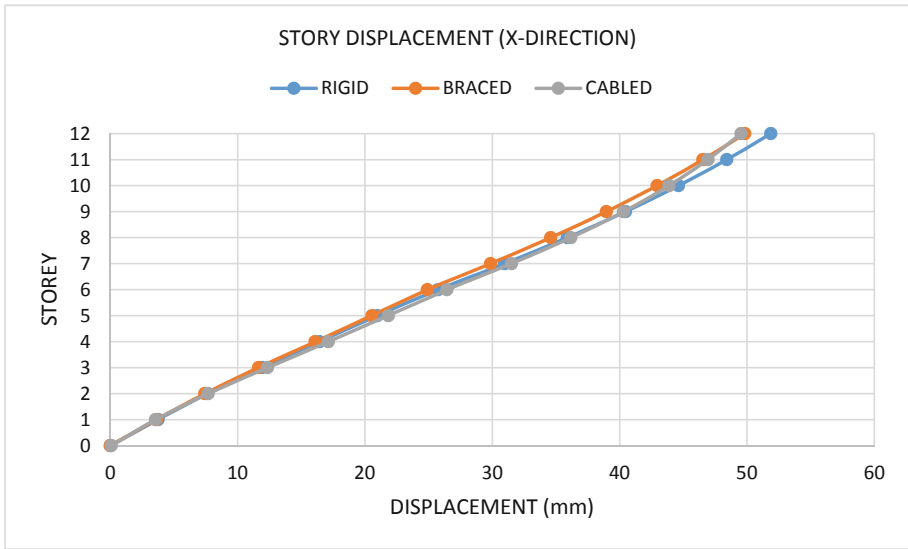


Fig. 11. Comparison of Story displacement in X-direction for Response spectrum method.

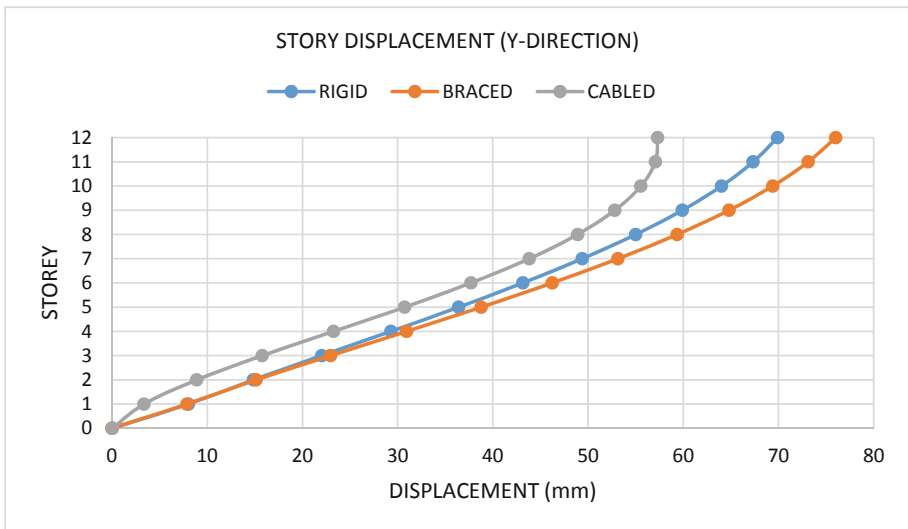


Fig. 12. Comparison of Story displacement in Y-direction for Response spectrum method.

Cabled structure performed pretty well in the response spectrum analysis in X-direction as well as Y-direction. As shown in Fig. 11 all the three structures shows almost similar performance in X-direction but as compared to all the structure cabled structure shows less deflection than both the structures. Cabled structure performed 0.6% better than braced structure and 4.5% better than rigid structure. Whereas in Y-direction braced structure showed poor performance than rigid and cabled structure as shown in Fig. 12. Around 24.4% less deflection is seen in cabled structure than the braced structure and 18% better performance of cabled structure with respect to rigid structure.

### 5.3 Time History Analysis

For Time history analysis, results of all the three earthquake records are compared together and the earthquake with highest issue will be compared with all the three models.

#### 5.3.1 Rigid Model

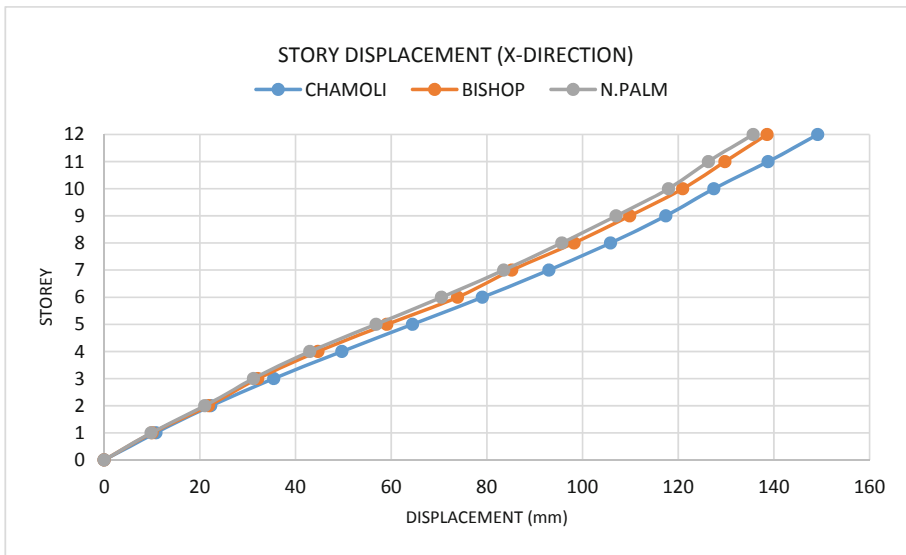
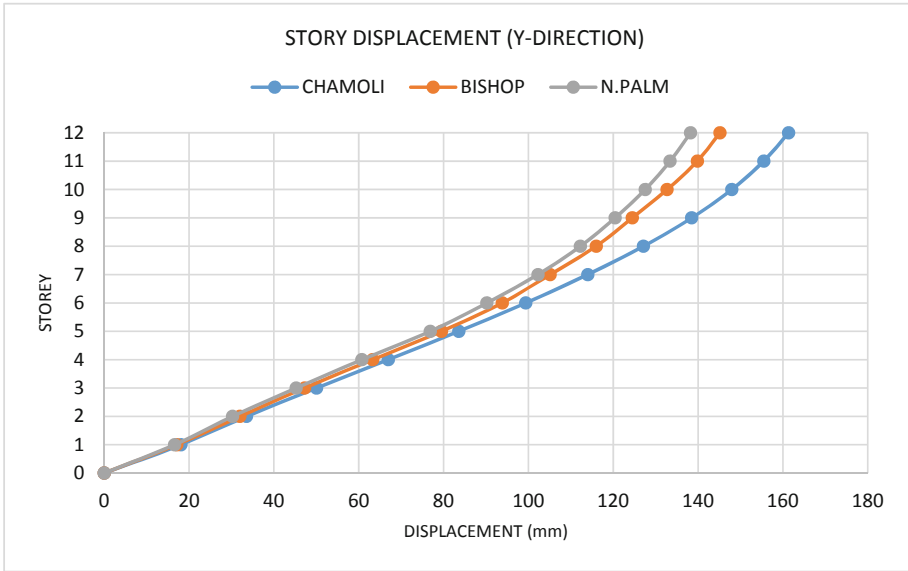


Fig. 13. Comparison of rigid frame in X-direction.



**Fig. 14.** Comparison of rigid frame in Y-direction.

It has been seen from the above Fig. 13, as well as Fig. 14 that while comparing all the three time history records in rigid frame, chamoli earthquake shows the highest displacement in X-direction as well as Y-direction.

### 5.3.2 Braced Model

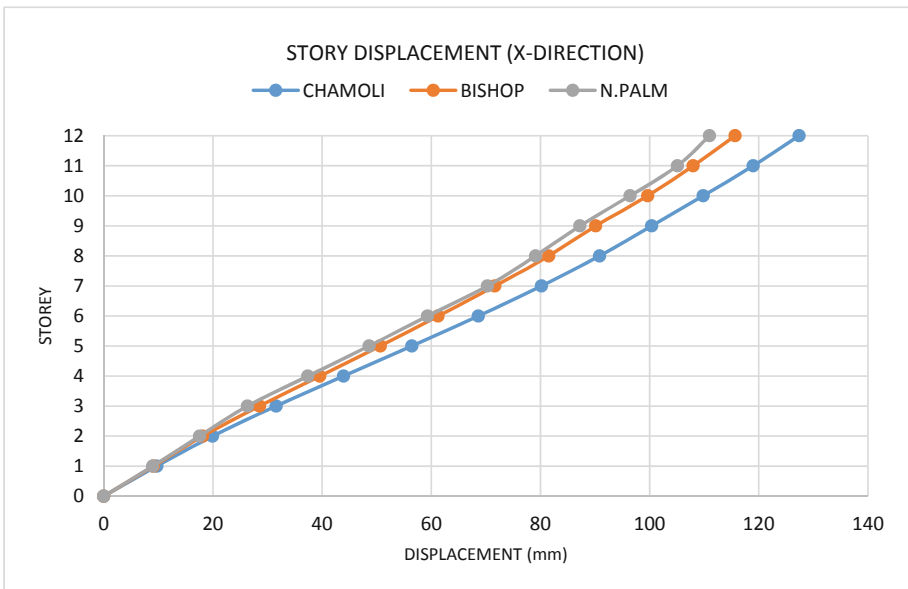


**Fig. 15.** Comparison of braced frame in X-direction.

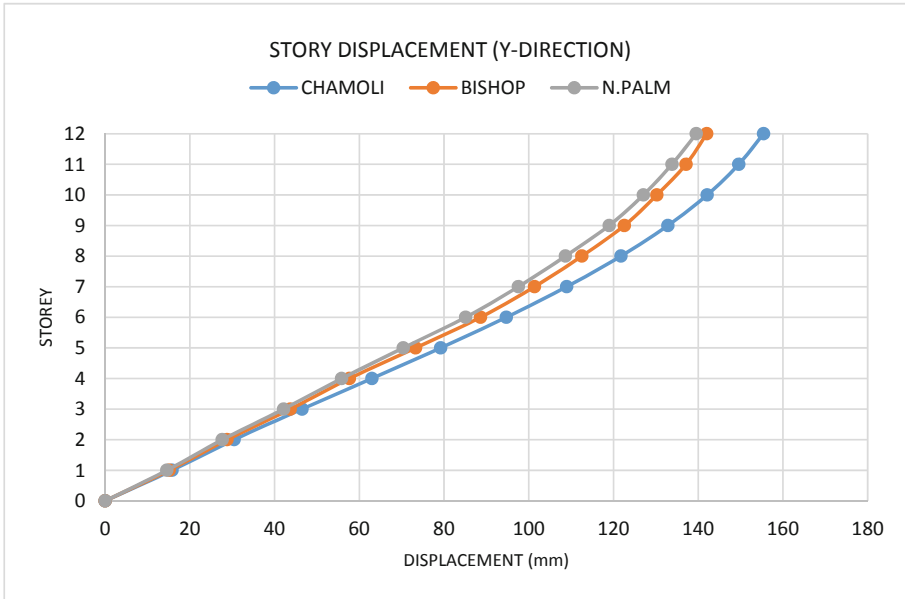


**Fig. 16.** Comparison of braced frame in Y-direction.

In the braced frame, chamoli earthquake shows the highest displacement in both X-direction as well as Y-direction as shown in Fig. 15 and Fig. 16.

### 5.3.3 Cabled Model

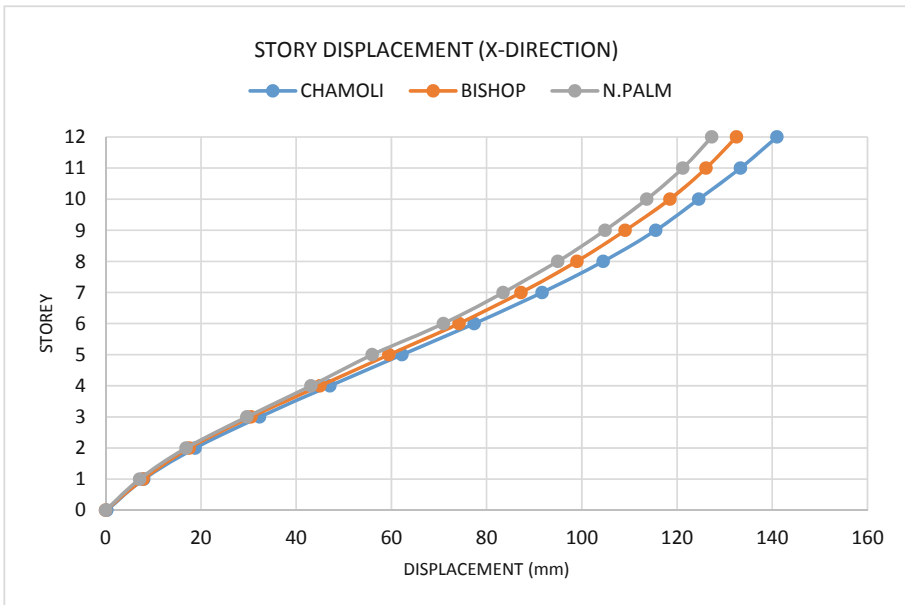


**Fig. 17.** Comparison of cabled frame in X-direction.

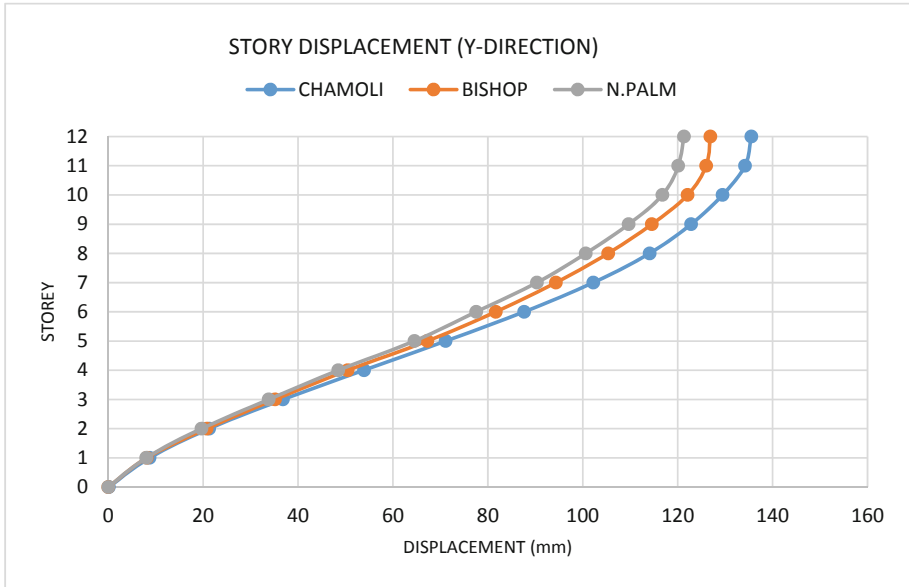


**Fig. 18.** Comparison of cabled frame in Y-direction.

It has been seen from the above Fig. 17. as well as Fig. 18 that while comparing all the three time history records in cabled frame, chamoli earthquake shows the highest displacement in X-direction as well as Y-direction.

### 5.3.4 Story Displacement Compared with all Models

As chamoli earthquake got highest displacement in all the models, it is considered to compare the maximum displacement with rigid structure, braced structure and cabled frame structure.

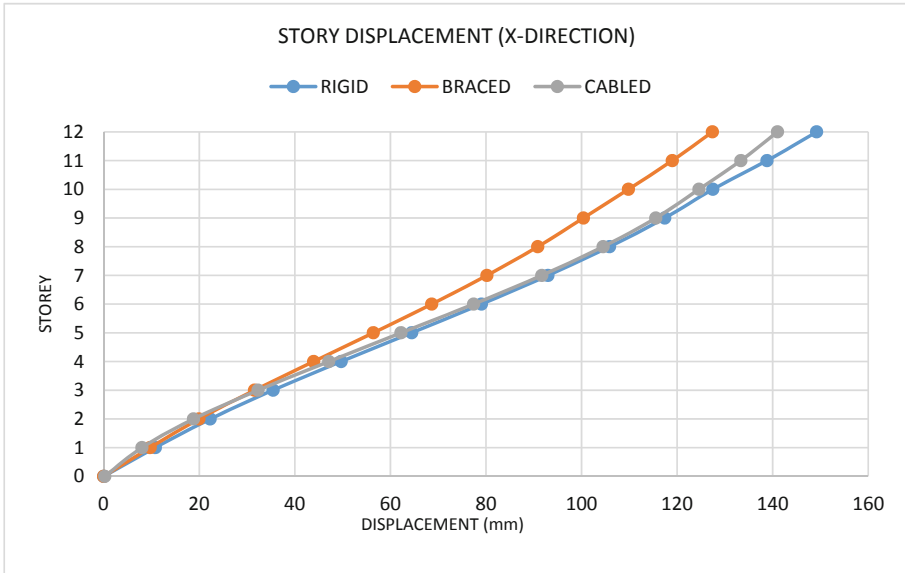


**Fig. 19.** Comparison of Story displacement in X-direction for Time History analysis.

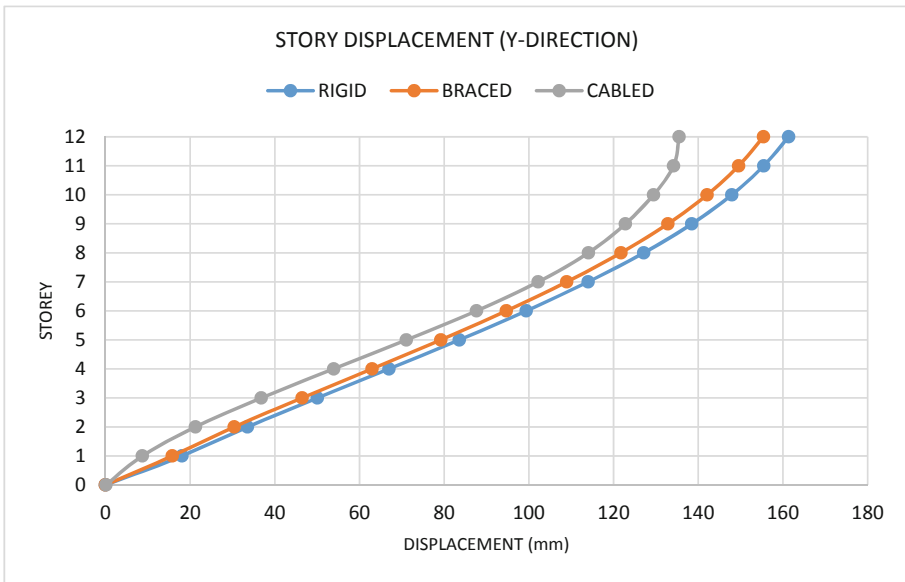


**Fig. 20.** Comparison of Story displacement in Y-direction for Time History analysis.

Cabled structure performed very well with good results in time history analysis. As shown in Fig. 19 cabled structure performed better than rigid structure in X-direction which is 5.49%. While braced structure shows 14% less displacement than rigid

structure. Whereas in Y-direction cabled structure shows 16% less deflection than rigid structure. And 12% better performance than braced structure as shown in Fig. 20.

#### 5.4 Time Period

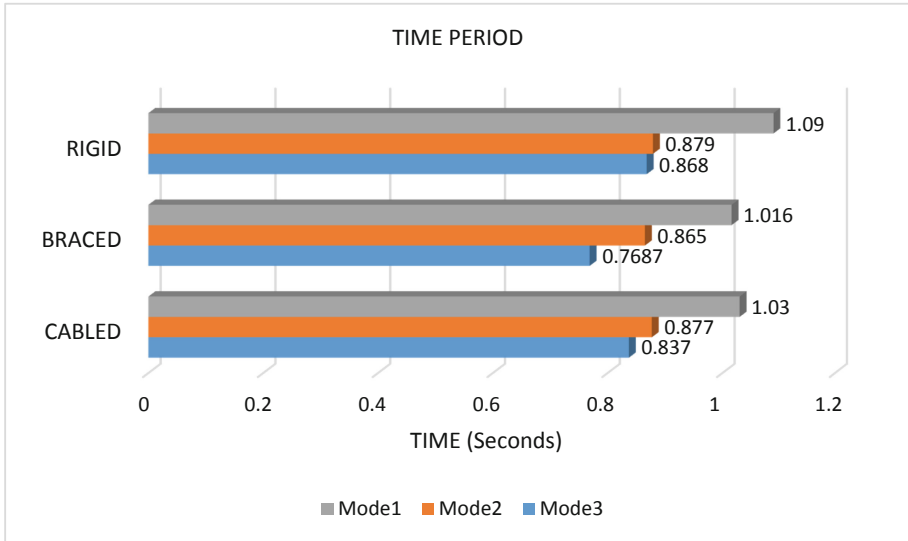


**Fig. 21.** Comparison of time period.

For comparison of time period of the structure first three modes are taken into consideration. In which braced structure and cabled structure showed almost similar results with a difference of 0.014 s as shown in Fig. 21. In other words braced structure performed 1.35% better than cabled structure. Also cabled structure performed 5.5% better compared to rigid structure.

## 6 Conclusion

In this work, Analysis of all the three modelled structure has been carried out. Effect of CFRP cabled frame with steel X-braced frame and rigid frame under earthquake loads was studied, it is concluded that:

- It has been observed that for CFRP cabled structures, the direction in which more cables are positioned, resulted in better output which is Y-direction.
- In cabled structure there is 5% to 28% decrease in story displacement than rigid structure for equivalent static method, response spectrum method and time history analysis.

- In maximum story drift, it has been observed that as the story height increases the story drift keeps decreasing until 11<sup>th</sup> floor and shows better results as compared to braced and rigid structure.
- In time period, the braced structure outperformed the cabled structure by 1.35%.
- Cabled structure comparatively performed better than the other structures. So as a result it can be used to improve the seismic stability of the structure,
- CFRP cables can be used for high strength and efficiency, but they are relatively costly than steel.

## References

- IS 456:2000: Plain and Reinforced concrete – Code of practice. Bureau of Indian Standards, New Delhi
- IS 1893-2002(Part-1): Criteria for Earthquake resistant design of structures. General provisions and buildings, Bureau of Indian Standards, New Delhi
- Eshelman, L.D.P.: Strand rods and high-performance fiber-reinforced cementitious composites: alternative options for seismic retrofit of existing structures. *Eng. Struct.* **111**, 323–332 (2019)
- Santoh, N.: CFCC (carbon FRP cable). *Dev. Civ. Eng.* **42**, 223 (1993)
- Mochida, Y., Imoto, Y.: Development of carbon fiber reinforced thermoplastic strand rod. *Int. J. Geomate* **16**(57), 109–115 (2019)
- Liu, Y., Zwingmann, B., Schlaich, M.: Carbon fiber reinforced polymer for cable structures—a review. *Polymers* **7**(10), 2078–2099 (2015)





# Analysis of Accidental Collision of Blue Whale with Submerged Floating Tunnel

Sahil Rana<sup>(✉)</sup>, M. Abdul Akbar, Rachit Sharma, and Ankush Thakur

Department of Civil Engineering, Dr. B R Ambedkar National Institute of Technology, Punjab, India

{sahilr.sc.19, akbarma}@nitj.ac.in,  
sahilrana3030@gmail.com

**Abstract.** Submerged Floating Tunnel (SFT) is a tunnel that floats in water, supported by its buoyancy acting as a means of connecting countries and continents and if built will become the largest man-made structure underwater. Apart from the complexities and challenges involved in its design and construction, the threat the structure may pose to aquatic life and the disruption of natural habitats and feeding regimes is a serious concern. In this work, a 20 span SFT anchored firmly to the seabed with tethers spaced at 100 m is modelled in ABAQUS/CAE. The model after validation with available results of the impact load of a steel ball is subjected to a load of a Blue whale (with isotropic properties) hitting at speeds of 9 m/s, 7 m/s, 5 m/s, 3 m/s. The 3D geometry of Blue whale is developed in AutoCAD 2017 and imported into ABAQUS 6.14. Parametric studies have been carried out by varying the grades of concrete (M30, M35, M40, M50) for different velocities of the Blue whale. Explicit dynamic analysis is carried out for the determination of Bending stress and deflection developed in the SFT due to the Blue whale. Based on the results obtained from the analysis, conclusions were drawn on the minimum size and grade of concrete of SFT that can withstand a collision.

**Keywords:** Submerged floating tunnel · Blue whale · Aquatic life · Stress analysis · Impact loading · Collision · Finite element analysis · Structural design

## 1 Introduction

Through the advancement of transportation, people are able to travel long distances in a shorter time. Land travel is restricted by geography in many cases and various types of infrastructures, such as bridges and tunnels are designed and constructed to facilitate transportation lines. When these lines are interrupted by the rivers and seas, bridges, undersea tunnels, an immersed tunnel can serve as a solution. The modern approaches are not efficient and economical as well if the ocean disturbs these transportation lines. In these cases, a more useful and economical approach is a Submerged Floating Tunnel (SFT). Submerged Floating Tunnel is also known as the Archimedes Bridge (Xiang and Yang 2017) or Suspended Tunnel or Submerged Floating Tube Bridge (SFTB) as shown in (Fig. 1). It generally consists of tubes, anchoring devices, underwater foundations, and revetment structures (Mazzolani et al. 2010). The SFT has many advantages over conventional bridges and tunnels such as higher efficiency, better

environmental adaptability, all-weather operation, and a comparatively lower construction cost (Zhang et al. 2010).

A Submerged Floating Tunnel is a tunnel that floats in water and is supported by its buoyancy (Lu et al. 2011). It maintains balance and stability by the combined effect of deadweight, buoyancy, and anchoring system. SFT is an underwater channel by which vehicles and trains can move (Østlid 2010). Historical records indicate that Sir James Reed, UK, in 1886 and later Trygve Olsen Dale, Norway in 1924 are the pioneers of this technology who are accredited with the development of the conceptual idea. During the last part of the 1960's, a revival of interest in SFT was marked by the beginning of some research ventures, which gathered momentum in Italy, Japan, and Norway during the years that followed.



**Fig. 1.** Inside view of SFT.

The glamorous concept of SFT first conceptualized as early as the 19<sup>th</sup> century has lagged significantly in its implementation and widespread acceptance by developed countries owing to the many factors underlying this brazen infrastructure. On one hand, persistent ambiguity exists in the SFT life cycle, due to the large demand of investment and the long construction duration as well as the innumerable unforeseen factors underlying it (Xiang et al. 2010). The unknown hazards concealed during project planning, design, construction and working worried engineers and planners. Apart from that, many technical issues, for instance, the reliability of the connection of segments, wave load mechanism, and seismic effects on SFT have still not been addressed. There are still no universally accepted guidelines and requirements for SFT design and construction (Xiang et al. 2010).

SFT is a massive marine structure which once implemented will revolutionize the transportation system, However, on account of the immense structure, it will also have a serious impact on the ecosystem of marine life. This study is carried out to quantify the effect of the collision of aquatic animals with SFT. The collision or strike of large fish with the underwater structure may lead to serious damage to structure or often

results in physical trauma or death of animals (Schoeman et al. 2020). The collision of the small fishes is less reported but the collisions of the large fishes like whales, dolphins, sharks etc. are reported widely throughout the globe. This collision may not be the biggest threat to the underwater structure but, it surely has a bad impact on marine lives.

## 2 Literature Review

### 2.1 Inclination Mooring Angle

Independent studies have shown that the IMA of  $45^\circ$  for mooring lines is the most efficient. As per the study (Lu et al. 2011) carried out with a focus on the slacking phenomenon of tethers on a 100 m deep tunnel, it was concluded that  $45^\circ$  is the ideal orientation among the range of angles considered ( $0^\circ$  to  $45^\circ$ ). As per a different study conducted on a 150 m long SFT (Marina et al. 2015) for IMA of  $30^\circ$ ,  $45^\circ$ , and  $65^\circ$ , minimum slacking and maximum tension was observed with  $45^\circ$  orientation of mooring lines. Thus  $45^\circ$  has emerged as a good starting point for IMA as per multiple researches works.

### 2.2 Influence of Impact Load

Under the influence of impact load, spatial dynamic response analysis was carried out (Xiang and Yang 2017) for an SFT. In this study, the SFT tube is treated as a beam on the elastic foundation (BOEF) with 3 degrees of freedom (horizontal displacement, vertical displacement, and torsion angle). The modal superposition and Runge-Kutta method were used to calculate the spatial displacement response of SFT. The effect of parameters such as BWR, IMA, anchorage stiffness, and hydraulic resistance was studied. Analysis shows that an increase in BWR ratio resulted in an increase in the maximum displacement and natural frequency and it recommends an IMA range between  $45^\circ$  to  $60^\circ$ . Earlier studies (Lu et al. 2011; Marina et al. 2015) have shown that  $45^\circ$  is the most suitable angle for tethers. Hydraulic resistance also has a significant effect on SFT and hence should be considered in the design. The anchor stiffness is found to have an inverse relationship with the maximum displacement of SFT and hydraulic resistance.

### 2.3 Accidental Sudden Breakage of Tethers

Studies have been carried out in which the behavior of SFT has been investigated in the unlikely event of sudden breakage of cables (tethers) (Xiang et al. 2018, 2020). A theoretical approach is proposed (Xiang et al. 2018), in which the analysis of SFT was simplified and the Alternate load Path method (AP method) is adopted to simulate the cable-breakage process. The theoretical model developed was found to be in good agreement with the FEM model. The behavior of SFT under the sudden failure of cable was studied (Xiang et al. 2020) by installing a set of sensors on the SFT. The model was analyzed using ABAQUS and the results were found to be in good agreement with

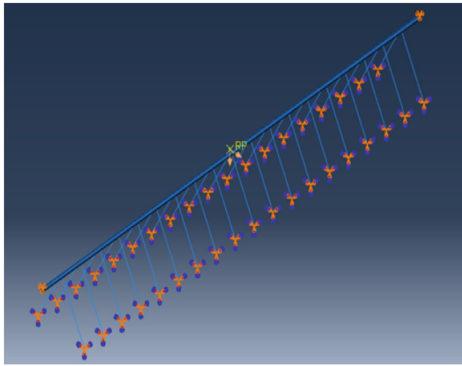
the experimental model. Both studies conclude that the anchor cables neighboring the cable with rupture are the most affected ones. AP method was found to be a suitable method for modeling of SFT vibration effects initiated by cable-loss. Based on the common conclusion that the cables neighbouring the location of cable rupture are the most severely affected, cable failure events can be avoided by providing multiple pairs of anchor-cables.

#### 2.4 Effect of Resonance on SFT

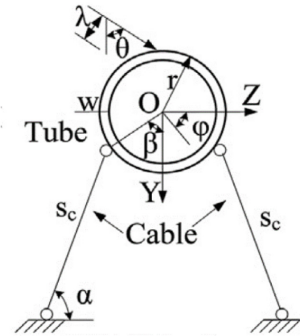
Some studies considering resonance were carried out (Lin et al. 2019; Sun et al. 2020). In these parametric studies, the behavior of tethers was observed when resonance occurs. To analyze the vehicle-tunnel coupled vibration of SFT due to the parametric excitation (Lin et al. 2019), the theoretical model was conceptualized by the Hamilton principle and D'Alembert's principle. The model was solved by the fourth-order Runge-Kutta method. The beam on the elastic foundation (BOEF) model was proposed to verify the results obtained from the theoretical model. Study shows that if the vehicle-tunnel vibration is confined to a smaller region, then its effect can be reduced. The vehicle having less velocity is most affected by the tethers vibration when travelling through the tunnel. Study also suggests the ideal range of gravity-buoyancy ratio (GBR) considering slack risk to lie between 0.75–0.85.

### 3 Numerical Modelling

In this study, a 20 span SFT is fixed at its ends and supported by 19 sets of cables spaced at regular intervals is modelled and detailed Finite element analysis is carried out using ABAQUS 6.14. The spacing of cables is 100 m. Cables are modelled as truss elements. The Finite element model of SFT is shown in (Fig. 2a) (isotropic view). For the validation of the model, the SFT model tube is impacted at the mid-span, with a steel ball of 10 m diameter (Xiang and Yang 2017). The speed of the ball is 5 m/s. The incidence angle is  $45^\circ$  and the eccentric distance of impact point to cross-section centroid is 5 m as shown in (Fig. 2b). The connection between the cable and tube is modelled as a hinge. In order to consider the effect of water on SFT model, the Eulerian domain was modelled and SFT and its components are submerged in it completely. The dimensions of the Eulerian domain are  $500 \times 500$  m and it is filled with water completely to the top. For the validation of model, a convergence study has been carried out. For the convergence study, mesh size was varied from 50 m to 10 m intervals of 10 m and further reduced to 6 m uniformly. Since the part of interest was at the center of 2000 m SFT, adaptive meshing was performed with 6 m mesh size for the 200 m length at the center and 50 m mesh size at other locations. The validation of SFT is done with the horizontal displacement given in the literature (Xiang and Yang 2017) with the 3% error.



(a) Isotropic view



(b) Side view (Xiang and Yang, 2017)

**Fig. 2.** Finite element analysis model of SFT in ABAQUS.

The properties of the SFT used in validation is given in Table 1.

**Table 1.** Parameters of SFT used for validation (Xiang and Yang 2017)

Component	Item	Symbol	Value	Units
Tube	Elasticity modulus	E	$3.55 \times 10^{10}$	$\text{Nm}^{-2}$
	Mass per unit length	$M_0$	$1.1 \times 10^5$	Kg
	Length	L	2000	m
	Outer diameter	D	15	m
	Wall thickness	W	1	m
Cable	Length	$S_c$	231	m
	Diameter	$d_c$	0.347	m
	Elastic modulus	$E_c$	$1.95 \times 10^5$	MPa
	Inclination angle	$\alpha$	$\pi/3$	radians
	Installation angle	$\beta$	$\pi/3$	radians
	Cable interval	L	100	m
Water	Density	$\delta$	1000	$\text{Kgm}^{-3}$

Blue whale is the largest mammal in the sea and the SFT might be an interruption to its natural feeding path. Blue whale is known to generate speeds up to 9 m/s. As the study deals with the accidental collisions of Blue whale with SFT, there is a probability that the Blue whale which is moving at its top speed of 9 m/s may decelerate to lower velocities after seeing the SFT from a distance. Hence considering this, the velocities of Blue whale considered in this study are 3 m/s, 5 m/s, 7 m/s in addition to a maximum speed of 9 m/s.

After validation of model with available results for the impact load of a steel ball the model is subjected to the impact load of a Blue whale assumed to be analytically rigid. The 3D geometry of the Blue whale was initially developed in Google SketchUp

and thereafter converted to an AutoCAD drawing and finally imported in to ABAQUS (Fig. 3). It is assumed that Blue whale is hitting the tube at an angle of  $45^\circ$  as shown in (Fig. 4). Explicit dynamics analysis is carried out for 10 s and the results are obtained. A full-grown Blue whale is considered in this study with its length extending up to 30 m. The exact point of contact of the whale with SFT was determined geometrically as per the hitting point shown in (Fig. 2b) and in the impact analysis using ABAQUS, the velocity of Blue whale is entered in the term of its components along the coordinate axis. The density of the whale is assumed to be  $1040 \text{ kg/m}^3$  and the mass of whale is  $5.01 \times 10^5 \text{ kg}$ , with 35% of its weight is to be considered as added mass for all calculations. The contact between whale and tube is defined for the impact analysis. In order to study the detailed effects of whale on SFT a total of 16 models has been made by varying the grades of concrete and velocities of Blue whale.

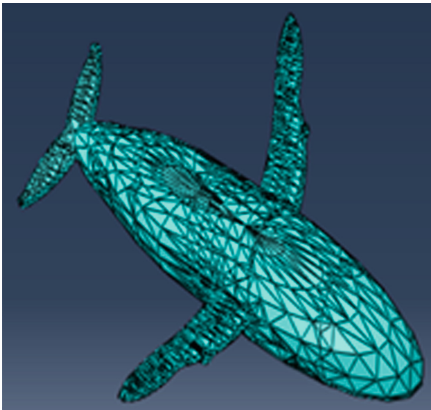


**Fig. 3.** Side view of Blue whale.

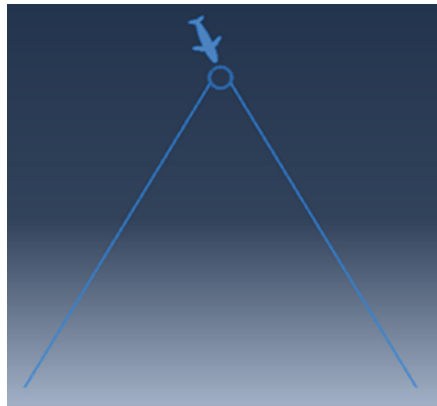


**Fig. 4.** Illustration of whale hitting SFT.

The 16 models considered were the combination of changing the grade of concrete (M50, M40, M35 and M30) along with the change in velocity of the Blue whale (9 m/s, 7 m/s, 5 m/s, 3 m/s).

## 4 Results and Discussion

In this study, a fully grown Blue whale is analyzed for accidental collision with the SFT. By varying the grade of concrete (M50, M40, M35, M30) of the SFT tube, corresponding to the velocities of the whale (9 m/s, 7 m/s, 5 m/s, 3 m/s) the response of SFT is obtained in terms of bending stress, horizontal displacement at the mid-span (which corresponds to maximum values). Further, obtained results are compared with the codal provisions of Indian concrete code (IS 456 : 2000) and obtained results are plotted in a graph, and inferences are obtained. The displacement and bending stress for the 16 models were obtained and were compared with the limits of displacements and

stresses as per IS:456 (2000) to arrive at detailed guidelines on the effect of SFT on Blue whale and vice-versa.

**1. Displacement**

After analysis, the obtained horizontal displacements are plotted in graph (Fig. 5) and compared with the codal provision of Indian concrete code (IS 456 : 2000). According to clause 23.2 (IS 456 : 2000) the maximum allowable deflection for a structure should not normally exceed span/250. Here, in this study the span is 100 m (between cables) and hence the corresponding maximum allowable deflection for the SFT is 400 mm. It is observed through analysis that maximum deflection is observed for a velocity of 7 m/s for each grade of concrete (considered in this study) except for M50. All the maximum displacement corresponding to each grade is shown in Table 2. As expected, the horizontal deflection at mid-span decreases with an increase in the grade of concrete.

**Table 2.** Maximum deflection for each grade.

Grade	M50	M40	M35	M30	Max-displacement IS:456
Displacement (mm)	68.84	76.72	77.69	78.03	400

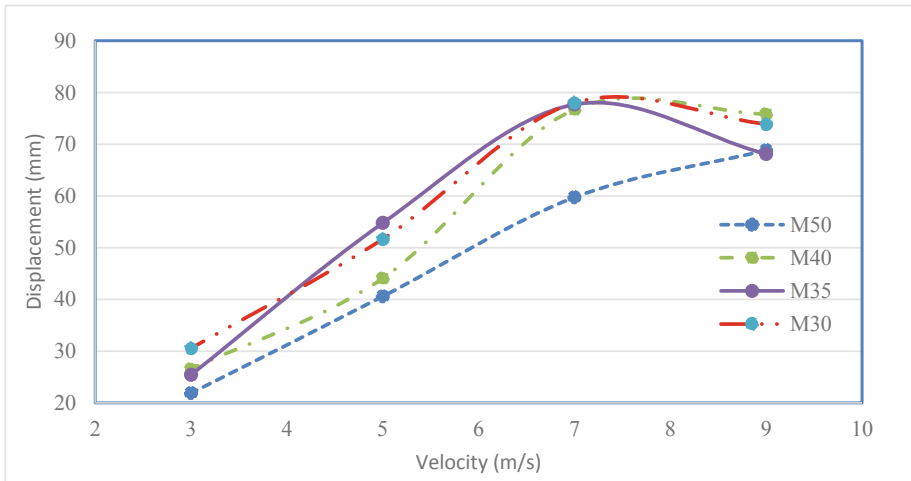


**Fig. 5.** Variation of displacement with velocity.

**2. Bending Stress**

Due to the hitting of Blue whale at the mid-span, the bending stresses are induced in SFT, the 20 span SFT will behave like a 20 span continuous beam with elastic supports (cables) in between. These induced stresses are plotted in the graph shown in (Fig. 6) and the values are compared with (IS 456 : 2000), (Table 2) limits pertaining to a different grade of concrete. It is observed that as we move from high-grade concrete (M50) to low grade (M30) the bending stress increases as expected but all the stresses

are within the specified limit in (IS 456 : 2000). The maximum value of bending stresses is obtained corresponding to 9 m/s velocity. The maximum value of bending stresses and corresponding allowable bending stresses for each grade are shown in Table 3.

**Table 3.** Maximum bending stresses and allowable stresses

Grade	Bending stress (N/mm <sup>2</sup> ) for analysis	Allowable stress (IS:456 2000) (N/mm <sup>2</sup> )
M50	4.47	16
M40	6.12	13
M35	6.509	11.5
M30	6.901	10

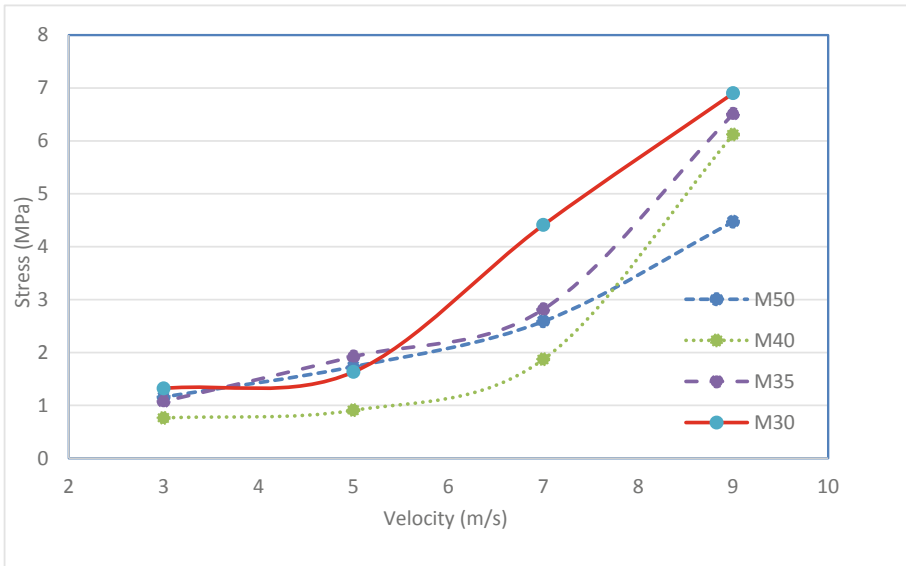


**Fig. 6.** Variation of stresses with velocity.

## 5 Conclusion

This study shows that, although the Blue whale is the world's largest mammal found in the sea, when it will collide with SFT having 15 m diameter and wall thickness of 1m, then it will not lead to any catastrophic damage within the proposed grades of concrete. All the parameters like displacement and bending stress are within the limits stated by the Indian concrete code and hence the structure is safe. As the Blue whale was modelled as analytical rigid further studies are required to quantify the effect of the collisions on the Blue whale considering its actual elastic nature.



## References

- IS 456 : 2000: Plain and Reinforced Concrete - Code of Practice, Bureau of Indian Standards, New Dehli (2000)
- Lin, H., Xiang, Y., Yang, Y.: Vehicle-tunnel coupled vibration analysis of submerged floating tunnel due to tether parametric excitation. *Mar. Struct.* **67**, 102646 (2019). <https://doi.org/10.1016/j.marstruc.2019.102646>
- Lu, W., Ge, F., Wang, L., Wu, X., Hong, Y.: On the slack phenomena and snap force in tethers of submerged floating tunnels under wave conditions. *Mar. Struct.* **24**, 358–376 (2011). <https://doi.org/10.1016/j.marstruc.2011.05.003>
- Marina, D., Wardhana, W., Walujo, R.: Dynamic response analysis on submerged floating tunnel due to hydrodynamic loads. *Procedia Earth Planet. Sci.* **14**, 220–227 (2015). <https://doi.org/10.1016/j.proeps.2015.07.105>
- Mazzolani, F.M., Faggiano, B., Martire, G.: Design aspects of the AB prototype in the Qiandao Lake. *Procedia Eng.* **4**, 21–33 (2010). <https://doi.org/10.1016/j.proeng.2010.08.005>
- Østlid, H.: When is SFT competitive? *Procedia Eng.* **4**, 3–11 (2010). <https://doi.org/10.1016/j.proeng.2010.08.003>
- Schoeman, R.P., Patterson-Abrolat, C., Plön, S.: A global review of vessel collisions with marine animals. *Front. Mar. Sci.* **7**, 1–25 (2020). <https://doi.org/10.3389/fmars.2020.00292>
- Sun, S.-N., Su, Z.-B., Feng, Y.-F., Xu, X.: Parametric vibration analysis of submerged floating tunnel tension legs. *China Ocean Eng.* **34**(1), 131–136 (2020). <https://doi.org/10.1007/s13344-020-0013-9>
- Xiang, Y., Chen, Z., Bai, B., Lin, H., Yang, Y.: Mechanical behaviors and experimental study of submerged floating tunnel subjected to local anchor-cable failure. *Eng. Struct.* **212**, 110521 (2020). <https://doi.org/10.1016/j.engstruct.2020.110521>
- Xiang, Y., Chen, Z., Yang, Y., Lin, H., Zhu, S.: Dynamic response analysis for submerged floating tunnel with anchor-cables subjected to sudden cable breakage. *Mar. Struct.* **59**, 179–191 (2018). <https://doi.org/10.1016/j.marstruc.2018.01.009>
- Xiang, Y., Liu, C., Zhang, K., Wu, Q.: Procedia engineering risk analysis and management of submerged floating tunnel and its application. *Procedia Eng.* **4**, 107–116 (2010). <https://doi.org/10.1016/j.proeng.2010.08.013>
- Xiang, Y., Yang, Y.: Spatial dynamic response of submerged floating tunnel under impact load. *Mar. Struct.* **53**, 20–31 (2017). <https://doi.org/10.1016/j.marstruc.2016.12.009>
- Zhang, K., Xiang, Y., Du, Y.: Research on tubular segment design of submerged floating tunnel. *Procedia Eng.* **4**, 199–205 (2010). <https://doi.org/10.1016/j.proeng.2010.08.023>



# Structural Audit of Mutha River Bridge Using Displacement Sensors

Husain Anandwala and Hanamant Magarpatil<sup>(✉)</sup>

School of Civil Engineering, Dr. Vishwanath Karad MIT World Peace  
University, Pune, India

hanamant.magarpatil@mitwpu.edu.in

**Abstract.** The purpose of this research is to undertake a structural audit of the Mutha river bridge, which is located near Warje, Pune, on the Mumbai-Bangalore National Highway. In this study, a number of audit methodologies are combined to provide an overview of the bridge condition. To begin, a visual assessment of the bridge construction is conducted to identify any obvious defects in the members that require more care. The study considers traditional procedures such as the Rebound Hammer Test and the Ultrasonic Pulse Velocity Test. In the bridge structure, there are only a few ways for measuring deck displacement. As a result, an institutionally designed displacement sensors equipment is utilized in this investigation to determine the displacement in the deck of the bridge construction. Following a visual inspection, it was agreed to do a displacement test on all of the bridge decks. During the visual assessment, all of the deck beams were found to be damaged in some way. An 18.5 tons two-axle truck was driven across the bridge and displacement data were recorded at the same time for real-time loading. Then, compare the resulting displacement reading to the AASTHO-LFRD standard. The general condition of the bridge was assessed after completing the structural audit and evaluating the data, and the major areas that needed repairs were noted.

**Keywords:** Structural audit · Mutha river bridge · Displacement sensors

## 1 Introduction

Bridges are structures built over rivers, roads, and other obstacles that carry roads, railways, paths, etc. In India there are many old bridges which were constructed during the British Rule and are even used today. Loads on bridges act very differently than any other structure. They are used every day and throughout the day. They are exposed to the atmospheric conditions and continuous traffic which can cause the deterioration of the bridge structure. Bridges are exposed to fatigue loading as the loads acting on the structure varies continuously throughout the day. It can be very high during the day time and very low during night which can cause deterioration of the structure.

Structural Auditing of a structure is normally done in a span of three to five years, which depends upon the guideline established by the authorities. Bridge auditing has gained importance during recent years after few accidents on old bridges took place. For the safety of the people, it's very important to regularly audit a bridge structure.

The method of auditing for building and a bridge are not totally same even if they are of RCC. As the components in a bridge and a building are not same. The first and the most important step in audit of any structure is visual inspection.

Following the visual inspection, further tests are carried out as appropriate based on the findings. During the visual examination, the bridge members judged to be crucial are subjected to a Rebound Hammer test and an Ultrasonic Pulse Velocity test. It was also found out during the inspection that most of the decks showed exposed reinforcement and corrosion was seen in them so sensor test was considered to check the displacement of the decks. The bridge undertaken for the study is Mutha River Bridge which is situated on the Mutha river on Mumbai-Bangalore National Highway near Warje, Pune. It is situated on the lane from Bangalore towards Mumbai. The bridge has a span of 174.15 m. it has total of 9 decks, 8 piers and 2 abutments. Length of each deck is 19.35 m. Width of the bridge is 12 m. Length of each pier is 9.65 m and the width is 1.85 m.

Permission required for the audit work was taken from the National Highways Authority of India (NHAI) department. And according to the NHAI officials, plans for bridge structure were not available. The sensors can be used to get the displacement of the decks under different loading conditions. In this study the sensors were used to check the displacement of the individual decks under the constant loading condition. Normally this analysis is done using software's such as ETABS where a model is prepared and then the loads are applied but, in this study, an onsite method is used to check the condition of the decks.

## 2 Literature Review

Gromicko and Shepard (2006) discussed the methods for visually inspecting concrete in this document. Concrete and the problems that inspectors may see can be affected by many factors. The properties of concrete's constituent ingredients, as well as how its hardness, strength, and the attributes of its surface, are all affected by a variety of factors. Inspectors benefit from able to pinpoint the cracking source because it allows them to establish if the situation that generated the cracking has stabilised, making it less possible to cause new cracks or stimulate the increase of existing fissures. Cracks, such as those created by concrete shrinkages, are low fissures caused by force that allow condition to reset rapidly and does not cause structure issue. Others, such as those generated by changes in volume of soil, are the result of long-term factors that impact concrete. Long-term structural difficulties may arise as a result of this long-term instability. Detailed procedures to visually inspect concrete are explain in the document.

Indian Railway Institute of Civil Engineering (2014) the guidebook was created to assist field engineers in checking the health of critical bridges on a regular basis, as required by the Indian Railways Bridge Manual (IRBM). This version includes numerous novel NDT testing procedures that were not included in the original edition. Because our current inspection method is insufficient to detect internal faults in structures, non-destructive testing of bridges has taken on significant importance in the current environment. With recent bridge failures in India and other nations, objective bridge inspection has become essential. Indian Railway Bridge Manual (IRBM) calls

for an independent body to conduct periodic health monitoring of Very Important Bridges, which includes monitoring of corrosion, deterioration of materials, system damages, and retrofitting, among other things. All of this can be accomplished with the use of appropriate NDT techniques. Because the work will be done by a third party, it is important that the engineer has a thorough understanding of testing procedure, as engineer could be asked to watch the working on site. NDT tests for concrete, steel, and masonry bridges are described in depth, along with their procedures.

The study of Lasisi et al. (2018) looks at the use of non-destructive testing as a tool for observing structural performance of concrete constructions. The examination was divided into four phases, the first of which comprised evaluating concrete strength on cube specimens using destructive and non-destructive techniques. The second phase of the investigation used a rebound hammer and an ultrasonic pulse velocity metre to analyse the site for a dual engineering theatre at the University of Lagos Faculty of Engineering. The final phase involved establishing a relation between calibrated strengths and ultrasonic pulse velocity with their associated compressive strengths values on cube and value collected from present structures using a linear regression analysis model with MATLAB. Ultrasonic pulse velocity test appeared to be ideal for analysing concrete member strengths than rebound hammer at first, but additional research revealed that second was appropriate for early age concrete while the first was better suitable for ageing concrete. As a result, in this project, a hybrid approach is proposed.

Mahadik and Jaiswal (2014) aims to raise awareness among civil engineers, inhabitants, and building owners on the importance of conducting a structural audit on existing concrete structures. The aim of structural audit is to prevent accidents and save valuable human life by maintaining and repairing existing structures that are more than 30 years old. Because of its low cost, ease of manufacture, and wide range of applications, concrete is frequently utilized as a construction material. The building sector is more concerned than ever before with enhancing social, economic, and environmental sustainability characteristics. The structural audit must adhere to auditing standards, non-destructive testing procedures, and code requirements. Structural auditing will aid in the timely implementation of maintenance and repair work, resulting in the building's longevity and occupant safety. Structural diagnosis is a large, significant, and high-risk task that involves people's lives. Periodic structural audits of buildings by experienced specialists are required and recommended, and quick action should be taken in response to the audit report's recommendations. Repairs and restorations are always successful when they are based on full information, right diagnosis, and in-depth studies of building problems, competent repair procedures, and finally socio-economic factors. Effective auditing extends the life of a structure and prevents it from deteriorating, resulting in its long-term viability.

Raikwad and MagarPatil (2020) aims to undertake a structural auditing of Sadhu Vaswani Bridge, it is a Railway Over Bridge in Pune. Also, to validate the displacement sensor test developed at the university as a credible testing for structural audit of bridge deck. This study took into account traditional auditing procedures. There are few ways for testing decks displacement, and the issue has been addressed here. The unique aspect of study is that deck displacements of the chosen bridge is determined using institutionally designed displacement sensors. These sensors have never been utilised previously, and there are no on-site methods for measuring deck deflections in real

time. The decks were subjected to displacement testing. Displacement sensors were used to test the key decks that had been identified during the Visual Inspections. The displacement values were taken simultaneously when load was passed over bridge surface. The deflection of the deck under a consistent rolling force was determined using this displacement value. The displacements acquired were then checked against the standard criteria. Following the foregoing tests, the general condition of the bridge was established, as well as the key areas that needed to be repaired.

### 3 Methodology

#### 3.1 Visual Inspection

The first and the most important step to be considered in auditing of a structure is visual inspection. By using this method, we can check the condition of the structure. Drawings of the structure can be studied if they are not available can be prepared. Safety of the structure is needed to be checked if not safe the critical sections are to be marked for further testing. Changes or alterations in the structure are also checked by analyzing the drawings.

Because the bridge is located on the national highway, due to heavy traffic, it was necessary to pay attention for personal safety when visually inspecting the bridge during peak hours. It is easy to enter under the bridge from both ends. There is a straight road at one end and from other end it was required to walk down from a sloping ground. Since all bridge components are easily accessible, it is easier to carry all test instruments on site and perform all tests on selected components.

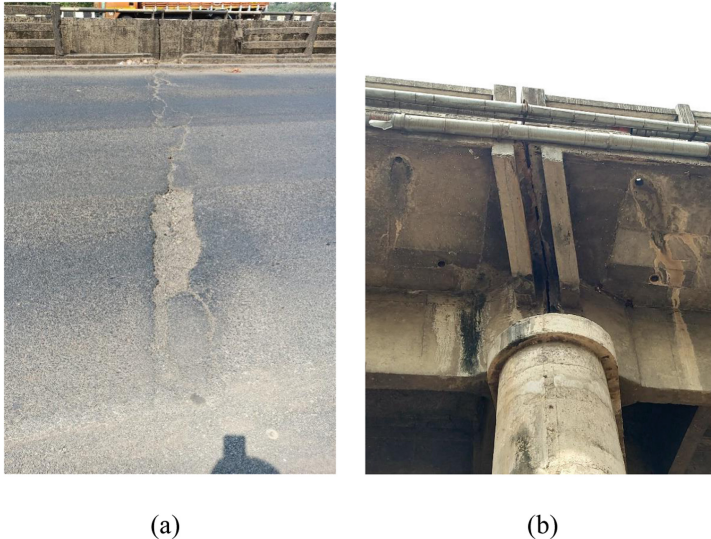


**Fig. 1.** Expansion joints filled with bitumen material causing seepage.

While conducting visual inspection, it was observed that there are many horizontal and vertical cracks present in the piers of the bridge. Most of the deck girders had exposed reinforcement and the reinforcements had started to corrode. Following critical sections were selected for further testing.

Pier Numbers. -1, 2, 3, 4, 6, 7, 8, 9.

Abutment No.- 1, 2.

Deck Numbers. - 1, 2, 3, 4, 5, 6, 7, 8, 9.

Expansion joints were filled with bitumen material to close the gaps in the joints. The improper work done to close the expansion joints is cause water seepage through it below on the piers. As seen from the Fig. 1, same type of bitumen filling is observed in all the expansion joints. Due to the seepage of water on the decks and piers algae growth was observed.

Horizontal and Vertical Cracks were observed on the piers surfaces as seen in the Fig. 2. Concrete from the surface of the piers has started to deteriorate in many places. It was even observed that the quality of concrete was not satisfactory according to the present specifications. Random mixture of sand was seen in the concrete used in the piers and which can be easily scraped of using a spatula. Concrete railing on the bridge for the side walk was observed to be damaged in many places.



**Fig. 2.** Horizontal and vertical cracks in the piers.



**Fig. 3.** Surface damage on the piers.





**Fig. 4.** Damage to girder on deck 4.



**Fig. 5.** Damage to girder on deck 6.

Cracks were observed in every deck girder and the concrete cover had started to come off. As seen in Figs. 4 and 5, the concrete cover of the girder has come off and the reinforcements are totally exposed. Corrosion was also observed in the reinforcement. Repairing work was also observed to be done on the piers where plaster was applied to fill up the horizontal and vertical cracks. Pier number 5, being surrounded by water, was observed from some distance, horizontal and vertical cracks were seen and concrete deterioration was also observed.

After observing damage to the deck girder, a large amount of vibrations was also felt when standing on the bridge deck. So, a deflection test on the decks using sensors was decided to be conducted. During the visual inspection, all factors need to be considered when selecting key sections for further testing, and what tests are required.

### 3.2 Deck Displacement Test

The test chosen to find out the condition of the bridge decks is Deck displacement test. There are three components in the whole setup of the test-

1. Displacement Sensor.
2. Recording Instrument.
3. Laptop for getting the results.

The experimental equipment was developed in the institutional laboratory by the writers. These sensors can measure displacement occurring on site and can give real time results. The sensor measures displacement in millimeters, and its sensitivity is two decimal places.

As shown in Fig. 6, the displacement sensors are small black components. In each sensor, the recorder will record in one direction, which will be its main direction. The direction is engraved on them. Sensors record readings in all three axes i.e., X, Y and Z and it can measure Acceleration, Displacement and Velocity. The sensors are to

be placed at the center of the bridge decks and displacement reading will be shown in the Y direction when a two-axel truck having weight of 18.5 ton is moved over the bridge deck.



Fig. 6. Displacement sensors position.

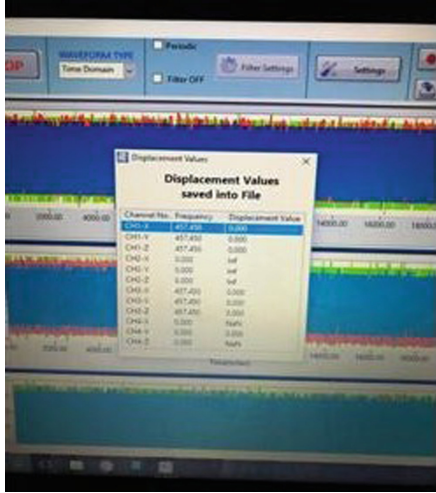


Fig. 7. Zero displacement when no load is passed.

The instrument shown in Fig. 8 is the recording instrument. The whole apparatus works on external power supply. It has four connection points, from where you can use wires to connect the sensor. Laptop is to be connected to the device using the connecting cord in the main port which is in front of the device. The recording device records the values obtained from the sensors and sends them to the laptop so that the user can evaluate readings such as acceleration, velocity and displacement. The graphs of displacement, acceleration and velocity readings can be viewed on laptop screen where they are shown in real time. Figure 9 shows the result screen on the laptop when the instrument is setup. Only the displacement data was used for study and was shown on the Y direction.



Fig. 8. Recording device connected to the sensors using wires.

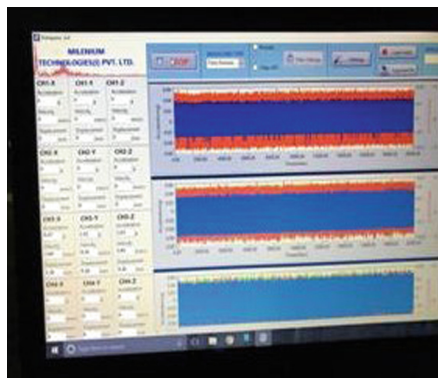


Fig. 9. Laptop screen showing the readings.



All the decks were considered for the sensor test as all deck girders showed cracks and concrete deterioration. The sensor was placed in the center of the bridge deck, and the apparatus was installed together. For reference, a zero-load reading was taken. As predicted, the laptop displayed zero readings of acceleration, velocity, and displacement, as illustrated in Fig. 9. When the setup was installed and connected, a two-axle truck was passed over the deck to measure the real time deflection readings. The channel in which the sensor was connected showed the displacement reading other showed zero readings as no sensors were connected. The software used on the laptop to get the readings from the recording device is “KAMPANA”. The sensors were placed on the ground and held in position by using the double-sided tape. The sensor was connected to the recording device using a wire, which was connected to the channel of the device. A USB wire was connected to the laptop from the device to access the readings. A UPS was used on the bridge to power the whole setup. Once the equipment was in place and running the “KAMPANA” software on the laptop was opened. Vehicle was signaled to move once the application was running. The option “record log” was clicked to record the readings of displacement which can be analyzed later. It was required to be careful that no other vehicle passes over the bridge at the same time. By not allowing any other vehicle we could make sure that the displacement was not occurring because of any other additional load. The readings of deck displacement obtained are mentioned in the Result chapter.

## 4 Analysis and Design

### 4.1 Rebound Hammer Test

Rebound hammer test was conducted on Pier number 1, 2, 3, 4, 6, 7 and 8 and two abutments. Pier number 5 was not accessible due to river water around so it was not considered for the test. The rebound hammer test reading was obtained at a height of one meter over the ground level. A total of 21 readings were obtained at the same height for this test. The equivalent compressive strength was determined by taking the average of these values and utilizing the compressive strength versus rebound number graph. Before taking the readings, the surface was levelled with a grinding stone.

**Table 1.** Rebound hammer test readings

Sr. no.	Abutment 1	Pier 1	Pier 2	Pier 3	Pier 4	Pier 6	Pier 7	Pier 8	Abutment 2
1	45	34	32	26	24	25	27	42	41
2	44	38	30	25	32	24	26	45	50
3	40	30	28	28	34	26	27	46	26
4	45	44	36	34	28	27	31	40	28
5	38	34	32	25	30	27	26	41	43
6	46	33	32	26	30	20	26	30	38
7	44	30	35	30	30	25	38	40	42
8	40	32	32	32	28	23	28	34	28
9	44	28	28	32	30	21	37	28	30

(continued)

**Table 1.** (continued)

Sr. no.	Abutment 1	Pier 1	Pier 2	Pier 3	Pier 4	Pier 6	Pier 7	Pier 8	Abutment 2
10	36	26	34	33	33	32	26	30	29
11	30	26	28	30	40	30	24	38	31
12	32	32	42	34	34	26	28	28	36
13	45	32	33	30	30	26	27	32	32
14	30	28	28	34	32	28	29	31	27
15	38	26	26	35	37	27	26	34	37
16	36	38	25	33	29	32	24	28	33
17	45	34	34	34	37	28	38	25	37
18	40	30	30	38	29	24	32	28	35
19	36	32	32	27	33	25	24	27	33
20	46	26	35	30	31	27	26	28	35
21	43	34	36	27	30	26	33	34	32
Average	40.1428	31.7619	31.8095	30.6190	31.4761	26.1428	28.7142	33.7619	34.4285

A Total of 21 readings were noted down at each location (as per IS 13322 Part 2). Readings all around the piers and on whole length of abutment was taken so that all the sides are duly tested. Test procedure was followed as per the IS code. During the visual inspection of the bridge, a visual inspection was conducted and the critical sections for the test were selected. The Rebound Hammer number obtained are shown in Table 1 above.

After recording all the rebound numbers obtained from the test, the graph of the relationship between rebound numbers and compressive strength was used to obtain the compressive strength of the component. Value from all faces is averaged as shown in Table 1 and then compressive strength is obtained which is shown in the Results chapter.

## 4.2 Ultrasonic Pulse Velocity Test

The second test carried out is Ultrasonic Pulse Velocity Test. The components selected for the test are pier number 1, 2, 3, 4, 6, 7, 8 and abutment 1 and 2. As pier 5 was surrounded by river water it was not considered for the test. Similarly, to the rebound hammer test, a total of 21 measurements at a height of 1 m were taken around the pier and along the whole length of the abutment and averaged. Then the average velocity in km/sec from the table was checked against the table given in IS 13322 Part 1. According to the velocity obtained the table gives difference between the quality of concrete. Same procedure used for the ultrasonic pulse velocity test was obtained here. A grinder stone was used to smooth the surface of pier and abutment. Petroleum jelly was used to cover the transducers to remove the air gap between it and the concrete surface which can cause fluctuations in the readings. The table below lists the readings obtained from the test. Readings at a height of one meter around the entire pier were taken, and attention was given to avoid the area covered by steel bars for testing. Table 2 shows average velocity readings obtained from the test from pier 1, 2, 3, 4, 6, 7, 8 and abutment 1 and 2.

**Table 2.** UPV test velocity of piers and columns

Sr. no.	Element	Time (in Micro sec.)		Velocity (km/s)	
		L = 350 mm	L = 750 mm	L = 350 mm	L = 750 mm
1	Abutment 1	165	324	2.121212	2.314815
2	Pier 1	147	340	2.380952	2.205882
3	Pier 2	137	310	2.554745	2.419355
4	Pier 3	134	229	2.611940	3.275109
5	Pier 4	95	218	3.684211	3.440367
6	Pier 6	145	264	2.413793	2.840909
7	Pier 7	145	250	2.413793	3.000000
8	Pier 8	130	255	2.692308	2.941176
9	Abutment 2	127	245	2.755906	3.061224

The rebound hammer test and the ultrasonic pulse velocity test are combined to compare the rebound number and the ultrasonic velocity to obtain the quality of concrete. If the rebound number shows good compressive strength and the quality of concrete is good then the concrete can be considered as safe. When the concrete quality is seen as medium then proper care must be taken to compare the readings but if the concrete quality seen as doubtful or poor then no comparison must be made and the concrete must be considered to be repaired using proper repair techniques. IS 13322 Part 1 and IS 13322 Part 2 were studied to perform Rebound Hammer and Ultrasonic Pulse Velocity Test.

The quality of the concrete compared to the velocity obtained is compared from the quality table in IS 13322 Part 1 and is shown in the Results chapter.

## 5 Results and Discussions

The maximum displacement of the deck as referred from AASTHO-IFRD section on deck displacement is given by Eq. (1) and (2) (LRFD Bridge Design Manual 2017).

$$\Delta = L/800 \quad (1)$$

For Bridge without sidewalk and,

$$\Delta = L/1000 \quad (2)$$

For Bridge with sidewalk.

where, L = Total span of the bridge.

It was observed during visual inspection that the bridge does have a side walk thus L/1000 formula is to be considered. Also, during the visual inspection, when standing on the bridge, heavy vehicles will feel a lot of vibration when they cross the bridge. As most of the bridge deck girders were having some cracks with concrete deterioration and reinforcement where also exposed. Some amounts of Vibration were felt on every

deck so test was to be conducted on all the decks. Vibration on the deck is structurally unsafe because it will cause the concrete in the girders to further deteriorate and expose more steel bars. Table 3 below shows the displacement readings of the deck 1, 2, 3, 4, 5, 6, 7, 8 and 9 as all were selected for testing.

$$\Delta = L/1000 \tag{3}$$

where, L = Total span of the bridge  
 L = 174.15 m

$$\begin{aligned} \Delta &= 174.15/1000 \\ \Delta &= 0.17415 \text{ m} \\ \Delta &= 0.5713 \text{ ft} \end{aligned}$$

Thus, the displacement of the decks obtained from the test should be not more than 0.17415 m or 174.15 mm or 0.5713 ft.

From Table 3 below we get the maximum value of displacement as 125.21 mm or 0.12521 m. Since this value and other displacement value that we get are less than the value obtained from AASTHO-IFRD formula, thus we can conclude that the decks are safe. The deflection readings show that severe damage to the bridge has not yet occurred. But due to further vibrations in the decks and removal of the concrete cover from the girders which is exposing and corroding the reinforcement can increase the deck deflections in the future and make the bridge unsafe. Bearings were seen to be damaged below the bridge decks, so it could further increase the vibrations. Proper decks treatment is required, bearings should be installed and the girder are to repaired as early as possible before further damage to the decks. There is already seen some amount of gap in the expansion joints and the vibrations may lead to further increase in the gap, causing unbalanced load distribution to the piers. Moreover, the penetration of water into internal components will cause corrosion, which may cause serious problems in the future, which will be more financially difficult and long-term process as compared with the current situation.

**Table 3.** Displacement readings

Sr. no.	Deck no.	Deck displacement (mm)
1	1	41.94
2	2	52.64
3	3	73.37
4	4	108.36
5	5	98.76
6	6	125.21
7	7	107.31
8	8	96.86
9	9	82.11

After getting proper results from this test, we can say that this test can be used on site to get real time deflection of the bridge decks. As a result, this test may be used to inspect bridge decks or any other component that requires displacement testing. The compressive strength of the piers and abutments are mentioned in the Table 4. The average of all 21 readings was taken. The compressive strength of all components is determined from the graph of rebound hammer vs compressive strength and presented in the Table.

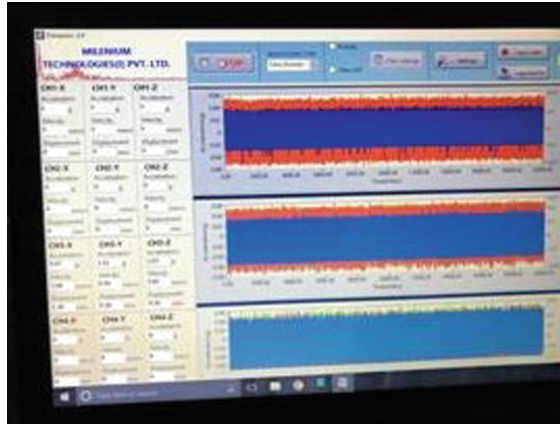


**Fig. 10.** Displacement reading of deck 6

Abutments show better compressive strength than the piers. As abutment 1 has compressive strength of 34.60 MPa, which is highest among all. Pier 6 shows the lowest at 15.59 MPa. This can be due to inconsistency of the materials used during the construction, as it was concluded during the visual inspection that the concrete used for construction is not up to the specifications. Random sand materials were seen in the concrete. The surface concrete in many places was seen to be deteriorating which is to be looked after immediately. The ultrasonic pulse velocity test velocity results were compared to the quality table in IS 13322 Part-1, and Table 5 shows the quality of each abutment and pier.

**Table 4.** Rebound hammer test results

Sr. no.	Member	Average	Strength (N/mm <sup>2</sup> )
1	Abutment 1	40.14286	34.60
2	Pier 1	31.76191	22.92
3	Pier 2	31.80952	23.00
4	Pier 3	30.61905	21.20
5	Pier 4	31.47619	22.42
6	Pier 6	26.14286	15.59
7	Pier 7	28.71429	18.35
8	Pier 8	33.76191	25.26
9	Abutment 2	34.42857	26.34

**Table 5.** UPV test concrete quality

Sr. no.	Element	Time (in Micro sec.)		Remark	
		L = 350 mm	L = 750 mm	L = 350 mm	L = 750 mm
1	Abutment 1	165	324	165	324
2	Pier 1	147	340	147	340
3	Pier 2	137	310	137	310
4	Pier 3	134	229	134	229
5	Pier 4	95	218	95	218
6	Pier 6	145	264	145	264
7	Pier 7	145	250	145	250
8	Pier 8	130	255	130	255
9	Abutment 2	127	245	127	245

Piers and abutments showing very low velocity means that there is no longer a homogeneity of materials, and there are many internal cracks or discontinuities in the members. As seen during the visual inspection that most of the piers and abutments were observed to have many horizontal and vertical cracks which may be showing very low velocity in the above test. Readings were taken on all faces of the piers and abutments. It was observed that when the quality of concrete was shown as doubtful the value of rebound hammer for the same was also low so a correlation can be made between both the test to analyze the results. Thus, from the Table 4 and Table 5, we can conclude that abutment 1 and 2 show good compressive strength and the velocity obtained from the pulse velocity test is also satisfactory. So, it can be concluded the condition of the abutments is good only surface treatment is required. Where as in pier numbers 3 and 4 show low compressive strength of the concrete but the velocity test shows results from Medium to Good. So, it can be said that the piers have lost its surface hardness but the homogeneity of the element is still maintained.

Further pier numbers 1, 2, 6, 7 and 8 show very low compressive strength and the quality of concrete found from the pulse velocity test is also from doubtful to medium. This confirms that the surface hardness and the strength of the elements is reduced. The inside of the columns is damaged, cracked and lost homogeneity. Many of these piers have shown some chunks of concrete to have been removed from its surface. Proper maintenance repair of these elements is required to be done. Thus, by using this combined test we can recognize the condition of the piers and abutments and also by conducting the tests it can be verified.

## 6 Conclusion

We may conclude that the bridge is in workable condition based on the results of the tests performed above. The outcomes of the testing were not entirely satisfactory. Many of the above-mentioned key areas required to be examined as soon as feasible. In addition, correct maintenance procedures must be utilized to improve the bridge's safety and lifespan. Because the bridge is located on a major route, a large volume of

traffic passes over it every day, it is critical to begin repairs as soon as possible to ensure the safety of those who use it. The primary goal of this research was to employ an institutionally designed displacement sensor to conduct a bridge structure audit. Following the positive results of the testing, it can be concluded that the test may be utilized on site to get real-time displacement readings of bridge parts. The entire test gear is quite compact and can be carried in a small suitcase. Because the equipment was powered by a UPS, provided a continuous power source is controlled on site, the equipment can be permanently installed. So, by installing it full-time real time data of whole day can be obtained. Obtaining real-time data is critical, and this sensor displacement approach can help with that. This approach may be added to the list of techniques for monitoring the structural health of bridges and decks.

Normally audit work is done every three to five years on every bridge, by using this method the results of acceleration, velocity and displacement can be obtained in a very short period of time. This setup can be installed on those critical bridges whose life span is about to end or is in critical condition. By doing this the critical bridges can be kept under observation. Being under observation serious damage can be caught and disasters can be avoided. As the main aim of doing structural audit is to avoid disasters and save human life. This method can be further developed by using the acceleration and velocity data obtained using the sensors. The sensor was placed at the mid span of the decks in this study. If the sensors are placed under the deck surface more accurate and precise readings can be obtained. And further development can be made to this method to get real time data directly by using a wireless less device into the office. So, by doing this it won't be necessary to go on the site every time and thus time and efforts to go on site can be saved.

## References

- Bureau of Indian Standard: Non-Destructive testing of Concrete-Methods of Test, Part 2- Rebound Hammer. IS 13311 (Part: 2) (1992)
- Bureau of Indian Standard: Non-Destructive testing of Concrete-Methods of Test, Part 1- Ultrasonic Pulse Velocity. IS 13311 (Part: 1) (1992)
- Gromicko, N., Shepard, K.: Visual inspection of concrete. *Int. Assoc. Certif. Home Insp.* **4**( 3), 125–127 (2006). <http://www.nachi.org/visual-inspection-concrete.html>
- Indian Railway Institute of Civil Engineering: Non Destructive Testing of Bridges, October 2014
- Lasisi, A., Sadiq, O.: Combined use of ultrasonic pulse velocity and rebound hammer for structural health monitoring of reinforced concrete structures. December (2018). <https://doi.org/10.13140/RG.2.2.10379.75040>
- LRFD Bridge Design Manual (2017)
- Mahadik, B., Jaiswal, M.H.: Structural audit of buildings. *Int. J. Civil Eng. Res.* **5**(4), 411–416 (2014)
- Raikwad, M., MagarPatil, H.R.: Structural audit of Sadhu Vaswani Pul using institutionally developed displacement sensors. *Int. J. Innov. Technol. Expl. Eng.* **9**(9), 387–391 (2020)



# Analysis and Cost Comparison of Framed Structure Using Different Building Materials

Jinka Lakshmi Narayana, Gutti Nikhil Vamsi,  
Boddu Venkata Sai Prakash, and P. Bhuvaneshwari<sup>(✉)</sup>

School of Civil Engineering, SASTRA Deemed University,  
Thanjavur 613 401, India  
bhuvaneshwari@civil.sastra.edu

**Abstract.** In the present study, the cost comparison of framed structures using different building materials subjected to seismic analysis was carried out. G+6 storey framed structure of 18 m high was analyzed for 72 different types of seismic parameters (2 types of support conditions -fixed, pinned; 3 types of building materials -concrete, steel, and composite; 3 types of soils -hard, medium, soft; 4 types of earthquake zones -Zone-II to zone-IV) using STAAD.Pro CONNECT V22. The comparison shows that the framed structure with pinned support condition showed a 50% reduction in base shear for composite and steel as building materials. Whereas, in the case of concrete, the base shear was found to be the same irrespective of the support conditions. Since the material cost plays a major role in construction projects, the total cost of material utilized for all the 72 combinations was calculated. The comparison shows that the framed structures with fixed support were about 20% costlier than the pinned structure, using composite building material. Whereas the difference was negligible when concrete was used as a building material.

**Keywords:** Response spectrum analysis · Schedule of rates · Parallel flange beams · Optimal building material

## 1 Introduction

The compressive strength of concrete helps to withstand the heavy gravity loads which are offered by the frame, whereas steel structures provide sufficient ductility to the structure, which is beneficial in resisting dynamic loads like earthquakes and wind. Instead of using reinforced concrete (RCC) in all site conditions, it is suggested to prefer the best-suited material for the site or even integrate more than one and make a composite structure or built-up section. Despite many advantages, it is very difficult to find residential steel or steel-concrete composite structure in India.

Savadi and Hosur (2019) carried out the comparative study of RCC, steel, and composite structures for G+2 industrial building in earthquake zone-3 by using the equivalent static method of analysis in STAAD.Pro V8i. It was observed that the cost of the composite structure was less than that of the RCC and steel structures and concluded that composite structures were more suitable for multi-storeyed constructions. Shah and Pajgade (2013) concentrated on analysis of RCC and composite G+15



structure which was situated in earthquake zone-IV along with a wind speed of 39 m/s. It was observed that the weight of the composite structure was quite less when compared to the RCC structure, due to which the foundation cost was decreased significantly. This study concluded that composite structures were preferred for high-rise constructions. Ghabussi *et al.* (2020) studied the improvement in the seismic performance of portal frame structures with steel curved dampers. The study focused on using five different steel curved dampers (SCD) systems in studying the structural behavior of steel portal frames. It was found that among all five dampers, the maximum energy dissipation and frame strength were achieved with 60° damper and 30° damper in the mono-pitch portal frame and pitched roof symmetric portal frame respectively.

Chintakrindi *et al.* (2020) worked on the analysis and design of a multi-storey building with a single column using STAAD.Pro and explained the suitability of the software for analysis. Gagandeep (2020) has carried out the time and cost comparison of reinforced cement concrete and steel structure. Response Spectrum analysis of 3D model of building with ETABS has been carried out and various parameters like time period, deflection, storey drift, base shear etc. were studied. It was observed that lateral forces acting on the RCC structures were much more than steel and the steel structures were found to be less susceptible to seismic action.

Lian *et al.* (2020) concentrated on the experimental and numerical study of seismic performance of high-strength steel-framed structures (SFTS). The high-strength steel fabricated steel framed-tube structures along with bolted web-connected replaceable shear links (HS-FTS-RSL) were proposed to improve the ductility and energy dissipation capacities of traditional steel framed-tube structures. It was proved that good ductility and energy dissipation capacity were achieved using a bolted web-connected replaceable shear link with a back-to-back double-channel section. Limbare and Dode (2018) studied the performance of reinforced concrete framed structures and steel-concrete composite structures, subjected to static and dynamic loading. The different materials were used for G+20 storey building which was situated in earthquake zone-2. It was reported that the displacement of the composite structure was 20.93% more than RCC and the axial force in the composite structure was 20.48% lesser when compared to RCC. Muffassir and Kalurkar (2016) carried out wind analysis of multi-storey RCC and the composite structure for different plan configurations under the effect of wind using ETABS. It was observed that the U-shape buildings were vulnerable in wind prone zone due to large displacement and less stiffness. It was reported that the composite structures were performing well under wind loads than that of RCC. Surender *et al.* (2020) considered a general commercial G+8 apartment at Hyderabad, Telangana along with wind load, earthquake, and gravity loads as per Indian standards and adopted the design as per IS:456-2000 in ETABS and STAAD.Pro. It was concluded that both the software ended with similar results. Ali and Bhalchandra (2015) worked on the seismic analysis of RCC and steel-concrete composite structures and carried out the cost comparison with different support conditions. It was observed that the self-weight of RCC frames was more than that of the composite frames. The study concluded that the composite constructions are best suited for high-rise buildings. Past literature depicts that there is a scope of increase in the structural performance by choosing appropriate building material for constructions.

In the current study, symmetric framed structures are to be analyzed under different seismic conditions. The base shear, storey drift, and cost are to be compared for framed structure using 3 building materials (concrete, steel, steel-concrete composite) under 2 support conditions (fixed and pinned), 3 types of soil (hard, medium, and soft), and 4 seismic zones (zone 2, zone 3, zone 4 and zone 5). Parametric analysis is to be carried out for 72 models to arrive at appropriate conclusions.

## 2 Methodology

The analysis and cost comparison of framed structures using different building materials were carried out. G+6 storey framed structure of 18 m high was analysed for 72 different types of seismic parameters (2 types of support conditions-fixed and pinned; 3 types of building materials -concrete, steel, and composite; 3 types of soils-hard, medium and soft; 4 types of earthquake zones -Zone-II to zone-IV). The analysis was achieved through the licensed version of STAAD.Pro CONNECT V22. IS 456-2000 and IS 800-2007 design codes are referred for concrete and steel design respectively. IS 1893 (Part-III) was referred for earthquake analysis.

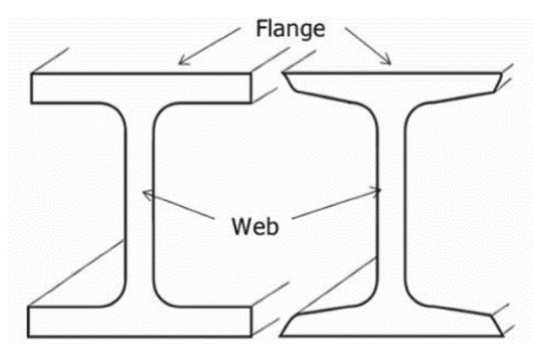


**Fig. 1.** Parallel flange beams and Tapered flange beams.

M35 grade concrete and Fe415 Grade steel had been used adopted for RCC and steel structures respectively. The parallel flange beams of yield strength  $250 \text{ N/mm}^2$  were used. The parallel flange beams, unlike the Tapered flange beams, contain the flanges perfectly parallel to the horizontal plane as shown in Fig. 1. As per suggestions offered by INSDAG, these beams reduce the steel requirement by 10–25% and make the structure more economical. The composite structure was made using concrete columns and steel beams with the grades mentioned above. Figure 2 depicts the flow chart for the work carried out.

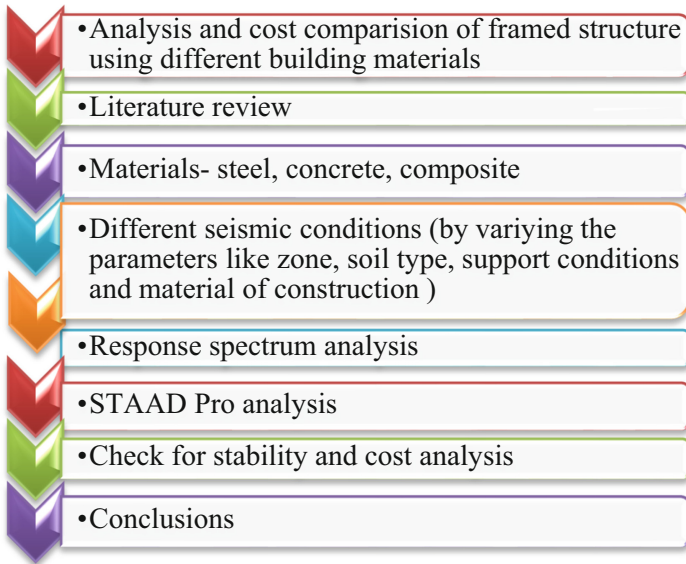


**Fig. 2.** Flow chart for seismic analysis.

### 3 Materials and Cost Analysis

Steel, concrete, steel-concrete composite structures were utilized. The unit costs as per Standard schedule of rates were mentioned in Table 1.

**Table 1.** Standard unit cost

Material	Cost per unit
Concrete	3300 ₹/m <sup>3</sup>
Reinforcement steel	38.5 ₹/kg
Structural steel	43.5 ₹/kg

## 4 Seismic Analysis

### 4.1 Modelling

The nomenclature for each model was as per data shown in Table 2. The first part represents the type of analysis namely, Response spectrum analysis abbreviated to RSA. The second part represents building material. It can be “COMP” abbreviated for composite, “CONC” abbreviated for concrete, and “STEEL” for steel models. The third part represents the support condition. “P” for pinned support and “F” for fixed support. The fourth part represents soil type -“S” for soft soil, “M” for medium soil, and “H” for hard soil. The fifth part represents the earthquake zone -Zone-II, III, IV, and V. The nomenclature of individual models is displayed in Tables 3, 4, and 5.

**Table 2.** Different parts of the nomenclature of a model

Type of analysis	Building material	Support	Soil type	Zone
RSA	COMP, CONC, STEEL	P, F	H, M, S	II, III, IV, V

- RSA- Response spectrum analysis.
- COMP- Composite, CONC- Concrete, STEEL- Steel.
- P- Pinned, F- Fixed.
- H- Hard Soil, M- Medium Soil, S- Soft Soil.

**Table 3.** Composite models for analysis

S. no.	Nomenclature	S. no.	Nomenclature
1	RSA_COMP_FH2	13	RSA_COMP_PH2
2	RSA_COMP_FH3	14	RSA_COMP_PH3
3	RSA_COMP_FH4	15	RSA_COMP_PH4
4	RSA_COMP_FH5	16	RSA_COMP_PH5
5	RSA_COMP_FM2	17	RSA_COMP_PM2
6	RSA_COMP_FM3	18	RSA_COMP_PM3
7	RSA_COMP_FM4	19	RSA_COMP_PM4
8	RSA_COMP_FM5	20	RSA_COMP_PM5
9	RSA_COMP_FS2	21	RSA_COMP_PS2
10	RSA_COMP_FS3	22	RSA_COMP_PS3
11	RSA_COMP_FS4	23	RSA_COMP_PS4
12	RSA_COMP_FS5	24	RSA_COMP_PS5

**Table 4.** Concrete models for analysis

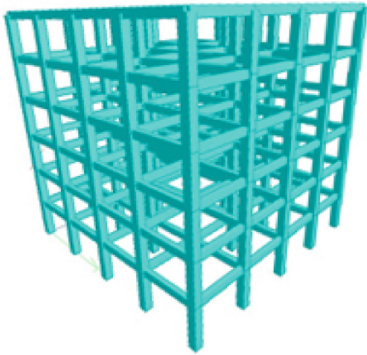
S. no.	Nomenclature	S. no.	Nomenclature
25	RSA_CONC_FH2	37	RSA_CONC_PH2
26	RSA_CONC_FH3	38	RSA_CONC_PH3
27	RSA_CONC_FH4	39	RSA_CONC_PH4
28	RSA_CONC_FH5	40	RSA_CONC_PH5
29	RSA_CONC_FM2	41	RSA_CONC_PM2
30	RSA_CONC_FM3	42	RSA_CONC_PM3
31	RSA_CONC_FM4	43	RSA_CONC_PM4
32	RSA_CONC_FM5	44	RSA_CONC_PM5
33	RSA_CONC_FS2	45	RSA_CONC_PS2
34	RSA_CONC_FS3	46	RSA_CONC_PS3
35	RSA_CONC_FS4	47	RSA_CONC_PS4
36	RSA_CONC_FS5	48	RSA_CONC_PS5

**Table 5.** Steel models for analysis

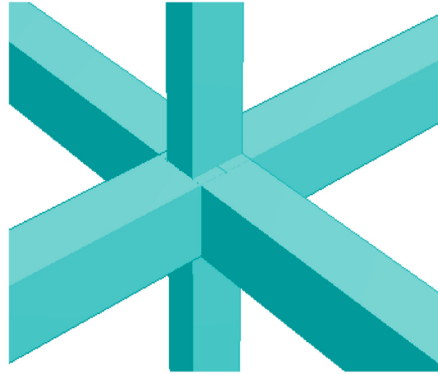
S. no.	Nomenclature	S. no.	Nomenclature
49	RSA_STEEL_FH2	61	RSA_STEEL_PH2
50	RSA_STEEL_FH3	62	RSA_STEEL_PH3
51	RSA_STEEL_FH4	63	RSA_STEEL_PH4
52	RSA_STEEL_FH5	64	RSA_STEEL_PH5
53	RSA_STEEL_FM2	65	RSA_STEEL_PM2
54	RSA_STEEL_FM3	66	RSA_STEEL_PM3
55	RSA_STEEL_FM4	67	RSA_STEEL_PM4
56	RSA_STEEL_FM5	68	RSA_STEEL_PM5
57	RSA_STEEL_FS2	69	RSA_STEEL_PS2
58	RSA_STEEL_FS3	70	RSA_STEEL_PS3
59	RSA_STEEL_FS4	71	RSA_STEEL_PS4
60	RSA_STEEL_FS5	72	RSA_STEEL_PS5

## 4.2 Analysis of Framed Structures

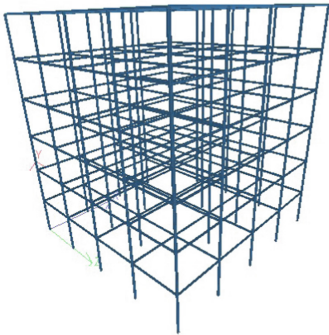
The numerical models were created for all 72 models using a licensed version of STAAD.Pro CONNECT V22. Figure 3(a), Fig. 3(c), and Fig. 3(e) show the 3D view of concrete, steel and composite buildings. Figure 3(b), Fig. 3(d), and Fig. 3(f) depict the typical beam-column junction of concrete, steel, and composite buildings.



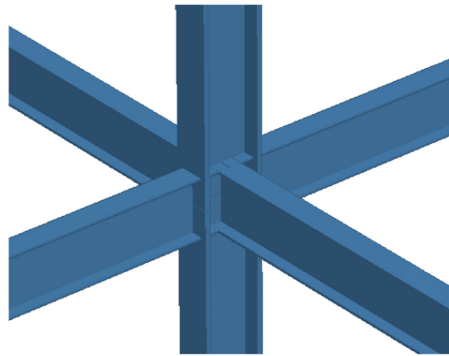
(a) 3D view of the concrete building



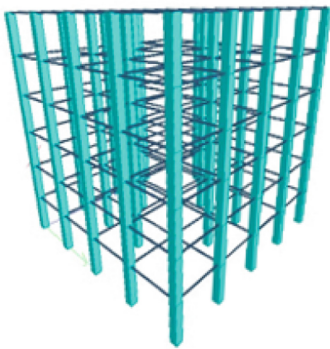
(b) Beam-Column Junction of Concrete building



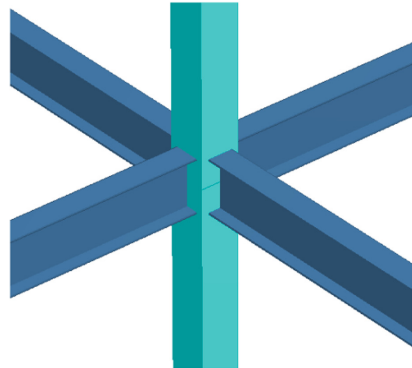
(c) 3D view of steel building



(d) Beam-Column Junction of Steel building



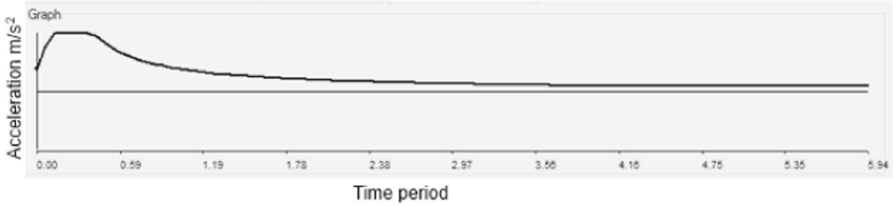
(e) 3D view of the composite building



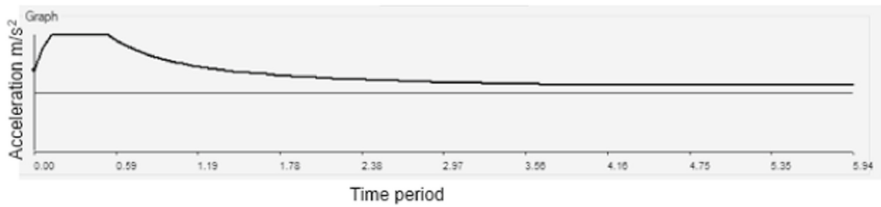
(f) Beam-Column Junction of Composite building

**Fig. 3.** Numerical models.

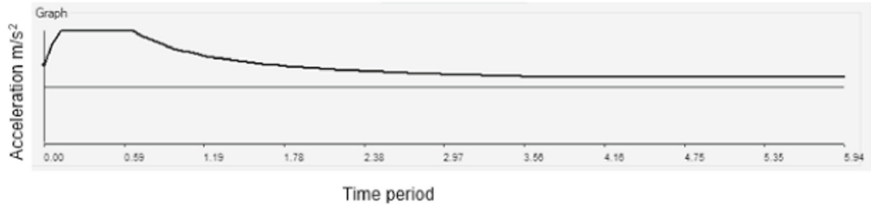
Figure 4(a), Fig. 4(b), and Fig. 4(c) represent response spectrum curves for hard, medium and soft soils respectively, for which the analysis was carried out. The stability was checked as per IS:456-2000 and IS:800-2007.



(a) Response spectrum curve of Hard soil.



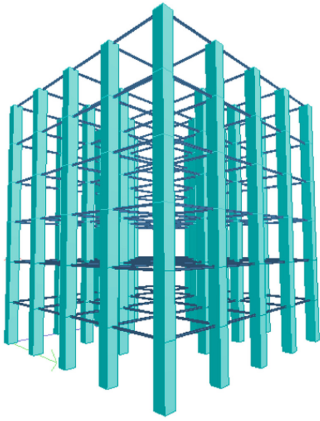
(b) Response spectrum curve of Medium soil.



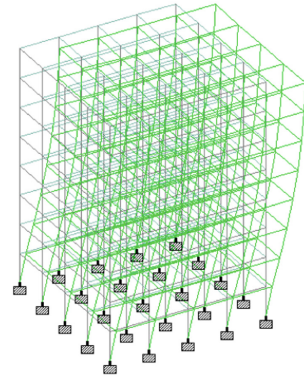
(c) Response spectrum curve of Soft soil.

**Fig. 4.** Response spectrum curves.

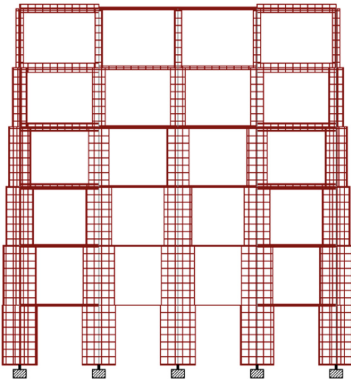
The model, deflection, shear force, and bending moment of RSA\_COMP\_FH2 are as given in Fig. 5(a), Fig. 5(b), Fig. 5(c) and Fig. 5(d) respectively.



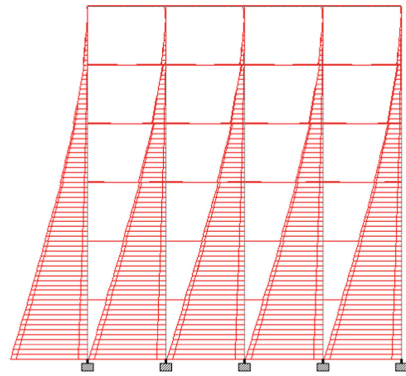
(a) 3D view of RSA\_COMP\_FH2



(b) Deflection of RSA\_COMP\_FH2



(c) Shear force of RSA\_COMP\_FH2



(d) Bending moment of RSA\_COMP\_FH2

**Fig. 5.** Analysis outputs from Staad.Pro.

The combination method for the Response analysis was a continuous quadratic combination (CQC) and by default, the software uses six modes for combination. The six mode shapes for the Model: RSA\_COMP\_FH2 are as shown in Fig. 6(a), Fig. 6(b), Fig. 6(c), Fig. 6(d), Fig. 6(e) and Fig. 6(f) respectively.



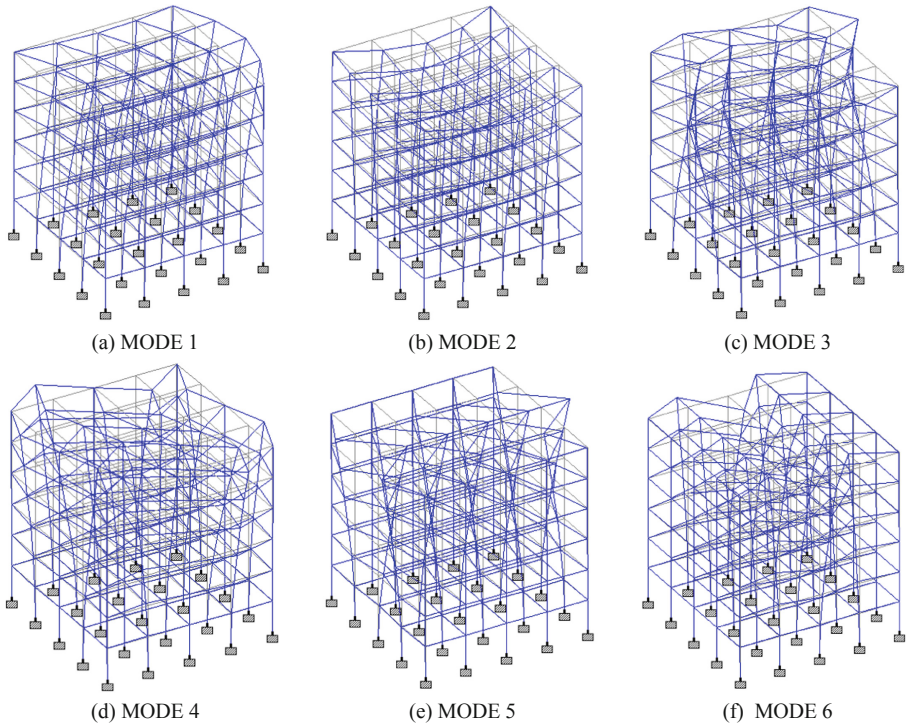


**Fig. 6.** Mode shapes of models.

## 5 Results and Discussion

### 5.1 Structural Response of Frame Structures

#### 5.1.1 Fixed Composite Models

The variation of base shear and storey drift with earthquake zone for fixed composite models are as shown in Fig. 7(a) and Fig. 7(b) respectively.

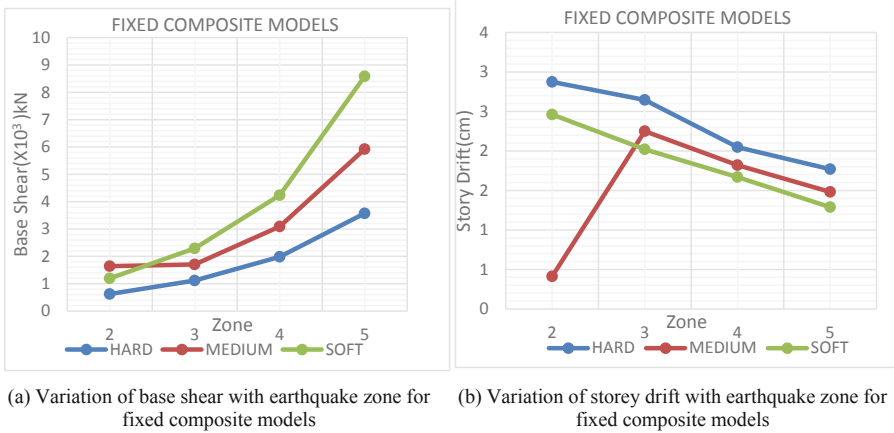


Fig. 7. Charts of variation of output parameters for fixed composite models.

It was found that the soft soil and hard soil contribute to maximum and minimum base shear respectively. At zone II, medium soil contributes to maximum base shear, and later that soft soil contributes to maximum base shear.

The soft soil and hard soil contribute to a minimum and maximum storey drift respectively. At zone II medium soil contribute to minimum storey drift and later that soft soil contributes to a minimum value.

### 5.1.2 Pinned Composite Models

The variation of base shear and storey drift with earthquake zone for pinned composite models was as shown in Fig. 8(a) and Fig. 8(b) respectively.

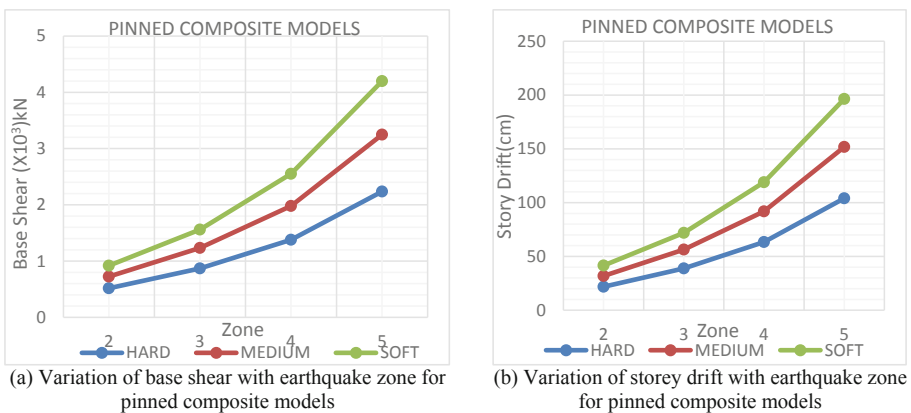
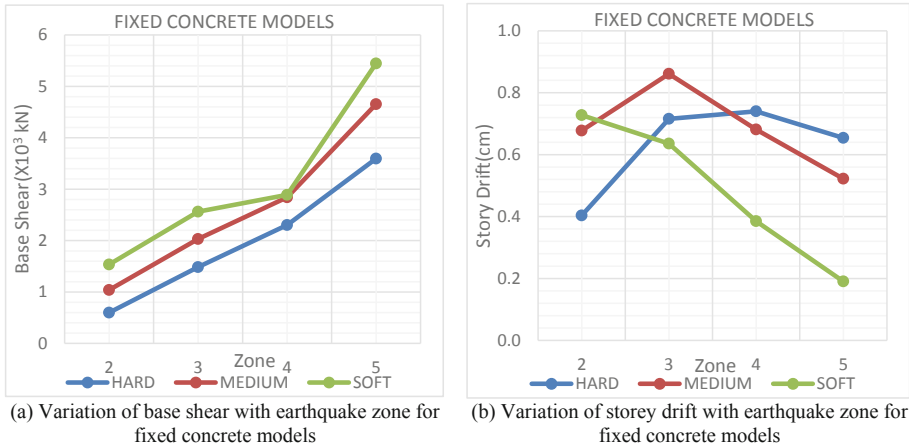


Fig. 8. Charts of variation of output parameters for pinned composite models.

The soft soil and hard soil contribute to maximum and minimum base shear respectively in all zones. Similar behaviour was noticed for storey drift respectively in all zones. Compared to other cases the trend for the storey drift was reversed.

**5.1.3 Fixed Concrete Models**

The variation of base shear and storey drift with earthquake zone for fixed concrete models are as shown in Fig. 9(a) and Fig. 9(b) respectively.

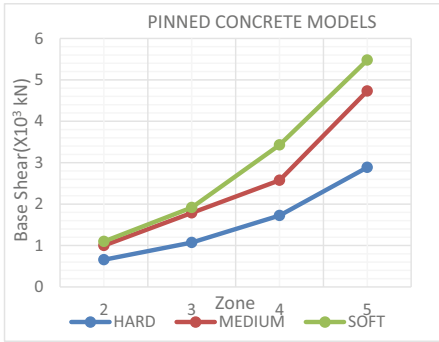


**Fig. 9.** Charts of variation of output parameters for fixed concrete models.

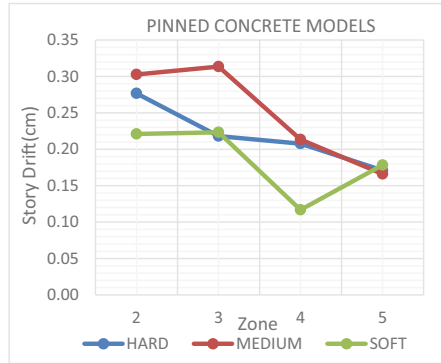
The maximum base shear was contributed by the soft soil. The storey drift followed a zig-zag trend. In zone II, the soft soil has contributed to maximum storey drift and in zone III, the medium soil has contributed for maximum storey drift. In zone V the hard soil has contributed to the maximum storey drift.

**5.1.4 Pinned Concrete Models**

The variation of base shear and storey drift with earthquake zone for pinned concrete models are as shown in Fig. 10(a) and Fig. 10(b) respectively.



(a) Variation of base shear with earthquake zone for pinned concrete models



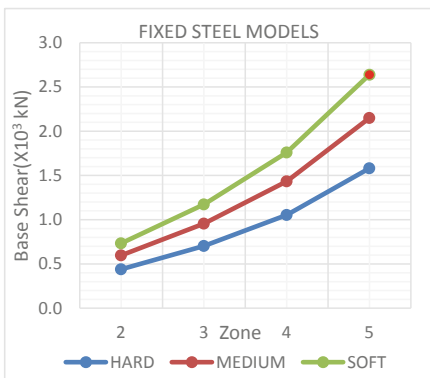
(b) Variation of storey drift with earthquake zone for pinned concrete models

**Fig. 10.** Charts of variation of output parameters for pinned concrete models.

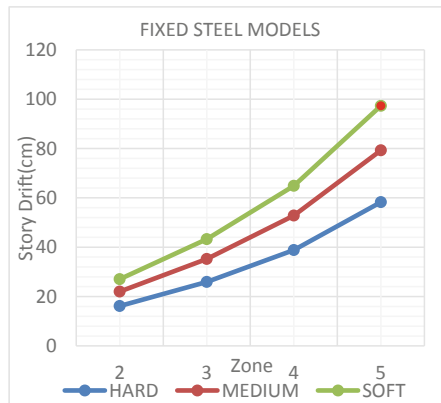
The maximum base shear was contributed by soft soil and the minimum base shear was contributed by the hard soil in all zones. It was noticed that the base shear between zone II and zone III, for both soft and medium soils showed little difference. The medium soil has the maximum contribution at zone II and as the zone increased to V there were some undulations.

### 5.1.5 Fixed Steel Models

The variation of base shear and storey drift with earthquake zone, for fixed steel models are as shown in Fig. 11(a) and Fig. 11(b) respectively.



(a) Variation of base shear with earthquake zone for fixed steel models



(b) Variation of storey drift with earthquake zone for fixed steel models

**Fig. 11.** Charts of variation of output parameters for fixed steel models.

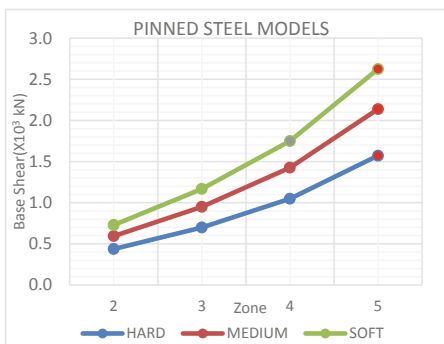
The soft soil contributed to the maximum base shear and the hard soil to the minimum base shear in all zones. The soft soil contributed to the maximum storey drift and the hard soil to the minimum storey drift in all the zones. The trend for the storey drift was reversed compared to other cases. The model under soft soils has failed in zone V (RSA\_STEEL\_FS5) and no variation in trends were noticed for the different soil types in all the zones. Though the values differ from the trends, the response was found to be similar to the pinned composite framed structures.

**5.1.6 Pinned Steel Models**

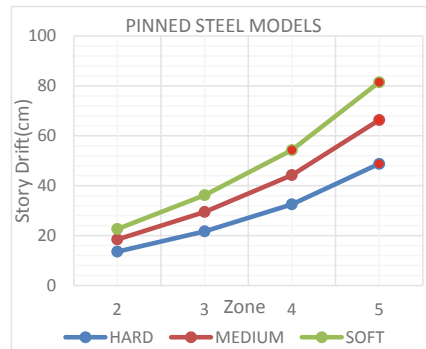
The variation of base shear and storey drift with earthquake zone for pinned steel models are as shown in Fig. 12(a) and Fig. 12(b) respectively. The soft soil contributed to the maximum base shear and the hard soil to the minimum base shear in all zones. The soft soil contributed to the maximum storey drift and the hard soil to the minimum storey drift in all the zones. The trend for the storey drift was opposite to that of the other cases. All the models in zone V and the soft soil model in zone IV were structurally failed and no variation was noticed concerning soil types.

**5.2 Cost Analysis**

The cost of concrete and composite models was given in Table 6. As the steel models were failing under some conditions, they were excluded from the cost analysis. The fixed structure was found to be nearly 20% costlier than the pinned structure. From the above table, it could be found that the soft soil models were costlier than the hard soil models. Similarly, the cost of the framed structure was found to increase with the increase in the severity of the seismic zone.



(a) Variation of base shear with earthquake zone for pinned steel models



(b) Variation of storey drift with earthquake zone for pinned steel models

**Fig. 12.** Charts of variation of output parameters for pinned steel models.

**Table 6.** Cost of each model in lakh Rupees as per SOR, SSR

Composite models	Total cost (in lakh Rupees)	Concrete models	Total cost (in lakh rupees)
RSA_COMP_FH2	27.7	RSA_CONC_FH2	23.8
RSA_COMP_FH3	35.1	RSA_CONC_FH3	62.8
RSA_COMP_FH4	45.5	RSA_CONC_FH4	68.9
RSA_COMP_FH5	64.6	RSA_CONC_FH5	77.3
RSA_COMP_FM2	63.8	RSA_CONC_FM2	43.5
RSA_COMP_FM3	45.4	RSA_CONC_FM3	66.6
RSA_COMP_FM4	56.0	RSA_CONC_FM4	62.1
RSA_COMP_FM5	78.9	RSA_CONC_FM5	75.8
RSA_COMP_FS2	36.0	RSA_CONC_FS2	63.8
RSA_COMP_FS3	48.8	RSA_CONC_FS3	71.0
RSA_COMP_FS4	66.0	RSA_CONC_FS4	47.5
RSA_COMP_FS5	105.8	RSA_CONC_FS5	64.7
RSA_COMP_PH2	24.7	RSA_CONC_PH2	28.7
RSA_COMP_PH3	31.8	RSA_CONC_PH3	31.6
RSA_COMP_PH4	41.0	RSA_CONC_PH4	38.8
RSA_COMP_PH5	54.0	RSA_CONC_PH5	50.7
RSA_COMP_PM2	29.2	RSA_CONC_PM2	38.7
RSA_COMP_PM3	38.3	RSA_CONC_PM3	51.8
RSA_COMP_PM4	50.2	RSA_CONC_PM4	49.2
RSA_COMP_PM5	67.2	RSA_CONC_PM5	67.4
RSA_COMP_PS2	32.4	RSA_CONC_PS2	31.7
RSA_COMP_PS3	43.7	RSA_CONC_PS3	41.3
RSA_COMP_PS4	58.5	RSA_CONC_PS4	56.9
RSA_COMP_PS5	79.1	RSA_CONC_PS5	73.3

## 6 Conclusion

In the present study, the cost and performance comparison of a framed structure using different building materials subjected to seismic analysis was carried out. Totally 72 models were analysed and the following conclusions have arrived:

- Steel structures show less base shear value and storey drift, compared to composite and concrete models irrespective of the support condition.
- In the case of earthquake-prone zones, the structural behaviour of composite and steel structures was found to be highly unpredictable.
- The steel structures are showing significant storey drifts and fail at higher earthquake zones. Usage of better grades could avoid these failures.
- Structure modelled with fixed support was 20% costlier than that modelled with pinned support, irrespective of the material.
- The cost of the framed structure was found to increase with the increase in the severity of the seismic zone.

Regarding the better structural performance and economical construction, concrete could be preferred as a building material for structures put up in seismic zones.

## References

- Anil, S.S., Hosur, V.: Comparative study of RCC, steel and composite structures for an industrial building. *Int. J. Adv. Res. Innov. Ideas Ed.* **5**(4), 637–647 (2019)
- Anish, N.S., Pajgade, P.S.: Comparison of RCC and composite multistoried buildings. *Int. J. Eng. Res. Appl.* **3**(2), 534–539 (2013)
- Ghabussi, A., Marnani, J.A., Rohanimanesh, M.S.: Improving seismic performance of portal frame structures with steel curved dampers. *Structures* **24**, 27–40 (2020). <https://doi.org/10.1016/j.istruc.2019.12.025>
- Chintakrindi, V.K., Sarath, A.K., K., Lingeshwaran, N., VigneshKannan, S. and Pratheba, S.: Study on analysis and design of a multi-storey building with a single column using STAAD. *Pro. Mater. Today Proc.* **33**, 728–731 (2020). <https://doi.org/10.1016/j.matpr.2020.06.073>
- Design Manual for Effective Use of Parallel Flange Sections Prepared For JSPL, INSDAG, Kolkata, India
- Draft common schedule of rates as per A.P. revised standard data for the year (2019), Government of AP, Vijayawada, India
- Gagandeep: Time and cost comparison of reinforced cement concrete and steel Structure, *Mater. Today Proc.* **37**, 2917–2920 (2020). <https://doi.org/10.1016/j.matpr.2020.08.672>
- IS 456-2000: Code of Practice for Plain And Reinforced Concrete, Burea of Indian Standards, New Delhi, India
- IS 800-2007: Code of Practice For General Construction in Steel, Burea of Indian Standards, NewDelhi, India
- IS 875-2002: Code of Practice for Design Load (Other Than Earthquake) for Buildings And Structures, Burea of Indian Standards, New Delhi, India
- IS 875(Part3)-1987: Code of practice for design loads (other than earthquake) for buildings and structures, Burea of Indian Standards, New Delhi, India
- Lian, M., Guan, B., Cheng, Q., Zhang, H., Mingzhou, S.: Experimental and numerical study of seismic performance of high-strength steel fabricated framed-tube structures with replaceable shear links. *Structures* **28**, 2714–2732 (2020). <https://doi.org/10.1016/j.istruc.2020.10.081>
- Parag, P.L., Dode, P.A.: Comparative study of reinforced concrete frame structure & steel-concrete composite structure subjected to static and dynamic loading. *Int. J. Eng. Appl. Sci.* **5** (3), 29–32 (2018)
- Schedule of rates for building works for the year: Government of Andra Pradesh, Vijayawada, India (2018)
- Muffassir, S., Kalurkar, L.G.: Comparative study on wind analysis of multi-storey RCC and composite structure for different plan configuration. *Int. Organ. Sci. Res. J. Mech. Civ. Eng.* **13**(4), 42–49 (2016). <https://doi.org/10.9790/1684-1304074249>
- Standard schedule of rates for building works for the year: Office of the Chief Engineers, Hyderabad, India (2009)
- Surender Kumar, K., Lingeshwaran, N., Jeelani, S.H.: Analysis of residential building with STAAD. Pro & ETABS. *Mater. Today Proc.* **33**, 1221–1228 (2020). <https://doi.org/10.1016/j.matpr.2020.08.329>
- Ali, S.F., Bhalchandra, S.A.: Study on seismic analysis of RCC and steel concrete composite structure and cost comparison with different support conditions. *Int. J. Sci. Res. Devel.* **3**(9), 354–359 (2015)



# Study of Simply Supported Skew Composite Bridge Decks Under IRC Loading

J. Jane Regita and A. Sofi<sup>(✉)</sup>

Vellore Institute of Technology, Vellore, India  
a.sofi@vit.ac.in

**Abstract.** Skewness alters the behaviour of a bridge deck significantly. Though it gives rise to complex load distribution patterns, they are adopted due to the obstructions present at the site. Today's highway network consists of many such skew bridges generally restricted to a skew angle of 30°. In this paper, the behaviour of Simply supported skew steel -concrete composite bridge decks having spans ranging from 25 m to 50 m and with skew angles 20°, 30° and 45° are studied. Grillage analogy method, a popular procedure followed in design offices. Analysis of these decks is done using STAAD Pro software. IRC live loads Class A, 70R (l), (m) and (n) wheeled vehicle, 70 R tracked type vehicle and Special Vehicle loading as given in IRC:6-2017 is adopted. This work aims to study simply supported skew bridge decks under all possible load combinations suggested by the latest version of IRC codes. Guidelines for width of bridge deck provided in IRC: SP: 87-2019 are followed. 18 bridge deck models are studied and their responses are compared and presented in a form that can be understood by the readers.

**Keywords:** Skew bridges · Steel concrete composite · Grillage analogy · IRC

## 1 Introduction

Slab girder bridges are the widely used bridge type in today's highway network. In places where the bridge alignment crosses a river or roadway or railway line or any other obstruction at an inclination different from 90°, the bridge is termed as a skew bridge. The skew angle is the angle between the axis of support (pier or abutment) and a line normal to the longitudinal axis (centreline) of a bridge. Bridge designs with higher skew angles are not desirable and should be avoided whenever possible. When a skew cannot be avoided it should be reduced as much as possible. In skewed bridges, the centre of mass usually does not coincide with the centre of stiffness which causes large displacements at the supports. Unlike squared decks, the load distribution in skew decks is non-uniform and complicated. The load coming on deck is transferred to the nearest support or along the shortest distance. The load travels along the shortest distance to the obtuse corner of the bridge deck and the participation of acute corners in load transfer is minimal. Skew support arrangements also give rise to torsional effects (Nouri and Ahmadi 2012). However, the effect of skew is less critical in slab girder bridges than solid slab or cellular slab bridges (Hambly 1991).



Slab girder bridges can be built over a longer span as a steel-concrete composite structure. Steel-concrete composite slab-girder bridge decks consist of a concrete deck slab that spans over longitudinal steel girders. They are normally adopted up to a span of 50 m. Steel concrete composite girder bridges offer advantages like high strength-to-weight ratio, design flexibility, and increased service life. Efficient use of the material in composite design also reduces the size and weight of the structure. The composite behaviour is attained through the longitudinal shear force transferred by the shear connectors that increases the bending resistance greatly (Chun 2010). This paper illustrates the behaviour of simply supported skew composite bridge decks under live loads as per IRC recommendations. The study is undertaken by varying the span of the bridge deck from 25 m to 50 m at every 5 m interval and at 20°, 30° and 45° skew angle each. Initially, a preliminary design is performed to proportion the bridge deck and work out the section properties. Detailed transverse and longitudinal analysis of the bridge deck models are performed in STAAD Pro. The response of the bridge decks under dead load and moving load is discussed and represented graphically.

## 2 Skew Deck Behaviour

Skew has the tendency to affect the geometry and the behavior of the structure. Skewness has a considerable effect on behaviour of the deck and critical design stresses. The load is transferred more to the nearest support or along the shortest distance. The effect of skew is ignored in bridges with small skew angles (i.e.) decks skewed at less than 20° are considered as squared bridge decks. Higher skew angles affect shear force, bending moment, torsion, deflection and support reactions of the bridge deck. Warping of the deck slab causes higher deflection at obtuse angled corners. Skew decks generate twisting moments which is more acute for higher skew angles (Kar et al. 2012; McConnell et al. 2020). The ratio between skew length and width of the deck (aspect ratio) also alters the deck slab deflection. Maximum deflection moves from the obtuse corner to the mid-span as the aspect ratio increases. Support reactions and shear forces are also maximum at the obtuse corners. Excessive twisting and out of plane rotation of the girders, uplift at support locations and development of lateral bending stresses in flanges were also observed. Previous studies have also discussed the construction issues associated with skewed bridges during different phases of the construction. Skewness of the bridge affects activities like girder erection, cross frame fitting and concrete deck placement (Hambly 1991; Gull et al. 2017).

Transverse reactions are transferred from the mid-span to the supports. They are further distributed vertically through the bearings. These bearings are restrained in translation in the transverse direction. Thus the generated shear forces are transferred to the pier cap or abutment or column bent. To ensure a continuous transverse load path adequate composite action should be provided between the girders and the deck. Designing the top chord of the end cross frames to act compositely with the deck was found to be effective in previous numerical analysis. In areas vulnerable to seismic activity, the girders can be made fully composite both in positive and negative moment regions. This increases its load-carrying capacity of the deck. For longitudinal ground

motion, the shear connectors play an integral part in transferring inertia forces along the entire length of the bridge (Maleki 2002).

### 3 Bridge Analysis

Bridge deck analysis is generally performed in both transverse and longitudinal directions and their respective behaviours are obtained.

#### 3.1 Transverse Analysis

Transverse analysis is done for proportioning of the bridge deck slab like deck thickness and girder spacing. The deck slab is modeled as a continuous member simply supported at girder locations. One portion of a 6 lane highway bridge deck (i.e.) 3 lane deck is considered for study. The 3 lane carriageway is 17 m wide, the girders are spaced at 3.5 m c/c and has a cantilever projection of 1.5 m on either sides. Width of carriageway, paved shoulders of 2.5 m, footpath of 1.5 m and shy away distance of 0.5 m are provided (IRC:SP:87-2019). For purpose of analysis a deck slab of 1 m width is considered. The nodes indicating the support locations are chosen on the center-line of the girder. The idealised deck slab for transverse analysis is shown in Fig. 1. Self-weight of the deck and wearing coat is calculated and applied as uniformly varying load. Crash barrier and parapet wall loads are applied as concentrated loads at appropriate locations. Transverse analysis is done as per the Effective width method given in Annexure B-3 of IRC:112-2019.

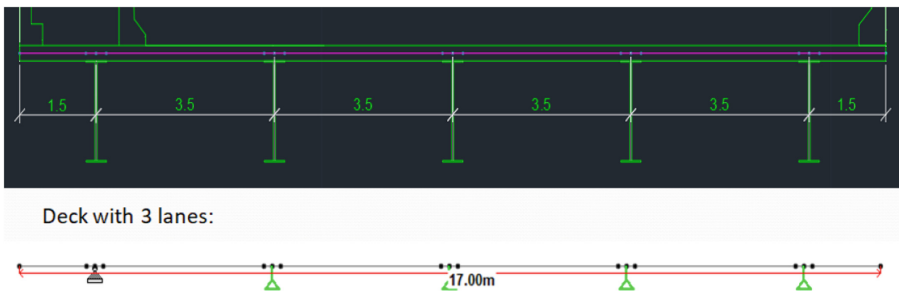


**Fig. 1.** Idealisation of bridge deck.

IRC recommends the effective width method for analysing the effect of wheel loads on bridge deck transversely. Effective width is the width that resists the bending moment due to applied wheel loads. IRC 112 provides formulae for solid slabs spanning in one direction and cantilever slabs to find out the effective width. These formulae depend upon several factors like effective span of the deck, distance of centre of gravity of the load from the nearest support, the breadth of concentration of the load and the ratio between the width and effective span of the slab. Figure 2 visualises the concept of effective span and effective width of the deck slab. The wheel loads are

applied as concentrated loads at various positions of the deck and the response is studied. Slabs designed by the above method need not be checked for shear (IRC:112-2019).

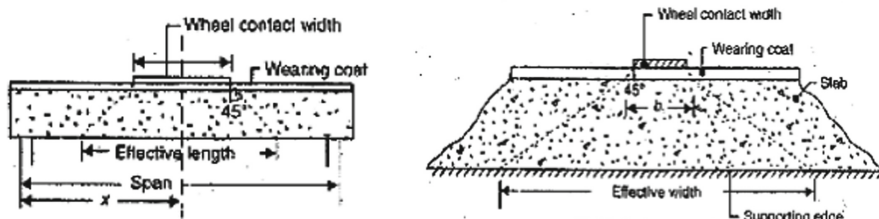


Fig. 2. Load dispersion as per effective width method (Shreedhar and Kharde 2013).

In STAAD Pro software, the idealised deck slab is subjected to vehicular loading and its behaviour is studied. The partial safety factors for the loads for various limit states are used as given in Annexure B of IRC:6-2017. Their results are discussed later in Sect. 4 of this paper.

### 3.2 Longitudinal Analysis

Longitudinal analysis is carried out using grillage analogy method where the deck is idealized as a series of interconnected beams. This grillage is identical to the actual bridge deck so that, obtained reactions and displacements are similar to the actual structure. This technique is versatile and is also easy to visualize the grillage model. It can reflect complex features like high skew angle, deep haunches, decks with stiffened edge beams etc. which significantly alters the live load distribution in slab girder bridge decks. Gridlines of a grillage are formed along the ‘strength lines’ (i.e.) centreline of the main girders and along the edge beams longitudinally. The properties of intermediate and end cross girders or diaphragms are also represented by grillage lines drawn transversely along the centreline of the diaphragms. Such cross-frames or diaphragms provide lateral load resistance, help to distribute moving load among girders and reduce the buckling length in the compression flanges of girders. Under gravity loads, the main girders bend along its major axis resulting in a differential vertical displacement of cross frames (Surana and Agarwal 1998).

The ratio between the transverse and longitudinal grid line spacing is recommended to be maintained between 1 and 2. Preferably the number of transverse lines must be odd and a minimum of 7 lines are suggested. They must also extend up to the outermost longitudinal gridline. Grillage for bridge decks with a footpath on one or both sides includes an additional gridline along its centreline. An increase in the number of gridlines increases computational efficiency and accuracy (Seo et al. 2013). The grid lines can be arranged either orthogonally or non-orthogonally as shown in Fig. 4. In an orthogonal grillage, the transverse grid lines are perpendicular to the main girders whereas in non-orthogonal grillage they are placed parallel to the skew support line.

Orthogonal models are found to be realistic and give accurate results and yield economic sections during design. Models with skew or parallelogram grillage mesh do not have grid members closer to the dominant direction. Therefore they overestimate deflection and moment values which in turn increases the amount of steel required (Shreedhar and Kharde 2013). Though they can be accurate for decks with skew angles less than  $15^\circ$ , orthogonal grillage is recommended by many authors and practicing engineers. The below Fig. 3 shows a typical skew deck model with skew angles of  $30^\circ$  and  $45^\circ$ .

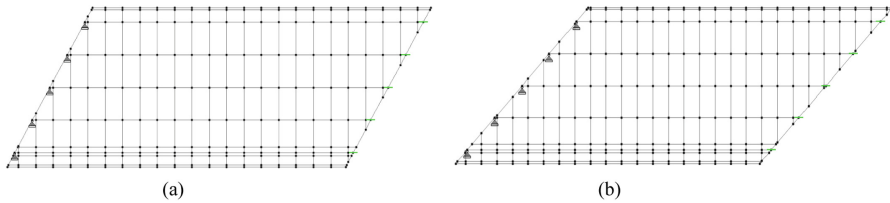


**Fig. 3.** Grillage model of (a)  $30^\circ$  deck (b)  $45^\circ$  deck.

The modelled deck is simply supported at one end and free to translate along the vertical axis at the other end. The section properties for longitudinal and transverse girders are then assigned to the deck model. A trial section of the plate girder is adopted and checked for its shear capacity and bending resistance. The properties of the section which satisfy the required conditions and limitations are adopted further. The two general design considerations include: 1) The spacing between the main girders is preferred to be more than  $1/20$ th of the effective span. This spacing must be sufficient enough to resist the overturning effect due to lateral loads. 2) Depth of the plate girders is considered to be not less than  $1/25$ th of the effective span. The proportion of the steel web and flange plates are checked as per IRC recommendations. This is done to ensure the safety of the section under serviceability criteria and compression flange buckling criteria (Duggal 2017).

The properties of the concrete slab are converted to its equivalent composite section property after dividing it by the  $E_s/E_c$  modular ratio (IRC:22-2015). Dead loads due to self-weight of girders, deck slabs, superimposed dead load due to crash barrier, parapet wall and wearing coat, footpath live load and vehicular live loads are assigned. The bridge deck is subjected to Class A, 70 R wheeled 'l' 'm' and 'n' type, 70 R tracked and Special vehicle loading. Live load generations and combinations are adopted as per IRC:6-2017. A total of 24 live load combinations are checked by placing the set of vehicles at different positions of the deck slab. Transversely, the set of wheel loads are placed at both extreme ends of the carriageway, at the centre of carriageway and by aligning the wheel with centre line of girder to get the maximum effect. Load generations along the traffic direction of the deck are studied with 0.25 m increment of live loads. Congestion factor, Impact factor and Reduction factor for longitudinal effect of live loads in bridges are all considered (IRC:6-2017).

## 4 Results and Discussion

### 4.1 Transverse Analysis

The bending moment envelope is shown below (Fig. 4):

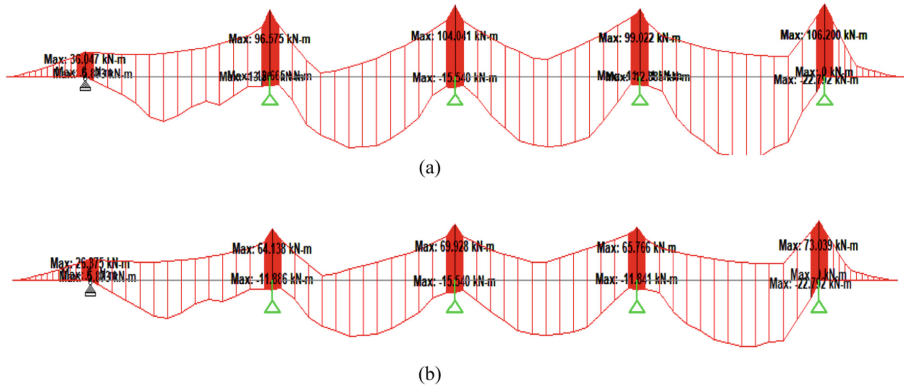


**Fig. 4.** (a) BM envelope under ULS (b) BM envelope under SLS.

- The bending moment values obtained from the analysis are used to design the deck slab both under ultimate limit state (ULS) and serviceability limit state (SLS) conditions.
- The combined effect of dead and live load is slightly unsymmetric due to the presence of footpath at one end.
- Guidelines as per IRC:112-2019 are adopted in design procedures. Based on the design bending moment and effective depth, area of transverse and longitudinal reinforcements for the deck slab are calculated.
- Similarly, maximum compressive stress in concrete and crackwidth is calculated and is found to be within the permissible limits as given in IRC:112-2019.

### 4.2 Longitudinal Analysis

#### 4.2.1 Maximum Response of Bridge Decks vs Span

The maximum midspan bending moment, torsional moment and shear force are represented graphically. The variation of these parameters for spans ranging from 25 m to 50 m and skewed at 20°, 30° and 45° can be interpreted from the graphs (Figs. 5, 6, and 7).

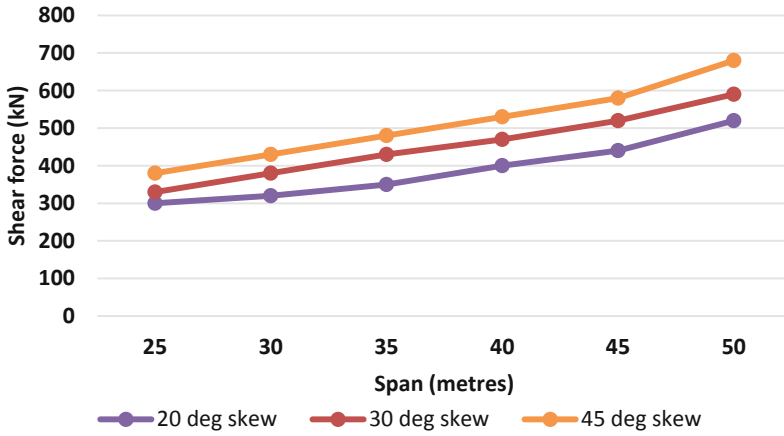


Fig. 5. Variation of maximum shear force with span.

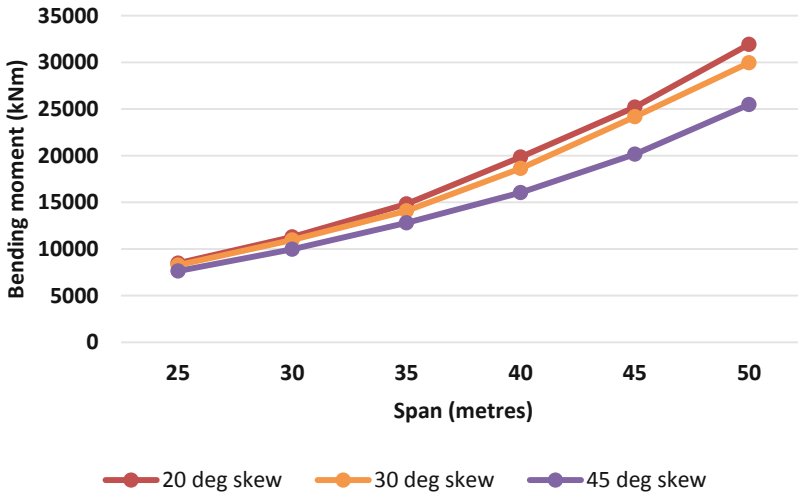


Fig. 6. Variation of midspan bending moment with span.

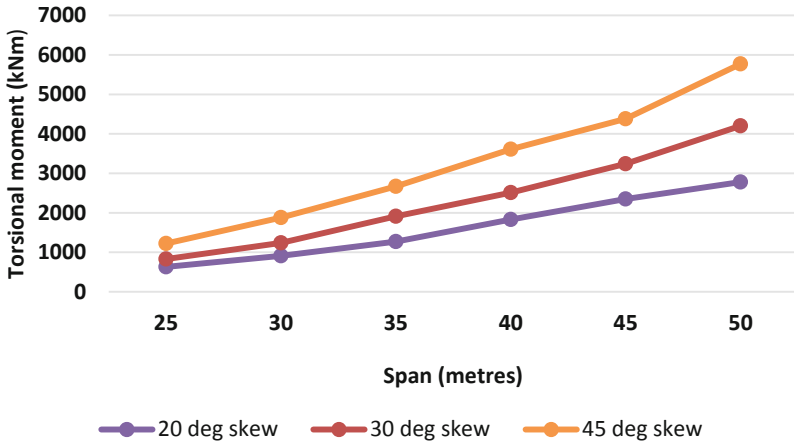


Fig. 7. Variation of midspan torsional moment with span.

- The load combination  $1.35DL + 1.35SIDL + 1.75Wearing\ Coat + 1.5Footpath\ LL + 1.5LL$  is used to compute the design moment and shear values.
- Responses of the most critical girder is used here.
- Maximum midspan bending moment increases with an increase in span and reduces with an increase in skew angle.
- Torsion (i.e.) the twisting moment along the horizontal axis increases steadily with an increase in span and skew angle.
- Shear force values follow an increasing trend as the span increases similar to torsion

#### 4.2.2 Check for Deflection

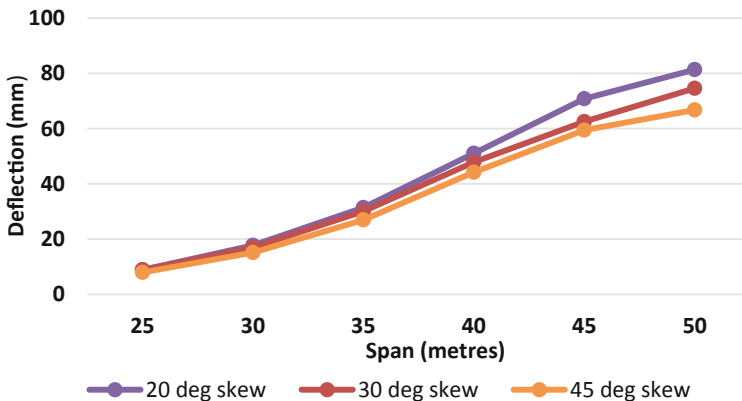


Fig. 8. Variation of maximum deflection with span.

Total permissible deflection as per IRC:22-2015 is effective span ( $l$ )/600. The actual deflection obtained is within the permissible limits (Fig. 8) (Table 1).

**Table 1.** Deflection check

Span (m)	Skew angle (degrees)	Total deflection (mm)	Permissible deflection (mm)
25	20	8.88	40
	30	8.854	
	45	7.959	
30	20	17.736	48.33
	30	16.981	
	45	15.125	
35	20	31.426	56.67
	30	30.095	
	45	26.956	
40	20	51.072	65
	30	47.839	
	45	44.195	
45	20	70.802	73.33
	30	62.492	
	45	59.47	
50	20	81.32	81.67
	30	74.544	
	45	66.738	

**4.2.3 Effect of Different Wheel Load Combinations**

An effort has also been made to capture the variation of bending moment for the bridge decks under each type of vehicular loading separately. This gives a clear idea about the most critical live load combination for each deck (Figs. 9, 10, 11, 12, 13, 14, 15, 16, 17, 18, 19, 20, 21, 22, 23, 24, 25 and 26).

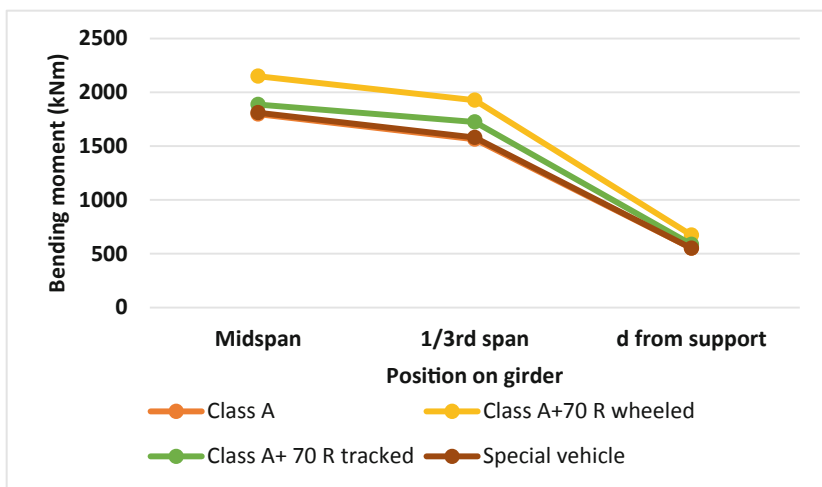


**Fig. 9.** Effect of wheel load on 25 m 20° skew bridge deck.



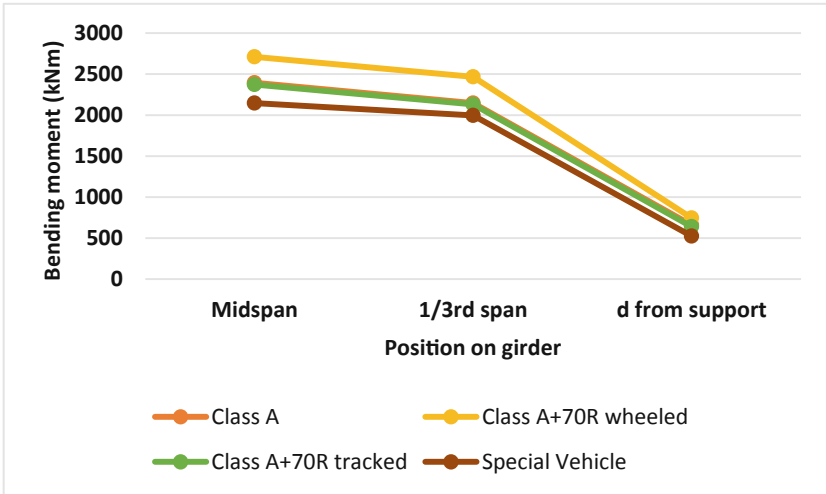


Fig. 10. Effect of wheel load on 30 m 20° skew bridge deck.

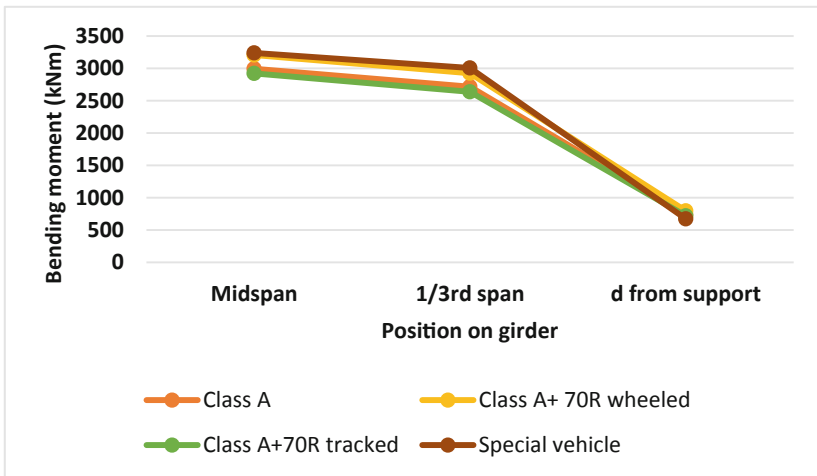


Fig. 11. Effect of wheel load on 35 m 20° skew bridge deck.

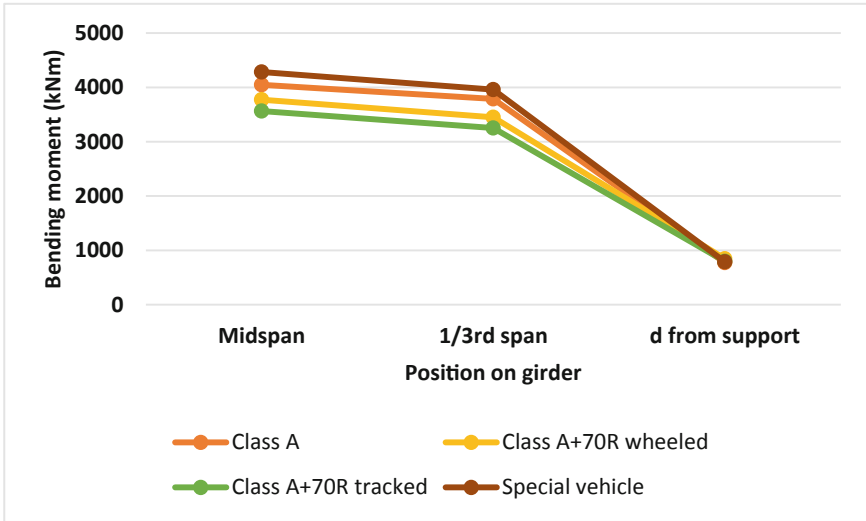


Fig. 12. Effect of wheel load on 40 m 20° skew bridge deck.

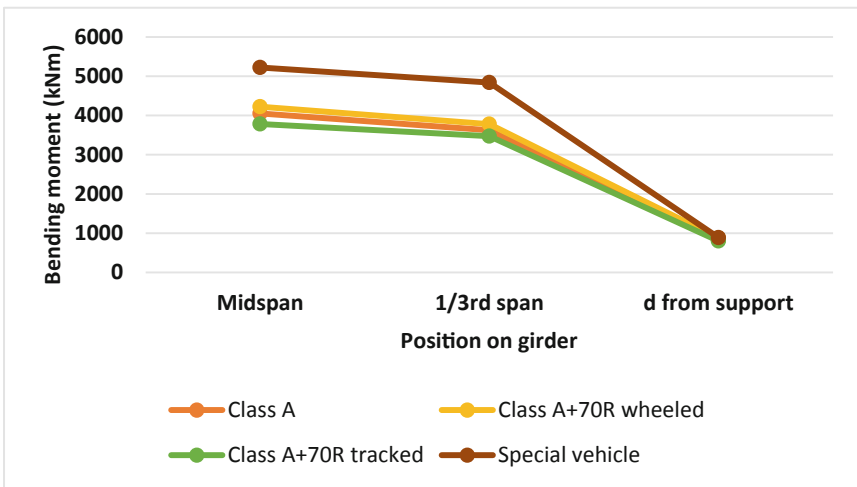


Fig. 13. Effect of wheel load on 45 m 20° skew bridge deck.

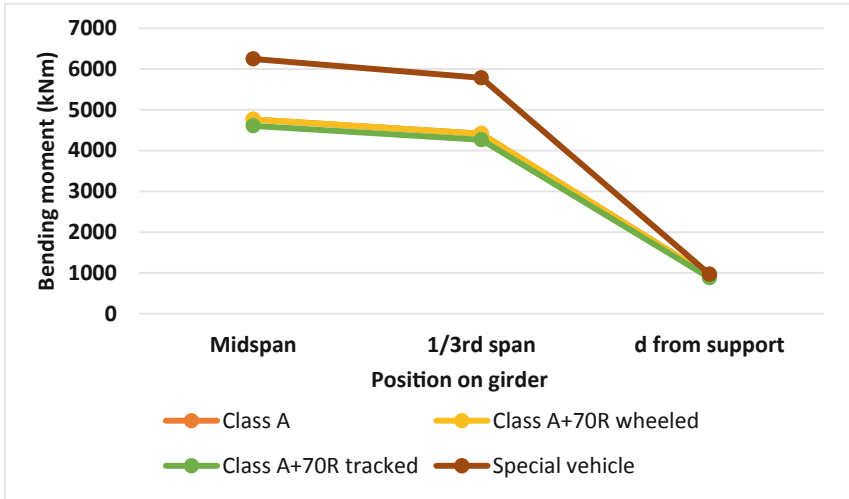


Fig. 14. Effect of wheel load on 50 m 20° skew bridge deck.

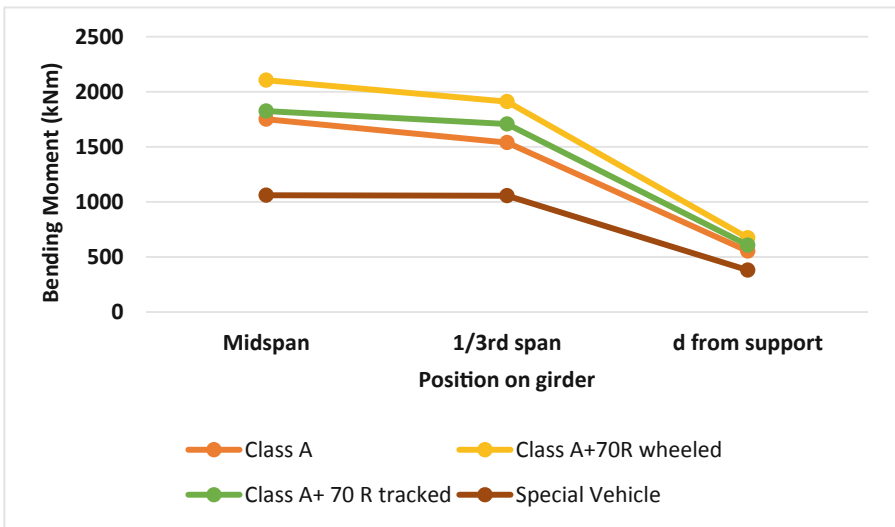


Fig. 15. Effect of wheel load on 25 m 30° skew bridge deck.

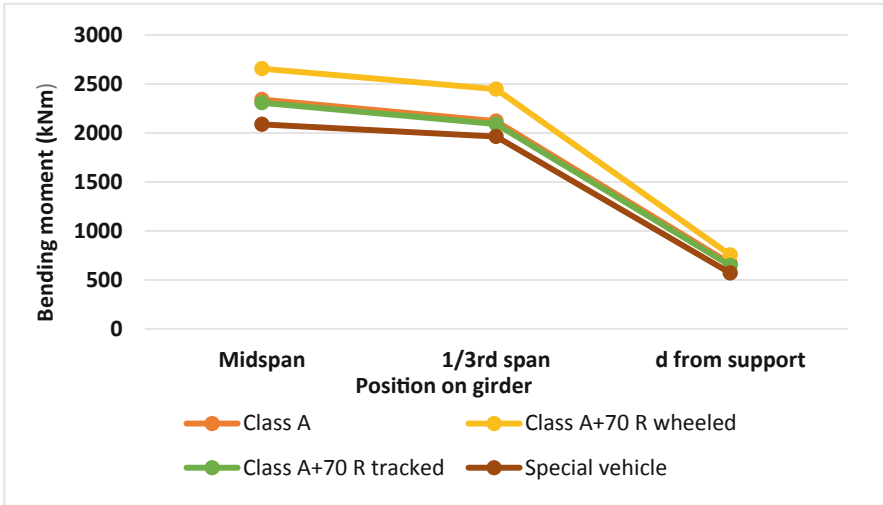


Fig. 16. Effect of wheel load on 30 m 30° skew bridge deck.

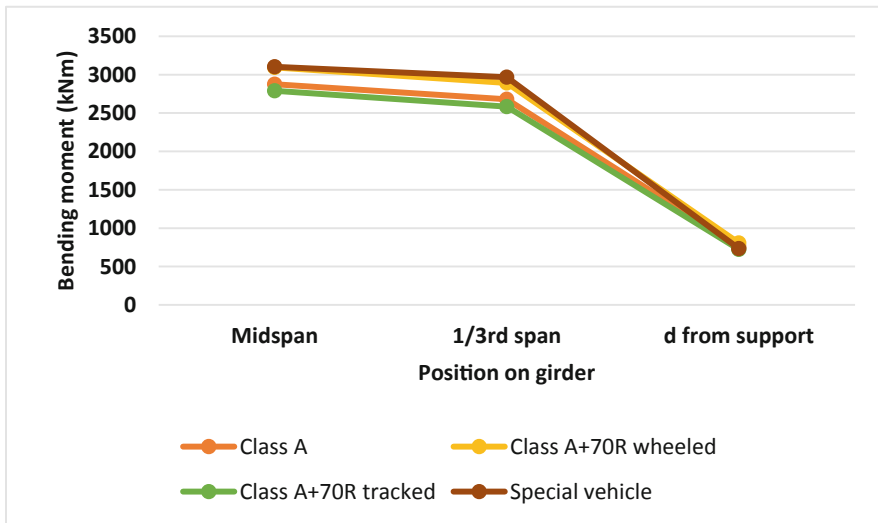


Fig. 17. Effect of wheel load on 35 m 30° skew bridge deck.

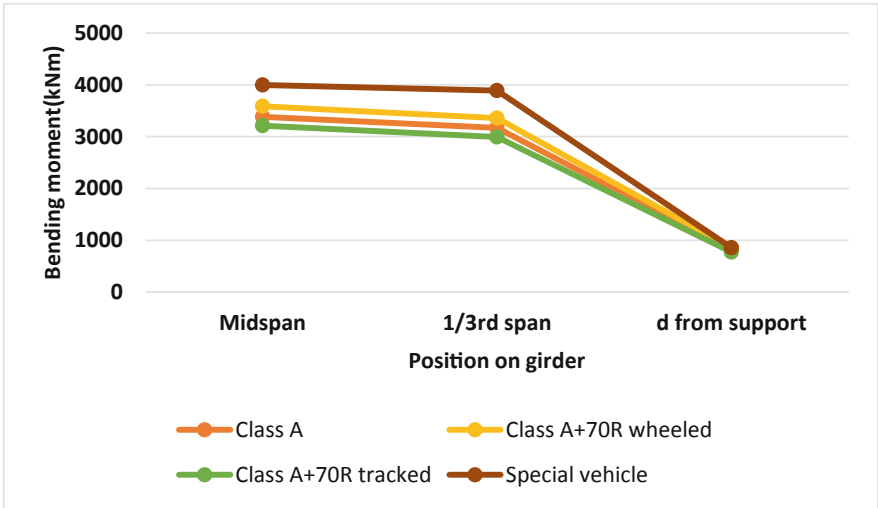


Fig. 18. Effect of wheel load on 40 m 30° skew bridge deck.

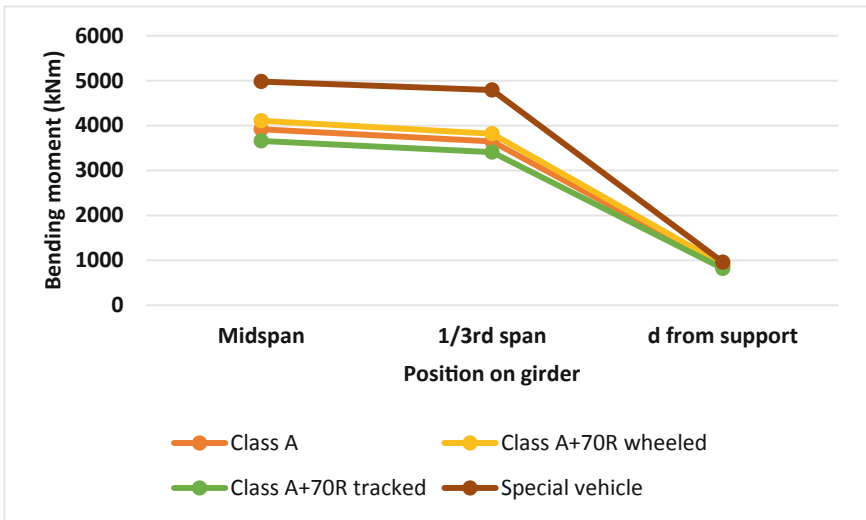


Fig. 19. Effect of wheel load on 45 m 30° skew bridge deck.

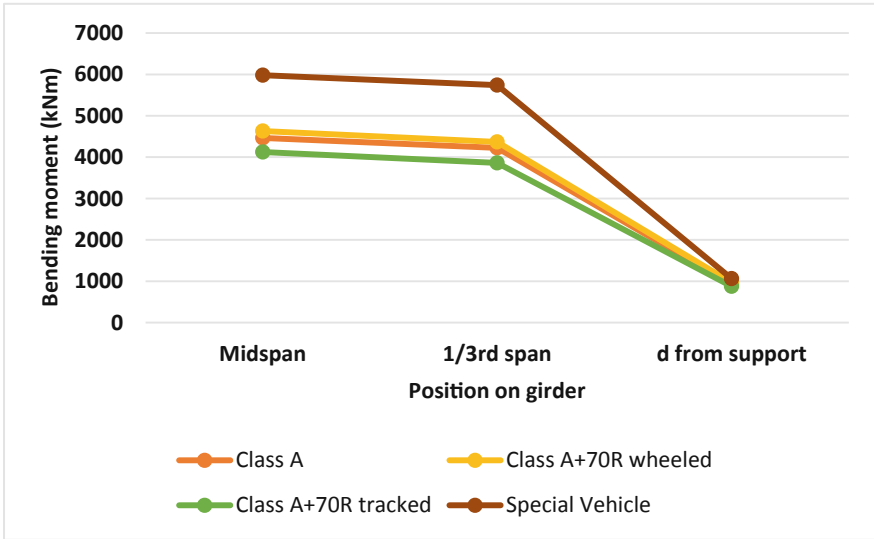


Fig. 20. Effect of wheel load on 50 m 30° skew bridge deck.

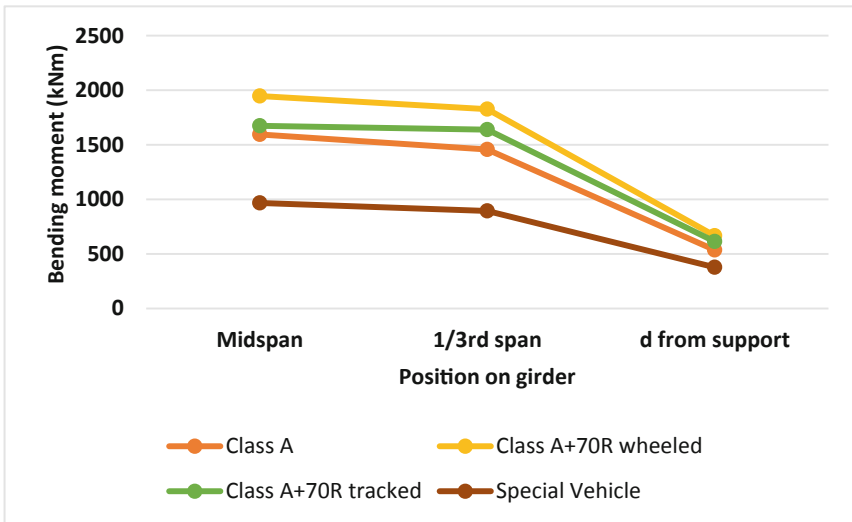


Fig. 21. Effect of wheel load on 25 m 45° skew bridge deck.

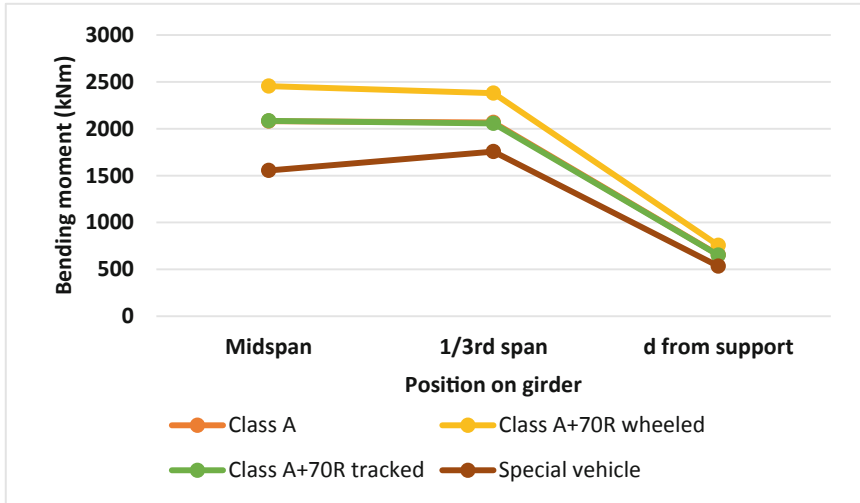


Fig. 22. Effect of wheel load on 30 m 45° skew bridge deck.

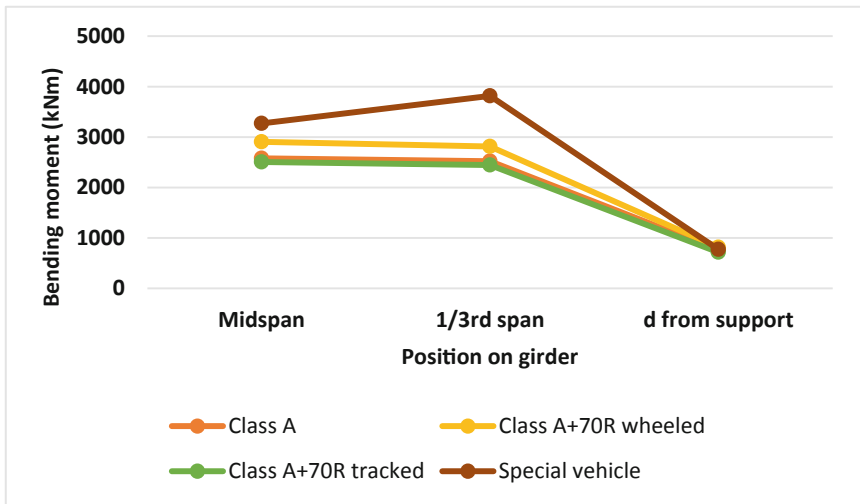


Fig. 23. Effect of wheel load on 35 m 45° skew bridge deck.

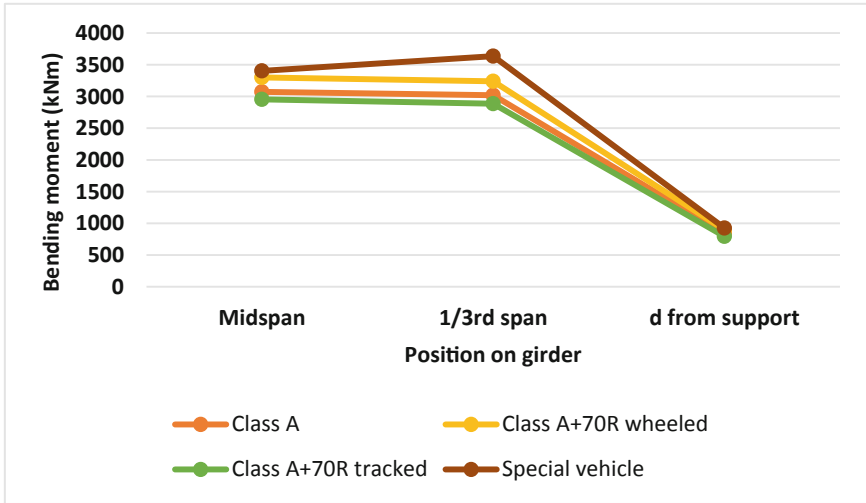


Fig. 24. Effect of wheel load on 40 m 45° skew bridge deck.

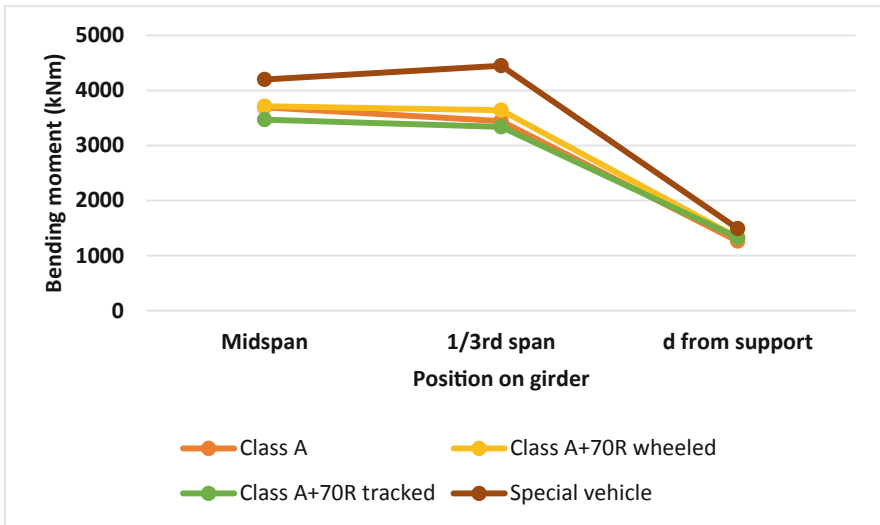


Fig. 25. Effect of wheel load on 45 m 45° skew bridge deck.



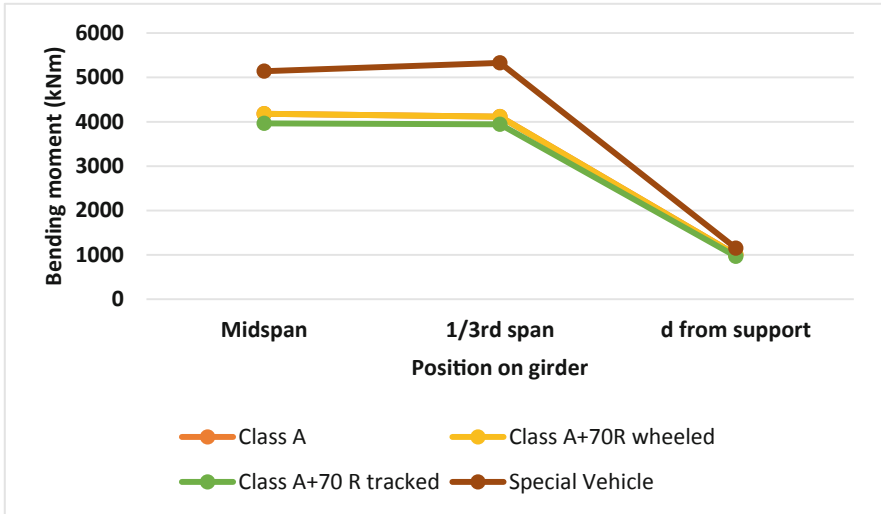


Fig. 26. Effect of wheel load on 50 m  $45^\circ$  skew bridge deck.

- Bending moment values corresponding to the load generation giving maximum effect is depicted above.
- Three different locations midspan of girder, one-third of effective span and 'd' from support is chosen. Here, effective span is the centre to centre distance of bearings and 'd' represents the effective depth of girder. Moment values obtained from these locations are further used to design the section.
- It is understood that for spans 35 m to 50 m special vehicle loading has maximum effect on bending moment followed by class A+70 R wheeled loading and class A loading and lastly class A+70R tracked vehicle combination.
- For spans 25 m and 30 m, the effect of special vehicle is not dominant and maximum bending moment is due to class A+70 R wheel loading type.
- It can also be observed that at the maximum skew angle of  $45^\circ$ , the effect of Special vehicle at one-third is more dominant than at midspan.
- This indicates that the longer bridge decks are most critical for longer spans under load exerted by special vehicles. But this loading is not considered in many works of literature as it takes place occasionally.

## 5 Conclusion

Based on the analytical study of 3 lane simply supported of steel -concrete composite skewed bridge decks it is observed that there is a reduction in the bending effect of the longitudinal girder for larger skew angles. This could be due to the reason that, as the skew increases the wheel loads might be transferred to the support closer to it (Bishara et al. 1993). Torsion is higher at larger skew angles, bridges skewed at  $45^\circ$  exhibit 48.68% more torsion than the minimum skew angle of  $20^\circ$ . Torsional reinforcements to withstand

such high moments should be provided accordingly. The lateral buckling strength of the plate girder section under torsion, can also be checked as per guidelines provided in clause 509.2.2 in IRC:24-2010. Unlike torsion, shear force increases steadily and a variation of only 23.5% was observed between the maximum and minimum values. Overall deflection of the bridge deck increases with increase in span. It also increases with decrease in skew angle. This work will be helpful for students and engineers studying the effect of skew decks under various vehicular loading, all pertaining to Indian standards.

## References

- Bishara, A.G., Liu, M.C., El-Ali, N.D.: Wheel load distribution on simply supported skew i-beam composite bridges. *J. Struct. Eng.* **119**(2) (1993). ISSN 0733-9445/93/0002-0399
- Chun, B.J.: Skewed Bridge Behaviours: Experimental, Analytical, and Numerical Analysis. Doctoral report submitted to Wayne State University, Michigan (2010)
- Dhanush, S., Rao, K.B.: Behaviour of segmental composite skew slabs subjected to flexure loading, In: Paper Submitted in Conference on Technological Innovations for Sustainable Infrastructure, NIT Calicut, 13–14, March 2015
- Duggal, S K.: *Limit State Design of Steel Structures*, 2 edn., McGraw Hill Education (India) Private Limited (2017)
- Gull, J.H., Aziznamini, A., Helwig, T.A.: Comparison of detailing methods for straight skewed steel I-girder bridges. *J. Constr. Steel Res.* **2017**, 24–34 (2017). <https://doi.org/10.1016/j.jcsr.2017.05.003><sup>nd</sup>
- Hambly, E.C.: *Bridge Deck Behavior*, 2nd edn, E & FN Spon Publications (1991)
- Huang, H., Shenton, H.W., Chajes, M.J.: Load distribution for a highly skewed bridge: testing and analysis. *J. Bridge Eng.* **9**(6) (2004). [https://doi.org/10.1061/\(ASCE\)1084-0702\(2004\)9:6\(558\)](https://doi.org/10.1061/(ASCE)1084-0702(2004)9:6(558))
- IRC:5-2015 Standard Specifications and Code of Practice for Road Bridges, Section I – General features of design (2015)
- IRC:6-2017 Standard Specifications and Code of Practice for Road Bridges, Section II – Loads and Load combinations (2017)
- IRC: 22–2015 Standard Specifications and Code of Practice for Road Bridges SectionVI Composite Construction (Limit State Design)
- IRC: 24-2010 Standard Specifications and Code of Practice for Road Bridges SectionV Steel Road Bridges (Limit State Design)
- IRC:SP:87-2019 Manual of Specifications and Standards for Six laning of highways (2019)
- IRC: 112-2019 Code of practice for Concrete Road Bridges (2019)
- Kar, A., Khatri, V., Maiti, P.R., Singh, P.K.: Study on effect of skew angle in skew bridges. *Int. J. Eng. Res. Dev.* **2**(12), 13–18 (2012). ISSN: 2278-067X
- Maleki, S.: Deck modeling for seismic analysis of skewed slab-girder bridges. *Eng. Struct.* **24**, 1315–1326 (2002)
- McConnell, J., Radovic, M., Keller, P.: Holistic finite element analysis to evaluate influence of cross-frames in skewed steel I-girder bridges. *Eng. Struct.* **213**, 110556 (2020). <https://doi.org/10.1016/j.engstruct.2020.110556>
- Nouri, G., Ahmadi, Z.: Influence of skew angle on continuous composite girder bridge. *J. Bridge Eng.* **17**(4) (2011). [https://doi.org/10.1061/\(ASCE\)BE.1943-5592.0000273](https://doi.org/10.1061/(ASCE)BE.1943-5592.0000273)
- Razzaq, M.K., Sennah, K., Ghrib, F.: Moment and shear distribution factors for the design of simply supported skewed composite Steel I-Girder bridges due to dead loading. *J. Bridge Eng.* **25**(8) (2020). [https://doi.org/10.1061/\(ASCE\)BE.1943-5592.0001552](https://doi.org/10.1061/(ASCE)BE.1943-5592.0001552)

- Seo, J., Linzell, D.G., Hu, J.W.: Nonlinear seismic response analysis of curved and skewed bridge system with spherical bearings. *Adv. Civil Eng.* **2013**, 248575 (2013)
- Shreedhar, R., Kharde, R.: Comparative study of grillage method and finite element method of RCC bridge deck. *Int. J. Sci. Eng. Res.* **4**(2) (2013). ISSN: 2229-5518
- Surana, C.S., Agarwal, R.: *Grillage Analogy in Bridge Deck Analysis*, Narosa Publishing House, New Delhi (1998)
- Théoret, P., Massicotte, B., Conciatori, D.: Analysis and design of straight and skewed slab bridges. *J. Bridge Eng.* **17**(2) (2011). [https://doi.org/10.1061/\(ASCE\)BE.1943-5592.0000249](https://doi.org/10.1061/(ASCE)BE.1943-5592.0000249)



# Structural Assessment of Composite Concrete Members for Waterproofing and Thermal Insulation

Hanamant Magarpatil, Ankita Thorat, and Vedang Patil<sup>(✉)</sup>

School of Civil Engineering, MIT World Peace University, Pune, India  
ankita.thorat@mitwpu.edu.in, vedpatil10@gmail.com

**Abstract.** The thermal performance of any structure depends on the thermal characteristics of the structural material. Thus, it is crucial to study the behavior of that material for thermal resistance and thermal insulation. The performance of that material is governed by its thermal conductivity, which describes the ability of the material to allow the flow of heat across it in the presence of differential temperature. Thermal variations are highly hazardous from the point of view of durability of the structure and needs more attention to improve the structural properties. It has been proved that thermocol (Polystyrene foam) has good insulating properties and also has a low thermal conductivity and therefore a good thermal insulating material. In this study, experimental tests are conducted on concrete slab with and without using thermocol for flexure and as an insulating material in R.C. slab for studying the behavior of slab for thermal insulation. Concluding from the results of thermal conductivity it is proved that the thermocol is a good insulating material and the slab is good in thermal insulation compared to RCC slab.

**Keywords:** Composite concrete · Waterproofing · Thermal insulation · Flexure · Thermal conductivity

## 1 Introduction

Materials used in civil engineering are changing rapidly. Structural steel and concrete are stronger than even just a few years ago. And new construction materials such as inorganic fibers, composites, plastics and polymers are being used more frequently and with satisfactory mechanical behavior than ever before (Campbell-Allen and Throne 1963). As a part of this evolution, the use of Polystyrene (a polymer compound) in engineered construction is growing fast. Polystyrene foam (Thermocol) is a polymer having good insulatory, water proofing (as it floats on water freely), light weight, low thermal conductivity, fire resistant, moisture resistant and frost resistant and excellence shock absorption properties. The material consists of 98% air, the best natural heat insulator. It has good dimensional stability and compressive strength. Other applications include warehousing and factories, agricultural sheds, cold storage, cavity wall insulation, under concrete slabs, roofs, walls, suspended concrete slabs flooring, and sandwich panels with various laminates.

The chain polymer is produced from polymerization of the monomer by chain initiation reaction. Heat transfer through takes place by conduction, convection and radiation. Due to its closed cell structure water molecules cannot pass through it and thus acts as a waterproofing material (Yucel et al. 2003). Brittle failure of expanded polystyrene (EPS) under compression is not observed and, therefore, its ultimate strength cannot be accurately determined. The characteristic of compression behaviour is often defined conditionally as a stress corresponding to 10% deformation of specimens (Ivan et al. 2001).

In places of cold and hot external atmospheres, it acts as a regulator to prevent the excess heat loss (Abela 2006). Expanded Polystyrene Foam has a typical thermal conductivity of 0.038 (W/m<sup>o</sup>K) and coefficient of linear thermal expansion CLTE as  $5 \times 10^{-5}$  to  $8 \times 10^{-5}$  mm/mm/<sup>o</sup>C. EPS ISOBOARD is used in construction purposes which have uniform density distribution, resistance to water vapour distribution and provides protection to concrete slab and gives good waterproofing from thermal shock (ZarrRobert et al. 1991). Used with either wood or metal stud framing, EPS foam insulation provides a highly moisture-resistant thermal break to sheath and insulate all framing. EPS products were also good at handling the water at the outside contact with soil thus showing that EPS has good resistance to water ingress. (Swinton et al. 1999). EPS has very poor absorption which decreases as density increases as shown in. EPS with over 10 years of usage period has 8–9% of its volume of groundwater as its contents. The cellular structure of EPS is water resistant, vapor permeable, and possesses zero capillarity (Mustapa et al. 2019).

### 1.1 PS has Very Poor Water

A good insulation of buildings not only saves cooling energy but also provides a more comfortable indoor climate due to lower wall insides surface temperature and protects the building structure from daily temperature changes (Spitzner Martin 2003). EPS offers significant insulating performance while also reducing air infiltration. New or retrofit siding, brick and stucco finishes can then be applied. The long term R-value, high-compressive strength, exceptional moisture resistance and excellent resistance to chemicals typically found in soil make EPS ideal for use as foundation insulation. The properties and requirements of the EPS are stated in the Table 1.

**Table 1.** Requirement of expanded polystyrene (EPS) thermal insulation performance as per ASTM standard

Property	Units	ASTM test	Type IX
Density	pcf, minimum	C303	1.80
Thermal resistance values (R)	Per inch thickness At 75 °F (23.9 °C)	C518	4.20
Flexural strength	psi, minimum	C203	50
Water absorption by total immersion	% by Vol Max	C272	2.0

## 2 Methodology

In the methodology for the experimental work and corresponding tests are discussed. For conducting the thermal conductivity test a standard size of slab panel is considered. Hence a slab panel of size  $500 \times 500 \times 55$  mm is used for the test procedure. A total of 72 such slabs are casted for the design methodology for testing across 7 days, 14 days and 28 days and the results of 28<sup>th</sup> day are presented. Concrete used is M20 grade and steel as Fe 415. Design of the slab panel to be tested is done in accordance with the steps given below:

### 2.1 Design of Slab

Design of one way slab, simply supported on all edges.

Concrete used is M20 grade and steel as Fe 415.

$$\sigma_{cbc} = \frac{7N}{mm^2}, \sigma_{st} = 230 \text{ N/mm}^2$$

From IS 456–2000 we have,

### 2.2 Design Constants

The design constants as per IS 456 are as mentioned in the Eq. (1). Equation (2) and Eq. (3) as per IS 456 give the calculations for the bending moment and shear force for that particular slab specimen.

$$m = 13.33, k = 0.29, j = 0.9036, Q = 0.913 \quad (1)$$

Load due to self-weight of slab + Superimposed load = 1320 N + 2500 N

Total UDL per meter run of slab (W) = 3820 N

$$\text{Total bending moment (M)} = \left( \frac{W \times L^2}{8} \right) 119.375 \text{ Nm/m} \quad (2)$$

$$\text{And Shear force (V)} = \left( \frac{W \times L}{2} \right) = 955 \text{ N at the face of the support} \quad (3)$$

### 2.3 Design of Section

We have  $D = 55$  mm

$$d = 55 - 10 - 4 = 41 \text{ mm}$$

## 2.4 Main Reinforcement

When we design the slab, a minimum reinforcement in order to sustain the weight load is given and considered as mentioned in the Eq. (4)

$$\text{Minimum reinforcement} = 0.12\% \times Ast_{min} \times b \times D = 66 \text{ mm}^2 \quad (4)$$

$$\text{Using } 8 \text{ mm } \Phi \text{ bars, } A_{\Phi} = \frac{\pi \times 8^2}{4} = 50.26 \text{ mm}^2, \text{ Spacing } S = 100 \text{ mm} \quad (5)$$

Provide 8 mm  $\Phi$  bars @ 100 mm c/c. From Eq. (5) we understand the total reinforcement needed of the 8 mm bars used.

Deflection check is required to check whether the deflection occurring in the element is within the limiting value or not, and in case it exceeds the limiting value additional reinforcement is to be provided.

## 2.5 Check for Development Length

$$\frac{1.3M_1}{V} + L_0 \geq L_d \quad (6)$$

$$\begin{aligned} L_0 &= 125 \text{ mm}, L_d = 255.55 \text{ mm} \\ &= \frac{1.3 \times 42.826 \times 10^3}{955} + 125 = 183.27 \text{ mm} \end{aligned}$$

## 2.6 Check for Shear

$$\tau_v = \frac{V}{b \times d} = 0.0232 \quad (7)$$

$\tau_v = 0.0232$  which is less than permissible value,  $\tau_c = 1.3 \times 0.22 = 0.29$  (IS 456, 2000).

Equation (6) gives the expression for the bond development length as per IS456 and Eq. (7) the check for the shear resistance in the slab specimen. The shear check is done to find out whether the shear resistance is enough to resist the shear force due to applied loading and adding additional shear reinforcement if needed.

## 2.7 Distribution Reinforcement

$$\begin{aligned} A_{sd} &= 82.5 \text{ mm}^2 \text{ Using } 6 \text{ mm } \Phi \text{ bars, } A_{\Phi} = 28.27 \text{ mm}^2 \\ &\text{Provide } 6 \text{ mm } \Phi \text{ bars @ } 100 \text{ mm c/c.} \end{aligned}$$

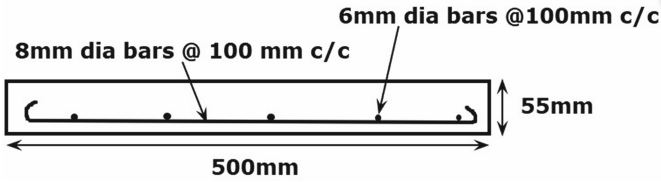


Fig. 1. Reinforcement detail for one way slab.

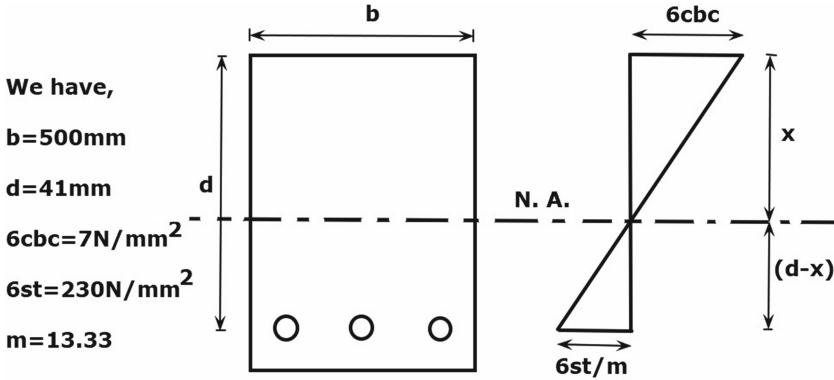


Fig. 2. Position of neutral axis.

$$\frac{\sigma_{cbc}}{\frac{\sigma_{st}}{m}} = \frac{x}{d - x} \tag{8}$$

$x = 11.83 \text{ mm}$ , N.A. about 12 mm from top. From Eq. (8) we come to know about the depth of neutral axis.

The section properties so required have been designed as per IS 456:2000 and the suitable reinforcements have been provided. The reinforcement detailing can be seen from Fig. 1 and the depth of neutral axis can be estimated from the Fig. 2.

The strain and stress diagram as per our assumptions are shown below, Maximum compressive stress in concrete is  $8.92 \text{ N/mm}^2$ .

From calculation of total compressive and tensile force we get the following values as seen in Fig. 3 which shows the forces in compression and tension zone.



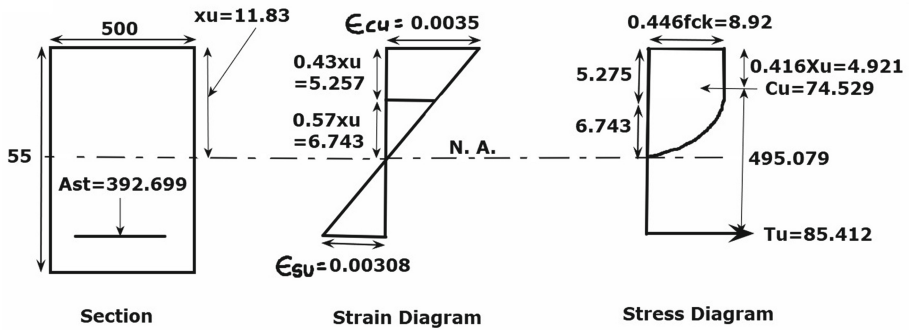


Fig. 3. Stress and strain diagram.

## 2.8 Concrete Mix Design

As per M20 grade, the concrete in the necessary proportions is prepared.

The quantities of water, cement, sand, coarse aggregate are designed considering the following requirements are in the Table 2.

1. Characteristic strength of concrete at 28 days = 20 N/mm<sup>2</sup>
2. Maximum size of aggregate is 20 mm.
3. Degree of workability is 0.85 cf.
4. Type of exposure is mild.
5. Degree of quality control is good.

Table 2. Mix proportions

Water	Cement	Sand	Coarse aggregate
186 kg	372 kg	650 kg	1208 kg
0.5	1	1.6	3.2

Hence the mix proportion is **1:1.5:3** for M20 grade of concrete.

## 3 Experimentation

In this experimental work, for calculating the thermal conductivity of concrete and composite concrete i.e. concrete using Thermocol, 24 nos. of slabs of size 500 mm × 500 mm × 55 mm are casted for testing purpose. The concrete used for slab is of M<sub>20</sub> grade and water cement ratio is taken as 0.5.

In this experimental work for measuring the thermal conductivity value, a thermal conductivity meter is manufactured as per requirements.

For measuring the flexural strength of concrete slab with Thermocol we use three types of methods of placing the Thermocol sheets at various layers and for comparing the results concrete slabs without Thermocol are casted. The Thermocol sheet is placed at zero stress level i.e. the portion below the Neutral Axis of slab and above the reinforcement.

In the first case the Thermocol sheet is placed below the neutral axis with anchor bars provided as shown,

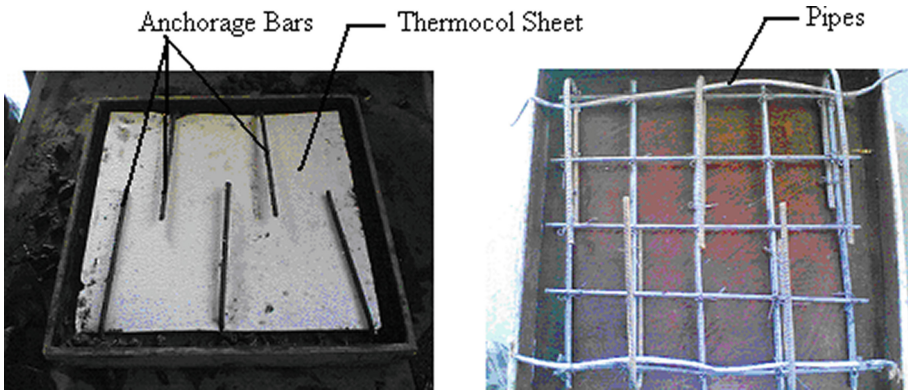


**Fig. 4.** Arrangement of Thermocol Sheet for Case 1.

The arrangement of Thermocol is as shown above in Fig. 4, in this case due to the arrangement of Thermocol and anchor bars the bonding between concrete and Thermocol is achieved. Also when the slab is constructed using such type of arrangement due to layer of Thermocol sheet the curing of concrete below the sheet is not possible since Thermocol is good waterproofing material, to overcome this difficulty we can provide plastic pipes with holes and these pipes are inserted in water at the ends which helps in supplying water inside the concrete for curing as shown in above figure.

In the second case, the Thermocol sheet is placed same as in first case i.e. below the N.A. but with perforations in the sheet i.e. 3 holes are provided in the sheet of 10% area of area of the sheet i.e. 3 holes of 10 mm diameter. These holes are provided for making the bond between Thermocol and the concrete below and above the sheet. In the places of holes some anchor bars are provided which are attached to the below reinforcement bars as shown in Fig. 5 below.

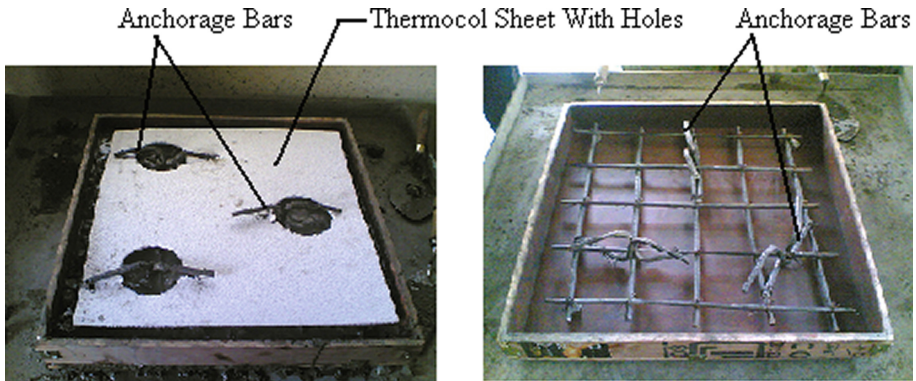


**Fig. 5.** Arrangement of Thermocol Sheet for Case 2.

Due to these holes in the sheet the concrete above and below the sheet mix together and holds the Thermocol sheet properly, which gives best bonding results compared to the first case.

In the third case in the Fig. 6 below, the Thermocol sheet is placed below the reinforcement, the sheet is covered with chicken mesh from bottom side and the upper part of chicken mesh is placed above the reinforcement in the concrete which gives good type of bond between Thermocol, reinforcement and concrete. The bottom portion of slab is then plastered using concrete plaster or plaster of Paris.

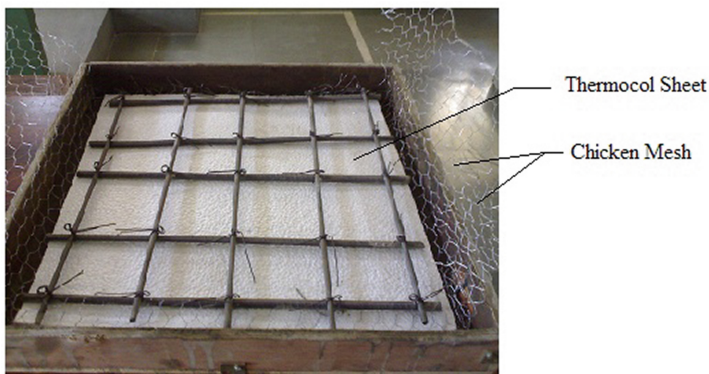


**Fig. 6.** Arrangement of Thermocol Sheet for Case 3.

Using such type of arrangements of placing Thermocol sheets in the concrete slab at various levels we can measure the strength and bond of the composite concrete slab.

#### Flexural Strength Test:

For measuring the flexural strength of slab panel the above discussed slabs are used for testing. The test is carried out on a universal testing machine (UTM) which is of 100

ton capacity. The test setup apparatus is shown in the Fig. 7 below and the experiments and then performed.

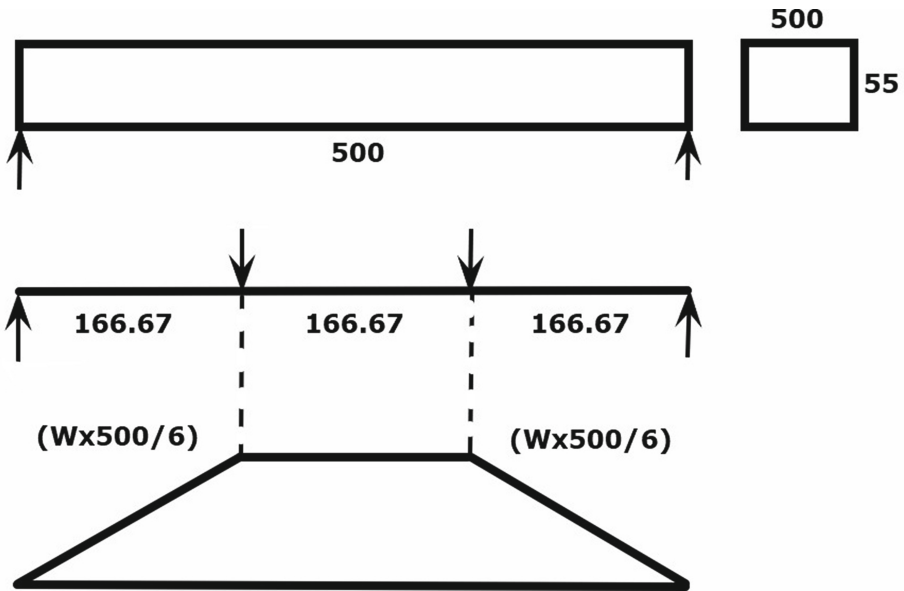


Fig. 7. Apparatus setup for Flexural test.

### 3.1 Procedure for Measuring Thermal Conductivity Value

Start the supply and consider the steady state condition for the thermocouple wires i.e. the temperature at the time interval of 10 min should be same passing through the Thermocouple wire. Control the supply of required current and voltage by the controller and check the readings for Thermocouple wires at different positions using dimmer stat. Using these values of Thermocouple wires we can calculate the Thermal Conductivity (K value) as below,

We know,

$$Q = Power = V \times I \times \cos\Phi = \text{Reading from Voltmeter (Voltage)},$$

$I$  is Reading from Ammeter (Current)

$\cos \Phi$  is power factor, generally taken as 0.8 (Assume)

Also,  $q = \frac{Q}{2}$  (Assume)

$$q = \frac{\Delta T}{\Sigma R_{th}} \tag{9}$$

$$q = \frac{\frac{T_5+T_6}{2} - \frac{T_7+T_8}{2}}{\frac{Thickness}{K_{slab} \times A_s}} = \frac{T' - T''}{\frac{Thickness}{K_{slab} \times A_s}} \tag{10}$$

Where  $T_5, T_6, T_7, T_8$  are Thermocouple wires readings,  
 $K_{slab}$  is Thermal Conductivity of Slab  
 $A_s$  = Area of slab.

$$K_{slab} = \frac{q \times Thickness}{(T' - T'') \times A_s} \tag{11}$$

Thus, from Eq. (9), Eq. (10) and Eq. (11), we can calculate the thermal conductivity of slab. Another method of calculating the value of thermal conductivity in which the arrangement is same as that of above explained. Only instead of Thermocouple wires we use two Sensors and which are connected to the Indicators which separate for each Sensor and to Voltmeter and Ammeter. These sensors are very much sensitive and which measures the direct value of heat transfer through a material. In the two sensors one is placed with the heater inside the assembly and another one is placed at the outer face of the slab by drilling a small hole in the slab at outer side. The arrangement and the Thermal Conductivity Meter are shown in Fig. 8 below, and then the experiments procedures are begun.

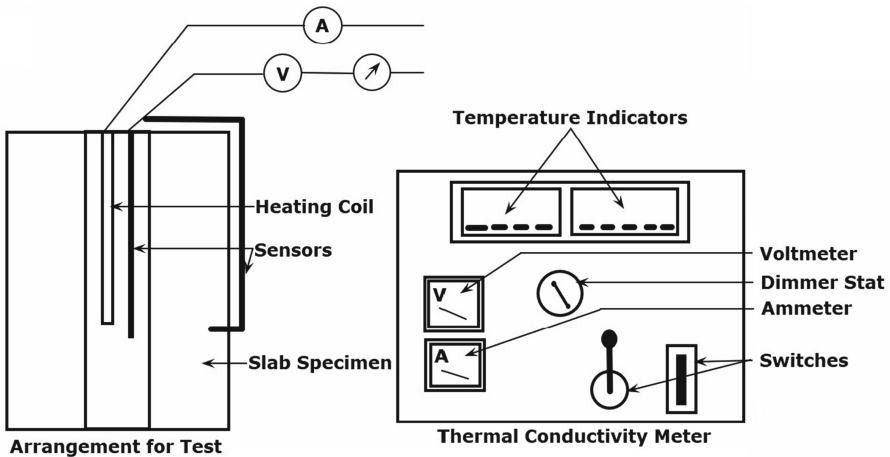


Fig. 8. Thermal conductivity meter and test setup.

In the test procedure first both sensors displays the surrounding temperature while supplying the current to the inside of slabs through the heater, the sensor which is inside the assembly will show the inside temperature. After supplying the required temperature to inside, the outer sensor shows how much heat is transferred from the slab in the Indicator. And the value by deducting the surround temperature will give

directly the heat transfer through the slab i.e. nothing but the Thermal Conductivity value. Hence due to its easiness this method is used in this work and which gives the accurate values.

But in this work using six slab panels a room is casted with all corners sealed using plaster of Paris. All the four slab panels of four faces used are of all cases i.e. one is only concrete slab, the next one is slab with Thermocol below the reinforcement, the next is slab with Thermocol sheet with anchor bars and the last one is slab with Thermocol and sheet with perforations. Using such an assembly as seen in Fig. 9 we can find out value of Thermal Conductivity of all slabs in a single attempt by changing the outer sensor to one slab to the other.

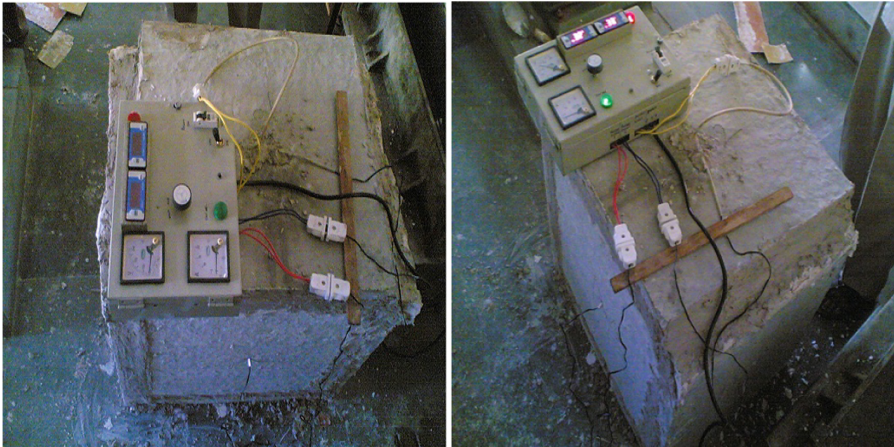


Fig. 9. Thermal conductivity meter and arrangement.

In the test procedure the starting value of surround temperature is 32 °C and inside temperature of the room is 33 °C. The supply to the room is started and the supply is stopped at 57 °C. The result at this temperature of slab without Thermocol is 33.60 °C and for the case 1 slab panel is 32.04 °C, case 2 panel is 32.05 °C and for the case 3 panel is 32.04 °C. These results with setup are as shown below.



Fig. 10. Test result for thermal conductivity.



In above Fig. 10 we see the result of slab with Thermocol at 57 °C temperature on the left and the result for the concrete slab without Thermocol on right. Experiment has used as a design mix for the concrete used in every setup that is been experimented throughout all the tests.

The arrangement is used for testing all the samples taken under consideration throughout the experiment and the results are provided further. Flexural tests are to be performed on each of the 4 cases of arrangements of thermocol with the reinforced concrete and the most efficient design is to be analyzed.

Water Absorption Test:

The sample of thermocol was tested for its water absorption in order to check its waterproofing capacity.

Weight of wet sample;  $W_1 = 25$  gms.

Weight of oven dry sample;  $W_2 = 24.99$  gms.

Percentage Water absorption =  $\frac{W_1 - W_2 \times 100}{W_2} = 0.04\%$

## 4 Results

From the tests conducted on concrete cubes and casted slab samples for flexure tests the results are tabulated for 7, 14 and 28 days strength in Table 3.

**Table 3.** Compressive strength results

	No.	Load (KN)	Compressive strength (N/mm <sup>2</sup> )	Avg. compressive strength (N/mm <sup>2</sup> )
7 Days strength	A1	350	15.55	15.40
	A2	340	15.11	
	A3	340	15.11	
	A4	350	15.55	
	A5	345	15.33	
	A6	355	15.77	
14 Days strength	A7	400	17.77	17.70
	A8	410	18.22	
	A9	405	18.00	
	A10	390	17.33	
	A11	390	17.33	
	A12	395	17.55	
28 Days strength	A13	600	26.66	26.96
	A14	630	28.00	
	A15	610	27.11	
	A16	590	26.22	
	A17	595	26.44	
	A18	615	27.33	

**Table 4.** 28 days flexural strength results

No.	Load (KN)	Flexural strength (N/mm <sup>2</sup> )	Avg. compressive strength (N/mm <sup>2</sup> )
A13	59.0	17.553	18.049
A14	62.0	18.446	
A15	60.0	17.851	
A16	61.0	18.148	
A17	60.5	18.000	
A18	61.5	18.297	
B13	53.0	15.768	18.049
B14	53.5	15.917	
B15	53.0	15.768	
B16	52.0	15.471	
B17	52.5	15.619	
B18	52.0	15.471	
C13	55.0	16.363	16.338
C14	56.0	16.661	
C15	55.5	16.512	
C16	54.5	16.214	
C17	54.0	16.066	
C18	54.5	16.214	
D13	59.0	17.553	17.230
D14	58.5	17.404	
D15	56.0	16.661	
D16	59.5	17.702	
D17	57.0	16.958	
D18	57.5	17.107	

The results as in Table 4 show us the strengths of the M20 grade casted cubes and its strength across 28 days and can be concluded to have good compressive strength. From the results of flexural test it is observed that the Flexural Strength of the composite slab using Thermocol as an insulating material are of good strength compared to RCC slab.

Figures 11, 12, 13, and 14 below show the results for Flexural strength test results of 28 days for RCC slab, case 1, case 2, case 3 arrangements respectively. Graphs of Load vs Deflection curve are plotted as below.

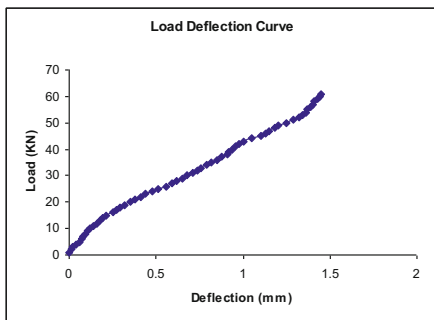


**Fig. 11.** Load deflection curve for 28 days flexural strength of RCC slab.

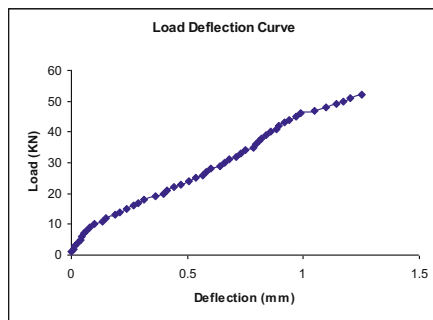


**Fig. 12.** Load deflection curve for 28 days flexural strength of case 1.



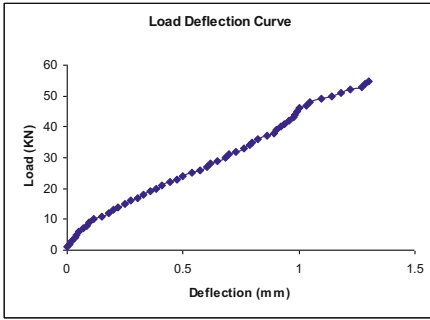


**Fig. 13.** Load deflection curve for 28 days flexural strength of case 2.

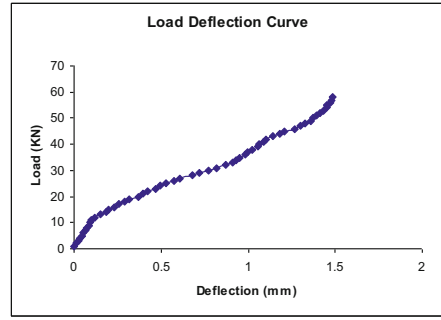


**Fig. 14.** Load deflection curve for 28 days flexural strength of case 3

The experimental result on thermocol shows following results in Table 5 tell us about the water absorption capacity and thermal conductivity.

**Table 5.** Thermal conductivity of Thermocol

Thermal conductivity, (W/m <sup>2</sup> K)	0.035
Water absorption (%)	0.04%

The average Thermal Conductivity, Thermal Resistivity and Thermal Resistance results at room temperature of 37 °C is as tabulated below,

**Table 6.** Thermal properties results

Sr. no.	Case	Thermal conductivity value (W/m <sup>2</sup> K)	Thermal resistivity (m <sup>2</sup> K/W)	Thermal resistance (m <sup>2</sup> K/W)
1	RCC slab	1.60	0.625	0.0343
2	Composite slab with Thermocol with anchor bars (Case 1)	0.050	20	1.1
3	Composite slab with Thermocol with perforations (Case 2)	0.040	25	1.375
4	Composite slab with Thermocol sheet below the reinforcement (Case 3)	0.050	20	1.1

The thermal absorption capacity for the Thermocol is 0.04% which makes Thermocol an excellent water proofing material. From the flexural test results case 2 and 3 show good bond strength but weaker for case 1. The Table 6 concludes about the

properties and slab specimen best suited for use from the thermal resistivity and resistivity values.

## 5 Conclusions

1. From the thermal insulation results it is concluded that the RCC slab panel has high thermal insulation value and by using the Thermocol sheet in slab as an insulating material, the thermal insulation value of the panel is very much less.
2. Hence it is concluded that Thermocol is a good insulating material and which can be used in various structures like residential buildings, hospitals, school buildings and offices.
3. The result of water absorption test shows that Thermocol is good waterproofing material.
4. From flexural results it is found that the bond between Thermocol and concrete is good, in this work for case 2 and 3 the bond is good but in case 1 the bond is somewhat weak and to be improved.

## References

- Abela A.: Thermal Performance of Insulation Samples: Applications to Malta, pp. 1–4. University of Malta, June 2006
- Campbell-Allen D., Thorne C.P.: Thermal conductivity of concrete. *Mag. Concr. Res.* **15**(43), 39–48 (1963)
- Ivan, G., Vladislovas, K., Saulius, V., Sigitas, V.: Assessment of strength under compression of expanded polystyrene (EPS) slabs. *Mater. Sci.* **10**(4), 326–329 (2001)
- IS 456:2000: Design of plain and reinforced concrete
- Mustapa, S.A.S., Sulong, N.H.R., Rashid, M.K.A.: Applications of Expanded Polystyrene (EPS) in buildings and constructions. *J. Appl. Polym. Sci.* **2019** (2019)
- Spitzner Martin, H.: Thermal insulation of buildings: materials, properties and systems. In: *The Annual Insulation Conference 2003, Dubai*. 30 November 2003, pp. 1–17 (2013)
- SternalJohn, R., TheDutcher Group: Extruded Polystyrene Foam Insulation Association Background, vol. 15, pp. 12–15. Dutcher Group Publications (2015)
- Swinton, M.C., Bomberg, M.T., Kumaran, M.K., Normandin N., Maref, W.: Performance of thermal insulation on exterior of basement wall. *Constr. Technol. Update* **36**, 1–20 (1999)
- Yucel, K.T., Basyigit, C., Ozel, C.: Thermal insulation properties of expanded polystyrene as construction and insulating materials. Technical Paper, Suleyman Demirel University, Civil Engineering Department, Isparta/Turkey, pp. 1–13 (2003)
- ZarrRobert, R.: Insulation materials: testing and applications. *ASTM STP*, 3rd vol., 1320, pp. 91–105



# Use of Polyvinyl Acetate and Glass Fiber for Improving Expansive Soil

Vijay Kumar<sup>(✉)</sup>, R. P. Tiwari, and Deepak Kumar

Civil Engineering Department, MNNIT Allahabad, Allahabad 211004, India  
{vkr, rpt}@mnnit.ac.in

**Abstract.** Population of world is increasing at alarming rate which has led to large scale urbanization. For this, construction activities over expansive soil has increased in last decade. For stability and reliability of any structure on the poor soil, bearing capacity of soil should be enhanced for structural security. In this research, the influence of two additives Poly Vinyl Acetate (PVAc) and Glass fiber were used on expansive clayey soils for engineering properties examined. The impact of polymers with fiber on the unconfined compression strength and free swell index of the prepared soil was assessed. PVAc added in dosage of 0%, 2%, 4% and 5%, also the Glass fibers are added in proportions of 0.25% and 0.50%. Soil samples with glass fiber are cured for 1 and 14 days. Outcome of UCS tests on stabilized expansive clay samples with different PVAc together with fiber contents after curing for 1 and 14 days stated that such hydrophilic polymers significantly enhance the compressive strength of expansive clay soils. It also increases their strength with curing period. Soil behavior changes from fragile to ductile with the addition of glass fiber and increasing resistance at the identical time are important advantages in developed clay. The reduction in free swell index occurred due to physiochemical connection which moderate the potential expansion of the soil. The effectiveness of the additives however, depends greatly on the soil type, fiber length and testing conditions.

**Keywords:** Unconfined compressive strength · Stabilisation · Organic polymer · Expansive soils · Free swell index

## 1 Introduction

In the 1970s, soil stabilizer was introduced in developing countries such as the Japan and US as a new material for environmentally sustainable soil development. Development objectives have created the need of construction in each locality of the country's area this has led in utilization of the Expansive soil in construction as nearly 20% area of India is covered with Expansive soil i.e., Black Cotton (BC) Soil. Traditional methods of stabilization incorporate the implementation of various blends of cementitious material, lime, bitumen products and fly ash. Significant investigation on the use of conventional stabilizers has been performed (Yong and Ouhadi 2007; Soltani et al. 2017). Using cement in soil stabilization, shrinkage occurs caused due to hydration of the cement and drying of cement, is commonly observed fact, which significantly increases the permeability as well as reduces the strength (Nakayama and

Handy 1965). Traditional stabilization technique often require longer cure times and comparatively large amounts of additives for a considerable improvement in strength. However no selection criteria is available for Non-traditional stabilizers (including enzymatic emulsions, polymers, Lignosulfonates, emulsions of tree-resin, and industrial waste materials), and extremely little research has been done on these materials, but have shown encouraging leads to stabilizing expansive clays. Although these materials vary in nature also chemical characteristics, they will be wont to diminish porousness, lessen liquefaction, surge soil strength by occupying the voids and created bonding between the particles (Ajalloeian et al. 2013; Mohammad et al. 2015; Naeini et al. 2012). With the growth of the global economy in addition engineering construction have rapidly impacted the natural climate, leading to a number of natural hazard, such as soil erosion, land-slides and dust pollution, etc. The average soil loss in the US is  $8.7 \times 10^6$  kg/km<sup>2</sup> each year, according to some investigations (Orts et al. 2000). Approach of using stabilizing agents on soil has a long history, for e.g. the use of fiber in Great Wall of China around 2000 years' earlier (Hongu and Philips 1990). A concoction of unrealized stabilizers recognized by the USACE during 1946–1977 were advanced (Oldham et al. 1997). The result of the findings were divided by soil type and illustrated that product performance differed for varying soil types. This was also reported that the stabilization functions for particular stabilizing compounds, such as salts, were especially suited to different regimes. Azm et al. (1997) revealed that, alligator cracking, rutting, depression and swelling damage are most frequent failures of pavement of Ibrid City principally due to the lack of proper drainage path.

Glass fibers, incorporated in this research are very much in demand these days. These are used to enhance unconfined compressive strength (UCS), volumetric reduction and swelling (Tang et al. 2007). Soil strengthened by fibre serves as a synthesized material in which comparatively higher tensile strength fibers are used in the soil. Shear strength of soil mobilize tensile resistance in soil fibres that, in effect, give the soil greater strength. Maher and Ho (1993) concluded that incorporating 1% fiber and 4% cement in sand result in the increase of 1.5 times in UCS on comparing to no fiber reinforcement in cement stabilized sand. Consoli et al. (1998) revealed that incorporating fibers (GF) in silty sand constructively enhances strength. Hejazi et al. (2012) stated that the surge in stiffness and strength was a function of fiber properties and test conditions such as confining pressure. In all, it is important to note that the work into the use of cohesive-soil fibers was tighter. Though fibre-reinforcement cohesive strength was increased, these reinforcements of soils requires further evaluation, since interface loading mechanisms between fiber and soil matrix are not appreciated.

The main objective is to analyze geotechnical properties of soil, glass fiber with polymer (Polyvinyl acetate) and to know its optimal quantity. Polymerization of vinyl acetate monomer leads to PVAc is an artificial elastic polymer. The different mixes were tested for UCS and free swell index after curing period 1 and 14 days.

## 2 Materials

### 2.1 Soil

Expansive soil samples was procured from Chakghat Village, Rewa (M.P.). The BC soil was procured after removing the upper soil of 500 mm (disturbed sample). Black Cotton soil are mostly inorganic clays. In India these soils covers almost 520000 km<sup>2</sup> area of land. These soils have a high property of shrinkage and swelling. The soil becomes very hard when it is dry and as soon as it intercepts moisture it loses its bearing capacity. Upon soil drying it shrinks and cracks are really large. The Grain size distribution is plotted in Fig. 1. The basic geotechnical properties of the soils tested for Atterberg limits, Particle size, compaction parameters and Free Swell index are shown in Table 1.

**Table 1.** Geotechnical properties of soil

Physical Properties	Value
Specific Gravity (G)	2.59.
<b>Grain Size</b>	
Clay (%)	52.64
Silt (%)	24.55
Sand (%)	3.16
Gravel (%)	0
<b>Compaction Parameters</b>	
MDD (Max. dry density)	1.65 gm/cm <sup>3</sup>
OMC(Optimum moisture content)	19.17%.
Natural moisture content	10.11%.
<b>Atterberg limits</b>	
Liquid limit	69.76%.
Plastic Limit	30.27%.
Plasticity Index	39.49%.
Free swell index	67.27%.
IS Classification System	CH.

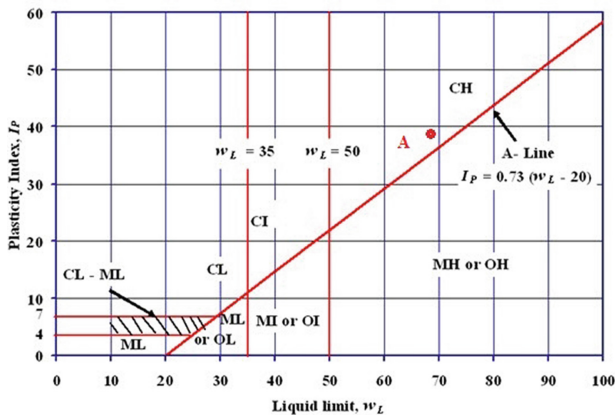


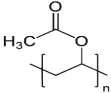
**Fig. 1.** Plasticity chart (IS:1498, 1970).

## 2.2 Poly-Vinyl Acetate (PVAc)

Polymerization of vinyl acetate monomer results to PVAc. It is an artificial polymer. PVAc emulsions are functional as glues for various provisions, like cloth, timber and paper (Matinmanesh 2010). It's being employed to shield soil and seed from either wind erosion or water erosion or both. PVAc may additionally be used for surface treatment of agricultural land and as stabilizing sand (Wolfgang et al. 1998). It its risk-free and biologically favorable polymer (Crowley et al. 2009). The hydrophilic groups ( $-\text{OOCCH}_3$ ) reacts with the clay particles ions in its molecular structure and create physico-chemical bonding between PVAc molecule and soil particles. The bonds are of the ionic and hydrogen varieties. Via these bond the long-chain polymer macro molecules enclose and interlink the soil grain surfaces around them to create viscous membrane structure that decreases ability of expansive soil to swell and shrink. Table 2 represents the important physical and chemical properties of the PVAc. PVAc has the subsequent primary advantages:

- It's soluble in water and might be further thinned to different concentrations.
- Soil can form an elastic and viscous film in the presence of PVAc.
- It's an ecologically friendly product and price effective product.

**Table 2.** Physiochemical properties – PVAc

Property	Value
Chemical Formula	 $\left[ \text{CH}_2 - \text{CH} \left( \text{COOCH}_3 \right) \right]_n$
Physical occurrence	Fluid (Liquid)
Color	White
B.P. °C	100
pH	6.5-7.5
Viscosity MPa	420
Density, gm/cm <sup>3</sup>	1.07
Solid, %	45

## 2.3 Glass Fiber

Strength of silty sand improves with the inclusion of glass fibers (Consoli et al. 1998). In another study, (Consoli et al. 2004) verified the effect of Polypropylene (PP), Polyester (PET) and glass fibers on the mechanical behavior of cemented soils reinforced by fiber. The result shown that the incorporating of PP fibers greatly improved the brittleness of cement treated soils, while very slight decrease in deviator stress during failure. The inclusion of PET and glass fibers is slightly different to the case of PP fibers because it led to increase within the deviator stress at failure and considerably reduced the brittleness of soil sample. Conversely, Al-Refeai (1991) said polypropylene fiber surpassed glass fibers. The physical and mechanical properties of the glass fibers utilized during this study are shown in Table 3.

**Table 3.** Glass fiber property

Property	Value
Single strand Strength (Tension)	3.7 GN/m <sup>2</sup>
Young's modulus as per ASTM D2256	76 GN/m <sup>2</sup>
Specific gravity	2.59
Diameter	0.4 mm
Length	10 mm

### 3 Experimental Studies

The project's approach seeks to assess the engineering properties of soil for its application in various construction such as retaining walls, road, rail pavements and light loaded structures etc. Upon determining soil type and engineering properties, a distinction can be made between the properties of untreated soil and soil mixed with polyvinyl acetate (PVAc) with Glass fiber as it is blended to improve soil properties. The properties of the soil to be determined, decides the laboratory tests to be performed on the soil samples. In this research work the following laboratory tests are performed. (i) UCS test – IS: 2720 (Part 10) – 1991. (ii) Free Swell Index (FSI) test – IS: 2720 (Part 40) – 1977. During the conduct of the experiments the Indian standard codes were followed. To study the efficacy of chemical additives included in this study the UCS and Free swell index of expansive soils. For UCS the soil specimen is compacted to a maximum dry density of 16.67 kN/m<sup>3</sup>. A series of UCS tests is done to assess the optimum amount of PVAc and Glass Fiber to stabilize the soil samples at pre-established unit weight. In the very first, the UCS sample prepared at max dry unit weight of 16.7 kN/m<sup>3</sup>. Prepared sample was kept for 1 day and 14 days curing after that samples were tested and determined. On the next move, series of unconfined compression strength tests on the soil samples were performed to optimize the PVAc material. Soil sample equipped with 0–5% PVAc with 1 and 14 day curing for both compact samples at 16.67 kN/m<sup>3</sup> of dry unit weight.

## 4 Results and Discussion

### 4.1 Deviation in U.C.S. with PVAc Variation

As illustrated in Fig. 2, adding the polyvinyl acetate in the soil sample increases the UCS value up to 69% for a rise up to 4% in PVAc content from 0% PVAc. But on further increasing the PVAc to 5% of dry weight the UCS value slightly decreased. This decrease in UCS could be due to the fact that, PVAc used in soil to add the fraction of the interfaces between soil particles and not in filling voids so on further increasing the PVAc content will not be efficient. On other side, polymer has lower compressive strength than soil grains. If increasing PVAc content fills the voids, lower UCS value will be obtained. By the process of penetration and phase diffusion, the PVAc matrix with soil forms reticular membrane between soil particles, which

improves the bonds between the soil grains and uplift the strength of soil samples. With the increase of the PVAc proportions, the interaction of the PVAc and the soil is also strengthened up to 4% polymer; hence the compressive strength of the soil increases with the increase in PVAc concentration.

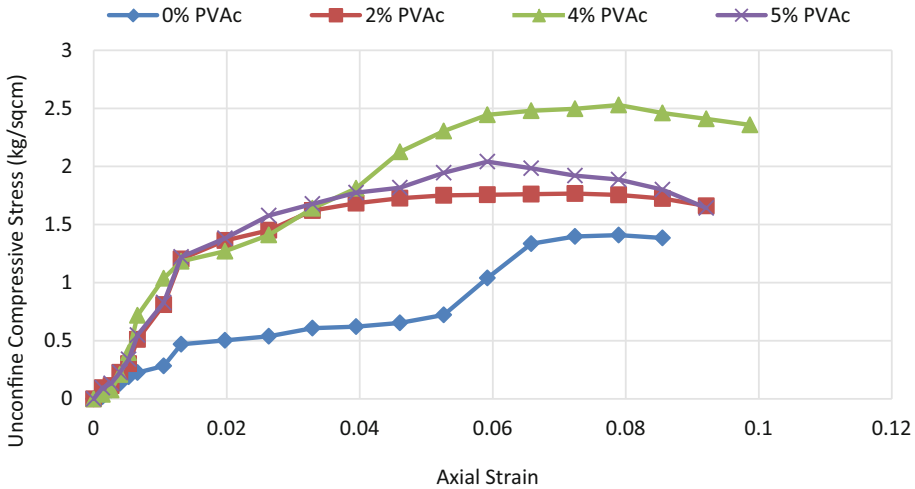


Fig. 2. Stress – Strain curve for different percentage of PVAc.

#### 4.2 Deviation in UCS due to Curing Time

To find out the effect of cure time on UCS value, three soil sample were made, tested at 1 day and 14 day of curing time and their average is taken. The result of UCS test of both treated and untreated soil is present in Table 4. Prolonged contact with soil particles, PVAc is adsorbed by electrostatic attraction on to the soil outer surface (Fig. 3a). On the surface of the soil particles the carboxyl groups form hydrogen bonds with hydroxyl groups of water present on soil surface (Fig. 3b). Because of the large amount of hydrogen Bonds available, soil structure is steadier. This bond formation increased with curing as initially the number of bonds formed would be less that results in low UCS improvement of soil specimen. On curing it for 14 days with PVAc the UCS value increased of about 28%.

Table 4. Results of unconfined compressive strength on PVAc treated Soils (kg/cm<sup>2</sup>)

Soil type	Polymer content (%)	Cure time	
		1 day	14 day
Black cotton soil	0	1.492	1.509
	2	1.581	1.767
	4	1.974	2.529
	5	1.869	1.954



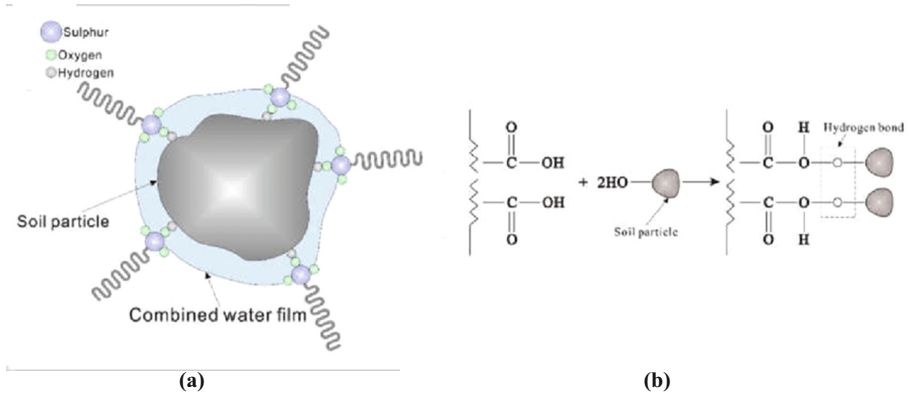


**Fig. 3.** (a) Interaction of PVAc with soil particle (b) Formation of hydrogen bond b/w soil and PVAc.

### 4.3 Deviation in UCS Due to Fiber Addition

Figure 5 states that with a constant amount of PVAc content, the U.C.S. of the reinforced soil increases with an increase in fiber content. The fiber reinforcement increases the peak stress of soil. According to Fig. 4 the optimum quantity of Fiber is 0.25% by dry weight of soil and 10 mm length. The value of UCS increased from a value of 2.529 kg/cm<sup>2</sup> to 2.928 kg/cm<sup>2</sup> about 16% further surge in the UCS value of the soil treated with 4% PVAc. Large amount of fibers in the soil further decreases the UCS value it is due to the fact that large amount of fiber-fiber interaction instead of fiber-soil interaction. There could be possibly two reasons for explaining using short fiber in UCS value. Firstly, longer strands bends over and above themselves. Secondly, in a particular percentage there would be more strands of short fiber then using the long fiber.

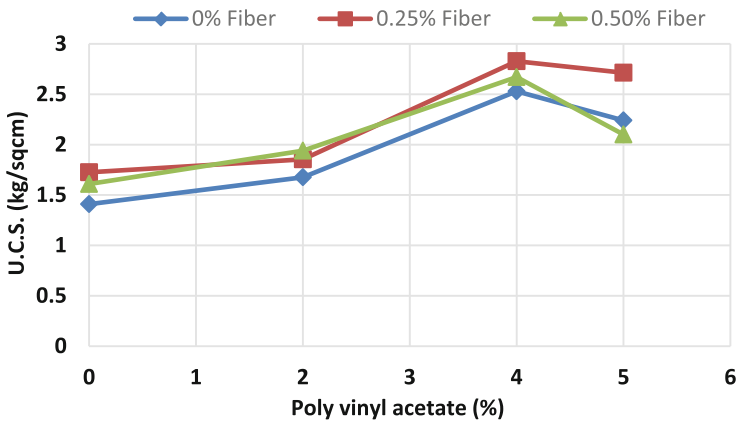


**Fig. 4.** Graph of UCS test for different percentage of PVAc and fibers.

### 4.4 Effect of PVAc-Fiber on FSI

The influence of PVAc at varying quantities (0%, 2%, 4%, and 5%) on FSI of the PVAc-reinforced soil is presented in Fig. 5, also the results are tabulated in Table 5. FSI value of the treated soil specimen is reducing with increasing PVAc content is shown in Fig. 5. The dip in FSI value of the soil with 5 percent of PVAc is sort of 49% while comparing to pure soil. This dip happened owed to chemical bonding which reduce the particular expansion of the soil. The upper swelling and shrinkage characteristics is because of more Na & Ca contents. Curing the sample for 14 Days after addition of PVAc to soil is more effective, because there is complete and uniform propagation of the polymer between soil particles.

**Table 5.** Variation of FSI for different percentage of PVAc and fibers

Soil type	Polymer (%)	Glass fiber (%)		
		0%	0.25%	0.50%
Black cotton soil	0%	112	97	90
	2%	102	81	71
	4%	85	64	62
	5%	68	61	57

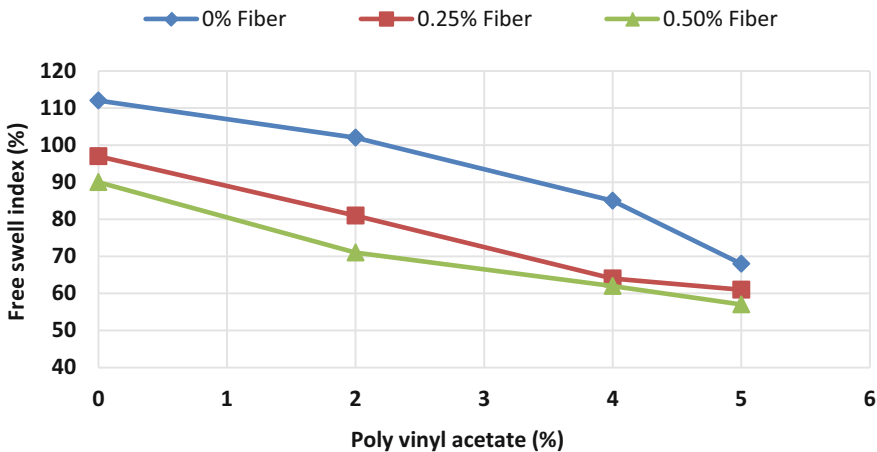


**Fig. 5.** Variation of FSI for different percentage of PVAc and fibers.

## 5 Conclusion

This research was conducted to study the suitability and use of polymer with glass fiber and curing time on the UCS of treated along with on untreated soil sample also the FSI is observed on the soil sample. Study findings are reported in the subsequent conclusions:

- The UCS value increases with the curing time of soil specimen. Initially with curing time the Gain of strength was higher and after 7 days the growth rate slowed down.
- The U.C.S. Of treated soil can be constructively boosted by PVAc polymer and GF. Keeping the dry density same, the strength soared with increasing PVAc and fiber. The sample with dry unit wt. of  $16.7 \text{ kN/m}^3$ , the UCS improved with PVAc content of 4% and 0.25% glass fiber from a value of  $1.509 \text{ kg/cm}^2$  to  $2.928 \text{ kg/cm}^2$  about 94% increase.
- The FSI of soils is additionally found to be decreasing with increasing polymer content and further decreases with increase in fiber.

Findings from this research showed that PVAc can be effectively used as soil stabilizer to increase its compressive strength and swelling shrinkage of soil by a nontoxic and organic polymer. This research is still ongoing, and the present paper is based on the partial results to this level.

## References

- Ajalloeian, R., Matinmanesh, H., Abtahi, S.M., Rowshanzamir, M.: Effect of polyvinyl acetate grout injection on geotechnical properties of fine sand. *Geomech. Geoeng.* **8**(2), 86–96 (2013)
- Azm, A., Obaidat, A., Turki,: Loss in serviceability of pavements due to expansive clay subgrades. *Environ. Eng. Geosci.* **3**, 277–294 (1997)
- Al-Refeai, T.: Behavior of granular soils reinforced with discrete randomly oriented inclusions. *Geotext. Geomembr.* **10**, 319–333 (1991)
- Bureau of Indian Standards. Classification and Identification of Soil. IS : 1498–1970
- Bureau of Indian Standards. Determination of free swell index. IS: 2720 (Part 40) – 1977
- Bureau of Indian Standards. Determination of Unconfined Compressive Strength. IS: 2720 (Part 10) – 1991
- Consoli, N.C., Montardo, J.P., Donato, M., Prietto, P.: Effect of material properties on the behavior of sand–cement–fiber composites. *Proc. Inst. Civil Eng. Ground Improve.* **8**(2), 77–90 (2004)
- Consoli, N.C., Prietto, P.D.M., Ulbrich, L.A.: Influence of fiber and cement addition on behavior of sandy soil. *J. Geotech. Geoenviron. Eng.* **124**(12), 1211–1224 (1998)
- Crowley, J., Bell, D., Holtwiesche, B.K.: Environmentally favorable erosion control with a polyvinyl acetate based formulation Quattro Environmental Inc., Technical Report (2009)
- Hejazi, S.M., Sheikhzadeh, M., Abtahi, S.M., Zadhoush, A.: A simple review of soil reinforcement by using natural and synthetic fibers. *Constr. Build. Mater.* **30**, 100–116 (2012)
- Hongu, T., Philips, G.: New fibers Ellis Horwood Series in Polymeric Science and Technology. New York (1990)
- Maher, M., Ho, Y.: Behavior of fiber-reinforced cemented sand under static and cyclic loads. *Geotech. Test. J.* **16**(3), 330–338 (1993)
- Matinmanesh, H.: Laboratory study of fine graded sand improvement using polyvinyl acetate injection. In: *The 4th International Conference on Geotechnical Engineering and Soil Mechanics*. Tehran, Iran (2010)
- Mohammed, L., Ansari, M.N.M., Pua, G., Jawaid, M., Islam M.S.: A review on natural fiber reinforced polymer composite and its applications. *Int. J. Polym. Sci.* **15**, 1–15 (2015)
- Naeini, S.A., Naderinia, B., Izadi, E.: Unconfined compressive strength of clayey soils stabilized with waterborne polymers. *KSCE J. Civil Eng.* **16**(6), 943–949 (2012)

- Nakayama, H., Handy, R.L.: Factors Influencing Shrinkage of Soil-Cement. Highway Research Record 86 (1965)
- Oldham, J.C., Eaves, R.C., White, D.W.: Materials evaluated as potential soil stabilizers. U.S. Army Engineer Waterways Experiment Station, pp. 77–15 (1997)
- Orts, W.J., Sojka, R.E., Glenn, G.M.: Biopolymer additives to reduce erosion-induced soil losses during irrigation. *Ind. Crops Prod.* **11**, 19–29 (2000)
- Wolfgang, R., Stephan, V.T., Heinz, M., Hartmut, B.: Use of selected polyvinyl acetate dispersions for the surface stabilization of sand and/or soil. United State Patent, Patent Number: 5846601, pp. 846–601 (1998)
- Soltani, A., Taheri, A., Khatibi, M., Estabragh, A.R.: Swelling potential of a stabilized expansive soil: a comparative experimental study. *Geotech. Geol. Eng.* **35**, 1717–1744 (2017)
- Tang, C., Shi, B., Gao, W., Chen, F., Cai, Y.: Strength and mechanical behavior of short polypropylene fiber reinforced and cement stabilized clayey soil. *Geotext. Geomemb.* **25**(3), 194–202 (2007)
- Yong, R.N., Ouhadi, V.R.: Experimental study on instability of bases on natural and lime/cement-stabilized clayey soils. *Appl. Clay Sci.* **35**, 238–249 (2007)



# Effect of Terrain Category, Aspect Ratio and Number of Storeys on the Shear Lag Phenomenon in RCC Framed Tube Structures

Sapna Kumari<sup>1</sup>(✉), Ashish Singh<sup>2</sup>, and Sasankasekhhar Mandal<sup>2</sup>

<sup>1</sup> IEST Shibpur, Howrah, West Bengal, India  
kumarisapna785@gmail.com

<sup>2</sup> IIT BHU, Varanasi, Uttar Pradesh, India  
{ashishsingh.rs.civ18, smandal.civ}@iitbhu.ac.in

**Abstract.** Nowadays many tall structures and high rise buildings are being built all around the world. Wind load is found to be dominant load in analysis of tall structures. The IS 875 (Part-3): 2015 deals with wind loads on different types of structures. Effect of wind is predominant on tall structures depending on location of the structure and height of the structure. Tubular structures, when subjected to lateral load such as wind load, the corner columns experience much higher axial load due to the shear lag phenomenon. Several studies investigated tall tubular structures for its shear lag responses. In this study, both tubular and realistic framed buildings have been studied for the understanding of relative shear lag effect subjected to wind loading. This study presents the shear lag effects on buildings with different terrain categories as per IS 875 (Part3), with varying plan aspect ratio using STAAD.Pro. Both tubular and framed models are analyzed with aspect ratio 0.5, 0.75, 1 and 1.167. Also the effect of height variation on amplified axial forces is studied by varying height from 16 to 40 storeys.

**Keywords:** Shear lag phenomenon · Amplification factor · Plan aspect ratio · Tubular structure · STAAD.Pro

## 1 Introduction

Generally, the lateral load resistance of framed tube system is largely enhanced with the help of tube action. When subjected to lateral load, the tube behaves like a cantilever box beam, where the column deflects in lateral direction and beam deflects in bending. Shear lag effect is a major phenomenon that controls the design of tall buildings using framed tube system. During the tube action, the shear lag occurs. The wind becomes the governing factor as the structure height increases. Positive shear lag occur in the lower part of the building where as in upper storeys negative shear lag prevails. The axial force in column, immediately adjacent to the corner, increases and with further increase in height of structure, it starts to shift towards central columns. Some columns of compression flange may also develop tension right from the support depending upon height of the structure.

**Citation:** The popular framed tube structural system was introduced by Khan (1961) as an additional exterior structure in tall buildings. Coull and Ahmed (1978), Ha et al. (1978) analyzed structural system of framed tube building by using equivalent plane frame elements method. Kwan (1994) assumed that the distribution of axial displacement of web is independent of flange panel and noted that shear lag is also influenced by the variation of loads on structure. Singh and Nagpal (1994) and Jain and Mandal (2012) investigated negative shear lag by modeling a 40-storey framed tube building. They also noted that positive shear lag occurs in the bottom part of the building while negative shear lag occurs at the top part. Lee et al. (2000) used numerical methods to analyze shear lag effect in framed tube structures comprising of multiple internal tubes. Nouri and Ashtari (2013) examined shear lag in braced tube tall structures compared to framed tube tall structures as an alternate solution to resist shear lag phenomenon. Nagvekar and Hampali (2014) analyzed a 30 storey tubular framed building hollow structures by using ETABS software. They found that negative shear lag occurs only after positive shear lag has occurred and becomes the maximum at top portion of building. Singh et al. (2013) showed that additional corner columns provided at the outer side of the corner reduce shear lag significantly. Singh et al. (2013) investigated the effect of additional corner column on shear lag phenomenon in tubular multi-storied building in greater details. Singh et al. (2015) carried out a study on shear lag phenomenon in RCC tube structures.

## 2 Objective

The paper is dedicated to the modeling and the analysis of RCC building with varying terrain category, aspect ratio and building height using STAAD Pro software. An attempt has been made to improve the understanding of shear lag phenomenon in framed tube structures under the action of wind loads. The study quantifies the variation of axial force in web and flange panel columns by varying the plan aspect ratio as 0.5, 0.75, 1 and 1.167. It also looks into the effect of variation of total height of the building on shear lag effect. The height of the building varies as 48 m, 60 m, 72 m, 84 m, 96 m, 108 m, and 120 m. The effect of these parameters on shear lag amplification factor has also been investigated.

## 3 Mathematical Calculation and Codal Provision

Design wind speed ( $V_z$ ) at any height  $z$ , can be mathematically expressed as:

$$V_z = V_b k_1 k_2 k_3 k_4 \quad (1)$$

where,  $V_z$  = design wind speed at any stature  $z$ , in m/s,  $V_b$  = basic wind speed for the location,  $k_1$  = probability factor (Risk coefficient),  $k_2$  = terrain roughness and height factor,  $k_3$  = topography factor,  $k_4$  = importance factor for cyclonic regions.

The values of  $k_1$ ,  $k_2$ ,  $k_3$  and  $k_4$  are adopted from different relevant Tables in IS 875 (Part-3) 2015. The wind pressure at any height above mean ground level should be obtained as:

$$P_z = 0.6V_z^2 \quad (2)$$

where,  $P_z$  = wind pressure in  $N/m^2$  on the structure.

## 4 Description of Structural Configuration

See Table 1.

**Table 1.** Parameters considered for study

Structure height	G+15 to G+39 (Varied)
Floor to floor height	3 m
Number of bays in length	14 bays
Number of bays in width	12 bays
Each bay size	2.5 m $\times$ 2.5 m
Column size	0.8 m $\times$ 0.8 m
Thickness of the plate	0.2 m
No. of stories considered	16, 20, 24, 28, 32, 36, 40
Aspect ratio	0.5, 0.75, 1, 1.167
Wind speed	47 m/s
Modulus of elasticity, E	$2.17 \times 10^7$ kN/m <sup>2</sup>
Poison's ratio, $\mu$	0.17
Types of footings	Fixed foundation
Live load	3.34 kN/m <sup>2</sup>

## 5 Modelling

STAAD Pro is structural analysis and design software which helps in modeling the building frames by varying different parameters of building structures. By changing terrain categories, aspect ratio and number of storey, a total of 22 building frames have been modeled and analyzed using STAAD Pro software. Figures 1, 2, 3, 4, and 5 show few typical layout of columns, model of frame, live load, 3D view of model, applied wind load respectively (Fig. 6).

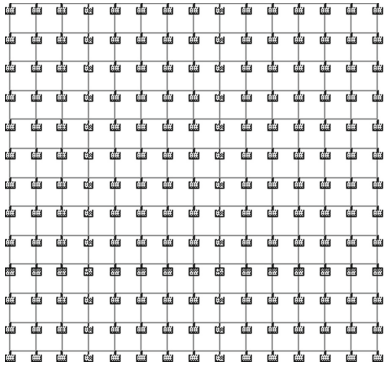


**Fig. 1.** Plan view of model.

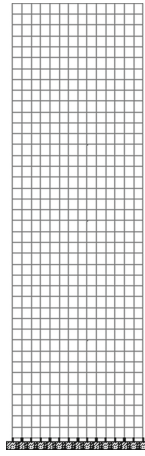


**Fig. 2.** Elevation of model.

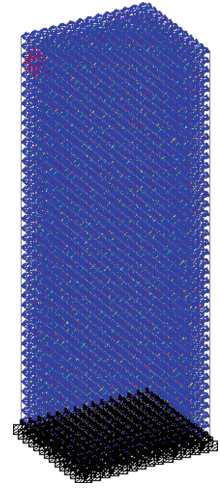


**Fig. 3.** Live load applied.

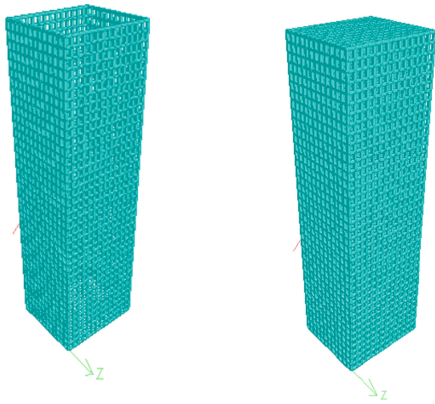


**Fig. 4.** 3D view of tubular structure and bay structure.

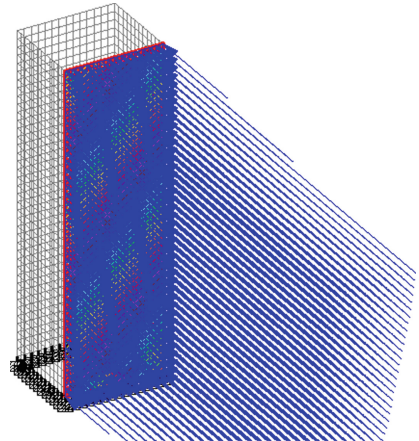


**Fig. 5.** Wind load applied.



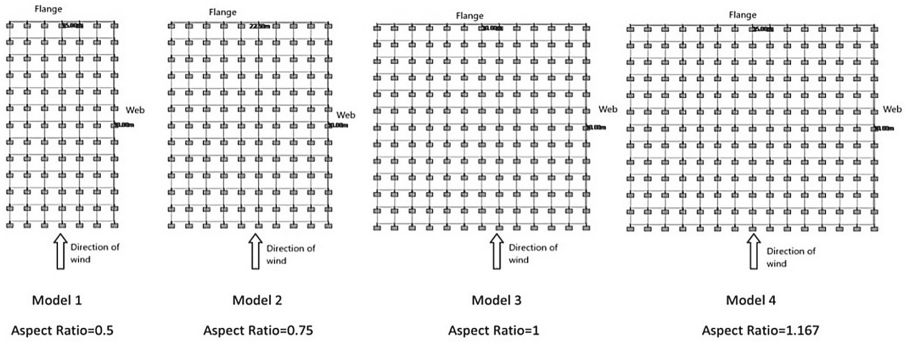


Fig. 6. Models with different aspect ratio considered for study (Plan View).

## 6 Calculation of Amplification Factor

The amplification factor is defined as the maximum force in corner column divided by the average force in the flange columns, expressed as

$$\text{Amplification Factor (AF)} = \frac{\text{Maximum force in the corner column}}{\text{Average force in the flange column}}$$

This factor gets altered due to change in the terrain categories, aspect ratio and total building height.

## 7 Results and Discussion

The variations of axial forces in the flange and web panels along the height of the tubular structure and bay structure have been presented in this section.

### 7.1 Variation of Axial Force in Web Panel Columns and Flange Panel Columns

To study the pattern of axial force distributions in the web and flange panels column and to see the variation of it with terrain category variation, axial force in columns of web and flange panel at every ten storeys have been plotted in each plot (Figs. 7, 8, 9 and 10), so that comparison can be made on between tubular structure and bay structure for plan aspect ratio of 1.167.

Similar kind of variation of axial force along web panel and flange panel columns are obtained for other terrain categories and aspect ratio 0.5, 0.75 and 1 for both tubular structure as well as Bay structure.

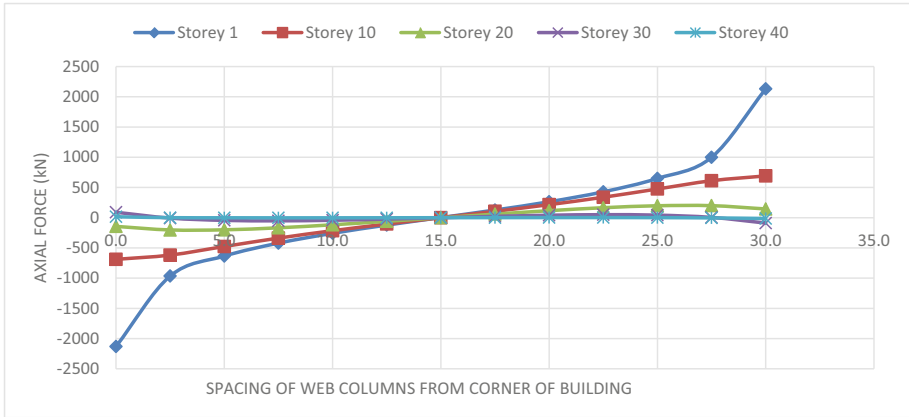


Fig. 7. Variation of axial forces along web panel columns in tubular structure for category 1.

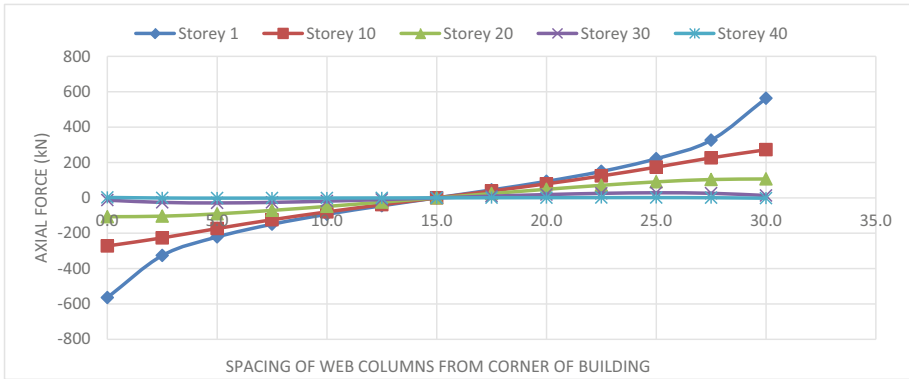


Fig. 8. Variation of axial forces along web panel columns in bay structure for category 1.

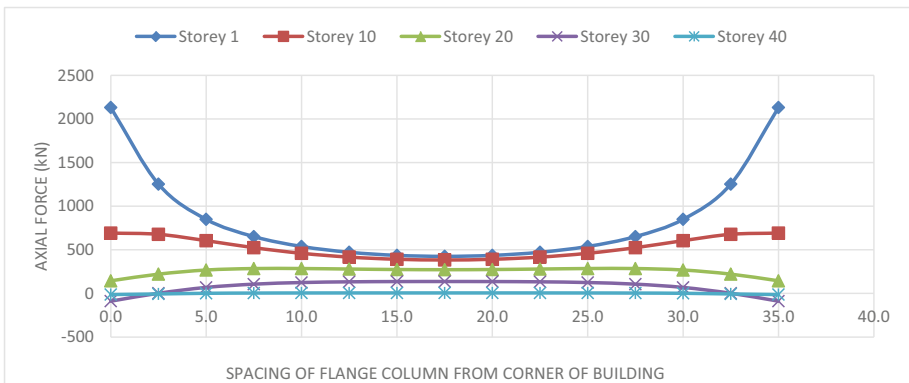
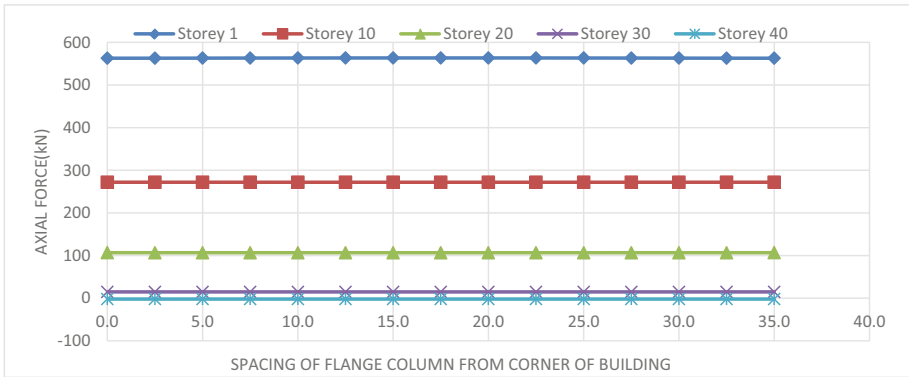


Fig. 9. Variation of axial forces along flange panel columns in tubular structure for category 1.



**Fig. 10.** Variation of axial forces along flange panel columns in bay structure for category 1.

## 7.2 Variation of Axial Force on Varying Terrain Category

Effect of different terrain categories causes variation of axial forces in columns of both web and flange panels. This influence of terrain category, in which the structure stands, has been assessed and the axial forces at foundation level for  $30\text{ m} \times 35\text{ m} \times 120\text{ m}$  building are presented below. It can be noted that as the wind load is maximum in terrain category 1, the axial forces are also more for this category. However, as the bay structures are more rigid than tubular structures, effect of shear lag is lesser in such structures. This supports the fact that a near rigid structure experience negligible shear lag effect (Tables 2, 3, 4 and 5).

**Table 2.** Variation of axial forces (in kN) along web panel columns for category 1, 2, 3 and 4, aspect ratio = 1.167 at foundation level for tubular structure

Distance from corner column (m)	Category 1	Category 2	Category 3	Category 4
0.0	-2130.503	-2055.272	-1898.526	-1824.321
2.5	-964.74	-928.386	-826.054	-844.858
5.0	-634.884	-610.933	-567.488	-556.83
7.5	-420.378	-404.74	-376.083	-369.299
10.0	-258.092	-248.534	-230.996	-226.986
12.5	-122.276	-117.757	-109.46	-107.602
15.0	2.233	2.155	2.01	1.984
17.5	126.974	122.289	113.682	111.759
20.0	263.666	253.897	235.974	231.839
22.5	428.273	412.296	383.043	375.895
25.0	649.351	624.841	580.119	568.061
27.5	998.555	960.06	890.247	867.902
30.0	2130.503	2043.515	1888.239	1816.469

**Table 3.** Variation of axial forces (in kN) along web panel columns for category 1, 2, 3 and 4, aspect ratio = 1.167 at foundation level for bay structure

Distance from corner column (m)	Category 1	Category 2	Category 3	Category 4
0.0	-563.887	-541.354	-500.889	-484.265
2.5	-325.981	-313.538	-291.028	-284.617
5.0	-221.254	-213	-197.885	-194.17
7.5	-149.261	-143.741	-133.606	-131.306
10.0	-92.97	-89.549	-83.257	-81.893
12.5	-44.69	-43.05	-40.032	-39.396
15.0	0.121	0.116	0.107	0.096
17.5	44.93	43.278	40.241	39.583
20.0	93.199	89.766	83.456	82.066
22.5	149.465	143.933	133.78	131.447
25.0	221.406	213.14	198.007	194.25
27.5	325.976	313.606	291.069	284.613
30.0	562.846	540.39	500.037	483.59

**Table 4.** Variation of axial forces (in kN) along flange panel columns for category 1, 2, 3 and 4, aspect ratio = 1.167 at foundation level for tubular structure

Distance from corner column (m)	Category 1	Category 2	Category 3	Category 4
0.0	2130.503	2043.515	1888.238	1816.469
2.5	1253.099	1204.221	1115.869	1084.034
5.0	848.955	816.851	758.302	742.156
7.5	651.525	627.295	582.887	572.245
10.0	538.412	518.586	482.14	474.125
12.5	471.789	454.519	422.712	416.074
15.0	436.209	420.292	390.948	384.994
17.5	424.987	409.495	380.924	375.18
20.0	436.209	420.292	390.948	384.994
22.5	471.789	454.519	422.712	416.074
25.0	538.412	518.586	482.14	474.125
27.5	651.525	627.295	582.887	572.245
30.0	848.955	816.851	758.302	742.156
32.5	1253.099	1204.221	1115.869	1084.034
35.0	2130.503	2043.515	1888.238	1816.469
<b>Amplification factor</b>	<b>2.442</b>	<b>2.436</b>	<b>2.429</b>	<b>2.399</b>

**Table 5.** Variation of axial forces (in kN) along flange panel columns for category 1, 2, 3 and 4, aspect ratio = 1.167 at foundation level for bay structure

Distance from corner column (m)	Category 1	Category 2	Category 3	Category 4
0.0	562.846	540.39	500.037	483.59
2.5	562.88	540.423	500.065	483.614
5.0	563.02	540.553	500.179	483.702
7.5	563.165	540.689	500.299	483.797
10.0	563.29	540.806	500.403	483.88
12.5	563.382	540.892	500.479	483.943
15.0	563.438	540.944	500.526	483.981
17.5	563.457	540.962	500.541	483.993
20.0	563.438	540.944	500.526	483.981
22.5	563.382	540.892	500.479	483.943
25.0	563.29	540.806	500.403	483.88
27.5	563.165	540.689	500.299	483.797
30.0	563.02	540.553	500.179	483.702
32.5	562.88	540.423	500.065	483.614
35.0	562.846	540.39	500.037	483.59

### 7.3 Variation of Axial Force on Varying Aspect Ratio

The axial force along web and panels columns varies with variation in plan aspect ratio of the building. For the same height, a structure having more plan aspect ratio, is vulnerable to higher shear lag. The variation of axial forces is shown below at foundation level for 30 m × 35 m × 120 m building located at terrain category 1. It is to be noted that the oblong structures experience higher shear lag (Tables 6 and 7) .

**Table 6.** Variation of axial forces (in kN) along web panel columns for aspect ratio = 1.167, 1, 0.75, 0.5 and terrain category 1 at foundation level for tubular structure

Distance from corner column (m)	Aspect ratio = 0.5	Aspect ratio = 0.75	Aspect ratio = 1	Aspect ratio = 1.167
0.0	-1086.434	-1456.72	-1879.464	-2130.503
2.5	-538.892	-682.091	-856.476	-964.74
5.0	-346.59	-454.437	-565.819	-634.884
7.5	-245.462	-303.186	-375.655	-420.378
10.0	-152.505	-187.182	-231.068	-258.092
12.5	-73.041	-89.201	-109.716	-122.276
15.0	0.575	1.03	1.685	2.233
17.5	74.208	91.327	113.239	126.974
20.0	153.738	189.562	235.172	263.666
22.5	246.893	306.287	381.338	428.273
25.0	366.807	460	576.369	649.351
27.5	545.238	696.886	882.113	998.555
30.0	1081.344	1448.565	1868.484	2130.503

**Table 7.** Variation of axial forces (in kN) along web panel columns for aspect ratio = 1.167, 1, 0.75, 0.5 and terrain category 1 at foundation level for bay structure

Distance from corner column (m)	Aspect ratio = 0.5	Aspect ratio = 0.75	Aspect ratio = 1	Aspect ratio = 1.167
0.0	-518.139	-553.007	-557.756	-563.887
2.5	-299.276	-307.153	-322.309	-325.981
5.0	-203.18	-208.295	-218.821	-221.254
7.5	-137.074	-140.423	-147.62	-149.261
10.0	-85.379	-87.429	-91.949	-92.97
12.5	-41.04	-42.016	-44.2	-44.69
15.0	0.114	0.117	0.12	0.121
17.5	41.265	42.246	44.436	44.93
20.0	85.594	87.649	92.174	93.199
22.5	137.267	140.621	147.823	149.465
25.0	203.336	208.448	218.973	221.406
27.5	299.377	307.249	322.398	325.976
30.0	517.14	531.994	556.731	562.846

**7.4 Variation of Axial Forces on Varying Building Height**

The axial forces along web and flange panel’s columns vary with variation in number of storey. As the building height increases, shear lag experienced by the structure also increases. The variation is shown for 16, 20, 24, 28, 32, 36, 40 storey building at foundation level having terrain category 1 for both tubular and bay structure (Tables 8 and 9).

**Table 8.** Variation of axial forces (in kN) along web panel columns on varying building height for aspect ratio = 1.167 and terrain category 1 at foundation level for tubular structure

Distance from corner column (m)	16 storey	20 Storey	24 storey	28 storey	32 storey	36 storey	40 storey
0.0	-444.615	-659.004	-901.002	-1170.421	-1467.463	-1792.119	-2130.503
2.5	-108.122	-198.681	-301.132	-442.309	-595.458	-769.766	-964.74
5.0	-61.811	-117.841	-189.15	-276.108	-379.211	-498.805	-634.884
7.5	-36.485	-72.523	-119.044	-176.587	-245.775	-327.044	-420.378
10.0	-19.757	-41.688	-70.172	-105.605	-148.524	-199.329	-258.092
12.5	-7.734	-18.18	-31.805	-48.767	-69.367	-93.847	-122.276
15.0	2.255	2.24	2.192	2.176	2.187	2.21	2.233
17.5	12.475	22.833	36.406	53.344	73.972	98.499	126.974
20.0	25.332	47.19	75.606	111.041	154.001	204.857	263.666
22.5	44.216	80.231	126.749	184.334	253.577	334.898	428.273
25.0	75.939	132.192	203.613	290.65	393.81	513.445	649.351
27.5	140.947	232.167	343.833	476.084	629.258	803.576	998.555
30.0	432.259	646.545	888.469	1157.831	1454.832	1779.462	2130.503

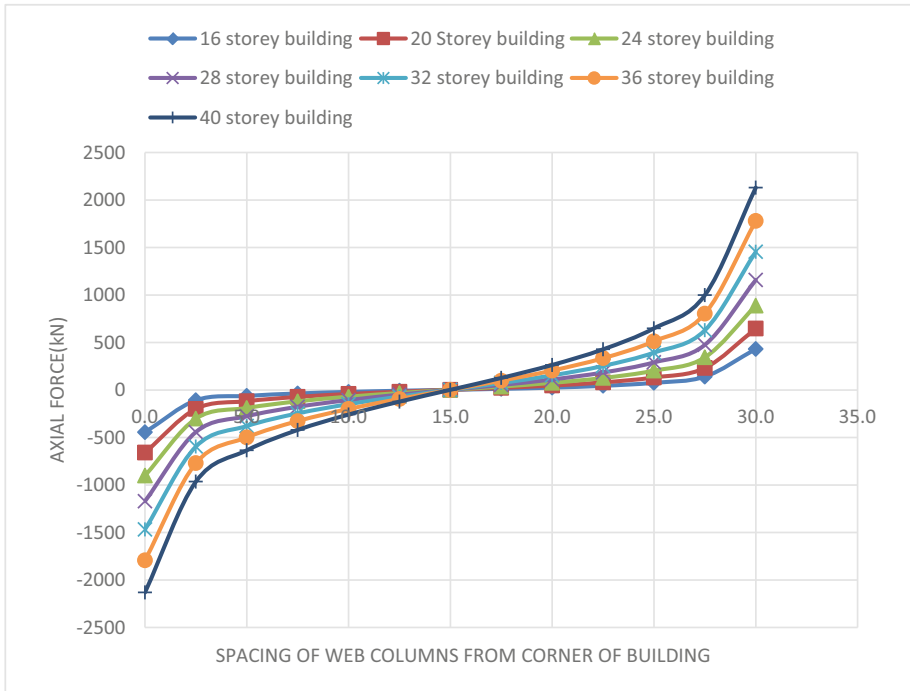


**Fig. 11.** Variation of axial force along web panel's columns for tubular structure.

**Table 9.** Variation of axial forces (in kN) along flange panel columns on varying building height for aspect ratio = 1.167 and terrain category 1 at foundation Level for tubular structure

Distance from corner column (m)	16 storey	20 Storey	24 storey	28 storey	32 storey	36 storey	40 storey
0.0	432.259	646.545	888.469	1157.831	1454.832	1779.462	2130.503
2.5	185.206	302.085	443.167	608.576	798.69	1013.732	1253.099
5.0	91.39	162.894	255.335	369.583	506.38	666.236	848.955
7.5	52.812	102.7	171.08	259.286	368.374	499.087	651.525
10.0	32.785	70.556	125.266	198.397	291.138	404.374	538.412
12.5	21.647	52.261	98.977	163.25	246.267	348.97	471.789
15.0	15.916	42.642	85.089	144.651	222.269	319.492	436.209
17.5	14.144	39.627	80.724	138.803	214.982	310.208	424.987
20.0	15.916	42.642	85.089	144.651	222.269	319.492	436.209
22.5	21.647	52.261	98.977	163.25	246.267	348.97	471.789
25.0	32.785	70.556	125.266	198.397	291.138	404.374	538.412
27.5	52.812	102.7	171.08	259.286	368.374	499.087	651.525
30.0	91.39	162.894	255.335	369.583	506.38	666.236	848.955
32.5	185.206	302.085	443.167	608.576	798.69	1013.732	1253.099
35.0	432.259	646.545	888.469	1157.831	1454.832	1779.462	2130.503
<b>Amplification factor</b>	<b>3.864</b>	<b>3.469</b>	<b>3.161</b>	<b>2.923</b>	<b>2.731</b>	<b>2.573</b>	<b>2.442</b>

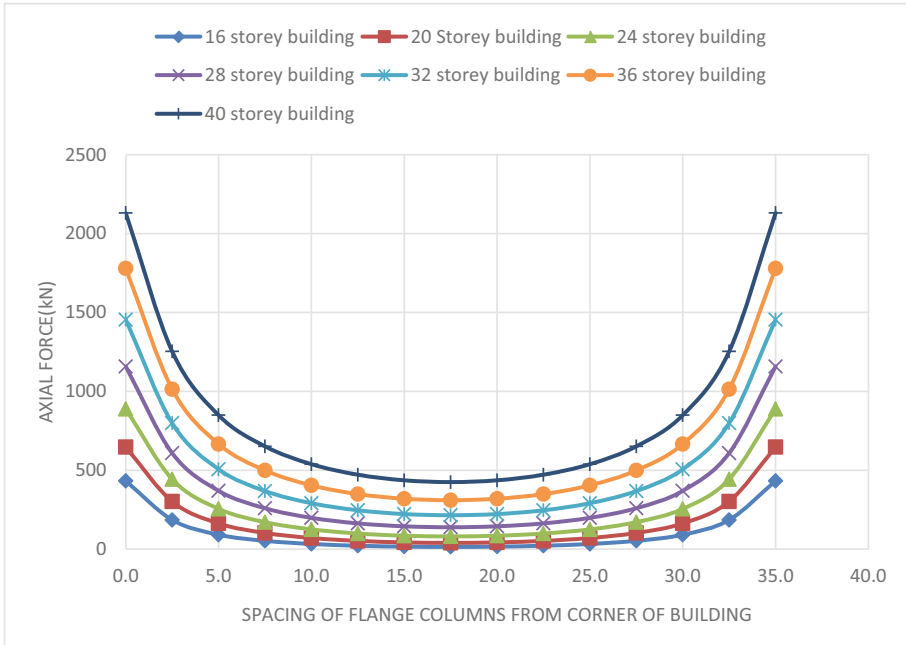


Fig. 12. Variation of axial force along flange panel’s columns for tubular structure.

### 8 Variation of Amplification Factor

As stated above, the amplification factor is altered by changing the aspect ratio, terrain categories and total building height. The variation is depicted in the following Tables and Figures. The values presented here pertain to foundation level of 30 m × 30 m × 30 m building. As noted in Fig. 11, the amplification factor increases with plan aspect ratio. Figure 12 shows that as the wind load value is lowest in category 4, the amplification factor is also the least. The taller the building, the higher is the amplification factor (Fig. 13) (Figs. 14, 15 and Tables 10, 11, 12).

Table 10. Effect of plan aspect ratio

Plan aspect ratio	Amplification factor
1.167	2.442
1.0	2.178
0.75	1.801
0.50	1.442

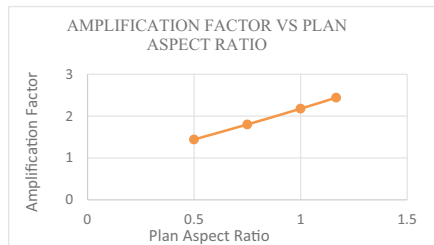
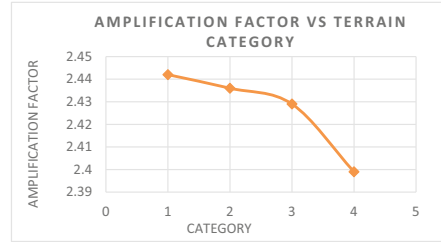


Fig. 13. Variation of amplification factor with plan aspect ratio.

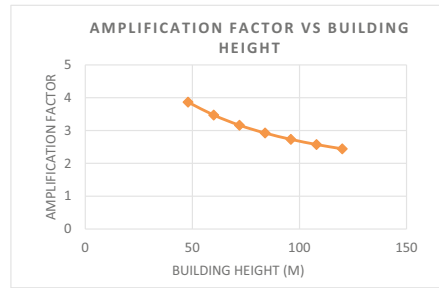


**Table 11.** Effect of terrain category

Terrain category	Amplification factor
Category 1	2.442
Category 2	2.436
Category 3	2.429
Category 4	2.399

**Fig. 14.** Variation of amplification factor with terrain category variation.**Table 12.** Effect of building height

Building height (m)	Amplification factor
48	3.864
60	3.469
72	3.161
84	2.923
96	2.731
108	2.573
120	2.442

**Fig. 15.** Variation of amplification factor with building height.

## 9 Conclusion

The typical data presented in Tabular forms and figures, obtained after performing the analysis of the framed and tubular structures using STAAD Pro software, the following conclusions can be drawn:

- For the same plan aspect ratio, a building in category 1 shows maximum amplification factor. The axial forces as well as the amplification factor along both web and flange panels decreases if terrain category changes from category 1 to category 4.
- As the plan aspect ratio increases, the axial forces as well as the amplification factors increases.
- As the height of the building increases, axial forces in the columns along web panel and flange panel also increases. However, it is noted that as the height of the building increases, the magnitude of the amplification factor also decreases.

## References

- Coull, A., Bose, B.: Torsion of frame–tube structures. *J. Struct. Div. ASCE* **102**(12), 2366–2370 (1976)
- Coull, A., Ahmed, A.A.: Deflections of frame-tube structures. *J. Struct. Div. ASCE* **104**(5), 857–862 (1978)
- Chang, S.T., Zheng, F.Z.: Negative shear lag in cantilever box girder with constant depth. *J. Struct. Eng.* **113**(1), 20–35 (1987)
- IS: 875(Part 3): Code of practice for design loads for building and structures: Wind Loads published by Bureau of Indian Standards, New Delhi (2015)
- Jain, Y.K., Mandal, S.: A case study on shear lag phenomenon in tubular structures under wind load. In: 6th National Conference on Wind Engineering, CRRI, pp. 237–248. New Delhi (2012)
- Kristek, V., Studnicka, J.: Negative shear lag in flanges of plated structure. *J. Struct. Eng.* **117**(12), 3553–3569 (1991)
- Kwan, A.K.H.: Simple method for approximate analysis of framed tube structures. *J. Struct. Eng. ASCE* **120**(4), 1221–1239 (1994)
- Lee, K.-K., Guan, H., Loo, Y.-C.: Simplified analysis of shear lag in framed tube structures with multiple internal tubes. *Comput. Mech.* **26**(5), 447–458 (2000)
- Luo, Q.Z., Tang, J., Li, Q.S.: Negative shear lag effect in box girders with varying depth. *J. Struct. Eng.* **127**(10), 1236–1239 (2001)
- Luo, Q.Z., Tang, J., Li, Q.S.: Shear lag analysis of beam columns. *Eng. Struct.* **25**(9), 1131–1138 (2003)
- Luo, Q.Z., Wu, Y.M., Li, Q.S., Tang, J., Liu, G.D.: A finite segment model for shear lag analysis. *Eng. Struct.* **26**(14), 2113–2124 (2004)
- Ronvak, M., Duricova, A.: Discussion on negative shear lag effect in box girders with varying depth. *J. Struct. Eng.* **127**(10), 1236–1239 (2004a)
- Ronvak, M., Duricova, A.: Discussion on analysis of shear lag anomaly in box girders. *J. Struct. Eng.* **128**(11), 1860–1861 (2004b)
- Rovnak, M., Rovnakova, L.: Discussion on negative shear lag in framed-tube buildings. *J. Struct. Eng.* **122**(6), 711–713 (1996)
- Shushkewich, K.W.: Negative shear lag explained. *J. Struct. Eng.* **117**(11), 3543–3546 (1991)
- Singh, G.J., Mandal, S., Kumar, R.: Investigation on shear lag phenomenon in RCC framed tube structures. *i-Manager's J. Struct. Eng.* **4**(3), 28–35 (2015)
- Singh, G.J., Mandal, S., Kumar, R.: Effect of column location on plan of multi-story building on shear lag phenomenon. In: 8th Asia Pacific Conference on Wind Engineering (APCWE VIII), pp. 978–981 (2013)
- Singh, Y., Nagpal, A.K.: Negative shear lag in framed-tube buildings. *J. Struct. Eng.* **120** (1994). ASCE, ISSN 0733-9445/94/0011-3105. Paper No. 6972
- Nagvekar, Y.D., Hampali, M.P.: Analysis of shear lag effect in hollow structure. *Int. J. Eng. Res. Technol.* **3**(7), 936–937 (2014)
- Zhou, S.J.: Shear lag analysis of box girders. *Eng. Mech.* **25**(2), 204–208 (2008)



# Flexural and Torsional Moment of Clamped RC Curved Beam: A Parametric Study

Abhishek Kumar, Anjani Kumar Shukla<sup>(✉)</sup>, and P. R. Maiti

Department of Civil Engineering, IIT (BHU), Varanasi, India  
akshukla.rs.civ16@iitbhu.ac.in, prmaiti.civ@iitbhu.ac.in

**Abstract.** A both-end fixed curved beam is a statically indeterminate structure according to the structural boundary condition. Since the center of gravity of loads and reactions to one side of any section does not lie along the axis of the beam, it is subjected to torsional moment, in addition to bending moment (flexural moment) and shear force. They are capable of exchanging loads through the combined action of twisting and stretching compared to a straight beam. The difference in analysis and design between the beams curved in plan and the straight beams is mainly due to the presence of torsional movement induced by the vertical load. This paper deals with the distribution and variation of flexural and torsional moment developed in the curved beam with different geometric parameters such as radius of curvature and depth to width ratio of the beam.

**Keywords:** Curved beam · Fixed ends · Flexural moment · Torsional moment

## 1 Introduction

Beams curved in plan are used to support circular water tanks (reservoirs), curved balconies, curved ramps, skew bridges or other similar structures having a curved boundary. Such curved beams may be circular, elliptical or polygonal in plan, and the line joining the supports lies away from the curved longitudinal axis of the beam. A curved beam is a statically indeterminate structure according to the structural boundary condition, and it develops torsional moment subjected to a self-weight and live load. The difference in analysis and design between the beams curved in plan and the straight beams is mainly due to the presence of torsional movement induced by the vertical load. The capability of resisting torsional moment is expressed by torsional rigidity, which is defined as the torsional moment, when applied to one end, free to rotate, and produces a unit angle of twist with respect to the other end assumed to be fixed entirely. The higher the torsional rigidity increases the resistance to carry higher torque. The value of torsional rigidity depends on the shape and size of the beam section.

Badawy et al. (1977) presented a theoretical study to calculate a collapse load for reinforced concrete horizontally curved beams. In this study, the effect of shear on ultimate load, failure modes, and internal moments and forces in the curved beams were investigated. Shanmugam et al. (1995) conducted an experiment on two sets of I-beams (one comprising rolled sections and the other built-up sections) to analyze the ultimate

load behavior of I-beams curved in plan and compared with the corresponding values predicted by using the elasto-plastic finite- element analysis. The effects of residual stresses and radius of curvature to span length ratios (R/L) were considered. Each beam was subjected to a concentrated load applied at an intermediate point where the beam was laterally restrained. Test results indicated that the load-carrying capacity decreases with the decrease in the R/L ratio. Authors tested four (1/12) liner scale simply supported curved composite concrete deck-steel multi-cell bridge model to substantiate and verify the analytical model presented using finite element method. Al-Mutairee (2008) conducted a theoretical study on the behavior of horizontally curved beams under static and dynamic loads using nonlinear finite element method by writing two computer programs NFHCBSL and NFHCBDL for static and dynamic analyses respectively. The subject of HCRCB was addressed in several researches and papers. Tan and Uy (2009) had presented a model to represent the bending-torsion interaction for curved in plan composite steel- concrete beams with full and partial shear connection. They designed composite steel-concrete beams with different span/radius of curvature ratios and tested eight curved in plan composite steel-concrete beams under a single applied load at mid-span. They found out that in the presence of flexure, there will be an increase in the torsional moment capacity, but the flexural moment capacity does not greatly increase in the presence of torsion. Al-Mutairee (2013) studied the effects of non-uniform distribution of longitudinal reinforcements on the behavior of reinforced concrete (RC) horizontally curved beams with fixed ends under static loads The results showed that the effect of non-uniform distributions of longitudinal reinforcement of RC horizontally curved beams with fixed-ends is effective and can be used to improve the strength of this type of beams, and the increment in the ultimate load obtained was equal to 23.5%. Al-Shaarbaf and Abbas (2014) presented nonlinear analysis using finite element method to study a pre-stressed concrete box section beam. The authors concluded that the ultimate load increases as the wall thickness of the box section increased. Subramani et al. (2014) had analyzed three-dimensional horizontal reinforced concrete curved beam using ANSYS by varying various parameters like shear length to effective depth ratio, curvature of beams and by increasing transverse and lateral reinforcements. Muralidharan et al. (2017) did an analytical investigation of RC curved beams. Many researchers used the analytical and ANSYS to find the optimum grade of concrete, diameter of rebar, depth of the RC curved beam under two-point loading condition and compared the corresponding results with the conventional beam.

In the present study an attempt has been made to study the behavior and distribution of flexural and torsional moment of curved beam for different angle of curvature and D/b ratio of the curved beam. Seven different angles of curvatures are considered for this study, i.e., 10°, 20°, 30°, 40°, 45°, 50° and 60° and D/b ratio is varied from 3 to 7 and presented.

## 2 Mathematical Formulation

Figure 1 shows a curved beam ABC, fixed at end A and B, and subtending an angle  $2\theta$  at the centre. The beam carries a uniformly distributed load  $w$  per unit length of the beam. Because of fixity, there will be three reaction components at each support (i) shear

force  $F_O$  (ii) bending moment  $M_O$  and (iii) twisting moment  $M'_O$ . The beam is therefore, statically indeterminate to first degree. We shall use the method of strain energy to solve the problem.

Because of symmetry, shear force and torsional moment at the middle point C will be zero. Let the bending moment at this point be M. If we cut the beam at C, in two portions Mc will be the reaction component at C. This component is evidently about the radial axis C O. Consider a point P at angular distance  $\phi$  with OC. Load on section CP is given by  $W_\phi = wR\phi$ , and its C.G. will be at point D such that

$$OD = \frac{R \sin \frac{\phi}{2}}{\frac{\phi}{2}}$$

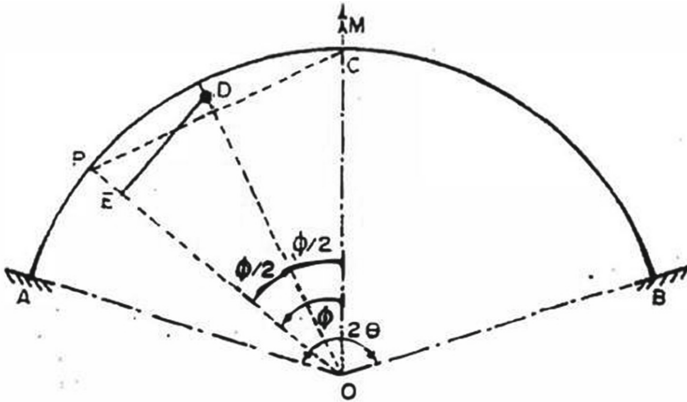


Fig. 1. Curved beam fixed at ends.

From D, drop perpendicular DE on radial axis PO

$$\begin{aligned} \therefore DE &= DO \cdot \sin \frac{\phi}{2} = \frac{R \sin^2 \frac{\phi}{2}}{\frac{\phi}{2}} \\ EO &= DO \cdot \cos \frac{\phi}{2} = \frac{R \sin \frac{\phi}{2} \cos \frac{\phi}{2}}{\frac{\phi}{2}} = \frac{R \sin \phi}{\phi} \\ PE &= PO - EO = R - \frac{R \sin \phi}{\phi} = R \left( \frac{\phi - \sin \phi}{\phi} \right) \end{aligned}$$

Now,  $F_\phi = W_\phi = wR \cdot \phi$  (1)

The bending moment  $M_C$  (sagging) can be resolved in component  $M_C \cos \phi$  about PO and  $M_C \sin \phi$  about tangential axis at P. The moment  $M_C \cos \phi$  about PO will evidently be the bending moment component at P, while  $M_C \sin \phi$  about tangential axis at P will be the torsional moment component.

$$\therefore M_\phi = M_C \cos \phi - W_\phi ED$$

$$\text{Or } M_\phi = M_C \cos \phi - wR\phi \left( \frac{R \sin^2 \frac{\phi}{2}}{\frac{\phi}{2}} \right)$$

$$M_\phi = M_C \cos \phi - wR^2(1 - \cos \phi) \tag{2}$$

Similarly,  $M_\phi^t = M_C \sin \phi - W_\phi PE$

$$M_\phi^t = M_C \sin \phi - wR\phi \cdot R \left( \frac{\phi - \sin \phi}{\phi} \right)$$

$$M_\phi^t = M_C \sin \phi - wR^2(\phi - \sin \phi) \tag{3}$$

Let U be the strain energy of half the portion (CA) of the beam consisting of strain energy due to B.M and that due to torsional moment. The strain energy due to S.F. is extremely small and maybe neglected. Hence,

$$U = \int_0^\theta \frac{M_\phi^2 ds}{2EI} + \int_0^\theta \frac{(M_\phi^t)^2 ds}{2GJ^t}$$

where,  $ds = Rd\phi$ .

In order to determine  $M_C$ , put  $\frac{\partial U}{\partial M_C}$  equal to zero.

$$\int_0^\theta \frac{M_\phi}{EI} \frac{\partial M_\phi}{\partial M_C} R \cdot d\phi + \int_0^\theta \frac{M_\phi^t}{GJ^t} \frac{\partial M_\phi^t}{\partial M_C} R \cdot d\phi = 0$$

where  $G = \text{modulus of rigidity} = \frac{E}{2(1-\mu)}$

$J^t = \text{torsion factor (rotational constant), depending upon the shape of the section.}$

In the expression,

$$\frac{\partial M_\phi}{\partial M_C} = \cos \phi$$

$$\frac{\partial M_\phi^t}{\partial M_C} = \sin \phi$$

Putting  $\frac{EI}{GJ} = T_F$ , we get

$$\int_0^\theta [M_C \cos \phi - wR^2(1 - \cos \phi)] \cos \phi d\phi + T_F \int_0^\theta [M_C \sin \phi - wR^2(\phi - \sin \phi)] \sin \phi d\phi = 0$$

On integration, we get  $M_c$

$$M_C \left\{ \frac{\theta}{2} + \frac{\sin 2\theta}{4} + T_F \left( \frac{\theta}{2} - \frac{\sin 2\theta}{4} \right) \right\} + wR^2 \left\{ \left( \frac{\theta}{2} - \sin \theta + \frac{\sin 2\theta}{4} \right) + T_F \left( \theta \cos \theta - \sin \theta + \frac{\theta}{2} - \frac{\sin 2\theta}{4} \right) \right\} = 0 \tag{4}$$

### 3 Results

All results for flexural and torsional moment are solved with the help of MATLAB. In this paper angle of curvature and D/b ratio are varied to understand the behavior and distribution of flexural and torsional moment of curved beam. A total udl of 30 kN/m and radius of curvature 20 m is considered for present study. Seven different angles of curvatures are considered for this study, i.e., 10°, 20°, 30°, 40°, 45°, 50° and 60°. D/b ratio is varied from 3 to 7.

Results of flexural moment and torsional moment are shown below in tabular manner.

#### 3.1 Curved Beam Subtending Angle at Centre = 10°

The purpose of this study is to understand the best depth/width (d/b) of curved RC beam. In this analysis two major parameter were consider: d/b ratio and angle of curvature. Flexural moment  $M_\phi$  and torsional moment  $M_\phi^t$  have been calculated at three points: at centre line, at point of contraflexure and at supports for 7 orientations starting from 10° to 70° at interval of every 10°. The five different d/b ratio 3, 4, 5, 6 and 7 has taken for analysis the behaviour of curved beam.

Table 1, 2, 3, 4 and 5 consists the values of flexural and torsional moment for different d/b ratio and subtending angle of 10° and d/b = 3 to 7. The maximum flexural moment was observed at the support at d/b = 7 and maximum torsional moment at the point of contraflexure at d/b = 3.

**Table 1.** Variation of flexural and torsional moment for D/B = 3

Location	$\phi$ (Degree)	$M_\phi$ (kN-m)	$M_\phi^t$ (kN-m)
Centre line	0°	15.1267	0
Point of Contraflexure	2.8754°	0	0.5061
Support	5°	-30.5945	-0.0103

**Table 2.** Variation of flexural and torsional moment for D/B = 4

Location	$\phi$ (Degree)	$M_\phi$ (kN-m)	$M_\phi^t$ (kN-m)
Centre line	0°	15.0604	0
Point of Contraflexure	2.8691°	0	0.5027
Support	5°	-30.6605	-0.0160

**Table 3.** Variation of flexural and torsional moment for D/B = 5.

Location	$\phi$	$M_\phi$ (kN-m)	$M_\phi^t$ (kN-m)
Centre line	0°	14.9786	0
Point of Contraflexure	2.8613°	0	0.4987
Support	5°	-30.7420	-0.0232

**Table 4.** Variation of flexural and torsional moment for D/B = 6.

Location	$\phi$	$M_\phi$ (kN.m)	$M_\phi^t$ (kN.m)
Centre line	0°	14.8827	0
Point of Contraflexure	2.8521°	0	0.4939
Support	5°	-30.8376	-0.0315

**Table 5.** Variation of flexural and torsional moment for D/B = 7.

Location	$\phi$	$M_\phi$ (kN.m)	$M_\phi^t$ (kN.m)
Centre line	0°	14.7742	0
Point of Contraflexure	2.8417°	0	0.4885
Support	5°	-30.9456	-0.0410

### 3.2 Curved Beam Subtending Angle at Centre = 20°

Table 6, 7, 8, 9 and 10 contain the values of flexural and torsional moment for different d/b ratio and subtending angle of 20° and d/b = 3 to 7. The maximum flexural moment



was observed at the support at  $d/b = 3$  and also the maximum torsional moment at the point of contraflexure at  $d/b = 3$  (Figs. 2, 3, 4, 5 and 6).

**Table 6.** Variation of flexural and torsional moment for  $D/B = 3$ .

Location	$\phi$	$M_\phi$ (kN.m)	$M_\phi^t$ (kN.m)
Centre line	0°	59.33	0
Point of	5°	13.4436	3.8426
Contraflexure	5.6859°	0	3.9248
Support	10°	-128.8753	-0.3139

**Table 7.** Variation of flexural and torsional moment for  $D/B = 4$ .

Location	$\phi$	$M_\phi$ (kN.m)	$M_\phi^t$ (kN.m)
Centre line	0°	58.4007	0
Point of	5°	12.5148	3.7613
Contraflexure	5.6413°	0	3.8328
Support	10°	-124.7935	-0.4758

**Table 8.** Variation of flexural and torsional moment for  $D/B = 5$ .

Location	$\phi$	$M_\phi$	$M_\phi^t$
Centre line	0°	57.3254	0
Point of	5°	11.4436	3.6676
Contraflexure	5.5893°	0	3.7275
Support	10°	-125.8525	-0.6625

**Table 9.** Variation of flexural and torsional moment for  $D/B = 6$ .

Location	$\phi$	$M_\phi$ (kN.m)	$M_\phi^t$ (kN.m)
Centre line	0°	56.1593	0
Point of	5°	10.2820	3.5660
Contraflexure	5.5324°	0	3.6145
Support	10°	-127.009	-0.8650

**Table 10.** Variation of flexural and torsional moment for  $D/B = 7$ .

Location	$\phi$	$M_\phi$ (kN.m)	$M_\phi^t$ (kN.m)
Centre line	$0^\circ$	54.9489	0
Point of Contraflexure	$5^\circ$	9.0762	3.4605
Support	$10^\circ$	-128.1928	-1.0752

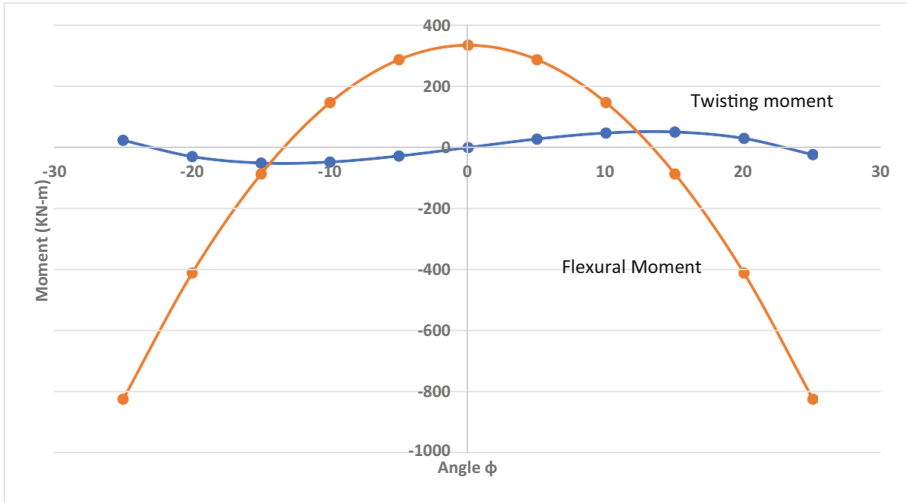


**Fig. 2.** Flexural moment and Twisting moment distribution of curved beam with angle subtended at the centre =  $50^\circ$ .

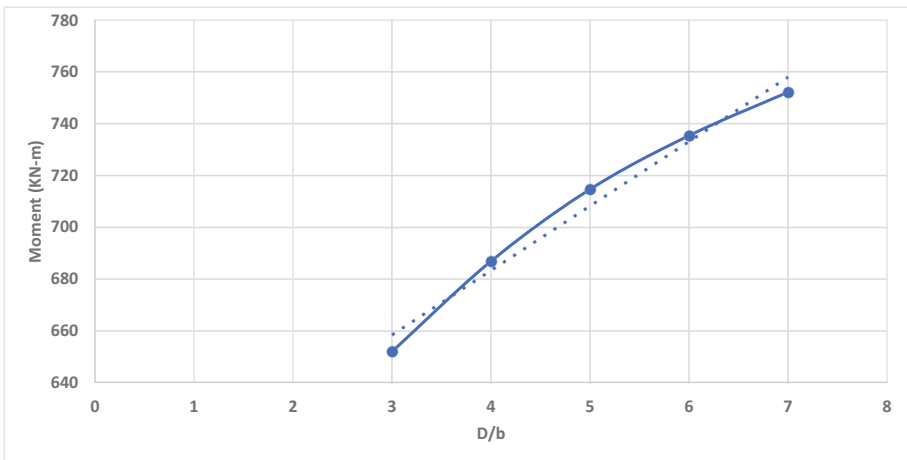


**Fig. 3.** Variation of maximum Mid-span moment with  $D/b$  ratio of the curved beam with angle subtended at the centre =  $50^\circ$ .

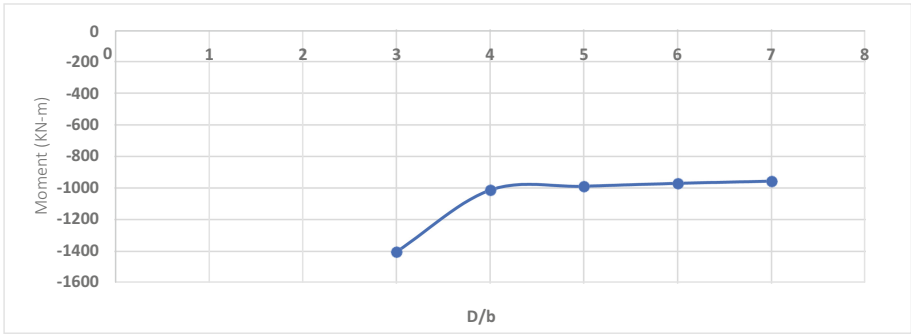


**Fig. 4.** Variation of maximum support moment (flexural) with D/b ratio of curved beam with angle subtended at the centre = 50°.

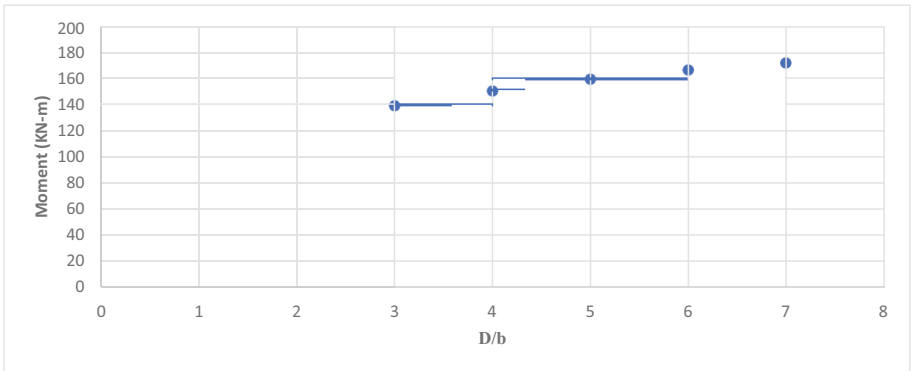


**Fig. 5.** Variation of maximum Twisting Moment with D/b ratio of curved beam with angle subtended at the centre = 50°.

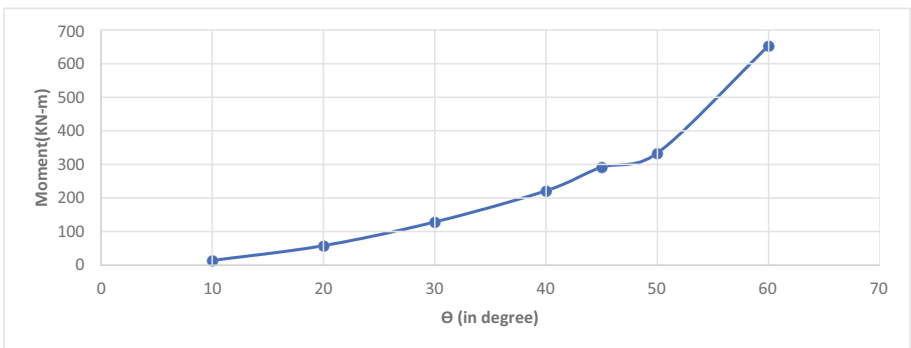


**Fig. 6.** Variation of maximum Twisting Moment with D/b ratio of curved beam with angle subtended at the centre = 50°.

## 4 Conclusion

From the data obtained for curved beam using MATLAB, the following conclusions were made:

Maximum flexural moment occurs at the mid span of the curved beam and twisting moment is zero at mid span. Maximum twisting moment occurs when flexural moment changes its sign, i.e., from negative to positive and vice versa. This point is also known as point of contraflexure. Maximum mid span moment, maximum negative flexural moment and maximum positive flexural moment increases with increase in  $D/b$  ratio. Maximum twisting moment increases gradually with increase in  $D/b$  ratio.

## References

- Al-Mutairee, H.M.K.: Effect of non-uniform distribution of longitudinal reinforcement on the behaviour of reinforced concrete horizontally curved beams with fixed-ends. *J. Babylon Univ. Eng. Sci.* **21**(3), 2013 (2013)
- Al-Mutairee, H.M.K.: Nonlinear static and dynamic analysis of horizontally curved beams, Ph.D. Thesis, University of Babylon (2008)
- Al-Shaarbaf, I.A., Abbas, H.E.: Nonlinear finite element analysis of pre-stressed concrete box section beams. *Nahrain Univ. College Eng. J.* **16**(2), 156–167 (2014)
- Badawy, H.E.I., Jordaan, I.J., McMullen, A.E.: Effect of shear on collapse of curved beams. *J. Struct. Div. ASCE* **103**(ST9), 1849–1866 (1977). (Proceedings Paper 13185)
- Khaled, S., John, B.K.: Simply supported curved cellular bridges: simplified design method. *J. Bridge Eng.* **4**(2), 85–94 (1999)
- Muralidharan, R., Jeyashree, T.M., Krishnaveni, C.: Analytical investigation of RC curved beams. *J. Indust. Pollut. Control* 1387–1392 (2017)
- Punmia, B.C., Jain, A.K., Jain, A.K.: *Comprehensive RCC Designs*. Laxmi Publications (1998)
- Shanmugam, N.E., Thevendran, V., Liew, J.R., Tan, L.O.: Behaviour and design of horizontally curved steel beams. *J. Construct. Steel Res.* **32**(1), 37–67 (1995)
- Subramani, T., Subramani, M., Prasanth, K.: Analysis of three-dimensional horizontal reinforced concrete curved beam using ANSYS. *J. Struct. Eng.* **4**, 156–161 (2014)
- Tan, E.L., Uy, B.: Experimental study on curved composite beams subjected to combined flexure and torsion. *J. Construct. Steel Res.* **65**(8–9), 1855–1863 (2009)



# Effect of Infill Walls on Seismic Behaviour of Buildings: A Review

Azeel P. Kassim<sup>(✉)</sup> and Satyabrata Choudhury

Department of Civil Engineering, National Institute of Technology Silchar,  
Silchar, India

azeel\_pg@civil.nits.ac.in

**Abstract.** Infill walls are used as interior partition as well as exterior barrier. It is considered to be a non-structural element. But it contributes to the enhancement of strength and stiffness of a structure, hence is accounted as beneficial to the structural performance. Generally, in design, the effect of infill is ignored. Open ground floor, however, may lead to soft storey. To study these pros and cons, researchers started including infill panels as two equivalent diagonal compression struts in the analytical models while performing analysis. Studies revealed that infill walls can provide lateral resistance to seismic and wind loads, it increases the stiffness thus the time period of the structure get reduced and reduces the inter-storey drift. During an earthquake, infill panels also aid in energy dissipation. Reinforcing infill avoids the out-of-plane collapse of the masonry wall and it enhances the ductility. The cross-laminated timber infill walls for steel moment-resisting frames are also in use. A thorough review of the effect of infill has been made in this paper.

**Keywords:** Equivalent diagonal compression strut · Masonry infill · Inter-storey drift ratio · Floor spectra · Floor response amplification

## 1 Introduction

The infill wall is a panel that supports the facade system and is installed in between the floors of the structural frame of the building. Although infill walls are not load-bearing, they can survive wind and seismic loads applied to the facade. It switches the structural load-transferring mechanism from frame to truss. Infill walls have conventionally been made of masonry or wood, but modern construction practices use steel C-sections of light weight. Unreinforced masonry infill walls are commonly used in all types of buildings across the world. For enhancing ductility and reducing out of plane collapse, reinforced masonry walls are used in which a pair of mild steel bars is placed after every three layers of masonry. These reinforcement bars are sometimes welded to a steel plate that is anchored to the column to strengthen it. The position of infill panels influences the plastic hinge location on structural elements. Since it is not considered as a structural element, the influence of infill in seismic behaviour of structure is not studied in the past. In recent earthquakes, many buildings have been badly damaged or collapsed as a consequence of neglecting the influence of infill walls while designing. Likewise, buildings with infill walls which are not designed for seismic loads are found

to show excellent performance under moderate earthquakes. These observations made the researchers to extend their studies to infill walls which results in many relevant findings.

## 2 Influence of Infill Walls on Structures

From the records of past earthquakes, it is evident that buildings with masonry infill show excellent performance even though they are not designed for seismic response. The brick infill walls, according to Murty and Jain (2000), contribute significantly to strength, overall ductility, lateral stiffness and energy dissipation capacity. The studies were done in the differential behaviour of RC frame buildings with and without infill wall, difference in responses of reinforced from unreinforced masonry infill wall with and without anchorage to frame column. Different sized bricks in different orientation was tried in those studies. Infills obstruct the frame's lateral deformation, infill and frame separation occurs on one diagonal, while the compression strut forms on the other. As a result, infill adds lateral rigidity to the structure. Infilled RC frames have an initial rigidity nearly four times that of bare RC frames.

Further studies by Razzaghi and Javidnia (2015) proves that the infill wall will dissipate a major portion of the seismic energy, thus safeguard the frame from large lateral loads. It shows that the infilled frame has 70% higher strength than the bare frame. If the infill bricks are placed in an angle with horizontal, the strength of the building will increase since it prevents the formation of weak horizontal plane of sliding. The yield displacement of the infill frame is small as compared to the bare frame, causes ductility increase for the infilled frame (Murty and Jain 2000).

Hyun et al. (2014) evaluated the seismic behaviour of reinforce concrete (RC) moment-resisting frame with brick infilled walls. The force-displacement curve obtained from the analysis shows that the building on low seismic zone have considerable overstrength due to infill wall, so they don't show ductile behaviour against ground motion. The slope of force-displacement curve is decreasing after each cycle of loading in case of partially and fully infilled models in moderate and high seismic region is because of the reduction in stiffness of the structure caused by cracking of infill wall. Interstorey Drift Ratio (IDR) for fully infilled building is found to be least because of the increased system stiffness. Buildings without infill only at first floor have IDR value similar to fully infilled building except for first floor. IDR for building without infill is high comparing to others except for the first floor which is less than that of building with soft storey. By applying a new technique of structural design for structures with soft storey, the IDR value for structure without infill only in the ground floor shows enhanced seismic resistance similar to fully infilled structure (Ko et al. 2014).

Under seismic loads, masonry infills trigger a number of adverse effects, including the short column effect, torsion, soft storey effect, and out-of-plane collapse. If the infills are not evenly distributed, a mixed structural load transfer mechanism involving both truss and frame action will emerge. In those cases, certain elements may face large ductility demand. In the case of a storey having no infill or comparatively less infill than the adjoining storey results in a large difference in the stiffness between the two

storeys and the storey with no infill is considered as a soft storey. Due to the large difference in stiffness the interstorey drift ratio becomes high and as a result the columns of soft storey will be subjected to large deformation out of its limit which leads to collapse of the entire floor (Murty and Jain 2000; Guevara 2012).

In case, the walls are elevated only up to a particular column height, during a ground motion, the lower portion of the column will be firmly held by the infill which concentrates all deformation in the upper portion of the column. This is called short column effect in which short column have to bear high load from earthquake which makes them to fail. The structural responses will be dominated by the plan torsion effect when infills are asymmetrically positioned in plans. This will impose an excessive amount of ductility demand on frame columns, causing the collapse mechanism to be significantly altered (Murty and Jain 2000).

## 2.1 Novel Structural Design Method for Soft Storey Buildings

Ko et al. (2014) proposed a new structural design method for structures with soft storey. To improve the seismic resistance capability of the soft storey, he proposed a method of incorporating extra shear force proportionate to the design seismic base shear force in the design of structural elements. To achieve desired performance equivalent to an infilled frame, the authors employed an extra shear force of 1.5 times the base shear in the design. He kept the size of structural elements unchanged while increasing the shear force by increasing the yield moment of column and beams with additional reinforcement. But the extra shear load factor used in his study should be recalculated for other structures.

## 2.2 Influence of Reinforcement on Masonry Infill

In studies done by Murty and Jain (2000), they provided reinforcement in masonry with a pair of 6 mm mild steel bars that is placed after three layers of brick of full-scale length. The size of bars can be reduced while using brick of reduced scale of length. Reinforced masonry infill will increase the ductility of the frame. When inserting the reinforcing bars in the masonry, a thicker layer of mortar is used than usual. In comparison to unreinforced masonry (URM) frames, the weak horizontal planes thus introduced have a negative impact on the strength, stiffness and energy dissipation of reinforced masonry (RM) frames. So, RM frames show less separation at failure between frame and infill and this indicates that infilled frame has a better out-of-plane response. Similarly, reinforcement bars anchored to the plate provided in the inside face of column shows less stiffness, energy dissipating capacity compared to unanchored reinforced infill walls because of larger mortar thickness in the vicinity of joint. But the anchored reinforcement increases the strength of the infill frame. On application of a cyclic load, the reinforced masonry infill shows a smaller drop in stiffness in the second cycle of loading than unreinforced masonry infill because the reinforcement aids in minimising infilled frame damage (Murty and Jain 2000).

By altering the arrangement of the infill walls, the position of plastic hinges in structural elements changes. It is also confirmed that infill walls are critical for energy dissipation during an earthquake. It was also found noticeable changes in the seismic

performance of the structure with different infill wall arrangements (Razzaghi and Javidnia 2015) and varying infill percentage (Dinar et al. 2013).

In brief, the infill brick wall will improve the structure's stiffness, strength, energy dissipation capacity, and ductility, lowering the deformation and ductility demand on the frame components. This is why some old buildings sustains moderate earthquakes even if it is not detailed and designed for seismic force. And, reinforcement in masonry actually reduces the stiffness of the wall but it avoids the out-of-plane collapse.

### **3 Modelling of Infill Strut**

#### **3.1 Concrete Frame with Infill**

Concrete frame with infill is built in such a way that the frame and the infill interact with each other when subjected to lateral and vertical loads (FEMA 356).

##### **3.1.1 Masonry Infill**

While modelling masonry infill, we consider two cases. The infill and frame are treated as a homogenous element if the infill wall would break when subjected to design lateral pressures. The infills which allow cracks when subjected to design lateral forces is modelled as a diagonally braced frame in which the beams function as horizontal ties, the columns as vertical chords and the infill as an analogous compression strut.

##### **3.1.2 Concrete Infill**

The strength, stiffness and capacity against deformation of structural elements, concrete infills, and other linkages shall be represented using the analytical model for a concrete infilled RC frame. For low deformation levels when the frame is reasonably flexible, the infilled frame is depicted as a shear wall with holes. In other cases, the infilled frame is modelled as a braced frame similar to the case of frame with masonry infill.

The impact of strut compression forces applied to the beam and column, eccentric from the beam-column junction, is examined on the frame with full height masonry infill. The frames with infills up to partial height is assessed by the decreased effective length of the columns above the infilled area of the bay.

#### **3.2 Steel Frame with Infill**

The interaction between the steel frame and the infill is identical to that between the concrete frame and the infill, as described in the preceding subsection. The seismic force will be carried by the infill walls and frames in composite action, taking into account the relative stiffness of each part, until the walls have completely failed. Some or all of this stiffness may be negated by gaps between the wall and the frame. These spaces might be between the wall and the columns, or between the wall and the top beam. With varied types and locations of discontinuities, variable strength and stiffness conditions must be predicted. As a result, any breaks or discontinuities between the frame and infill walls must be identified and taken into consideration during the design



and restoration process. The rigidity produced by the infilled steel frame is determined by the level of integrated action between the wall and the steel frame.

### 3.3 Compression Strut Mechanism

Under earthquake conditions, infill walls can offer lateral load resistance and are often partially detached from boundary frames, revealing a compression strut mechanism (Klingner and Bertero 1976).

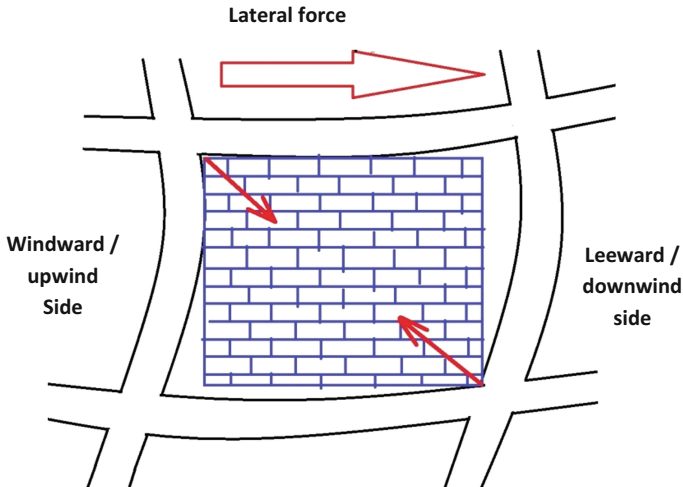


**Fig. 1.** Seismic behaviour of masonry infilled frame.

Due to interactions between the infill and the impounding frame, the lateral stiffness of an infilled frame system is not equal to the sum of the frame and infill stiffnesses. Studies have revealed that when lateral forces are applied, the frame separates from the infill around the upwind lower and downwind higher corners of the infill panels, resulting in compressive contact stress between the infill and the frame at the other diagonally opposite corners. Identifying this behaviour, the stiffness contribution of the infill is represented by an analogous compression strut linking the infilled frame's windward upper and leeward lower corners (FEMA 356 2000; ASCE/SEI 41-13 2014).

In simple words, when lateral load is imparted to the building in any one direction, the infill walls cannot take tensile force but can resist compressive force diagonally, as shown in Fig. 1. So, the wall acts like a compressive strut along diagonal direction. The corners of wall subjected to tensile force will get separated from the frame. The thickness of the strut and elastic modulus are considered to be the equal to that of the infill wall. The calculation of the effective width of the strut was proposed by Dolsek and Fajfar (2002).

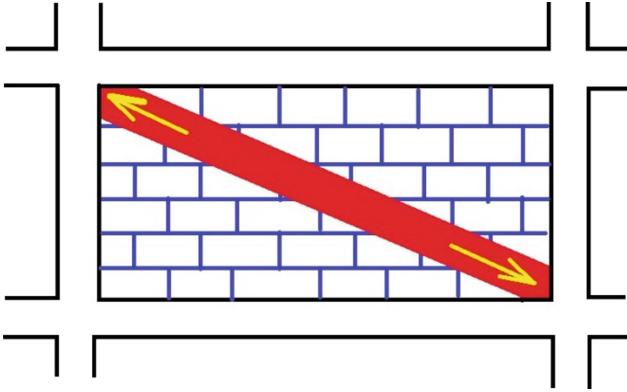


**Fig. 2.** Concentric compression strut.

For global building analysis purpose, the compression struts denoting infill panels can be positioned concentrically across the frame's diagonals, resulting in a concentrically braced frame as shown in Fig. 2. The forces imposed on the frame's columns by the infill are not correctly reflected in this design. Compression struts may be positioned eccentrically inside the frames to accommodate for these effects as shown in Fig. 3. If eccentrically placed compression struts are included in the analytical models, the findings should immediately result in infill effects on the column (FEMA 356 2000).

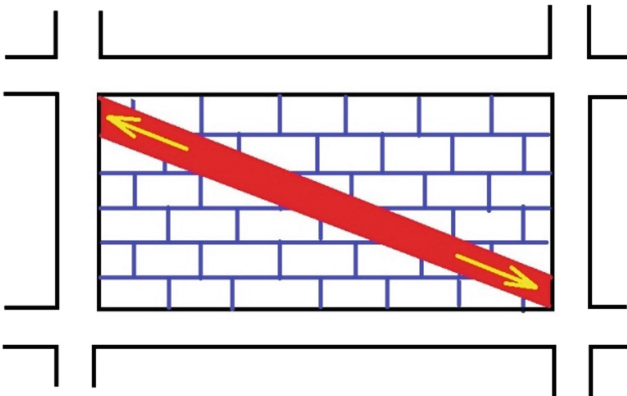


**Fig. 3.** Eccentric compression strut.

Infill panel stiffnesses may also be incorporated in analytical models for infill panels with openings, such as doors or windows using diagonally concentric analogous struts, provided that the equivalent stiffness of the infill is obtained from suitable analysis methods in a consistent manner with the global analytical model. Analysis of local impacts must consider many conceivable stress fields that can potentially form

inside the infill. A potential depiction of these stress fields using numerous compression struts is illustrated in Fig. 4 which is suggested by Hamburger and Chakradeo (1993).

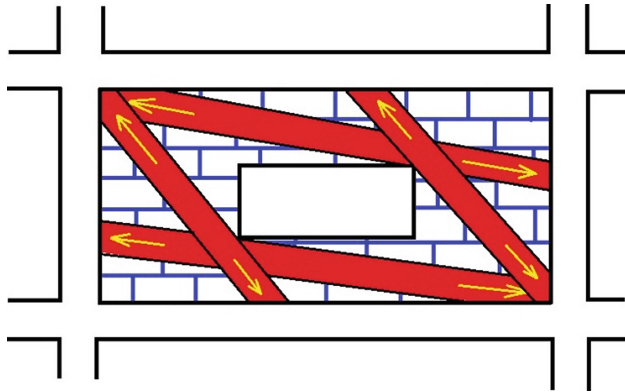


Fig. 4. Strut analogy in perforated infill panel.

### 3.4 Modelling Parameters

For estimating maximum strength and initial stiffness of walls, the maximum strength, initial stiffness ( $K_{in}$ ) and the effective width ( $W_{ef}$ ) of the analogous diagonal compression strut are needed to be calculated (FEMA 365 2000; Dolsek and Fajfar 2002; ASCE/SEI 41-13 2014; IS 1893 (Part 1) 2016).

The effective width of the infill strut is given by Eq. (1).

$$W_{ef} = 0.175 (\lambda_h H)^{-0.4} \sqrt{H^2 + L^2} \tag{1}$$

where the parameters  $\lambda_h$  and  $\theta$  are given by Eqs. (2) and (3) respectively.

$$\lambda_h = \sqrt{4 \frac{E_w t_w \sin(2\theta)}{4E_c I_c H_{in}}} \tag{2}$$

$$\theta = \arctan\left(\frac{H}{L}\right) \tag{3}$$

where,  $E_c$  and  $E_w$  are the modulus of elasticity of concrete and infill wall in kilo pound per square inches correspondingly,  $\theta$  is the slope of the diagonal in radians,  $t_w$  is the infill wall thickness in inches,  $I_c$  is the moment of inertia of the column adjacent to wall in  $\text{inch}^4$ , and  $H_{in}$ ,  $H$ ,  $L$  are the net height of the infill wall, the storey height and the bay length of the frame in inches correspondingly.

The initial lateral stiffness is given by Eq. (4).

$$K_{in} = \frac{E_w W_{ef} t_w}{\sqrt{H^2 + L^2}} \cos^2 \theta \quad (4)$$

The maximum strength of the infill wall is given by Eq. (5).

$$F_{max} = 0.818 \frac{L_{in} t_w f_{tp}}{C_1} \left( 1 + \sqrt{C_1^2 + 1} \right) \quad (5)$$

where  $C_1$  is given by Eq. (6).

$$C_1 = 1.925 \frac{L_{in}}{H_{in}} \quad (6)$$

where,  $f_{tp}$  is the breaking resistance of the infill which can be acquired from diagonal compression test, and  $H_{in}$  and  $L_{in}$  are the height and length of the wall correspondingly.

The infill rigidity is calculated as proposed by Eq. (7) (Razzaghi and Javidnia 2015).

$$K = \frac{E_w W_{ef} t_w}{\sqrt{H^2 + L^2}} \quad (7)$$

For infill panel with opening, a reduction coefficient ( $R$ ) was applied to the width of diagonal strut.  $R$  can be calculated as per Eq. (8).

$$R = 0.6 \left( \frac{A_{open}}{A_{panel}} \right)^2 - 1.6 \left( \frac{A_{open}}{A_{panel}} \right) + 1 \quad (8)$$

where,  $A_{panel}$  and  $A_{open}$  are the area of panel and opening correspondingly. The crack resistance of the infill is computed as per Eq. (9).

$$R_{cr} = W_{ef} t_w f_m \quad (9)$$

where  $f_m$  is the compressive strength of infill material. Furthermore, the shear strength of the infill panel is computed by using Eq. (10).

$$R_{shear} = A_n f_v \quad (10)$$

where  $A_n$  is the area of cross-section of mortar between adjacent rows of the infill panel and  $f_v$  is the shear strength of the infill panel. Infill shear strength is calculated using Mohr-Coulomb criterion (Eqs. (11) to (13)).

$$f_v = \tau + \mu \sigma \quad (11)$$

$$\tau = 0.04 f_m \quad (12)$$

$$\mu = 0.654 + 0.00515f_j \quad (13)$$

$\tau$  is the adhesive coefficient and  $\mu$  is the friction coefficient,  $f_j$  is the compressive strength of the mortar between the infill rows and  $\sigma$  is the vertical compressive stress (Razzaghi and Javidnia 2015).

## 4 Timber Infill in Steel Structures

Light weight, speed of construction, good acoustic and thermal performance, good for environment are some of the reasons for preferring timber as infill panels. Bezabeh et al. (2016) investigated a hybrid construction that uses *cross-laminated timber* (CLT) shear infill panels in steel moment-resistant frames (SMRF). As connections, L-shaped brackets are attached to the steel frame and fixed by nailing to the CLT panel. A gap is provided between the wall and the frame to allow the brackets to flex and release energy under earthquake stress. The proposed design begins with the assumption of modelling parameters of CLT infilled steel frame such as bracket spacing, panel thickness, post-yield stiffness and panel strength. To assure deformation in pure shear, the CLT shear panels are separated at the top and bottom of each storey. 70% of the base shear of the hybrid system is allocated to the frame. The shear resistance for CLT wall is then estimated by Eq. (14) (Bezabeh et al. 2016).

$$\frac{V_{i,CLT}}{V_b} = \frac{V_{i,total}}{V_b} - \frac{V_{i,frame}}{V_b} \quad (14)$$

where,  $V_{i,CLT}$  is the shear resisted by the CLT infill panel at storey  $i$ ,  $V_b$  is the design base shear, and  $V_{i,total}$  is the total shear at storey  $i$ , total number of storeys being  $n$ , the shear relation is given by Eq. (15) (Bezabeh et al. 2016).

$$\frac{V_{i,total}}{V_b} = 1 - \frac{i(i-1)}{n(n+1)} \quad (15)$$

### 4.1 Design Method

Bezabeh et al. (2016) developed a new iterative direct displacement-based design technique for SMRF with CLT infill. The features of a similar SDOF system are determined by the drift limit of lower stories of SMRF and an anticipated displacement profile. Under seismic stimulation, the displacement profile is related to the structure's inelastic response of fundamental mode (Priestley et al. 2007). The drift limit considered in the study was 2.5%. The displacement profile is then formed from Sullivan et al. (2010) and is given by Eq. (16).

$$\Delta_i = \omega_0 \theta_c h_i \left( \frac{4H_n - h_i}{4H_n - h_1} \right) \quad (16)$$

where  $\Delta_i$  is the level  $i$  displacement,  $h_i$  is the  $i^{th}$  level height from the ground,  $H_n$  is the total height of the structure,  $\omega_\theta$  is the factor which accounts for higher modes and is given by Eq. (17).

$$\omega_\theta = 1.15 - 0.0034H_n \leq 1 \tag{17}$$

At low drift levels, panel crushing at the nail contact occurs, and the ductility associated with it is high. In the case of SMRFs, the inelastic response occurs at a higher drift value. This impact is integrated for design purposes by calculating the weighted average ductility of both and is provided as follows,

The displacement ductility value of CLT panels is given by Eq. (18).

$$\mu_{CLT} = \frac{\Delta_d}{\Delta_{crush,CLT}} \tag{18}$$

where, the crushing displacement ( $\Delta_{crush,CLT}$ ) is calculated by provided elastic modulus ( $E_0$ ), diagonal crushing strength of CLT panel ( $f_{CLT}$ ) and diagonal length of infill panel ( $d$ ), as shown in Eq. (19).

$$\Delta_{crush,CLT} = \frac{df_{CLT}}{E_0 \cos\theta} \tag{19}$$

The displacement ductility of the SMRF is computed as per Eq. (20).

$$\mu_{frame,i} = \frac{\Delta_i - \Delta_{i-1}}{h_i - h_{i-1}} \left( \frac{1}{\theta_{y,steelframe}} \right) \tag{20}$$

Where yield drift of the steel frame is given by Eq. (21).

$$\theta_{y,steelframe} = 0.65 \varepsilon_y \frac{L_b}{h_b} \tag{21}$$

where,  $h_b$  and  $L_b$  are the depth and length of beam respectively. The weighted system ductility is determined by the corresponding overturning moment resistance and is given by Eq. (22).

$$\mu_{sys} = \frac{M_{CLT} \mu_{CLT} + M_{frame} \mu_{frame,average}}{M_{frame} + M_{CLT}} \tag{22}$$

where  $M_{frame}$  and  $M_{CLT}$  are the overturning moment resistance of frame and CLT panel correspondingly.

Equivalent system damping is given by Eqs. (23) and (24).

$$\xi_{hyst} = C \left( \frac{\mu_{sys} - 1}{\mu_{sys} \pi} \right) \tag{23}$$

$$\xi_{eq} = \xi_{hyst} + \xi_{elastic} \quad (24)$$

The effective time period of the system is derived from the EC-8 displacement spectrum and effective stiffness and base shear distribution is calculated then.

The plastic moment strength for the columns and beams is computed using the distributed storey shear in each floor element. The plastic section modulus of available structural members is calculated in order to select an acceptable section that meets the need. The element portions are chosen for the gravity and seismic forces that are greater (Bezabeh et al. 2016).

## 5 Effect of Infill in the Design of OFCS

### 5.1 Floor Spectra Response

Debnath and Choudhury (2015) investigated the impact of unreinforced masonry infill on the parameters including floor amplification factor in infilled frame buildings constructed using the Unified Performance-Based Design approach (Choudhury and Singh 2013). For the design of operational and functional components (OFCs), the floor spectra are a significant parameter. These are non-structural components, equipment and services in a building. When the mass of the OFCs are small in comparison with the mass of the building, uncoupled analysis was done between OFCs and building. The spectra of floor acceleration were derived using floor acceleration histories. The average floor spectra of the buildings designed as per Unified Performance Based Design for 5% damping was marginally decreased with the incorporation of infill struts. The reduction is less in lower floors but it varies from 11% to 29% in middle and top floors (Debnath and Choudhury 2015).

### 5.2 Response Amplification

The floor response amplitudes are multiplied as the building rises in elevation. The Floor Amplification Factor (FAF), Component Amplification Factor (CAF) and Total Amplification Factor (TAF) are the most significant factors. According to the findings, FEMA gives a reasonable estimate for FAF values in structures without infill struts, but it overestimates in buildings with infill struts. For all types of structures, FEMA provision for CAF is found to be underestimated, whereas provision for TAF is found to be overstated. As a result of these provisions, floor-mounted equipment will be designed in an inefficient manner. The relationship for these parameters from best fit curves obtained from the analysis study, are shown in Eqs. (25) to (29).

$$FAF_{with\ infill} = 1.63 \left( \frac{h}{H} \right) + 0.734 \quad (25)$$

$$CAF_{without\ infill} = 2.5 \left( \frac{h}{H} \right) + 2.96 \quad (26)$$

$$CAF_{with\ infill} = 2.33 \left( \frac{h}{H} \right) + 3.31 \quad (27)$$

$$TAF_{without\ infill} = 1.56 \left( \frac{h}{H} \right) + 0.23 \quad (28)$$

$$TAF_{with\ infill} = 1.41 \left( \frac{h}{H} \right) + 0.16 \quad (29)$$

It is also observed variation in roof displacement such that it is found to be reduced 32% to 38% with the introduction of infill walls (Debnath and Choudhury 2015).

## 6 Conclusion

The seismic behavioural effects of infill walls on buildings are studied by comparing three types of structures such as, framed structure without infill wall, framed structure with infill walls on all storeys but ground storey (partially infilled) and framed structure with infill wall (fully infilled). Inclusion of infill enhances the seismic performance of buildings as it increases the ductility, lateral stiffness, energy dissipation capacity and strength of the building. The unreinforced masonry infill dissipates a major portion of seismic energy through its out-of-plane collapse thus reduces the energy demand on frame members. The reinforced masonry infill will increase the ductility of the system but reduces the energy dissipating capacity but preferable for preventing the out-of-plane collapse. The infill walls reduce the Interstorey Drift Ratio of the building because of the increased stiffness. The roof displacement is also got reduced due to infill walls. The undesirable effects of infill walls on the structure like soft storey effect, plane torsion, short column effect and out-of-plane collapse are discussed in the paper. For the modelling aspect, infill walls are considered as a pair of diagonal compression struts with specific characteristics. The compression strut is positioned concentrically across the diagonals of the frame for global building analysis purposes, and the pressures exerted on columns by the infill are not represented. Compression struts may be positioned eccentrically inside the frame to accommodate for these effects. The weighted average of ductility and damping are taken for the design purpose knowing the fact that the total ductility of the system is not equal to the sum of ductility of frame and infill taken separately, since the frame wall interaction cannot be neglected. The infill also affects the design of Operational and Functional Components in a building as the parameters such as floor spectra response and floor amplification factors get reduced. It is found that FEMA provisions for these parameters are unsatisfactory and new relations are obtained from analytical experiments. The beneficial behaviour of infill in frame structures under seismic load can be utilised for reducing the design dimensions of structural elements which is needed to be explored in future researches.



## References

- ASCE/SEI 41-13: Seismic Evaluation and Retrofit of Existing Buildings, American Society of Civil Engineers (2014)
- Bezabeh, M.A., Testamariam, S., Stiemer, S.F., Popovski, M., Karacabeyli, E.: Direct Displacement-Based Design of a Novel Hybrid Structure: Steel Moment-Resisting Frames with Cross-Laminated timber Infill Walls, *Earthquake Spectra*, vol. 32, no. 3, pp. 1565–1585. Earthquake Engineering Research Institute (2016).
- Choudhury, S., Singh, S.M.: A unified approach to performance based design of RC frame building. *J. Inst. Eng. (I)-Ser. A*, Springer **94**(2), 73–82 (2013)
- Debnath, P.P., Choudhury, S.: Effect of unreinforced masonry infill on floor amplification and other parameters in frame-wall buildings. *Mech. Based Des. Struct. Mach.* **43**(4), 450–465 (2015)
- Yousuf, D., Nazmul, A., Paul, S.C.: Performance based analysis of RC building consisting shear wall and varying infill percentage. *Euro. Acad. Res.* **1**(9) (2013)
- Dolsek, M., Fajfar, P.: Mathematical modelling of an infilled RC frame structure based on the results of pseudo-dynamic tests. *Earthquake Eng. Struct. Dyn.* **31**, 1215–1230 (2002)
- FEMA 356: Prestandard and Commentary on the Seismic Rehabilitation of Buildings. Federal Emergency Management Agency, Washington, D.C (2000)
- Guevara-Perez, L.T.: “Soft Storey” and “Weak Storey” in earthquake resistant design a multidisciplinary approach. In: 15th World Conference on Earthquake Engineering (2012)
- IS 1893 (Part 1): Criteria for Earthquake Resistant Design of Structures (sixth revision), Bureau of Indian Standards (2016)
- Klingner R.E., Bertero V.V.: *Infilled Frames in Earthquake Construction*, 292 p. National Science Foundation, Washington D.C. (1976)
- Ko, H., Kim, H.-S., Kang, J.-W.: Evaluation of seismic behaviour of RC moment resisting frame with masonry infill walls. *J. Asian Arch. Build. Eng.* **13**(3), 641–648 (2014)
- Murty, C.V.R., Jain, S.K.: Beneficial influence of masonry on seismic performance of RC frame buildings. In: 12th World Conference on Earthquake Engineering, February 2000, Volume 2: Earthquake Engineering Practice. Social and Economic Issues (2000)
- Priestley, M.J.N., Calvi, G.M., Kowalsky, M.J.: Displacement-based seismic design of structures. In: *New Zealand Conference on Earthquake Engineering*, vol. 2007. Iuss Press (2007)
- Razzaghi, M.S., Javidnia, M.: Evaluation of the effect of infill walls on seismic performance of RC dual frames. *Int. J. Adv. Struct. Eng.* **7**, 49–54 (2015)
- Sullivan, T.J., Reyes, G., Gaetano, C.D.: Development of a displacement-based design method for steel frame\_RC wall buildings. *J. Earthquake Eng.* **14**(2), 252–277 (2010)
- Hamburger, R.O., Chakradeo, A.S.: Methodology for seismic capacity evaluation of steel frame buildings with infill unreinforced masonry. In: *Proceeding of 1993 National Earthquake Conference, Earthquake Hazard Reduction in the Central and Eastern United States*, Memphis, Tennessee (1993)



# Seismic Base Isolation of 7 Storey RC Structure Using Single Friction Pendulum System

Sumbul Iqbal<sup>1</sup>(✉) and Nazrul Islam<sup>2</sup>

<sup>1</sup> Department of Civil Engineering (Earthquake Engineering),  
Jamia Millia Islamia, New Delhi, India  
sumbuliqball@gmail.com

<sup>2</sup> Department of Civil Engineering, Jamia Millia Islamia, New Delhi, India

**Abstract.** Base isolation is an advance technique to prevent our structure from the disastrous effect of the earthquake. Several attempts had been made in history in research and development fields for anti-seismic structure or for the development of structure that can withstand the effect of earthquake. Due to increase activity of tectonic movement, the seismic hazard and its effect are now a major concern, especially in earthquake-prone areas. Base isolation is the answer to the above problems. It is an advanced technique to deal with the behavior of structure during seismic loading. As an example, a 7-storey simple RC structure is analyzed by using SAP 2000 software in which two different models are framed. The first model is the building with a fixed base and the second one is the model with single friction pendulum. In the analysis of the aforementioned models base shear, time period and inter storey drifts are compared. Furthermore, the parameter of friction pendulum is compared like the radius of curvature and the coefficient of friction. Basically, two cases have been taken, in the first case the value of coefficient of friction of pendulum and radius of curvature is varied and accordingly the results are compared. In the second case, the coefficient of friction is fixed ( $\mu = 0.1$ ) and the radius of curvature of pendulum is varied, and then results are compared. Non-linear time history analysis using the El-Centro TH earthquake record has been taken.

**Keywords:** Base isolation · Friction pendulum system · Radius of curvature · Coefficient of friction · SAP 2000

## 1 Introduction

The analysis of medium rise building is the motive of present study and the importance of base isolated structure is clearly depicted at the end of our research. Concept of ductility was used in the olden building but such buildings have performance below the expected level (Scheaua 2011). Researchers have developed many methods to deal with the pre and post effect of earthquake, but among all the alternatives, base isolation is the best technique and now a days this method is being widely use (El-Bayoumi 2015). It is important to note that this technique can be easily applied on new as well as for retrofitting the old structure (Scheaua 2011). In the year 1891 the wooden logs in several layers were used in lateral and longitudinal direction at the base of the building

to isolate it from the ground, this technique was used in Japan (Lousidis 2015). In the year 1985 in USA the first isolator used as the base isolator.

The idea of invention of base isolation was to reduce the ground shaking effect of the structure supported above the ground. In base isolation technique a support mechanism is installed which helps in separating our structure from ground which in turn decouples the effect of ground shaking (Thomas and Mathai 2015). Base isolation reduces absorption of seismic forces and energy which can be done by placing the structure on such a mechanism so that our building is flexible in horizontal direction or in other words our structure has very low lateral stiffness and at the same time introduce such a feature that restrict the amount of motion caused by the earthquake forces.

Among all the types of base isolation devices friction pendulum is one of them (Kamrava 2015). There is a pure friction system in which no restoring force is available. But in the recent development new type of sliding isolator are developed which has restoring forces so when the earthquake strike, the building restores its original position this type of isolators is known as the friction pendulum system.

### 1.1 Friction Pendulum Bearing

The working principle of friction pendulum bearing is same as that of simple pendulum. The bearing is made up of an articulated slider having radius of curvature  $R$  and concave surface at the bottom, the top portion is flat and there is a bearing at the middle with low friction (Mansouri and Nazari 2017). When earthquake strike this articulated slider moves along the concave surface due to which the structure move following a simple harmonic motion and there is increase in the time period of structure (Thomas and Mathai 2016). The friction pendulum separates the superstructure from ground and also the damping ratio and time period of superstructure increases (Torunbalci and Ozpalkanlar 2008). There is a production of frictional forces during the course of dynamic action of pendulum, this frictional force act as a damping system. Hence the response of structure to the seismic forces decreases. Friction pendulum system has more advantages compare to that of previous isolators as it has high durability and has stability over time and most importantly it has resilience and has re-centering capacity at the end of earthquake which makes it different from all the other type of devices available in the market (Nguyen et al. 2018) (Fig. 1).

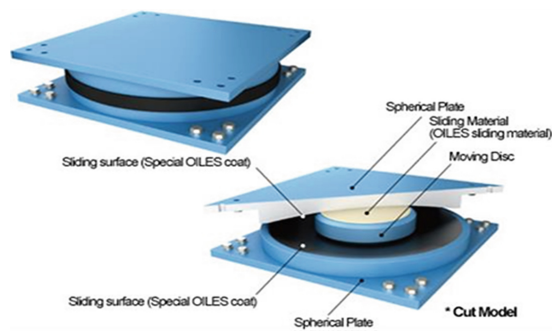


**Fig. 1.** Friction pendulum system slider (<https://www.oiles.co.jp/en/menshin/building/menshin/products/fps/>).

## 2 Modelling of Structure

**Table 1.** Modelling data of structure

Elements in the model	Dimension(mm)	Total storey	Loads	Each storey height
Beams	300 × 500	7-storey level	Floor Finish =1 KN/m <sup>2</sup>	3 m
Columns	500 × 500		Live load= 4 KN/m <sup>2</sup>	
Slab	150			

**Table 2.** Plan data

Direction	Total number of Bays in each direction	Length of each Bay
Along X axis	4	6 m
Along Y axis	4	4 m

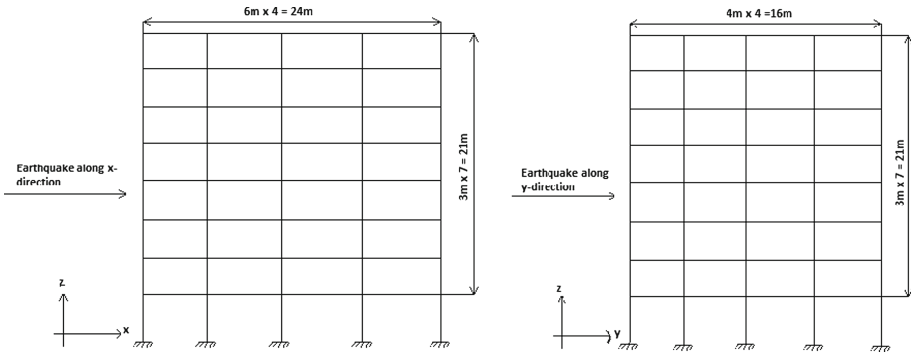


**Fig. 2.** Schematic diagram of 7 storey building and load exerted in x and y direction.

The peak ground acceleration is taken as 0.24 g for the analysis of structure (Fig. 2 and Tables 1, 2).

### 3 Modelling of Friction Pendulum

The main modelling criteria of friction pendulum is as stated below:

$$T = 2\pi\sqrt{R/g} \quad (1)$$

$R$  = radius of curvature for sliding surface of friction pendulum

$\mu$  = Coefficient of friction under dynamic condition, generally taken in between 3–10% (Scheaua 2011)

$T$  = Time period of isolated structure

$K_I$  = Device horizontal stiffness

$W_I$  = Design vertical load

$K_{eff}$  = Device effective stiffness in horizontal direction

$\beta_{eff}$  = Effective damping

$$K = \frac{W_I}{R} \quad (2)$$

$$K_{eff} = \frac{H}{\delta} = \frac{W_I}{R} + \frac{\mu W_I}{\delta} \quad (3)$$

$$\beta_{eff} = \frac{2}{\pi} \frac{(\mu)}{\mu + \frac{\delta}{R}} \quad (4)$$

### 4 Analysis Data

Parameters of the friction pendulum with three-dimensional behavior used in SAP 2000 are as follows:

U1 linear effective stiffness = 10000000 KNm<sup>-1</sup>

U2 = U3 = Linear effective stiffness = 1209 KNm<sup>-1</sup>

U2 = U3 = Nonlinear effective stiffness = 89500 KNm<sup>-1</sup>

Coefficient of friction in slow = 0.02

Coefficient of friction in fast = 0.04

Rate parameter = 5.5

Radius of curvature for sliding surface of friction pendulum = 2.24 m

Effective damping = 0.165

These parameters affect the behavior of friction pendulum system

Below are the models of 7 storey building having friction pendulum at the base modelled in SAP 2000 software (Figs. 3, 4 and 5).

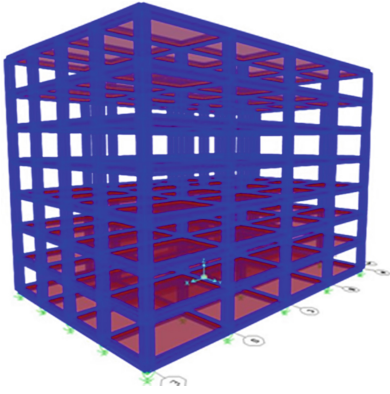


Fig. 3. Model with friction pendulum.

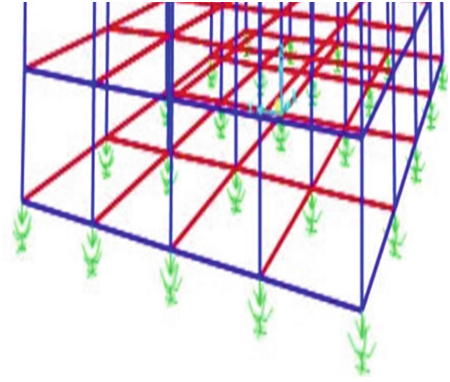


Fig. 4. Nonlinear link support (FPS).

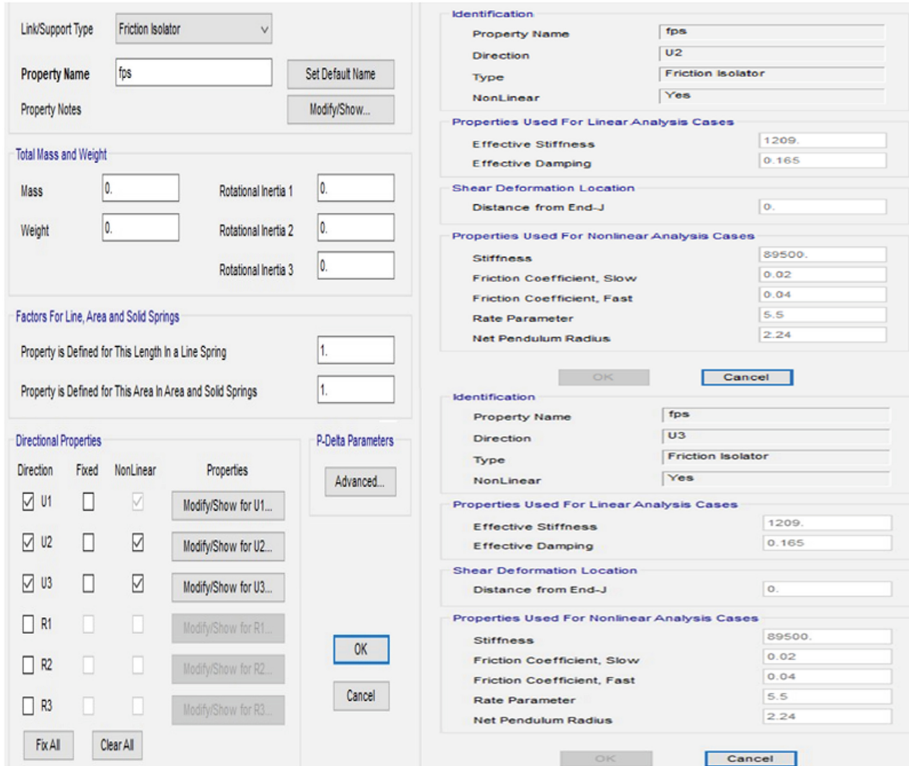


Fig. 5. Properties of FPS to be used in SAP 2000.

Nonlinear time history analysis is done by using El-Centro TH earthquake records by taking aforementioned data and parameters like base shear in X and Y direction, time period and inter storey drift are monitored.

Furthermore, the radius of curvature (R) and fast coefficient of friction is varied from 2.24 m to 6.2 m and 0.04 to 0.08 respectively in the first case.

In the second case the value of coefficient of friction is fixed as 0.1 and the radius of curvature is varied from 1.5 m to 4.5 m, in both the cases base shear is compared.

## 5 Result and Discussion

### 5.1 Base Shear

See Figs. 6, 7 and Table 3.

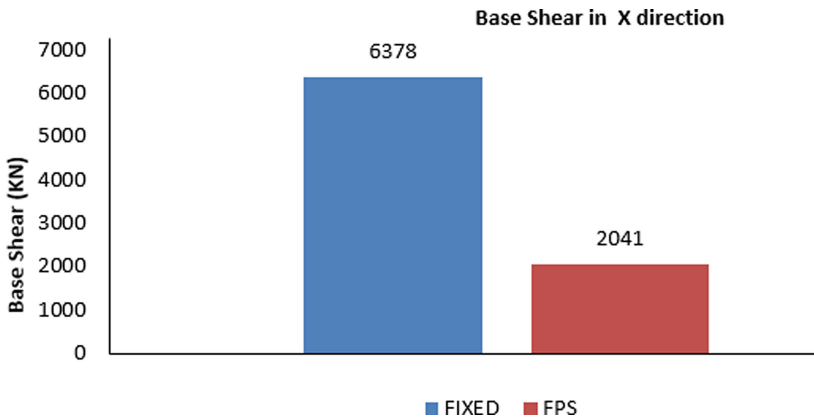


Fig. 6. Base shear in X direction.

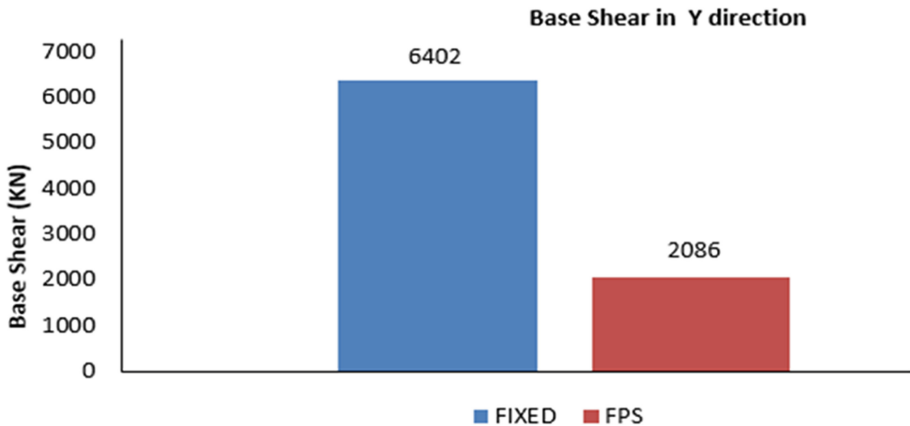
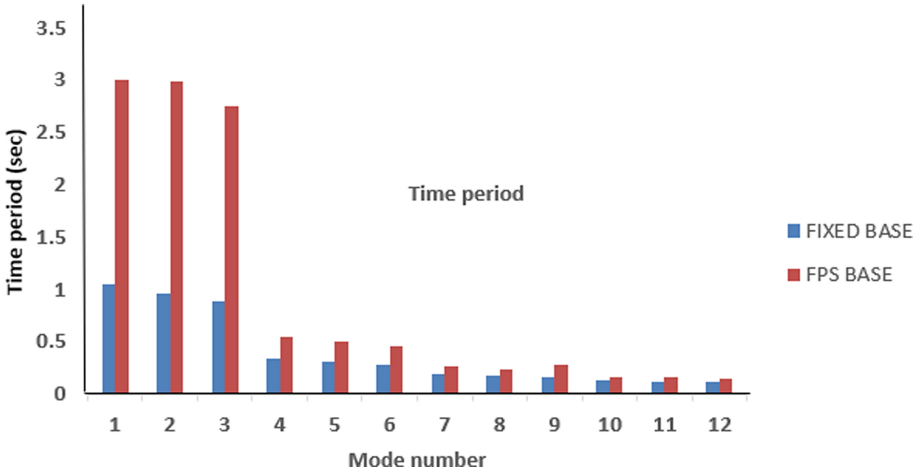


Fig. 7. Base shear in Y direction.

**5.2 Time Period**

See Fig. 8 and Table 4.



**Fig. 8.** Time period.

**Table 3.** Time period

MODE	FIXED BASE	FPS BASE	%INCREASE
1	1.050	3.00	65.00
2	0.957	2.99	67.99
3	0.892	2.75	67.56
4	0.339	0.55	38.36
5	0.310	0.499	37.87
6	0.289	0.46	37.17
7	0.191	0.268	28.73
8	0.177	0.243	27.16
9	0.165	0.277	27.31
10	0.127	0.169	24.85
11	0.120	0.156	23.08
12	0.112	0.145	22.76



### 5.3 Inter Storey Drift

See Fig. 9.

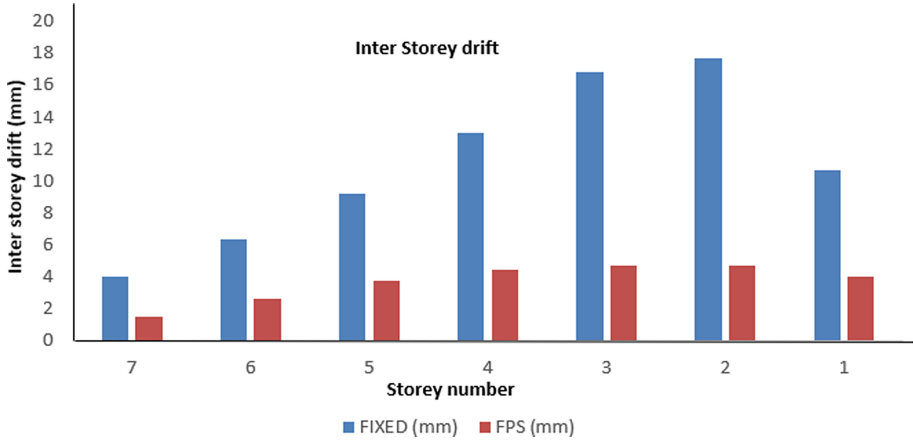


Fig. 9. Inter storey drift.

Table 4. Inter storey drift

STOREY	FIXED (mm)	FPS (mm)	%REDUCTION
7	4.03	1.45	64.02
6	6.36	2.64	58.49
5	9.18	3.75	59.15
4	13.03	4.45	65.84
3	16.82	4.70	72.06
2	17.7	4.67	73.62
1	10.65	4.03	62.16

### 5.4 Base Shear with Varying R and $\mu$

Table 5. R and  $\mu$  varying

R(m)	Time period(sec)	$\mu$	Y(KN)	Base shear in X (KN)	Base shear in
2.24	3.0	0.04		2041	2086
3.04	3.5	0.05		2109	2185
3.97	4.0	0.06		2222	2344
5.0	4.5	0.07		2372	2536
6.2	5.0	0.08		2550	2737

### 5.5 Base Shear with Varying R and $\mu$ (0.1)

See Table 6.

**Table 6.** R varying and  $\mu = 0.1$

R(m)	Base shear in X direction (KN)	Base shear in Y direction (KN)
1.5	2826	3130
2.5	2904	3159
3.5	2933	3161
4.5	2938	3178

## 6 Conclusion

### 6.1 Result with R = 2.24 m and $\mu = 0.04$

As from the analysis it is clear that the base shear reduction in X direction is about 68% whereas in Y direction reduction is 67% when friction pendulum is used compared to that of fixed base. From the time period result there is a maximum increase of 68% which occur in 2nd mode. From the inter-storey drift result there is a reduction of about 74% to 58% compare to fixed base model.

From all the above result it is very clear that the friction pendulum system proves to be very effective during seismic response and helps in safeguarding our structure during the course of earthquake.

### 6.2 Result with Variation of R and $\mu$

As we vary R (from 2.24 to 6.2 m) and  $\mu$  (0.04 to 0.08) simultaneously we can clearly notice that the base shear increases. From R = 2.24 m at  $\mu = 0.04$  to R = 6.2 m at  $\mu = 0.08$ , the base shear in X direction increases by 20.4% and in Y direction it increases by 23.7% (as in Table 5). It can be clearly inferred that for getting a better response the higher value of R and  $\mu$  should be avoided.

### 6.3 Result by Varying of R and Keeping $\mu$ as 0.1

By simply varying R and keeping  $\mu$  as constant (0.1) the base shear both in X and Y direction increases and therefore higher values of radius of curvature should be avoided for better response during earthquake.

## References

- El-Bayoumi, K.: Dynamic analysis of high rise seismically isolated buildings. *Am. J. Civil Eng.* **3**(2), 43 (2015). <https://doi.org/10.11648/j.ajce.20150302.13>
- Kamrava, A.: Seismic isolators and their types. *Curr. World Environ.* **10**(1), 27–32 (2015). <https://doi.org/10.12944/cwe.10.special-issue1.05>
- Lousidis, A.P.: Technical University of Crete Dynamic Analysis of a Friction Pendulum Isolation System (FPS) under earthquake excitation Declaration of Authorship (2015)
- Mansouri, S., Nazari, A.: The effects of using different seismic bearing on the behavior and seismic response of high-rise building. *Civil Eng. J.* **3**(3), 160–171 (2017)
- Nguyen, N.V., et al.: Performance of Single Friction Pendulum bearing for isolated buildings subjected to seismic actions in Vietnam. *IOP Conf. Ser. Earth Environ. Sci.* **143**(1) (2018). <https://doi.org/10.1088/1755-1315/143/1/012048>
- Scheaua, F.: Seismic base isolation of structures using friction pendulum bearings. *J. Mech. Eng.* **1**, 61–64 (2011)
- Thomas, T., Mathai, A.: Friction pendulum system- a parametric study of friction coefficient. *Int. J. Sci. Technol. Eng.* **2**(6), 14–16 (2015). <http://www.slideshare.net/IjsteJournal/friction-pendulum-system-a-parametric-study-of-friction-coefficient>
- Thomas, T., Mathai, A.: Study of base isolation using friction pendulum bearing system, pp. 19–23 (2016)
- Torunbalci, N., Ozpalkanlar, G.: Earthquake response analysis of mid-story buildings isolated with various seismic isolation techniques. In: 14th World Conference on Earthquake Engineering (14WCEE) (2008)



# A Vision-Based Data-Analytics Tool for Crack Characterization in Reinforced Concrete Structures

Sandeep Das<sup>1(✉)</sup>, Subhrajit Dutta<sup>1</sup>, Dibyendu Adak<sup>2</sup>,  
and Shubhankar Majumdar<sup>2</sup>

<sup>1</sup> NIT Silchar, Silchar, India  
sandeepdas.510@gmail.com,  
subhrajit.dutta@civil.nits.ac.in

<sup>2</sup> NIT Meghalaya, Shillong, India  
shub@nitm.ac.in

**Abstract.** Civil engineering structures are the basic needs of the society and proper functioning of these structures is of paramount importance. However, these systems after construction may not be in the original state due to various environmental events, undergoing ageing and deterioration, thus degrading the health of the structure during their operation time. To mitigate the adverse effects of these events, proper and periodic maintenance of infrastructures is necessary. The need for early prediction and detection plays a crucial role in the smooth functioning of the structure. Several structural health monitoring (SHM) techniques were developed in the past to evaluate the condition of these structures. To study and monitor these systems, researchers have come up with many tools and techniques by making use of sensors to acquire data. Proper analysis of the acquired data is necessary to identify the present state and future prediction. In this study, the main emphasis is laid on studying cracks using image processing techniques and finally developing a data driven framework based on real time data. Dynamic mode decomposition has been used for predicting cracks, and level set method for quantification. Experimental investigation has been done on a simply supported beam. A vision-based data driven numerical tool has been developed and validated on the real time data collected. This tool can be used by researchers/practicing engineers for predicting and quantifying cracks. A robust predictions of future health state for the existing infrastructure systems will be valuable to stakeholders for sustainable development. Based on such predictions, a risk-informed decision making can be done for maintenance and/or demolishing the existing infrastructure systems.

**Keywords:** Structural health monitoring · Prognostics and health management · Data-driven · Dynamic mode decomposition · Level set method

## 1 Introduction

Degrading structure and infrastructure are a major concern across the world. The primary design purpose of a concrete structure is to suit the needs for which it was designed. The structural designer's goal is to make the structure safe and serviceable

for as long as possible, with a low chance of failure within the design lifetime. To satisfy the serviceability limit states, the structure must be serviceable and capable of performing its intended function during its working life. Excessive deflection undermines the structure's function whilst being unattractive aesthetically. Cracks should not be visible or large enough to compromise the structure's integrity, and vibrations must not pose risks to the occupants. A reinforced concrete structure is composed of beams, columns, slabs, and walls. Beams support slabs and are prone to flexure or bending. As and when the bending moment of these beams surpasses the moment carrying capability of the beam, cracks form, allowing moisture to enter the reinforced member through the fractures and start the reinforcement corrosion process.

Reinforced concrete beams under the action of serviceable loads deflects and forms cracks. Such cracks are temporary in nature and ceases to exist after the removal of loads. However, when the applied loads exceed the load carrying, the developed cracks are permanent in nature. These cracks reduce the strength of the beam. The ingress of moisture through these cracks corrodes the reinforcement and reduces the life of the structure. Indian codal design aid SP 25:1984 (BIS 1984) mentions the causes and prevention of cracks on concrete surface. Cracks behave randomly and is influenced by the concrete-reinforcing steel bond, cross-sectional dimensions of the member, loading and boundary conditions. Addressing the problem of cracks is one of the major concerns in today's world that demands a sustainable and resilient infrastructure systems.

## 2 Literature Review

A thorough literature review of formulae for crack-width calculation is given in the paper by Lapi et al. (2018), Basteskår et al. (2019). To study the behaviour of cracks, (Bazant and Oh 1983; Bazant and Oh 1984) compared experimental results with theoretical calculations, they also tried to quantify cracks along with the spacing of cracks Kim and White (1991) proposed a model to localize cracks with no web reinforcement. Gerstle et al. (1992) developed formulae to study the growth of cracks based on fracture mechanics approach. The effect of concrete cover on the flexural strength of beams was studied by Makhlouf and Malhas (1996). The behaviour of cracks in beams subjected to repetitive loads was done by Oh and Kim (2007), and the concept of transfer length (length of load transfer from steel to concrete) was introduced. The relation between the splitting action and cracks, a model was proposed by Giuriani et al. (1998). Cracks reduces the moment of inertia, which in turn changes the natural frequency of the beam. This change in natural frequency of beams was used to detect cracks by Chasalevris and Papadopoulos (2006). The formation of cracks with time and due to shrinkage was done by Gilbert (2008). Steel fibre-reinforced concrete shows good performance with respect to crack-width and deflection (Yang et al. 2010). Application of fracture mechanics proves to be better than elastic theory in predicting crack-widths, as suggested by Słowik (2018), Correia et al. (2013).

With the advancement of technology, numerical investigations were done on the data acquired from advanced tools (accelerometer, strain gauge, ultra-sonic pulse velocity meter, etc.). Such investigations involve data cleansing techniques to gain

useful information. Image processing techniques are been used with the advancement of computer vision tools. Such techniques do not require contact with the surface for detection and quantification. In the review paper by Mohan and Poobal (2018), the various tools and techniques, advantages and disadvantages of image processing for crack detection is highlighted. Huang et al. (2018) assessed the condition of damaged structure using deep-learning techniques. Liu et al. (2016) anticipated a model for locating cracks by constructing 3D image from 2D images. Genetic programming and percolation model was used by Qu et al. (2019) to identify surface cracks Zhu et al. (2010) gathered the properties of crack (width, length, orientation and location) by making use of image-based system identification tools. Physics-based models with images, wavelength transformation was used by Nigam and Singh (2020) to detect cracks.

Based on the literature review, it was observed modal-based techniques can typically predict the presence, location, and absolute severity of damage. Minor changes in a building's dynamic attributes result from damage. Local monitoring tactics have a much better probability of discovering and measuring damage. The usage of vision-based buildings monitoring techniques is becoming more common and frequent. Sensors are typically used in contact with structures, which can contribute to measurement inaccuracies. Structures must be kept in good repair on a regular basis. Because the data obtained from structures is massive (also known as big data), it must be thoroughly scrutinized. Structures must be maintained on a regular basis. Sensor-based crack detection has been shown to be successful when the crack occurs close to or in direct contact with the sensors. The underlying physics of the problem may not be explicitly reflected in data-driven inverse problems of health monitoring, and the outcomes may be erroneous. High-resolution imaging makes it difficult to identify extremely light cracks, and calculating crack propagation is as difficult. It's difficult to detect the tip of a fracture, and it can be deceitful at times. Only a little amount of research has been done on how cracks evolve or propagate over time. It has been observed that vision-based tools and techniques are gaining popularity and perform well in detecting cracks on a standing structure since it is non-destructive and contactless. This makes it suitable for health assessment of structures. However, the propagation of cracks with changing percentages of steel using image processing techniques has not been studied, and this forms the objective of this paper. The objectives of the frame-work proposed are:

1. To study the crack-width by changing the steel reinforcement in the flexural zone.
2. To develop an image-based data-driven tool to quantify cracks and validate it with experimental results.

### **3 Materials and Methodology**

#### **3.1 Experimental Setup**

Portland pozzolana cement, crushed aggregates and fine river sand was used to prepare M25 grade concrete mix design that was used in this study. The concrete mix was

prepared as per the guideline provided in IS 10262:2019 (Bureau of Indian Standards 2019). High yield strength deformed (HYSD) steel bars of Fe500 grade was used for the beam of size  $150 \times 150 \times 700$  mm. Three-point bending test was conducted on a simply supported beam. The details are shown in Fig. 1. The beams have been grouped into three categories with percentages of steel as 0.25, 0.37 and 0.45 (Table 1). Three beams for each category were used (in total 9 beams were tested). The test was conducted on a hand operated flexural testing machine to detect the load at which the 1<sup>st</sup> crack appears and the ultimate load at failure. The loads were applied at a uniform rate of 1 kN/s. Three cameras were used to capture the spatio-temporal phenomenon of the beams under the gradually increasing loads. The cameras were placed in the front, back and bottom of the beam. Theoretical 1<sup>st</sup> cracking moment and crack-width were calculated as per IS 456:2000 (Bureau of Indian Standards 2000). In the flexure zone, crack widths were computed at the bottom corner and in between the bars.

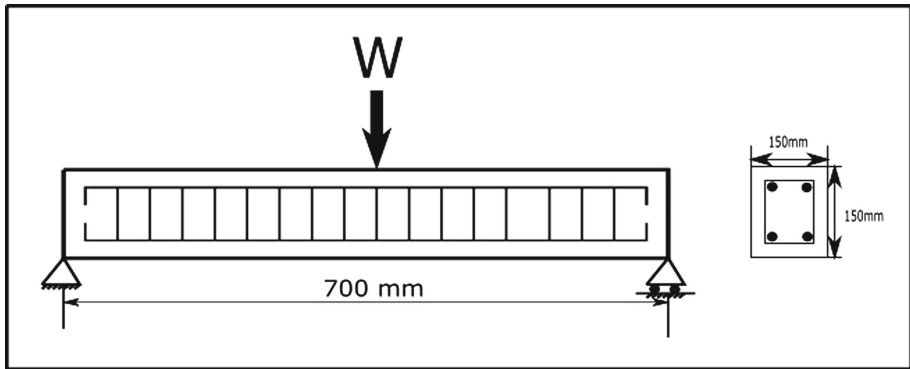


**Fig. 1.** Loading arrangement and cross-section detail of beam.

**Table 1.** Beam details

Beam mark	Length (mm)	Reinforcement		Shear spacing (6 $\Phi$ ) (mm)
		Compressive (top)	Tensile (bottom)	
B1	700	2-6 $\Phi$	2-6 $\Phi$	75
B2	700	2-6 $\Phi$	3-6 $\Phi$	75
B3	700	2-6 $\Phi$	2-8 $\Phi$	75

### 3.2 Methodology for Crack Quantification

A video of the beam being tested was recorded and images were obtained from the video file. To identify the beam specimen, the photos were cropped to reduce background noise and compress the data. Image segmentation was carried out to quantify and measure the crack-widths. Cracks are represented using the Level Set Method (LSM) (Stolarska et al. 2001). LSM represents the boundary interface by using the

interface as the zero-level surface of an implicit one-dimensional function and is based on initial value formulation to solve partial differential equations. As shown in Fig. 2, the interfaces are represented as contours of the zero-valued function of  $(x)$  defined within the complete object or crack, so that 0 (if inside the curve) and  $>0$  (if outside the curve). Consider an implicit surface  $(x)$  that represents a crack’s interface as a zero-level surface.

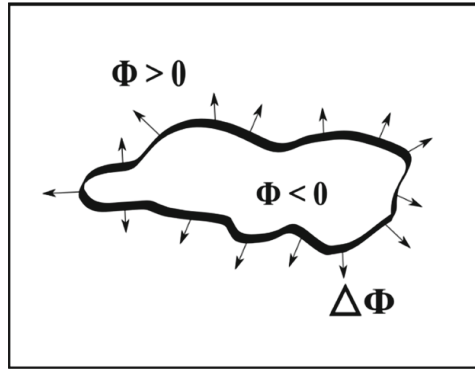


Fig. 2. A dynamic surface representing zero level set.

Signed distance function is efficient for representing  $\varphi$  (Stolarska et al. 2001; Jovičić et al. 2005) and has been selected to represent cracks. Crack-width  $s(x_e)$  (in Fig. 3) is derived mathematically at time  $t$  by reducing the arc distance  $ds$ , stated as an optimization problem

$$s = \operatorname{argmin}_{s \in x_e} \int_0^{x_e} ds \cdot \varphi(x_e, t) \cdot \left( \frac{\nabla \varphi}{\|\nabla \varphi\|} \right) dx dy \tag{1}$$

where  $s = \sqrt{dx^2 + dy^2}$  is the curved distance (of the crack-width) formed by the sections  $dx$  and  $dy$  in the  $x$  and  $y$  direction of the crack-width. A python code was developed for the implementation of LSM.

The main benefit of this image-based data-driven technology is that it can quantify cracks to a high level of precision, and the data collection process is contactless.



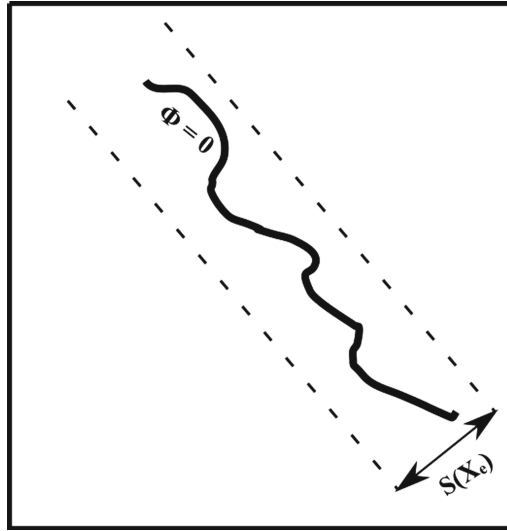


**Fig. 3.** Crack width using geodesic active contour.

## 4 Results and Discussion

Upon testing of the beams, it was observed that the cracks were located at the mid-span of the beam where the bending moment is maximum (Cracked image of Beam 1 is shown in Fig. 4). The details of the video recorded while testing the beam are:

1. 1. The total duration of the video for Beam 1, 2 and 3 are 27, 30, and 115 s respectively.
2. 2. The frames of the video were captured at an average frame rate of 35 frames/second.

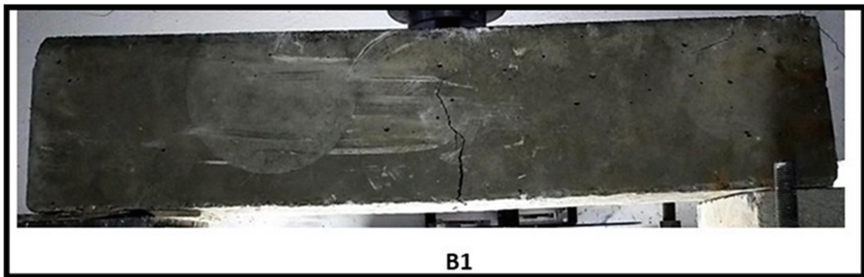


**Fig. 4.** Cracked image of Beam 1.

After 28 days of curing, the average compressive strength of a 150 mm concrete cube was found to be 32 MPa. Table 2 shows the experimental initial cracking load and moment obtained from a three-point loading test on reinforced concrete beam. The

experimental initial cracking moment exceeds the first cracking moment obtained from theoretical calculations while falling short of the ultimate load/moment. B3 has maximum percentage of steel and hence has maximum load carrying capacity. The crack-width (in mm) for theoretical, experimental, and numerical calculations is shown in Table 3. The first crack width decreases as the amount of steel increases, whereas the crack-width at ultimate load increases as the percentage of steel increases. A comparison between the crack-width values is given in Table 4. The numerical model is validated by the observation that the relative percentage error between the numerical and experimental crack widths is low. Theoretical calculation of crack-width is underestimated.

**Table 2.** Load and moment values

Beam	1st cracking moment				Ultimate load & moment	
	Theoretical		Experimental		Experimental	
	Load (kN)	Moment (kNm)	Load (kN)	Moment (kNm)	Load (kN)	Moment (kNm)
B1	13.83	2.42	14	2.45	25	4.38
B2	13.94	2.42	16.5	2.89	29	5.08
B3	13.83	2.44	17	2.98	49	8.58

**Table 3.** Crack-width at different loads

Beam mark	1st cracking load						Ultimate load	
	Crack-width theoretical (mm)		Crack-width experimental (mm)		Crack-width numerical (mm)		Crack-width experimental load (mm)	
	In between bars	At bottom corner	In between bars	At bottom corner	In between bars	At between corner	In between bars	At bottom corner
B1	0.14	0.11	0.17	0.14	0.15965	0.1377	0.34	0.27
B2	0.14	0.11	0.2	0.16	0.1852	0.1503	0.42	0.33
B3	0.12	0.1	0.15	0.13	0.1441	0.1184	0.52	0.43

**Table 4.** Percentage error of crack-width values

Numerical			Experimental		Error	
Time (sec)	In between bars (mm)	At bottom corner (mm)	In between bars (mm)	At bottom corner (mm)	In between bars (%)	At between bars (%)
15	0.1485	0.1335	0.15	0.12	1	11.25
17	0.1748	0.1518	0.18	0.14	2.88	8.43
19	0.2037	0.1647	0.21	0.16	3	2.94
23	0.2490	0.1867	0.26	0.21	4.23	11.1

## 5 Conclusions and Future Perspectives

A concrete structure's predominant design goal is to meet the requirements for which it was built. The structural designer's objective is to keep the structure safe and serviceable, with a low probability of failure within the design lifetime. The structure should be serviceable and perform its intended purpose throughout its working life in order to satisfy the serviceability limit states. Excessive deflection compromise's the structure's function and be aesthetically unappealing. Cracks should not be unattractive or big enough to cause durability issues, and vibrations should not damage the structure that discomforts the occupants.

Ageing and prolonged loads applied on the structure are the principal cause of RC structural element deterioration, which is influenced by a number of factors. One of the key characteristics used to evaluate the serviceability criterium of a RC structure is the formation of cracks. The present study investigates the behaviour of flexural cracks in reinforced concrete beam members both experimentally and numerically. By altering the amount of tensile steel in the beam sections, the experimental examination focuses on the influence of flexural cracks of RC beam sections. A vision-based data-driven tool for modelling and quantifying crack-widths is created and validated by making use of real-time video surveillance data of beam tested under three-point loading. The model may be used to quantify cracks accurately. From the standpoint of beam serviceability requirements, this approach is advantageous. Cracks with various design factors can be studied using the model (cross-section dimension, concrete grade, area of steel, etc.). The proposed numerical tool can be used by practicing engineers and researchers to develop a dependable serviceability-based design of structural systems from experimental measurements.

This research is restricted to the study of flexural behaviour of cracks in RC beams. However, a more in-depth analysis of additional failure limits, such as variation in shear and compression steel on cracks, should be carried out both experimentally and numerically. The crack width is measured by making use of static image in this study; however, the framework can be applied for dynamic and predictive modelling. Predictive modelling and quantification in combination can provide crucial information regarding health management techniques. The frame-work can then be applied on an existing bridge to quantify cracks. Designers and practitioners will be able to utilize these estimates to make judgments and anticipate the remaining useful life of the structure, enabling for effective repair and retrofitting of established cracks such as grouting, epoxy injection, stitching, and other methods.




## References

- Basteskår, M., Engen, M., Kanstad, T., Fosså, K.T.: A review of literature and code requirements for the crack width limitations for design of concrete structures in serviceability limit states. *Struct. Concr.* **20**(2), 678–688 (2019)
- Bazant, Z.P., Oh, B.H.: Spacing of cracks in reinforced concrete. *J. Struct. Eng. (United States)* **109**(9), 2066–2085 (1983)

- Bazant, Z.P., Oh, B.H.: Crack spacing in reinforced concrete approximate solution. *J. Struct. Eng.* **109**(9), 2207–2211 (1984)
- BIS: Handbook on Causes and Prevention of Cracks in Buildings (1984)
- Bureau of Indian Standards: IS 456-2000 Plain and reinforced concrete- Code of practice (2000)
- Bureau of Indian Standards: IS 10262- 2019, Concrete mix proportioning- guidelines (2019)
- Chasalevris, A.C., Papadopoulos, C.A.: Identification of multiple cracks in beams under bending. *Mech. Syst. Signal Process.* **20**(7), 1631–1673 (2006)
- Correia, J.A.F.O., De Jesus, A.M.P., Fernández-canteli, A.: Local unified probabilistic model for fatigue crack initiation and propagation: application to a notched geometry. *Eng. Struct.* **52**, 394–407 (2013)
- Gerstle, W.H., Dey, P.P., Prasad, N.N.V., Rahulkumar, P., Xie, M.: Crack growth in flexural members. A fracture mechanics approach. *ACI Struct. J.* **89**(6), 617–625 (1992)
- Gilbert, R.I.: Control of flexural cracking in reinforced concrete. *ACI Struct. J.* **106**(2), 301–307 (2008)
- Giuriani, E., Plizzari, G.A., Member, A.: Interrelation of splitting and flexural cracks in RC beams. *J. Struct. Eng.* **124**(9), 1032–1040 (1998)
- Huang, H., Li, Q., Zhang, D.: Deep learning based image recognition for crack and leakage defects of metro shield tunnel. *Tunnel. Underground Space Technol.* **77**, 166–176 (2018). (Elsevier)
- Jovičić, G., Živković, M., Jovičić, N.: Numerical modeling of crack growth using the level set fast marching. *FME Trans.* **1**, 11–19 (2005)
- Kim, W., White, R.N.: Initiation of shear cracking in reinforced concrete beams with no web reinforcement. *ACI Struct. J.* **88**(3), 301–308 (1991)
- Lapi, M., Orlando, M., Spinelli, P.: A review of literature and code formulations for cracking in R/C members. *Struct. Concr.* **19**(5), 1481–1503 (2018)
- Liu, Y.F., Cho, S., Spencer, B.F., Fan, J.S.: Concrete crack assessment using digital image processing and 3d scene reconstruction. *J. Comput. Civ. Eng.* **30**(1), 1–19 (2016)
- Makhlouf, H.M., Malhas, F.A.: The effect of thick concrete cover on the maximum flexural crack width under service load. *ACI Struct. J.* **93**(3), 257–265 (1996)
- Mohan, A., Poobal, S.: Crack detection using image processing: a critical review and analysis. *Alexandria Eng. J.* **57**(2), 787–798 (2018). (Faculty of Engineering, Alexandria University)
- Nigam, R., Singh, S.K.: Crack detection in a beam using wavelet transform and photographic measurements. *Structures* **25**, 436–447 (2020). (Elsevier)
- Oh, B.H., Kim, S.H.: Advanced crack width analysis of reinforced concrete beams under repeated loads. *J. Struct. Eng.* **133**(3), 411–420 (2007)
- Qu, Z., Chen, Y.X., Liu, L., Xie, Y., Zhou, Q.: The algorithm of concrete surface crack detection based on the genetic programming and percolation model. *IEEE Access* **7**, 57592–57603 (2019). (IEEE)
- Słowik, M.: The analysis of failure in concrete and reinforced concrete beams with different reinforcement ratio. *Arch. Appl. Mech.* **89**(5), 885–895 (2018). <https://doi.org/10.1007/s00419-018-1476-5>
- Stolarska, M., Chopp, D.L., Moes, N., Belytschko, T.: Modelling crack growth by level sets in the extended finite element method. *Int. J. Numer. Meth. Eng.* **51**(10), 943–960 (2001)
- Yang, I.H., Joh, C., Kim, B.S.: Structural behavior of ultra high performance concrete beams subjected to bending. *Eng. Struct.* **32**(11), 3478–3487 (2010). (Elsevier Ltd)
- Zhu, Z., German, S., Brilakis, I.: Visual recognition and assessment of concrete crack properties. In: EG-ICE 2010 - 17th International Workshop on Intelligent Computing in Engineering (2010)



# Response of Two-Way RCC Slab with Unconventionally Placed Reinforcements Under Contact Blast Loading

Qurat ul Ain<sup>1</sup> , Mehtab Alam<sup>2</sup> , and S. M. Anas<sup>3</sup> 

<sup>1</sup> Civil Engineering Department, Jamia Millia Islamia, Delhi 110 025, India  
waniquurat111@gmail.com

<sup>2</sup> Department of Civil Engineering, Netaji Subhas University of Technology,  
New Delhi 110 073, Delhi, India  
mehtab.alam@nsut.ac.in

<sup>3</sup> Jamia Millia Islamia, Delhi 110 025, India  
s1910521@st.jmi.ac.in

**Abstract.** Failure of building structures by blast-induced loading is quite common and is of considerable interest. Consequences of blast loading may result in the progressive collapse of the buildings and as noticed by a number of researchers, some elements of reinforced concrete structures subjected to such extreme loading of short duration may not respond with plastic behaviour at mid-span and fail by suffering severe damage. In order to control the explosive induced damage, it is indispensable to comprehend response of the structural elements under such intensive loadings. A plate element is considered to represent slab and wall in a structure. With this concern, a finite element model of a slab reinforced with conventional rebar mesh has been developed and validated using the ABAQUS/CAE software. To improve the blast resistance of the two-way concrete slab, the slab models are provided with the same reinforcement ratio in three layers with first- and third-layer having layouts of (a) 60° and 120°, (b) 45° and 135°, and (c) 30° and 150°. Finite element simulations are executed to scrutinize the effect of layout of the reinforcements in the slab and compared their blast performance with the conventionally reinforced one. CDP, damage plasticity model with strain rate effects has been invoked in this work. Maximum displacement, damage dissipation energy, and crack patterns have been evaluated and discussed.

**Keywords:** Blast loading · RC slab · Reinforcement layout · Blast pressure · Damage dissipation energy · Stresses · Cracks

## 1 Introduction

Structural engineers and designers have taken cognizance of accidental as well as intentional explosive-induced blasts and structural damage caused by such explosive-induced loading (Luccioni et al. 2003). Some recent explosions are like that triggered by ammonium nitrate detonation in Beirut (August 2020) the chemical explosion at Chemours Plant in the US (December 2020) and two bomb blasts in Kabul (February 2021) (Ain et al. 2021; Anas et al. 2020a, b). Reinforced concrete shows a complex

behavior under the action of blast loads (Kumar et al. 2019). Blast load acts for a short duration, from the local region of high pressure and temperature (Tai et al. 2011). The shock wave generated from the blast propagates through the concrete as a compressive wave and reflects after interacting with the free surface as a high tensile stress wave producing spallation of target concrete (Zhao et al. 2019). Concrete structures respond differently under close-in detonation and contact detonation. Spalling and craters are formed under contact detonation whereas flexural failure or flexure-shear damage can be seen in the case of close-in detonation (Anas et al. 2021a, b, c). According to ASCE/SEI 59-11 (2011), the explosive charge detonated at close proximity to the structure is termed as close-in or near range explosion, it corresponds to the scaled distance less than  $1.20 \text{ m/Kg}^{1/3}$ . On the other hand, standoff distance is negligible in case of contact detonation i.e., the explosive is in contact with the target. Urban areas with congregated traffic, public buildings, metros, and other engineering structures are most susceptible to huge damages and losses induced by any explosion, either intentional or accidental.

## 2 Literature Survey

A number of researchers have experimentally, theoretically, and numerically studied the effect of blast loading on structures (Yu and Hao 2001; Silva and Lu 2009; Wang et al. 2012; Guo et al. 2017; Iannitti et al. 2018; Zhao et al. 2019; Kumar et al. 2019; Habbobi and Wazni 2020; Anas et al. 2021a, b, c; Ain et al. 2021; Dar et al. 2021; Ahmadi et al. 2021; Anas and Alam 2021a, b; Anas et al. 2021d, e; Anas and Alam 2022a, b, c; Anas et al. 2022c, d, e, f, g, h, i, j, k; Shariq et al. 2022; Tahzeeb et al. 2022a, b, c). Yu and Hao (2001) used coupled single degree-of-freedom systems to analyse the failure modes of the RCC slabs under blast loading. It was concluded that the blast with high amplitude load and short duration leads to the failure of slab in direct shear mode, and blast with comparatively low amplitude load with longer duration causes the slab to fail in flexure mode. Silva and Lu (2009) studied the RC slabs and their behaviour using SDOF in aggregation with displacement-based design technique for the assessment of the explosive load and standoff distance which caused a particular level of damage in RC slab. The results were verified by the experiment carried out on the same and found to be consistent. Wang et al. (2012) performed a field study on scaling the blast resistance of the one-way square RC slab exposed to the near-field explosion. Based on the results, they proposed two empirical equations for the scaling up of the model to prototype. Guo et al. (2017) experimentally studied the effectiveness of glass-FRP retrofitted RC slab subjected to blast loading by 400–1400 g of TNT. It was concluded in the test results that externally bonded GFRP slabs efficiently increased the ultimate blast-resistant capacity against conventional explosive blast loading. Iannitti et al. (2018) numerically analysed the RC slab samples without and with partition exposed to blast loading by adopting the explicit FE code in LS-DYNA. The main result of their study was the identification of a mechanism that determined the damage generation, which could be potentially utilized in order to

invoke higher effective blast resistance in the structures by taking partition elements into account. Zhao et al. (2019) performed a numerical study on the Novel RC slab and compared its dynamic behavior with the ordinary RC slab subjected to near-range blast loading. Blast performance of the NRC slab was found superior. Habbobi and Wazni (2020) used the new steel reinforcement method i.e., they embedded computer numerical control CNC steel plate configuration for a one-way concrete slab model and investigated it under the blast loading. They concluded that this new method increases the overall ductility of the slab and hence had been promising for blast-resistant design of structures. Kumar et al. (2019) performed the experimental and finite element investigation on six reinforced concrete RC slabs at varying standoff distances with different quantities of Gelatine explosives. A detailed study was done on the response of RC slabs like damage pattern, cracks, spalling and crater diameter, etc. Anas et al. (2020a, b, 2021a, b, c) performed numerical simulation of slabs on ABAQUS/CAE by making finite element models. Analysis was carried out with 25% and 50% replacement of conventional steel rebars with FRP rebars. Maximum mid-span displacement and damage underwent by the reinforced slab were computed.

In most of the above-mentioned literature survey, research has been focussed on retrofitting new materials into the slab for resilience against blast loading. In the present study, reinforcement is placed in three layers, with first-, and third-layers having layouts of (a)  $60^\circ$  and  $120^\circ$ , (b)  $45^\circ$  and  $135^\circ$ , and (c)  $30^\circ$  and  $120^\circ$  (Fig. 1) to increase the resistance against blast loading. The percentage steel is kept the same as in the case of the conventionally reinforced slab with isotropic rebars placed parallel to the supports.

### 3 Numerical Modelling

A high-fidelity finite element program, ABAQUS/CAE has been employed in this study to simulate the behavior of two-way simply supported reinforced concrete slab of size  $1000 \text{ mm} \times 1000 \text{ mm} \times 40 \text{ mm}$  subjected to the blast loading. In the first of the four FE models generated, the slab is conventionally reinforced with isotropic rebars parallel to the supports. In the 2<sup>nd</sup>, 3<sup>rd</sup> and 4<sup>th</sup> models, each model is provided with three layers of rebars at  $60^\circ/90^\circ/120^\circ$ ;  $45^\circ/90^\circ/135^\circ$ ; and  $30^\circ/90^\circ/150^\circ$  respectively, (Fig. 1) each layer consisting of an equal area of the reinforcement. Concrete is of compressive strength 39.50 MPa. The slabs are singly reinforced with steel rebar mesh of diameter 6 mm of yield strength 600 MPa, elastic modulus 210 GPa, and Poisson's ratio 0.30. The spacing of the rebars in the first slab model is 75 mm c/c, while it is 100 mm c/c in all the other three slab models. Steel reinforcement has been discretized with a 3-node explicit quadratic beam element (B32) with a fine mesh of unity, while the slab is modeled using the 8-node explicit solid element (C3D8R) with a mesh size of 5 mm.

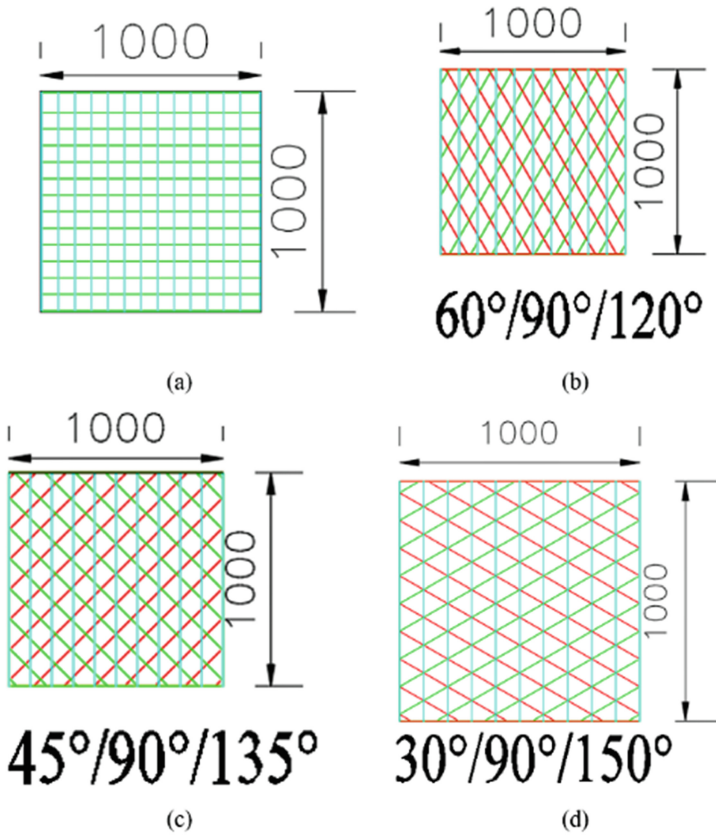


**Fig. 1.** RC slabs with different reinforcement layouts: (a) 90°/180°, (b) 60°/90°/120°, (c) 45°/90°/135°, and (d) 30°/90°/150°.

**Table 1.** Experimental values of blast parameters at 0.40 m standoff distance

$W_{TNT}$ (kgTNT)	$Z$ ( $m/kg^{1/3}$ )	$P_{OP}$ (MPa)	$t_A$ (ms)	$t_I$ (ms)	$t_2$ (ms)	$t_d$ (ms)	$t = t_A + t_d$ (ms)
0.31	0.59	4.02	0.35	0.96	0.21	1.17	1.52



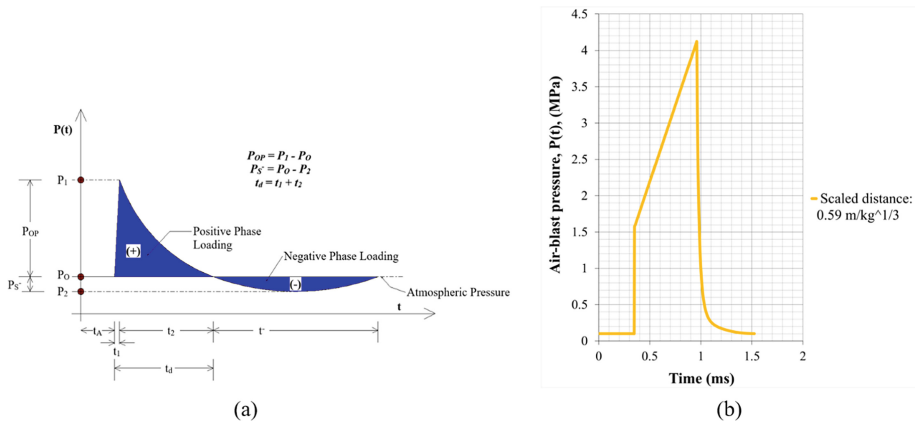


**Fig. 2.** (a) Idealized blast pressure-time history, and (b) Calculated blast time history.

### 3.1 Blast Loading

Explosion is a phenomenon of the sudden discharge of energy with hot gases at high pressure into the atmosphere (TM 5-1300 1990). Due to this fierce outburst of hot gases adjacent air condenses, forming a compressive layer of air in front of these gases called blast wave containing of the blast energy (Mays and Smith). The blast waves continue to expand and while propagating outward, pressure starts decreasing with an increase in distance and momentarily becomes equal to the atmospheric pressure (Fig. 2(a)) (TM 5-1300 1990; Wu and Hao 2005). The continuation of expansion leads to a fall of pressure below atmospheric pressure thus creating a suction zone in the blast wave (Fig. 2(a)) (TM 5-1300 1990; Wu and Hao 2005). Table 1 lists the blast parameters values. Following the current blast design guidelines (Goel and Matsagar 2014; TM 5-1300 1990; Wu and Hao 2005) the influence of the suction blast phase on the performance of the considered models has been neglected in the present work. Figure 2(b) shows the predicted blast pressure profile at a scaled distance of  $0.59 \text{ m/kg}^{1/3}$ , calculated using the empirical model proposed by Wu and Hao (2005) (Wu and Hao 2005).

Positive phase duration of a wave is compared with the natural period of vibration of the target structural element and three cases of loading can occur: (a) Impulsive loading where the load duration is shorter than the natural time period of the structure, (b) Quasi-static loading has the duration longer than the fundamental period of the structure, and (c) the third category lies in the mid of the above two cases, where the load duration and natural period of vibration are similar and it is called dynamic loading (Mays and Smith). Blast loading comes under the category of impulsive loading, having a short duration and very high strain rates, so the response of the structure is governed by its ductility and natural period of vibration (Mays and Smith).

### 3.2 Material Model

In the ABAQUS/CAE, different types of models are provided for concrete modeling which include: (a) Smeared crack model, (b) Discrete crack model, and (c) Concrete damaged plasticity (CDP) model. In this work, the CDP model, a precise elastoplastic constitutive model with isotropic compressive and tensile plasticity to incorporate the inelastic concrete behavior, is utilized for concrete modeling. This model is based on the yield function given by Lee and Fenves (1998) and later on modified by Lubliner et al. (2003), to account for the plasticity of concrete under tension and compression. Concrete possesses the nonlinear behaviour due to plasticity and damage occurs. Micro-cracking, coalescence, de-cohesion, etc., are included under the damage process. The characterization of plasticity of concrete comprises progressive deterioration, strain softening, and volumetric expansion. These lead to the reduction of stiffness and strength of concrete (Tao and Chen 2014).

To describe this stiffness degradation in CDP, stresses can be represented by:

$$\sigma_t = (1 - d_t)E_O(\varepsilon_t - \varepsilon_t^{pl}) \quad (1)$$

$$\sigma_c = (1 - d_c)E_O(\varepsilon_c - \varepsilon_c^{pl}) \quad (2)$$

where,  $d_t$  and  $d_c$  are the scalar stiffness degradation variables, which varies from 0 (undamaged) to 1 (completely damaged);  $E_O$  is the initial modulus of elasticity; and  $\sigma_t$ ,  $\sigma_c$ ,  $\varepsilon_t$ ,  $\varepsilon_c$ ,  $\varepsilon_t^{pl}$ , and  $\varepsilon_c^{pl}$  represent, the stress, total strain, and plastic strain in tension and compression respectively. As shown in Fig. 3(a), the response of concrete during the unloading is weakened due to elastic stiffness degradation described by damage variables,  $d_t$  and  $d_c$  for tension and compression respectively (Tao and Chen 2014). The stress-strain curve of concrete experiencing uniaxial tension shows a linear elastic response till it attains failure stress (Failure point),  $\sigma_{to}$ . Initiation of micro-cracking is represented by the failure point corresponding to maximum tensile stress. Post failure point region represents softening stress-strain response macroscopically in the form of micro-cracking which induces strain localization in the concrete. The stress-strain curve under uniaxial compression is linear till initial yield  $\sigma_{co}$ , followed by strain hardening and subsequently strain-softening of concrete occurs as shown in Fig. 3(b) (ABAQUS/CAE Manual). The properties of the concrete used in the CDP model are from Hafezolzhorani et al. (2018).

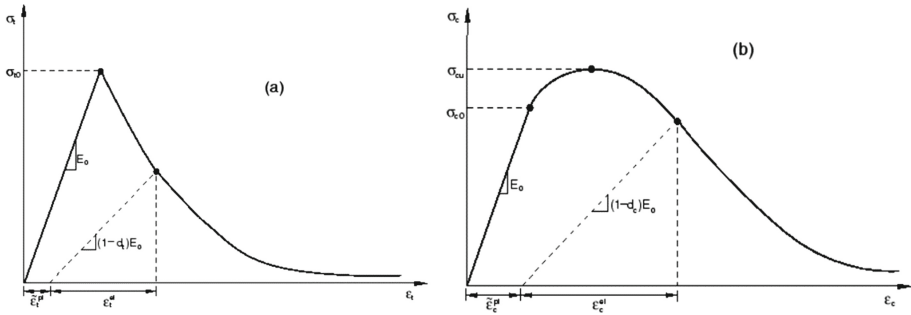


Fig. 3. Response of concrete in (a) uniaxial tension and (b) uniaxial compression.

## 4 Results and Discussion

Damage in the form of spalling of concrete has been found in the slab at the center on the blast surface followed by circumferential cracks of increasing diameter with some eventual radial cracks, Fig. 4. On the back surface of the slab, the concrete spalling occurs with predominant radial cracks propagating towards the corners of the slab (Fig. 4). Table 2 shows that the computed maximum central displacement of the slab with isotropic rebars parallel to the supports is closed to the maximum central displacement measured by Wang et al. (2012) with a percentage difference less than 8%. The crack patterns developed on the top and bottom surfaces of the slab as depicted in Fig. 4 and the crater with average size of 170 mm are closely matching with Wang et al. (2012) results approve the application of the employed software in predicting the dynamic response of the slab. The maximum central displacement, damage dissipation energy (DDE), principal tensile stress in the reinforcement, and mean depth of crack penetration in the slab with isotropic rebars are found to be 13.89 mm, 738.95 J, 600 MPa, and 32 mm, respectively (Table 2 to Table 5 and Figs. 5, 6, 7, 8 and 9). The slab with 60/90/120-degree reinforcement layouts reduce the DDE, principal tensile stress in the reinforcements, average depth of radial cracks, and maximum central displacement by 40, 45, 25, and 51%, respectively as compared with the slab having isotropic rebars only (Tables 2, 3, 4, 5 and 6 and Figs. 5, 6, 7, 8, 9, 10, 11, 12, 13, 14, 15, 16, 17 and 18). The application of 45/90/135-degree reinforcement layouts in the slab decreases the maximum central displacement, damage dissipation energy, principal tensile stress in the reinforcements, and the maximum average depth of cracks by 77, 75, 55, and 38% respectively (Tables 2, 3, 4 and 5). The slab with 30/90/150-degree reinforcement layouts reduce the maximum central displacement, damage dissipation energy, principal tensile stress in the reinforcements, and the maximum average depth of radial cracks by 84, 86, 63, and 44%, respectively (Tables 2, 3, 4, 5 and 6 and Figs. 5, 6, 7, 8, 9, 10, 11, 12, 13, 14, 15, 16, 17 and 18). It has been observed that the reinforcement orientation significantly improves the behavior of the slabs. However, the slab with 30/90/150-degree reinforcement layouts give the best performance under the 0.31 kg TNT contact explosive load at 0.40 m standoff distance.

**Table 2.** Summary of maximum central displacement (mm) of the slabs

W (kg TNT)	Z (m/kg <sup>1/3</sup> )	Wang et al. (2012) experimental result (with isotropic re-bars)	ABAQUS/CAE (2017) results			
			Slab with isotropic re-bars	Slab with 60/90/120° reinforcement layouts	Slab with 45/90/135° reinforcement layouts	Slab with 30/90/150° reinforcement layouts
0.31	0.59	15	13.89 ( <sup>a</sup> 7)	7.32 ( <sup>a</sup> 51)	3.38 ( <sup>a</sup> 77)	2.36 ( <sup>a</sup> 84)

<sup>a</sup>percentage decrease (%) in displacement with respect to Wang et al. (2012) slab model

**Table 3.** Summary of damage dissipation energy (J) of the slabs

Z (m/kg <sup>1/3</sup> )	Damage dissipation energy (J)			
	Slab with isotropic re-bars	Slab with 60/90/120° reinforcement layouts	Slab with 45/90/135° reinforcement layouts	Slab with 30/90/150° reinforcement layouts
0.59	738.95	446.08 ( <sup>a</sup> 40)	184.61 ( <sup>a</sup> 75)	104.84 ( <sup>a</sup> 86)

<sup>a</sup>percentage decrease (%) in damage dissipation energy with respect to the conventionally reinforced slab

**Table 4.** Summary of principal tensile stress in the reinforcements of the slab

Z (m/kg <sup>1/3</sup> )	Maximum tensile stress (MPa) in the reinforcements of the slabs with			
	Isotropic re-bars	60/90/120° reinforcement layouts	45/90/135° reinforcement layouts	30/90/150° reinforcement layouts
0.59	600	330.29 ( <sup>a</sup> 45)	272.65 ( <sup>a</sup> 55)	223.95 ( <sup>a</sup> 63)

<sup>a</sup>percentage decrease (%) in tensile stress with respect to the conventionally reinforced slab

**Table 5.** Summary of crack depth (mean)

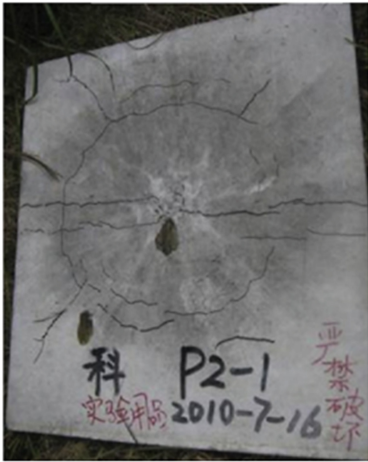
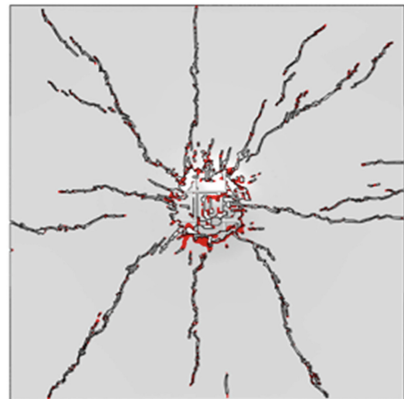
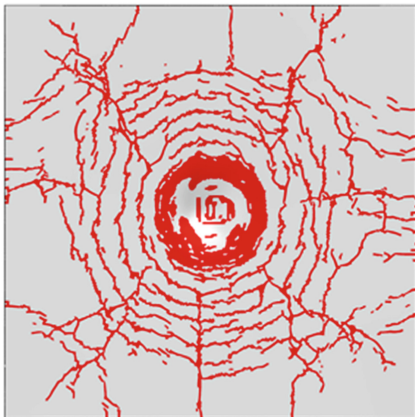
Z (m/kg <sup>1/3</sup> )	Mean depth (mm)			
	Slab with isotropic re-bars	Slab with 60/90/120-degree reinforcement layouts	Slab with 45/90/135-degree reinforcement layouts	Slab with 30/90/150-degree reinforcement layouts
0.59	32	24 ( <sup>a</sup> 25)	20 ( <sup>a</sup> 38)	18 ( <sup>a</sup> 44)

<sup>a</sup>percentage decrease (%) in average crack depth with respect to the conventionally reinforced slab

**Table 6.** Crater average size (mm)

W (kg TNT)	Z (m/kg <sup>1/3</sup> )	Wang et al. (2012) experimental result (with isotropic re-bars)	ABAQUS/CAE (2017) results			
			Slab with isotropic re-bars	Slab with 60/90/120° reinforcement layouts	Slab with 45/90/135° reinforcement layouts	Slab with 30/90/150° reinforcement layouts
0.31	0.59	180	170 ( <sup>a</sup> 6)	135 ( <sup>a</sup> 25)	70 ( <sup>a</sup> 61)	45 ( <sup>a</sup> 75)

<sup>a</sup>percentage decrease (%) in crater diameter with respect to Wang et al. (2012) slab model

**FRONT SURFACE****BACK SURFACE****Wang et al. (2012) experimental observations****ABAQUS/CAE crack patterns****Fig. 4.** Comparison of crack patterns (t = 1.52 ms).

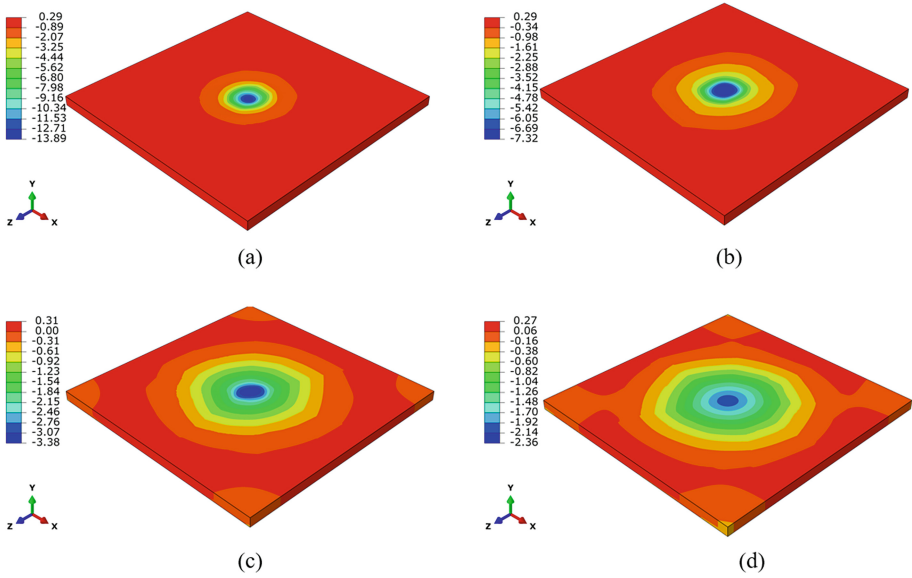


**Fig. 5.** Distribution of Y-displacement (mm) of the slabs with (a) isotropic rebars, (b) 60/90/120, (c) 45/90/135, and (d) 30/90/150-degree reinforcement layouts ( $t = 1.52$  ms).

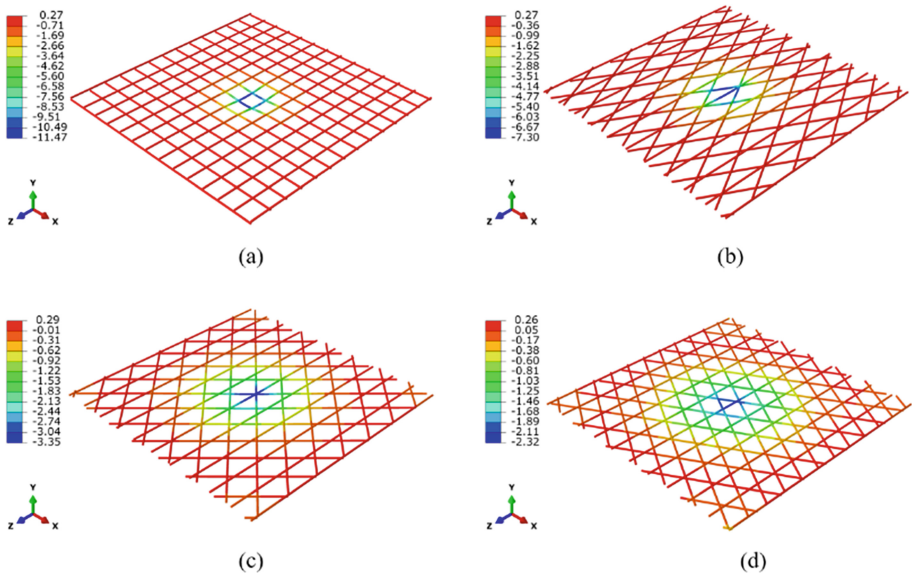


**Fig. 6.** Distribution of Y-displacement (mm) of the reinforcements in the slabs with (a) isotropic rebars, (b) 60/90/120, (c) 45/90/135, and (d) 30/90/150-degree reinforcement layouts ( $t = 1.52$  ms).

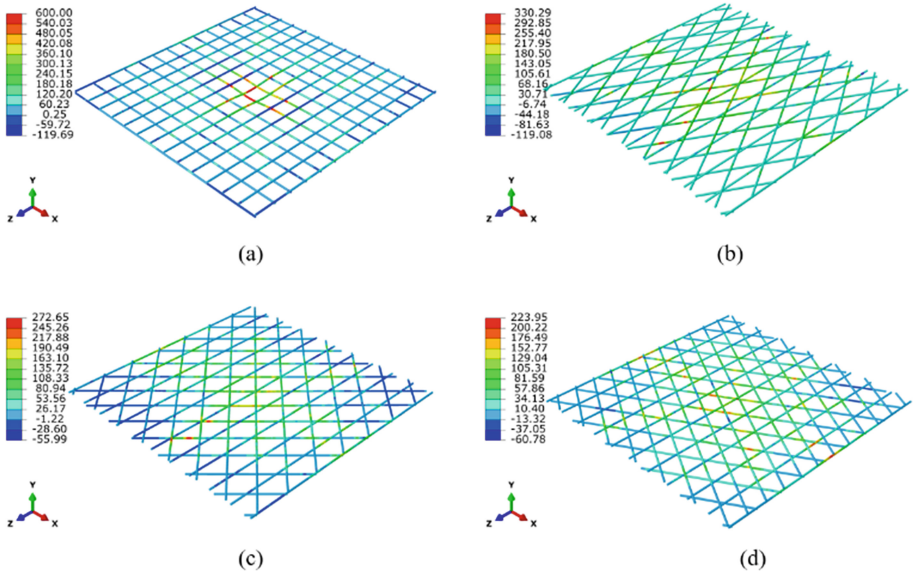


**Fig. 7.** Distribution of principal stresses (MPa) of the reinforcements in the slabs with (a) isotropic rebars, (b) 60/90/120, (c) 45/90/135, and (d) 30/90/150-degree reinforcement layouts ( $t = 1.52$  ms).

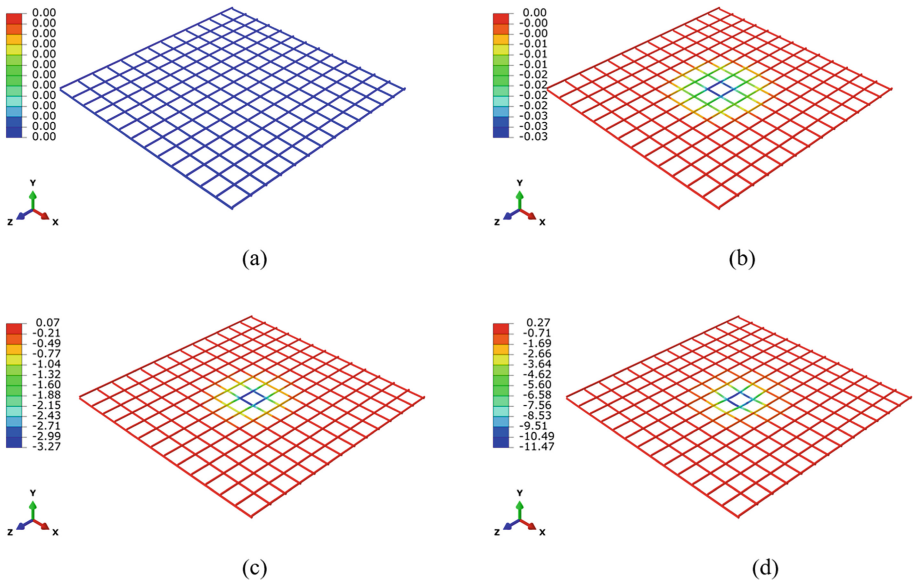


**Fig. 8.** Distribution of Y-displacement (mm) of the reinforcements in the slabs with isotropic rebars at different time steps: (a)  $t = 0$  ms, (b)  $t = 0.35$  ms, (c)  $t = 0.96$  ms, and (d)  $t = 1.52$  ms.



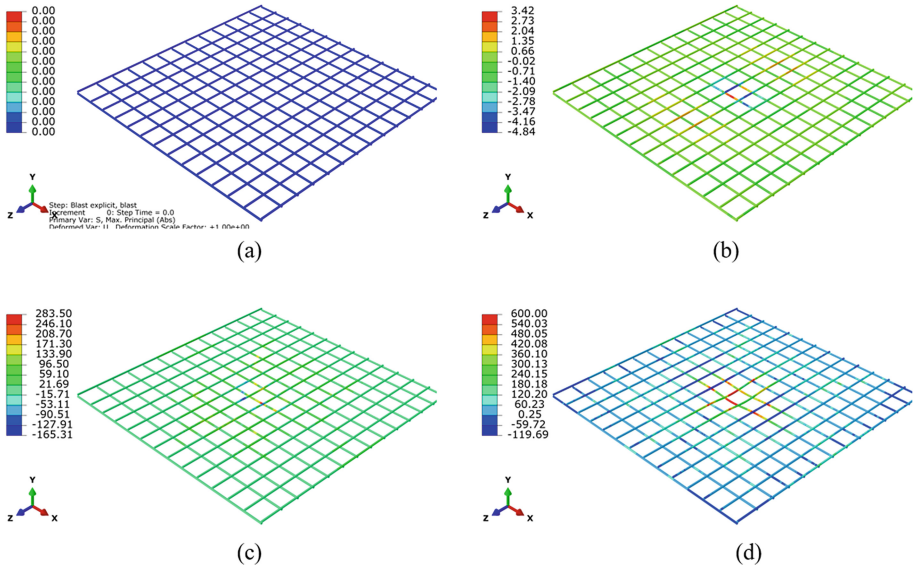


**Fig. 9.** Distribution of principal stresses (MPa) of the reinforcements in the slabs with isotropic rebars at different time steps: (a)  $t = 0$  ms, (b)  $t = 0.35$  ms, (c)  $t = 0.96$  ms, and (d)  $t = 1.52$  ms.

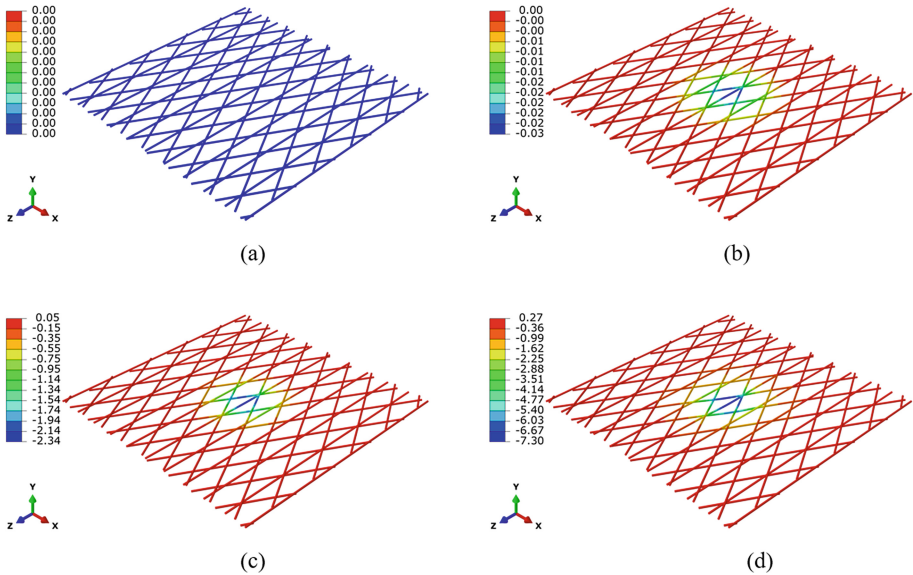


**Fig. 10.** Distribution of Y-displacement (mm) of the reinforcements in the slabs with 60/90/120-degree reinforcement layouts at different time steps: (a)  $t = 0$  ms, (b)  $t = 0.35$  ms, (c)  $t = 0.96$  ms, and (d)  $t = 1.52$  ms.



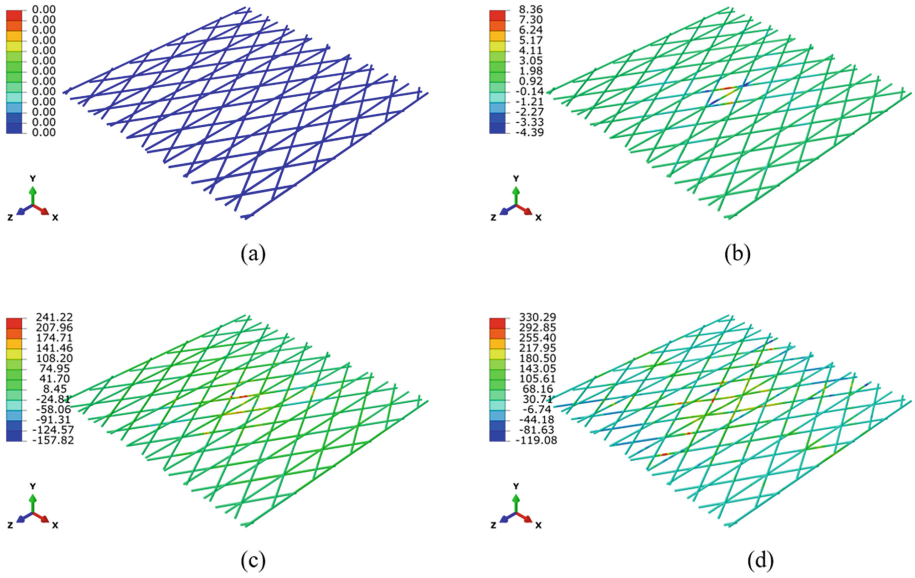


**Fig. 11.** Distribution of principal stresses (MPa) of the reinforcements in the slabs with 60/90/120-degree reinforcement layouts at different time steps: (a)  $t = 0$  ms, (b)  $t = 0.35$  ms, (c)  $t = 0.96$  ms, and (d)  $t = 1.52$  ms.

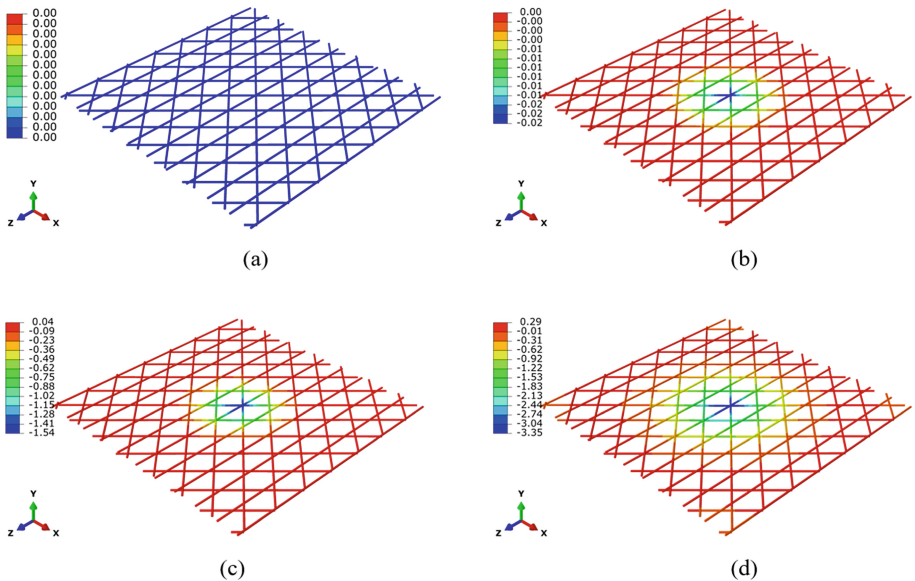


**Fig. 12.** Distribution of Y-displacement (mm) of the reinforcements in the slabs with 45/90/135-degree reinforcement layouts at different time steps: (a)  $t = 0$  ms, (b)  $t = 0.35$  ms, (c)  $t = 0.96$  ms, and (d)  $t = 1.52$  ms.

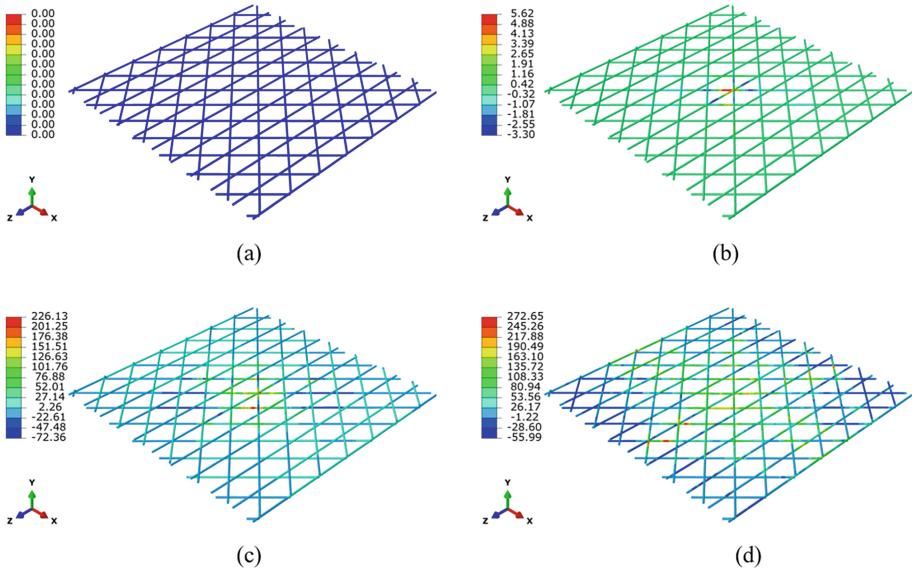


**Fig. 13.** Distribution of principal stresses (MPa) of the reinforcements in the slabs with 45/90/135-degree reinforcement layouts at different time steps: (a)  $t = 0$  ms, (b)  $t = 0.35$  ms, (c)  $t = 0.96$  ms, and (d)  $t = 1.52$  ms.

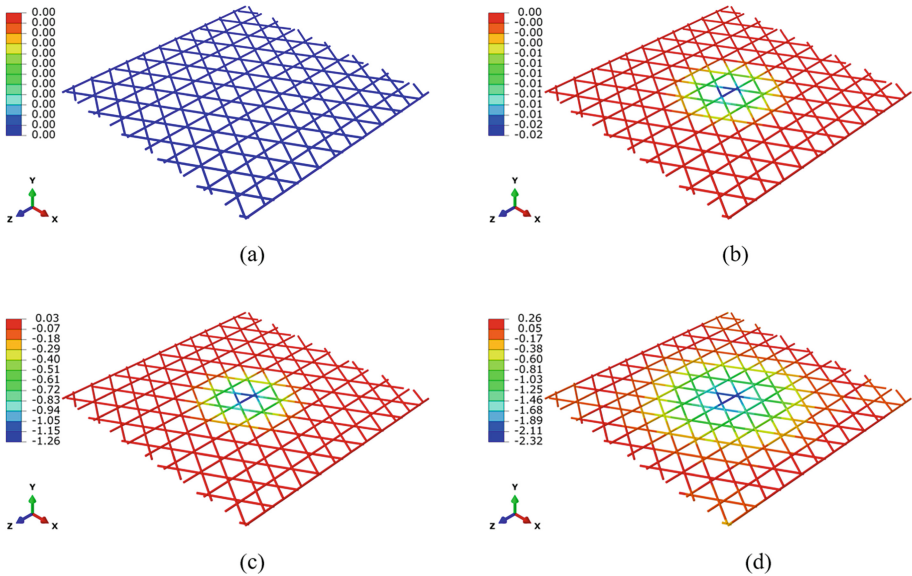


**Fig. 14.** Distribution of Y-displacement (mm) of the reinforcements in the slabs with 30/90/150-degree reinforcement layouts at different time steps: (a)  $t = 0$  ms, (b)  $t = 0.35$  ms, (c)  $t = 0.96$  ms, and (d)  $t = 1.52$  ms.

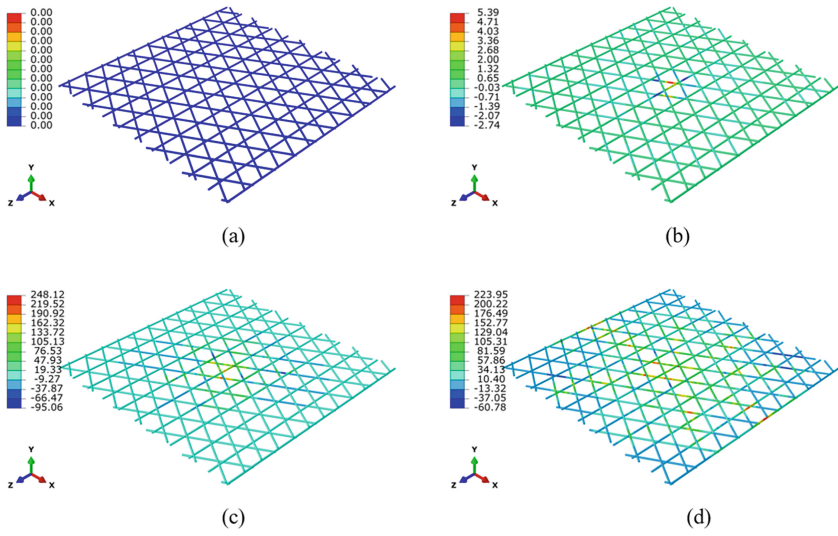


**Fig. 15.** Distribution of principal stresses (MPa) of the reinforcements in the slabs with 30/90/150-degree reinforcement layouts at different time steps: (a)  $t = 0$  ms, (b)  $t = 0.35$  ms, (c)  $t = 0.96$  ms, and (d)  $t = 1.52$  ms.

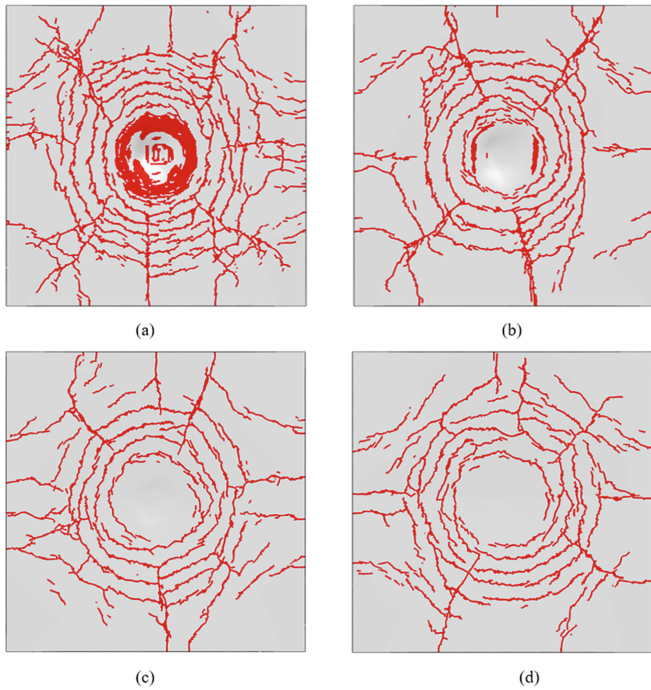


**Fig. 16.** Pattern of cracks on the front face of the slabs with (a) isotropic rebars, (b) 60/90/120, (c) 45/90/135, and (d) 30/90/150-degree reinforcement layouts ( $t = 1.52$  ms).

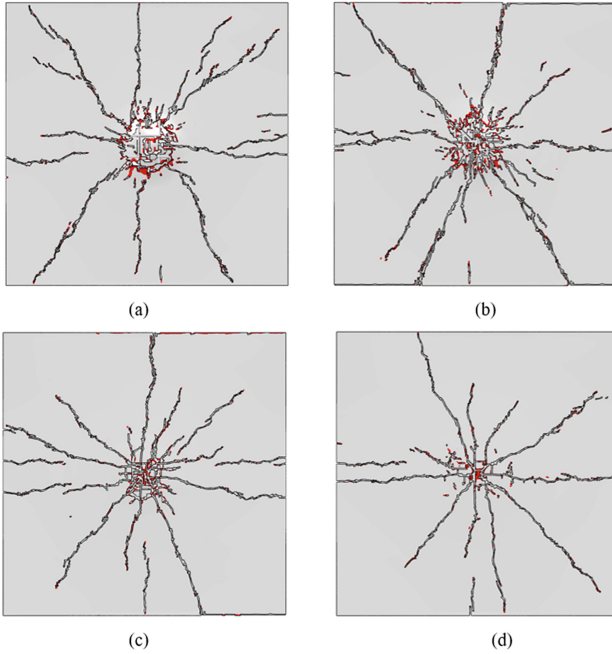


**Fig. 17.** Pattern of cracks on the rear face of the slabs with (a) isotropic rebars, (b) 60/90/120, (c) 45/90/135, and (d) 30/90/150-degree reinforcement layouts ( $t = 1.52$  ms).

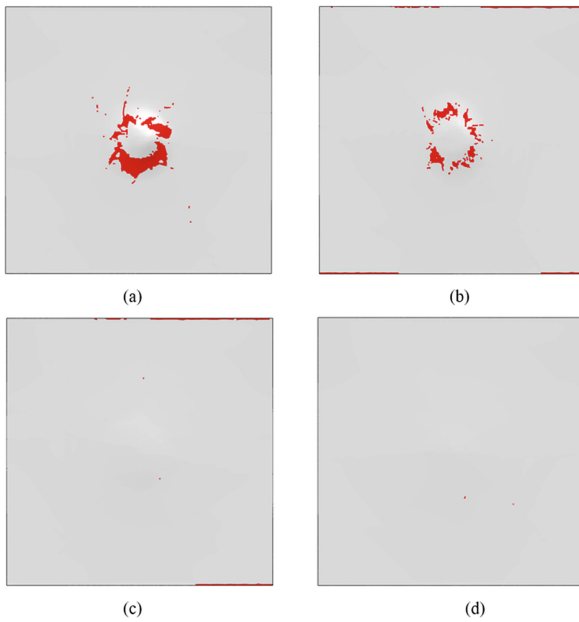


**Fig. 18.** Crushing on the bottom surface of the slabs with (a) isotropic rebars, (b) 60/90/120, (c) 45/90/135, and (d) 30/90/150-degree reinforcement layouts ( $t = 1.52$  ms).

## 5 Conclusion

In this paper, a 1000 mm × 1000 mm × 40 mm RC slab with isotropic rebars has been modeled using ABAQUS/CAE software and subjected to the 0.31 kg TNT contact load to estimate maximum central deflection and damage pattern in the slab. The deflection and damage pattern obtained are found closely matching with the available experimental results. In order to enhance the behavior of the slab under blast loading, the models have been provided with the same reinforcement ratio in three layers with first- and third-layer having a layout of (a) 60° and 120°, (b) 45° and 135°, and (c) 30° and 150°. Results reveal that the slab performs the best with 30/90/150-degree reinforcement layout under the contact explosion loading. Therefore, it can be concluded that the orientation of the reinforcement plays a major role in enhancing the performance of the slab under the contact explosion and the nominal flexural reinforcements in the form of equiangular triangular grid enhance the blast performance of the RC slab.

## References

- Al-Habbobi, A.M., Al-Wazni, S.J.: Blast loading response of a special concrete slab reinforced with embedded CNC steel plate. *J. Eng. Sci. Technol.* **15**(6), 3803–3819 (2020)
- ABAQUS/CAE FEA program. Concrete-damaged plasticity model, explicit solver, three-dimensional solid element library. ABAQUS DS-SIMULIA User Assistance Manual (2017)
- Ahmadi, E., Alam, M., Anas, S.M.: Blast performance of RCC slab and influence of its design parameters. In: Kolathayar, S., Ghosh, C., Adhikari, B.R., Pal, I., Mondal, A. (eds.) *Resilient Infrastructure*. LNCE, vol. 202, pp. 389–402. Springer, Singapore (2021). [https://doi.org/10.1007/978-981-16-6978-1\\_31](https://doi.org/10.1007/978-981-16-6978-1_31)
- Ain ul, Q., Alam, M., Anas, S.M.: Behavior of ordinary load-bearing masonry structure under distant large explosion, Beirut scenario. In: Kolathayar, S., Ghosh, C., Adhikari, B.R., Pal, I., Mondal, A. (eds.) *Resilient Infrastructure*. Lecture Notes in Civil Engineering, vol. 202, pp. 239–253. Springer, Singapore (2022). [https://doi.org/10.1007/978-981-16-6978-1\\_19](https://doi.org/10.1007/978-981-16-6978-1_19)
- Anas, S.M., Alam, M.: Air-blast response of free-standing: (1) Unreinforced brick masonry wall, (2) Cavity RC wall, (3) RC walls with (i) Bricks, (ii) Sand, in the cavity: a macro-modeling approach. In: Marano, G.C., Ray Chaudhuri, S., Unni Kartha, G., Kavitha, P.E., Prasad, R., Achison, R.J. (eds.) *Proceedings of SECON'21*. SECON 2021. LNCE, vol. 171, pp. 921–930. Springer, Cham (2021a). [https://doi.org/10.1007/978-3-030-80312-4\\_78](https://doi.org/10.1007/978-3-030-80312-4_78)
- Anas, S.M., Alam, M.: Comparison of existing empirical equations for blast peak positive overpressure from spherical free air and hemispherical surface bursts. *Iran. J. Sci. Technol. Trans. Civ. Eng.* **46**, 965–984 (2021b) <https://doi.org/10.1007/s40996-021-00718-4>
- Anas, S.M., Ansari, M.I., Alam, M.: Performance of masonry heritage building under air-blast pressure without and with ground shock. *Australian J. Struct. Eng.* **21**(4), 329–344 (2020a). <https://doi.org/10.1080/13287982.2020.1842581>
- Anas, S.M., Alam, M., Umair, M.: Performance of one-way concrete slabs reinforced with conventional and polymer re-bars under air-blast loading. In: Chandrasekaran, S., Kumar, S., Madhuri, S. (eds.) *Recent Advances in Structural Engineering*. LNCE, vol. 135, pp. 179–191. Springer, Singapore (2021a). [https://doi.org/10.1007/978-981-33-6389-2\\_18](https://doi.org/10.1007/978-981-33-6389-2_18)

- Anas, S.M., Alam, M., Umair, M.: Performance of one-way composite reinforced concrete slabs under explosive-induced blast loading. In: 1st International Conference on Energetics, Civil and Agricultural Engineering 2020, ICECAE 2020, Tashkent, Uzbekistan, December 2020, vol. 614 (2020b). <https://doi.org/10.1088/1755-1315/614/1/012094>
- Anas, S.M., Ansari, M.I., Alam, M.: A study on existing masonry heritage building to explosive-induced blast loading and its response. *Int. J. Struct. Eng.* **11**, 387–412 (2021b)
- Anas, S.M., Alam, M., Umair, M.: Experimental and numerical investigations on performance of reinforced concrete slabs under explosive-induced air-blast loading: a state-of-the-art review. *Structures*. **31**, 428–461 (2021c). <https://doi.org/10.1016/j.istruc.2021.01.102>
- Anas, S.M., Alam, M., Umair, M.: Performance of on-ground double-roof RCC shelter with energy absorption layers under close-in air-blast loading. *Asian J. Civ. Eng.* **22**, 1525–1549 (2021d). <https://doi.org/10.1007/s42107-021-00395-8>
- Anas, S.M., Alam, M., Umair, M.: Air-blast and ground shockwave parameters, shallow underground blasting, on the ground and buried shallow underground blast-resistant shelters: a review. *Int. J. Prot. Struct.* **13**(1): 99–139 (2021e). <https://doi.org/10.1177/20414196211048910>
- Anas, S.M., Alam, M.: Performance of simply supported concrete beams reinforced with high-strength polymer re-bars under blast-induced impulsive loading. *Int. J. Struct. Eng.* **12**(1): 62–76 (2022a). Article in press
- Anas, S.M., Alam, M.: Performance of brick-filled reinforced concrete composite wall strengthened with C-FRP laminate(s) under blast loading. *Mater. Today Proc.* (2022b) Elsevier. <https://doi.org/10.1016/j.matpr.2022.03.162>
- Anas, S.M., Alam, M.: Role of shear reinforcements on the punching shear resistance of two-way RC slab subjected to Impact loading. *Mater. Today Proc.* (2022c, in press). Elsevier
- Anas, S.M., Alam, M., Umair, M.: Out-of-plane response of clay brick unreinforced and strengthened masonry walls under explosive-induced air-blast loading. In: Kolathayar, S., Ghosh, C., Adhikari, B.R., Pal, I., Mondal, A. (eds.) *Resilient Infrastructure*. LNCE, vol. 202, pp. 477–491. Springer, Singapore (2022a). [https://doi.org/10.1007/978-981-16-6978-1\\_37](https://doi.org/10.1007/978-981-16-6978-1_37)
- Anas, S.M., Alam, M., Umair, M.: Influence of charge locations on close-in air-blast response of pre-tensioned concrete u-girder. In: Kolathayar, Sa., Ghosh, C., Adhikari, B.R., Pal, I., Mondal, A. (eds.) *Resilient Infrastructure*. LNCE, vol. 202, pp. 513–527. Springer, Singapore (2022b). [https://doi.org/10.1007/978-981-16-6978-1\\_40](https://doi.org/10.1007/978-981-16-6978-1_40)
- Anas, S.M., Shariq, M., Alam, M.: Performance of axially loaded square RC columns with single/double confinement layer(s) and strengthened with C-FRP wrapping under close-in blast. *Mater. Today Proc.* (2022c). Elsevier. <https://doi.org/10.1016/j.matpr.2022.01.275>
- Anas, S.M., Shariq, M., Alam, M.: Strengthening of braced unreinforced brick masonry wall with (i) C-FRP wrapping, and (ii) Steel angle-strip system under blast loading. *Mater. Today Proc.* (2022d). Elsevier. <https://doi.org/10.1016/j.matpr.2022.01.335>
- Anas, S.M., Shariq, M., Alam, M.: Effect of design strength parameters of conventional two-way singly reinforced concrete slab under concentric impact loading. *Mater. Today Proc.* (2022e). Elsevier. <https://doi.org/10.1016/j.matpr.2022.02.441>
- Anas, S.M., Shariq, M., Alam, M.: Performance based strengthening with concrete protective coatings on braced unreinforced masonry wall subjected to close-in explosion. *Mater. Today Proc.* (2022f). Elsevier. <https://doi.org/10.1016/j.matpr.2022.04.206>
- Anas, S.M., Alam, M., Shariq, M.: Damage response of conventionally reinforced two-way spanning concrete slab under eccentric impacting drop weight loading. *Def. Technol.* (2022g, in press)
- Anas, S.M., Shariq, M., Alam, M., Umair, M.: Evaluation of critical damage location of contact blast on conventionally reinforced one-way square concrete slab applying CEL-FEM blast modeling technique. *Int. J. Prot. Struct.* (2022h, in press). <https://doi.org/10.1177/20414196221095251>



- Anas, S.M., Shariq, M., Alam, M., Umair, M.: Performance of (1) Concrete-filled double-skin steel tube with and with-out core concrete, and (2) Concrete-filled steel tubular axially loaded composite columns under close-in blast. *Int. J. Prot. Struct.* (2022i, in press)
- Anas, S.M., Alam, M., Umair, M.: Air-blast response of axially loaded clay brick masonry walls with and without reinforced concrete core. In: *Advances in Structural Mechanics and Applications*, ASMA 2021, STIN 19, pp. 1–18 (2022j, in press). [https://doi.org/10.1007/978-3-030-98335-2\\_4](https://doi.org/10.1007/978-3-030-98335-2_4)
- Anas, S.M., Alam, M., Shariq, M.: Behavior of two-way RC slab with different reinforcement orientation layouts of tension steel under drop load impact. *Mater. Today Proc.* (2022k, in press). Elsevier
- ASCE/SEI 59-11: Blast protection of buildings. ASCE/SEI 59-11, American Society of Civil Engineers (2011)
- Dar, R.U.N., Alam, M.: Damage evaluation of reinforced concrete bridge subjected to blast loading. In: Chandrasekaran, S., Kumar, S., Madhuri, S. (eds.) *Recent Advances in Structural Engineering*. LNCE, vol. 135, pp. 131–142. Springer, Singapore (2021). [https://doi.org/10.1007/978-981-33-6389-2\\_14](https://doi.org/10.1007/978-981-33-6389-2_14)
- Goel, D.M., Matsagar, A.V.: Blast-resistant design of structures. *Practice Periodical on Structural Design and Construction*. ASCE. **19**(2), 1–9 (2014). [https://doi.org/10.1061/\(ASCE\)SC.1943-5576.0000188](https://doi.org/10.1061/(ASCE)SC.1943-5576.0000188)
- Guo, Z., Xu, Z., Chen, C., Zhang, B., Lehman, D. E., Cao, S.: Behaviour of GFRP retrofitted reinforced concrete slabs subjected to conventional explosive blast. *Mater. Struct.* **50**, 236 (2017). <https://doi.org/10.1617/s11527-017-1107-6>
- Hao, H., Hao, Y., Li, J., Chen, W.: Review of the current practices in blast-resistant analysis and design of concrete structures. *Adv. Struct. Eng.* Sage **19**(8), 1193–1223 (2016). <https://doi.org/10.1177/1369433216656430>
- Hafezolgborani, M., Hejazi, F., Vaghei, R., Jaafar, B.S.M., Karimzade, K.: Simplified damage plasticity model for concrete. *Struct. Eng. Int.* **27**(1), 68–78 (2018). <https://doi.org/10.2749/101686616X1081>
- Iannitti, G., et al.: Analysis of reinforced concrete slabs under blast loading. *Struct. Integr. Proc.* **9**, 272–278 (2018). <https://doi.org/10.1016/j.prostr.2018.06.035>
- Kumar, V., Kartik, K.V., Iqbal, M.A.: Experimental and numerical investigation of reinforced concrete slabs under blast loading. *Eng. Struct.* **206**, 110125 (2019). <https://doi.org/10.1016/j.engstruct.2019.110125>
- Lee, J., Fenves, L.G.: Plastic-damage model for cyclic loading of concrete structures. *J. Eng. Mech. ASCE*. **124**(8), 892–900 (1998). [https://doi.org/10.1061/\(ASCE\)0733-9399\(1998\)124:8\(892\)](https://doi.org/10.1061/(ASCE)0733-9399(1998)124:8(892))
- Lubliner, J., Oliver, J., Oller, S., Onate, E.: A plastic-damage model for concrete. *Int. J. Solids Struct.* **25**(3), 299–326 (2003). [https://doi.org/10.1016/0020-7683\(89\)90050-4](https://doi.org/10.1016/0020-7683(89)90050-4)
- Luccioni.B.M., Ambrosini.R. D and Danesi.R. F (2003), Analysis of building collapse under blast loads. *Eng. Struct.* **26**, 63–71 (2004). <https://doi.org/10.1016/j.engstruct.2003.08.011>
- Low, H.Y., Hao, H.: Reliability analysis of direct shear and flexural failure modes of RC slabs under explosive loading. *Eng. Struct.* **24**(2), 189–198 (2001). [https://doi.org/10.1016/S0141-0296\(01\)00087-6](https://doi.org/10.1016/S0141-0296(01)00087-6)
- Mays, G., Smith, D.P.: *Blast Effects on Buildings: Design of Buildings to Optimize Resistance to Blast Loading*. Thomas Telford, London (1995)
- Silva, F.P., Lu, B.: Blast resistance capacity of reinforced concrete slabs. *J. Struct. Eng.* **135**(6), 708–716 (2009). [https://doi.org/10.1061/\\_ASCE\\_ST.1943-541X.0000011](https://doi.org/10.1061/_ASCE_ST.1943-541X.0000011)
- Shariq, M., Alam, M., Husain, A., Anas, S.M.: Jacketing with steel angle sections and wide battens of RC column and its influence on blast performance. *Asian J. Civ. Eng.* (2022). Springer. <https://doi.org/10.1007/s42107-022-00437-9>

- Tao, Y., Chen, J.F.: Concrete damage plasticity model for modelling FRP-to-concrete bond behaviour. *J. Compos. Constr.* **19**(1), 04014026 (2014). [https://doi.org/10.1061/\(ASCE\)CC.1943-5614.0000482](https://doi.org/10.1061/(ASCE)CC.1943-5614.0000482)
- Tai, Y.S., Chu, T.L., Hu, H.T., Wu, J.Y.: Dynamic response of a reinforced concrete slab subjected to air blast load. *Theoret. Appl. Fract. Mech.* **56**, 140–147 (2011). <https://doi.org/10.1016/j.tafmec.2011.11.002>
- Tahzeeb, R., Alam, M., Mudassir, S.M.: A comparative performance of columns: reinforced concrete, composite, and composite with partial C-FRP wrapping under contact blast. *Mater. Today Proc.* (2022a). Elsevier. <https://doi.org/10.1016/j.matpr.2022.03.367>
- Tahzeeb, R., Alam, M., Mudassir, S.M.: Effect of transverse circular and helical reinforcements on the performance of circular RC column under high explosive loading. *Mater. Today Proc.* (2022b). Elsevier. <https://doi.org/10.1016/j.matpr.2022.04.676>
- Tahzeeb, R., Alam, M., Mudassir, S.M.: Performance of composite and tubular columns under close-in blast loading: a comparative numerical study. *Mater. Today Proc.* (2022c). Elsevier. <https://doi.org/10.1016/j.matpr.2022.04.587>
- TM 5-1300: Structures to resist the effects of accidental explosions. Technical Manual, Joint Department of the Army, the Navy, and the Air Force, US (1990)
- Wang, W., Zhang, D., Lu, F., Wang, S.C., Tang, F.: Experimental study on scaling the explosion resistance of a one-way square reinforced concrete slab under a close-in blast loading. *Int. J. Impact Eng.* **49**, 158–164 (2012). <https://doi.org/10.1016/j.ijimpeng.2012.03.010>
- Wu, C., Hao, H.: Modeling of simultaneous ground shock and airblast pressure on nearby structures from surface explosions. *Int. J. Impact Eng.* **31**(6), 699–717 (2005). <https://doi.org/10.1016/j.ijimpeng.2004.03.002>
- Yu, L.H., Hao, H.: Reliability analysis of reinforced concrete slabs under explosive loading. *Struct. Saf.* **23**(2), 157–178 (2001). [https://doi.org/10.1016/S0167-4730\(01\)00011-X](https://doi.org/10.1016/S0167-4730(01)00011-X)
- Zhao, C., Wang, Q., Lu, X., Wang, J.: Numerical study on dynamic behaviors of NRC slabs in containment dome subjected to close-in blast loading. *Thin-Walled Struct.* **135**, 269–284 (2019). <https://doi.org/10.1016/j.tws.2018.11.013>





# Response Mitigation of Structure Using Tuned Liquid Column Ball Damper: A Review

Shulanki Pal<sup>(✉)</sup>, Bijan Kumar Roy, and Satyabrata Choudhury

Department of Civil Engineering, National Institute of Technology Silchar,  
Silchar, India

shulanki@gmail.com, {bijan, chou\_s}@civil.nits.ac.in

**Abstract.** In the last few years, a new type of passive damping device, named as tuned liquid column ball damper (TLCBD) has been introduced to mitigate the response of the structures. It is a modified form of tuned liquid column damper (TLCD), where the orifice in the middle of the horizontal part of the column is replaced by a metal ball. During the recent past, many investigations have been carried out to prove the better performance of TLCBD over TLCD. Different kinds of modifications and analytical and experimental studies considering various kinds of loadings are a significant part of it. The concise studies that have been performed on various fields of TLCBD till now are discussed in this paper.

**Keywords:** Tuned liquid column ball damper · Tuned liquid column damper · Response mitigation · Passive dampers

## 1 Introduction

The advancement of current urbanization has seen an impressive expansion in the number of uses of high-rise structures. The engineers are compelled to plan and design such high-rise structures as flexible and lightweight designs because of the expansion in population, cost reduction, and constraint of space. Such designing leads to practically low damping properties of the structures which create inhabitant discomfort and poor serviceability condition during excessive vibration induced by external forces such as earthquake (Abdel-Mooty et al. 2009; Debbarma et al. 2010) or, wind (Wu et al. 2005; Lin and Yaojun 2013) or, waves (Lee et al. 2006b; Chatterjee and Chakraborty 2014). In this regard, understanding the vibration control of such structures plays a vital role in improving the comfort, safety, and usefulness of the construction. The excessive lateral displacement results in total structural collapse due to its inability to dissipate high energy. The trash of the devastated constructions has claimed numerous lives. To encounter such challenges structural engineers are trying to develop and incorporate innovative design concepts for protecting structures along with their occupants and as well as the material constituents and elements. This type of protection system has to fulfil the criteria of reliability and survivability along with comfort.

In general, the combination of strength, energy absorption capability, and deformability of a structure has been considered during its design for resisting natural

hazards. The structural components like braced frames, shear walls, diaphragms, moment-resisting frames, and horizontal trusses are combined to achieve resistance against lateral displacements (Egor 1983; Yang et al. 2019; Dániel et al. 2013; Razak et al. 2018; Dalal et al. 2015; Shreyas and Sridhar 2018; Resmi and Yamini 2016; Deepna et al. 2018; Ambreshewar et al. 2018; Behrouz et al. 2009; Castro et al. 2008; Ahiwale and Khartode 2021; Piotr and Marcin 2013; Tarigan et al. 2018; Bishay-Girges 2019; Mali and Patil 2020).

In view of this, researchers and structural engineers are working on alternate structural protective systems or vibration control devices to mitigate the damaging effects caused by natural hazards (Sarwar et al. 2019; Li and Huo 2010; Ikeda et al. 2019). These vibration control devices are capable of absorbing or reflecting a portion of the input energy from seismic activity or strong winds. Hence the presence of such a device reduces the severe harmful vibration of the most critical members of the structures. One of the important concerns is, most of the existing building has been constructed without earthquake-resistant features and reconstruction of such buildings to resist earthquake as per conventional method may be uneconomical and replacing the damaged parts after an earthquake may prove to be cumbersome. Hence, structural control methods may be a viable solution to protect newly constructed buildings from natural hazards. This type of vibration control mechanism can be adopted for the new buildings also to protect them from hazardous earthquakes. To date, various vibration control devices have been used successfully and newly proposed designs are also considered that give the opportunity of extending its applications with improved efficiency (Symansa and Constantinou 1999; Han et al. 2006; Heysami 2015; Ricciardelli et al. 2003). The most important three key factors of vibration control devices are efficiency, applicability to existing structures, and cost. Primarily, good vibration control devices should be able to decrease the risk of damage to an adequate level (Housner et al. 1997; Spencer and Nagarajaiah 2003). These kinds of control devices have to be designed and analyzed properly before installing, as they are normally attached to the existing structures. Another important factor about these devices is the cost of production and maintenance. A vibration control device should fulfill all these criteria to be considered as a good response control device.

These vibration control systems are mainly characterized into four different groups as: (1) Passive systems (2) Active systems (3) Semi-active systems (4) Hybrid systems.

The most common structural control devices are passive control systems which are being used to dissipate a significant amount of vibrational energy. The viscous dampers, metallic yield braces, fiber reinforced concrete, friction dampers are generally categorized as passive control systems. The advantage of such devices is that they do not use any external power which makes them very economical. They simply work by changing the mass, stiffness, or damping of the structures. Another advantage of such systems is that they can create a higher damping force when the structural response becomes higher. Generally, passive control systems are designed and tuned for particular dynamic loading where they perform well (Ciampi et al. 1996; Iemura and Pradono 2002).

Passive damping devices are considered as a very good solution for the response mitigation process in the current scenario due to their low cost, easy maintenance, and high efficiency. As no external power source is needed to continue the response

mitigation process, therefore, these kinds of dampers are very reliable at the time of electricity loss during natural hazards. Another vital quality of passive damping devices is the inability to destabilize the structure, as they cannot inject energy into the system (Parulekar et al. 2009; Bishay-Girges 2004).

Some of the vastly used passive dampers and their details are as follows:

- (1) Tuned mass damper (TMD)
- (2) Tuned liquid damper (TLD)
- (3) TLCD
- (4) TLCBD and others.

TMD consisting of a mass, a spring, and a damper is one of the reliable and effective passive structural vibration control devices used to suppress the undesirable vibrations induced by various kinds of forces. It dissipates a large amount of vibrational energy caused by high wind or earthquake loads irrespective of the type and design of the structure as it can be easily tuned to the fundamental mode of the structure (Lee et al. 2006a; Rana and Soong 1998; Abe and Fujino 1994; Abe 1996; Pinelli et al. 2003; Lukkumaprasit and Wanitkorkul 2001; Chakraborty and Roy 2013).

In TLD the mass of the damper is replaced by water in a tank. When a rectangular tank is partially filled with water of a shallow depth, then such dampers are classified as TLD (Welt and Modi 1989a, b). The TLDs are a very practical device, where the sloshing property of liquid present in existing water tanks is being used to mitigate the response of the structure (Konar and Ghosh 2021; Shankar and Balendra 2002). The functionality of this kind of dampers is enhanced by simply getting modified with the addition of internal partitions within them (Kaneko et al. 1999).

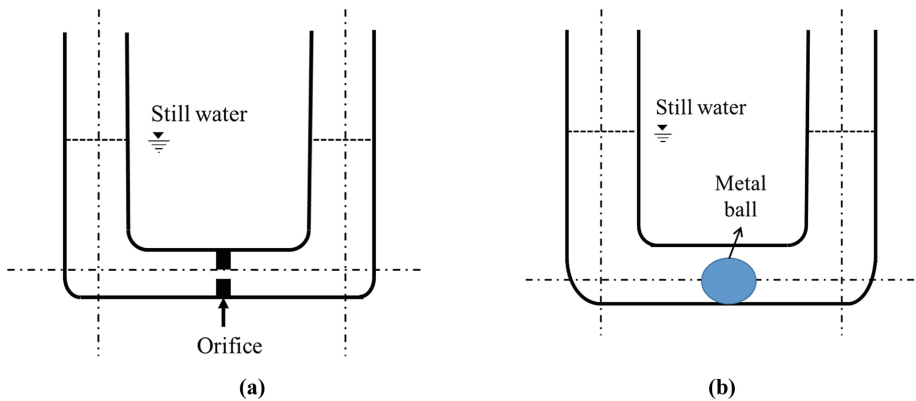


**Fig. 1.** (a) Schematic diagram of TLCD (b) Schematic diagram of TLCBD.

TLCD consists of a U-shaped tube filled with water, shown in Fig. 1(a). Sakai et al. (1989) proposed this kind of dampers with uniform cross-sectional areas to mitigate the response of the structure and provided the nonlinear mathematical description for the above. In this type of damper, the damping ratio is dependent on the area ratio, length ratio, and vertical column height (Mansour et al. 2018). In liquid column dampers, the gravitational force gets generated by the mass of liquid present in the column, the viscous interactive force developed by the liquid interaction with the rigid container,

and the transitional force generated by the liquid movement within the horizontal and vertical columns. To determine the natural frequency of TLCD, two major parameters are responsible which are the length of the column and the geometric configuration of the damper (Gao et al. 1997). The liquid column vibration absorber (LCVA) is a variation of TLCD with a different cross-sectional area for the intermediary horizontal column than the cross-sectional area provided in the vertical portion of it (Chang and Hsu 1998; Hitchcock et al. 1997a, b). The efficiency of TLCD can be increased by introducing an orifice in the horizontal column portion due to the enhanced damping property (Chakraborty and Debbarma 2011; Balendra et al. 1999; Di 2016). Generally, an orifice is used in the middle part of the TLCD to increase the damping property by improving its head loss coefficient.

Various studies proved that if a metal ball is used as a rolling orifice instead of an immovable orifice then its performance will be further improved as the damping property of the TLCD gets enhanced. The modified TLCD introduced with a metal ball is named as TLCBD. In this paper, the performance study, optimization study, reliability-based study of response mitigation of structure is highlighted in detail considering the past literatures.

## 2 Brief Literatures on Performance of TLCBD in Response Mitigation

In the last decade, one modification of TLCD is introduced in the literature, which is referred to here as TLCBD shown in Fig. 1b. The various studies on this topic are discussed in the following sections.

### 2.1 Performance of TLCBD on Structure

Saif et al. (2011) first proposed the concept of TLCBD schematically, to overcome the difficulties of conventional TLCDs. The fixed orifice of TLCD restricts the capability of response reduction of dampers whereas, the moving orifice of TLCBD improves it significantly when similar mass was considered. To prove the importance of TLCBDs they developed a mathematical model of the absorber attached to a single degree of freedom (SDOF) structure. The mathematical model was developed to compute the response of the structure where the damping factor was measured through experimentation by a single-point laser vibrometer. Responses of both TLCD and TLCBD attached structures were evaluated by the mathematical model and the performance of the TLCBD was found excellent with up to 67% vibration reduction. The ball-tube diameter ratio and the mass ratio were the most influencing parameters that influence the performance of the TLCBD and it was revealed that the performance of TLCBD could be improved by selecting the optimum ball-tube diameter ratio and by increasing the mass ratio to an acceptable and practical limit.

Following this work, Chatterjee and Chakraborty (2014) compute the efficiency of TLCBD to control the wave-induced vibration response and compared it with the same of TLCD. Accordingly, they obtained the performance of both TLCBD and TLCD by a parametric study. During this parametric study, the stochastic dynamic analysis of

structure was done in the frequency domain considering both the presence and absence of the dampers.

In continuation Kalva et al. (2015) further established that TLCBD performs better compared to various types of other passive TLCDs such as LCVA, V-shaped TLCD, and U-shaped TLCD in order to suppress the harmonic vibration. In this regard, harmonic excitation of different excitation levels and frequencies were considered and the response of the uncontrolled and controlled structure was evaluated. The efficiency was assessed in terms of percentage response reduction. They obtained the frequency response curves and depicted that the efficiency of TLCBD decreases at frequency ratios around 0.95 and 1.05 compared to other TLCDs.

Though from the above-mentioned studies the better performance of TLCBD has been confirmed, still more improvements mechanisms were introduced for further perfection. Gupta et al. (2017) developed a newer version of TLCD and named it spring loaded liquid column ball damper. The damper was developed from TLCD where a steel ball is placed in the horizontal part of the column using a spring of same material. Both viscosity of the fluid and the stiffness of the spring were considered for the analysis. They considered an SDOF system that attached with the damper for the mathematical model. As the mass ratio and the ball-tube diameter ratio were found as the most influencing parameters, hence both the parameters were assessed by the parametric study to find out the absorber capacity. It was observed that an improvement in efficiency can be done by appropriately selecting these two ratios up to a certain limit. The author performed a comparative study of conventional type TLCD with the spring-loaded TLCBD in terms of results gained by the numerical simulation. These results were obtained based on the related optimum parameters. Around 74% of the vibration absorption was claimed using the modified TLCD.

In the previous works, the applicability of TLCBD was confirmed for the SDOF systems. Tanveer et al. (2019) studied the applicability and effectiveness of TLCBD on a steel frame structure of four-story height with the help of an analytical model. The analytical models were further examined with the help of experimentation. A numerous number of shake table tests was performed to establish the fact considering the structure subjected to harmonic and seismic excitations of different level. In this regard, time history analysis was also done and the better effectiveness of TLCBD to control response generated by earthquake forces compared to harmonic loading was ensured. The results were used to obtain the effectiveness of TLCBD compared to that of TLCD. The peak values of acceleration and the root mean square acceleration for structure with and without damper were evaluated using the loading mentioned above. It has been observed that various works were going on TLCBD to design better structures with efficient vibration control under different loads (wind, offshore, earthquake). In continuation to these works, recently various other authors considered the design and development of TLCBD itself as mentioned below. Later in the year 2020, an extended part of the previous work was reported, where different types of liquid and ball combinations were studied. The percentage response reduction was evaluated for a better understanding of the decrease in the response of the structure. The better performance of TLCBD with high-density ball and liquid than the one with the lower ball and liquid density was confirmed from this study. The enhanced efficiency of TLCBD

against seismic excitation than the harmonic excitation was also established from this experimental-based study.

## 2.2 Optimization Studies on TLCBD in Mitigation of Response of the Structure

An investigation was done by Chatterjee and Chakraborty (2014) to study the effectiveness of TLCBD over TLCD in terms of optimum response reduction of the structure. Root mean square displacement (RMSD) of the offshore structure under a particular condition was used for optimization and related optimum parameters were evaluated to compare the performance. In general, for the optimal performance evaluation of the damper, the RMSD of the structure is considered as an objective function. In stochastic structural optimization (SSO), random excitation is considered to evaluate the response by minimizing the stochastic structural response (Mrabet et al. 2015; Marano and Greco 2008; Alkmima 2017; Debbarma et al. 2010). An appropriate set of design variables are obtained by performing unconstrained optimization in this regard. MATLAB optimization tools are used to assess the above.

A numerical study was performed by Chatterjee and Chakraborty (2014) to explore the effectiveness of both the TLCD and TLCBD. TLCBD was found better than TLCD, in the case of offshore structure as less displacement of liquid was noticed in case of response mitigation, which is very much preferable for this type of flexible structure. For an extensive range of parametric variations, the optimum blocking ratio of TLCBD remains almost unchanged. Both frequency domain and time domain study were performed to ensure the robustness of TLCBD over TLCD. Similarly, to that Gur et al. (2015) performed an analytical study considering the earthquake excitation. They have worked on reducing the response of the structure as well as the liquid column with the help of TLCBD which was showing an improved performance compared to that of TLCD. They used stochastic analysis to evaluate the response of a SDOF system subjected to random earthquakes. The system was analyzed once with TLCBD and TLCD separately to compare their performance. Similar to the work of Saif et al. (2011), it was also revealed that the ball-to-tube diameter ratio and the optimum tuning ratio, were the important parameters that affect the performance of the structure-TLCBD system. To prove the robustness of TLCBD over the TLCD, they performed extensive numerical simulations. During the simulations, the optimum ball-to-tube diameter ratio and the optimum tuning ratio of the structure-TLCBD system were identified as the design variables. To ensure the capability of TLCBD to mitigate the response of the structure subjected to real earthquakes, a set of real ground motion data was considered and the similar behavior of the damper was achieved.

Pandey and Mishra (2018) investigated the efficiency of a combined TLCBD and circular shaped TLCBD, to control the vibration of a structure. Lateral-torsional coupled vibration due to Wind force was considered to perform the study. Lagrange's approach was used to establish the equations of motion for the structure-TLCBD system. By minimizing the stochastic response of the structure, the optimal performance was evaluated for random vibration. Further, the results were verified by performing experimental tests using a shake table and time history analysis for simulated wind excitation.

Though the metal ball is used in the Conventional type TLCD to enhance the response mitigation of the structure but the effect of the area ratio on the TLCBD has never been studied before. Pal et al. (2020a) incorporated a ball within the LCVA to enhance the efficiency of conventional TLCBD. A comparative study was performed to analyze the response of an SDOF structure attached with LCVA and LCVA with the ball (TLCBD), subjected to non-stationary earthquakes. Stochastic structural optimization was used to find out the optimal response of the structure-damper system. A numerical problem was performed and the improvement was confirmed for LCVA with the ball than the conventional type LCVA for all the parameters considered.

It has been noticed that during strong earthquakes the response of the structure increases which leads to an exaggerated response of the liquid present in the columns and may result in instability and changes in damping properties of TLCBD (Chakraborty et al. 2012). Pal et al. (2020b) performed a study where the optimum response of the structure has been evaluated using TLCBD for limited liquid displacement. As the vertical movement of the liquid increases, it may create an L-shape of damper instead of a U-shaped and during this process, air may get entrapped in the horizontal part of the column. To solve this kind of issue, limitations on the vertical movement of the liquid are provided by using constrained optimization. A numerical study has been performed to establish the fact and further the proper design of a TLCBD can be done by using this kind of constrained optimization.

### 2.3 Reliability-Based Performance Studies on TLCBD in Response Mitigation

Only the consideration of the response reduction of the structure is not enough to determine the strength or serviceability condition (Lin and Yaojun 2013; Papadimitriou et al. 1997; Taflanidis et al. 2008). Important structures like hospitals, schools, fire stations, police stations, bridges, civil defence centres, etc. should be designed in such a way so that they can provide service after any strong vibration caused by natural hazards. In this regard, it is important to find out the failure of the structure. To investigate the reliability and the safety of the structure, rather than the minimization of the response reduction is of prior interest. In this context, minimization of the failure probability of the system by using RBDO is a better way to define the condition. Pal et al. (2021) performed a comparative study of reliability-based design optimization of TLCBD and TLCD for different structure, damper and earthquake parameters. In this study, the probability failure of the structure was evaluated considering the system parameters as deterministic. The better safety by using TLCBD over TLCD for risk reduction of the structure was confirmed from this investigation.

## 3 Conclusion

The passive control devices are well known for their response mitigation property in consideration of applicability, efficiency, and cost. Within various kinds of passive dampers, TLCD has established its own place by its advanced response mitigation property and adeptness with different kinds of structures and loads. The modifications

of conventional type TLCD has been directed to create an innovative and improved version of it named as TLCBD where the orifice present in the horizontal part of the column has been replaced by a rolling orifice. Different studies have confirmed its adaptability and robustness in response reduction of structure using TLCBD the better performance in response mitigation over TLCD is established in literature. Though numerous numbers of analysis have been performed on TLCBD but still there are several fields remain to explore in this regard.

## References

- Abdel-Mooty, M., Al-Atrpy, H., Ghouneim, M.: Modeling and analysis of factors affecting seismic pounding of adjacent multi-story buildings. In: *Earthquake Resistant Engineering Structures VII* (2009). WIT Trans. Built Environ. **104**, 127–138
- Abe, M., Fujino, Y.: Dynamic characterization of multiple tuned mass dampers and some design formulas. *Earthq. Eng. Struct. Dyn.* **23**, 813–835 (1994)
- Abe, M.: Tuned mass dampers for structures with bilinear hysteresis. *J. Eng. Mech.* **122**, 797–800 (1996)
- Alkmima, M.H., De-Moraiss, M.V.G., Fabro, A.T.: Optimum parameters of a tuned liquid column damper in a wind turbine subject to stochastic load. In: *IOP Conference Series: Materials Science and Engineering*, vol. 280, no. 012007 (2017)
- Al-Saif, K.A., Aldakhan, K.A., Foda, M.A.: Modified liquid column damper for vibration control of structures. *Int. J. Mech. Sci.* **53**, 505–512 (2011)
- Ambreshwar, Nithinchary, Mahesh, D., Baag S., Sachin: Study of shear walls in different locations of multi-storied building with uniform thickness in seismic zone-III. *Int. J. Innov. Res. Technol.* **4**(12), 393–402 (2018)
- Balendra, T., Wang, C.M., Rakesh, G.: Vibration control of various types of buildings using TLCD. *J. Wind Eng. Ind. Aerodyn.* **83**, 197–208 (1999)
- Behrouz, A., Arezoo, S., Pejman, A.: Seismic response of moment resisting frames through incremental dynamic analysis. In: *Computational Methods in Structural Dynamics and Earthquake Engineering*, Rhodes, Greece (2009)
- Bishay-Girges, N.W.: Seismic protection of structures using passive control system. Ph.D. thesis, Department of Civil Engineering, University of Canterbury, New Zealand (2004)
- Bishay-Girges, N.W.: An alternative system for eccentrically braced frames resisting lateral loads. *Eng. Technol. Appl. Sci. Res.* **9**(3), 4281–4286 (2019)
- Castro, J.M., Elghazouli, A.Y., Izzuddin, B.A.: Performance assessment of composite moment-resisting frames. In: *The 14th World Conference on Earthquake Engineering*, Beijing, China, 12–17 October 2008 (2008)
- Chatterjee, A., Chakraborty, S.: Vibration mitigation of structures subjected to random wave forces by liquid column dampers. *Ocean Eng.* **87**, 151–161 (2014)
- Chakraborty, S., Debbarma, R.: Stochastic earthquake response control of structures by liquid column vibration absorber with uncertain bounded system parameters. *Struct. Saf.* **33**(2), 136–144 (2011)
- Chakraborty, S., Debbarma, R., Marano, G.C.: Performance of tuned liquid column dampers considering maximum liquid motion in seismic vibration control of structures. *J. Sound Vib.* **331**(7), 1519–1531 (2012)
- Chakraborty, S., Roy, B.K.: Reliability based optimum design of tuned mass damper in seismic vibration control of structures with bounded uncertain parameters. *Int. J. Mech. Sci.* **75**, 123–133 (2013)



- Chang, C.C., Hsu, C.T.: Control performance of liquid column vibration absorbers. *Eng. Struct.* **20**(7), 5811–5816 (1998)
- Ciampi, V., De-Angelis, M.: Optimal design of passive control system based on energy dissipation for earthquake protection of structures. In: Proceedings of the European Conference on Structural Dynamics, EUROLYN 1996, Firenze, Italy (1996)
- Dalal, S.P., Patoliya, D., Dalal, P.D.: Performance based plastic design of concentrically braced frame attuned with indian standard code and its seismic performance evaluation. *J. Mater. Eng. Struct.* **2**, 168–179 (2015)
- Merczel, D.B., Hugues, S., Jean-Marie, A., János, L.: On the behaviour of concentrically braced frames subjected to seismic loading. *Periodica Polytechnic Civ. Eng.* **57**(2), 113–122 (2013)
- Debbarma, R., Chakraborty, S., Ghosh, S.K.: Optimum design of tuned liquid column dampers under stochastic earthquake load considering uncertain bounded system parameters. *Int. J. Mech. Sci.* **52**(10), 1385–1393 (2010)
- Deepna, U., Arjun, S.M., Balamurugan, S.: A comparative study on shear wall concept in accordance to its seismic behaviour. *Int. J. Eng. Technol.* **7**(4.5), 182–187 (2018)
- Ahiwale, D.D., Khartode, R.R.: Parametric study for long-span roof truss subjected to vertical ground motion. *Asian J. Civ. Eng.* **22**(3), 381–404 (2020). <https://doi.org/10.1007/s42107-020-00320-5>
- Di, M.A., Di, P.M., Pirrotta, A.: Innovative modeling of tuned liquid column damper controlled structures. *Smart Struct. Syst.* **18**(1), 117–138 (2016)
- Egor, P.P.: Recent research on eccentrically braced frames. *Eng. Struct.* **5**(1), 3–9 (1983)
- Gao, H., Kwok, K.C.S., Samali, B.: Optimization of tuned liquid column dampers. *Eng. Struct.* **19**(6), 476–486 (1997)
- Gupta, A., Kakulate, M., Jopale, A.: Spring loaded liquid column ball damper for vibration control with forced vibration. In: International Conference on Ideas, Impact and Innovation in Mechanical Engineering (ICIIME 2017), vol. 5, no. 6, pp. 433–439 (2017)
- Gur, S., Roy, B.K., Mishra, S.K.: Tuned liquid column ball damper for seismic vibration control. *Struct. Control Health Monit.* **22**, 1325–1342 (2015)
- Han, S.J., Tsopelas, P., Baz, A.: Active/passive seismic control of structures. *J. Earthq. Eng.* **10**(4), 509–526 (2006)
- Heysami, A.: Types of dampers and their seismic performance during an earthquake. *Curr. World Environ.* **10**(1), 1002–1015 (2015)
- Hitchcock, P.A., Kwok, K.C.S., Watkins, R.D., Samali, B.: Characteristics of liquid column vibration absorbers (LCVA)—I. *Eng. Struct.* **19**(2), 126–134 (1997a)
- Hitchcock, P.A., Kwok, K.C.S., Watkins, R.D., Samali, B.: Characteristics of liquid column vibration absorbers (LCVA)—II. *Eng. Struct.* **19**(2), 135–144 (1997b)
- Housner, G.W., Bergman, L.A., Caughey, T.K., Chassiakos, A.G.: Structural control: past, present, and future. *J. Eng. Mech.* **123**(9), 897–971 (1997)
- Iemura, H., Pradono, M.H.: Passive and semi-active seismic response control of a cable-stayed bridge. *J. Struct. Control* **9**, 189–204 (2002)
- Ikeda, Y., Yamamoto, M., Furuhashi, T., Kurino, H.: Recent research and development of structural control in Japan. *Jpn. Archit. Rev.* **2**(3), 219–225 (2019)
- Kalva, M., Ray-Chaudhuri, S.: Comparison of performance of different tuned liquid column dampers (TLCDs). In: Matsagar, V. (ed.) *Advances in Structural Engineering*, pp. 1257–1269. Springer, New Delhi (2015). [https://doi.org/10.1007/978-81-322-2193-7\\_98](https://doi.org/10.1007/978-81-322-2193-7_98)
- Kaneko, S., Ishikawa, M.: Modeling of tuned liquid damper with submerged nets. *J. Press. Vessel Technol.* **121**(3), 334–343 (1999)
- Konar, T., Ghosh, A.D.: Flow damping devices in tuned liquid damper for structural vibration control: a review. *Arch. Comput. Methods Eng.* **28**(4), 2195–2207 (2021). <https://doi.org/10.1007/s11831-020-09450-0>

- Lee, C., Chen, Y., Chung, L., Wang, Y.: Optimal design theories and applications of tuned mass dampers. *Eng. Struct.* **28**, 43–53 (2006a)
- Lee, H.H., Wong, S.H., Lee, R.S.: Response mitigation on the offshore floating platform system with tuned liquid column damper. *Ocean Eng.* **33**, 1118–1142 (2006b)
- Li, H., Huo, L.: Advances in structural control in civil engineering in China. *Math. Probl. Eng.* **2010**, 1–23 (2010). Article ID: 936081
- Lin, Z., Yaojun, G.E.: Wind induced buffeting reliability of long-span cable-stayed bridge using stochastic finite element method. *Disaster Adv.* **6**(3), 32–40 (2013)
- Lukkunaprasit, P., Wanitkorkul, A.: Inelastic buildings with tuned mass dampers under moderate ground motions from distant earthquakes. *Earthq. Eng. Struct. Dyn.* **30**, 537–551 (2001)
- Mali, U.L., Patil, S.N.: Review on lateral load resisting system for different geometric shapes of high-rise buildings. *Int. J. Eng. Dev. Res.* **8**(2), 193–199 (2020)
- Mansour, H.A., Adriano, T.F., Marcus, V.G., De, M.: Optimization of a tuned liquid column damper subject to an arbitrary stochastic wind. *J. Braz. Soc. Mech. Sci. Eng.* **40** (2018). Article number: 551. <https://doi.org/10.1007/s40430-018-1471-3>
- Marano, G.C., Greco, R.: Stochastic optimum design of linear tuned mass dampers for seismic protection of high towers. In: *The 14th World Conference on Earthquake Engineering*, Beijing, China, 12–17 October 2008 (2008)
- Mrabet, E., Guedri, M., Ichchou, M.N., Ghanmi, S.: Stochastic structural and reliability based optimization of tuned mass damper. *Mech. Syst. Sig. Process.* **60–61**, 437–451 (2015)
- Pal, S., Roy, B.K., Choudhury, S.: Comparison of effectiveness of TLCBD over LCVA in vibration control of structure under non-stationary earthquake. In: Das, B., Barbhuiya, S., Gupta, R., Saha, P. (eds.) *Recent Developments in Sustainable Infrastructure*. LNCE, vol 75, pp. 311–323. Springer, Singapore (2020a). [https://doi.org/10.1007/978-981-15-4577-1\\_26](https://doi.org/10.1007/978-981-15-4577-1_26)
- Pal, S., Roy, B.K., Choudhury, S.: Comparative performance study of tuned liquid column ball damper for excessive liquid displacement on response reduction of structure. *IJE Trans. B Appl.* **33**, 753–759 (2020b)
- Pal, S., Roy, B.K., Choudhury, S.: Comparative study of reliability-based optimum performance analysis of structure using TLCBD and TLCD. *Disaster Adv.* **14**(4), 59–67 (2021)
- Pandey, D.K., Mishra, S.K.: Moving orifice circular liquid column damper for controlling torsionally coupled vibration. *J. Fluids Struct.* **82**, 357–374 (2018)
- Papadimitriou, C., Katafygiotis, L.S., Au, S.K.: Effects of structural uncertainties on TMD design: a reliability based approach. *J. Struct. Control* **1**(4), 65–88 (1997)
- Parulekar, Y.M., Reddy, G.R.: Passive response control systems for seismic response reduction: a state-of-the-art review. *Int. J. Struct. Stab. Dyn.* **09**(01), 151–177 (2009)
- Pinelli, J.P., Hu, S., Gutierrez, H., Casier, F.: Multiple distributed tuned mass dampers: an exploratory study. In: *Proceedings of Response of Structures to Extreme Loading (XL 2003)*, CD-ROM, Toronto, Canada, 3–6 August 2003. Elsevier (2003). Paper 7
- Piotr, I., Marcin, K.: 3D buckling analysis of a truss with horizontal braces. *Mech. Mech. Eng.* **17** (1), 49–58 (2013)
- Rana, R., Soong, T.T.: Parametric study and simplified design of tuned mass dampers. *Eng. Struct.* **20**(3), 193–204 (1998)
- Razak, S.M., Kong, T.C., Zainol, N.Z., Adnan, A., Azimi, M.: A review of influence of various types of structural bracing to the structural performance of buildings. In: *E3S Web of Conferences*, vol. 34, no. 01010 (2018)
- Resmi, R. and Yamini, S.R. (2016), A review on performance of shear wall, *International Journal of Applied Engineering Research*, Volume 11, Issue 3
- Ricciardelli, F., Pizzimenti, D., Mattei, M.: Passive and active mass damper control of the response of tall buildings to wind gustiness. *Eng. Struct.* **25**, 1199–1209 (2003)

- Sakai, F., Takaeda, S., Tamaki, T.: Tuned liquid column damper – new type device for suppression of building vibration. In: *Proceeding of International Conference on High-Rise Building*, Nanjing, China, pp. 926–931 (1989)
- Sarwar, W., Sarwar, R.: Vibration control devices for building structures and installation approach: a review. *Civ. Environ. Eng. Rep.* **29**(2), 074–100 (2019)
- Shankar, K., Balendra, T.: Application of the energy flow method to vibration control of buildings with multiple tuned liquid dampers. *J. Wind Eng. Ind. Aerodyn.* **90**, 1893–1906 (2002)
- Shreyas, K.N., Sridhar, R.: Comparative analysis of moment resisting frames of steel and composite materials. *Int. Res. J. Eng. Technol.* **05**(06), 832–840 (2018)
- Spencer, B.F., Nagarajaiah, S.: State of the art of structural control. *J. Struct. Eng. ASCE* **129**(7), 845–856 (2003)
- Symansa, M.D., Constantinou, M.C.: Semi-active control systems for seismic protection of structures: a state-of-the-art review. *Eng. Struct.* **21**(6), 469–487 (1999)
- Taflanidis, A.A., Beck, J.L.: An efficient framework for optimal robust stochastic system design using stochastic simulation. *Comput. Methods Appl. Mech. Eng.* **198**(1), 88–101 (2008)
- Taflanidis, A.A., Scruggs, J.T., Beck, J.L.: Reliability-based performance objectives and probabilistic robustness in structural control applications. *J. Eng. Mech.* **134**(4), 291–301 (2008)
- Tanveer, M., Usman, M., Khan, I.U., Ahmad, S., Hanif, A., Farooq, S.H.: Application of tuned liquid column ball damper (TLCBD) for improved vibration control performance of multistorey structure. *PLoS ONE* **14**(10), 1–15 (2019)
- Tanveer, M., Usman, M., Khan, I.U., Farooq, S.H., Hanif, A.: Material optimization of tuned liquid column ball damper (TLCBD) for the vibration control of multi-storey structure using various liquid and ball densities. *J. Build. Eng.* **32**, 101742 (2020)
- Tarigan, J., Manggala, J., Sitorus, T.: The effect of shear wall location in resisting earthquake. In: *Materials Science and Engineering*, vol. 309 (2018)
- Welt, F., Modi, V.J.: Vibration damping through liquid sloshing, part I: a nonlinear analysis. *Proc. Diagn. Veh. Dyn. Spec. Top ASME Des. Eng. Div.* **18**, 149–156 (1989a)
- Welt, F., Modi, V.J.: Vibration damping through liquid sloshing, part 2: experimental results. *Proc. Diagn. Veh. Dyn. Spec. Top ASME Des. Eng. Div.* **18**, 157–165 (1989b)
- Wu, J.C., Shih, M.H., Lin, Y.Y., Shen, Y.C.: Design guidelines for tuned liquid column damper for structures responding to wind. *Eng. Struct.* **27**(13), 1893–1905 (2005)
- Yang, T.Y., Sheikh, H., Tobber, L.: Innovative methodologies for resilient buildings and cities. *Front. Built Environ.* (2019). <https://doi.org/10.3389/fbuil.2019.00027>



# Numerical Analysis of One-Way Flexural Strength of Voided Slab

N. Nareshnyak<sup>(✉)</sup> and B. N. Rao

IIT Madras, Chennai, India  
nareshnyk8448@gmail.com, bnrao@iitm.ac.in

**Abstract.** This article presents a nonlinear finite element approach on the one-way flexural strength determination of biaxial hollow slabs (voided slab). Voided slab appears as traditional solid slab. Primary advantage of voided slab is lighter than conventional solid slab, as a result of it, studies have done on capacity analysis of voided slabs. In the paper, four node tetrahedron finite element slab model was analysed. Nonlinearities of concrete and reinforcement bars was incorporated in the numerical programme using stress-strain relationship of each material. Numerical load-deflection plot was compared with experimental plot. Experimental and numerical results are matched appropriately in terms of ultimate load and deflection but not in first crack location. A parametric study was performed to study the impact of change of grade of concrete on the deflection and ultimate load. Numerical findings were shown. Results obtained from the numerical analysis showed that grade change of concrete will not significantly affect the ultimate load and deflection.

**Keywords:** Biaxial hollow slab · Voided slab · Flexural strength · Numerical · Capacity analysis · Parametric study · Ultimate load · Deflection · Grade of concrete

## 1 Introduction

Slab with inside plastic inserts is generally termed as voided slab. Under some loading, load carrying capacity is different for normal reinforced concrete slab and voided slab (Valivonis et al. 2014). Plastic material (void former) create voids inside the slab, by which certain amount of concrete consumption arrested (Ahmed 2014). Plastic inserts can be made from recycling of household plastic waste which can reduce atmospheric pollution. It will become one of the solution method to lower environment pollutants. For creating voids in the slab, using of household recycled plastic waste can reduce the consumption of natural non-renewable resources like crude oil and coal. Atmospheric air will not be more polluted. This will in turn improve human health (Valivonis et al. 2014; Ahmed 2014). Slab is the only structural component, which takes huge amount of concrete than other structural components so it's self-weight is high (Chung et al. 2010). Primary aim of insertion of plastic materials inside the slab is to produce light weight two-way and one way slabs compared with conventional solid slab (Mota 2010).

Typical example of voided slab was shown in Fig. 1. Initially, some companies at the end of the year 2000 and after beginning of the year 2000 tried to reduce the weight

of the slabs by insertion of different plastic shapes. They are Bubble deck slab, Cobiax and U-boot slab etc. Bubble deck is the first company to execute voided slab structure in the world. This paper gives a brief detail on numerical analysis of voided slab flexural behaviour. Finite element programme used for numerical analysis is DIANA software, numerical simulation results were presented.

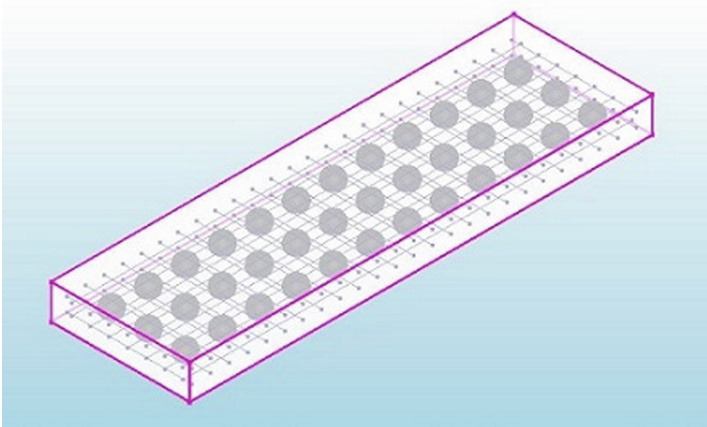


**Fig. 1.** Typical voided slab.

## 2 Literature Review

Gasham et al. (2019) carried out experiments to estimate void size effect on the one-way flexural performance of voided slabs compared with similar solid slab result. Flexural behaviour variables such as crack pattern, ultimate load, ductility and flexural stiffness were studied based on ball size/slab thickness ratio of voided slab. Flexural behaviour variables of void slabs with different ball size/slab thickness ratio are compared with similar solid slab capacity. Plan dimension of slab is 2000 mm  $\times$  500 mm. depth of slab is 120 mm. Total four slab specimens are casted, out of which one slab with no voids, is the control specimen. The remaining three slabs ratio of ball diameter to the slab depth is 58.3%, 75% and 50%. Spheres used for creating voids in slabs are of diameter 60 mm, 70 mm and 90 mm. Ultimate strength and yield stress of rebar is 670 MPa and 570 MPa. 45 MPa is the concrete grade of slab. Eight 10 mm rebar used in transverse direction of slab and thirty-four 10 mm rebar used in longitudinal direction of the slab. Effective length of each slab was 1650 mm. Slab was loaded at two points as line loads along the width of the slab. Loading was continuously increased until failure of the slab. Rate of increment of loading is 1 kN/min. Failure mode and crack pattern were influenced by presence of voids in the slab. The percentage reduction in ductility of voided slabs having 90 mm, 60 mm and 70 mm void slab was 67%, 10.3% and 11.1% respectively. Drop in ultimate flexural strength of 60 mm voided slab is insignificant. Larger balls inserted voided slabs flexural strength percentage reduction was significant,

21.3% for 90 mm void slab and 17% for 70 mm void inserted slab. Slab with 90 mm voids, failure mode changed from flexure to shear.

Sagadevan and Rao (2019) Sphere and cuboid void shape effect on flexural capacity of voided slab was studied, individually. Two void slab specimens are casted. 180 mm diameter sphere void used in one slab specimen. 450 mm × 450 mm 160 mm size cuboid shaped voids used in the other specimen. The characteristic compressive strength of concrete cube is 25 MPa. To test flexural capacity of the slab, load was applied two places along the width. Roller support provided at one end of slab and hinge support provided at other end. Deformation based loading was provided on the steel loading pads at a deformation rate of 0.05 mm/s. Experimental load deformation result concluded that voided slab flexural behaviour was similar to solid slab capacity. Voided slabs limited deflection for the given span length as per Indian reinforced concrete code is 12 mm. 75% of ultimate load was in the limited deflection. Reduction in cross sectional area of sphere voided slab was 33% and 39% cross section reduction happened in cuboid voided slabs.

Valivonis et al. (2014) numerical and experimental works were conducted to investigate the flexural capacity of reinforced concrete slabs with plastic voids inserted. Found deflection and flexural strength of reinforced voided slab. Experimentally, numerically and theoretically obtained ultimate load and deflection results are compared. Slab plan dimension is 6000 mm × 2960 mm and 300 mm of total depth. Plastic insert shape is oval, plan size is 350 mm × 350 mm and oval void height is 180 mm. centre to centre spacing of longitudinal bars is 415 mm. Reinforcement bar diameter is 25 mm. Yield strength of rebar is 534 MPa. Two-line forces are applied on the top of the slab. Theoretical, numerical and experimental deflection results compared with experimental deformation plot, difference in deformation is 7% and 10% respectively. Experimental flexural load and EN 1992-1-1 methodology flexure load difference is 8%. Load deflection results obtained from finite element analysis matched well with experimental plots. It shows, numerical study can better estimate flexural capacity of voided slabs.

Kim (2010) the paper expresses about numerical analysis and experimental works on the flexural capacity of the void slabs. The slab types (solid and void slab), thickness of slab, position of voids and plan size of polystyrene inserts of voided slabs are the main parameters of the experimental tests. Dimension of reinforced concrete slab with polystyrene voids is 3400 mm × 400 mm × 310 mm. Concrete compressive strength is 25.2 MPa. Diameter of reinforcement bar is 13 mm. Three rebar in the top portion of slab and three rebar at bottom of the slab are provided along the length of the slab. Experimental results show that as polystyrene form volume increases in the void slab, the second stiffness and initial stiffness were decreased.

### 3 Numerical Simulation of One-Way Flexure Test

Flexural capacity of slab with plastic inserts was experimentally investigated by Sagadevan and Rao (2019). In the current article, sphere voided slab load deformation plot was reproduced in the finite element analysis programme DIANA. Experimental slab details are shown in Fig. 2. Modelled slab dimension was 3300 mm × 1500 mm × 260 mm. Finite element TE12L was used for numerical modelling of the full

slab. TE12L represent a four node, three side isoparametric solid tetrahedron element. Element TE12L is shown in Fig. 3. Each side support was provided at 150 mm from the end of the slab. To produce experimental deformation-controlled loading condition, deformation load was applied in the programme at 1000 mm from each support of the slab. This was shown in Fig. 4. Triangular/tetra meshing was done with element mesh size 50 mm.

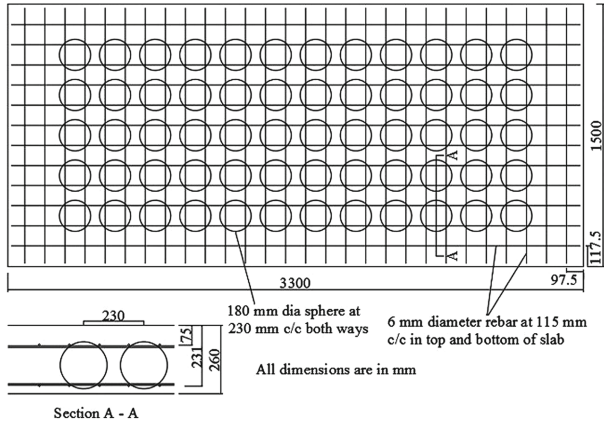


**Fig. 2.** Experimental slab specimen details of Sagadevan and Rao (2019).

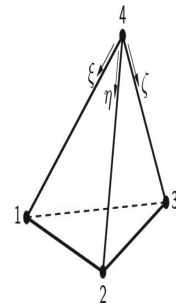


**Fig. 3.** Element TE12L.

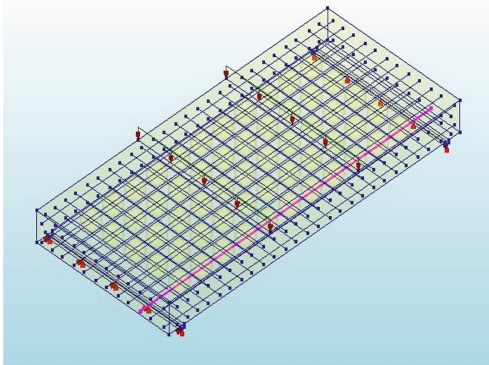


**Fig. 4.** Modelled voided slab with loading.

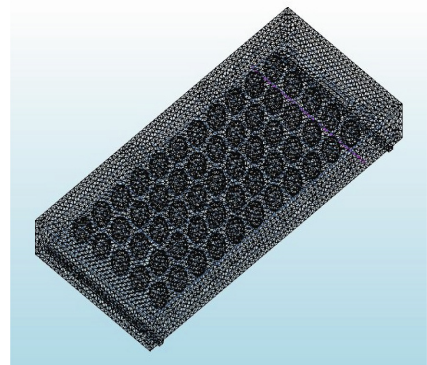


**Fig. 5.** Meshed voided slab.

To model reinforcement of voided slab in the programme, stress strain behaviour graph of steel is incorporated in nonlinear uniaxial stress strain model. The nonlinear uniaxial stress strain model is available in DIANA material library and full bond is automatically adopted in between steel and concrete. Voided slab concrete has particular tensile strength and compressive strength. Compressive strength value of void



slab got from cube test and generally tensile strength is one fifteenth of cube compressive strength. Concrete of voided slab modelled as total strain-based crack model available in DIANA numerical programme. Compressive and tensile strength values from the cube test are assigned in the total strain-based crack model. Figure 4 indicates reinforced voided slab with 180 mm diameter spheres, Fig. 5 shows meshed voided slab (Table 1).

**Table 1.** Material properties table

Parameter	Adopted value
Modelled slab size	3300 mm × 1500 mm × 260 mm
Concrete fracture energy ( $G_f$ )	0.04 N.mm
Grade of concrete ( $f_{ck}$ )	25.7 N/mm <sup>2</sup>
Concrete tensile strength ( $f_t$ )	1.5 N/mm <sup>2</sup>
Rebar yield strength ( $f_y$ )	560 N/mm <sup>2</sup>
Mesh size	50 mm

For analysing the voided slab model various analysis methods are available in the numerical programme. Structural nonlinear analysis was chosen and analysis was carried out until the ultimate failure of the slab. Initial applied deformation on the slab is 1 mm. load steps was increased from 0.05 mm to failure of the slab. This can be made in the user load steps section of the analysis menu. The results of the present numerical model were shown in Fig. 6 along with the experimental results.

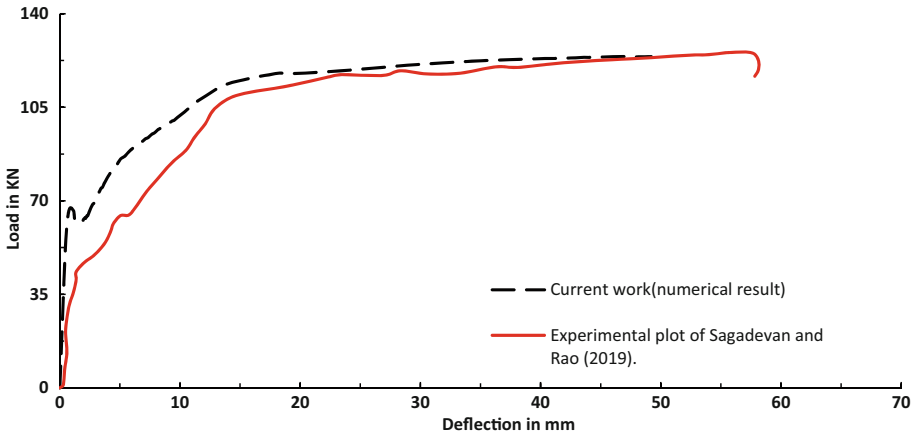


**Fig. 6.** Numerical and test Load versus deformation graph.



## 4 Conclusions

1. The current worked-out numerical model matched with the test results obtained by Sagadevan and Rao (2019).
2. Initial stiffness of numerical model was high because invisible micro cracks were not evaluated in the numerical model. To form first visible crack in the experiment, certain invisible cracks form at weak sections of concrete slab before the visible crack. Along with applied loading and the resultant of the invisible cracks will lead to form first visible crack in the laboratory experiment. Experimental any bond slip failure effect between steel and concrete were not taken into consideration in the numerical model.
3. Numerical results matching with experimental results indicate that numerical studies can be done to investigate the voided slab flexural behaviour.
4. Effect of change of concrete grade, Steel grade and change of spacing of voids can be studied.

### 4.1 Study of Effect of Change of Concrete Grade

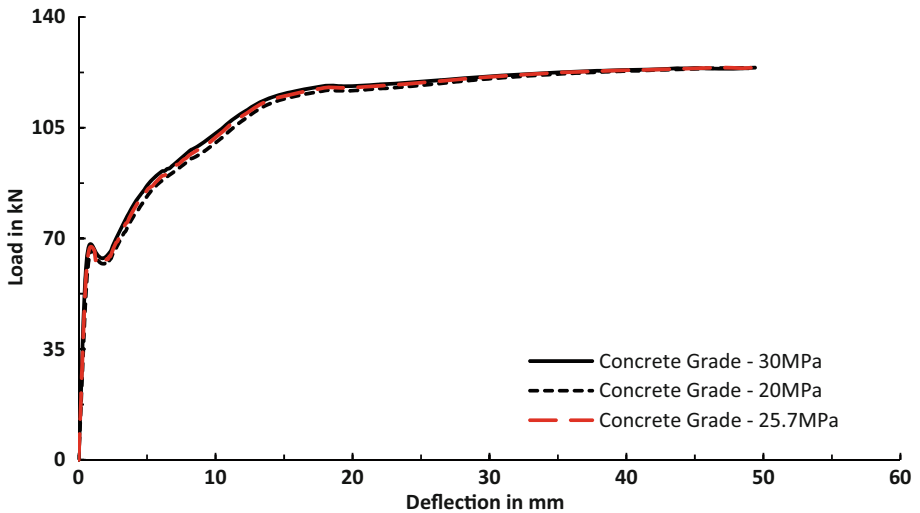


Fig. 7. Load-deformation response with different slab compressive strength.

Investigated the effect of change of concrete grade on load versus deformation graph and results are shown in Fig. 7. Result obtained from the finite element programme showed that grade change of concrete will not significantly affect the load versus deformation behaviour of slab.

## References

- Ahmed, Q.W.: Punching shear behaviour of bubbled reinforced concrete slabs. *Diyala J. Eng. Sci.* **09**, 55–66 (2014)
- Al-Azzawi and Ali Omar, A.A.: A state of the art review on reinforced concrete voided slabs. *ARPN J. Eng. Appl. Sci.* **13**, 1678–1700 (2018)
- Chung, J.H., Park, J.H., Choi, H.K., Lee, S.C., Choi, C.S.: An analytical study on the impact of hollow shapes in bi-axial hollow slabs. In: *Korea Concrete Institute Journal, Proceedings of Fracture Mechanics of Concrete and Concrete Structures*, pp. 1729–1736, May 2010
- Chung, J.H., Jung, H.S., Bae, B., Choi, C.S., Choi, H.K.: Two-way flexural behaviour of donut type voided slabs. *Int. J. Concr. Struct. Mater.* (2018). <https://doi.org/10.1186/s40069-018-0247-6>
- Chung, J.H., Choi, H.K., Lee, S.C., Choi, C.S.: One-way shear strength of circular voided reinforced concrete floor slabs. *Inst. Civ. Eng.* **168**, 336–350 (2015). <https://doi.org/10.1680/stbu.14.00044>
- Churakov, A.: Bi-axial hollow slab with innovative types of voids. *Construction of Unique Buildings and Structures*, pp. 70–88 (2014)
- DIANA FEA BV: *DIANA-10.2 User's Manual - Analysis Procedures*, The Netherlands (2017)
- Dwivedi, A.K., Joshi, H.J., Raj, R., Mishra, P.P., Kaldhane, M., Mohabey, B.: Voided slab design review paper. In: *Third International Conference on Multidisciplinary Research and Practice* (2016). *Int. J. Res. Sci. Innov. (IJRSI)* **4**(1), 220–226
- Al-Gasham, T.S., Hilo, A.N., Alawsi, M.A.: Structural behaviour of reinforced concrete one-way slabs voided by polystyrene balls. *Case Stud. Constr. Mater.* 1–13 (2019). <https://doi.org/10.1016/j.cscm.2019.e00292>
- Ibrahim, A.M., Ali, N.K., Salman, D.W.: Flexural capacities of reinforced concrete two-way bubble-deck slabs of plastic spherical voids. *Diyala J. Eng. Sci.* **6**, 9–20 (2013)
- Ing, A.C.: *Bubble deck floor system - an innovative sustainable floor system report*. Fuchs Deputy Director, BubbleDeck, Netherlands (2009)
- Mota, M.: Voided slabs then and now. *Concr. Int.* **32**(10), 41–45 (2010)
- Sagadevan, R., Rao, B.N.: Effect of void former shapes on one way flexural behaviour of biaxial hollow slabs. *Int. J. Adv. Struct. Eng.* 297–307 (2019). <https://doi.org/10.1007/s40091-019-0231-7>
- Kim, S.H.: Flexural behavior of void RC and PC slab with polystyrene forms. In: *Key Engineering Materials, Advances in Fracture and Damage Mechanics IX*, pp. 61–64, 11 November 2010
- Schnellenbach-Held, M., Pfeffer, K.: Punching behaviour of biaxial hollow slabs. *Cem. Concr. Compos.* **24**(6), 551–556 (2002)
- Valivonis, J., Skuturana, T., Daugevicius, M., Sneideris, A.: Flexural capacity and stiffness of monolithic biaxial hollow slabs. *J. Civ. Eng. Manag.* **20**, 693–701 (2014). <https://doi.org/10.3846/13923730.2014.917122>



# Influence of Hot Air Exposure on CFRP Shear Strengthened RC T-Beams

Franklin F. R. Frederick<sup>1</sup>(✉), U. K. Sharma<sup>2</sup>, and V. K. Gupta<sup>2</sup>

<sup>1</sup> Global Institute of Engineering and Technology, Hyderabad, India  
drfranklincivil@gmail.com

<sup>2</sup> Indian Institute of Technology Roorkee, Roorkee, India

**Abstract.** This paper presents an experimental study on the influence of different environmental exposures on shear resistance of Carbon Fiber Reinforced Polymer (CFRP) strengthened reinforce concrete (RC) - beams using Externally Bonded Fiber Reinforced Polymer (EB-FRP) technique, Self-End Anchorage (SEA) technique and Sandwich Anchorage (SWA) technique. In this experimental investigation, the long-term durability of shear deficient reinforced concrete beams strengthened with CFRP strap fabrics is examined under different independent environmental exposures such as natural laboratory condition and Hot Air Condition at 60 °C temperature. A total of twenty one R.C T-beams were cast in seven different series including a series of control un-strengthened beam. CFRP strap and CFRP laminated strip were used for this study. The shear strength ratio, energy absorption and mode of failure show the significance of anchorage in improving the efficiency of strengthening method under all the chosen environmental conditions. The employed FRP anchorage materials were resisted the environmental problems and eliminated the premature debonding.

**Keywords:** RC beam strengthening · External bonded-FRP · Durability · Shear behavior · End anchorage

## 1 Introduction

The existing structures suffer deterioration in their structural performance due to aggressive environmental conditions. Reinforced concrete elements are considered to be one of the major infrastructure elements in need of continuous maintenance and repair. Long-term stability of the materials used in construction is necessary to ensure desired performance over the anticipated lifespan of a structure. Fiber-Reinforced Polymer (FRP) products are being used worldwide for the retrofitting and repair of deficient and old structures such as bridges and buildings. They have been used to retrofit parking garages, marine and industrial structures, highway bridges and reinforced concrete piers (Sandeep et al. 2008).

However Reinforced Concrete (RC) beams, which are externally reinforced with FRP laminates and fabrics, when exposed to aggressive environmental circumstances, the bond between the FRP plate and the surface of the RC beam may affect the strength of externally reinforced RC beams (Nabil et al. 2005). Alkanline environment has significant influence on strength and stiffness behaviour of FRP strengthened RC

members. (Benmokrane et al. 2000). The environmental factors affect the tensile strength and glass transition temperature of composite matrix resins Chin et al. (1998); Karbhari et al. (1996) studied the effect of aqueous solutions on the bonding between different FRP composites and concrete. It is concluded that the FRP composites exposed to aqueous solutions have significant effect on the bonding behaviour. (Dai et al. 2013) developed the bond-slip model for FRP laminates externally bonded to concrete at elevated temperature. Further, Surface-bonded FRP for civil structure applications does not have proven history of long-term durability based on actual in-service performance.

Many studies show the influence of FRP in shear strengthening of shear deficient RC beams (Sheikh 2002; Adhikary et al. 2004; Chen et al. 2003; Dai et al. 2007; Zhang et al. 2005; Cao et al. 2005; Galal et al. 2010; Boussselham et al. 2006; Chaallal et al. 2010). But only very few have focused on the effect of different environmental exposures on the efficiency of FRP strengthened beams. Due to this, in most critical condition, the FRP application has been limited by the rehabilitation engineers. Thus there is a need for an elaborate study on FRP strengthening on structures that are exposed to environmental attack such as dry hot air areas and high temperature areas.

This work attempts to investigate the influence of hot air exposure and natural laboratory condition on shear resistance of CFRP strengthened RC beams using Externally Bonded Fiber Reinforced Polymer (EB-FRP) technique, Self-end anchorage (SEA) technique and Sandwich anchorage (SWA) technique. In this experimental study, the long-term durability of shear deficient reinforced concrete beams strengthened with CFRP strap fabrics is tested.

## 2 Experimental Programs

### 2.1 Details of RC T-Beam Specimens

The experimental program consists of RC T – beams of 1.4 m length. The cross section and reinforcement particulars of test specimen are showed in Fig. 1. It shows that the load point is positioned in the beam elevation as to split the length of the beam into a tested span (750 mm) on the right side and the shorter span (500 mm) on the left side. In test span, 6 mm dia. steel stirrups are used at 250 mm center to center. The unrepresentative span is confined with 8 mm dia. stirrups at 100 mm spacing to prevent any significant shear distress during testing so that shear failure always occurs in the test span.

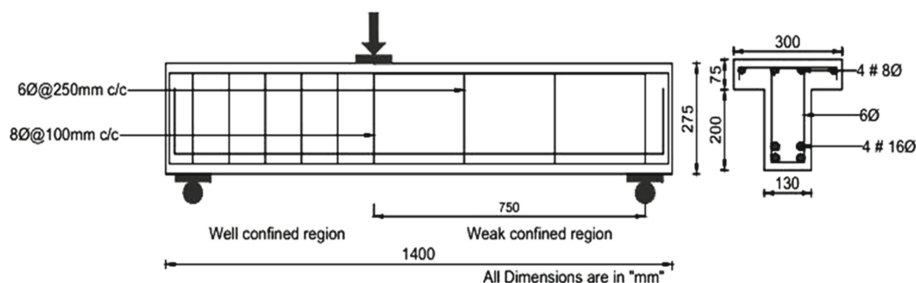


**Fig. 1.** Typical cross section details of RC T-beams.

## 2.2 Materials Specifications

Ordinary Portland Cement (OPC-43 grade) and coarse aggregates 12.5 mm graded were used in concrete preparation. The average cube compressive strength of 37 MPa for 28 days was obtained for all the concrete specimens. Fe 415 for stirrups and Fe 500 grade steel for main reinforcement were used in this experimental study. CFRP sheet with an average tensile strength of 4137 MPa, 0.15 mm thickness and elastic modulus of 242 GPa; CFRP laminated strip with 1.2 mm thickness and 50 mm width with an average 196 GPa elastic modulus and tensile strength of 1700 MPa were used for strengthening works. Table 1 shows the properties (provided by the manufacturer) of CFRP sheet and CFRP laminate.

**Table 1.** Properties of dry carbon fiber sheet/strips\*

Sl. no	Typical dry fiber properties	Units	CFRP fabrics	CFRP laminate
1	Tensile strength	MPa	4137	1,700
2	Tensile modulus	GPa	242	196
3	Fiber diameter	Microns	7.2	-
4	Density	g/cm <sup>3</sup>	1.81	1.7
5	Ultimate elongation	%	-	0.107

\*As provided by the supplier

## 2.3 Test Specimens and Strengthening Schemes

The experimental study consists of three types of strengthening technique to study the influence of CFRP sheets on strengthening of shear deficient R.C T-beams with and without end-anchorage system under various independent environmental exposures such as natural laboratory condition and Hot Air Condition at 60 °C temperature. The reinforcement ratio and detailing were kept same for all the beams in order to compare the performance of dissimilar CFRP strengthening methods. Three different shear strengthening methods have been used in this experiment namely Externally Bonded Fiber Reinforced Polymer (EB-FRP), Self-End Anchorage (SEA) method and Sandwich Anchorage (SWA) method strengthening as shown in Fig. 2. Detailed processes are as follows.

The control specimens are branded as TBC whereas the specimens strengthened with U-jacket Externally Bonded Fiber Reinforced Polymer (EB-FRP) method are branded as TBE. The specimens strengthened with U-jacket EB-FRP method using Self-End Anchorage (SEA) method are branded as TBSA and specimens strengthened with U-jacket EB-FRP method using Sandwich Anchorage (SWA) method are labelled as TBSW. The strengthened RC T beams which are exposed to hot air condition are labelled as TBHE, TBHSA and TBHSW according to their strengthening technic viz. Externally Bonded Fiber Reinforced Polymer (EB-FRP) method, Self-End Anchorage (SEA) method and Sandwich Anchorage (SWA) method.

### 3 Strengthening Procedure

#### 3.1 EB-FRP Strengthening Process

In EB-FRP fortify work, surface of the fortify zone was ground thoroughly until the surface got dirt free; the bottom corners of the beam web were chamfered approximately at a radius of 12 mm in order to avoid stress concentration and early rupture of the CFRP sheet and cleaned by compressed air. Later a tinny layer of primer coat was applied over the ground surface to fill the voids and to smooth the surface. After 24 h, a film of epoxy coating was applied over primer coat. Finally CFRP strap was wrapped in U-shape over the epoxy coating on the web portion of beam specimen as shown in Fig. 2(b). An acceptable roller was used to roll over the wrapped surface to remove the air voids, which is a common practice in CFRP wrapping. The above procedural steps were followed in all the strengthened beams. The typical details of strengthening procedure for specimen TBE and TBHE are shown in Fig. 2(c).

In Self-End Anchorage (SEA) specimens TBSA and TBHSA, after surface grinding, a trench was made with an average width of 5–7 mm and depth of 15–17 mm along two sides of the test span at the flange-to-web junction in order to provide self-end anchorage. Before CFRP wrapping, trenches were filled with epoxy concurrently at the time of epoxy coating on the fortify surface. Later, the CFRP strap free end portions were slot in and fully wrapped on the walls of the groove at both the sides of the test span at the flange-to-web junction. After FRP fixing, the grooves were filled with epoxy in order to fill the remaining empty space inside the grooves as shown in Fig. 2(d) to 2(f).

To implement the SWA technique, anchorage holes were first made by drilling in perpendicular direction to the beam web surface with a diameter of 12 mm and 50 mm depth at a pitch of 30 mm as shown in Fig. 2, 11 mm dia. holes were made in CFRP laminates with proper care to place the laminate very carefully over the drilled anchorage holes in the beam web in order to avoid mismatching with each other. CFRP rod of 10 mm dia. and 75 mm length was used in anchorage work. The one end of CFRP anchorage rod was ground to make the edge sharp to penetrate CFRP sheet while anchoring. For the duration of CFRP wrapping, the unrestricted end of CFRP strap was rolled with 50 mm width CFRP laminated strip. As soon as the wrapping work has been finished, the adhesive treated CFRP rods were introduced into the holes through the laminated strip holes. The complete step by step procedure of sandwich

anchorage method is showed in Fig. 2(g) to 2(i). Figure 2(i) shows the typical details of SWA anchorage technique.

## 4 Environmental Conditioning

Two different types of environmental condition such as natural laboratory and hot air exposure condition were adopted in this study. The detailed explanation about the environmental condition is as follows.

### 4.1 Natural Laboratory Condition

All the test beams were cast and strengthened after 28 days of curing. The strengthened beams were kept in room temperature in the laboratory for 60 days. These natural laboratory condition specimens were used as control specimens for comparative performance.

### 4.2 Hot Dry Air Condition

To evaluate the influence of hot air conditioning on the beams fortified with CFRP strap, nine T-beam specimens were subjected to hot air environment. Specially designed hot air environmental chamber having outer dimensions of 1 m wide  $\times$  1.5 m long  $\times$  2.1 m height, capable of attaining a maximum temperature of 70 °C as shown in Fig. 3 was employed. The temperature inside the environmental chamber was recorded with the help of thermocouples. The heating system was accomplished by electric resistance heater elements. The elements responded rapidly to instrument demand with minimum residual heating effects minimizing overshoot. Blowers were used to provide hot air circulation within the conditioned area. The blowers were designed to assure proper hot air distribution and to prevent hot air stratification throughout the chamber.

Nine T-beams strengthened with different strengthening methods (EB-FRP, SEA and SWA technique) were marked and the surface condition of each beam was documented. Beams were stacked in three rows, each composed of three beams strengthened with CFRP strap fabrics. The chamber was then heated to 140 °F (60 °C) and maintained at this temperature for the entire period of exposure. The beams were kept under steady heat for duration of 1440 h (60 days) and were spaced apart to ensure an adequate hot air circulation and exposure. Past weather records show some particular places having temperature history of 51 °C to 60 °C. In India highest temperature was recorded 51 °C in Phalodi, Thar desert, Rajasthan. Therefore, a maximum target temperature of 60 °C was considered to be reasonable for the accelerated long-term durability test. After exposing specimens to the target temperature for the desired time duration, the environmental chamber was switched off and the samples were left in the chamber to allow natural cooling to room temperature. Each beam was then instrumented and loaded to failure under three-point flexural loading.

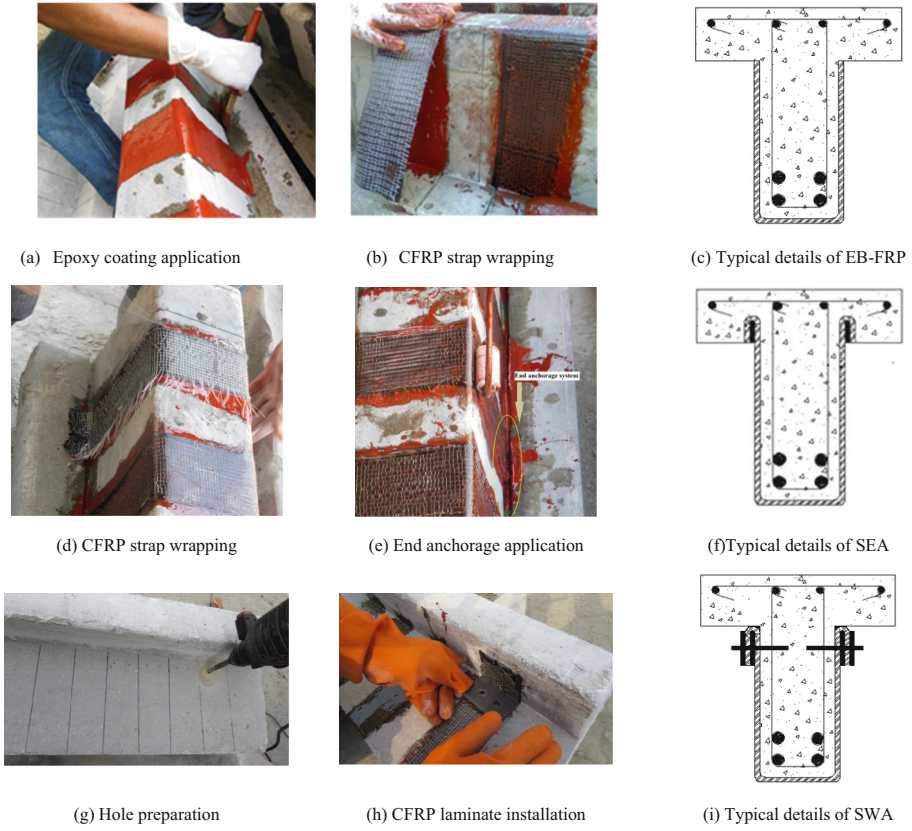


**Fig. 2.** Detailed strengthening system of RC T- beams

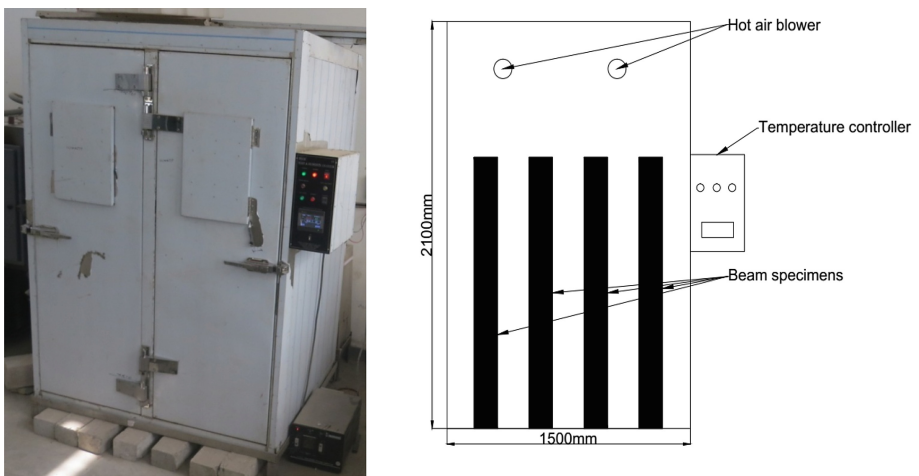


**Fig. 3.** A view of hot air environmental chamber and arrangement of specimens.



## 5 Observations After Environmental Conditioning

The specimens kept in the environmental chamber were taken out from the chamber after 60 days for visual inspection. In this inspection the external changes in the FRP and adhesive nature of epoxy were closely monitored. It is understood that there were no cracks, delamination or rupture over the FRP in the strengthened region. Also it is observed that there was no change in the epoxy adhesion and its hardness range. This assessment proves that the employed CFRP and epoxy effectively resist the environmental effect without any physical damages.

## 6 Test Setup and Arrangement

All the RC T-beam specimens were tested under three point static loading with shear span-to-effective depth ( $a/d$ ) ratio of 3.2. Figure 4 shows the test setup and location of strain gauges. The tests were carried out using 100 ton hydraulic jack and the equivalent load and deflections were observed using load cell and Linear Variable Displacement Transducers (LVDT). Strain gauges were positioned on the side of beam web portion of CFRP fortified beams for the most part in the shear-span and oriented along the fiber direction of the section. Six strain gauges were attached on the expected plane of CFRP surface where shear cracks and high strains would be expected. The data from LVDT, strain gauges and load cell were noted using a data acquisition system.

## 7 Results and Discussions

### 7.1 Failure Analysis

#### 7.1.1 Laboratory Condition

RC beam specimens with different exposures were tested under monotonic loading to evaluate the influence of environmental exposures in FRP strengthening. The experimental outcomes are summarized in Table 2. The load resistance offered by the different strengthening method subjected to different environment exposure and the variation in load resistance compared to control specimen are shown in Fig. 5.

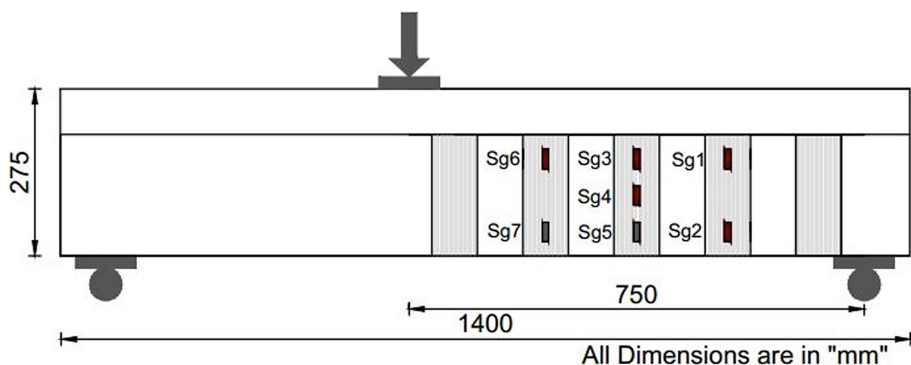
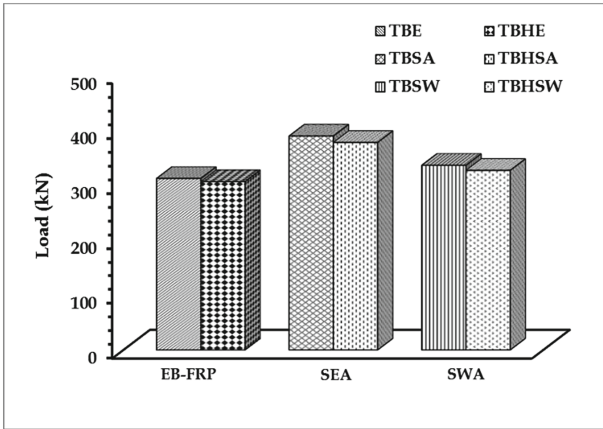


Fig. 4. Test setup and location of strain gauges on CFRP.



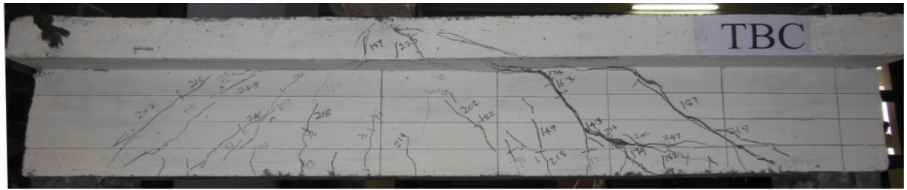
**Fig. 5.** Comparison performance of different strengthening.

Shear failure with web shear crack was observed in all the test specimens. Figures 6 and 7 show the typical failure patterns of tested samples. In control beam specimen TBC, the initial vertical cracks turned inclined as the load rises to higher extent. During further loading, shear cracks were spread across the span and finally failure occurred in the test zone at an ultimate load of 284 kN. In beam TBE, the inclined shear cracks were noticed at 166 kN but the observed FRP debonding led the beam to fail in brittle shear as depicted in Fig. 6(b). The Specimen TBSA with self-end anchorage technique shows similar kind of inclined crack formation in test span at 171 kN. Later, the growth of inclined cracks was hindered and popping sound was made out as an evidence of cracking in the fortified region. Finally, it exhibits brittle failure with a maximum load of 389 kN. The self-end anchorage restricts the CFRP strap delamination and led the FRP to fracture. As a result of CFRP rupture, delamination was observed on the top of the beam flange junction as shown in Fig. 6(c). The SWA anchorage in Specimen TBSW enhances the strengthening performance better than the TBSE beam and also completely prevented the FRP debonding until the complete failure occurs. In this technique, the provided anchorage kept the FRP in active until it ruptures, thus the FRP rupture was noticed as shown in Fig. 6(d) as because of high stress concentration.

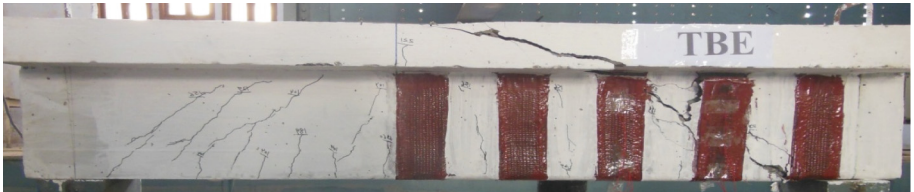
**7.1.2 Hot Air Condition**

The specimens exposed to hot air conditions also exhibits shear failure. As the load increases, shear cracks in progress to spread across the span in specimen TBHE but the intensity of secondary cracks was less as compared with TBE but finally failed in brittle shear as depicted in Fig. 7(a). The Specimen TBHSA with self-end anchorage shows lesser primary crack width as compared with TBSA. The self-end anchorage restricts the CFRP strap delamination and led the FRP to fracture near flange in TBSA whereas same kind FRP rupture was observed near the tension zone in TBHSA as shown in

Fig. 7(b). The Specimen TBHSW with SWA anchorage shows failure behaviour as alike as the specimen TBHSA. The provided SWA anchorage works perfectly under hot air condition and hence it completely prevented the FRP debonding and kept the FRP in active until it ruptures, thus the rupture of FRP occurred at tension zone as shown in Fig. 7(c).



(a) TBC



(b) TBE

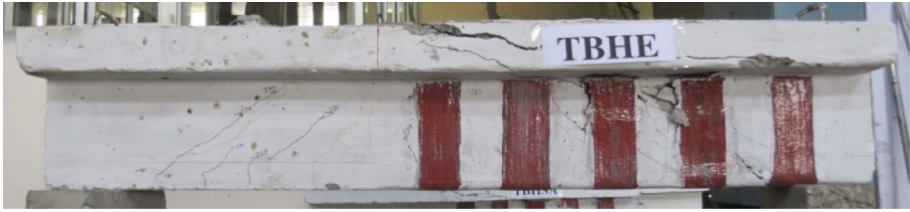


(c) TBSA



(d) TBSW

**Fig. 6.** Failure pattern of tested beam specimens.



(a) TBHE



(b) TBHSA



(c) TBHSW

**Fig. 7.** Failure pattern of tested beam specimens.

## 7.2 Load-Displacement Behaviour

Figure 8 shows the load-deflection curve of tested beam specimens and the outcomes are summarized in Table 2. Figure 8(d) shows sudden drop in load after peak in the specimen TBC. The absence of external strengthening led the specimen TBC to fail in brittle shear within 5.2 mm deflection at 284 kN. The load-deflection curve of strengthened specimens TBE, TBSA and TBSW shows tremendous difference in the case of load carrying capacity as compared to specimen TBC. It authenticates the effectiveness of the strengthening. Also the comparative response unveils the role of anchorage in shear strengthening. The observed peak load in specimen TBE is 312 kN, which is 8% lesser than the specimen TBSW and it is 25% lesser than TBSA. The provided anchorage holds the specimen active at higher deformation with increased load carrying capacity. Also the load deformation envelope of specimen TBSA shows gradual rate of post peak degradation than specimen TBSW. The observed post peak response of TBSW shows sudden drop in load whereas in TBSA it is gradual with slower rate. It authenticates the influence of self-end anchorage efficacy than sand-wich anchorage.

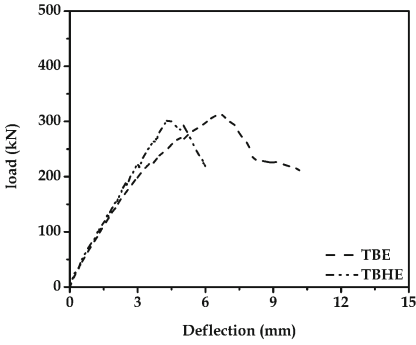
The specimens exposed to hot air condition show slight reduction in load carrying capacity. This is possibly because of the heat reaction between the epoxy and concrete surface. But the post peak response varies with respect to the employed anchorage technique. The response of TBHE is comparable with that of TBSE. The initial tangent of the load-deformation curve of TBHSA and TBHSW shows improved stiffness behavior over the specimens under laboratory condition as shown in Figs. 8 (b) and (c). The post peak response shows sudden drop in load after peak. Although the observed load carrying capacity of anchored specimens emphasizes the prominence of anchorage in shear strengthening. The observed load enhancement with anchored specimens is not possible to attain by usual method.

**Table 2.** Test outcomes of T-beam specimens

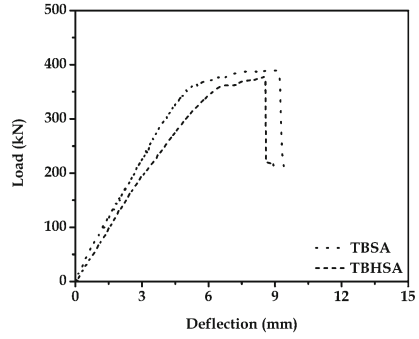
Specimen ID	Environmental condition	Peak load	Total shear resistance	Shear resistance due to CFRP	Gain due to CFRP	Gain due to anchorage	Deflection at load point	Ductility factor	Energy absorption
		(kN)	(kN)	$V_f$ (kN)	(%)	(%)	(mm)	( $\mu$ )	(kN.mm)
TBC	Laboratory	284	113.6	×	×	×	5.2	1.17	1171
TBE		312	122.4	8.8	9.85	×	6.5	1.08	2153
TBSA		389.3	155.7	42.1	37.0	25	9.13	1.18	2614
TBSW		336	134.4	20.8	18.3	8	8.52	1.37	2341
TBHE	Hot air	306.2	116.3	2.7	7.7	×	4.37	1.25	1146
TBHSA		377.6	151.0	37.4	32.9	23.3	8.5	1.44	2128
TBHSW		326.7	130.6	17	15.0	6.7	7.8	1.5	2181

### 7.3 Ductility and Energy Absorption

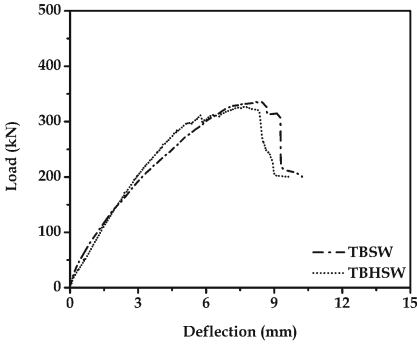
Figure 9 shows the absence of strengthening in TBC led the specimen to fail in small deflection thus the energy absorption is less as compared to the strengthened specimens. The absorbed energy of TBC is 100% lesser than the strengthened specimens. The specimen with EB-FRP external strengthening shows gradual increase in energy absorption with respect to the deflection. The external strengthening helped the specimen to deform higher than unstrengthened specimen, as a result of this it exhibits better energy absorption. The self-end anchorage specimen shows higher energy absorption over other specimens. The early shear failure in EB-FRP strengthened specimens shows lesser energy absorption over SWA technique strengthened specimens. The provided additional anchorage in specimen (TBSA and TBHSA) holds the specimen active at larger deformation. Thus the specimens show higher energy absorption over all other specimens. The sandwich anchorage specimen shows higher energy absorption in lesser deformation. This authenticates the effect of anchorage in strengthening. The strengthened specimens exposed to hot air condition show higher energy in lesser deflection as compared with control specimens. The difference in energy between different anchorages is negligible. Thus it proves that irrespective of anchorage technique it supports the load carrying capacity and improves the overall performance.



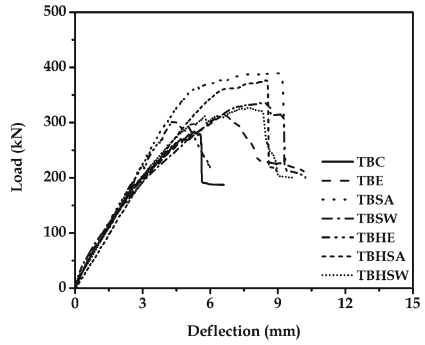
(a) EB-FRP strengthened specimens



(b) SEA strengthened specimens



(c) SWA strengthened specimens



(d) All specimens

**Fig. 8.** Load - deflection curves of R.C beams exposed to hot dry air condition.

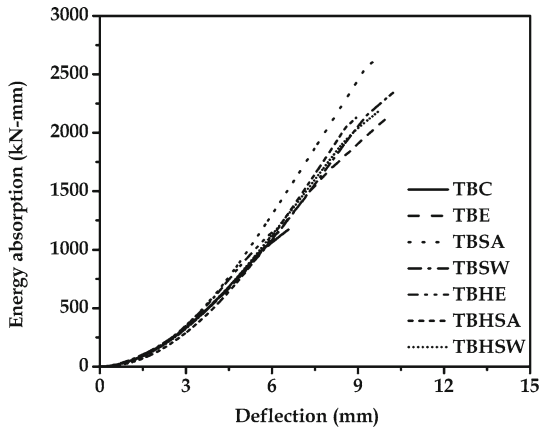


**Fig. 9.** Energy absorption.

#### 7.4 Efficiency of the Anchorage Methods

To measure the efficiency of employed strengthening techniques with EB-FRP strengthening methods on shear strengthening, an effective assessment was also carried out. The efficiency of FRP strengthening is demarcated as the ratio between the shear strength contribution of CFRP ( $V_f$ ) to the CFRP ultimate tensile capacity per unit length ( $f_{fu}^*$ ). The computed efficiency levels of all the FRP strengthening techniques are listed in Table 3. The specimens TBE and TBHE strengthened with EB-FRP sheet shows an average of 8.8% and 2.7% efficiency level. The specimens TBSA and TBHSA strengthened with SEA technique exhibited an average of 42.1% and 37.4% efficiency levels which is attained the uppermost FRP efficiency over all the strengthened beams. The specimens TBSW and TBHSW show an average of 20.8% and 17% efficiency level.

**Table 3.** Efficiency of the anchorage method

Specimen ID	Area of wrap fiber	Ultimate tensile capacity per unit length ( $f_{fu}^*$ )	$V_f$	$\psi_f$ Efficiency of FRP
	(mm <sup>2</sup> /m)	(kN/m)	(kN)	(% m)
TBE	225	315	8.8	2.8
TBSA	225	315	42.1	13.4
TBSW	225	315	20.8	6.6
TBHE	225	315	2.7	0.86
TBHSA	225	315	37.4	11.8
TBHSW	225	315	17	5.4

#### 7.5 Strain Response in CFRP

Figure 10 shows the load versus CFRP strain response of all the fortified specimens. It can be observed that at early stage of loading there was no strain growth in CFRP sheets and strain curves of all the fortified beams stay same up to a load of 200 kN. Figure 10 shows linearity in graph till 200 kN in control specimen whereas the anchored specimens show linearity for more than 300 kN. The strain behavior of specimens exposed to hot air condition where compared with laboratory condition, though the maximum strain observed with the anchored specimens are nearly same and shows the effectiveness of anchorage in improving the efficiency of the FRP shear strengthening over the strengthening without anchorage. Among the anchored specimens the employed self-end anchorage specimens shows better strain response over sand-wich specimens. This shows that the provided self-end anchorage holds the specimen to a higher extent and improves the efficiency of strengthening without any external support. The sand-wich anchorage shows competitive performance with self-end anchorage, in particular the performance of sandwich in hot air condition is exceptional over natural laboratory condition.



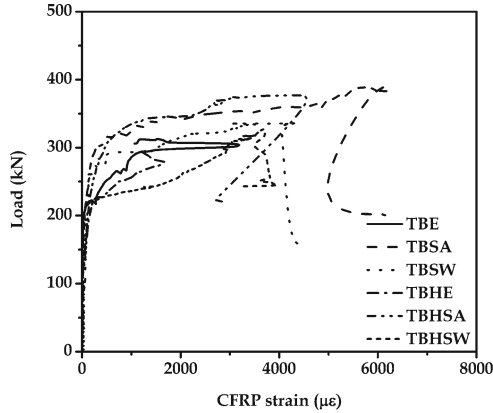


**Fig. 10.** Load versus strain in CFRP.

## 8 Concluding Remarks

This study aim investigates the effectiveness of different anchorage in CFRP strengthening subjected to different environmental conditions. Following concluding remarks are arrived from the study.

1. The load-deflection behavior of strengthened specimens shows the importance of anchorage in strengthening. An average of 8% increase in strength is observed with EB-FRP strengthened beam over unstrengthened specimen. But the shear strength enhancement of anchored specimen is ranging from 18–37% over control specimens. Even under different environmental conditions the shear resistance of FRP has been effectively supported by the provided anchorage.
2. The observed energy absorption of strengthened specimens is better than control specimens but the calculated energy absorption of anchored specimens commendably shows the influence of anchorage in shear strengthening.
3. The crack pattern and failure mode of test specimens evidenced the role of anchorage in strengthening. The usual delamination failure in conventionally strengthened specimens shows the early failure of strengthening. Whereas the FRP rupture at different location with respect to the anchorage and different environmental conditions authenticates the importance and need of anchorage in FRP strengthening to effectively utilize the advantages of FRP strengthening in practice.
4. The FRP strain behavior of anchored specimens show enhanced FRP efficiency than strengthened specimens without anchorage. In particular the specimens with end anchorage show higher FRP efficiency than the other anchored specimens. It proves that the end anchorage in FRP strengthening improves the efficacy and allows to resist higher load carrying capacity.



## References

- Adhikary, B.B., Mutsuyoshi, H.: Behavior of concrete beams strengthened in shear with carbon-fiber sheets. *J. Compos. Constr.* **8**(3), 258 (2004)
- Benmokrane, B., Faza, S., GangaRao, H.V.S., Karbhari, V., Porter, M.: Effects of Alkaline Environment, Gap Analysis for Durability of Fiber Reinforced Polymer Composites in Civil Infrastructure. ASCE Publications, pp. 24–28 (2000)
- Bousselham, A., Chaallal, O.: Behavior of reinforced concrete t-beams strengthened in shear with carbon fiber-reinforced polymer-an experimental study. *ACI Struct. J.* **103**(3), 339–347 (2006)
- Chin, J., Haight, M., Hughes, W., Nguyen, T.: environmental effects on composite matrix resins used in construction. In: Proceedings of CDCC 1998, Sherbrooke, Canada, pp. 229–242 (1998)
- Chen, J.F., Teng, J.G.: Shear capacity of fiber-reinforced polymer-strengthened reinforced concrete beams: fiber reinforced polymer rupture. *J. Struct. Eng.* **129**(5), 615 (2003)
- Cao, S.Y., Chen, J.F., Teng, J.G., Hao, Z., Chen, J.: Debonding in RC beams shear strengthened with complete FRP wrap. *J. Compos. Constr.* **9**(5), 417 (2005)
- Chaallal, O., Mofidi, A., Benmokrane, B., Neale, K.: Embedded through-section FRP rod method for shear strengthening of RC beams: performance and comparison with existing techniques. *J. Compos. Constr.* **15**(3), 374–383 (2010)
- Dai, J.G., Gao, W.Y., Teng, J.G.: Bond-slip model for FRP laminates externally bonded to concrete at elevated temperature. *J. Compos. Constr.* **17**(2), 217–228 (2013)
- Dai, J., Ueda, T., Sato, Y.: Bonding characteristics of fiber-reinforced polymer sheet-concrete interfaces under dowel load. *J. Compos. Constr.* **11**(2), 138–148 (2007)
- Galal, K., Mofidi, A.: Shear strengthening of RC T-beams using mechanically anchored unbonded dry carbon fiber sheets. *J. Perform. Constr. Facil.* **24**(1), 31–39 (2010)
- Karbhari, V.M., and Engineer, M. (1996), Effect of Environmental Exposure on the External Strengthening of Concrete with Composites—ShortTerm Bond Durability, *Journal of Reinforced Plastics and Composites*, pp. 1194–1216
- Grace, N.F., Singh, S.B.: Durability evaluation of carbon fiber-reinforced polymer strengthened concrete beams: experimental study and design. *ACI Struct. J.* **102**(1), 40 (2005)
- Sheikh, S.A.: Performance of concrete structures retrofitted with fibre reinforced Polymers. *Eng. Struct.* **24**, 869–879 (2002)
- Pendhari, S.S., Kant, T., Desai, Y.M.: Application of polymer composites in civil construction: a general review. *Compos. Struct.* **84**, 114–124 (2008)
- Zhang, Z., Hsu, C.T.T.: Shear strengthening of reinforced concrete beams using carbon-fiber-reinforced polymer laminates. *J. Compos. Constr.* **9**(2), 158–169 (2005)



# Mathematical Models for Seismic Analysis of Elevated Water Tanks: A Review

Kangkana K. Baruah<sup>(✉)</sup> and Satyabrata Choudhury

Department of Civil Engineering, National Institute of Technology Silchar,  
Silchar, India

{kangkana\_pg, chou\_s}@civil.nits.ac.in

**Abstract.** The conventional seismic analysis of elevated water tanks requires a simplified mathematical model in the form of a spring mass system. Several such models have been suggested by researchers, each with its own set of assumptions which make it applicable for certain problems but not suited for others. The study covers three such models namely, the most basic single lumped mass model and two other models considering fluid structure interaction for rigid and flexible tanks. These models are not exhaustive and each has its own shortcomings. The models discussed in this work do not take soil structure interaction into account and all of them assume a fixed base. This leaves the study of such models for a separate work.

**Keywords:** Mathematical model · Elevated water tank · Seismic analysis

## 1 Introduction

Elevated water tanks are lifeline structures and as such, the possibility of any damage to them due to seismic activity is a matter of grave concern. From providing safe drinking water to extinguishing fire, several of the basic utilities are dependent on the preservation of structural and functional integrity of the elevated water tanks in the post-earthquake scenario. In the past, there have been several cases of water tanks not being able to withstand seismic forces and suffering lot of damage (Steinbrugge and Flores 1963; Rai 2002). In the Jabalpur earthquake of 1997 and the Bhuj earthquake of 2001, much damage took place in elevated water tanks.

A very important aspect to consider in the seismic analysis and design for elevated water tanks is their simplified representation or mathematical model. Such a model is an idealized discrete mass system makes it easier to formulate equations of motion. An idealized lumped mass system is required by finite element model-based computer programs to predict the dynamic behaviour of such structures in response to earthquake excitation. Various such idealized models have been formulated to represent the fluid-structure interaction, with or without considering flexibility of tank wall and interaction of the overall structure with the soil. So far researchers have idealized water tanks as one mass, two mass and three mass structures.

The kind of model which will be applicable to a particular problem will of course depend on the nature of the problem. As for example as stated by Housner (1963), a closed tank completely full of water or completely empty can be idealized as a single

mass structure. However, if the tank is partially filled i.e., it has a free water surface then in order to account for the sloshing of water it has to be idealized as a two-mass structure.

## 2 Available Simplified Models

The simplified models for elevated water tanks can be classified as the single lumped mass model, models which consider fluid structure interaction and models which consider fluid- structure-soil interaction.

### 2.1 Single Lumped Mass Model

The single lumped mass model is the most simplified model of an elevated water tank. This was first used by Chandrashekhara and Krishna (1954). In this model the supporting structure, irrespective of its type (steel frame, concrete shaft, concrete frame or masonry pedestal) is assumed to behave as a cantilever of uniform rigidity throughout its height. The mass is considered to be concentrated at the top of this supporting structure as shown in Fig. 1. This mass ( $m$ ) constitutes of the mass of the tank structure, the water contained in it and a fraction of the mass of the supporting structure.

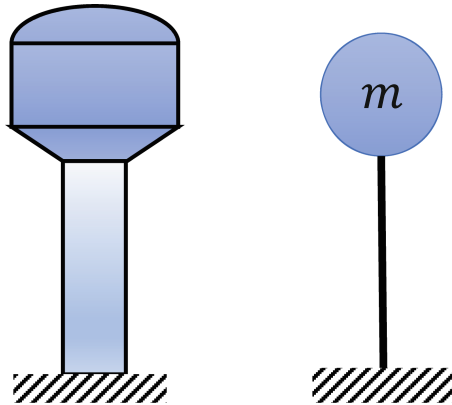


**Fig. 1.** One mass idealization of elevated water tank.

The stiffness of the supporting structure  $k_s$  may be estimated as given in Eq. (1) as it is idealized as a cantilever (Livaoglu and Dogangun 2006).

$$k_s = \frac{3EI_c}{l_{cg}^3} \quad (1)$$

Here  $E$  is the Young's modulus of the material,  $I_c$  is the moment of inertia of gross section about centroidal axis and  $l_{cg}$  is the distance of the base to the centroid of the stored water.

The time period  $T$  can be established using Eq. (2) as per ACI 371R-98 (1995).

$$T = 2\pi \sqrt{\frac{W_L}{gk_s}} \quad (2)$$

In Eq. (2),  $W_L$  represents the sum of the self-weights of the tank and the tank floor, maximum of two thirds of the total weight of the support structure and the weight of water in the tank. The ACI 371R-98 (1995) states that single lumped mass model is to be used only when water load is 80% or more of the total gravity load which includes the total dead load above the base, water load and a minimum of 25% of the floor live load in areas that are used for storage.

IS 1893 (Part 2): 2014 also gives a similar formula for the time period of single lumped mass model with the modification that the fraction of mass of the support structure that is to be considered is precisely specified to be one third of the total mass of the support structure. The earlier version of IS 1893 published in 1984 specified only the single lumped mass model irrespective of the problem statement. But the recent revision of this code, IS 1893 (Part 2): 2014, permits the single mass model to be used only in following cases: (i) RC tank of capacity upto 1000 kl considering rigid wall for tank and (ii) Steel tanks (flexile wall) up to capacity of 200 kl or for height to diameter (or length) ratio greater than or equal to 0.4.

Chandrashekharan and Krishna (1954) are of the view that for design of the staging sloshing of water does not cause any appreciable deformation in the staging and thus, the single lumped mass model is a good approximation for the design of staging.

Lakhade et al. (2017, 2018) while studying the nonlinear behaviour of the RC frame staging of elevated water tanks have used a single lumped mass model. The single mass model is also used by Kumbhar et al. (2019) for the direct displacement-based design of RC frame staging of elevated water tanks.

## 2.2 Models Representing Fluid Structure Interaction

### 2.2.1 Rigid Wall Tanks

Following the damage of some elevated water tanks in the Chilean Earthquake of 1960, Housner (1963) concluded that for accurate dynamic analysis of elevated water tanks, the motion of the water relative to the tank must also be taken into account. This was accounted for in the mechanical model by introducing an impulsive mass ( $m_i$ ) rigidly attached to the tank wall and one or more convective masses ( $m_c$ ) which are attached through springs to the tank wall.

The impulsive mass is the representation of that portion of the water that oscillates in tandem with the tank wall and exerts a reactive force on the tank wall of a magnitude which is same as that which will be exerted by the impulsive mass attached to the wall rigidly as shown in Fig. 2. The convective masses are representation of the portion of the water that will undergo a sloshing motion which in turn exerts an oscillating force

on the tank the magnitude of which will be same as that exerted by convective masses oscillating horizontally against a restraining spring. There can be several convective masses but Housner (1963) stated that the convective mass corresponding to the fundamental sloshing frequency is the one that is most significant for earthquake problems. As such other convective masses are ignored.

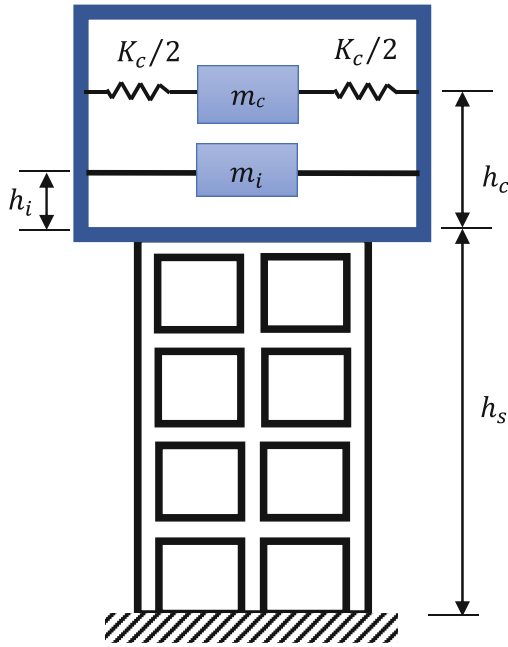


Fig. 2. Spring mass model for two mass idealization.

The main parameters of this model are  $m_i$ ,  $m_c$ ,  $h_i$ ,  $h_c$  and  $k_c$  which denote the impulsive mass, convective mass, height of impulsive mass, height of convective mass and spring stiffness of convective mode respectively (Fig. 2). The parameters for the two-mass idealization have been originally derived by Housner (1963). But these have been modified to some extent in ACI 350.3 (2001). These modified parameters have been added in the IITK GSDMA guidelines and in IS 1893 (Part 2): 2014. These parameters can be obtained for circular tank from the Eqs. (3) to (7) in terms of the total mass of liquid ( $m$ ), depth of liquid ( $h$ ) and diameter of tank ( $D$ ). Using these equations, the graphs in Figs. 3 and 4 are drawn.

$$\frac{m_i}{m} = \frac{\tanh(0.866 \frac{D}{h})}{0.866 \frac{D}{h}} \tag{3}$$

$$\frac{m_c}{m} = 0.23 \frac{\tanh(3.68 \frac{h}{D})}{\frac{h}{D}} \tag{4}$$

$$\frac{k_c h}{mg} = 0.836 \tanh^2\left(3.68 \frac{h}{D}\right) \tag{5}$$

$$\begin{aligned} \frac{h_i}{h} &= 0.375 \quad \text{for } \frac{h}{D} \leq 0.75 \\ &= 0.5 - \frac{0.09375}{h/D} \quad \text{for } \frac{h}{D} > 0.75 \end{aligned} \tag{6}$$

$$\frac{h_c}{h} = 1 - \frac{\cosh\left(3.68 \frac{h}{D}\right) - 1}{3.68 \frac{h}{D} \sinh\left(3.68 \frac{h}{D}\right)} \tag{7}$$

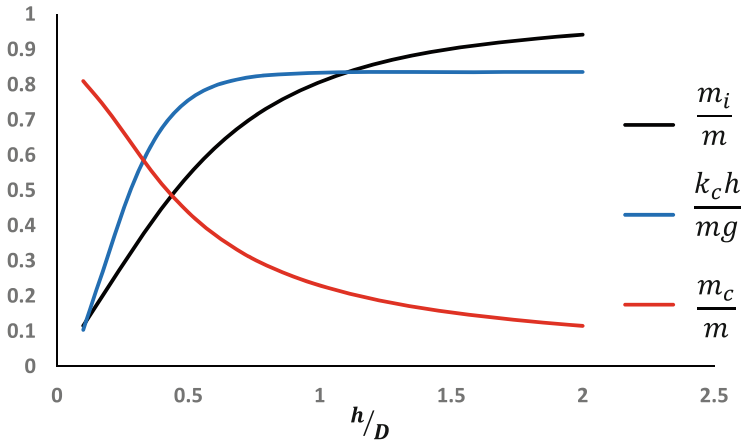


Fig. 3. Impulsive and convective mass and convective spring stiffness.

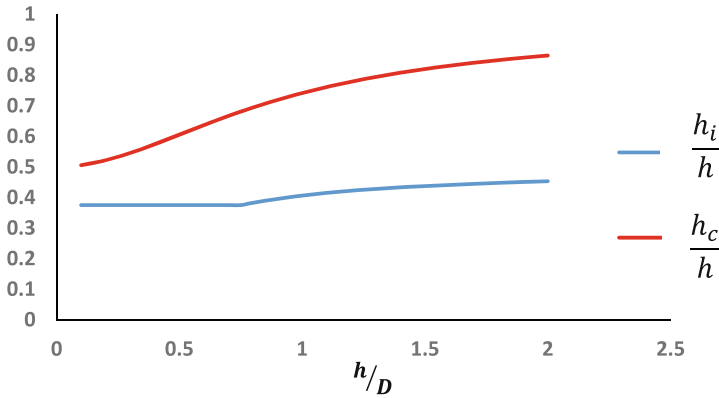


Fig. 4. Heights of impulsive and convective masses.

The time periods for the impulsive and convective mode of vibration can be found using Eqs. (8) and (9).

$$T_i = 2\pi\sqrt{\frac{m_i + m_s}{k_s}} \tag{8}$$

$$T_c = 2\pi\sqrt{\frac{m_c}{k_c}} \tag{9}$$

where  $m_s$  is mass of the container and one third mass of the staging and  $k_s$  is the lateral stiffness of the staging.

It has been found that usually the impulsive and convective time periods are well separated and as such the system can be considered as two uncoupled single degree of freedom system as shown in Fig. 5.

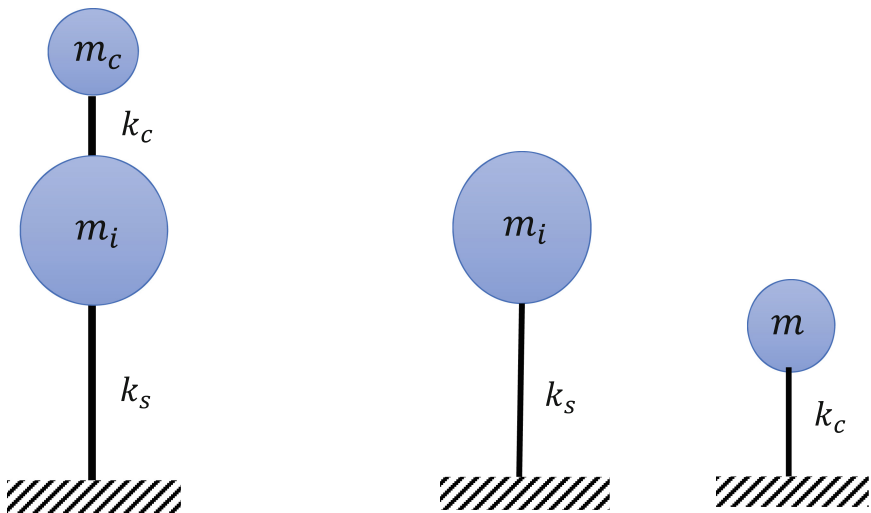


Fig. 5. Two mass idealization and equivalent single degree of freedom system.

Shepherd (1972) stated that the two-mass idealization given by Housner (1963) enables satisfactory prediction of frequency properties which is of significance when complex numerical integration of earthquake response is desired.

Priestly et al. (1986) stated that a two-mass model was recommended by the New Zealand Society of Earthquake Engineering for the seismic analysis of elevated water tank. Rai (2002) stated that the two-mass idealization was more accurate representation of elevated water tank than the single lumped mass model.

GSDMA guidelines on elevated water tank also advocates for the use of a two-mass model because most elevated tanks are never completely filled with liquid and thus sloshing will always be present.

**2.2.2 Flexible Wall Tanks**

Housner’s two mass model didn’t take into account tank wall flexibility which is important in case of steel tanks. It has been found that wall flexibility also has an effect on the dynamic behaviour of fluid containers.

Haroun and Elliathy (1985a) proposed a mathematical model for flexible tanks. This model is applicable to both elevated and ground-based tanks and considers rigid base rocking motion along with lateral translation. rigid base rocking motion was also considered. In their study they made certain assumptions, mentionable among them are: (i) The tank undergoes base translation, base rotation or both due to seismic excitation, (ii) Interaction of sloshing modes with shell deformation is weak, and (iii) Short period pressure component due to wall flexibility is taken into consideration.

The mathematical model proposed by Haroun and Elliathy (1985a), is as shown in Fig. 6. The short period pressure component due to wall flexibility is represented by the mass,  $m_f$ , located at a height,  $H_f$ , from tank bottom. Mass,  $m_r$ , is the impulsive mass located at height,  $H_r$ , from tank bottom.  $I_r$  is the central moment of inertia of mass  $m_r$ . The spring attaching mass,  $m_f$ , has an equivalent stiffness  $K_f$ . The sloshing effect of water is not considered as such there is no convective mass.

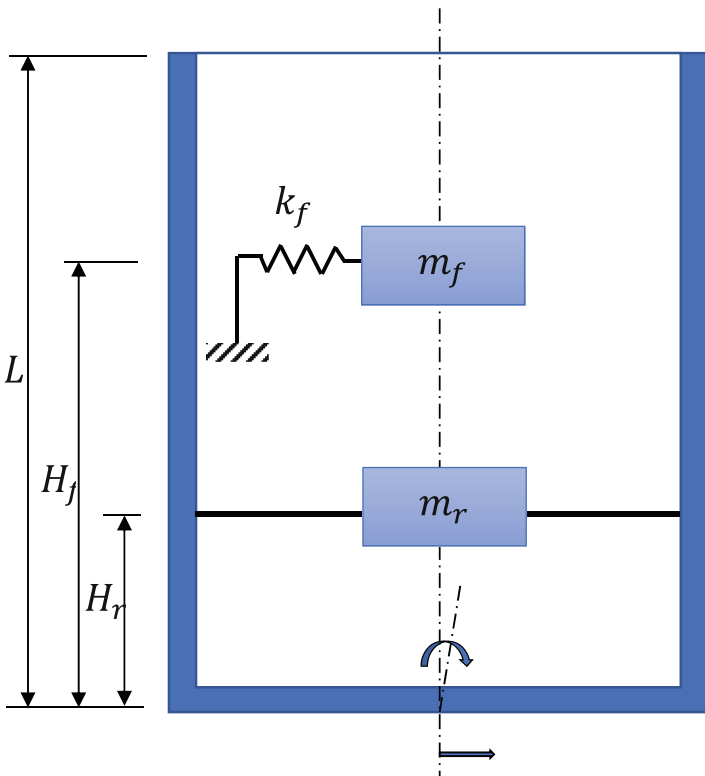


**Fig. 6.** Mathematical model for flexible tank.



Haroun and Elliathy (1985a) provided equations and graphs for explicit values of the parameters in the mathematical model. Haroun and Elliathy (1985b) stated that prior to employing this model in the analysis of supporting towers i.e. elevated tanks, the parameters  $m_r, m_f, H_r, H_f$  and  $I_r$ , are replaced by  $m_0, m_1, H_0, H_1$  and  $I_0$  by the Eqs. (10) to (14).

$$m_f = m_1 \tag{10}$$

$$m_r = m_0 + m_1 \tag{11}$$

$$H_f = H_1 \tag{12}$$

$$m_r H_r = m_1 H_1 + m_0 H_0 \tag{13}$$

$$m_r H_r^2 + I_r = m_1 H_1^2 + m_0 H_0^2 + I_0 \tag{14}$$

The stiffness  $K (= K_f)$  can be obtained by the expression given in Eq. (15) wherein  $H$  is the total depth of water in the tank,  $R$  is the radius of the tank and  $E$  is the Young’s modulus along with the rest of the notation consistent with the theory above.

$$K_f = \frac{4\pi^2 E h m_f}{m} \left\{ 0.01205 \left(\frac{H}{R}\right)^2 - 0.08466 \left(\frac{H}{R}\right) + 0.17042 \right\}^2 \tag{15}$$

After sorting out the parameters of the mechanical analogue, Haroun and Elliathy (1985b) obtained the equation of motion for the model while also taking into account mass and stiffness of the staging. Thereafter going for an eigenvalue analysis, they arrived at equivalent mass and equivalent height for different modes of vibration and an equivalent simple oscillator for each mode of vibration.

### 3 Discussion

The seismic analysis of elevated water tanks requires simplified mathematical models. The appropriate mathematical model to be used for a particular case depends on several factors which include water level in the tank, material of construction for the tank, the parameters for which seismic analysis is done etc. This has been tabulated in Table 1.

**Table 1.** Condition of applicability of different models

Type of model	Applicability
Single Lumped mass model	1. Narrow and tall tanks with depth to diameter ratio exceeding 0.4
	2. In the absence of possibility of sloshing i.e., for tank full and tank empty condition
	3. When the topic of interest in seismic analysis pertains to the staging and not to the tank such as nonlinear analysis of the staging for estimating drift
	4. Mostly rigid tanks, not suitable for flexible tanks
Models representing fluid structure interaction	1. Wider tanks with less depth
	2. Partially filled tanks with possibility of sloshing
	3. Partially filled tanks with flexible walls

The models studied in this work are the most basic ones to understand the seismic behaviour of elevated water tanks. These models are not inclusive of all the factors which affect the dynamic behaviour. As for example Housner's model (Housner 1963) didn't take into account tank flexibility and as such it is less appropriate for steel tanks. On the other hand, while Haroun and Elliathy (1985a) did consider tank flexibility, they didn't incorporate the sloshing effect. Another shortcoming of these models is that all of them considered a rigid base that is stiff soil condition which might not be the case always.

## 4 Conclusion

Mathematical models for elevated water tanks with and without considering fluid-structure interaction are important tools for seismic analysis. This study is an attempt to understand some of those mathematical models.

Each model has its own applicability and it depends on the researcher to seek out the model which is most appropriate with his problem statement. The models also come with their own set of shortcomings.

The models discussed in this work are not exhaustive of all parameters influencing the dynamic behaviour of elevated water tanks. There have been efforts to incorporate soil structure interaction in the mathematical models by many researchers. However, those have not been covered in this work and left for later study.

## References

- ACI 371R-98 1995: Guide to the Analysis Design and Construction of Concrete-pedestal Water Tower (American Concrete Institute)  
 ACI 350.3 2001: Seismic Design of Liquid-Containing Concrete Structures (American Concrete Institute)

- Chandrashekar, A.R., Krishna, J.: Water towers in seismic zones. In: Proceedings of the Third World Conference on Earthquake Engineering, New Zealand, vol. 4, pp. 161–171 (1954)
- Haroun, M.A., Elliathy, H.M.: Model for flexible tanks undergoing rocking. *J. Eng. Mech.* **111**(2), 143–157 (1985a). [https://doi.org/10.1061/\(ASCE\)0733-9399\(1985\)111:2\(143\)](https://doi.org/10.1061/(ASCE)0733-9399(1985)111:2(143))
- Haroun, M.A., Elliathy, H.M.: Seismically induced fluid forces on elevated tanks. *J. Techn. Topics Civil Eng.* **111**(1), 1–15 (1985). <https://doi.org/10.1061/JTCEDL.0000023>
- Housner, G.W.: The dynamic behaviour of water tanks. *Bull. Seismol. Soc. Am.* **53**(2), 381–387 (1963). <https://doi.org/10.1785/BSSA0530020381>
- IITK-GSDMA Guidelines for seismic design of liquid storage tanks, Indian Institute of Technology, Kanpur, India, 2005
- IS 1893 Part 2: Criteria for Earthquake Resistant Design of Structures Part 2 Liquid Retaining Tanks, Bureau of Indian Standards, New Delhi, India (2014)
- Kumbhar, O., Kumar, R., Panaiyappan, P.L., Farsangi, E.N.: Direct displacement based design of reinforced concrete elevated water tanks frame staging. *Int. J. Eng.* **32**(10), 1395–1406 (2019). <https://doi.org/10.5829/ije.2019.32.10a.09>
- Lakhade, S.O., Kumar, R., Jaiswal, O.R.: Estimation of response reduction factor of RC frame staging in elevated water tanks using nonlinear static procedure. *Struct. Eng. Mech.* **62**(2), 209–224 (2017). <https://doi.org/10.12989/sem.2017.62.2.209>
- Lakhade, S.O., Kumar, R., Jaiswal, O.R.: Damage states of yielding and collapse for elevated water tanks supported on RC frame staging. *Struct. Eng. Mech.* **67**(6), 587–601 (2018). <https://doi.org/10.12989/sem.2018.67.6.587>
- Livaoglu, R., Dogangun, A.: Simplified seismic analysis procedures for elevated tanks considering fluid-structure-soil interaction. *J. Fluids Struct.* **22**, 421–439 (2006). <https://doi.org/10.1016/j.jfluidstructs.2005.12.004>
- Priestley, M.J.N., et al.: Seismic design of storage tanks. Recommendation of a study group the New Zealand Society for Earthquake Engineering, New Zealand (1986)
- Rai, D.C.: Seismic retrofitting of R/C shaft support of elevated tanks. *Earthq. Spectra.* **18**(4), 745–760 (2002). <https://doi.org/10.1193/1.1516753>
- Shepherd, R.: The two mass representation of a water tower structure. *J. Sound Vibr.* **23**(3), 391–396 (1972). [https://doi.org/10.1016/0022-460X\(72\)90634-7](https://doi.org/10.1016/0022-460X(72)90634-7)
- Steinbrugge, K.V., Flores, R.: Engineering report on the Chilean earthquakes of May 1960 - a structural engineering viewpoint. *B.S.S.A.* **53**(2), 225–307 (1963). <https://doi.org/10.1785/BSSA0530020225>



# Seismic Vulnerability Assessment Methods: A Review

N. Sarma Roy<sup>(✉)</sup> and Satyabrata Choudhury

Department of Civil Engineering, NIT Silchar, Silchar, India  
{nirmalya\_rs, chou\_s}@civil.nits.ac.in

**Abstract.** Seismic vulnerability is defined as the tendency of the structure to undergo structural or non-structural damage in case of any seismic event. In such cases, the buildings lose its ability to bear the sudden effects of seismic forces. In risk analysis of a building, the vulnerability assessment of a structure plays a vital role. Over the years various methods have evolved for assessing the seismic vulnerability of a structure. The assessment procedures may be empirical, semi empirical or analytical. The assessment output may be quantitative or qualitative in nature. Seismic vulnerability based on empirical method are evaluated with the help of post-earthquake damage data collected over the years and thereafter the structures are compared with the structural details and typology prior to seismic event. The damage data and statistics are recorded year after year around the globe after every seismic event. On the other hand, in analytical method, the seismic vulnerability can be assessed through deriving numerical model and also performing various types of static and dynamic analyses, mainly the nonlinear analyses. However, some of the said, methods are time consuming and computationally intensive, hence there are various alternative vulnerability assessment strategies proposed by various researchers, which are briefly described in this article. Also, the prerequisite of a suitable seismic vulnerability assessment procedure is discussed.

**Keywords:** Seismic vulnerability · Empirical · Analytical

## 1 Introduction

Every year, there are significant amount of losses, including losses of human lives, caused by natural catastrophes like earthquake. This bears a significant impact if considered decade wise. Predicting seismic vulnerability of the built environment is required for saving losses, minimising causalities and also anticipating the extent of damage likely to take place. Vulnerability assessment is a significant component of an overall loss predicting model which identifies the seismic damage for a given scenario. This proves to be very useful for the insurance company for estimating premium and claim settlement. With the ever increase of population suitable vulnerability assessment methods are necessary for quick estimate of future losses and to formulate strategies to mitigate the risk. A successful and timely vulnerability assessment can mitigate the risk to a great extent and the subsequent rehabilitation and retrofitting strategies can be cost effective. Further the seismic vulnerability assessment of the existing building or stock

of buildings can provide all important details that are to be considered during construction and design of new buildings following the prevalent seismic code including the calibration of the codal guidelines as per requirement. As already defined the seismic vulnerability of a structure is its probable likelihood to damage by a given ground shaking intensity and therefore the structural vulnerability assessment under a scenario earthquake leads to the probability of achieving a prescribed damage level, which can be expressed qualitatively or quantitatively. In this regard various seismic vulnerability assessment methods have been proposed by seismic experts, earthquake engineer and researchers for a given building stock, based on the seismic demand and typology of the structure. This paper will review some of the important vulnerability assessment procedures.

## 2 Literature Review

Seismic vulnerability as defined is the likelihood of the building to damage during earthquake. It is an important parameter for various field workers, engineers, disaster management authority to know the vulnerability of a building stock before hand in order to anticipate the probable occurrence of damage post-earthquake. In this regard Kassem et al. (2019) proposed an index called Seismic Vulnerability Index (SVI), with its value ranging from 0 to 1. less vulnerable being indicated by 0 and more vulnerable by 1, in qualitative sense. Yakut (2004) proposed an index called basic capacity index method which reflects the probable or anticipated seismic performance of a structure during earthquake based on the structural details of existing RC structure. Japanese Seismic Index method (JBDPA 1990) is another popular method used in Japan since 1975 for existing RC buildings less than six storeys. A combination of empirical method and analytical method for seismic vulnerability assessment is popularly known as hybrid method of vulnerability assessment, Kappos et al. (1995, 1998) have derived damage probability matrices using a hybrid procedure. Bernardini et al. (1990), proposed a method for the vulnerability assessment of unreinforced masonry buildings (URMB) using the fuzzy-set theory and the definition of collapse multipliers. There is another method called FaMIVE which is based on collapse load factor where the most probable mechanism with lowest capacity considering both in plane and out of plane failure of masonry building is taken into consideration as proposed by D'Ayala and Speranza (2002). Calvi (1999) developed a methodology where displacements are considered to be the primary indicator of damage for any seismic event. Meléndez et al. (2018) proposed a probabilistic vulnerability index method which is termed as Vulnerability Index Method probabilistic (VIM\_P) for seismic risk and vulnerability assessment of the building stock in Barcelona. Whitman et al. (1973) introduced empirical damage probability matrix for the probabilistic prediction of damage to buildings from earthquakes based on previous earthquake damage data. Spence et al. (1992) have developed continuous vulnerability curves based on parameter less scale of intensity (PSI). Kircher et al. (1997), discussed about the capacity spectrum methods in which the performance point of a structure is derived from the intersection of an earthquake demand spectrum, and a capacity curve (pushover curve), where the demand spectrum representing the ground motion during earthquake.

### 3 Description of the Methods

#### 3.1 Seismic Vulnerability Index Method

A simpler method using nonlinear parametric analysis and subsequently deriving the seismic vulnerability index for the seismic vulnerability assessment of reinforced concrete (RC) was proposed by Kassem et al. (2019) (Fig. 2). The authors developed this approach to study the seismic vulnerability of a school building at Ranau, Malaysia post Ranau earthquake in 2015. However this method is useful to determine the vulnerability classes of building stock by classifying the buildings based on seismic resistant design capacity as Low, Medium or High ERD (ERD-Earthquake Resistant Design). The authors have further proposed eight types of parameters to finally derive the vulnerability index of each vulnerability class. The eight parameters considered are: connections at beam-column joint, support type at foundation level, types of horizontal diaphragm, soil type of the building foundation, ductility of the building, structural irregularity in terms of mass ratios and grade of concrete. A series of nonlinear static analysis and nonlinear dynamic analyses are performed to evaluate the weightage of each parameter mentioned. Seismic Vulnerability Index (SVI) is thus determined from the Eq. (1). SVI value is deterministic and it ranges from 0 to 1.

$$SVI_{Building} = \frac{1.5 \sum N_i^c x_i + 1.0 \sum N_i^b x_i}{\sum N_i^c + \sum N_i^b x_i} \tag{1}$$

where,  $N_i^c$  and  $N_i^b$  denotes the number of plastic hinge(s) formation- in columns and beams respectively, and ‘i’ represents number assessing the performance level, where ‘i’ ranges from 1 to 6.  $x_i$  is the weightage factor of the beams and columns. For performance level (PL) < B,  $x_i = 0.000$ ; PL:B-IO,  $x_i = 0.125$ ; PL:IO-LS,  $x_i = 0.375$ ; PL:LS-CP,  $x_i = 0.625$ ; PL:CP-C,  $x_i = 0.875$ ; PL: C-D, D-E, > E,  $x_i = 1.000$ , as proposed by Kassem et al. (2019) (Fig. 1).

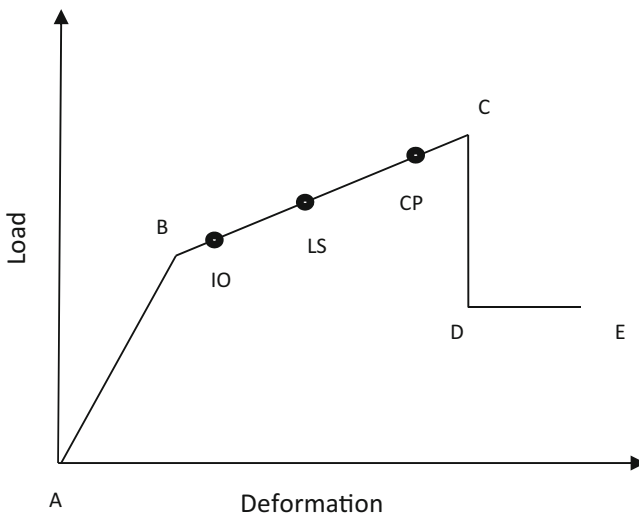
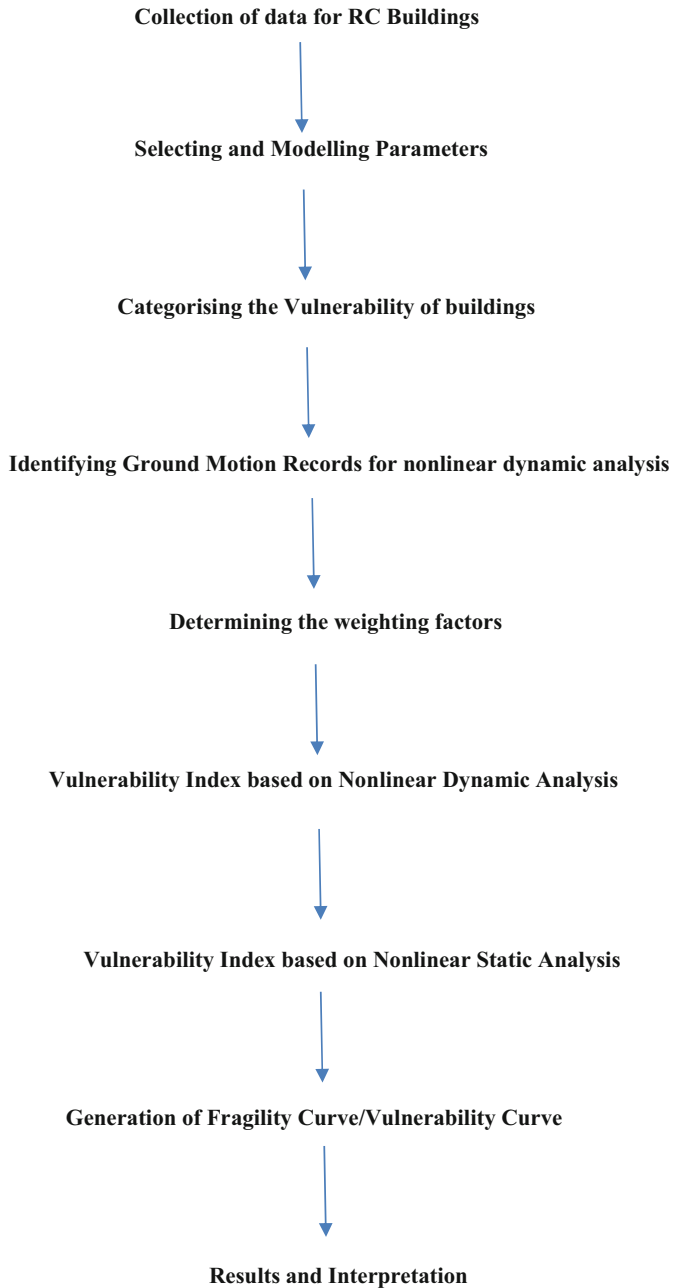


Fig. 1. Load-deformation curve indicating various performance level for the weight factor  $x_i$ .

**VARIOUS STEPS OF ANALYSIS IN SEISMIC VULNERABILITY INDEX (VI) METHOD**



**Fig. 2.** Various steps of Seismic Vulnerability Index (SVI) method as per Kassem et al. (2019).

Once the seismic vulnerability index (SVI) value is determined, the mean damage grade ( $\mu_D$ ) (where,  $(0 < \mu_D < 5)$ ) is evaluated for each building under study. For this purpose, a mean vulnerability function correlating seismic hazard with the said damage relating the SVI and the corresponding seismic intensity (PGA) is expressed. Subsequently using the SVI approach vulnerability curves relating mean damage grade vs. PGA can also be developed. This method may serve as an alternative to rapid visual screening method, as it is based on judgements and opinions of the experts, and previous damage record data. This method is analytically derived for vulnerability assessment of RC buildings, unlike the procedure from the Italian GNDT and European Macro seismic (EMS) approaches which were mainly focused on empirical data and vulnerability of masonry structures and steel structures. This method also serves as an effective tool to determine the economic damage index which is defined as the ratio of repair/renovation cost to replacement cost. The more is the index value the more is the economic losses. It also accounts for the rate of loss of human lives and other damages.

### 3.2 Basic Capacity Index Method

Capacity Index (Yakut 2004) is a method suited for low rise to mid-rise RC buildings. The method is of the concept that the higher the contribution of the concrete in a structural element, the higher would be the shear capacity of the reinforced concrete buildings and less will be the corresponding vulnerability. In this method, the capacity depends on the size, material property and the direction in which the capacity is computed for individual member, since as the direction changes the dimensions of individual structural element changes, and thus the shear strength capacity also changes for longitudinal direction and transverse direction for any RC buildings under considerations. The yield base shear capacity  $V_y$  generally does not take into account the effect of masonry infill walls, however one may relate the presence of masonry infill wall and its contribution to the shear capacity by calculating  $V_{yw}$  which is related to  $V_y$  by the equation

$$V_{yw} = V_y \left( 46 \frac{A_w}{A_f} + 1 \right) \quad (2)$$

where  $A_w$  indicates the total area of the infill wall and  $A_f$  indicates the total floor area of the building under consideration. The  $V_y$  is then used to calculate the  $V_c$ , the concrete base shear capacity which in turn is used to determine the Basic Capacity Index (BCPI). The BCPI (also known as yield over strength ratio) value is generally theoretical and is calculated as per Eq. (4). It does not consider the structural irregularities and the uncertainties in standard construction practices. To overcome this, the CPI is calculated by taking into consideration the limitations of BCPI and is calculated as per Eq. (6). The  $CPI_{limit}$  value is set by expert observation after survey and the calculated CPI value is expected to be of higher value than the  $CPI_{limit}$ , so that the building can have adequate life safety performance.



Following equations are used in finding the capacity index of the building:

$$V_y = (0.37n + 0.30)V_C \quad (3)$$

$$BCPI = \frac{V_y}{V_{code}} \quad (4)$$

$$CPI_{limit} = 0.05n + 0.45 \quad (5)$$

$$CPI = C_A \times C_M \times BCPI \quad (6)$$

where,

$V_c$  = The concrete base shear capacity.

$V_y$  = The yield base shear capacity.

$N$  = No. of stories.

$V_{code}$  = The base shear capacity as per codal provision.

$BCPI$  = Basic Capacity Index.

The CPI value has been taken by considering the architectural features and irregularity denoted by  $C_A$  and the variation in the standards of workmanship/construction practice denoted by  $C_M$ . CPI value is compared with the CPI limit value to know the probable performance of the structure. CPI limit values as already mentioned should be ideally smaller than the CPI value calculated. The higher the difference ( $CPI - CPI_{limit}$ ) the better is the performance expected from a building and lower will be the vulnerability. This method is based on strength based concept and the results may be inaccurate compared to the displacement based procedure. However quick vulnerability assessment of the large building stock is possible without detailed computation.

### 3.3 Japanese Seismic Index Method

As the name suggests, this method is widely used in Japan, for identifying the seismic performance of existing Reinforced Concrete buildings less than 06 (six) storeys. This method is prevalent in Japan since 1975 (JBDPA 1990). The performance of a building during a seismic event is evaluated by an index namely seismic performance index,  $I_S$ , which is calculated for individual storey in all possible frame direction within the particular building under study using the following equation:

$$I_S = E_0 S_D T \quad (7)$$

where  $E_0$  indicates the basic structural performance representing the energy dissipation capacity during the seismic event,  $S_D$  represents the index indicating the structural configuration for the particular building, and  $T$  is the index representing the time deterioration of the building under consideration.  $E_0$  can be calculated by the product of the shear force coefficient ' $\alpha$ ' and the ductility ' $\mu$ ' of the particular storey, under performance evaluation. Both  $S_D$  and  $T$  are empirically derived non-dimensional index.  $S_D$  takes into account the vertical or horizontal irregularity of a structure, the damage concentration of a structure, and the cumulative damage sustained by the structure.

The building deterioration and the development of cracks over time after the seismic event is accounted under the empirical index  $T$ , which is based on actual field survey data.

### 3.4 Hybrid Methods

Hybrid methods are the combination of empirical method and analytical method that are used to derive vulnerability curves. In this method the empirical data from previous earth quake record set along with damage statistics are used to simulate the numerical model of a particular building typology. It can be particularly useful where the empirical data reduces the computational effort to generate an analytical vulnerability curve using damage probability matrix. Kappos et al. (1995, 1998) in their study developed the damage probability matrices using hybrid methods, where the damage value against the respective intensity levels are selected using the previous ground motion record set following the Vulnerability Index method proposed by Benedetti and Petrini (1984).

### 3.5 Collapse Mechanism-Based Methods

Bernardini et al. (1990) proposed collapse mechanism-based methods by using ‘collapse multipliers’ for analytically assessing the vulnerability of a masonry building. The failure mechanism of the building during earthquake determines the value of collapse multipliers. It is calculated numerically for an in-plane shear failure during a seismic event and is denoted by  $I_1$ , where  $I_1$  can be defined, to be the ratio of the minimum value of shear strength considering both the directions  $x$  and  $y$  to the total weight  $W$  of the building.

$$I_1 = \frac{\min(V_x, V_y)}{W} \quad (8)$$

where  $V_x$  and  $V_y$  are the shear strengths at mid-storey level of the ground floor considering the  $x$  and  $y$  directions. The minimum value of  $V_x$  and  $V_y$  is considered for determining the collapse multiplier as the minimum shear strength will led to the cause of the early collapse of the masonry facade wall. The collapse mechanism occurring out of plane is defined by the collapse multiplier  $I_2$  where,  $I_2$  is the ratio of flexural strength of the facade/external wall to the total weight of the structure ( $W$ )

$$I_2 = \frac{\min(F_H + F_V)}{W} \quad (9)$$

where  $F_H$  and  $F_V$  are the minimum flexural strength of the horizontal and vertical strips of the most critical external wall.

### 3.6 Failure Mechanism Identification and Vulnerability Evaluation (FaMIVE) Method

FaMIVE as the name suggests is a procedure which identifies failure mechanism of the masonry structures mainly the URM (unreinforced masonry) buildings and the subsequent vulnerability evaluation. This method yields collapse load factor for each and every types of failure mechanism or collapse mechanism. A total of thirteen nos. of different failure mechanism are considered for the facade wall depending on the type of constraints between the facade wall and the rest of the structural members of the building. The said thirteen failure mechanism involves both in-plane failure mechanism, out of plane failure mechanism and the combined mechanism. The load factor is calculated for every individual facade of the building, and depending upon the masonry properties and connections between the structural members, the most probable failure mechanism is identified. It therefore helps in repair and renovation of the structure so as to mitigate or avoid the possible failure. It applies the pushover analysis for subsequent generation of the capacity curve and to locate the performance point graphically. Thus, this procedure helps to generate vulnerability functions for various masonry structures. This method has been used worldwide on various structures of historical importance for countries like India, Nepal, Italy etc. D'Ayala and Speranza (2002) have also used this procedure for vulnerability assessment of URM buildings.

### 3.7 Fully Displacement Based Method

This method as the name suggests is based on displacement of the structure due to seismic input, which serves as the damage indicator. It was first proposed by Calvi (1999), who proposed displacement as a damage parameter and developed seismic demand spectra for displacement. It is inspired by the principle introduced by Priestley (2003), who preferred direct displacement based design over strength based design approach of the framed structures. The multiple degree of freedom generally present in a framed building is simplified and modelled as a single degree of freedom (SDOF) structures (Fig. 3). In this approach  $K_e$  effective stiffness is considered instead of initial stiffness  $K_i$  unlike force based design approach. This method is non-iterative or very less iteration is required, hence it provides the displacement limit profile directly without any intensive computation for any given building stock. It is an effective tool for vulnerability assessment specially for a large building stock by estimating the losses in a cost-effective manner.

### 3.8 Rapid Visual Screening Method

This method was used for the first time in the year 1988 in the United States. It is basically an empirical method with a preliminary vulnerability approach without involving any detailed calculation and investigation. It is later on modified by introducing suitable modifications and assigning scores against each parameter detailed in FEMA P 154, 2015 (Third Edition). This procedures involves only visual inspection of the structures by a trained personnel while merely walking around the structures and collecting data. This procedure is not suitable for buildings having complex details,

however can provide a basic guidance for further detailed analysis and disaster mitigation process.

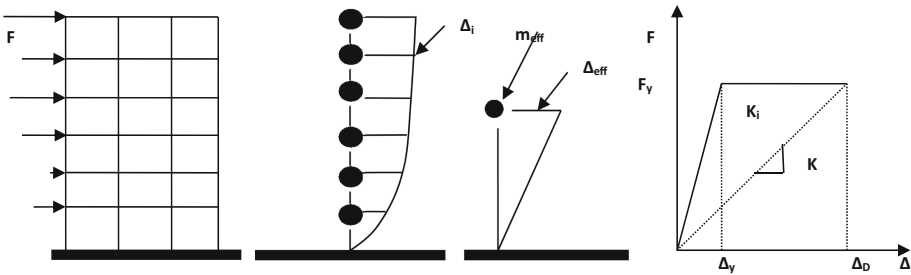


Fig. 3. Equivalent SDOF system.

### 3.9 The Analytic Hierarchy Process (AHP)

This method is the process of developing a hierarchy model to decide the most effective criteria and their relative weights to finalise a complex decision. This method is a part of Multi Criteria Decision Making (MCDM) process. This technique can also be used in seismic vulnerability assessment of a specific area and to generate a pair wise comparison matrix of different criteria related to vulnerability assessment. The criteria may be categorised with a single objective/goal or may be multi objective. The multi objective goals can be under a single primary goal. As for example, if we take preparation of a seismic vulnerability assessment map as a primary goal, there may be structural parameters and geological parameters as the secondary goal. Each secondary goal can have different criteria relevant to vulnerability assessment. The criteria are to be selected wisely based on knowledge and experience. The hierarchy model is developed with primary goal at level 1, secondary goals at level 2, various criteria at level 3, development of pairwise matrix at level 4 and evaluating the relative weights and consistency index (CI) and finalising the matrix. Level 5 is the last step that provides the result of the decision making process with a priority rank of each assessment criteria, which concludes the entire process of AHP. However the AHP method needs to be supplemented by empirical and analytical methods used for the buildings under consideration. A seismic vulnerability map can thus be developed with area having less vulnerable to more vulnerable structures. This method was first used and developed by the famous statistician Saaty in the decades of 1970s, which was subsequently modified as per the use by various researchers, statistician and mathematicians. A schematic flow chart of the AHP process is given below (Fig. 4).

### 3.10 GIS Method of Vulnerability Assessment

A geographic information system (GIS) is basically a framework that allows to capture and analyse the geographic and spatial data for vulnerability assessment of the area of interest. It also helps in identifying the topography of the building site and ascertains possibility of new construction. With technological advancements, this method has

become one of the fastest and cost-effective method for vulnerability assessment compared to the traditional method. GIS is also a semi-empirical assessment approach. A seismic hazard analysis of a particular city or town can be made by the help of the software called GIS Arc. Various other GIS based app and commercial software are also recently developed. Currently the GIS data can be digitally stored and a digital map can be developed for any area by converting and manipulating data as per requirement.

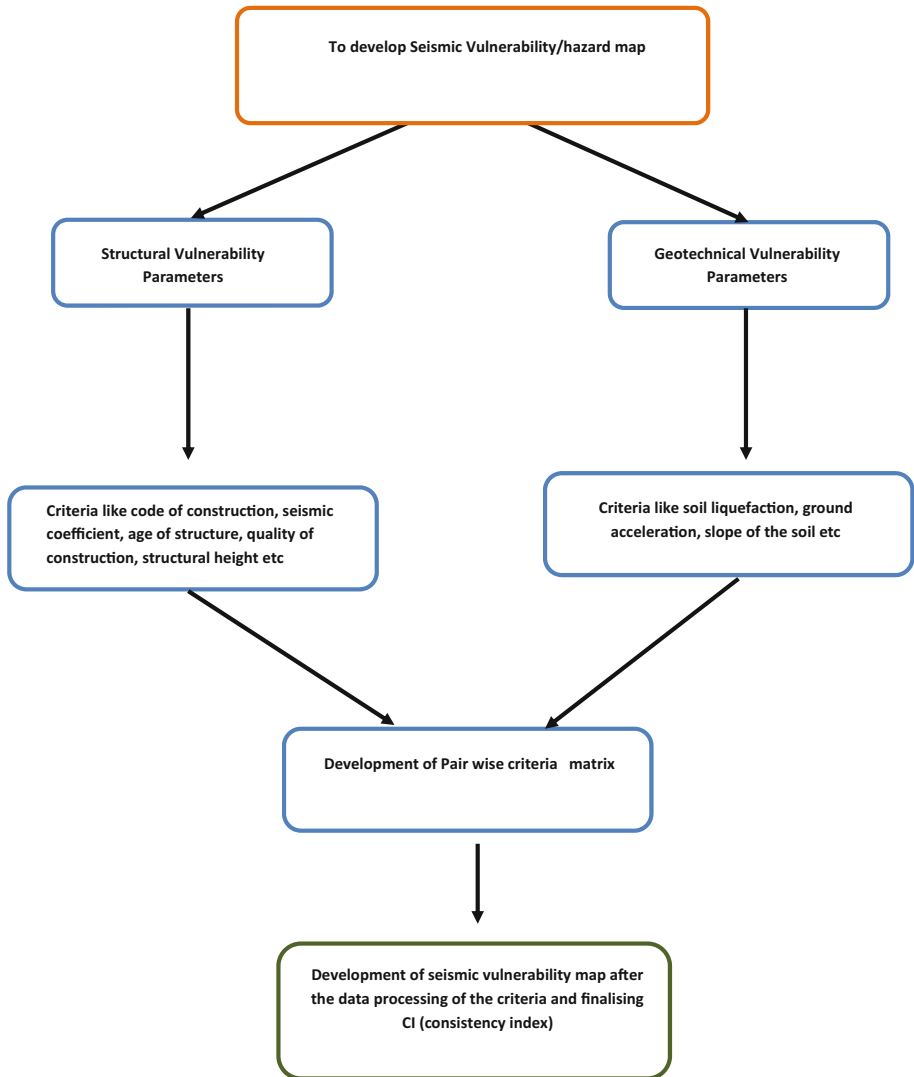


Fig. 4. Development of a seismic vulnerability map using AHP.

### 3.11 The Internet-Based Seismic Vulnerability Assessment Method

This method is developed as a preliminary step for seismic vulnerability assessment and cannot be considered decisive until reviewed and verified by the experts, as it involves the common people who are not technically qualified to judge every structural detail of their individual building. However it allows the common people staying on their individual residential buildings to access the primary server and to enter their respective building related information. The information are stored and processed serially. The users are provided with two types of approaches i) simple approach and ii) detailed and complex approach for vulnerability evaluation. The users may enter data accordingly depending on their level of competency and understanding. Once the data are entered and sent into the primary servers, the data are processed through a software to generate results with a detailed report about the seismic deficiency of the structure, site soil report, seismic hazard of the area where the building is located; along with many other important details, which can be obtained in a printed form. The reports are sent back to the user accordingly. Internet based approach combines multiple advantages but there are also associated disadvantages on its use. The advantages can be listed as follows:

- a) Different users are allowed to access the internet simultaneously.
- b) There is no time limitation of using the internet and the users can access the internet as per their own convenience and comfort.
- c) This method does not require any trained personnel to enter the building details which eliminate the hiring cost of the technical expert.
- d) This method does not involve any cost as such and hence it is beneficial for the lower income group to evaluate the seismic vulnerability of their buildings. The combined data of various users form a comprehensive database comprising of various details of the buildings, which further helps for additional assessment by the experts and formulate retrofitting strategies.

The main disadvantages of this method include:

- a) The data are not individually reliable and has to be supplemented by other established vulnerability assessment procedures or from previous valid data sources.
- b) There is no accountability for wrong data or inappropriate data entered by the users which may cause severe damages to the structure reported with low vulnerability, for future earthquakes and cannot have any legal locus standi.

The main intent of the said method is outlined in the following as follows:

- i) To develop a seismic vulnerability assessment tools (which is also cost effective) in an online platform for various types of existing and newly designed reinforced concrete structures.
- ii) To minimise the difficulties due to the lack of technical experts to collect data from the wide variety of buildings in a country.
- iii) To expedite the vulnerability assessment procedure, this will further help in retrofitting works in the worst affected area anticipating future major earthquake
- iv) To develop a global approach this may be useful for various countries of the world as well

- v) To make the common people literate at a primary level about earthquake risk and vulnerability of buildings.
- vi) To spread basic civil engineering knowledge and construction practices among the masses
- vii) To adjust and calibrate new weighting factors by matching with building information recorded at the database after occurrence of an earthquake, and in the process evolving a new coefficient by correlating with the damage level after each seismic event.

### 3.12 Probabilistic Vulnerability Index Method (VIM\_P)

The most widely used method for seismic vulnerability assessment is the Vulnerability Index Method (VIM), because of its simple approach which involves the seismic hazard analysis, seismic vulnerability analysis and damage evaluation by generating damage probability matrix. However the results obtained are deterministic in nature and does not include the structural uncertainties. Hence the VIM\_P is the extension of VIM method which quantifies the annual loss estimation in a probabilistic approach. It considers five damage grades (D1 to D5) based on physical damage observation and evaluates the probability of frequency exceedance of a certain damage grade determined annually, under a given macro seismic intensity and computed vulnerability index under VIM. As earlier mentioned VIM provides the deterministic value and it ranges between 0 to 1 from less vulnerable to more vulnerable depending on the structural characteristics, storey height and typology etc. The probabilistic approach studies the reliability of the vulnerability index calculated. In other words, suppose a building attains the value of 0.5 as a vulnerability index in the deterministic approach, however for the same value, a building may develop three types of vulnerability curves described by three types of probability density functions and the curves thus generated can be named *lower*, *best* and *upper*. The '*best curve*' is considered to be the probable vulnerability of a particular building with a minimum uncertainty compared to the lower and upper curves. This seismic vulnerability computed is linked with the seismic hazard of the area and the damage functions to evaluate the seismic risk. USERRISK 2015 software computes the seismic risk of the structure by using VIM\_P method. Melendez et al. (2018) have also determined the seismic risk of around 70000 buildings by using VIM\_P method.

### 3.13 Seismic Vulnerability Based on Current Seismic Code

Most of the seismic codes across the globe considers the building to sustain under minimum lateral earthquake force. The different standards provide the minimum design force related to the earthquake resistant design of buildings and for various other special structures. The latest Indian Code for earthquake resistant design of structures IS 1893:2016 (Part1) has been modified from its previous edition of IS 1893:2002 to

ensure better sustainability of structures with reference to strong ground shaking during earthquake. The codal standards of a particular country are related to the International Building Code standards, ASCE and FEMA guidelines of USA and other standard seismic regulations practised in different countries, keeping in view the standard practices and guidelines of its own country. However with every codal revision, the older structures especially the important structures require a vulnerability assessment for future earthquakes along with the structures constructed without any codal guidelines. In such a case various empirical and analytical methods can be applied for vulnerability assessment of such structures and can be compared with different limits proposed in the current seismic codes. The structures that are detected with low or insufficient earthquake resistance needs to be retrofitted and strengthened as far as practicable, if the re strengthening is economical compared to the replacement.

### 3.14 Damage Probability Matrices

Damage data of previous earthquakes on various structural typologies construct a damage probability matrix. As the name suggests, it gives a probabilistic idea of damage to be experienced by the structures from future earthquakes having similar typology. In this method all sorts of structural and non –structural damage are expressed in terms of damage ratio (repairing/renovation cost to the replacement cost) which in turn relates to the Modified Mercalli intensity scale. This method is basically an empirical approach where several thousands of earthquake data based on their extent of damage are quantified and expressed in the numerical range of damage ratios. The damage probability matrix initially derived by Whitman et al. (1973) to take stock of the extent of damage occurred after the 1971 San Fernando earthquake and it was further modified by Braga et al. (1982) based on MSK scale which was later on updated by Di Pasquale et al. (2005) where the damage is related to MCS scale. All the said DPMs are expressed in a discrete manner and the probability of reaching damage state ‘d’ corresponding to the ground motion intensity ‘i’ is expressed as  $P[D = d/i]$ .

### 3.15 Analytically Derived Vulnerability Curve and DPMs

In current era, with the technological development and evaluation of computer based program, computational analysis has become much easier, which led to the development of analytical vulnerability curves and damage probability matrix (DPMs). The analytical methods possess more detailed vulnerability algorithm, evaluation of numerical model and performing linear and nonlinear analysis through finite element software, which relates to the building stocks or representative building(s) under consideration. Various nonlinear dynamic analysis are carried out with various set of ground motion records (both near field and far field record) on different categories of buildings to evaluate the probable damage state of the structures, which are subsequently used for the derivation of analytical DPM s (using the Modified Mercalli Intensity Scale) by deriving damage index globally corresponding to damage state



obtained by using the Park and Ang (1985) Damage Index model because of its simplicity and reliability of use validated by statistical data of previous earthquakes. Analytical fragility or vulnerability curves are obtained using the spectral acceleration as the ground motion parameter and carrying out the nonlinear time history analysis to obtain the center of mass displacement of structure and to generate the IDA (incremental dynamic analysis) curve based on inter storey drift ratio, which further leads to the development of fragility curve. The analytical methods can be deterministic or probabilistic in nature. Singhal and Kiremidjian (1996) in their paper proposed the use of analytically derived fragility (or vulnerability) curves along with damage probability matrices for three types of RCC buildings that are low rise, mid-rise and high rise in elevation, using Monte Carlo simulation. The analytical method has proved to be useful where there is limited or no ground record data sets available for the previous earthquakes. However analytical methods are generally computationally intensive, which becomes a concern for vulnerability assessment when there is time constraint or limited time available to generate damage data for a large number of building stocks. Further there will always be a certain degree of uncertainty involved when vulnerability curves or DPMs are to be derived for variety of complex construction pattern of buildings developed with various seismic codes or non codal buildings. Singhal and Kiremidjian (1998) have done a reliability study post North Ridge earthquake 1994 made a detailed field survey of around 84 buildings and updated (with the help of Bayesian updating technique) their previous results based on analytical study in 1996. Thus it can be concluded that analytical method by itself may not be self-sufficient and therefore empirical data, previous reliable data sets need to be supplemented for a reliable analytical study.

### 3.16 Continuous Vulnerability Curves

Vulnerability curves based on continuous scale unlike the discrete scale of damage probability matrix (DPM) is called the continuous vulnerability curves. Spence et al. (1992) generated this curve using a parameter less scale of intensity (PSI) to obtain the continuous vulnerability function for the observed damage of the RC structures/buildings based on the MSK damage scale. Thus the conditional probability of obtaining various damage levels (D1 to D5) with respect to PSI is used to obtain the vulnerability curves (Fig. 5). Orsini (1999), derived similar kind of vulnerability curves with respect to the building stocks of Italy. PSI was subsequently converted to PGA (peak ground acceleration) by correlating with the empirical parameters with an aim to differentiate the ground motion intensity and damage intensity. In some cases, empirical vulnerability curves are obtained using  $S_a$  (spectral acceleration) or  $S_d$  (spectral displacement) as ground parameter instead of PGA and this has proved to obtain more realistic correlation between ground motion and damage incurred by the structure.

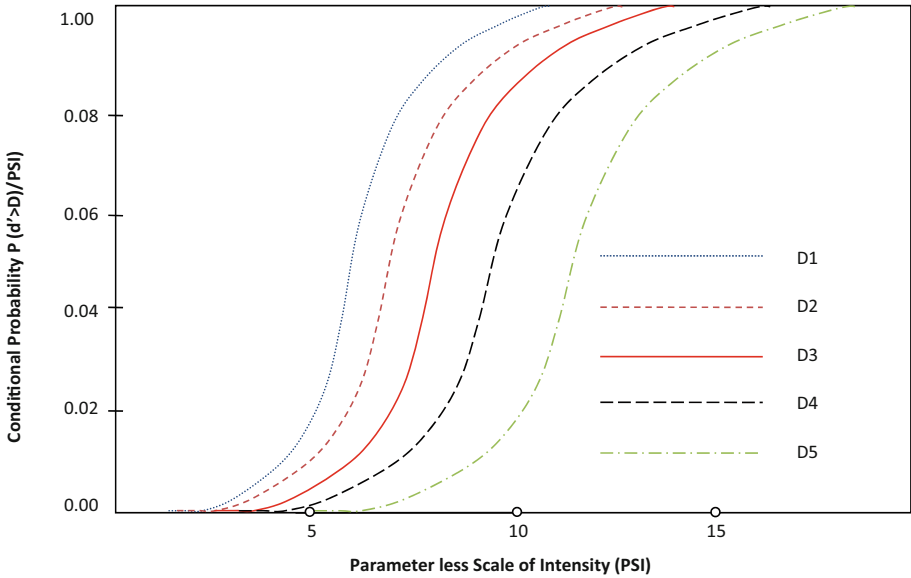


**Fig. 5.** Vulnerability curves using the parameter less scale of intensity (PSI); D1 to D5 relate to damage levels.

### 3.17 Capacity Spectrum Methods

Capacity spectrum methods or CSM is a rapid vulnerability assessment procedure based on performance based design concept. This method can be used for a large number of building stocks easily comprising of both new and existing structures. However a prior knowledge of the prevalent different types of structures is essential so as to generate the capacity spectrum of the area under study. This method can be useful for design proof checking of new buildings, damage state evaluation of existing buildings. The pushover analysis or nonlinear static analysis is performed for the geometric model of the particular buildings to obtain the push over curve or capacity curve having base shear (representing the ground motion input on the structure) at the x-axis and the corresponding roof displacement of the structure at the y-axis. The capacity curve so obtained is transformed to corresponding spectral acceleration and spectral displacement and by superimposing with the seismic demand spectra; the capacity spectrum is obtained (Fig. 6). The seismic demand spectra are basically a response spectra corresponding to the different levels of viscous damping percentage. The graphical intersection of capacity spectrum curve and response spectra curve depicts the ‘performance point’ of the structure with corresponding level of damping. This method was first used on 1970’s for vulnerability assessment of buildings of a naval shipyard at Bremerton, USA.

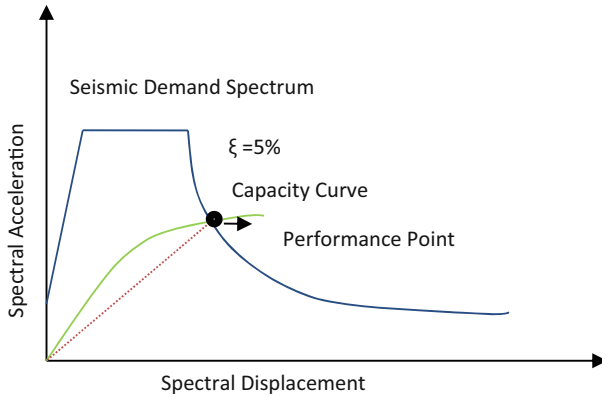


**Fig. 6.** A typical Capacity Spectrum (with 5% viscous damping) for a building.

## 4 Conclusions

A review of some of the significant methods to assess vulnerability, prevalent over the past few decades have been discussed and presented. This review might not consider the complete set of vulnerability assessment methods proposed or in use till date; however the popular and the widely accepted methods, for which detailed work procedures are in record, believed to be included.

From the above discussed methods, it may be concluded that an appropriate, ideal and reliable methods should include the following properties, mainly

- The state of art procedure of seismic hazard/vulnerability assessment should be taken into account.
- The vulnerability assessment procedures must be cost effective and should not be too complicated
- The vulnerability assessment procedures must be elaborative enough to incorporate all sorts of details related to the concerned building stock, uncertainties if anything considered should be described in qualitative terms or in quantitative terms as per necessity.
- The vulnerability procedure should be compatible to different types of structures suitable for various typologies, and also can be applied to different construction methods and practices around the world, as well as for new type of structures. It also should indicate the various estimated loss for the existing building, which will enable suitable retrofitting strategies.
- The vulnerability assessment should not be too computationally intensive as it will not be feasible in case of emergency management, however there must be sufficient reliability of the results obtained.

Overall, a single methodology might not incorporate all sorts of features, which meets the above requirements. As for example, an analytical method considering detailed data for a building stock might not be validated with the empirical data or from the past recorded data source. Similarly, an empirical method might not be feasible to

incorporate all sorts of structural details which can be tested in a lab and also the structural uncertainty involved for the existing buildings. Further the seismic demand to be experienced by a structure cannot also be accurately predicted. Thus an ideal methodology should minimise all sorts of uncertainty involved while generating results, and also an ideal methodology may incorporate all possible and positive features of various other assessment procedures. A multiple assessment approaches might also be taken into consideration so that the deficiencies of a particular method can be compensated with another method. With the development of seismic guidelines, codal provisions and performance based design; vulnerability assessment procedures are also expected to be more flexible along with large scope of application under different circumstances. Thus a suitable vulnerability procedure not only mitigates the effects of seismic hazard, but also with a continuous improvement in the prediction of losses will mitigate the disastrous impact on the society and the economy of the state.

## References

- Ashim, A., Rama Mohan, R.K., Dipendra, G., Hemchandra, C.: Seismic vulnerability and retrofitting scheme for low-to-medium rise reinforced concrete buildings in Nepal. *J. Build. Eng.* **21**, 186–199 (2019). <https://doi.org/10.1016/j.jobbe.2018.10.015>
- Antoniou, S., Pinho, R.: Development and verification of a displacement-based adaptive pushover procedure. *J. Earthq. Eng.* **8**(5), 643–661 (2004). <https://doi.org/10.1080/13632460409350504>
- Bernardini, A., Gori, R., Modena, C.: Application of coupled analytical models and experimental knowledge to seismic vulnerability analyses of masonry buildings. In: Koridze, A. (ed.) *Engineering Damage Evaluation and Vulnerability Analysis of Building Structures* Omega Scientific, Oxon (1990)
- Benedetti, D., Petrini, V.: Sulla Vulnerabilità Di Edifici in Muratura: Proposta Di UnMetodo Di Valutazione. *L'industriadelleCostruzioni* **149**(1), 66–74 (1984)
- Calvi, G.M.: A displacement-based approach for vulnerability evaluation of classes of buildings. *J. Earthq. Eng.* **3**(3), 411–438 (1999)
- Calvi, G.M., et al.: Development of seismic vulnerability assessment methods for the past 30 years. *ISET J. Earthquake Technol.* **43**(3), 75–104 (2006)
- Coskun, O., Aldemir, A., Sahmaran, M.: Rapid screening method for the determination of seismic vulnerability assessment of RC building stocks. *Bull. Earthq. Eng.* **18**(4), 1401–1416 (2019). <https://doi.org/10.1007/s10518-019-00751-9>
- D'Ayala, D., Speranza, E.: An integrated procedure for the assessment of seismic vulnerability of historic buildings. In: *Proceedings of the 12th European Conference on Earthquake Engineering*, London, U.K., Paper No. 561 (2002)
- Dilmaç, H.: Preliminary assessment approach to predict seismic vulnerability of existing low and mid-rise RC buildings. *Bull. Earthq. Eng.* **18**, 1–33 (2020). <https://doi.org/10.1007/s10518-020-00809-z>
- Earthquake Damage Evaluation Data for California Report ATC-13*, ATC (1985), Applied Technology Council, Redwood City, California, U.S.A
- Erdil, B., Ceylan, H.: A detailed comparison of preliminary seismic vulnerability assessment methods for RC buildings. *Iranian J. Sci. Technol. Trans. Civil Eng.* **43**(4), 711–725 (2019). <https://doi.org/10.1007/s40996-019-00234-6>

- JBDPA: Standard for Seismic Capacity Assessment of Existing Reinforced Concrete Buildings. Japanese Building Disaster Prevention Association, Ministry of Construction, Tokyo, Japan (1990)
- Kappos, A.J., Ptilakis, K. And Stylianidis, K.C.: Cost-benefit analysis for the seismic rehabilitation of buildings in Thessaloniki, based on a hybrid method of vulnerability assessment. In: Proceedings of the Fifth International Conference on Seismic Zonation, Nice, France, vol. 1, pp. 406–413 (1995)
- Kassem, M.M., Nazri, F.M., Farsangi, E.N.: Development of seismic vulnerability index methodology for reinforced concrete buildings based on nonlinear parametric analyses. *MethodsX* **6**, 199 (2019). <https://doi.org/10.1016/j.mex.2019.01.006>
- Kircher, C.A., Nassar, A.A., Kustu, O., Holmes, W.T.: Development of building damage functions for earthquake loss estimation. *Earthq. Spectra* **13**(4), 663–682 (1997)
- Aguilar-Meléndez, A., et al.: A probabilistic approach for seismic risk assessment based on vulnerability functions. application to Barcelona. *Bull. Earthq. Eng.* **17**(4), 1863–1890 (2018). <https://doi.org/10.1007/s10518-018-0516-4>
- Mosleh, A., Rodrigues, H., Varum, H., Costa, A., Arêde, A.: Seismic behaviour of RC building structures designed according to current codes. *Structures* **7**, 1–13 (2016). <https://doi.org/10.1016/j.istruc.2016.04.001>
- Nanda, R.P., Majhi, D.P.: Rapid seismic vulnerability assessment of building stocks for developing countries. *KSCE J. Civil Eng.* **18**(7), 2218–2226 (2014). <https://doi.org/10.1007/s12205-014-0050-0>
- Orsini, G.: A model for buildings' vulnerability assessment using the parameterless scale of seismic intensity (PSI). *Earthq. Spectra*. **15**(3), 463–483 (1999)
- Panahi, M., Rezaie, F., Meshkani, S.A.: Seismic vulnerability assessment of school buildings in Tehran city based on AHP and GIS. *Nat. Hazards Earth Syst. Sci.* **14**, 969–979 (2014). <https://doi.org/10.5194/nhess-14-969-2014>
- Patil, V.S., Tande, S.N.: Probabilistic seismic performance assessment of brick masonry infill reinforced concrete building. *Int. J. Adv. Struct. Eng.* **10**, 263–274 (2018)
- Park, Y.J., Ang, A.H.S.: Mechanistic seismic damage model for reinforced concrete. *J. Struct. Eng.* **111**(4), 722–739 (1985)
- Priestley, M.J.N.: *Myths and Fallacies in Earthquake Engineering, Revisited: The Mallet Milne Lecture, 2003*. IUSS Press, Pavia, Italy (2003)
- Rapid Visual Screening of Buildings for Potential Seismic Hazards: A Handbook FEMA P-154/January 2015. Third Edition (2015)
- Rapid Visual Screening of Buildings for Potential Seismic Hazards: A Handbook, Report ATC-21, ATC. Applied Technology Council, Redwood City, California, U.S.A (1988)
- Ricci, P., Domenico, M.D., Verderame, G.M.: Effects of the in-plane/out-of-plane interaction in URM infills on the seismic performance of RC buildings designed to Eurocodes. *J. Earthq. Eng.* **26**, 1595–1629 (2020). <https://doi.org/10.1080/13632469.2020.1733137>
- Ricci, P., Del Gaudio, C., Verderame, G.M., Manfredim, G., Pollino, M., Borfecchia, F.: Seismic vulnerability assessment at urban scale based on different building stock data sources. In: Conference Paper, June 2014 (2014). <https://doi.org/10.1061/9780784413609.104>
- Ródenas, J.L., Tomás, A., Garcia, A.S.: Advances in seismic vulnerability assessment of reinforced concrete buildings applied to the experience of Lorca (Spain) 2011 earthquake. *Int. J. Comp. Meth. Exp. Meas.* **6**(5), 887–898 (2018). <https://doi.org/10.2495/CMEM-V6-N5-887-898>
- El-Betar, S.A.: Seismic vulnerability evaluation of existing R.C. buildings. *Housing Build. Natl. Res. Center. (HBRC) J.* **14**, 189–197 (2018). <https://doi.org/10.1016/j.hbrcej.2016.09.002>
- Seismic Evaluation and Retrofit of Concrete Buildings, Report ATC-40, ATC. Applied Technology Council, Redwood City, California, U.S.A (1996)

- Singhal, A., Kiremidjian, A.S.: Method for probabilistic evaluation of seismic structural damage. *J. Struct. Eng. ASCE* **122**(12), 1459–1467 (1996)
- Singhal, A., Kiremidjian, A.S.: Bayesian updating of fragilities with application to RC frames. *J. Struct. Eng. ASCE* **124**(8), 922–929 (1998)
- Spence, R., Coburn, A.W., Pomonis, A.: Correlation of ground motion with building damage: the definition of a new damage-based seismic intensity scale. In: *Proceedings of the Tenth World Conference on Earthquake Engineering*, Madrid, Spain, vol. 1, pp. 551–556 (1992)
- Vicente, R., Parodi, S., Lagomarsino, S., Varum, H., Da Silva, J.A.R., Mendes: Seismic vulnerability assessment, damage scenarios and loss estimation case study of the old City Centre of Coimbra, Portugal. In: *The 14th World Conference on Earthquake Engineering* 12–17 October 2008, Beijing, China (2008)
- Whitman, R.V., Reed, J.W. and Hong, S.T.: Earthquake damage probability matrices. In: *Proceedings of the Fifth World Conference on Earthquake Engineering*, Rome, Italy, vol. 2, pp. 2531–2540 (1973)
- Yakut, A.: Preliminary seismic performance assessment procedure for existing RC buildings. *Eng. Struct.* **26**(10), 1447–1461 (2004)



# Advancement in Direct Displacement-Based Design: A Review

Manish Pal<sup>(✉)</sup> and Satyabrata Choudhury

Department of Civil Engineering, National Institute of Technology Silchar,  
Silchar, India

{manish\_pg, chou\_s}@civil.nits.ac.in

**Abstract.** Earthquakes are the most disastrous forces which cannot be stopped but their effects can be diminished with minimal casualties. Over the period of time, the seismic design procedure has evolved in many ways. Traditional force-based design cannot be design structure for a particular intended performance objective. The latest approach for seismic design of the structure is displacement-based, because displacement is a better indicator of damage. Direct displacement-based design is one kind of displacement-based design, firstly proposed by Priestley (1993). In this approach the structure is converted into an equivalent single-degree of freedom system. With the help of displacement spectrum for the known limit of design displacements one can determine the effective period. After calculating the effective time period, the stiffness and the base shear are calculated. Further, this design philosophy has been developed by other researchers and the multi-degree of freedom system also has been used in place of the equivalent single-degree of freedom system. This method not only consider the higher mode effect but also considers the P- $\Delta$  effect. Finally, unified performance-based seismic design also been advocated which can accommodate both drift and member performance level in the design process.

**Keywords:** Ductility · Direct displacement-based design · Equivalent single-degree of freedom system · Equivalent modal damping ratio · Unified performance-based design

## 1 Introduction

Over the last five decades, the design method for structural seismic design has been reviewed with the goal of addressing the flaws in conventional force-based codal design (FBD). The prime contrast from force-based design is that displacement-based design is able to design a structure for a particular intended target performance objective such as design drift, plastic rotation, crack width etc. Direct displacement-based design (DDBD) is one kind of displacement-based design (DBD) in which design displacement can be computed directly. In this approach the structure is to be designed for a particular intended target design displacement by an equivalent single-degree of freedom (ESDOF) representation but not considering the performance level

in the design philosophy. This is based on the Substituting the Structure to an equivalent SDOF system.

The basic principle behind the design philosophy is to design a structure which would achieve the target design drift as well as considering the performance level under a given seismic intensity. Among all of the philosophies of DBD, one can mention (Moehle 1992; Chopra and Goel 2001; Panagiotakos and Fardis 2001; Priestley 1993; Priestley and Kowalsky 2000; Pettinga and Priestley 2005; Priestley et al. 2007; Sullivan et al. 2006; Calvi and Sullivan 2008; Sullivan et al. 2012; Chandurkar and Pajgade 2013). The DBD method of Priestley and Kowalsky (2000); Priestley (2005) and Sullivan et al. (2006) are called direct migration-based approach (DDBD), which is very realistic and highly modern method. The complete book (Priestley et al. 2007), two example codes (Clavi and Sullivan 2008; Sullivan et al. 2012) and some articles (Priestley 1993; Priestley et al. 2008) are also helpful to understand.

The most important issue in DDBD is while designing the multi-degree of freedom system (MDOF), we convert the MDOF system into an equivalent SDOF system for our convenience. By doing that, we neglected the higher modes effects as well as the P- $\Delta$  effects. Which means we are considering that the structure is first mode dominating structure. This problem partially resolver by the researcher by introducing the factor on distributing the base shear (Calvi and Sullivan 2008; Sullivan et al. 2012).

The drawback of considering ESDOF system further eliminated by Muho et al. (2020), by considering an equivalent elastic MDOF system replaces with the original MDOF structure. Both the structure are equivalent in the work dissipation domain, means the dissipation of energy because of the hysteresis force is equivalent to the dissipation of energy by the viscous force. The modal displacement are inter-related to the target inter-storey drift ratios. The modal periods can thus be estimated from the displacement spectrum. The desired effective stiffness and modal base shear can be calculated using those modal periods. Combination rule can be used to find out the final design base shear.

Those modification on modern DDBD seismic design prosses can eliminate the disadvantages of FBD as well as the conventional DDBD design prosses. In the modern DDBD design process displacement spectrum is used instead of acceleration spectrum and the use of deformation dependant modal equivalent damping ratios makes the design process more accurate and the P- $\Delta$  effects and higher modes affects are also considered.

## 2 Force-Based Design Procedure

Over the past few years researcher and engineers says that the forces developed in the structure is a function of period and the ground accelerations. In this design method the main objective is to design a structure for a particular force. In the traditional method of designing, on the basis of the structure's estimated fundamental period and an elastic response spectrum, which represents the seismicity of the site, equivalent seismic base shear is determined. (*EC-8; IS-1893(1)-2016*). The type of structure, its location and significance, as well as the composition of the foundation soil, all influence the design base shear value. The base shear is adjusted along the height using an empirical



relationship based on weighted average to determine the story level forces. According to force-based design fundamental time period is estimated by some empirical-experimental formula for those first mode dominating structure within the elastic limit.

As per **IS:1893 part (1)-2016**

The design horizontal seismic co-efficient may computed and finally multiplied with the seismic weight of the system or structure to get design base shear.

Design horizontal seismic co-efficient ( $A_h$ ) is given by Eq. (1).

$$A_h = \frac{ZIS_a}{2Rg} \tag{1}$$

where,  $R$  is response reduction factor,  $Z$  is zone factor,  $I$  is importance factor,  $S_a/g$  is spectral acceleration ration.

Design base shear ( $V_b$ ) is given by Eq. (2).

$$V_b = A_h W \tag{2}$$

The final design base shear then finally distributed by some mass proportional based formula.

$$Q_i = V_b \frac{w_i h_i^2}{\sum w_i h_i^2} \tag{3}$$

where,  $w_i$  is seismic weight and  $h_i$  is the height of  $i$ -th floor and  $Q_i$  is force at level  $i$ .

As per **NZS 1170.5:2004**

Design horizontal base shear ( $V_b$ ) is given by Eq. (4).

$$V_b = C_d(T) W_t \tag{4}$$

where,  $C_d(T)$  is the horizontal design action co-efficient and  $W_t$  is the seismic weight of the structure. The horizontal design action co-efficient computed as

$$C_d(T) = \frac{C(T)S_p}{k_\mu} \tag{5}$$

where,  $C(T)$  is the ordinate of the elastic site hazard spectrum for horizontal loading,  $S_p$  is the structural performance factor.

$$C(T) = C_h(T) Z R N(T, D) \tag{6}$$

where,  $C_h(T)$  is spectral shape factor,  $Z$  is the hazard factor,  $R$  is return period factor,  $N(T, D)$  is the near-fault factor.

The final design base shear then finally distributed by Eq. (7).

$$F_i = F_t + 0.92(V_b) \frac{w_i h_i}{\sum_{i=1}^n (w_i h_i)} \tag{7}$$

where,  $F_t = 0.08V_b$  at the top level and zero elsewhere.

As per **UBC 1997**

Design base shear ( $V_b$ ) is given by Eq. (8).

$$V_b = \frac{C_v I}{RT} W \quad (8)$$

where,  $C_v$  is seismic co-efficient,  $I$  is importance factor,  $R$  accounting for ductility and overstrength,  $W$  is seismic weight,  $T$  is fundamental time period.

The final design base shear then finally distributed by some mass proportional based formula.

$$F_x = \frac{(V_b - F_t)W_x H_x}{\sum W_i h_i} \quad (9)$$

where,  $V_b$  is base shear,  $F_x$  is force at level  $x$ ,  $F_t$  is force at level  $t$  and  $h_i$  is the height of  $i$ -th floor.

As per **IBC 2006**

Design base shear ( $V_b$ ) is given by Eq. (10).

$$V_b = \frac{1.2S_{DS}}{R} W \quad (10)$$

where,  $S_{DS}$  is design elastic response acceleration at short period.

The final design base shear then finally distributed by Eq. (11).

$$F_x = \frac{1.2S_{DS}}{R} W_x \quad (11)$$

where,  $F_x$  is force,  $W_x$  is portion of seismic weight at level  $x$ .

As per **EC-8: (2004)**

Design horizontal base shear ( $F_b$ ) is given by Eq. (12).

$$F_b = S_d(T)m\lambda \quad (12)$$

where,  $S_d(T)$  is ordinate of design spectrum,  $m$  is total mass of the structure,  $\lambda$  is correction factor for time period.

The final design base shear then finally distributed by Eq. (13).

$$F_i = F_b \frac{s_i m_i}{\sum s_j m_j} \quad (13)$$

where,  $F_i$  is force,  $s_i, s_j$  are displacement of masses  $m_i, m_j$ .

It has been observed, that force is a bad indicator of damage and it is not possible for a designer to design a structure for some intended target displacement. Because of this limitation the design process has been developed and a new design philosophy came which overcomes all the drawbacks of FBD.

### 3 Displacement-Based Design Procedure

Overcoming the flaws of FBD a new concept of design has been introduced over the last few years. It has been seen that the structures are designed not for the particular force, it has been designed for the displacement satisfying some inter-storey drift ratio limits. As displacement is a better indicator of damage rather than force this design approach is much more appropriate and designer can design a structure for some design displacement.

In displacement-based design the structure is assumed to show inelastic behaviour which includes the ductility concept. Which also emphasized using displacement demand in proportional with target ductility to calculate required system capacity (Fig. 1).

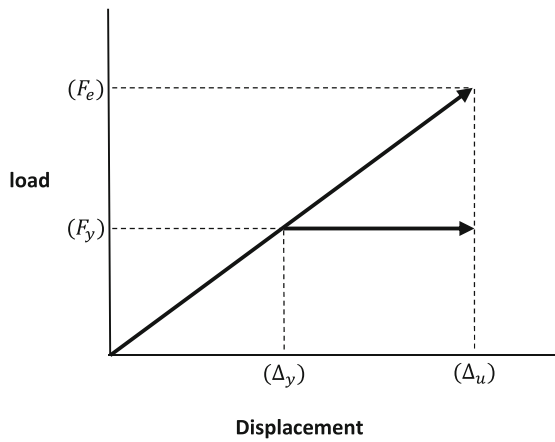


**Fig. 1.** Displacement ductility based on Equal-Displacement principle.

Displacement ductility ( $\mu_{\Delta}$ ) can be found out by Eq. (14).

$$\mu_{\Delta} = \frac{\Delta_u}{\Delta_y} = \frac{F_e}{F_y} \tag{14}$$

Displacement-based design procedure have been developed to design a structure to achieve a displacement that is less than a specified displacement limit. In this design philosophy, it is assumed that the structure will behave elasto-plastically, so the ultimate force experience by the structure is much less than the force experienced by the structure if the structure remains elastic till the failure. For this reason, ductility concept in introduced into the design philosophy.

The most common difference in design philosophy is the use of stiffness, in some design method the post-elastic stiffness is used and some initial stiffness is used like conventional force-based method. The equal-displacement or equal-energy approximations concept are implemented in this design philosophy which makes the design more realistic. In displacement-based design we set the target displacement and with

the help of secant stiffness, which is found out on the basis of equivalent viscous damping and the time period as per the desire target displacement from the design displacement spectrum and finally calculate the final design base shear.

### 3.1 Direct-Displacement Based Design Considering ESDOF System

The actual structure is turned into a comparable SDOF system via direct-displacement based design. While converting the system it should be checked that the total overturning moment of the actual system should be equal to the overturning moment of equivalent SDOF system. The properties of the equivalent SDOF system shown in Fig. 3, are then calculated.

Equivalent mass ( $m_e$ ), Design displacement ( $\Delta_d$ ), and Effective damping ( $\xi_e$ ) are the three qualities that must be present. Once they have been calculated, the design base shear of the substitute structure can be determined. The base shear is then distributed

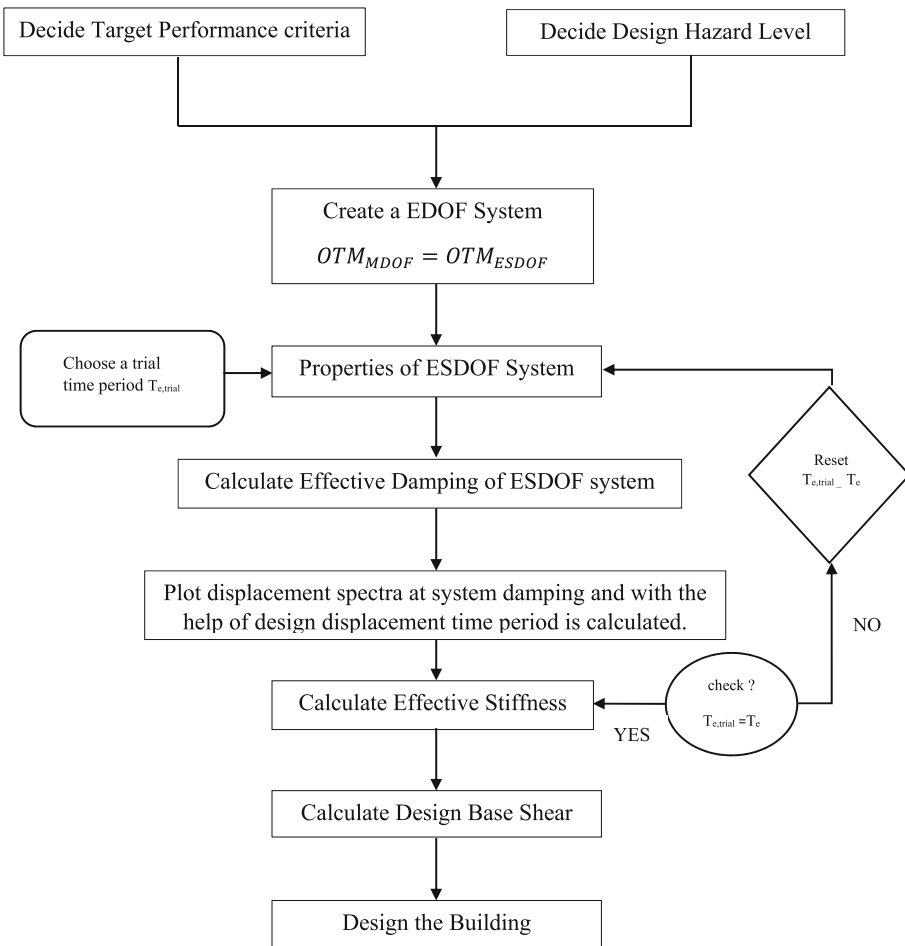


Fig. 2. A flowchart of Direct-displacement based design philosophy.

across the components of the real structure as inertia forces, and the structure is analysed using these forces to produce the design moments at plastic hinge points (Fig. 2).

**3.1.1 DDBD for RC Frame Structure**

Convert MDOF system into equivalent SDOF system by making sure the overturning moment of the MDOF system and ESDOF will be same and the system properties are determined.

Shape profile ( $\varphi_i$ ) is given by Eq. (15) and (16) as per Pettinga and Priestley (2005) for ready reference.

$$\text{For, } n \leq 4; \varphi_i = \frac{h_i}{H} \tag{15}$$

$$n > 4; \varphi_i = \frac{4h_i}{3H} \left( 1 - 0.25 \frac{h_i}{H} \right) \tag{16}$$

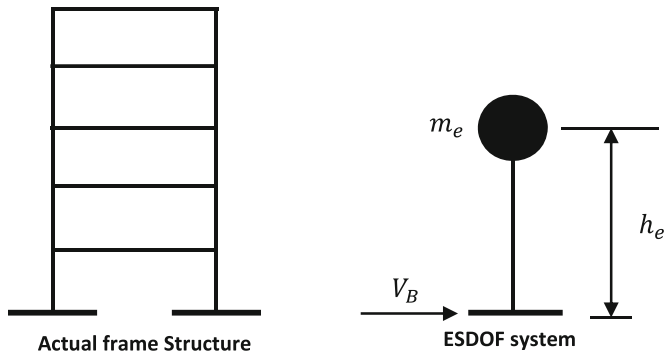


**Fig. 3.** Representation of actual structure into an equivalent SDOF system.

Critical storey displacement ( $\Delta_c$ ) is calculated by multiplying the critical storey height ( $h_{sc}$ ) with design drift ( $\theta_d$ ).

$$\Delta_c = h_{sc} \theta_d \tag{17}$$

The displacement profile ( $\Delta_i$ ) can be computed by using Eq. (18)

$$\Delta_i = \Delta_c \left( \frac{\varphi_i}{\varphi_c} \right) \tag{18}$$

where,  $\varphi_c$  is mode shape at the critical storey level.

The properties of the ESDOF system can be found by Eq. (19) to (21) as per Pettinga and Priestley (2005) for ready reference.

$$\text{Target displacement } (\Delta_d), \Delta_d = \frac{\sum m_i \Delta_i^2}{\sum m_i \Delta_i} \tag{19}$$

$$\text{Equivalent mass } (m_e), m_e = \frac{\sum m_i \Delta_i}{\Delta_d} \tag{20}$$

$$\text{Equivalent height } (h_e), h_e = \frac{\sum m_i \Delta_i h_i}{\sum m_i \Delta_i} \tag{21}$$

For varied damping, displacement spectra are generated using by Eq. (22), which correspond to design acceleration spectra.

$$S_d = \frac{S_a}{\omega^2} = \frac{S_a T^2}{4\pi^2} \tag{22}$$

The yield displacement ( $\Delta_y$ ) of ESDOF system is given by Eq. (23).

$$\Delta_y = h_e \theta_{yf} \tag{23}$$

The frame yield rotation is given by Eq. (24).

$$\theta_{yf} = \frac{0.5 \epsilon_y l_b}{h_b} \tag{24}$$

where,  $\epsilon_y$  is the yield strain of rebar,  $l_b$  and  $h_b$  is the length and depth of beam respectively.

The ductility of the frame in terms of displacement ( $\mu_\Delta$ ) is given by Eq. (25) (Fig. 4).

$$\mu_\Delta = \frac{\Delta_d}{\Delta_y} \tag{25}$$

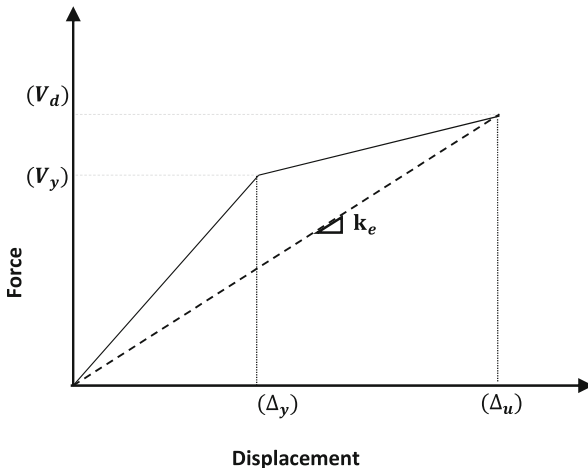


Fig. 4. Secant stiffness or effective stiffness.

Now, damping of ESDOF system is given by Eq. (26)

$$\zeta_e = 5 + 120 \frac{\left(1 - \frac{1}{\sqrt{\mu}}\right)}{\pi} \quad (26)$$

The effective time period is calculated by using displacement spectra associated with the equivalent damping curve and the intended displacement value. The ESDOF system's effective stiffness is defined by Eq. (27).

$$k_e = 4\pi^2 \frac{m_e}{T_{eff}^2} \quad (27)$$

Design base shear ( $V_b$ ), given by Eq. (28)

$$V_b = k_e \Delta_d \quad (28)$$

The design base shear has been distributed to each floors as per Eq. (29) and (30).

$$\text{For, } n \leq 10; F_i = V_b \frac{m_i \Delta_i}{\sum m_i \Delta_i} \quad (29)$$

$$n > 10; F_i = \begin{cases} 0.9V_b \frac{m_i \Delta_i}{\sum m_i \Delta_i} \\ F_{i,roof} + 0.1V_b \end{cases} \quad (30)$$

The design is done with expected strengths of materials as per FEMA. The load combinations are as below,

$$D + L$$

$$D + L \pm F_x$$

$$D + L \pm F_y$$

where,  $D$  is the dead load,  $L$  is the live load and  $F_x, F_y$  are the seismic loads in  $X$  and  $Y$  direction respectively (Table 1).

**Table 1.** Shape profile and Equivalent viscous damping of different DDBD approaches

Sr. no.	Approach	Shape profile		Equivalent viscous damping
1	Priestley and Kowalsky (2000)	$\varphi_i = h_i$ $\varphi_i = h_i \left( 1 - \frac{0.5(n-4)h_i}{16H} \right)$ $\varphi_i = h_i \left( 1 - \frac{0.5h_i}{H} \right)$	$n \leq 4$ $4 < n < 20$ $n \geq 20$	$\xi_e = 0.05 + \frac{1 - ((1-r/\sqrt{\mu}) - r\sqrt{\mu})}{\pi}$
2	Pettinga and Priestley (2005)	$\varphi_i = \frac{h_i}{H}$ $\varphi_i = \frac{4h_i}{3H} \left( 1 - 0.25 \frac{h_i}{H} \right)$	$n \leq 10$ $n \leq 10$	$\xi_e = 5 + 120 \frac{\left( \frac{1-\mu}{\mu\pi} \right) \varphi_0}{\pi}$
3	Priestley et al. (2007)	$\varphi_i = \frac{h_i}{H}$ $\varphi_i = \frac{4h_i}{3H} \left( 1 - 0.25 \frac{h_i}{H} \right)$	$n \leq 10$ $n \leq 10$	$\xi_{eq} = 0.05 + 0.565 \left( \frac{\mu-1}{\mu\pi} \right)$
4	Moghim and Saadatpour (2008)	$\varphi_i = h_i$ $\varphi_i = h_i \left( 1 - \frac{0.5(n-4)h_i}{16H} \right)$ $\varphi_i = h_i \left( 1 - \frac{0.5h_i}{H} \right)$	$n \leq 4$ $4 < n < 20$ $n \geq 20$	$\xi_e = 0.05 + \frac{1 - ((1-r/\sqrt{\mu}) - r\sqrt{\mu})}{\pi}$
5	Fakhraddini and Salajegheh (2012)	$\varphi_i = h_i$ $\varphi_i = h_i \left( 1 - \frac{0.5(n-4)h_i}{16H} \right) \varphi_i = h_i \left( 1 - \frac{0.5h_i}{H} \right)$	$n \leq 4$ $4 < n < 20$ $n \geq 20$	$\xi_e = 5 + 125 \frac{\left( \frac{1-\mu}{\mu\pi} \right) \varphi_0}{\pi}$
6	Dzacic et al. (2012)	$\varphi_i = \frac{h_i}{H}$ $\varphi_i = \frac{4h_i}{3H} \left( 1 - 0.25 \frac{h_i}{H} \right)$	$n \leq 10$ $n \leq 10$	$\xi_{eq} = 0.05 + 0.565 \left( \frac{\mu-1}{\mu\pi} \right)$

**3.1.2 Upgradations on Direct-Displacement Based Design Philosophy**

The most important issue in DDBD is, while designing the MDOF system we convert the MDOF system in an equivalent SDOF system for our convenience. By doing that we neglected the higher modes effects as well as the P-Δ effects. Which means we are considering that the structure is first mode dominating structure. This problem partially resolver by the researcher by introducing the factor in distributing the base shear (Sullivan et al. 2012).

The lateral displacement ( $\Delta_i$ ) at the storey  $i$  ( $i = 1, 2, \dots, n$ ) can be calculated from the expression given in Eq. (31), as per the target design inter-storey drift ratio ( $IDR_T$ ) and the inelastic displacement profile correspond to the fundamental mode.

$$\Delta_i = \omega_\theta IDR_T h_i \left( \frac{4H_n - h_i}{4H_n - h_1} \right) \tag{31}$$

where  $\Delta_i$  is the displacement at level  $i$ ,  $h_i$  is the height of  $i^{\text{th}}$  floor from ground,  $H_n$  is the total building height,  $\omega_\theta$  is the factor to account for the effects of higher modes and is given as,

$$\omega_\theta = 1.15 - 0.0034H_n \leq 1 \tag{32}$$

The properties of the ESDOF system can be found by Eq. (19) to (21), the yield displacement ( $\Delta_y$ ) of ESDOF system is given by Eq. (23), the yield rotation of the frame is given by Eq. (24), frame Displacement ductility ( $\mu_\Delta$ ) is given by Eq. (25).

Now, equivalent damping in the system is is given by Eq. (33)



$$\xi_{eq} = 0.05 + 0.565 \left( \frac{\mu - 1}{\mu\pi} \right) \tag{33}$$

A displacement design spectrum, such as the one depicted in Fig. 5, with the help of this spectrum for known data of  $\Delta_d$  and  $\xi_{eq}$  anyone can compute the design displacement ( $\Delta_{D,\xi}$ ) with equivalent amount of damping, and after that effective period  $T_{eff}$  is calculated stated in Eq. (34)

$$T_{eff} = \frac{\Delta_d}{\Delta_{D,\xi}} T_D \tag{34}$$

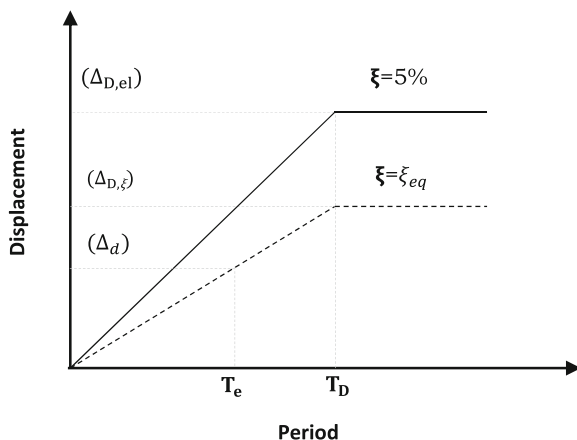


Fig. 5. Displacement spectra with different damping.

where  $T_D$  and  $\Delta_{D,\xi}$  are the corner period of design spectrum and the design displacement with equivalent amount of damping ( $\xi = \xi_{eq}$ ).

After calculating the effective stiffness by using Eq. (27) one can calculate the Design base shear ( $V_b$ ), is given by Eq. (35).

$$V_b = k_e \Delta_d + \mathfrak{C} \sum_{i=1}^n P_i \Delta_i / h_e \tag{35}$$

In the final design base shear formula Eq. (35), where the other quantity takes care of P-Δ effects. Where  $P_i$  is the total gravity load acting and  $\mathfrak{C} = 0.5$  for reinforced concrete frame.

The design base shear has been distributed to each floors as per Eq. (36) and (37).

$$\text{For floors } 1 \text{ to } n - 1: F_i = 0.9V_b \frac{m_i \Delta_i}{\sum m_i \Delta_i} \tag{36}$$

$$\text{For floors } n: F_i = F_{i,roof} + 0.1V_b \tag{37}$$

In the above force distribution formula Eq. (38–39), it has been assumed that 10% of the total base shear is separately added at top floor. Which ensure that because in order of higher-modes effects.

### 3.1.3 DDBD for RC Frame Structure with Linear Viscous Damper

Sometimes viscous damper are used to minimize the vibration in the main super-structure. However, use of such damper may not accumulative to the standard codal design procedure. Some papers are available on DDBD (Sullivan and Lago 2012), in which the DDBD procedure with linear viscous damper.

A viscous damper are consisting of viscous fluid filled cylinder with a piston with perforation. When the fluid passes through orifice energy will dissipate. The damping force is velocity dependent and varies according to Eq. (38).

$$F = C|v|^z \text{sign}(v) \quad (38)$$

where,  $F$  is the damping force,  $v$  is velocity and  $C$  is a constant with a value of 1 for linear viscous damper and for non-linear viscous damper value stay between 0.1 and 0.3.

First, the design displacement profile are calculated using Eq. (31). Then the shear proportion can be calculated that will carried by the damper. The other properties can be calculated as per the conventional DDBD procedure. Finally, the damping constant are calculated by proposed method by Sullivan (2012). The properties of the ESDOF system can be found by Eq. (19) to (21), the yield displacement ( $\Delta_y$ ) of ESDOF system is given by Eq. (23), the yield rotation of the frame is given by Eq. (24), frame Displacement ductility ( $\mu_\Delta$ ) is given by Eq. (25). The proportion of design base shear force taken by damper can be calculated by Eq. (39).

$$F_{d,i} = \beta_i V_i \quad (39)$$

where,  $F_{d,i}$  is the force for which a damper is designed at storey  $i$ ,  $V_i$  is the design shear force at level  $i$ .

Now, equivalent damping in the system is is given by Eq. (40)

$$\xi_{eq} = \xi_{eq,frame} + \frac{\beta}{2} \quad (40)$$

where,  $\beta$  is the proportion of force taken by damper at that level.

Equivalent damping in the frame is is given by Eq. (41)

$$\xi_{eq,frame} = 0.05 + 0.710 \left( \frac{\mu - 1}{\mu\pi} \right) \quad (41)$$

The effective time period is calculated by using displacement spectra associated with the equivalent damping curve, for the intended displacement value. The ESDOF system's effective stiffness is defined by Eq. (27). And, finally the base share can calculate.

Damping constant can be calculated by using Eq. (42).

$$C_i = \frac{F_{d,i} T_e}{2\pi \Delta_{d,j}} \tag{42}$$

where,  $F_{d,i}$  is the force for which a damper is designed at level  $i$ ,  $T_{eff}$  is the effective time period,  $\Delta_{d,j}$  is the relative axial displacement between the ends of the damper device at level  $i$ .

$$\Delta_{d,j} = \theta_{d,j} h_s \cos \theta_{damper} \tag{43}$$

where,  $h_s$  is storey height,  $\theta_{damper}$  is angle of damper,  $\theta_{d,j}$  is  $i$ -th level storey drift.

After knowing the damping constant one can compute the effective viscous damping ratio ( $\xi_d$ ) offered by the system of viscous damper by Eq. (44).

$$\xi_d = \frac{\sum_j C_j \omega \Delta_{d,j}^2}{2 \sum_i F_i \Delta_i} \tag{44}$$

where,  $C_j$  is damping constant for damper  $j$ ,  $\omega$  is the natural frequency of the structure,  $F_i$  is the storey level force and  $\Delta_i$  is the  $i$ -th level displacement.

### 3.1.4 DDBD for RC Frame-Wall Structure

Frame-wall dual system are combination of frame structure with shear wall. Shear wall are very good to take in plane lateral load. Shear wall are mainly provided along the periphery of the structure and symmetrically to avoid any torsional effects. In frame-wall structure 25% to 35% of base shear is taken by frame and rest of it was taken by shear wall. Frame bending action is different from the shear wall. Due to monolithic construction of frame and shear wall, the bending action of shear wall is predominant at bottom and frame action is predominant at the top. At bottom shear wall tries to push the frame on the other hand frame tries to pull the shear wall at the top.

Direct displacement-based design of frame-wall structure is given by Sullivan et al. (2006). In this article he proposed that how the design philosophy changed due to shear wall action. Shear taken by wall at any level above the ground cannot be calculated directly from the design base shear because the wall remain elastic. To obtain the shear taken by wall at any level one can subtract the frame shear from total shear at that level.

$$V_i = V_{i,F} + V_{i,W} \tag{45}$$

Here,  $i$  stands for  $i$ -th floor,  $F$  stands for frame and  $W$  stands for wall.

$$V_i = V_b \left( 1 - \frac{i(i-1)}{n(n+1)} \right) \tag{46}$$

where,  $V_b$  is design base shear and  $n$  is storey number.

Yield displacement can be calculated by Eq. (47) and (48).

$$\Delta_{i,y} = \frac{\varphi_{y,w} h_i H_{inflex}}{2} - \frac{\varphi_{y,w} H_{inflex}^2}{6} \quad \text{when } h_i \geq H_{inflex} \quad (47)$$

$$\Delta_{i,y} = \frac{\varphi_{y,w} h_i^2}{2} - \frac{\varphi_{y,w} h_i^3}{6H_{inflex}} \quad \text{when } h_i < H_{inflex} \quad (48)$$

where,  $\varphi_{y,w}$  is yield curvature,  $H_{inflex}$  is height of inflection,  $h_i$  is height of  $i$ -th storey.

$$\varphi_{y,w} = \frac{2\varepsilon_y}{L_w} \quad (49)$$

$L_w$  is length of shear wall.

The wall inflection height is established by assigning strength proportion to the member. The storey shear and moment of the wall are used to calculate the height of inflection where moment and curvature are zero.

Displacement of the  $i$ -th floor is given by Eq. (50).

$$\Delta_i = \Delta_{i,y} + \left( \theta_d - \frac{\varphi_{y,w} H_{inflex}}{2} \right) h_i \quad (50)$$

The properties of the ESDOF system can be found by Eq. (19) to (21).

Ductility are calculated using the following sets of equations.

Ductility of wall

$$(\mu_{wall}) = \frac{\Delta_d}{\Delta_{n_{e,y}}} \quad (51)$$

Curvature ductility of wall

$$(\mu_{\varphi,w}) = 1 + \frac{1}{L_p \varphi_{y,w}} \left( \theta_d - \frac{\varphi_{y,w} H_{inflex}}{2} \right) \quad (52)$$

$L_p$  is plastic hinge length and taken as minimum out of:

$$L_p = 0.2L_w + 0.03H_{inflex} \quad (53)$$

$$L_p = 0.022f_y d_b + 0.054H_{inflex} \quad (54)$$

where,  $d_b$  is diameter of rebar.

Ductility of frame at level

$$i(\mu_{i,frame}) = \left( \frac{\Delta_i - \Delta_{i-1}}{h_i - h_{i-1}} \right) \frac{1}{\theta_{y,F}} \quad (55)$$

$\theta_{y,F}$  can be computed using Eq. (24) and frame ductility ( $\mu_f$ ) can be computed by taking average of all values.

A trial time period is then then calculated by using Eq. (56)

$$T_{e,trial} = \frac{n}{6} \sqrt{\mu_{system}} \tag{56}$$

$$\mu_{system} = \frac{M_w \mu_w + M_{O,F} \mu_F}{M_w + M_{O,F}} \tag{57}$$

Now equivalent damping is found out by Eq. (58) and (59).

$$\zeta_{h,wall} = \frac{95}{1.3\pi} \left( 1 - \frac{1}{\mu_w^{0.5}} - 0.1r\mu_w \right) \left( 1 + \frac{1}{(T_{e,trial} + 0.85)^4} \right) \tag{58}$$

$$\zeta_{h,frame} = \frac{120}{1.3\pi} \left( 1 - \frac{1}{\mu_F^{0.5}} - 0.1r\mu_F \right) \left( 1 + \frac{1}{(T_{e,trial} + 0.85)^4} \right) \tag{59}$$

where,  $r$  is post-yield stiffness coefficient taken as 0.05 for new structure.

$$r = \frac{\text{stiffness after yield}}{\text{stiffness before yield}}$$

damping of the system is given by Eq. (60).

$$\zeta_{SDOF} = \frac{M_w \zeta_w + M_{O,F} \zeta_F}{M_w + M_{O,F}} \tag{60}$$

The effective time period is calculated by using displacement spectra associated with the equivalent damping curve and the intended displacement value. The ESDOF system’s effective stiffness is defined by Eq. (27). After calculating the effective stiffness one can calculate the Design base shear ( $V_b$ ), is given by Eq. (28) and distributed by Eq. (29) and (30).

### 3.1.5 DDBD for Steel-Braced RC Frame Structure

Frame-braced dual system are combination of frame structure with steel bracing. Steel bracing are very good to take in plane lateral load. Steel bracing are mainly provided along the periphery of the structure in frame plane and symmetrically to avoid any torsional effects.

Shear taken by steel bracing at any level above the ground cannot be calculated directly from the design base shear. To obtain the shear taken by steel bracing at any level one can subtract the frame shear from total shear at that level.

$$V_i = V_{i,F} + V_{i,brace} \tag{61}$$

where,  $V_i$  is shear at level  $i$  and can be computed from Eq. (45).

Yield displacement can be calculated by Eq. (62) given by Ghorbani-Asl (2007).

$$\Delta_{i,y} = \frac{F_y L_{brace}}{E \cos \theta_i} \tag{62}$$

where,  $F_y$  is yield stress of steel bracing,  $L_{brace}$  is length of bracing,  $E$  is modulus of elasticity of steel and  $\theta_{y,F}$  can be computed using Eq. (24).

Displacement profile as shown in Eq. (63).

$$\Delta_i = \Delta_{i,y} + (\theta_d)h_i \tag{63}$$

From the trial time period calculated on the basis of Eq. (56) one can assume a trial design displacement ( $\Delta_{spec}$ ) and ductility of the system is calculated on the basis of this.

$$\Delta_y = \frac{\Delta_{spec}}{\mu} \tag{64}$$

Time-history analysis is done check for maximum displacement obtained. If this is equal to the assumed value or within the 3% tolerance limit the proceed with those values, if not the do the same prosses. The constitutive model considered for the steel bracing to calculate the equivalent viscous damping is the Ramberg–Osgood model, and the loading curve complies with Eq. (65) Blandon (2004).

$$\frac{D}{D_y} = \frac{F}{F_y} \left( 1 + \left( \frac{F_0}{F_y} \right)^{\gamma-1} \right) \tag{65}$$

Finally, Blandon proposed the equivalent viscous damping factor for six different constitutive models using statistical approaches, and the equations are presented in Eq. (66) and (67).

$$\zeta_{brace} = \frac{a}{\pi} \left( 1 - \frac{1}{\mu^b} \right) \left( 1 + \frac{1}{(T_{e,trial} + c)^d} \right) \frac{1}{N} \tag{66}$$

$$N = 1 + \frac{1}{(0.5 + c)^d} \tag{67}$$

$a$ ,  $b$  and  $c$  are the constant coefficients defined for each hysteresis model,  $\mu$  is the ductility factor,  $T$  is the trial effective period and  $N$  is the normalization factor, and the model considered in this study is the Ramberg–Osgood model.

damping of the system is given by Eq. (68).

$$\zeta_{SDOF} = \frac{M_{brace}\zeta_{brace} + M_{O,F}\zeta_F}{M_{brace} + M_{O,F}} \quad (68)$$

After getting the damping one can compute the time period and progressively the base shear can be calculated. The rest of the process is similar to the DDBD approach of dual system. For more reference one can see Dashti (2013).

### 3.2 Direct-Displacement Based Design Considering MDOF System

This paper proposes a new approach in seismic design of structure. With the help of modal damping ratios and modal displacement in the direct displacement-based design one can consider a MDOF equivalent system rather than using a SDOF equivalent system used in the design philosophy. The method described here, can take care of the P-Δ effect because of the equivalent MDOF system, which is used instead of equivalent SDOF system. The design process also incorporate the higher modes effect, which contribute significantly to the response of the structure. On the other hand, this design method is a single stage design means only the checking of strength. An equivalent elastic MDOF system replaces with the original MDOF structure. Both the structure are equivalent in the work dissipation domain, means the dissipation of energy because of the hysteresis force is equivalent to the dissipation of energy by the viscous force. This method incorporate the theory of equivalent modal damping ratios as well as the modal displacement of those modes, which contribute significantly to the response of the structure, developed by Muho et al. (2020). The modal displacement are inter-related to the target inter-story drift ratios. The modal periods can thus be estimated from the displacement spectrum. The desired effective stiffness and modal base shear can be calculated using those modal periods. Combination rule can be used to find out the final design base shear.

#### 3.2.1 Modal Equivalent Damping Ratios

The main concept of deformation dependant equivalent modal damping ratio mainly introduced by Muho et al. (2020). On this paper he take a transfer function  $R(\omega)$  for a multi-degree-of-freedom system defined in the frequency domain as the ratio of the absolute roof acceleration  $\overline{U}_r(\omega)$  of the frame over the acceleration  $\overline{u}_g(\omega)$  at its base,

$$R(\omega) = \frac{\overline{U}_r(\omega)}{\overline{u}_g(\omega)} \quad (69)$$

where  $\overline{U}_r(\omega) = \overline{u}_g(\omega) + \overline{u}_r(\omega)$  with  $\overline{u}_g(\omega)$  and  $\overline{u}_r(\omega)$  being the earthquake motion and roof relative motion, respectively, in the frequency domain,  $\omega$  is the frequency and overbars denote Fourier transformation.

An equivalent elastic MDOF system replaces with the original MDOF structure. Both the structure are equivalent in terms of work dissipation, means the dissipation of energy because of the hysteresis force is equivalent to the dissipation of energy by the viscous force. As a result, this work equivalency notion can be viewed as a progression from Jacobsen’s (1930), as per this paper the behaviour of a SDOF structure due to

harmonic force is equivalent to the behaviour of an MDOF structure due to seismic force.

NLTH analyses incorporating significant displacement and P- $\Delta$  effects are used to assess the behaviour of the structure in the time domain for a greater number of earthquake excitation. A Fourier transform is used to bring the response into the frequency domain from the time domain to create the transfer function  $R(\omega)$ . With the help of these transfer function modal damping ratios ( $\zeta_k$ ) are determined. For each seismic motion, NLTH studies are run multiple times, progressively scaling the motion to record the target displacement values. As a result, the damping ratios ( $\zeta_k$ ) are related to displacement, so we can say that damping ratios are deformation dependent.

All of the aforementioned  $\zeta_k$  values were calculated under this concept are only relate to the hysteretic dissipation, in this approach the viscous damping ( $\zeta_v$ ) are not added. Thus, to get the total modal equivalent damping ( $\zeta_{eq,k}$ , we have to add those modal values, i.e.,  $\zeta_{eq,k} = \zeta_k + \zeta_v$ , where  $\zeta_v$  is assumed to 5% for RC structure and 2% for steel structure.

### 3.2.2 DDBD for RC Frame Structure Considering MDOF System

The suggested enhanced design philosophy of conventional direct displacement-based design has been modified by using an equivalent MDOF system instead of using an equivalent SDOF system, which makes the design philosophy more realistic than the conventional DDBD, Sullivan (2012), is detailed on this section. Thus, only considering the horizontal displacements ( $\Delta_i$ ) of only one mode in the conventional DDBD Sullivan (2012), one can use horizontal modal displacements ( $\Delta_{i,j}$ ) for every storey  $i$  and for every mode  $j$ , where  $i = 1, 2, \dots, n$ , and  $n$  is the storey number and  $j = 1, 2, \dots, n$ , where  $n$  denotes the number of modes, which contribute alluringly to the response of the structure. Again, instead of a single value of damping ( $\zeta_{eq}$ ) in equivalent SDOF system, equivalent damping ratio ( $\zeta_{eq,j}$ ) of those modes, which contribute significantly to the response of the structure, are determined.

The drawback of considering ESDOF system further eliminated by Muho et al. (2020), by considering an equivalent elastic MDOF system replaces with the original MDOF structure. Both the structure are equivalent in the work dissipation domain, means the dissipation of energy because of the hysteresis force is equivalent to the dissipation of energy by the viscous force.

Based on the first few modal shapes emerging from modal analysis, the displacement profile of each mode ( $\Delta_{i,j}$ ) for a target drift ratio ( $IDR_T$ ), are valued here. To accomplish this modal effect on target drift ratio ( $IDR_{Tj}$ ) one formula is given by Muho et al. (2020), which is shown in Eq. (70).

$$IDR_{Tj} = f_j IDR_T \quad (70)$$

where  $f_j$ , is denoted as mass participation factor.

The target modal displacements ( $\Delta_{i,j}$ ) corresponding to the  $IDR_{Tj}$  are determined by the uttered expression, in terms of the modal shapes ( $\varphi_{i,j}$ ), shown in Eq. (71).



$$\Delta_{i,j} = x_j \varphi_{i,j} \tag{71}$$

where  $x_j$ , is a modal multiplication factor.

The above Eq. (72) can be written as

$$\left( \frac{\Delta_{i+1,j} - \Delta_{i,j}}{h_{i+1} - h_i} \right) = x_j \left( \frac{\varphi_{i+1,j} - \varphi_{i,j}}{h_{i+1} - h_i} \right) \tag{72}$$

Also,

$$IDR_{Tj} = \max \left( \frac{\Delta_{i+1,j} - \Delta_{i,j}}{h_{i+1} - h_i} \right)_j \tag{73}$$

Putting Eq. (72) into Eq. (73), we may get

$$IDR_{Tj} = \max \left( \frac{\varphi_{i+1,j} - \varphi_{i,j}}{h_{i+1} - h_i} \right)_j x_j \tag{74}$$

Equation (74) can be solved for  $x_j$  and given by Eq. (75).

$$x_j = IDR_{Tj} / \max \left( \frac{\varphi_{i+1,j} - \varphi_{i,j}}{h_{i+1} - h_i} \right)_j \tag{75}$$

The modal target displacement in terms of  $IDR_{Tj}$  is given as Eq. (76).

$$\Delta_{i,j} = \frac{IDR_{Tj}}{\max \left( \frac{\varphi_{i+1,j} - \varphi_{i,j}}{h_{i+1} - h_i} \right)_j} \varphi_{i,j} \tag{76}$$

The design modal displacement can be found out by the given Eq. (77).

$$\Delta_{d,j} = \frac{\sum_{i=1}^n (m_{i,j} \Delta_{i,j}^2)}{\sum_{i=1}^n (m_{i,j} \Delta_{i,j})} \tag{77}$$

where  $m_{i,j}$ , is denoted as the percentage of mass activated in  $j$ -th mode.

The modal equivalent damping ratios,  $\xi_{eq,j} = \xi_j + 5\%$  are also calculated by the concept described before.

With the help of a displacement spectrum, with known values of  $\Delta_{d,j}$  and  $\xi_{eq,j}$  anyone may compute design damped target displacement ( $\Delta_{D,\xi}$ ), and also the period ( $T_{e,j}$ ) stated in Eq. (78)

$$T_{e,j} = \frac{\Delta_{d,j}}{\Delta_{D,\xi}} T_D \tag{78}$$

where  $T_D$  and  $\Delta_{D,\xi}$  are the corner period with damping  $\xi = \xi_{eq,j}$  at  $T_D$ , eventually.

As a result, Eq. (79) can be used to calculate the modal effective stiffness ( $k_{e,j}$ )

$$k_{e,j} = 4\pi^2 \frac{m_{e,j}}{T_{e,j}^2} \quad (79)$$

where the equivalent modal mass  $m_{e,j}$  can be computed by Eq. (80).

$$m_{e,j} = \sum_{i=1}^n (m_{i,j} \Delta_{i,j}) / \Delta_{d,j} \quad (80)$$

Equation (81) may be used to obtain the modal design base shear ( $V_{b,j}$ ).

$$V_{b,j} = k_{e,j} \Delta_{d,j} \quad (81)$$

The calculated design shear ( $V_{b,j}$ ) is then applied to the structure as a force ( $F_{i,j}$ ). The distribution pattern is given by Chopra (2011), shown in Eq. (82).

$$F_{i,j} = V_{b,j} \frac{m_{i,j} \Delta_{i,j}}{\sum m_{i,j} \Delta_{i,j}} \quad (82)$$

Finally, SSRS rule, which is a modal combination rule is then applied to calculate the lateral design force ( $F_i$ ) at each storey  $i$ , as shown in Eq. (83).

$$F_i = \sqrt{\sum_{j=1}^N F_{i,j}^2} \quad (83)$$

Static analysis may be utilised for designing the R/C frame using the maximum lateral design forces mentioned above. It is important to remember that, since the presented method is based on by considering an equivalent elastic MDOF system replaces with the original MDOF structure, can take care of the P- $\Delta$  effect because of the equivalent MDOF system, which is used instead of equivalent SDOF system. The design process also incorporate the higher modes effect, which contribute significantly to the response of the structure.

## 4 Unified Performance-Based Design

Unified performance-based design is a kind of displacement-based design methodology in which the intended target performance objective in terms of design drift or plastic rotation, and intended member performance levels both are considered. As a result, this method give some design data like member sizes as per the performance at the starting of the design which helps a designer to avoid a large number of iterations to get the member sizes. Choudhury (2008) improved the DDBD method of Sullivan et al. (2006) by incorporating both design drift limit and performance level together. The method can apply to frame structure as well as frame-wall structure also.

### 4.1 UPBD for RC Frame Structure

Choudhury and Singh (2013), presented the Unified Performance Based Design (UPBD) method for the design of RC Frame structures. The design methodology aims to meet both target design drift and member performance level requirements at the same time. The advantage of this method is that it may be used to determine the beam size that will meet the performance level criteria right at the start of the design process (Fig. 6).

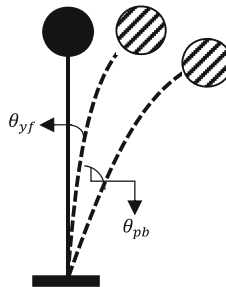


Fig. 6. ESDOF system.

Design drift and performance level are the major requirements of this design philosophy, with drift relating to the safety of drift-sensitive equipment and non-structural elements. Plastic rotation in beams according to design damage or strain is allowed as a performance level. Plastic hinges are allowed to develop in beams, not columns, according to the weak-beam strong-column principle, and therefore the column remains elastic up to the desired performance level.

The total design drift equalize to the summation of frame rotation and the plastic rotation of structural beam member as shown in Eq. (84).

$$\theta_d = \theta_{yf} + \theta_{pb} \tag{84}$$

Plastic rotation ( $\theta_{pb}$ ) in beam, is determined by the average allowable plastic rotation according to the performance level defined by FEMA-356 and available. According to standard design practise, the beam width should be between 1/3 and 1/2 of the beam depth.

The yield rotation of the frame is given by Eq. (85).

$$\theta_{yf} = \frac{0.5 \epsilon_y l_b}{h_b} \tag{85}$$

Putting the value of  $\theta_{yf}$  in Eq. (84), we will get a theoretically developed beam size is computed which will satisfy performance objectives.

The Beam depths are found out from Eq. (86).

$$\frac{h_b}{l_b} = \frac{0.5\varepsilon_y}{\theta_d - \theta_{pb}} \quad (86)$$

UPBD can accommodate both Design drift and performance level together. It also gives member sizes (Beam depth & width) so that we can avoid large iteration as compare to DDBD method. So UPBD is less time consuming and more accurate. UPBD method used the Expected strength of material.

#### 4.2 UPBD for RC Frame-Wall Structure

A MDOF structure is converted to an equivalent SDOF system. The target inter-storey drift is equal to the total rotation of ESDOF system. This can be encountered by equivalent rotational drift. Shear wall have the predominant effect in the dual system. In frame-wall structure 25% to 35% of base shear is taken by frame and rest of it was taken by shear wall. Frame bending action is different from the shear wall. Due to monolithic construction of frame and shear wall, the bending action of shear wall is predominant at bottom and frame action is predominant at the top. Choudhury (2008) first gave the UPBD design philosophy in-terms of hospital building. Moreover, the approach go through several investigation and more refine steps to get design data are developed (Debnath and Choudhury 2017).

The total rotation of the system then can be expressed as the sum of yield rotation and plastic rotation of the wall.

$$\theta_d = \theta_{yw} + \theta_{pw} \quad (87)$$

$\theta_{yw}$  can be computed by using by Eq. (88).

$$\theta_{yw} = \varphi_{y,w} \frac{H_{inflex}}{2} \quad (88)$$

Putting the value of Eq. (88) in Eq. (87) we will get the length of the wall at the starting of the design which will satisfy the performance level.

$$L_w = \frac{\varepsilon_y H_{inflex}}{\theta_d - \theta_{pw}} \quad (89)$$

where, Plastic rotation ( $\theta_{pw}$ ) in wall, is determined by the average allowable plastic rotation according to the performance level defined by FEMA-356 and available.

Thickness of the wall ( $t_w$ ) is obtained from Eq. (90).

$$t_w = \frac{V_{wall}}{0.8L_w\tau_cN_w} \quad (90)$$

where,  $V_{wall}$  is shear carried by the wall,  $\tau_c$  is permissible shear stress of concrete,  $N_w$  is number of shear wall in the considered direction,  $L_w$  is length of the wall. The factor

0.8 is used which says that 80% of the length of wall is effective in taking shear as per IS-456 (2000).

The rest of the design methodology is similar to the DDBD approach for frame-wall structure given by Sullivan et al. (2006).

The UPBD method, just like DDBD method, only considers the first mode motion of the structure and fails to consider the contribution of other modes to the overall motion of the structure. The Displacement Spectra used to acquire the Time period of the ESDOF system is derived from the Design Spectra for a given hazard or seismicity level. Hence, if an earthquake or ground motion of higher seismicity level hits the structure, the structure may land up collapsing entirely. To address simultaneous lateral and vertical ground motion effects, the approach needs to be improved.

## 5 Conclusions

For R/C MRFs, the design philosophy of conventional direct displacement-based design has been modified by using an equivalent MDOF system instead of using an equivalent SDOF system, which makes the design philosophy more realistic.

This method incorporates the concept of equivalent modal damping ratios as well as the modal displacement of those modes, which contribute significantly to the response of the structure, developed by Muho et al. (2020). The modal displacement are inter-related to the target inter-storey drift ratios.

The method described here, can take care of the P- $\Delta$  effect because of the equivalent MDOF system, which is used instead of equivalent SDOF system. The design process also incorporate the higher modes effect, which contribute significantly to the response of the structure. On the other hand, this design method is a single stage design means only the checking of strength.

Further, Unified performance-based design helps to design a structure by considering the design drift limit as well as the required performance level for structural safety. UPBD gives a range of depth of beam according to the desire performance level, so that we can avoid large iteration as compare to DDBD method.

## References

- Calvi, G.M., Sullivan, T.J.: Development of a Model Code for Direct Displacement-Based Seismic Design. IUSS Press, Pavia (2008)
- Chopra, A.K.: Dynamics of Structures, 4th edn. Pearson, Upper Saddle River (2011)
- Chopra, A.K., Goel, R.K.: Direct displacement-based design: use of inelastic vs. elastic design spectra. *Earthq. Spectra* **17**(1), 47–64 (2001)
- Choudhury, S.: Performance-based seismic design of hospital buildings. Ph.D. thesis, Department of Earthquake Engineering, IIT Roorkee (2008)
- Choudhury, S., Singh, S.M.: A unified approach to performance-based design of RC frame buildings. *J. Inst. Eng. India Ser. A* **94**(2), 73–82 (2013)
- Chandurkar, P.P., Pajgade, P.S.: Seismic analysis of RCC building with and without shear wall. *Int. J. Mod. Eng. Res.* **3**(3), 1805–1810 (2013)

- Debnath, P.P., Choudhury, S.: Nonlinear analysis of shear wall in unified performance based seismic design of buildings. *Asian J. Civil Eng.* **18**(4), 633–642 (2017)
- Dashti, F., Malekpour, S., Ghaffarzadeh, H.: Direct displacement-based design of steel-braced reinforced concrete frames. *Struct. Design Tall Spec. Build.* **22**, 1422–1438 (2013)
- Dzadic, D., Kraus, I., Moric, D.: Direct displacement-based design of regular concrete frames in compliance with Eurocode 8. *Techn. Gazette* **19**(4), 973–982 (2012)
- EC-8: Eurocode 8-design provisions for earthquake resistant structures. EN-1998-1: 2004, European Committee of Standardization, Brussels (2004)
- Fakhraddini, A., Salajegheh, J.: Optimum automated direct displacement-based design of reinforced concrete frames. In: *Proceedings of 15th World Conference of Earthquake Engineering*, Lisbon (2012)
- FEMA-356: Prestandard and commentary for the seismic rehabilitation of buildings, Federal Emergency Management Agency, Washington DC (2000)
- IS-1893(Part 1): Criteria for Earthquake Resistant Design of Structures, Part-I, General Provisions and Buildings, BIS, New Delhi (2016)
- Moehle, J.P.: Displacement-based design of RC structures subjected to earthquakes. *Earthq. Spectra* **8**(3), 403–428 (1992)
- Moghim, F., Saadatpour, M.M.: The applicability of direct displacement-based design in designing concrete buildings located in near-fault region. In: *Proceeding of 14th World Conference of Earthquake Engineering*, Beijing (2008)
- Muho, E.V., Papagiannopoulos, G.A., Beskos, D.E.: Deformation dependent equivalent modal damping ratios for the performance-based seismic design of plane R/C structures. *Soil. Dyn. Earthq. Eng.* **129**, 105345 (2020)
- Muho, E.V., Qian, J., Beskos, D.E.: A direct displacement-based seismic design method using a MDOF equivalent system: application to R/C framed structures. *Bull. Earthq. Eng.* **18**, 4157–4188 (2020)
- Panagiotakos, T.B., Fardis, M.N.: A displacement-based seismic design procedure for RC buildings and comparison with EC-8. *Earthq. Eng. Struct. Dyn.* **30**, 1439–1462 (2001)
- Priestley, M.J.N.: Myths and fallacies in earthquake engineering-conflicts between design and reality. *Bull. N Z Natl. Soc. Earthq. Eng.* **26**(3), 328–341 (1993)
- Priestley, M.J.N., Kowalsky, M.J.: Direct displacement-based seismic design of concrete buildings. *Bull. N Z Soc. Earthq. Eng.* **33**(4), 421–443 (2000)
- Pettinga, J.D., Priestley, M.J.N.: *Dynamic Behaviour of Reinforced Concrete Frames Designed with DBBD*, ROSE SCHOOL Research report, IUSS Press (2005)
- Priestley, M.J.N., Calvi, G.M., Kowalsky, M.J.: *Displacement-Based Seismic Design of Structures*. IUSS Press, Pavia (2007)
- Priestley, M.J.N., Calvi, G.M., Kowalsky, M.J., Powell, G.H.: Displacement-based seismic design of structures. *Earthq. Spectra* **24**(2), 555 (2008)
- Sullivan, T.J., Priestley, M.J.N., Calvi, G.M.: Direct displacement-based design of frame-wall structures. *J. Earthq. Eng.* **10**(SI 1), 91–124 (2006)
- Sullivan, T.J., Priestley, M.J.N., Calvi, G.M.: *A model code for the displacement-based seismic design of structures*, DBD12, IUSS Press, Pavia (2012)
- Sullivan, T.J., Lago, A.: Towards a simplified Direct DBD procedure for the seismic design of moment resisting frames with viscous dampers. *Eng. Struct.* **35**, 140–148 (2012)



# Study on High Strength Concrete with Hybrid Combination of Steel and Polypropylene Fibers

G. Prasanna and A. Sumathi<sup>(✉)</sup>

School of Civil Engineering, SASTRA Deemed to be University,  
Thanjavur 613401, India  
sumathi@civil.sastra.edu

**Abstract.** In this work, aimed to improve the mechanical properties of concrete with hybrid fibers (HF) for M50 grade of concrete with mix proportion of 1:1.67:2.22 with a w/c ratio of 0.40. Totally 13 mixes were prepared in that one mix is considered as control (without hybrid fibers) and other twelve mixes with different proportions of (HF)-Steel (S) and Polypropylene (P&PP) are added. The proportion of steel and polypropylene fibers are added, each with different hybridization ratio i.e. S0P0, S1%, S2%, S3%, P0.2%, P0.25%, P0.3% with the combination of steel fibers and PP with S0.8%P0.2%, S1.75%P0.25%, S2.7%P0.3%, S1%P0.2%, S2%P0.25%, S3%P0.3% are added in volume fractions. Nano-silica (NS) of 0.75% is added in to the concrete mix. The properties such as compressive strength, split tensile strength, impact resistance, and sorptivity for all the mixes were studied. Based on the test results, fiber combination of 2% steel with 0.25% PP fiber shows improved compressive strength, split tensile strength and less percentage of water absorption. Hybrid combination of 2% and 3% steel with 0.25% and 0.3% PP fiber enhanced the impact performance based on numbers of blows and impact energy at first and final failure. The hybrid steel – polypropylene fiber in the mix performs better in strength and durability properties than control and mix with only steel and polypropylene fibers.

**Keywords:** Hybrid fibers · Steel-fibre · Polypropylene · Nano-silica · Compressive strength · Split tensile strength · Sorptivity test · Impact strength

## 1 Introduction

In order to meet the structure's strength and durability criteria, there has recently been a major need to improve the properties of high-strength concrete (HSC) in terms of strength, durability, ductility, and performance as a structural material with cement. A new type of concrete has been produced as a result of high-strength concrete technologists' ongoing research to better understand, improve, and develop the properties of concrete. Bernard (2006) widely explained that Fiber Reinforced High Strength Concrete (FRHSC) is a type of concrete that incorporates fibres into the mix to improve strength, ductility, hardness, and toughness. Liu et al. (2020) examined the material properties of HFHSC could achieve the 10–20% improvement in the compressive and tensile strength. In this study, research was carried out to assess the

structural characteristics of steel-polypropylene as HSC with HF to increase the strength compared to normal concrete. Mezzal et al. (2021) had discussed the impact resistance, flexural, toughness of HSC with hybrid fibres (HF). Kanagavel et al. (2015) studied the mechanical properties on fibre dosage and the different combination of fibres in volume fraction were used. In that 12 different mix were used along with the control mix. In each mix having the different volume fraction of HF in HSC. It may be concluded that including HSC with HF has yielded benefits due to the fibers improved mechanical characteristics and the 'HSC-HFRC' good effect on concrete qualities. By using hybrid steel fibres gives greater result in compression as well as the impact energy in the concrete. Muzeyyen et al. (2020) explained how to improve the performance of hybrid fiber concrete by integrating fiber characteristics and the bending strength of fiber hybridization in concrete. If 0.25% polypropylene fibre is utilized, the steel fibre contribution ratio should be less than 2%, and the polypropylene fibre contribution ratio should be larger than 0.5%. The maximum pullout test reaches the maximum strength for fibre percent of 2% delivers the maximum strength of the hybrid fibre reinforced concrete, according to that paper. Fallah et al. (2017) investigate how different polypropylene (PP) and macro-polymeric (MP) fiber concentrations effect the mechanical properties and durability of HSC containing silica fume and nano-silica. Adding nano-silica and silica fume to concrete increases its mechanical properties and durability, according to the findings. Furthermore, introducing macro-polymeric fibers in the concrete mixture enhanced the mechanical properties. Furthermore, high volume percentages of polypropylene fibers in the concrete mixture had an adverse impact on the HSC physico-mechanical properties. The aim of this study is to examine at the mechanical performance of high-strength fiber reinforced concrete with varying volume percentages and the hybrid fiber concrete results has compared with the control concrete.

## 2 Experimental Programme

### 2.1 Material Properties

The OPC cement grade 53, with special gravity of 3.15, fine aggregate fineness modulus 2.7 and 4.75-mm size, coarse aggregate fineness modulus 6.7, and size ranges of 12.5 to 20 mm was used. A metal fiber with a diameter of 1 mm and a length of 50 mm is shown in Fig. 1. The material has a 50-aspect ratio, 7.86 specific gravity, and tensile strength of 800 to 1000 MPa. A fibrillated PP fiber with a length of 19 mm, a diameter of 0.04 mm, a specific gravity of 0.91, and a tensile strength of 350 to 450 MPa is shown in Fig. 2. Figure 3 shows nano silica with a density of 2.4 g/cm<sup>3</sup>, a molar mass of 59.96 g/mol, and a color of white powder shown in Tables 1 and 2.



**Table 1.** Physical properties of coarse and fine aggregate

Particulars	Coarse aggregate	Fine aggregate
Density	1830	1918
Fineness modulus	7.83	2.85
Specific gravity	2.74	2.65
Water absorption %	20	1.23
Moisture on the surface	Nil	Nil

**Table 2.** Properties of fibres and Nano silica

Properties	Steel fibre	Polypropylene	Nano silica
Diameter	1 mm	0.04 mm	-
Length of fibre	50 mm	45 mm	-
Aspect ratio	50	1125	
Shape of the fibre	Crimped end	Chopped strand	Powder form
Appearance	Steel black	White color	White
Specific gravity	7.86	0.91	2.4
Tensile strength	800–1000 MPa	350–450 MPa	-

**Fig. 1.** Steel fibre.**Fig. 2.** Polypropylene**Fig. 3.** Nano silica.

## 2.2 Mix Design and Methods

IS 10262-2019 was used to determine the concrete mix ratio for M50 concrete with a w/c ratio of 0.4, the mix percentage was 1:1.67:2.22 (C:FA:CA). Nano silica dosages used are substituted by 0.75% of cement. Fosroc conplastr 0.3% in concrete, super plasticizer is used as a water reducer. The role of Nano silica and hybrid fibers steel-polypropylene in compressive strength, split tensile strength, sorptivity test, and impact strength was investigated. The details of the mix proportions are presented in Table 3. Steel fibres and polypropylene with Nano silica were used to cast all the specimens.

Totally 13 mixes were prepared based on the hybrid combination of steel and polypropylene fibres and the details are presented in Table 4. Specimens such as Cubes (100 mm) for CS, acid and sulphate resistance, cylinders (100 mm diameter  $\times$  200 mm long) for STS, prisms (500  $\times$  100  $\times$  100 mm) and cylinders (50 mm  $\times$  100 mm) for sorptivity were cast and tested for different properties.

**Table 3.** Mix proportion ( $\text{kg}/\text{m}^3$ )

Mix grade	M50
Cement	477 $\text{kg}/\text{m}^3$
Fine aggregate	805 $\text{kg}/\text{m}^3$
Coarse aggregate	1073 $\text{kg}/\text{m}^3$
Super plasticizer (SP)	0.3%–1.43 $\text{kg}/\text{m}^3$

**Table 4.** Hybrid fibres combination

Mix id	Steel fibre (S) %	Polypropylene (P)%	Nano-silica (NS) %
S0P0-control	-	-	0.75
S1P0	1%	-	0.75
S2P0	2%	-	0.75
S3P0	3%	-	0.75
S0P0.2	-	0.2%	0.75
S0P0.25	-	0.25%	0.75
S0P0.3	-	0.3%	0.75
S0.8P0.2	0.8%	0.2%	0.75
S1.75P0.25	1.75%	0.25%	0.75
S2.7P0.3	2.7%	0.3%	0.75
S1P0.2	1%	0.2%	0.75
S2P0.25	2%	0.25%	0.75
S3P0.3	3%	0.3%	0.75

### 3 Results and Discussion

#### 3.1 Compressive Strength (CS)

Figures 4, 5 and 6 shows the results of cube CS with a fiber content rise up to 3% steel and 0.3% PP HSC content of fiber volume, the 7, 14, and 28-day CS is constantly enhanced. In HSC, the maximum strength was 67.54 MPa at 2% SF and 0.25% PP fibres volume fraction with the increase percentage of 29.065 for 28 days. The increase percentage of CS is shown in Fig. 7. As a result, HF can be used to increase the CS of high strength structural concrete. Compared to the specimens without steel and PP

fibers, the specimens with steel and PP fiber showed better results in CS. During testing of specimens with steel and PP fiber, it is noted that the cracks are formed at later stage and this shows that the steel and PP fibers and Nano materials are strongly bonded together to resist the crack formation.

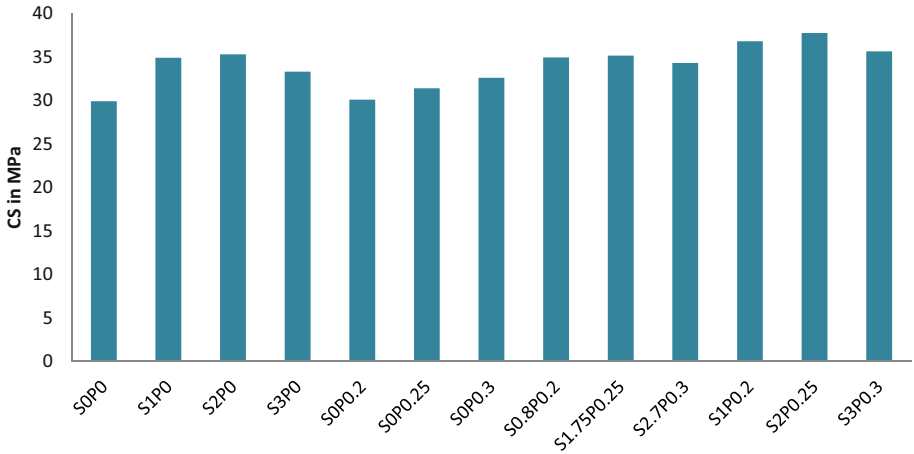


Fig. 4. CS at 7 days.

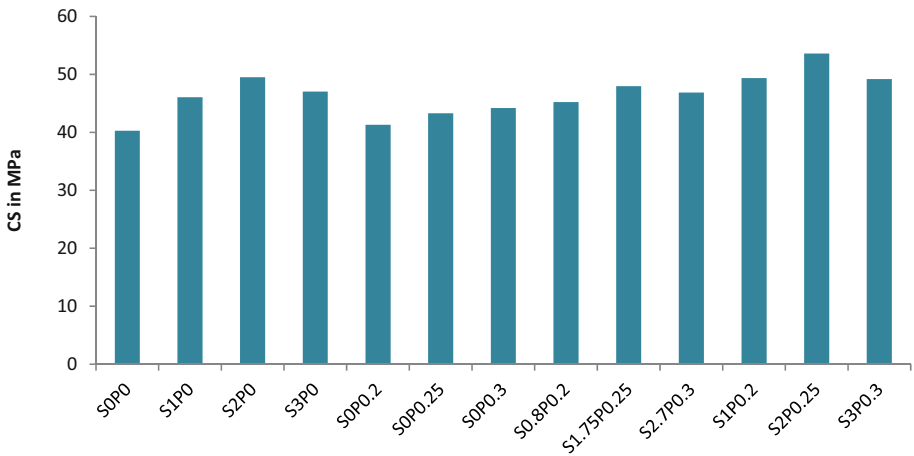


Fig. 5. Compressive strength at 14 days.

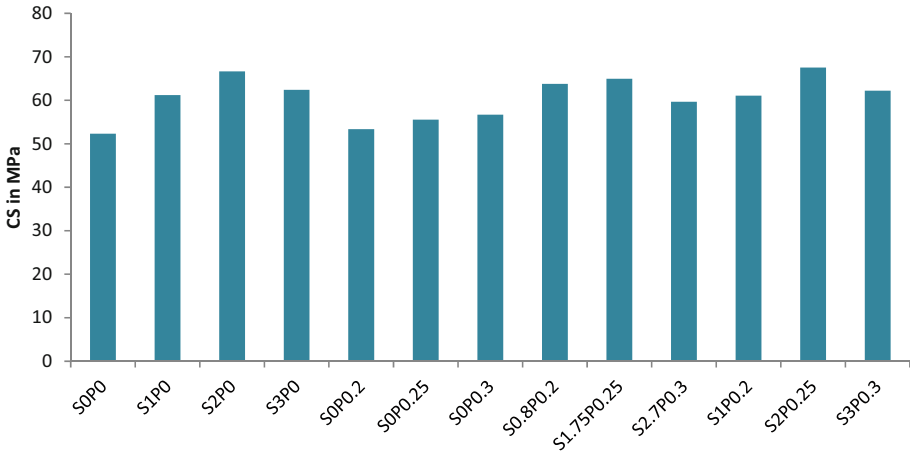


Fig. 6. Compressive strength at 28 days.

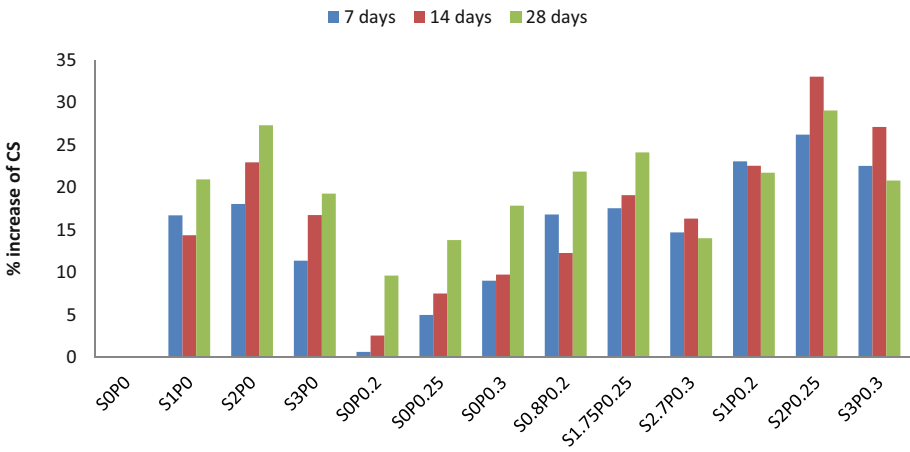


Fig. 7. % increase in compressive strength compared to control concrete.

### 3.2 Split Tensile Strength (STS)

The test results for STS on concrete employing a hybrid mixture of crimped SF and PP are presented in Fig. 8 for 28 days. The STS of HSC with crimped shaped steel fibers and PP is 7.8 MPa at 2% steel fiber volume fiber content and 9.32 MPa when 2% SF with 0.25% PP is added. It means that as the percentage of HF content increases, tensile strength of HSC increased. Figure 9 depicts the increase in percent STS, whereas Fig. 10 depicts the cylinder specimens' failure manner. As a result, the fibers are suitable for bridging internal concrete cracks to increase the STS of concrete.

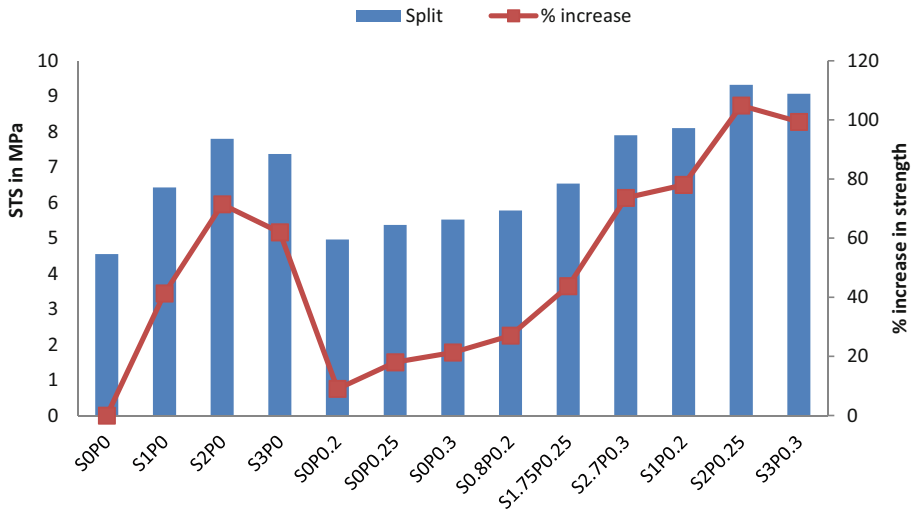


Fig. 8. Split tensile strength and % increase in strength.



Fig. 9. Final failure specimen of split tensile strength.

### 3.3 Impact Strength

The impact energy for 28 days of cure was computed on the basis of number of blows. At 28 days, the most powerful impact energy for the formation of the first fracture was about 2445.5 J, and the most possible impact energy for the creation of the final crack was about 3274.3 J. At the first and the specimens' ultimate failure, the maximum impact energy was obtained for mix S3P0 and S3P0.3 at 28 days in comparison to the control concrete. Figure 10 shows the test results of different mix and Fig. 11 shows the crack pattern of the specimens at failure. The control specimen with 0.75% Nano silica without steel and polypropylene fibers resulted in a smaller number of blows

compared to other specimens. Also, fibre with 3% steel and 0.3% polypropylene fibers has the maximum number of blows proving the crack bridging effect. The number of blows was also increased with increase in Nano content and addition of hybrid fiber content.

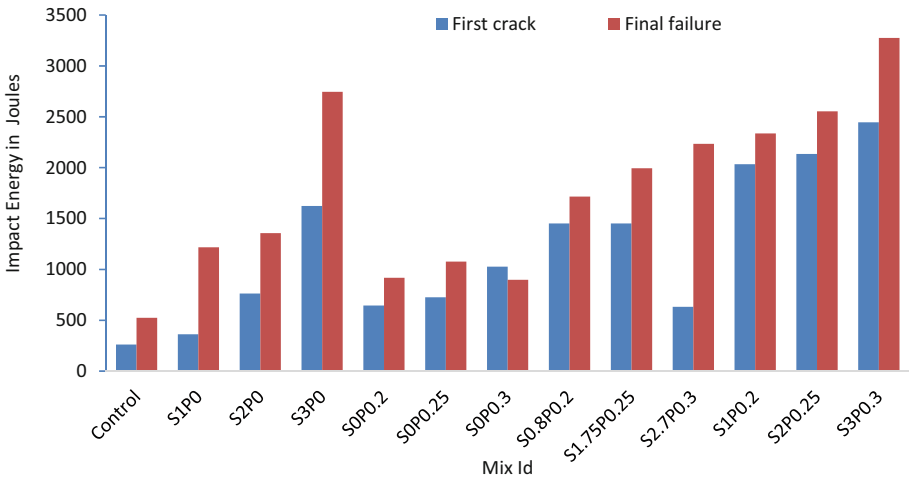


Fig. 10. Impact energy for first crack and final failure.



Fig. 11. Impact energy of final failed specimen.

### 3.4 Sorptivity Results

On fairly homogeneous material, the capillary increase absorption rate can be used to determine sorptivity. As a test fluid, water was used. After casting, the cylinder was placed in water for 28 days to cure. The specimen has a diameter of 100 mm and a height of 50 mm. The specimen’s surface water was wiped away. The specimen’s

surface water was wiped away. with a dampened tissue, and each weighting process was accomplished in less than an hour. Sorptivity is a material attribute that describes a porous substance’s Capillary action’s water-absorbing and water-transporting ability. The ability of capillary action to absorb and move water. Absorption rate (I) were calculated. The graph was plotted for I (mm) vs.  $\sqrt{\text{Time}} (\sqrt{s})$ , from that sorption coefficient was found a shown in Fig. 12. It is observed that the sorption coefficient was higher in case of control concrete, on comparison with other all cases. The initial absorption ends within a day and secondary absorption starts after it. The secondary absorption increases gradually up to day 1 and then decreases till there is no more absorption. Average secondary absorption rate is 0.4 mm and this rate is almost same for all cases except control concrete (with and without steel and PP fibers). It is noted that a minimum absorption rate was found in specimen with 3% SF and 0.3% PP. As the filaments expand, the droop values decrease. This is due to the fact that as the filaments are added, the drainage decreases and the mixture become strong. We may deduce from this that when the rate of fiber material increases, the workability decreases.

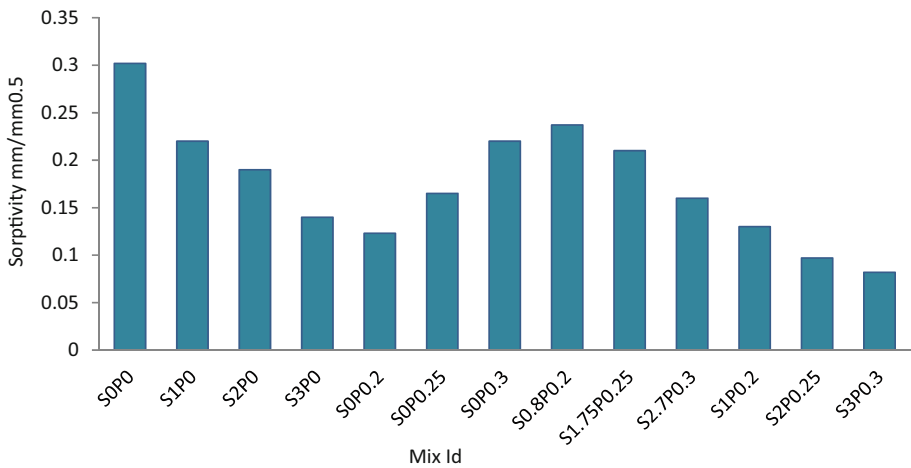


Fig. 12. Sorptivity results.

### 4 Conclusions

The conclusion that follows is based on the experimental results obtained.

1. Steel fiber clearly outperforms all other fibers in all tests. Steel fibers have more strength than polypropylene owing to the anchoring mechanism. Due to higher grade and combination of Nano silica resulted in brittle nature which has been compensated by the addition steel and PP fibre at different proportion.

2. According to the results of the tests, a fiber blend of 2% steel and 0.25% PP fiber yielded the best results shows improved compressive strength and split tensile strength.
3. Hybrid concrete has a high CS for 28 days, as does crimped steel, and polypropylene also has a high CS. This demonstrates that steel and its hybrid concrete have superior CS. Mix S2P0 and S2P0.25 gives the maximum compressive as 66.64 and 67.54 with the 273456% and 29.0655% increase in strength. In all hybrid combinations of fiber, mono steel and mono polypropylene reinforced cement.
4. The combination of 2% SF and 0.25% PP has a high strength in STS compared to all other hybrid combination these mix S2P0 and S2P0.25 gives the maximum tensile strength of 7.8 and 9.32 MPa and the increase percent of 71.84% and 104.83% with their combination of controls compares.
5. The impact performance of a hybrid of 2% and 3% steel with 0.25% and 0.3% PP fibre was improved based on the first and last failure, a number of blows and impact energy with the maximum of 2553.6 J and 3274.3 J.
6. The hybrid steel – polypropylene fibre reinforced concrete has superior strength and durability properties when compared to the control and mix with only steel and polypropylene fibers.
7. The inclusion of HSC mixed with hybrid fibers may be noted as having resulted in advantages due to increased mechanical properties of these fibers and a beneficial impact on concrete characteristics by the HSC-HFRC.

## References

- ACI committee 544.2R-89: Measurement of properties of fiber reinforced concrete
- American Society for Testing and Materials (ASTM): Standard test method for measurement of rate of absorption of water by hydraulic-cement concretes, ASTM C1585, ASTM International, West Conshohocken, Pennsylvania (2013)
- Bernard, E.S.: Influence of toughness on the apparent cracking load of fibre reinforced high strength concrete slabs. *J. Struct. Eng.* **132**, 1976–1983 (2006). [https://doi.org/10.1061/\(ASCE\)0733-9445\(2006\)132:12\(1976\)](https://doi.org/10.1061/(ASCE)0733-9445(2006)132:12(1976))
- Liu, F., Ding, W., Qiao, Y.: Experimental investigation on the tensile behavior of hybrid steel-PVA fiber reinforced concrete containing fly ash and slag powder. *Constr. Build. Mater.* **241** (11), 118000 (2020). <https://doi.org/10.1016/j.conbuildmat.2020.118000>
- IS 10262: Recommended guidelines for concrete mix design. Bureau of Indian standards, New Delhi (2019)
- Bankir, M.B., Sevim, U.k.: Performance optimization of hybrid fiber concrete according to mechanical properties. *Constr. Build. Mater.* **261** (2020). <https://doi.org/10.1016/j.conbuildmat.2020.119952>
- Kanagavel, R., Arunachalam, K.: Experimental investigation on mechanical properties of hybrid fiber reinforced quaternary cement concrete. *J. Eng. Fibers Fabrics.* **10**(4), 139–147 (2015). <https://doi.org/10.1177/155892501501000407>



- Mezzal, S.K., Al-Azzawi, Z., Najim, K.B.: Effect of discarded steel fibers on impact resistance, flexural toughness and fracture energy of high-strength self-compacting concrete exposed to elevated temperatures. *Fire Saf. J.* **121**(10), 103271 (2021). <https://doi.org/10.1016/j.firesaf.2020.103271>
- Fallah, S., Nematzadeh, M.: Mechanical properties and durability of high-strength concrete containing macro-polymeric and polypropylene fibers with nano-silica and silica fume. *Constr. Build. Mater.* **132**, 170–187 (2017). <https://doi.org/10.1016/j.conbuildmat.2016.11.100>



# Response of T-shaped Tall Building Under Wind Load

P. G. Priyadarsh<sup>(✉)</sup> and Neelam Rani

Department of Civil Engineering, Dr. B R Ambedkar National Institute of Technology, Jalandhar, Punjab, India  
priyadarshpg@gmail.com, ranin@nitj.ac.in

**Abstract.** This paper presents the results of wind load on T-shaped G+19 storey building located at Jalandhar, Punjab. The building is located in terrain category-3 as per IS 875 (part 3): 2015. Plan area of T shaped building is 343 m<sup>2</sup>. Unsymmetrical plan buildings cannot be analysed using data provided by wind codes. Wind incidence angles considered are from 0° to 180° at an interval of 45° for an isolated building. Interference effect due to another T-shaped building on an existing building also included in this study. Analysis was carried out using STAAD Pro V8i. The spacing between the buildings were varied from zero to twice the breadth of the flange. The deflection obtained were plotted in x–y graphs as a function of deflection of nodes. It was observed that at certain critical nodes deflection due to interference effect exceeded the deflection criteria specified in the code.

**Keywords:** Interference · Tall building · Wind load · Deflection · STAAD pro

## 1 Introduction

Need for high rise buildings are increasing day by day in developing countries like India due to rapid population rise. Advanced construction techniques and increased demand for aesthetic appearance culminated in the increased construction of unsymmetrical tall buildings. However, these unconventional plans of buildings are liable to lateral loads such as wind. Although the data available in most of the wind codes (ASCE 7, NBCC, GB50009) are adequate to calculate wind load for regular buildings, complex building configurations such as T, U shapes have not handled (Stathopoulos and Alrawashdeh 2020). Turbulence buffeting, galloping, vortex shedding resonance are some of the phenomena affecting wind load on high rise buildings.

In the past decade, studies conducted on wind loads mostly dealt with regular shaped buildings in isolated condition. Developments in the field of wind load and interference effects during 19<sup>th</sup> century are discussed by Khanduri et al. (1998) and Khanduri et al. (1998). Rapid advancements in computational capabilities in 20<sup>th</sup> century lead to the evolution of faster computers at feasible rate. Computational Fluid Dynamics (CFD) which are computationally intensive become simple and attracted the attention of many researches (Kataoka et al. 2020; Skytte et al. 2019). Gomes et al. (2005) studied wind effect on irregular plan shape building of “L” and “U” and compared the results with CFD calculated values (Gomes et al. 2005). Chakraborty

et al. 2014 used “+” plan shaped building and compared wind pressure obtained from wind tunnel testing and different CFD models (Chakraborty et al. 2014). Paul and Dalui (2016) conducted a study on “Z” plan shaped building using ANSYS (Paul and Dalui 2016). Sanyal and Dalui (2021) performed a CFD evaluation of wind pressure on “Y” plan shaped building and validation was performed by comparing wind tunnel test values of CAARC building. They noticed that K- $\epsilon$  model shows more realistic value (Sanyal and Dalui 2021). From another study conducted by Mohotti et al. (2018) K- $\omega$ SST model gave results closer to those obtained from wind tunnel experiment (Mohotti et al. 2018). Hou and Jafari (2020) performed an investigation about different methodologies for wind analysis like gust load factor, high frequency force balance, aeroelastic, numerical simulation and field measurements (Hou and Jafari 2020). Huang et al. (2018) introduced a new algorithm for computer vision based vibration measurements and discovered that computer vision based vibration measurement (VVM) is feasible to obtain dynamic response of tall building (Huang et al. 2018).

Interference effect is a complex phenomenon. It depends on many parameters like building geometry, location, spacing and many more. Hence IS 875 (part 3): 2015 introduced wind interference factor (IF) to compensate this phenomenon (Standards). Kumar (2020) reviewed IS 875 (part 3): 2015 and found out an increase of 7% to 35% in wind load due to implementation of IF. Author also states former version of AS1170.2 included IF, which was removed recently due to complexity (Kumar 2020). Xie and Gu (2004) performed study on interference effect on tall buildings based on their height, spacing and breadth and obtained an increment of about 20% compared to mean wind load. They also discussed about variation of height ratio with interference.. Author also found an increase of 10% in mean wind load on principal building when interfering building are located at (0,3.2b) due to channeling effect (Xie and Gu 2004). Same observation of 10% increase in pressure coefficient was found out by Yu et al. (2015) with a domain of  $2 < (y/b) < 5$  and  $H_r > 1$ . Yu et al. (2018) conducted a detailed study on interference effect on two tall building by varying breadth ratios from 0.4 to 1.4 with an increment of 0.2 (Yu et al. 2018). Zu and Lam (2018) done research work on shielding effect of row of building on a tall building (Zu and Lam 2018). Lam et al. (2008) studied interference mechanism of closely spaced row of high rise building whose breadth ratio ranges from 0.1B–0.5B (Lam et al. 2008). Hu et al. (2020) introduced machine learning models for interference analysis. They found GANs models gives more accurate results compared to other models (Hu et al. 2020).

## 2 Methodology

An experiment on T Shaped building was done by Ravinder Ahlawat at Civil Engineering Department, IIT Roorkee (Ahuja and Gupta 2013). Pressure measurement was done for wind incidence angles varying from  $0^\circ$  to  $180^\circ$  with the difference of  $45^\circ$  Fig. 2. Wind incident angles were varied in anti-clockwise direction. Interference effect was also studied on the existing T-shaped building of same specifications with spacing between them as  $0, b_f, 2b_f$  where  $b_f$  stands for breadth of flange. Dimension of the building model and direction of wind induced angles are shown in Figs.1 and 2. Two interference setups were studied, one with face E facing wind and other with face A facing wind (Fig. 2).

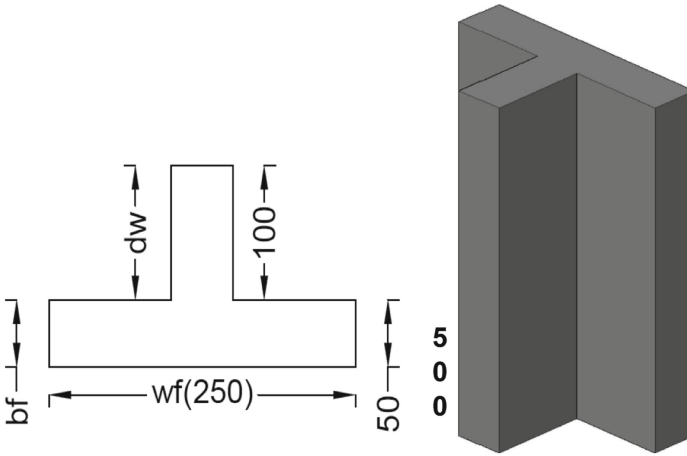


Fig. 1. Dimension of model (in mm) (Ahuja and Gupta 2013).

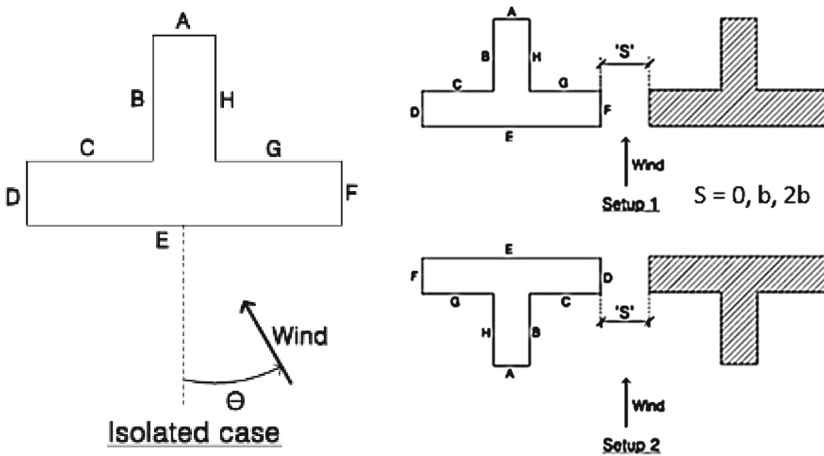


Fig. 2. Direction of wind incident angle for isolated and interference cases (Ahuja and Gupta 2013).

Pressure coefficients obtained from above wind tunnel tests are used to calculate the wind force according to IS 875 (part 3): 2015. The values of pressure coefficients are obtained by interpolating wind pressure contours using Surfer. The wind force obtained from isolated, interference condition and IS 875 (part 3): 2015 were compared using STAAD Pro V8i in this paper. Pressure coefficients are taken from code by considering T-shaped building as rectangular building. Deflection at various critical nodes are analysed by varying direction of wind load and interference conditions. Critical nodes taken are shown in Fig. 3.

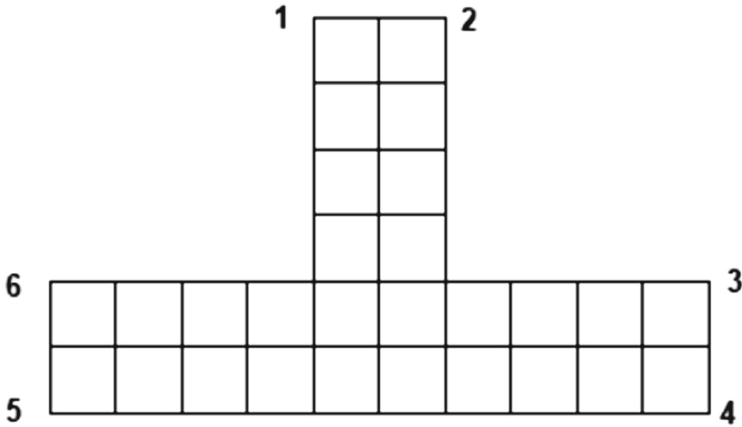


Fig. 3. Location of critical nodes.

### 3 Building Modeling

A T shaped building with same ratio of  $b_f$ :  $w_f$ :  $d_w$  (breadth of flange, width of flange, depth of web) is modelled in STAAD Pro V8i. Ratio of Building model is 7:14:35 and experimental model ratio is 50:100:250. The building was assumed to be located in Jalandhar, Punjab. Basic wind speed of 50 m/s and terrain category 3 has been selected as per IS 875 (part 3):2015 Standards. Wind load has been calculated by considering building without any opening and using equations provided in IS 875 (part 3):2015. Compressive strength of concrete taken as 27.579 MPa and density as 23.5616 kg/m<sup>3</sup>. Dead load and Live load are calculated using IS 875 Part 1 and Part 2. Base of the building assigned to be fixed. The different parameters of the building are shown in Table 1 (Figs. 4 and 5).

Table 1. Building specifications

S. no	Building specifications	Quantities
1	No of stories	G+19
2	Plan Area	343 m <sup>2</sup>
3	Floor to floor height	3.5 m
4	Dimension of beam	0.45 m × 0.45 m
5	Dimension of column	0.5 m × 0.5 m
6	Self-weight factor	1.5
7	Wall load	13.2 kN/m
9	Floor load	3.75 kN/m <sup>2</sup>
10	Live Load	2 kN/m <sup>2</sup>

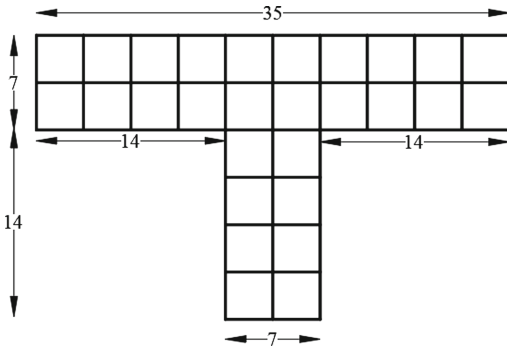


Fig. 4. Plan of T Building (in m).

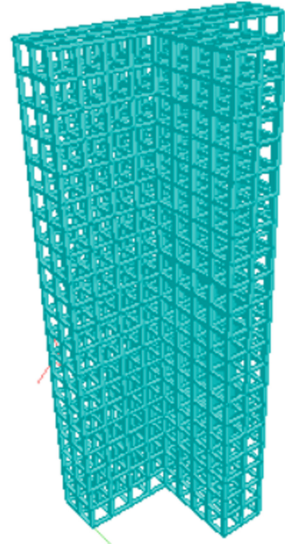


Fig. 5. Rendered View of Building.

## 4 Results and Discussion

### 4.1 Isolated Case

Figure 6 shows the variation of deflection of nodes at position 4 with respect to height of building for various wind incident angles. For all other cases, deflection obtained using IS 875 (part 3):2015 for  $0^\circ$  wind incident angle gives higher deflection of columns, followed by deflection obtained using experimental value for  $0^\circ$  isolated condition. However, at position 4 deflection obtained using IS 875 Part 3 for  $0^\circ$  and experimentally obtained value for  $45^\circ$  isolated condition found to be matching. Least deflection among all isolated conditions was observed with  $135^\circ$  wind incident angle.

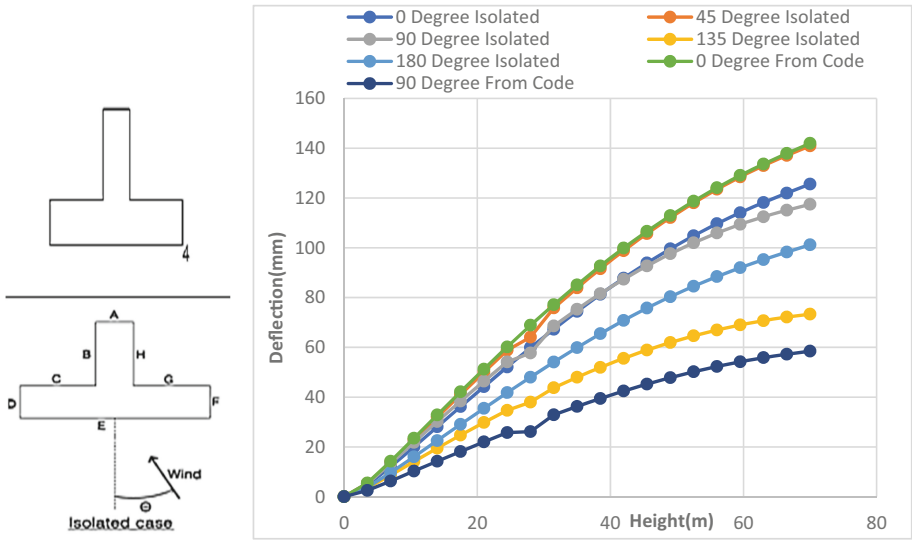


Fig. 6. Graph showing deflection at position 4 for various wind incident angles.

#### 4.2 Interference Setup 1 (Wind Incident on Face E)

Maximum deflection of the building (Fig. 7) obtained for columns located at position 4 for interference setup 1 with spacing between buildings equal to double the breadth of the flange. There is about 15.9% increment in deflection for columns located at position 4 with respect to average deflection of all columns located at top story.

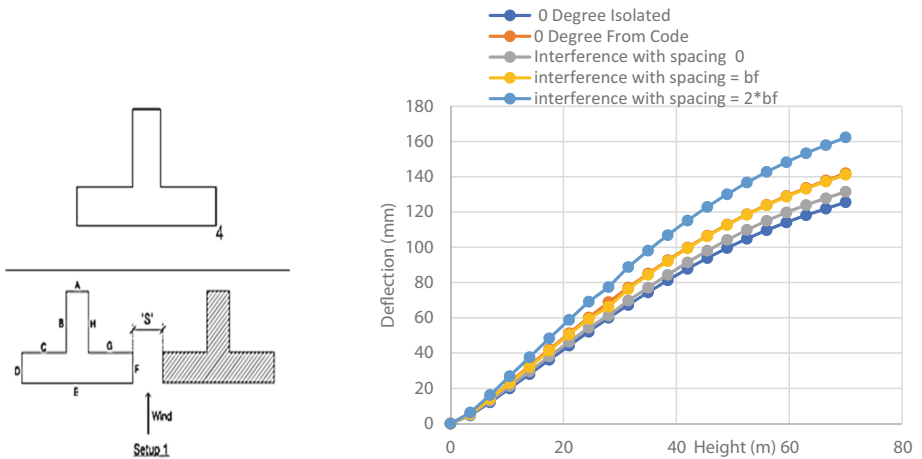


Fig. 7. Graph showing deflection at position 4 for wind incident at 0° and interference setup 1.

### 4.3 Interference Setup 2 (Wind Incident on Face A)

Unlike interference setup 1, the case without spacing gives maximum deflection for all critical nodes when compared with  $180^\circ$  isolated condition and other spacing scenarios in interference setup 2 (Fig. 8). Maximum deflection in this arrangement has been found at position 5.

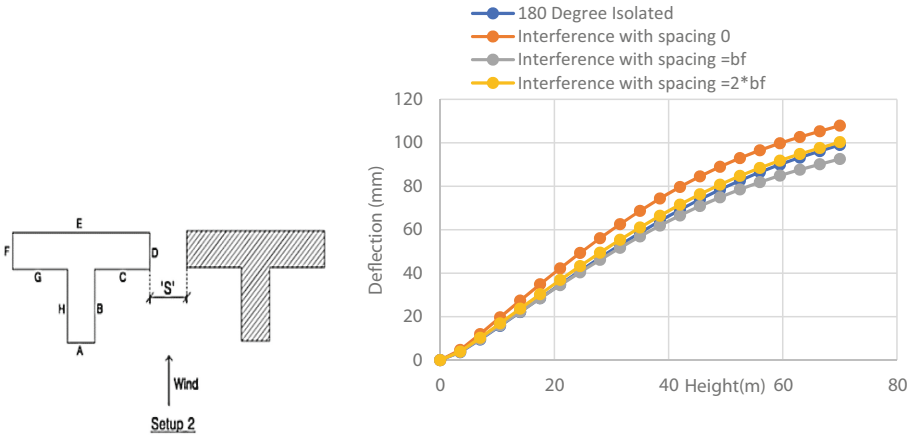


Fig. 8. Graph showing deflection for interference setup 2.

## 5 Conclusion

Maximum deflection observed at position 4 under interference setup 1 with spacing between building as double breadth of flange may due to channelling effect and formation of eddies. Least deflection was obtained for  $135^\circ$  wind incident angle and hence it can be considered that the ideal orientation of a T-building should be at an angle of  $135^\circ$  from the direction of maximum wind obtained from wind data.

Deflection observed from IS 875 Part 3 for  $90^\circ$  gave least value among all conditions while  $0^\circ$  condition obtained using IS 875 Part 3 gives highest deflection in most cases. It is evident that code cannot be used for irregular shaped buildings. It is desirable to perform CFD or wind tunnel test to get reliable results for the construction of irregular shaped buildings.

## References

- Ahuja, A.K., Gupta, P.K.: Wind loads on tall buildings. *Electr. J. Struct. Eng.* **7**, 41–54 (2013)
- Chakraborty, S., Dalui, S.K., Ahuja, A.K.: Wind load on irregular plan shaped tall building - a case study. *Wind Struct. Int. J.* **19**(1), 59–73 (2014). <https://doi.org/10.12989/was.2014.19.1.059>
- Gomes, M.G., Moret Rodrigues, A., Mendes, P.: Experimental and numerical study of wind pressures on irregular-plan shapes. *J. Wind Eng. Ind. Aerodyn.* **93**(10), 741–756 (2005). <https://doi.org/10.1016/j.jweia.2005.08.008>



- Hou, F., Jafari, M.: Investigation approaches to quantify wind-induced load and response of tall buildings: a review. *Sustain. Cities Soc.* **62**(May), 102376 (2020). <https://doi.org/10.1016/j.scs.2020.102376>
- Hu, G., Lingbo, T., Dacheng, S., Jie Tse, K.T., Kwok, K.C.S.: Deep learning-based investigation of wind pressures on tall building under interference effects. *J. Wind Eng. Ind. Aerodynam.* **201**, 104138 (2019). <https://doi.org/10.1016/j.jweia.2020.104138>
- Huang, M., Zhang, B., Lou, W.: A computer vision-based vibration measurement method for wind tunnel tests of high-rise buildings. *J. Wind Eng. Ind. Aerodyn.* **182**(September), 222–234 (2018). <https://doi.org/10.1016/j.jweia.2018.09.022>
- Kataoka, H., Ono, Y., Enoki, K.: Applications and prospects of CFD for wind engineering fields. *J. Wind Eng. Ind. Aerodynam.* **205**(July) (2020). <https://doi.org/10.1016/j.jweia.2020.104310>
- Khanduri, A.C., Stathopoulos, T., Bédard, C.: Wind-induced interference effects on buildings - a review of the state-of-the-art. *Eng. Struct.* **20**(7), 617–630 (1998). [https://doi.org/10.1016/S0141-0296\(97\)00066-7](https://doi.org/10.1016/S0141-0296(97)00066-7)
- Kumar, K.S.: Wind loading on tall buildings: review of Indian Standards and recommended amendments. *J. Wind Eng. Ind. Aerodyn.* **204**(May), 104240 (2020). <https://doi.org/10.1016/j.jweia.2020.104240>
- Lam, K.M.Á., Leung, M.Y.H., Zhao, J.G.: Interference effects on wind loading of a row of closely spaced tall buildings. *Aerodynamics* **96**, 562–583 (2008). <https://doi.org/10.1016/j.jweia.2008.01.010>
- Mohotti, D., Wijesooriya, K., Dias-da-Costa, D.: Comparison of Reynolds averaging Navier-Stokes (RANS) turbulent models in predicting wind pressure on tall buildings. *J. Build. Eng.* **21**, 1–17 (2018). <https://doi.org/10.1016/j.job.2018.09.021>
- Paul, R., Dalui, S.K.: Wind effects on ‘Z’ plan-shaped tall building: a case study. *Int. J. Adv. Struct. Eng.* **8**(3), 319–335 (2016). <https://doi.org/10.1007/s40091-016-0134-9>
- Sanyal, P., Dalui, S.K.: Effects of internal angle between limbs of “Y” plan shaped tall building under wind load. *J. Build. Eng.* **33**, 101843 (2021). <https://doi.org/10.1016/j.job.2020.101843>
- Skytte, M., Chr, J., Koss, H.H.H.: Review for practical application of CFD for the determination of wind load on high-rise buildings. *J. Wind Eng. Ind. Aerodyn.* **186**, 155–168 (2019). <https://doi.org/10.1016/j.jweia.2018.12.019>
- Standards, B. of I.: IS 875: Code of practice for design loads (other than earthquake) for building and structures - Part 3 : wind loads. BIS New Delhi **875**(1), 51 (2015)
- Stathopoulos, T., Alrawashdeh, H.: Wind loads on buildings: a code of practice perspective. *J. Wind Eng. Ind. Aerodyn.* **206**(August), 104338 (2020). <https://doi.org/10.1016/j.jweia.2020.104338>
- Xie, Z.N., Gu, M.: Mean interference effects among tall buildings. *Eng. Struct.* **26**(9), 1173–1183 (2004). <https://doi.org/10.1016/j.engstruct.2004.03.007>
- Yu, X.F. Xie, Z.N., Zhu, J.B., Gu, M.: Interference effects on wind pressure distribution between two high-rise buildings. *J. Wind Eng.* **142**, 188–197. <https://doi.org/10.1016/j.jweia.2015.04.008>
- Yu, X., Xie, Z., Gu, M.: Interference effects between two tall buildings with different section sizes on wind-induced acceleration. *J. Wind Eng. Ind. Aerodyn.* **182**, 16–26 (2018). <https://doi.org/10.1016/j.jweia.2018.09.012>
- Zu, G.B., Lam, K.M.: Shielding effects on a tall building from a row of low and medium rise buildings. *Wind Struct. Int. J.* **27**(6), 439–449 (2018). <https://doi.org/10.12989/was.2018.27.6.439>



# Source Localization in a Framed Structure for Effective Damage Detection Using Acoustic Emission Technique

Anupam Kumar Biswas<sup>1,2(✉)</sup>, Alope Kumar Datta<sup>3</sup>, Pijush Topdar<sup>3</sup>,  
and Sanjay Sengupta<sup>4</sup>

<sup>1</sup> NIT Durgapur, Durgapur, India

anupam.biswas@bcrec.ac.in, akb.l8cel502@nit.dgp

<sup>2</sup> Department of Civil Engineering, Dr. B C Roy Engineering College,  
Durgapur, India

<sup>3</sup> Department of Civil Engineering, NIT Durgapur, Durgapur 713209,  
W.B., India

<sup>4</sup> Dr. B.C. Roy Engineering College, Durgapur 713206, W.B., India

**Abstract.** Acoustic Emission (AE) technique is capable of detecting real time small-scale damage long before failure in a structure. However, the placement of sensors in a framed structure is an important issue for effective damage detection, which remains a challenge for many researchers. In this study, an experimental investigation is carried out for the localization of mounted AE sensors on a prototype rigid framed structure, and by detecting simulated AE source using Pencil Lead Break (PLB), on different beam and column locations of each floor levels of the framed structure. Then with the recorded AE signal waveforms, frequency analyses have been performed using the wavelet transform to get the signal's energy concentration. To localize the damage the wavelet transform is used in the time-frequency domain along with the group velocity. From the data comparison and analysis, it is found that for effective damage detection a single AE sensor can be placed at the beam-column joints of each floor level of framed structure on every plane of the frame.

**Keywords:** Acoustic emission technique · Structural health monitoring · Wavelet transformation · Hsu-Nielsen pencil lead break

## 1 Introduction

Steel Framed structures provide better resistance against collapse under seismic forces than compared to other building materials. Steel framed structures have wide range of application in different industries due to its immense strength and ductile properties. However, factors like fatigue weld fractures; corrosion etc. can hamper the structural performance severely and may lead to unexpected failure.

Structural Health Monitoring (SHM) is important for the evaluation of durability of structures during its service life & to make a warning or decision on maintenance of a structure. Acoustic Emission (AE) technique has been readily used for SHM as it is a precise damage detection technique in real-time. A crack which generates and propagates

in a structure produces stress waves. Once the signal is generated the AE event can be visualized in the Post-processing unit. Damage localization is a primary challenge in SHM. The common way of determining source location is time of arrival method in which a number of sensors are mounted on the surface of a structure and the location of source is identified by comparing the arrival time of the signals at the sensors and using triangulation techniques. Biswas et al. (2020) location of sensor to be placed of structure is a crucial to effectively detect damage. The installation of large number of sensors of effective damage detection could lead to huge investment and burden on the client. A considerable number of sensors would be required to effectively monitor damage initiation every part of the framed structure. Moreover, the number of sensors to be used for effective SHM can be reduced to least possible for cost-cutting. From the literature studies on the framed structure with AE technique damage localization it has been found that a limited experimental research work has been performed on the said topic till now.

The objective of this research is damage localization in framed structures with optimum no. of sensor placements for structural health monitoring. To carry research on the said topic, experimental work has been carried out on a prototype steel framed structure and various locations of the structure has been chosen for mounting the sensors. Damage has been simulated in structure by using mechanical pencil by using the technique of Pencil Lead Break (PLB). Once the time-dependent AE events are recorded, they are converted into frequency domain. Afterwards wavelet transformation in time-frequency domain is used is done to obtain the source location by using the group velocity in different symmetric and anti-symmetric modes.

Panjsetooni et al. (2013) investigated process of damage in reinforced concrete frame specimens. They tested reinforced concrete RC frames under loading cycle and monitored using AE. They used the AE test data to analyze the AE source location analysis method. The results obtained from AE source location in stage from micro-cracks, and concluded that AE method can be used to obtain the growth of internal microcracks at critical location. Also, the results show that first visible cracks at each location of RC frame specimen increased in cumulative absolute energy in those locations. Dong and Li (2012) simplified the source localization in three-dimensional bodies by placing sensors at selected corner points of a cube and then deriving an analytical expression for source localization.

From experimental studies carried out by Gorman and Prosser (1991) on rectangular aluminum plates by using pencil lead breaks Hsu Neilsen sources Hsu (1981) for producing AE signals, from this they found that for different plate modes the extent of damage and source localization measurements of the amplitudes can be used effectively. For determining AE source orientation, they used an approach which interprets AE signal for extensional and flexural mode of plate. One of the noteworthy advantages of the AE technique is that when sensors are located on different positions of the structure, based on the arrival times of an AE signals we can calculate spatial source location. When two sensors are placed in a line and the distance between them is known along with the velocity of propagating wave, then the source can be located along that line. Using two sensors source localization studies performed by Ziola and Gorman (1991) shows that, precise linear location can only be found out if the modal nature of AE signals is taken into consideration along and the arrival times of both the sensors which are determined on the same way. They have studied on the transducer

outputs with a single frequency cosine wave and cross correlated them to propose a method for finding AE source location. They found that accuracy of source location improved when locating phase points on the transducer outputs are determined to get the difference in arrival time. Finite element analysis has been found to be promising for validating the results for simple problems.

Schumacher et al. (2008) showed that by using waveforms and source mechanisms a relationship can be drawn by transforming the signal into frequency domain and calculating their coherence functions. The wavelet transform (WT) along with AE technique was first used by Suzuki et al. (1996) where he showed the usefulness of WT for analyzing the frequency components of an AE signal as a function of time and also demonstrates the ability of WT for separating valid signals from noise, by studying on the AE signals on glass-fibre reinforced composite sample under tensile loading where WT was performed.

In complex structures one of the major challenge is record of complete AE signals, as most of the weak signals get absorbed due to geometric spreading effects and dissipation of signals before they could reach the sensors. A considerable number of signals need to be stored for minimum number of events which causes problem for even sophisticated equipments, so to monitor large structures this is the possible limitation of signal-based techniques. Such limitations can be avoided by reducing the amount of data which is not related to the material failure by applying sophisticated trigger algorithms (Fig. 1).



Fig. 1. Preamplifier and sensor

To perform experimental investigation the pencil-lead break can proved to be a reliable source for simulation of AE source. Besides the advantage the limitations of pencil-lead break are that it can be only applied to outer surface of structure (as out-of-plane source) where the range of the source rise times and source dimensions are also limited. Besides Pencil-lead-break an AE source model can be simulated as done by Gary and Hamstad (1994) where they proposed a two-dimensional dynamic finite element method for thin plate specimens. The response recorded at a crucial location of structure can proof to be important regarding response-based damage detection. Hence, placement of sensors at crucial points on the structure is important aspect for effective damage detection by AE technique.

Extensive studies have been carried out on simple structures like plates for damage localization using simplified sources of AE and using FEM also by many

researchers. However, further investigation is required to make it implementable in real life structures.

Li et al. (2004) has determined the optimal sensor locations for structural vibration measurements. They presented an efficient method based on the uniform design theory, which is very different from the empirical method and is accurate and simple for implementation. A cantilever beam is used as an example to illustrate the effectiveness and application of the proposed method. It is shown through the example that in comparison with the conventional method, the use of the present method results in the reduction of workload above 90%.

Most of the research based on AE technique in damage localization with optimum sensor location explores on isotropic and/or anisotropic plates structures, RC beam and RC frame structures. Based on the literature review it is found that damage localization using AE technique in framed structure are rare in literature, therefore the present study is an effort to analyze the damage localization in framed structures with optimum no. of sensor placements using AE technique.

## 2 Methodology

The experimental setup consists of 0.9 m × 0.3 m × 0.3 m size steel bared frame structure, fixed at base. Sources were generated by breaking 0.5 mm mechanical pencil leads (Hsu-Nielsen source). Pencil- lead break (PLB). The lead is pressed firmly against the prototype structure until the lead breaks. These applications of pressure lead to breaking of lead and henceforth release acoustic waves. These acoustic waves propagate in structure and finally they are captures in sensors. Once the data are obtained in the form of AE waveform in (voltage verses time plot) to get the higher energy concentration of the AE event the time dependent data is converted to frequency domain by performing Fast Fourier transform (FFT) to identify the best position of sensors on the structure for effective damage detection (Figs. 2 and 3).

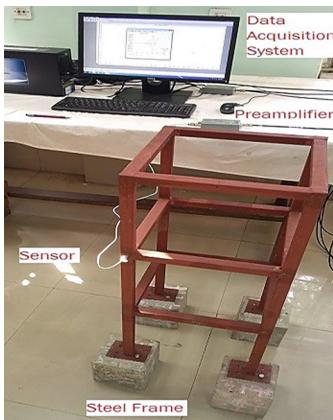


Fig. 2. Test setup

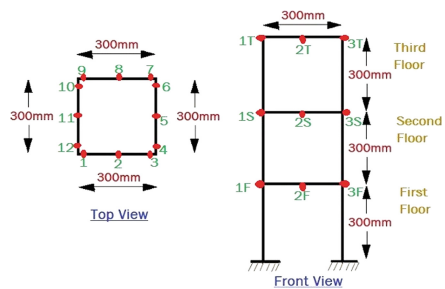


Fig. 3. Steel frame structure with nodal points

With the AE responses obtained Wavelet Transform was carried with help of AGU Vallen software. Group-velocity curves have been considered for longitudinal and shear velocity (i.e. P-wave and S-wave) as 5900 m/s and 3100 m/s respectively. The differential type R15D sensor was used with the frequency response between 20 kHz to 1 MHz.

### 3 Wavelet Transform and Surface Wave Equations

AGU-Vallen Wavelet Transform:-

The WT algorithm is used in this experiment for analyzing the characteristics of AE signals. Since, AE signal consists of more than one wave mode, the WT algorithm is useful to solve this process Zhang et al. (2015). The WT of a function  $f(t)$  of time  $t$  is defined as Hao et al. (2018):

$$\mathcal{W}_\psi^f(a, b) = \int_{-\infty}^{+\infty} f(t)\Psi_{a,b}(t)dt \tag{1}$$

where,  $\Psi_{a,b} = \frac{\psi(\frac{t-a}{b})}{\sqrt{b}}$ , and  $\Psi(t)$  is the complex conjugate of the mother function  $\psi(t)$ ,  $a$  is translation parameter and  $b$  is the scale parameter.

Rayleigh–Lamb (Surface Wave) Equations:-

Rayleigh–Lamb equations are used to calculate the group velocity curves. Generally, to understand the features of the AE signal, the group velocity curves are superimposed on the WT diagram. Rayleigh–Lamb equations are summarized in Eqs. (2)–(4).

$$\text{Symmetric modes: } \frac{\tan(qh)}{\tan(ph)} = -\frac{4k^2pq}{(k^2 - q^2)^2} \tag{2}$$

$$\text{Antisymmetric modes: } \frac{\tan(qh)}{\tan(ph)} = -\frac{(k^2 - q^2)^2}{4k^2pq} \tag{3}$$

Where

$$p^2 = \frac{w^2}{c_1^2} - k^2, \quad q^2 = \frac{w^2}{c_i^2} - k^2 \tag{4}$$

In the equations, ‘ $h$ ’ is half of the plate thickness, ‘ $w$ ’ is the angular frequency, ‘ $k$ ’ is the wave number, ‘ $c_1$ ’ is longitudinal wave velocity, and ‘ $c_i$ ’ is shear wave velocity.

Then, phase velocity:  $c_p = \omega/k$  and group velocity: ‘ $c_g$ ’ = ‘ $d\omega/dk$ ’ has been calculated.

The Discussion of Group-Velocity Curves in Beams:-

The group velocity curve has been calculated and plotted using the above-mentioned procedure. The group velocity curve has been converted to a time scale using the previously calculated propagation through the beam/column section to superimpose the

curve on the WT diagram. The different propagation distance has been calculated by square rooting the sum of the squared distance of the AE source. The beam/column section has a uniform thickness.

### 4 Results and Discussion

The AE waveform time dependent plot for Beam Member (Fig. 4) shows the AE waveform generated for the location of sensor is at node 2 of first floor, and the PLB is done at the 1 of first floor position of the prototype structure.

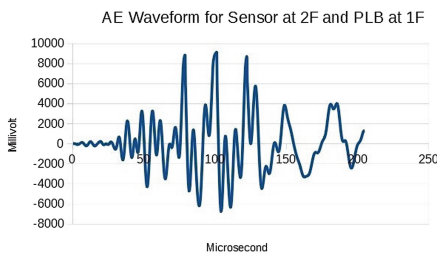


Fig. 4. AE event plot when the sensor is at node 2 PLB at 1 first floor.

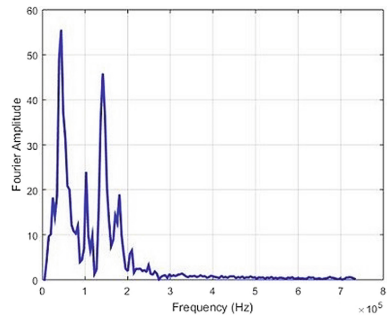


Fig. 5. FFT for Sensor at Node 2 and PLB at 1 first floor

The Fourier transform plot (Fig. 5) shows the amplitude to fall close to the 100 kHz range which is similar to PLB frequency range.

The 2D colour contour diagram of WT coefficient (Fig. 6) shows the maximum magnitude of WT lies with red colour indication and least in pink range. The group velocity curve in S0 mode is not passing through the maximum value, whereas A0 mode has been found to be passing the maximum magnitude of WT.

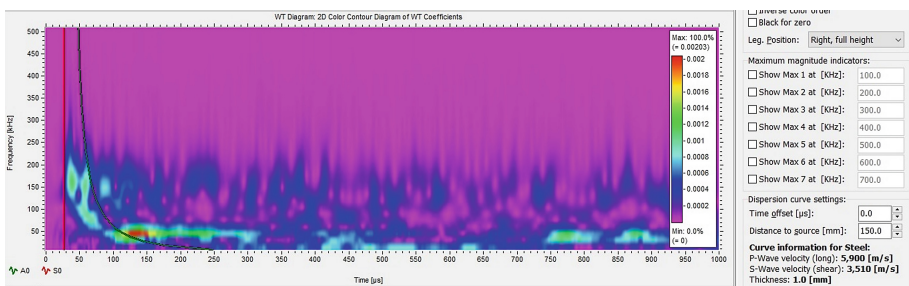


Fig. 6. Wavelet coefficient concentration node 2 and PLB at 1 first floor



Figure 6 shows the WT of the point node 2F when the PLB is done at point 1F on the frame. Here it can be found that the dispersion curve (S0 mode) reaches close to the maximum concentration of the wavelet coefficient, which gives close result of the actual source distance. Figure 7 shows the AE waveform generated when the sensor is at node 3 of first floor, and the PLB is done at the node 1 position of first floor.

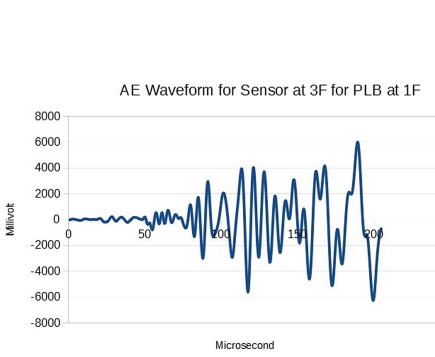


Fig. 7. Sensor is at node 3F, for PLB at 1F

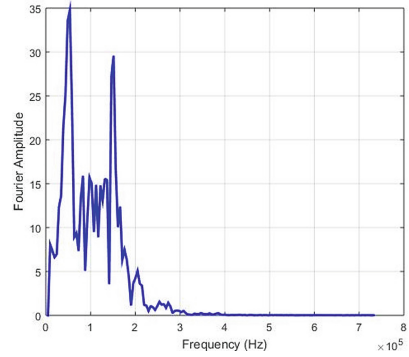


Fig. 8. FFT for Sensor at Node 3F and PLB at 1F.

The Fourier transform plot (Fig. 8) shows the amplitude to fall close to the 100 KHZ range which is similar to PLB frequency range.

The 2D colour contour diagram of WT coefficient (Fig. 9) shows the maximum magnitude of WT lies with red colour indication and least in pink range. The group velocity curve in S0 mode is not passing through the maximum value, whereas A0 mode has been found to be passing the maximum magnitude of WT (Table 1).

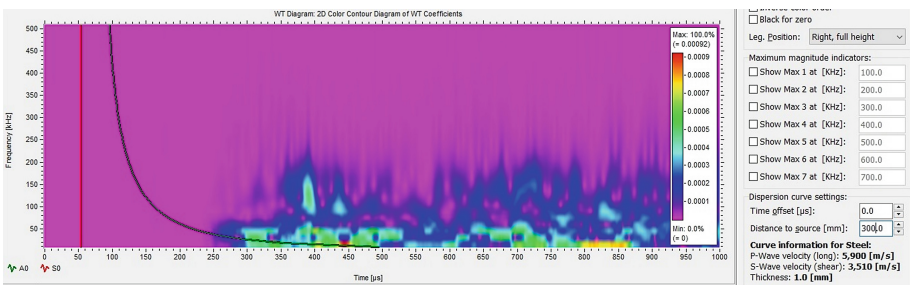


Fig. 9. Wavelet coefficient concentration node 3F PLB at 1F



**Table 1.** Distance between source to sensor and calculated distance when source is at 1F

Sensor location	Actual distance between source and sensor	Calculated distance (mm)
2F	145	143
3F	290	283.67
4F	300	287.78
5F	445	437.89
6F	590	575.43
7F	590	574.64
8F	445	439.16
9F	300	289.51
10F	290	287.62
11F	145	147.15
12F	10	11.36
1S	300	307.06
2S	445	441.23
3S	590	887.76
1T	600	608.26
2T	745	734.73
3T	890	877.84

## 5 Conclusion

From the test result and WT analysis performed for localization of damage in steel bared frame structure, it is found that when sensors are placed on the same beam or column location where damage has occurred, WT analysis along with group velocity can be used for localization considering A0 predominant mode with lesser error. Whereas, when the sensor location is shifted to adjacent beam or column with respect to the damage, the localization result shows erroneous, and with the increase in distance from the sensor the error also increases.

## References

- Biswas, A.K., Datta, A.K., Topdar, P., Sengupta, S.: On Effective placement of acoustic emission sensor in steel framed structure for damage detection. In: National Conference on Emerging Trends on Sustainable Technology and Engineering Applications (NCETSTEA-2020), pp. 1–5, IEEE, February 2020
- Datta, A.K., Shrikhande, M., Paul, D.K.: On the optimal location of sensors in multi-storeyed buildings. *J. Earthq. Eng.* **6**(01), 17–30 (2002)
- Isabelle, B., Gallimard, L., Nikoukar, S.: Optimal piezoelectric actuator and sensor location for active vibration control, using genetic algorithm. *J. Sound Vib.* **329**(10), 1615–1635 (2010)
- Dong, L., Li, X.: Three-dimensional analytical solution of acoustic emission or microseismic source location under cube monitoring network. *Trans. Nonferrous Metals Soc. China* **22**(12), 3087–3094 (2012)

- Gary, J., Hamstad, M.A.: On the far-field structure of waves generated by a pencil lead break on a thin plate. *J. Acoust. Emiss.* **12**(3–4), 157–170 (1994)
- Michael, G.R., Prosser, W.H.: AE source orientation by plate wave analysis. *J. Acoust. Emiss.* **9**(4), 283–288 (1991)
- Schumacher, T., Linzer, L., Grosse, C.U.: Signal-based AE analysis. In: Grosse, C.U., Ohtsu, M., Aggelis, D.G., Shiotani, T. (eds.) *Acoustic Emission Testing*. Springer Tracts in Civil Engineering, pp. 51–99. Springer, Cham (2022). [https://doi.org/10.1007/978-3-030-67936-1\\_5](https://doi.org/10.1007/978-3-030-67936-1_5)
- Hao, Q., Zhang, X., Wang, Y.S., Makis, V.: A novel rail defect detection method based on undecimated lifting wavelet packet transform and Shannon entropy-improved adaptive line enhancer. *J. Sound Vib.* **425**, 208–220 (2018)
- Hsu, N.N.: Characterization and calibration of acoustic emission sensors. *Mater. Eval.* **39**, 60–68 (1981)
- Li, Z.N., Tang, J., Li, Q.S.: Optimal sensor locations for structural vibration measurements. *Appl. Acoust.* **65**(8), 807–818 (2004)
- Alireza, P., Bunnori, N.M., Vakili, A.H.: Damage source identification of reinforced concrete structure using acoustic emission technique. *Sci. World J.* **2013** (2013)
- Sengupta, S., Datta, A.K., Topdar, P.: Structural damage localisation by acoustic emission technique: a state of the art review. *Latin Am. J. Solids Struct.* **12**(8), 1565–1582 (2015)
- Suzuki, H., Kinjo, T., Hayashi, Y., Takemoto, M., Ono, K., Hayashi, Y.: Wavelet transform of acoustic emission signals. *J. Acoust. Emiss.* **14**, 69–84 (1996)
- Zhang, X., Cui, Y., Wang, Y., Sun, M., Hu, H.: An improved AE detection method of rail defect based on multi-level ANC with VSS-LMS. *Mech. Syst. Signal Process.* **99**, 420–433 (2018)
- Zhang, X., Feng, N., Wang, Y., Shen, Y.: Acoustic emission detection of rail defect based on wavelet transform and Shannon entropy. *J. Sound Vib.* **339**, 419–432 (2015)
- Ziola, M.S., Gorman, M.R.: Source location in thin plates using cross-correlation. *J. Acoust. Soc. Am.* **90**(5), 2551–2556 (1991)



# Study on Evaluation of Angle Connection for Transmission Towers

Vinay Kumar Singh and Abhishek Kumar Gautam<sup>(✉)</sup>

Department of Civil Engineering, Madan Mohan Malaviya University  
of Technology, Gorakhpur 273010, India  
abhishek.gautam595@gmail.com

**Abstract.** In present time, the transmission line towers are older than 30–50 years and upgradation of towers are needed in terms of load and strength. Due to unfavourable environmental circumstances, the tower material will degrade. Due to voltage upgradation and the installation of additional antennas to the existing towers for new line of sight, the transmission and communication towers are subjected to increased loading. As a result, a cost-effective structural upgrade strategy that can be easily implemented by the electricity and communication sectors must be devised. In present study, component level analytical and experimental investigations of various researchers have been reviewed to carried out the suitable method for strengthening of existing angle section of transmission towers. Experimental investigation data has been examined from literature for the buckling capacity of steel single angle section of optimum suitable size with rational slenderness ratio to strengthen and to increase the compression capacity at component level showing various connection designs such as (i) double cross-plate, (ii) single cross-plate, (iii) friction grip, (iv) double angle, and (v) double cleat angle connections. Review for the numerical investigation of the above is also carried out using ABAQUS software. The numerical and experimental results are compared and found in good agreement, and the variation is within the suitable limits. It has been observed that the compression strength of angle section has been increased on the suitable average amount and same has been observed for the cleat angle connection method and double cross connection strengthening method from the experiment and analytical investigations perspectives. When compared to other types of strengthening patterns, the cleat angle connection is less expensive. The strengthening angle member shares substantial stress coming from the main member during the application of load in the cleat and friction grip connection. The primary angle member's buckling mode of failure is changed by the double angle connection.

**Keywords:** Transmission tower · ABAQUS · Strengthening · Cleat angle · Cross plate

## 1 Introduction

Transmission towers are frequently utilised for transmitting electric power because every developing country has a high need for electricity. Mexico was the first country to employ steel towers in 1903 (Roy and Kundu 2021). Many earlier transmission

towers were built with narrow diagonal elements and tension-only bracing methods. These towers will need to be modified to withstand the greater loads that will arise as a result of increased demand for power and altering worldwide climate patterns (Albermani et al. 2004). Because of the rising demand for electricity, existing lines must have voltage upgraded. As a result of the increased wind and gravity stresses, the present tower members are overstressed. The old tower members will also need to be reinforced. Because of change of wind zones, the wind loads are frequently changed. The increased wind loading necessitates tower strengthening (Balagopal et al. 2019). Current transmission towers may be under designed as a result of extra communication equipment mounted to them and enhanced design wind loads. Retrofitting existing getting old towers is more workable than building new towers because to economic efficiency, practicality, and environmental constraints (Lu et al. 2018). Members in transmission tower arms were retrofitted with vibration absorbers to reduce fatigue caused by wind loads. Wind loads generate modest amounts of vibration and they were found to be more cost effective than existing approaches such as altering crucial members (Kilroe 2000). This work discusses an evaluation for component-level experimental inquiry to strengthen an equal angle Section 65 mm × 65 mm × 5 mm for various connection patterns, including single cross-plate, double cross-plate, double angle, friction grip and double cleat angle connections. The ABAQUS software tool is used to carry out the analytical research. Based on the findings of investigations into various upgrade schemes, a suitable strengthening technique for transmission line tower and communication tower leg members is provided.

## 2 Literature Review

### 2.1 General Introduction

Lu et al. (2014) examine how many bolts are in the bolted connection, applied rotation, and Friction coefficient all influence as determined by prior study, the behavior of transmission tower legs made of reinforced steel when loaded, it is still necessary to enhance the strategy of retrofitting steel angle connectors in transmission towers.

Xie and Sum (2012) examined the retrofitting approach of a high voltage transmission line tower that had failed caused to an ice tragedy. The addition of diaphragm bracing was discovered to avoid deformation that is not in the plane of the bracing member and to increase the load bearing capability of the transmission tower's existing leg component.

Rao et al. (2012) executed Using 3D FEA of the lattice frame and towers, nonlinear analysis of angle compression members was carried out. The research takes into consideration the eccentricity of the members, the rotational stiffness of the connections, and the material nonlinearity.

Mills et al. (2012) retrofitting steel angle through bolted double steel angle connections to a steel lattice transmission tower. The bolted-splice connection was shown to successfully axial loads are transferred between the original and strengthening angle members.

Bekey et al. (2011) investigated the using fiber-reinforced polymer reinforcement to enhance the buckling strength of steel angles through numerous slenderness ratios. The failure mechanism, ductility, and buckling capability are all factors to consider. FRP strengthening has an impact on the ductility of existing angle sections.

Baskaran et al. (2011) investigated tower failure using basic ways to check tower capacity using existing given particular models. To analyze the collapse of these towers, preliminary structural study using a specialist structural analysis tool must be unified into standard steel tower design procedure. To increase its capacity, the transmission tower leg was upgraded with steel angles via bolted connections.

Albermani et al. (2009) developed a nonlinear analysis approach for transmission tower structures. Our estimates were validated through the results of a costly full-scale test, indicating that the proposed methodology may be used to reliably anticipate structural failure. Because of its precision, the methodology may be utilized for failure study and prediction, as well as design upgrades and revisions. As a result, tower designs may be quickly adjusted and upgraded, saving time and resources.

## 2.2 Need of Strengthening Tower

Thousands of tonnes of steel lattice towers are utilised across the world to deliver dependable power transmission and communication services to residential and commercial clients. As a result, they must be both safe and long-lasting. The majority of these towers have been operational for almost two decades. Furthermore, many older towers remain now designed to maintain bigger loads than individuals for which they were initially designed outstanding to newer, heavyweight devices and better wind design standards. As a result, the existing steel lattice transmission towers are physically inadequate (Lu et al. 2015). The global demand for electricity has recently increased, resulting in the construction of numerous large-scale transmission towers. High winds are a problem for many transmission towers on open terrain (Moon et al. 2009). Bridges, offshore platforms, big mining equipment, buildings, communication towers, and transmission towers are among the steel constructions that require upgrading. Cutting away and replacing plating, or attaching external steel plates, is the traditional way of repairing or strengthening steel structures (Zhao and Zhang 2007). The existing transmission line towers and communication towers must be strengthened due to increased demand for power. Due of land acquisition limits, it is more cost effective to strengthen existing towers rather than build new ones.

## 2.3 The Reasons for Tower Strengthening

### 2.3.1 Wind Load

The use of self-supporting steel towers to support antennas has increased dramatically in recent years as transmission systems have expanded. Wind forces are the key problem in the construction of these structures due to their small weight. High-intensity winds were the primary cause of transmission tower failure in many cases, with high strength winds accounting for 80–100% of all weather associated failures (Savory et al. 2001).

### 2.3.2 Ice Load

Transmission/communication towers are frequently designed with atmospheric icing in mind, especially in cold locations. Towers can be brought down by ice storms, which are a natural hazard. In cold climates, atmospheric icing is a common cause of tower failure. Liquid precipitation can cause ice to form on towers. Furthermore, ice build-up can increase the structure's section area, which increases wind loads. Signal intrusion, structural strain, wire strain, ice load injury as the ice shacks, and entire tower collapse can all be caused by ice load (Mulherin 1998).

### 2.3.3 Seismic Load

Wind impacts were frequently the sole source of lateral loads in latticed transmission tower construction, but earthquakes were rarely considered. Researchers investigated a basic static approach for determining member forces in self-sufficient lattice transmission towers owing to flat and perpendicular seismic irritations using the modal superposition analysis approach. These data clearly indicate that, in risky seismic locations, earthquake properties on towers may be more significant than wind impacts, and that it should be included as a design check. The best design for a latticed transmission tower that will withstand earthquakes. When designing a lattice tower, this research developed continuous and discrete variable optimization approaches to forecast seismic effects (Kocer and Arora 2002).

### 2.3.4 Bolt Slip

Legs, bracings, secondary bracings, and cross members make up latticed transmission towers. A small amount of rotation caused by joint bolt slide might cause extra tower distortion, which is difficult to predict and cannot be controlled for in the research. Bolt slippage may have minor effects on deflection, but it has small effect on the ultimate strength of lattice systems. The effects of deflections are often overlooked in tower analysis and design. Deflections will be significant if the tower is necessarily tall and flexible, and they cannot be ignored since they can produce secondary strains (Rao et al. 2012).

### 2.3.5 Corrosion

Corrosion is a typical problem with lattice towers, and it can be caused by a variety of factors, including temperature variations, the use of a lot of de-icing salts, and incorrect coating. When a latticed tower rusted, its load capacity was considerably reduced. It was also determined that the latticed tower's coating was linked to tower erosion. Corrosion of the lattice tower might also be caused by an improper painting system and upkeep (Chen et al. 2010).

## 3 Present Investigation

### 3.1 Description of Selected Section

An equal angle section with a slenderness ratio of 40 is reinforced to see how different types of patterns for connection is shown in Fig. 1, impact the component's compression capacity.

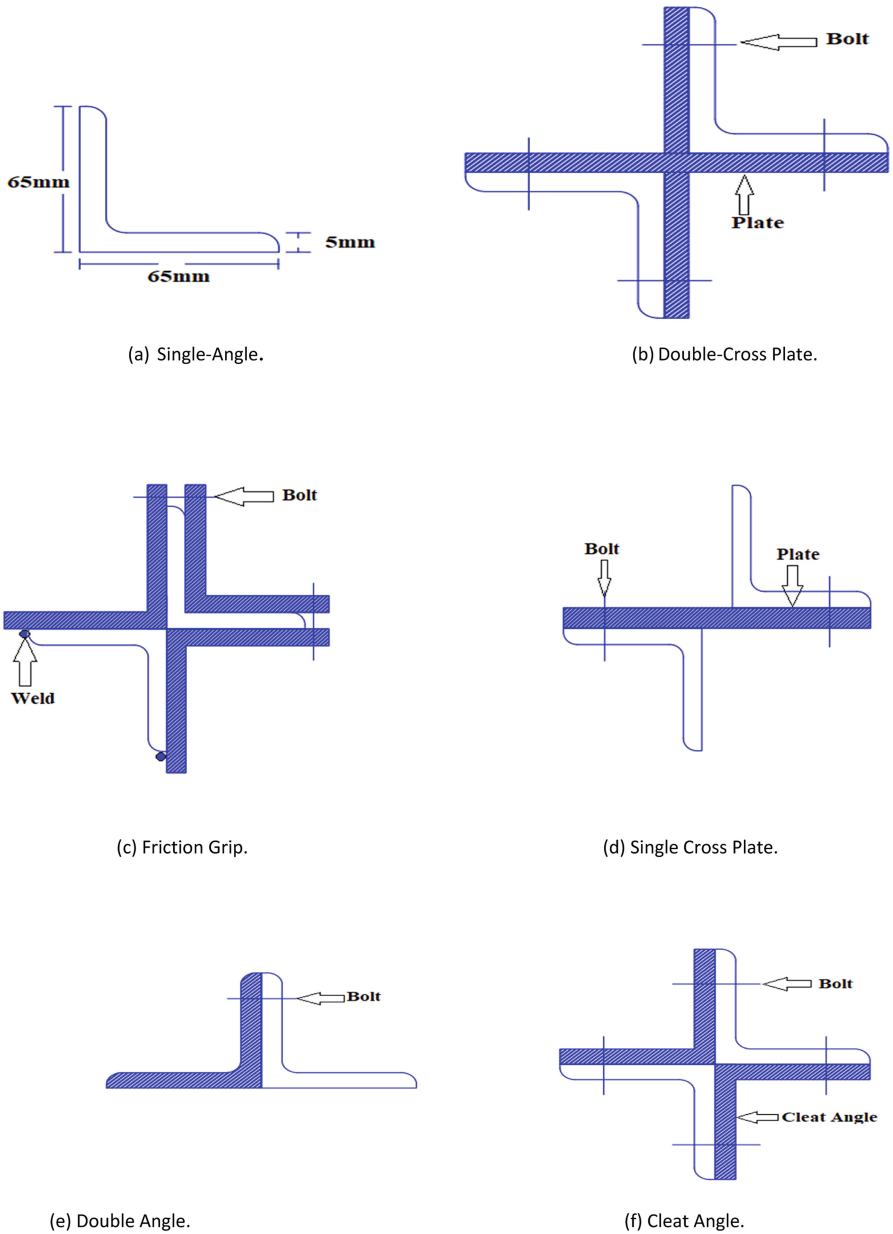


**Fig. 1.** Graphic view for different patterns of connection for strengthening.

### 3.2 Section Properties

In this review paper, a  $65 \times 65 \times 5$  mm (width  $\times$  thickness) section of equal angle with a slenderness ratio of 40 was chosen for various types of strengthening patterns.

To investigate how alternative connection patterns, like frictional grip, single cross-plate, double cross-plate, cleat angle and double angle connections affect compression capacity at the component level. The yield stress for different steel components like bolts, steel angles, and connecting plates is 250 MPa, the Young's modulus is  $2 \times 10^5 \text{ N/mm}^2$ , and the Poisson's ratio is 0.3. For mild steel, the nonlinear stress-strain curve defines the nonlinear material characteristics. Bolts with a diameter of 16 mm and an 8.8 grade, stiffened to a torque of 110 N-m, are used to connect the pieces.  $140 \times 65 \text{ mm}$  plates with a 300 mm centre-to-centre spacing are fastened together for single plate connections and double cross-plate connections.

#### **4 Experimental Investigation on Leg Member Strengthening**

For purpose of this review, five different connections are explored. For strengthening of angle member, one flange of each cleat angle is welded to the same angle member at a distance of 300 mm for friction grip attachment. These cleats' distinctive flanges are related to the flanges of the third cleat, which is attached to the main leg component. Due to friction formed between the cleat contact surfaces and the key leg member, the weight of the key leg member is transmitted to the firming angle. Two angle members are joined back-to-back together with cleats at a spacing of 300 mm centre to centre using bolts in the case of a double cleat connection, i.e., the reinforcing and existing leg member. Equally, with a double angle connection, bolts spaced 300 mm link the additional strengthening angle component to the main leg component. A compression load is supplied to the key leg (existing) component to replicate load allocation in the field. End plate fittings of size  $300 \times 300 \text{ mm}$  and 20 mm thick with thin strips welded to direct the location of the angle member are used to simulate the boundary situation. The load is transmitted through the major angle member's center of gravity. A 30-tonne compression jack is used to provide the axial force, and a digital wigmeter with a 100-tonne capacity is used to monitor the load. A hydraulic pump that is fully automated controls the compression jack. Dial and strain gauges are used to assess existing and strengthened angle components axial deformation and load transfer.

#### **5 Analytical Investigation on Strengthening of Leg Member**

ABAQUS software is used to conduct the numerical analysis. The C3D8R element has a lower integration level (1 Gauss point). This element alleviates shear locking however the stiffness matrix's rank insufficiency may result in spurious singular (hourglassing) modes (Bursi and Jaspart 1998). Two simple tee stub connections were used as standards in the authentication of a bolted connection FE software. Then, using a 3D finite element model, a viable framework for simulating these relationships in a realistic manner has been provided (Bursi and Jaspart 1998). The similar simulation applying C3D8 elements indicates that they are unable to cause bending-dominated issues, but C3D8R elements commonly underestimate the connection strength, as predicted (Bursi and Jaspart 1998). Since the tower pieces are connected by bolted joints, it's important in transmission line towers. The bolts are in clearance holes, and depending on the



applied stresses, they may slip into position. Elements-level studies on butt joints, which are equivalent to leg member connections in the steel tower, are done to analyze the behavior of bolted joints. A dial gauges and inclinometer are used to measure the joint rotation caused by bolt slide. Researches are conducted to determine the load at which the bolted joints will slide and the clamping force. A sequence of lap or butt joints connect the tower's leg member, and their effect on the tower deformation is investigated in depth (Rao et al. 2012). Solid C3D8R components are used to represent the steel angle and bolts in different type of angle connections shown in Fig. 1 (Sun et al. 2020). To describe the contact of frictional between plate sections and steel angle, surface-to-surface friction contact with a friction coefficient of 0.25 is employed. The coupling restriction is created at the bolted connection site for friction grip connections to confirm that the load is provided by friction. The yield stress of all steel bolts, angles, and connecting plates is 250 MPa, with a Young's modulus of  $2 \times 10^5$  N/mm<sup>2</sup> and a Poisson's ratio of 0.3 (Albermani et al. 2009). The nonlinear stress-strain curve characterizes mild steel's nonlinear material feature. The bottommost half of the composite angle section is meant to be kept in place and prevented from rotating along the longitudinal axis, while the upper half is designed to be free of rotation (Xie and Zhang 2021). All DOFs are constrained, with the exception of rotation and displacement in the axial direction. The mesh enhancement aspect ratio of 7.5 is used to mesh all of the components. The comparative movement of a bolted connection joint below shear is known as joint slip. The insertion of pretensioned cable separates the steel tower body may efficiently modify the external load transfer route on the structure, enhance the stress presentation of the structure's weak connections, and increase structural bearing capacity, stiffness, and stability in the vast majority of situations. This strategy has the potential to strengthen the tower component cross arm and body is characterized by simple structure, physical savings, economy, and high proficiency, has no impact on operation or manufacture, and may decrease direct economic losses (Albayrak and Morshid 2020). When it comes to the strengthening and reinforcing of transmission towers, it's difficult to rebuild and strengthen the nodes as well as to assure the stress. In the case of the angle steel transmission tower, the annular node plate can be added to the periphery of the original node to link new and old components. The new node plates may be bolted to the original primary materials to improve the reliability of the connection at the node area. Meanwhile, a stiffening beam is introduced to the weak area of novel node plates to improve node stress presentation and lessen the impacts of eccentricity-induced internal force redistribution (Cha et al. 2020). High power transmission tower lines passage high-speed railways have a greater goal dependability than regular lines. As a result, the iron tower's structural significance coefficient should be increased. If the operational stress is insufficient in the to-be-reinforced transmission tower, the principal materials, such as principal materials and diagonal members, can be reinforced by parallel component connection, oblique members and secondary materials can be strengthened by additional, and certain secondary materials can be correctly added (Baran et al. 2016).

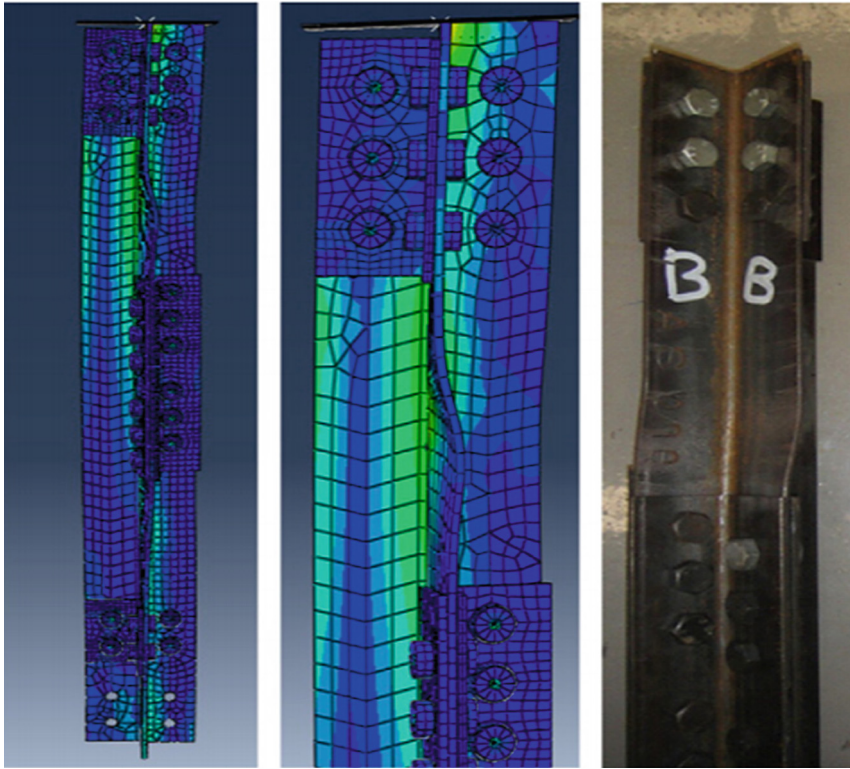


**Fig. 2.** ABAQUS model, ABAQUS model (close-up), and experimental specimen are the failure models (from left to right). Lu et al. (2014).

**Table 1.** Analytical and experimental results in a brief Balagopal et al. (2019)

Sl	Type of strengthening	Experimental failure load (kN)	FE analysis failure load (kN)	Increase in compression strength (experimental) % (w. r. to reference specimen)	Increase in compression strength (FEA) % (w. r. t reference specimen)
1	Single angle (Reference)	175	158	Parent member	Parent member
2	Double cross-plate	210	180	20	14
3	Single cross-plate	195	170	12	8
4	Friction grip	197	175	13	11
5	Double angle	195	175	11	11
6	Cleat angle	210	180	20	14

## 6 Results and Discussion

The investigational and FE analysis failure loads for various types of connections vary between 10% to 16% as shown in Table 1. Because of local buckling in the free length component of the primary angle section, the FE analytical findings differ from the experimental results. Load applied to the main member's centroidal axis generates local buckling in the connection of major angle sections. Strengthening the cleat angle connections, a larger increase in compression strength when associated to other types of connections. Other types of strengthening patterns are more expensive than the cleat angle then friction grip connection. The strengthening angle member in cleat angle and friction grip connections shares substantial stress rising from the main component through load submission, according to analytical and experimental data. The primary angle member's buckling mode is changed by the double angle connection pattern. The primary angle member's failure mode appears to be influenced by the strengthening pattern.

## 7 Conclusion

The current research on strengthened steel constructions has been reviewed in this study. The experimental and analytical failure loads for various types of connections have been shown to vary between 10% and 16%. The experimental and analysis for Finite element shows that the cleat angle's compression strength has been enhanced by 20% and the double cross-plate connection strength is increased by 14%. The cleat angle connection is less costly than other forms of strengthening arrangements. The strengthening angle element absorbs a substantial amount of stress as of the main component throughout the application of load in the cleat and friction grip connection. The primary angle component's buckling mode of failure is modified by employing a double angle connection.

## References

- Albayrak, U., Morshid, L.A.: Evaluation of seismic performance of steel lattice transmission towers. *Civil Eng. J.* **6**(10), 2024–2044 (2020). <https://doi.org/10.28991/cej-2020-03091600>
- Albermani, F., Kitipornchai, S., Chan, R.W.: Failure analysis of transmission towers. *Eng. Fail. Anal.* **16**(6), 1922–1928 (2009). <https://doi.org/10.1016/j.engfailanal.2008.10.001>
- Albermani, F., Mahendran, M., Kitipornchai, S.: Upgrading of transmission towers using a diaphragm bracing system. *Eng. Struct.* **26**(6), 735–744 (2004). <https://doi.org/10.1016/j.engstruct.2004.01.004>
- Balagopal, R., Rao, N.P., Rokade, R.P., Umesha, P.K.: Studies on Strengthening Techniques for Existing Transmission Line and Communication Towers. In: *Recent Advances in Structural Engineering*, Vol. 2, pp. 639–648. Springer, Singapore (2019). [https://doi.org/10.1007/978-981-13-0365-4\\_54](https://doi.org/10.1007/978-981-13-0365-4_54)
- Baran, E., Akis, T., Sen, G., Draisawi, A.: Experimental and numerical analysis of a bolted connection in steel transmission towers. *J. Constr. Steel Res.* **121**, 253–260 (2016). <https://doi.org/10.1016/j.jcsr.2016.02.009>

- Baskaran, K., Jeneevan, G., Jayasinghe, J.P.L.M., Hettiarachchi, H.H.A.N.C.: Strength assessment of steel towers (2011). <http://dl.lib.mrt.ac.lk/handle/123/11864>
- Bekey, S., Peng, F., Lieping, Y.: Experimental study on behavior of FRP anti-buckling strengthening steel members. In: Ye, L., Feng, P., Yue, Q. (eds.) *Advances in FRP Composites in Civil Engineering*, pp. 919–924. Springer, Heidelberg (2011). [https://doi.org/10.1007/978-3-642-17487-2\\_203](https://doi.org/10.1007/978-3-642-17487-2_203)
- Bursi, O.S., Jaspart, J.P.: Benchmarks for finite element modelling of bolted steel connections. *J. Constr. Steel Res.* **43**(1–3), 17–42 (1997). [https://doi.org/10.1016/S0143-974X\(97\)00031-X](https://doi.org/10.1016/S0143-974X(97)00031-X)
- Bursi, O.S., Jaspart, J.P.: Calibration of a finite element model for isolated bolted end-plate steel connections. *J. Constr. Steel Res.* **44**(3), 225–262 (1997). [https://doi.org/10.1016/S0143-974X\(97\)00056-4](https://doi.org/10.1016/S0143-974X(97)00056-4)
- Bursi, O.S., Jaspart, J.P.: Basic issues in the finite element simulation of extended end plate connections. *Comput. Struct.* **69**(3), 361–382 (1998). [https://doi.org/10.1016/S0045-7949\(98\)00136-9](https://doi.org/10.1016/S0045-7949(98)00136-9)
- Carril, C.F., Jr., Isyumov, N., Brasil, R.M.: Experimental study of the wind forces on rectangular latticed communication towers with antennas. *J. Wind Eng. Ind. Aerodyn.* **91**(8), 1007–1022 (2003). [https://doi.org/10.1016/S0167-6105\(03\)00049-7](https://doi.org/10.1016/S0167-6105(03)00049-7)
- Chen, Y., Qiang, C.M., Wang, G.G., Miao, W.H.: Corrosion and protection of transmission towers. *Electr. Power Constr./Dianli Jianshe* **31**(8), 55–58 (2010)
- Khedr, M.A., McClure, G.: A simplified method for seismic analysis of lattice telecommunication towers. *Can. J. Civ. Eng.* **27**(3), 533–542 (2000). <https://doi.org/10.1139/199-090>
- Kilroe, N.: Aerial method to mitigate vibration on transmission towers. In: 2000 IEEE ESMO-2000 IEEE 9th International Conference on Transmission and Distribution Construction, Operation and Live-Line Maintenance Proceedings. ESMO 2000 Proceedings. Global ESMO 2000, pp. 187–194. IEEE. <https://doi.org/10.1109/TDCLLM.2000.882820>
- Kocer, F.Y., Arora, J.S.: Optimal design of latticed towers subjected to earthquake loading. *J. Struct. Eng.* **128**(2), 197–204 (2002). [https://doi.org/10.1061/\(ASCE\)0733-9445\(2002\)128:2\(197\)](https://doi.org/10.1061/(ASCE)0733-9445(2002)128:2(197))
- Lu, C., Ma, X., Mills, J.E.: The structural effect of bolted splices on retrofitted transmission tower angle members. *J. Constr. Steel Res.* **95**, 263–278 (2014). <https://doi.org/10.1016/j.jcsr.2013.12.011>
- Lu, C., Ma, X., Mills, J.E.: Modeling of retrofitted steel transmission towers. *J. Constr. Steel Res.* **112**, 138–154 (2015). <https://doi.org/10.1016/j.jcsr.2015.04.005>
- Lu, C., Ma, X., Mills, J.E.: Cyclic performance of reinforced legs in retrofitted transmission towers. *Arch. Civil Mech. Eng.* **18**(4), 1608–1625 (2018). <https://doi.org/10.1016/j.acme.2018.07.001>
- Mills, J.E., Ma, X., Zhuge, Y.: Experimental study on multi-panel retrofitted steel transmission towers. *J. Constr. Steel Res.* **78**, 58–67 (2012). <https://doi.org/10.1016/j.jcsr.2012.06.004>
- Mohammadi Darestani, Y., Shafieezadeh, A., Cha, K.: Effect of modelling complexities on extreme wind hazard performance of steel lattice transmission towers. *Struct. Infrastruct. Eng.* **16**(6), 898–915 (2020). <https://doi.org/10.1080/15732479.2019.1673783>
- Moon, B.W., Park, J.H., Lee, S.K., Kim, J., Kim, T., Min, K.W.: Performance evaluation of a transmission tower by substructure test. *J. Constr. Steel Res.* **65**(1), 1–11 (2009). <https://doi.org/10.1016/j.jcsr.2008.04.003>
- Mulherin, N.D.: Atmospheric icing and communication tower failure in the United States. *Cold Reg. Sci. Technol.* **27**(2), 91–104 (1998). [https://doi.org/10.1016/S0165-232X\(97\)00025-6](https://doi.org/10.1016/S0165-232X(97)00025-6)
- Prasad Rao, N., Samuel Knight, G.M., Lakshmanan, N., Iyer, N.R.: Effect of bolt slip on tower deformation. *Pract. Period. Struct. Des. Constr.* **17**(2), 65–73 (2012). [https://doi.org/10.1061/\(ASCE\)SC.1943-5576.0000108](https://doi.org/10.1061/(ASCE)SC.1943-5576.0000108)

- Rao, N.P., Knight, G.S., Mohan, S.J., Lakshmanan, N.: Studies on failure of transmission line towers in testing. *Eng. Struct.* **35**, 55–70 (2012). <https://doi.org/10.1016/j.engstruct.2011.10.017>
- Roy, S., Kundu, C.K.: State of the art review of wind induced vibration and its control on transmission towers. *Structures* **29**, 254–264. <https://doi.org/10.1016/j.istruc.2020.11.015>
- Savory, E., Parke, G.A., Zeinoddini, M., Toy, N., Disney, P.: Modelling of tornado and microburst-induced wind loading and failure of a lattice transmission tower. *Eng. Struct.* **23** (4), 365–375 (2001). [https://doi.org/10.1016/S0141-0296\(00\)00045-6](https://doi.org/10.1016/S0141-0296(00)00045-6)
- Sun, L., Trovato, M., Stojadinović, B.: In-situ retrofit strategy for transmission tower structure members using light-weight steel casings. *Eng. Struct.* **206**, 110171 (2020). <https://doi.org/10.1016/j.engstruct.2020.110171>
- Xie, Q., Sun, L.: Failure mechanism and retrofitting strategy of transmission tower structures under ice load. *J. Constr. Steel Res.* **74**, 26–36 (2012). <https://doi.org/10.1016/j.jcsr.2012.02.003>
- Xie, Q., Zhang, J.: Experimental study on failure modes and retrofitting method of latticed transmission tower. *Eng. Struct.* **226**, 111365 (2021). <https://doi.org/10.1016/j.engstruct.2020.111365>
- Zhao, X.L., Zhang, L.: State-of-the-art review on FRP strengthened steel structures. *Eng. Struct.* **29**(8), 1808–1823 (2007). <https://doi.org/10.1016/j.engstruct.2006.10.006>



# Performance-Based Seismic Design on Bridge Piers: A Review

Gaddam Sudheer<sup>(✉)</sup> and Satyabrata Choudhury

Department of Civil Engineering, NIT-Silchar, Silchar, India  
{gaddam\_pg, chou\_s}@civil.nits.ac.in

**Abstract.** Recent advances in mathematical analysis and computing power have pushed the current specification of the bridge in terms of PBSD juxtapose to the standard force-based method. One of the major features of this PBSD is keeping the bridges in place and reducing repair costs by reducing global and local disability to acceptable levels under estimated loads. The aim of this fact-finding sheet is to develop a PBSD recommendations for RC bridge column. Some sort of earthquake design requirements is there, these demands are based mainly on the value of the building, the degree of disability placed on the building, in topsoil state, and the ductility of building components, specifically bridge pier and support. In the PBD method, the composition is very much concentrated on conference the performance objective, which is in pipeline with the required level of work. Presently, efforts to implement this PBD approach in building and bridge construction are ongoing the United States and some other parts of globe.

**Keywords:** Bridge · Bridge pier · Performance-based seismic design · AASHTO

## 1 Introduction

Performance-based seismic design method (PBSD) was invented in New Zealand in Seventies (Priestley 2000) and gained importance within the United States of America in the 1980 (Hamburger et al. 2004). It's been taken up in a very range of bridge design codal provisions round the earth in modern years (CSA 2014; NZT 2016). The PBSD utilizes the quantitative methods named as reinforcement strain, along with a quality process similar to the apparent damage to the connection. It's a design approach that expressly illustrate performance level of structures (Gibson 1982). One among the foremost necessary options of performance-based seismic design is that it straightly connects structural performance with the planning method and removes inborn unpredictability (Lehman et al. 2004; Chemist 2000). The unreliability of conventional earthquake design may be caused by impractical presumptions like equal displacement, that isn't reasonable for structural buildings with terribly small and large time periods. In addition, this structural malleability issue isn't constant certainly structures. It's enthusiastic about several aspects like axial force, lateral restraint, and footing flexibility, that are unheeded by several style codal provisions while using force-based design method.

The meaning of PBD has been developing from past few decades. In seventies, capacity design terms regarded as PBD. Due to this capacity designed building focuses on energy dispersion and yielding tool enclosed by the system, in place of the total shear value (Priestley 2000). John Hollings is thought to be the 'father of ductile design' of design idea revealed in 1969 (Megget 2006). In eighties, PBD formation was re-formulated in the U.S.A, which added assessed vandalism state of structure (Hamburger et al. 2004). The aim is to provide the house holder with clear explanations of the decisions. The current phase of PBD was developed in the 1990s, later 1994 Northridge and 1995 Kobe earthquake (Ghobarah 2001). In 2 large ground motions, as much buildings remains good, financial disaster they were more elevated than anticipated. Accordingly, engineering bodies have agreed that earthquakes not bound to only last avoid falls in addition to its face service performance. This report focuses on present PBSB defined as the combination of one or more performance levels at different risks.

PBSB not just removes irrational thinking in addition to it results in superior mitigate the risks. In PBD, needs as well as capabilities in accordance with potential examples by Mackie and Stojadinovic (2005). As a result, the cost of the life cycle analysis includes multiple risks and progression-Your deterioration is possible (Akiyama et al. 2013; Gidaris et al. 2017; Kameshwar and Padgett 2014; Wen 2001).

Performance-based design is predicted makes it effortless for resolution creators and shareholders to share wealth found on factual information (Marsh and Stringer 2013). The design work begins with a possible hazard analysis and design process selection. After that, the original building materials and size of the members are decided. Depend on with earthquake requirements and structural components resisting, structural damage for instance steel flexibility, concrete fragmenting is findable. By guessing the performance and serviceability of the structure, unintended failure due to traffic slow down and more might be limited once it required. The layout is takes account accomplished when losing and structure member damage are allowable.

Focus on earthquake design in the present structures especially in building and bridge codal provisions of alternative life security devoid the capability to view multiple building performance standards from different load conditions. As a result, even though falls are prevented by seismic load, there is no guarantee that structure will always be used so it may need to be demolished in the event of a major earthquake in the form of a dynamic design. Even though the death can be preventable, financial losses can be dramatic. There is none design process against high seismic magnitude once in every 475 years. For an earthquake event to a large extent, all buildings are subject to failure.

In retaliation to such, the evolution of a PBSB construction method needs to developed as more detailed prediction methodology, in under a definite level of faith, is earthquake of a building based on a design level set. So, financial losses suffered through supply earthquakes can be restricted, and reduce the lethality and emerging services of post-earthquake operations.

The purpose of this research is to analyze what is happening in performance established on the ongoing operation of the building properties and to scrutinize the outcome of this design methodology especially as it's works on bridges. This research will focus the use of PBSB in place of earthquake formation, the alternate is needed in



the current construction practice installing these improvement procedures. Lot of whack had made from the past few years to improve PBD. ATC-13 (1985) is the first reports to introduce PBD formulations. This research showcase methods and data estimates of losses in building inspections and repair costs in the California USA. It is a guide to measuring loss of life, wounds, financial losses and time to repair. As look into, ATC-36 (Rojahn et al. 1997) provides loss and method of measuring losses with data from Salt Lake County, Utah. Triumphant incident from ATC-13 (1985) in California transferred to other provinces and to the world. After some years, FEMA-356 (FEMA 2000) was published for provision guidelines for earthquake rehabilitation. According to FEMA-356 (FEMA 2000), most buildings the redesign of the guide will meet the requirements for the design of the earthquake design. By file development of PBD, many modified analytical procedure were suggested by experimenter, such as N2 Road (Fajfar 2000), PBD method (Powell 2008) and PEER (Günay and Mosalam 2013) systematically looking at the demand and capability of the system. As aforesaid texts established a design foundation based on performance in structural engineering. Although some texts were present it is designed especially for buildings, paths and terminals and also for bridges.

## 1.1 PBSD Criteria for Overpass

Many more importance sheet has been placed on the construction of Performance-based design. The similar system is required for bridges. Vision fact sheet 2000 (SEAOC 1995) of structures can be usable like framework for the issues of earthquake design that will need to be convey overpass. nevertheless, the distinguish between bridges and buildings codes should be very cautiously considered when designing a bridge codal provisions on the basis of building codes. In improving PBD for express flyovers, important problems to be considered.

They represent demonstrated in this way:

- The importance of current project requirements (provided by the AASHTO and California Departments Travel routes (Caltrans) elaborated below) in performance-based seismic design method.
- The choice of goal to be used in such construction that the required level of work to be complete. On this view, the structural engineer able to choose to specify over all needs of the you are given a bridge and point out a road map plan to reach these conditions.

### 1.1.1 Current Earthquake Design Methods for Bridges

The AASHTO provisions for the construction of the bridge the apply all over United States of America by defining a specific area of variables of coefficient of acceleration (A), the separation of significance (IC), seismic performance class (SPC), location equity (S), and earthquake response coefficient (C). Further consideration of earthquakes is attributed to the modification of the response feature (R), min seat width conditions, and loading combination. AASHTO will issue a diagram of the USA with accelerated coefficient values provided by the means of lines. The earthquake forces described to accelerate coefficients 10% chance of jumping in 50 years (approximately



equal to 15% chance of exceeding 75 years). This equates to a recovery timelapse of about 475 years. Under some special situation of proximity to practical error, long-term earthquake anticipation, or bridge value (requiring long-term return), specialized research is needed to find the site- and to create definite acceleration coefficients.

four test methods are listed below:

1. uniform load method
2. single-mode spectral method
3. multimode spectral method and
4. time history method

Choosing any specific examinations route is found by the earthquake classification “regularity” of bridge, furthermore the number of spans to the bridge. Typical overpass is explained as less than 7 spans, without sudden or unusual differences in mass, stiffness, shape as well as there are no major differences in the abovementioned boundaries from span-to-span or external support (exclusion eliminated). Flow chart for the standard definition of AASHTO (1995) has been acquired through the Earthquake Design for expressway overpasses (U.S. The Department of Transport (U.S. DOT) of 1993). California earthquake systems are based Standard specification of AASHTO. However, there is a lot more significant differences exist in loading and earthquake zones to be reported. Caltrans has advanced a “standard elastic design spectra” is called as ARS curves. These weeks are over acceleration rock (A), rock spectra (R), and soil augmentation factors (S). Spectra is created of the four types of sites separated by depth of cohesionless alluvium (sand or rock) over a “rock-like” object. This depth is 0–3 m, 3–25 m, 25–45.7 m also >45.7 m alluvium. Even though an identical static force for earthquake construction was allowed for conventional construction, most bridges are in California they are designed to use dynamic analysis. This allows design designers to have computing machine software as well accessible information. In the previous design experts, stretch forces from strong or partial static analyzes converted by Z coefficient, equivalent to R coefficient in AASHTO, to account of ductility and hazard. From the last decade, however, Caltrans have been used the ductility project in much of pennsylvania bridges.

- This seismic force reduction factor is being used by “The Force Based Approach” method that exists in many engaging states. But the reduction factor is a rapid measurement that means the same ductility requires intimidation. Many bridges can be seen in this the way can’t be explainable.
- improvements within the meaning of tremor action (i.e., response spectra) also therefore the extent of earthquake action are required
- Some codal provisions area is much prescriptive, and additional privilege for designers to decide on the design method is required.
- There is disagreement over the analysis processes
- The design of the earthquake is more concentrating this ultimate limit state and one desired levels of designed seismic.
- Bridge codal provisions are often found in building codes and use.

- PBSD of bridges must be considered during the bridge layout was designed. In addition to the design procedures for many California bridges, earthquake formation is often considered afterwards the bridge was designed on behalf of vertical forces.

Besides to this, of course in number of bridges need specific considerations not directly addressed with present codal provisions. Among each other are skewed also curved overpass, flyovers bearing non-construction parts (like pipes), and existing bridges are considered a landmark.

## 2 Bridge Applications

### 2.1 Japan Seismic Design Procedures

Specification of the Japan earthquake design codes in 1996 of the high-way overpass (Kawashima 1997) are exemplar from that implementation of PBSD in preceding codal provisions. This 1995 Hyogo-Ken tremor has raised a number of serious problems that needed to be conveyed in earthquake resist construction as well reinforce of flyover in cities. A study from that damaged flyovers concluded that almost the pipes were damaged are designed conforming to the 1964 or older design specification. These codes only provide for lateral requirement force coefficient. Preventing destruction from future earthquake of regions near the field, subsequent moderations were made for design guidelines.

- The lateral strength and ductility of all parts of the structure, where the magnitude of the earthquake has increased, had improved to strengthening the ductility of the overall bridge program. A ductility design method has been used in all parts of construction.
- Earthquakes made in Kobe were needed as seismic design in ductility design way
- Input ground motion was described in respect of the acceleration response spectra for dynamic response analysis with more enthusiasm.
- Strengthening is extended with intermediate bonds increased ductility at piers introduced.
- An ongoing multi-span bridge was approved for expansion the level of degree of redundancy from that cross over structure.
- Elastic bearing was suggested for lateral deflection between super and, under ground member.
- Menshin's scheme (as discussed afterwards in this paper) of base-isolation through earthquakes were inserted.
- Power, ductility, and power distribution extent of unseating prevention devices is expanded.
- The effect of lateral propagation has been considered associated with landslides in the construction of foundations in areas at risk of spreading in the background.

Revised design specifications provide seismic performance standards depend on two sections of bridges. These sections with standard bridges, called category- A bridges, and important bridges, called B-category bridges. Because underground motion bridges have a greater chance of occurring, both common and important bridges

should be in each form in a flexible way with minimum structural damage. Because ground-moving movements are less likely to occur, critical bridges will be damaged to the limit, and a standard bridge should intercept the critical failure. Two designs the procedures designed to meet the need of bridges, the 'seismic coefficient' methods also the 'ductility design method'. This previous approach utilizes a lateral load method coefficient (0.2 to 0.3) depending on a valid pressure construction method. The last method is deleted in consideration of the construction of the main plastic hinge in down the hill and the same power. Ductility design cannot be usable in the situations listed as follows:

- (1) Principal mode shapes of the overpass retaliation mode are alter than the considering this method of ductility design.
- (2) beyond two modes grant important to bridge to respond;
- (3) the main elastic hinges in more than 2 locations, or unknown places; also
- (4) Response modes where this notion of equivalent power is hardly applicable.

This coefficient of lateral load utilized in this construction of the ductility the approach was reversed in the 1996 specification. Type-I earthquakes may occur in a plate-boundary with a magnitude of eight. I-type seismic, utilized from 1990, it is thought to be the lateral load coefficient of stiff soil below the balanced also smooth ground because of extensive advanced harm in smooth areas of topsoil. However, the acceleration of spectral response in short natural duration is greater in hard areas than in soft soils sites. Type-II types of earth were introduced in 1996 to show real earth movement. Type-II ground movement will occur over a small lengths with a magnitude on the richter scale of 7 to 7.2. This must be pointed out this ground type-I movements extended in acceleration compared to Type-II, i.e., Supposed to be taken into account while determining the permissible displacement ductility factor of bridge pillar. The dynamic response analysis utilizes earth movements such are spectrally included in this Type-I and Type II acceleration response fields, adjusted zone wise and damping ratio.

Special guidelines for the Menshin design method are related to non-residential prevention programs. Steps require that (1) the opening of a large building from the foundations be even prevented under the unexpected failure of the members of the premises; (2) unseating protection arrangement consist of a sufficient seat length, a fall device, a device that limits movement, and a device to prevent the release of a very large structure; (3) sufficient seat height and blocking device fall to the end of the super structure of the long-term response; and (4) in some samples, the installation of a deflection restriction facility on each central support of the continuous bridge facing long and flexible response. The 1996 review of Specification of the Japanese earthquake design of expressway overpasses maybe prescribed as a PBSB method. Examples of these are presented in 2 earthquake design methods through the levels of soil vibration, the usage of a pushover analysis needed till assess bridge pier safeguard also foundations, permissible limits of drift, additionally non-linear analysis reaction is required and utilized in favor of complex overpasses.

## 2.2 Use of PBSD in Bridge Piers

In their research, Taylor and Stone (1994) introduced PBSD methods, formulae to find this permissible wreck indicator also designed model that includes earthquake retrofitting of a bridge pillar to show how to predict expected reinforced damage concrete bridge column. One cantilever flyover model pillar on silt soil utilized in the construction of a PBSD method. Earth motion describe a “target response spectra” based on a quick review of U.S. city history records. Active computer algorithm wrote to choosing the design data corresponding to this intended response spectrum. In such system, magnitude amplification devices are available inside the scope of 0.5–2.0, but no horizontal measurements are available allowed. Using the 1D shear-wave distribution system, the rock movements are spread over the surface to find the acceleration information is indicated in the column. The inelastic analysis system was then used to measure the inelastic cyclic load response in a column. Studies have used the computed risk index to measure the range of hazard to a RC flyover column. These indicators are revealed as a ductility coefficient (or drift capacity) and a word relevant to the accumulated energy occupied with these structural components. The hazard index could be checked with each analysis step, its true that the record could be traced across the entire loading period. Previous testing of cyclic lateral loads in the R.C columns have determined the limitations of 0.11, 0.40, and 0.77 yields, high lateral loading and failure injuries, correspondingly. A suggested prototype of acceptable flaw scales was obtained from a research by Taylor and Stone (1994). Directing 4 methods was applied to its progress. First, a complete fall it should be avoided to avoid death. Second, only a little damage should occur in small events over a much more distance from causative errors. Injury indicators of current status must be dormant within the state of not visible hazard and amongst of the 1<sup>st</sup> yield. 3rd, major tremor (in magnitude-8) may be severely damaged even in the normal distances (40 km) with a casual error. Hence, the damage indications may be close to the failure status of some cases. Fourth, the permissible level of damage of classified bridges should be less than the unthinkable it is important. Damage indicators for bridges classified as important are declining rapidly with higher distances and reduced seismic magnitude.

## 2.3 Current Obstacles to Usage of PBSD

A PBD approach can lead to more an expensive bridge due to the increase in construction processes and needed to achieve the purpose of operation. However, high initial costs will be compensated for with minimal damage as well the necessary repairs following the earthquake event. Since small range financial performance to longer-run capital protection supposed to be transformed by these stakeholders. Woefully, competition and misunderstanding will hinder change. Because of this severe damage you have suffered recently tremor, so, the designers and town architecture word probably re-examining this terminology “cost-prohibited” (Fairweather 1994). for the full price of about twenty-five billion dollars, the north ridge tremor was one of most valuable also most hazards one of the most expensive also most destructive tragedy in United States record (Nigg 1997). Obviously, it’s important to use the designer codal provisions that will manage this will influence of the associated financial crises events.

Over the use of performance-based seismic approaches, major differences are needed in the name holder, engineer, also contractor during such as method the procedure is performed. This step to a much complicated as well as duration-taking process is likely to be he met within considerable resistor. This part of constructional designer will be at the center of its execution. The engineer will need to execute within the householder to improve operation level purpose, provided the site also significance from overpass, that meets the appropriate degree of service after an earthquake incident. These decisions will depend on performance instead of money consideration. Ensuring this performance level choosing, the engineer will need to complete a thorough bridge concept analysis to develop an accurate design meets the standard set procedure. It will be obligatory in engineering work to adapt to complex and perhaps time-consuming analytical methods and design. In the end, the design work cannot be accomplished provided that the body formally meets the conditions of engineering design. The engineer needs to keep an eye on it a construction methodology to make sure that norms should be followed. Right sustenance also testing be undertaken required next fabrication towards to keep this integrity level of the building the required performance level. The closest obstacle to the implementation of performance-based seismic method was evolution of designed method, it is important to find exactly the operation level of overpass at a specific earthquake incident. The present study was a procedure of construction of bridges analysis systems as well components that will allow for seamless testing of performance and expected damage criteria. But, much more remained to be done to achieve the degree of assurance it is important to make a PBSD construction plan.

### 3 Conclusion

Several reports have presented various methods to the construction of the bridge to better respond to the priority of the structure. This paper incorporated these performance standards and improved the performance matrix of bridges depend on the performance matrix set upped for the buildings. Proposed operating level in Performance based design of bridges are fast service, limited service, and fall. The earth movements used are those previously accepted in structural building: repeated, occasional, unusual, and very rarely. This priority from the overpass is considered crucial, essential, or standard. Active implementation of PBSD the bridges route had been completed, as indicated by a review of the design of the highway seismic design overpass in Japanese later the Hyogo earthquake. Present investigation on operational level also the anticipated risk to the various elements of the bridge after the earthquake are examples of the research needed to build a complete suggested bridge codal provisions. but we observe financial, scientific, as well as societal barriers this need to defeat prior to the PBSD code for bridges possibly executed. Much more investigations also evolution in the places of PBD, earthquake design, scientific processes, also knowledge is required.

## References

- American Association of State Highway and Transportation Officials (AASHTO). Standard specifications for highway bridges, 16th edn., Washington, D.C. (1995)
- Applied Technology Council (ATC). A critical review of current approaches to earthquake-resistant design. ATC-34, Redwood City, California (1995)
- Applied Technology Council (ATC). Improved seismic design criteria for California bridges: Provisional recommendations. ATC-32, Redwood City, California (1996)
- Applied Technology Council (ATC). Seismic design criteria for bridges and other highway structures: Current and future. ATC-18, Redwood City, California (1997)
- California Department of Transportation (Caltrans). Bridge design specifications manual. Division of Structures, Sacramento, California (1993)
- Fajfar, P., Krawinkler, H. (eds.): Seismic design methodologies for the next generation of codes. In: Proceedings of International Conference at Bled, Slovenia. A.A. Balkema, Rotterdam/Brookfield, 411 pp (1997)
- Fairweather, V.: Performance based design application to seismic analysis of bridges-an overview. Master's thesis, Illinois Institute of Technology, Chicago (1994)
- Fazli, H., Pakbaz, A.: Performance-based seismic design optimization for multi-column RC bridge piers, considering quasi isolation. *Int. J. Optim. Civil Eng.* **8**(4), 525–545 (2018)
- Moehle, J.P.: Displacement-based design of RC structures subjected to earthquakes. *Earthq. Spectra* **3**(4), 403–428 (1992)
- Marsh, M.L., Stringer, S.J.: Performance-based seismic bridge design, Washington, D.C., Transportation Research Board (2013)
- Priestley, M.J.N.: Performance based seismic design. In: 12th World Conference on Earthquake Engineering (2000)
- Nigg, J.M.: Research needs for improving earthquake hazards reduction, Hearings on the National Earthquakes Hazards Reduction Program, Earthquake Engineering Research Institute, Oakland, California (1997)
- Prendergast, J.: Seismic isolation in bridges. *Civil Eng.* **65**(12), 58–61 (1995)
- NCHRP: Comprehensive Specification for the Seismic Design of Bridges. ATC/MCEER Joint Venture (2001)
- Saiidi, M.S.: Working group on bridge design issues. In: Conclusions and Recommendations of the Workshop on Seismic Design Methodologies for the Next Generation of Codes held in Bled, Slovenia (1997)
- Saiidi, M.S., Maragakis, E.M., Isakovic, T., Randall, M.: Performance-based design of seismic restrainers for simply-supported bridges. In: Fajfar, P., Krawinkler, H. (eds.) *Seismic Design Methodologies for the Next Generation of Codes*, Balkema, Rotterdam, The Netherlands (1997)
- Structural Engineers Association of California (SEAOC). Performance based seismic engineering of buildings-Volume I, Sacramento, California (1995)
- Taylor, W.T., Stone, W.C.: Performance-based seismic design of reinforced concrete bridge columns. In: Proceedings of 5th U.S. National Conference on Earthquake Engineering, Earthquake Engineering Research Institute, Oakland, California (1994)
- U.S. Department of Transportation (U.S. DOT). Seismic design of highway bridges. FHWA HI-93-040, Federal Highway Administration, Washington D.C (1993)
- Zhang, Q., Alam, M.S.: Performance-based seismic design of bridges: a global perspective and critical review of past, present and future directions. *Struct. Infrastruct. Eng.* **15**(4), 539–554 (2019)



# Vibration and Stability Characteristics of the Laminated Composite Plates (LCPs) for Various Delamination Positions

H. S. Rakshith<sup>1</sup>(✉), L. Ravi Kumar<sup>2</sup>, D. L. Prabhakara<sup>1</sup>,  
and T. Rajanna<sup>2</sup>

<sup>1</sup> Sahyadri College of Engineering and Management,  
Adyar, Mangaluru 575007, India  
rakshithhs.mech@gmail.com,  
director.engineering@sahyadri.edu.in

<sup>2</sup> BMS College of Engineering, Bull Temple Road, Bangalore 560019, India  
ravi.mech@bmsce.ac.in

**Abstract.** Most often, the laminated panels undergo delamination due to the manufacturing defects or complicated loading conditions during its working life cycle. In the present work, the effect of position of delamination on the vibration and stability behavior of laminated composite plate (LCP) are examined numerically by developing FE formulation. In relation to this, an eight-noded plate element is taken to mesh the plate by taking in to account of effect of shear deformation. The accuracy of the formulation is assured by co-relating the proposed model with the literature. Various control parameters such as delamination size and position, thickness of the plate, ply orientation and boundary conditions (BCs) are included to study the effect on vibration and stability characteristics. The study shows that the positioning of delamination significantly affects the stability characteristics of delaminated panels.

**Keywords:** Laminated composites · Delamination · Vibration · Static stability

## 1 Introduction

Modern days requirements of material being light in weight with a high strength has made composite materials as most extensively used alternative for structural materials used by mechanical, aeronautical, and civil engineers. As the use of composite materials have increased, many researchers has done extensive work on the buckling and vibration characteristics of LCPs without considering effects of delamination as well as discontinuities (Anderson et al. 1968; Bert and Birman 1987). The vibration of a rectangular plate having internal crack was analyzed using Ritz method by Huang et al. (2011). The free vibration study of rectangular isotropic plates for fifteen possible cases of BCs were done by Leissa (1973). Prabhakara and Datta (1996) and Prabhakara and Datta (1997), investigated the effects of internal damage, position of damage, different types, position and sizes of cutouts to study the vibration, buckling and parametric instabilities on an isotropic plate. Stability and vibration characteristics for isotropic and orthotropic thin, moderately thick and thick plates were studied by (Reddy 1984a, b, Reddy and Chao

(1981) and Reddy and Phan (1985) by considering shear deformable theory. The buckling, vibration and dynamic instabilities of composite plates cutouts and no cutouts under in-plane compressive and tensile loads was studied by Ravi Kumar et al. (2005), Ravi Kumar et al. (2004b), Ravi Kumar et al. (2003) and Ravi Kumar et al. (2004a). Rajanna et al. (2016), Arya and Rajanna (2020) and Rajanna et al. (2017) studied the vibration and buckling behavior of composite panels with and without stiffeners under various loading conditions for different combinations of BCs. Laminated composites may lead to premature collapse/failure at lower magnitude of compressive loads, this collapse/failure is due to one of the failure mode known as delamination. The delamination is nothing but the separation of lamina from the adjacent lamina, it may occur due to the improper fabrication techniques, external impact, high stress concentration in some areas etc. Delamination is one of the major concern which need to be addressed as the presence of delamination severely hinders the static and dynamic stability of the material. Chai et al. (1981) studied a 1-D model to understand the effect of delamination under compressive load. Kim and Kedward (1999) presented a technique to model the local and global buckling delaminated polymer composite. Krawczuk et al. (1997) developed a cracked model to study the dynamics of composite material using finite element method. Naganarayana and Atluri (1996) have used finite method to analyze the delamination growth in stiffened laminated composite shell with central elliptical delamination along the thickness of the shell. Lee and Park (2007) analyzed the composite laminated plate considering through- the – width delamination for various delamination sizes. Experimentation carried out to know the effects of global and local buckling of the single delamination along with numerical investigation was done by Juhász and Szekrényes (2017). Single and multiple delaminations in various composite plate subjected to in-plane periodic loads were investigated numerically and experimentally by Jayaram Mohanty et al. (2013), Jayaram Mohanty et al. (2015) and J. Mohanty et al. (2012) to know its effect on vibration and buckling behavior by considering BC and aspect ratio however, the author did not consider the effects of ply orientation and extent of delamination in his study. Buckling behavior of delaminated composite plate (DLCP) having delamination at different location were examined by Akbarov et al. (2010). From all the above literatures it can be inferred that large amount investigations are done to know the effects on buckling and vibration under various in-plane loads in the composite materials nevertheless enormous amount of scope is available to study the effects of delamination present in laminated composite plates and its significance on buckling and vibration. Hence, in the proposed study the effect of static stability and vibration behavior of DLCP will be studied by considering the extent of delamination, position of delamination along the thickness of the layer for different aspect ratio, thickness ratio and BCs.

## 2 Theory and Mathematical Formulation

Figure 1 shows an eight layered LCP with central square delamination, length and breadth of delamination  $b_l$ , length of the plate  $a$ , breadth of the plate  $b$  and height of the plate  $h$  along  $x$ -,  $y$ - and  $z$ -axes respectively.  $u$ ,  $v$  and  $w$  being mid-plane displacements  $\theta_x$  and  $\theta_y$  being mid-plane rotations along  $y$ - and  $x$ - axes respectively.



The governing equations are formulated by considering the Hamilton’s principle.

$$\delta \int_{t_1}^{t_2} (T - U) dt = 0 \tag{1}$$

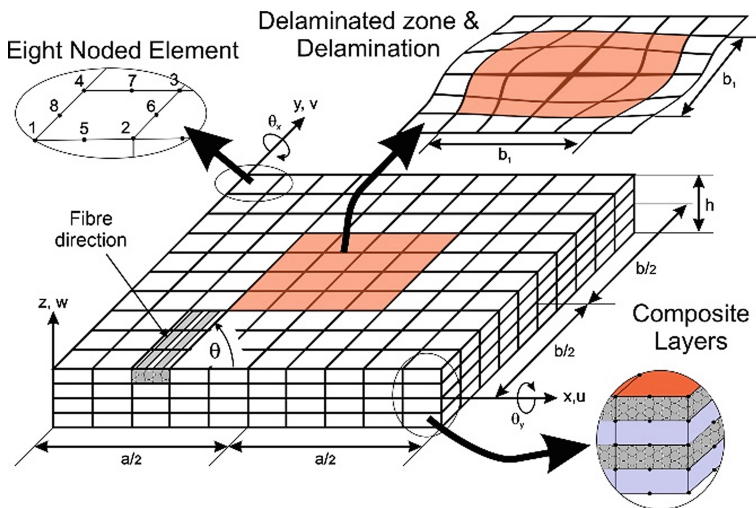


Fig. 1. Geometry of the eight layered square DLCP.

The K.E.,  $T$  of the plate can be expressed as

$$T = \frac{1}{2} \rho \int \int \int (\dot{u}^2 + \dot{v}^2 + \dot{w}^2) dv \tag{2}$$

The strain energies are expressed as linear and non-linear strains denoted as  $U_1$  and  $U_2$  respectively.

$$U_1 = \frac{1}{2} \int \int \int (\{\epsilon_l\}^T [D] \{\epsilon_l\}) dv \tag{3}$$

where  $\{\epsilon_l\} = [B] \{d^0\}$

$$U_2 = \frac{1}{2} \int \int \int (\{\sigma^0\}^T \{\epsilon_{nl}\}) dv \tag{4}$$

The expressions for the energy can be written by considering  $[K]$  - elastic stiffness matrix,  $[K_G]$  - geometric stiffness matrix and  $[M]$  - consistent mass matrix using standard FE procedure as (Cook 2007)

$$U_1 = \frac{1}{2} \{d\}^T [K] \{d\} \quad (5)$$

$$U_2 = \frac{1}{2} \{d\}^T [K_G] \{d\} \quad (6)$$

$$T = \frac{1}{2} \{\dot{d}\}^T [M] \{\dot{d}\} \quad (7)$$

On substituting the Eq. 5, Eq. 6 and Eq. 7 in Eq. 1 we obtain the equation of equilibrium and is as in Eq. 8

$$[M] \{\ddot{d}\} + ([K] - P_{cr}[K_G]) \{d\} = 0 \quad (8)$$

In the above equation  $[M]$  denotes mass matrix,  $[K]$  denotes elastic stiffness matrix,  $[K_G]$  denotes geometric stiffness matrix,  $P_{cr}$  is in-plane load applied and the vector for nodal displacement is denoted by  $\{d\}$ . By reducing the Eq. 8 the static stability and vibration governing equations can be derived as follows.

### **Static Buckling Problem**

By substituting  $\{\ddot{d}\} = 0$ , in Eq. 8 and the Eq. 8 reduces to static vibration problem.

$$[[K] - P_{cr}[K_G]] \{d\} = \{0\} \quad (9)$$

### **Vibration Problem**

An in-plane compression load is responsible for the panel to vibrate harmonically in that case the Eq. 8 reduces to vibration problem and can be expressed as

$$[[K] \pm P_0[K_G]] \{d\} - \omega^2 [M] \{d\} = \{0\} \quad (10)$$

If  $P_0$  is set to zero, then the panel experiences free vibration and if  $P_0$  is not equal to zero then the squares of the frequency i.e.  $\omega^2$  will become zero at some point and the corresponding load is known as critical buckling load.

## **3 Problem Definition**

For the present problem the plate was modelled using FE method by considering an eight noded iso-parametric element. The node numbering pattern and fiber direction is as shown in Fig. 1, mesh control parameter of  $m = 20$  and  $n = 20$  are considered to obtain accurate results. Each node is having five degrees of freedom out of which three translatory ( $u$ ,  $v$  and  $w$ ), two rotary ( $\theta_x$  and  $\theta_y$ ) degrees of freedom. *FSDT* is used and with the consideration of shear correction factor  $5/6$  (Reddy 1984b) for his problem. The plate aspect ratio ( $a/b$ ) of 1.0 and breadth to height ratio ( $b/h$ ) of 100. An individual MATLAB code has been written and code has been validated for elastic stiffness

matrix, geometric stiffness matrix, mass matrix, mesh size needed using various available resources.

### 4 Results and Discussions

The plate is having the various material constants as listed in Table 1. In the Table 1 two types of materials are mentioned  $M_1$  and  $M_2$ .  $M_1$  denotes the material constants for an iso-tropic material and  $M_2$  denotes the material constants for a composite material.  $M_1$  materials are used to validate the various matrices and  $M_2$  material constants are considered for the analysis throughout the paper unless otherwise specified.

**Table 1.** Properties of material

Material	Material constants					
	$E11$	$E22$	$\nu12$	$G12$	$G13$	$G23$
$M_1$	1	1	0.30	0.3854	0.3584	0.3584
$M_2$	40	1.0	0.23	0.60	0.60	0.50

The plate is analyzed for different set of BCs denoted as S; C and F. In the study  $S$  denotes simply supported;  $C$  denotes Clamped; and  $F$  denotes free edge BCs. The degrees of freedom to be arrested for different BCs are as follows (Ravi Kumar et al. 2004a):

**BCs for Simply supported plate (S)**

$$u = w = \theta_y = 0 \text{ when } x=0 \text{ and } a$$

$$v = w = \theta_x = 0 \text{ when } y=0 \text{ and } b$$

**BCs for Clamped plate (C)**

$$u = v = w = \theta_x = \theta_y = 0 \text{ when } x=0 \text{ and } a$$

$$u = v = w = \theta_x = \theta_y = 0 \text{ when } y=0 \text{ and } b$$

**BCs for Free Edge plate (F)**

No restraint

Table 2 describes the governing equations for natural frequencies and non-dimensional buckling load for isotropic and composite plates used in the present study (Ravi Kumar et al. 2004a).

**Table 2.** Governing equations

Parameter	Plates/Shells	
	Isotropic	Composite
Natural frequencies	$\omega a^2 \sqrt{\frac{\rho}{D}}$	$\omega a^2 \sqrt{\frac{\rho h}{E_{22} h^3}}$
Non-dimensional buckling	$\frac{Pa^2}{Db}$	$\frac{Pa^2}{E_{22} b h^3}$

Note:  $D = \frac{Et^3}{12(1-\nu^2)}$

### 4.1 Convergence Study

In FE method convergence analysis is one of the important step in achieving accurate results. Convergence study helps to decide mesh size required. Mesh control parameters *m* and *n* are given in the Table 3. An isometric plate having an aspect ratio (*a/b*) of 1.0 with simply supported condition with a UDL on the entire panel is imposed and the central deflection of the plate is evaluated for various meshing parameters and the results are represented in the following table.

**Table 3.** Maximum deflection for lateral uniformly distributed load for simply supported isotropic plate for different mesh control parameters

Mesh size		Number of elements	Central deflection	Central deflection
<i>m</i>	<i>n</i>	<i>m</i> × <i>n</i>	Present	(Timoshenko 1964)
2	2	4	0.00191	0.00406
4	4	16	0.00401	
6	6	36	0.00405	
8	8	64	0.00406	
10	10	100	0.00407	

It can be noticed from Table 3 that total elements of 64 and 100 are sufficient to arrive in to the very close approximation to the exact solution and further if the number of elements are increased accuracy of the results will not change significantly. Hence it can be inferred that the panel with a mesh size of *m* = 10 and *n* = 10 are sufficient for the proposed study.

#### 4.1.1 Comparison with the Previous Studies

While finding a solution for a problem using scientific computational techniques and iterative methods, it is very essential to carry out a comparative study. In the present section, the MATLAB code is verified and validated with the various available resources and the same is presented in the below tables.

A S-S-S isotropic plate having an UDL on the surface to find central deflection and UDL on one of the end to find the critical buckling load with various aspect ratios are examined. It is evident from the Tables 4 and 5 that the obtained FEA results are very much agreeing with the exact results.

**Table 4.** Central deflection for an isotropic plate for different aspect ratios

Aspect ratio ( $\alpha$ )	Central deflection	
	Present	(Timoshenko 1964)
1.0	0.004059	0.00406
1.5	0.007719	0.00772
2.0	0.010129	0.01013
3.0	0.012233	0.01223

**Table 5.** Comparison study on non-dimensional buckling loads for an isotropic plate for different aspect ratios

Aspect ratio ( $\alpha$ )	Non-dimensional buckling load ( $\lambda$ )	
	Present	(Timoshenko et al. 1962)
0.2	26.729	27.00
0.4	8.369	8.41
0.6	5.129	5.14
0.8	4.19	4.20
1.0	3.98	4.00
1.2	4.112	4.13

Table 6 shows the comparative study done with the available literature for a S-S-S-S composite panel having ply orientation of 0/90 subjected to an in-plane loading for different thickness ratios and results are found matching with the (Reddy 1984a).

**Table 6.** Non-dimensional buckling load for LCP for simply supported for different thickness ratios

Thickness ratio ( $b/h$ )	Non-dimensional buckling load ( $\lambda$ )	
	Present	(Reddy 1984a)
10	11.104	11.099
20	12.422	12.268
50	12.858	12.569
100	12.923	12.614

## 4.2 Buckling Behavior of the LCP Under Compression

The first six mode shapes for a panel under an in-plane compressive load is given in the following Figs. 2\_a to 2\_f.

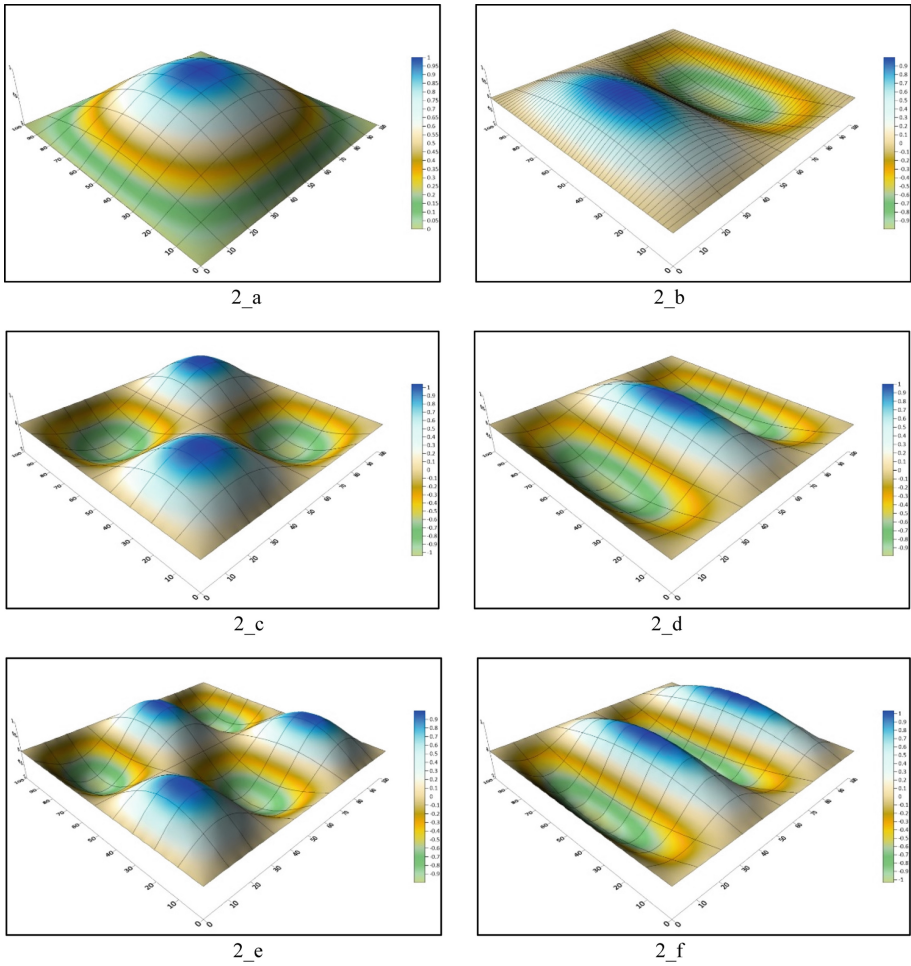


Fig. 2. Buckling mode shapes LCP.

### 4.3 Buckling and Vibration Results of DLCP Under Compressive In-plane Loads

Here in the present section the static stability and vibration behavior of eight layered LCP are evaluated by considering different parameters like, ply orientation, position of delamination, area of delamination and aspect ratio.

#### 4.3.1 Buckling Behavior of DLCPs Under an In-plane Uniform Loading for Various BCs

An LCP having aspect ratio of 1.0 and a ply orientation of  $(\pm 45/0/90)_S$  with a delamination at centre of the plate in x-y plane and mid plane of the plate ( $h_1/h = 0.5$ ) in x-z and y-z plane. The panel is subjected to an in-plane uniformly distributed load from one side and the non-dimensional buckling load is plotted and is as given in

Fig. 3 for various BCs, the extent of delamination is varied from 0.1 to 0.7 i.e. 1% to 49% as the panel is assumed to have a mesh size of  $20 \times 20$ .

It is evident from the Fig. 3 and Table 7 that as the extent of delamination enhance the non-dimensional buckling load reduces, it is obvious that as the extent of delamination increases the plate tend to become week and reduces its stability. Further is can be seen from the Fig. 3 the panel with C-C-C-C BC has highest stability and the plate with the combination of S-S and F-F possess least stability.

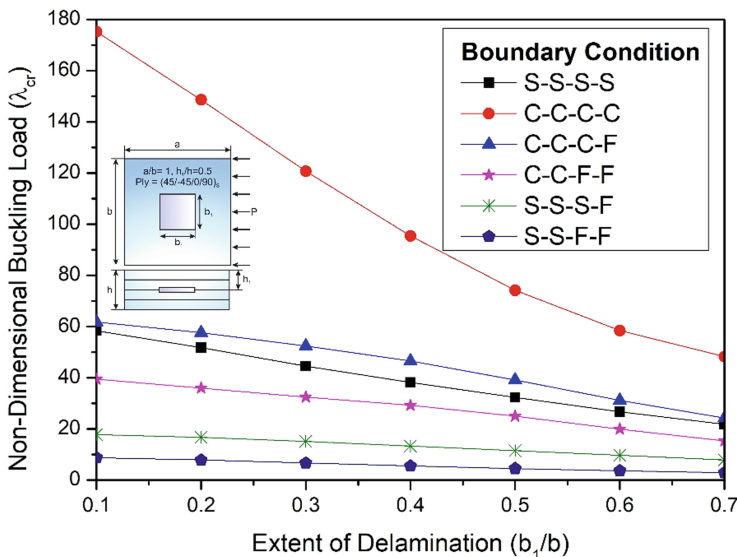


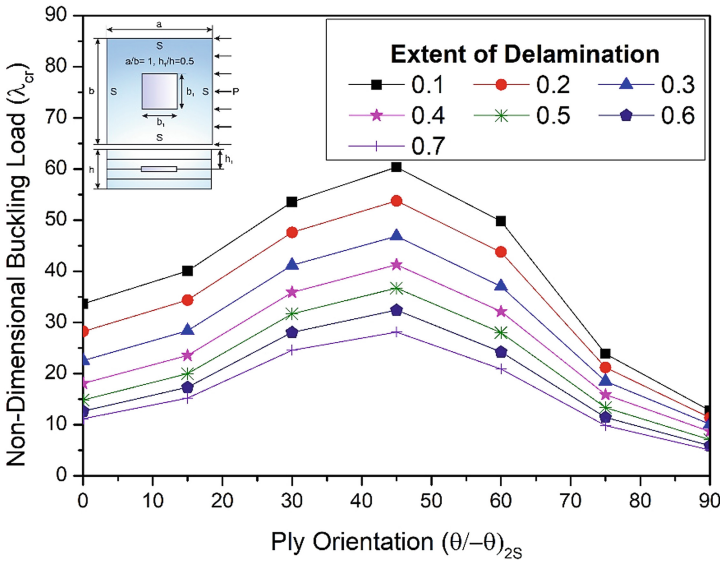
Fig. 3. Non-dimensional buckling load for various BCs under varying delamination.

Table 7. Non-dimensional buckling load values for LCP under different BCs for various extent of delamination

Extent of delamination ( $b_1/b$ )	BCs					
	S-S-S-S	C-C-C-C	C-C-C-F	C-C-F-F	S-S-S-F	S-S-F-F
0.1	58.343	175.194	61.774	39.413	17.811	8.770
0.2	51.760	148.622	57.647	35.963	16.671	7.881
0.3	44.509	120.722	52.456	32.469	15.064	6.718
0.4	38.188	95.430	46.587	29.216	13.277	5.550
0.5	32.325	74.160	39.171	25.000	11.463	4.515
0.6	26.703	58.456	31.157	19.923	9.670	3.643
0.7	21.844	48.241	24.236	15.278	7.893	2.917

**4.3.2 Buckling Behavior of DLCP Under In-plane Uniform Loading for Different Extent of Delamination**

A S-S-S-S composite panel having aspect ratio of 1.0 with an UDL at one end is examined to find the critical buckling load. The panel is examined for different set of ply orientations and results are plotted for different extent of delamination from 0.1 to 0.7.



**Fig. 4.** Non-dimensional buckling load for different extent of delamination having different ply angle.

The delamination is assumed at the centre of the plate in x-y plane and mid plane of the plate ( $h_1/h = 0.5$ ) in xz and yz plane. The Fig. 4 shows that all the plats having a trend that the buckling load increases up to certain point and falls after that. It can also be seen from the Fig. 4 the buckling load in maximum when the panel having a ply orientation of angle ply i.e.  $(45/-45)_{2S}$  and least for the cross ply i.e.  $(90/-90)_{2S}$ . It is also seen from the Fig. 4 that panel with less extent of delamination is more stable than any other panel with higher extent of delamination for any given ply orientation.

**4.3.3 Buckling Behavior of DLCP Under an In-plane Uniform Loading for Different Ply Orientation**

A S-S-S-S composite panel having aspect ratio of 1.0, extent of delamination 0.4 and with an UDL at one end is examined to find the critical buckling load. The panel is examined for different delamination position from 0.125 to 0.50 in x-z and y-z planes. The results are plotted for angle ply, cross ply and quasi isotropic ply orientations. Quasi isotropic ply orientation is nothing but the combination of angle and cross ply orientations. It is understood from the Fig. 5 that the buckling load increase up to the position of delamination value 0.25 (i.e. delamination is in between 2<sup>nd</sup> and 3<sup>rd</sup> layer



from the top layer) and after reduces for cross ply and angle ply. For Quasi isotropic ply orientation, the buckling load reduces continuously till it reaches mid plan and it is expected to show symmetry in the buckling loads as the delamination moves deeper.

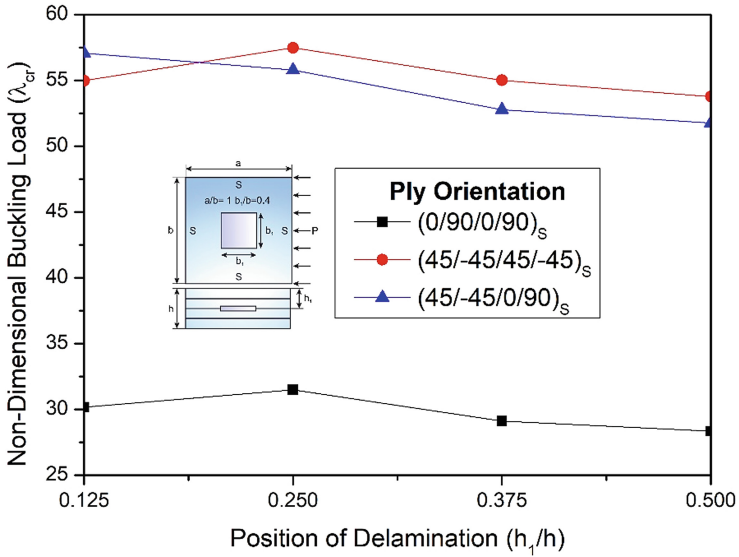


**Fig. 5.** Non-dimensional buckling load for different ply orientation with different delamination position.

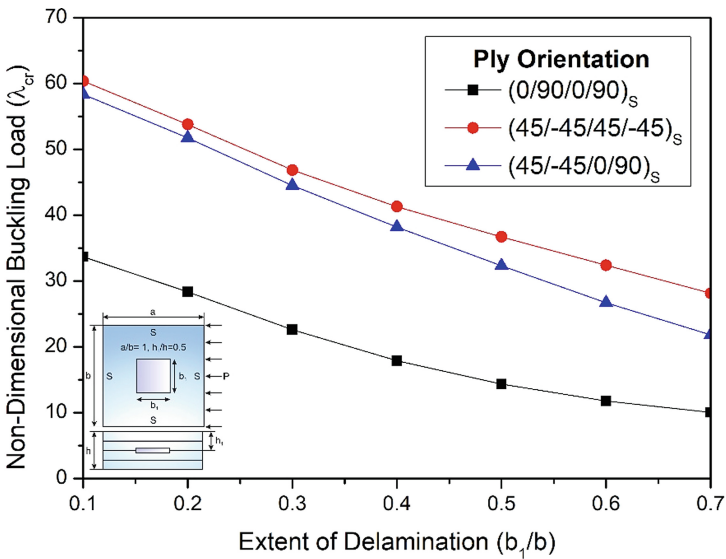


**Fig. 6.** Non-dimensional buckling load for different ply orientation under varying delamination.

For a similar plate varying extent of delamination and delamination is positions at the centre of the plate in x-y plane and mid plane of the plate ( $h_1/h = 0.5$ ) in x-z and y-z plane is shown in Fig. 6 and it briefs us that the buckling load reduces as the extent of delamination increases and in both the Fig. 5 and Fig. 6 it is noted that angle ply shows more stability then cross ply orientation however Quasi isotropic ply orientation shows good stability almost having same stability as angle ply.

**4.3.4 Buckling Behavior of DLCP Under In-plane Uniform Loading for Different Aspect Ratios**

A S-S-S-S cross ply composite panel for different extent of delamination from 0.1 to 0.7 and with an UDL at one end is examined to find the critical buckling load. The panel is examined for different aspect ratios from 0.5 to 3.0 and delamination positioned at the centre of the plate along the x-y plane and mid plane of the plate ( $h_1/h = 0.5$ ) in x-z and y-z plane. The plate with an aspect ratio is shows more stability than any other panel and as evident in previous Figs. 3, 4 and 6. The panel becomes less stable as the extent of delamination increases (Fig. 7).

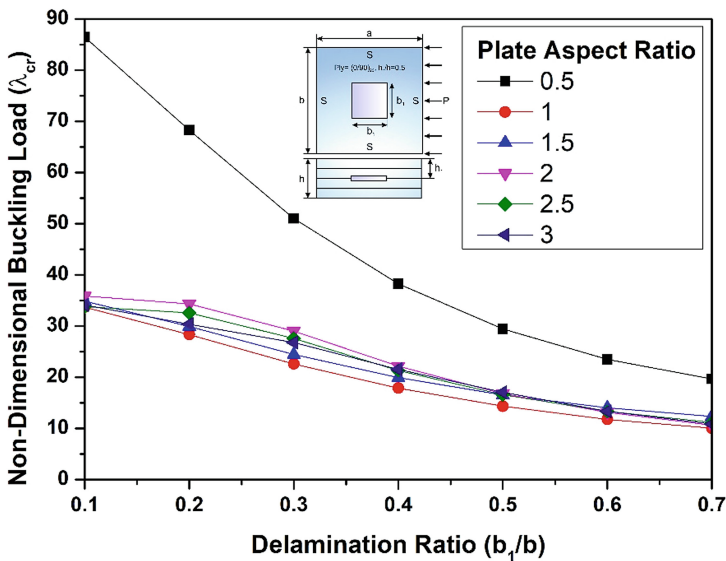


Fig. 7. Non-dimensional buckling load for different aspect ratio under varying delamination.

### 4.3.5 Buckling Behavior of DLCP Under In-plane Uniform Loading for Different Thickness Ratios

**Table 8.** Non-dimensional buckling load values for DLCP for simply supported for different thickness ratios.

Thickness ratio ( $b/h$ )	Non-dimensional buckling load ( $\lambda$ )		
	$(0/90)_{2S}$	$(\pm 45)_{4S}$	$(45/-45/0/90)_S$
100	28.345	53.772	51.760
50	27.918	52.571	50.658
25	26.521	48.514	46.977
20	25.624	45.885	44.590
10	16.607	30.1344	30.574
5	4.084	10.787	7.688

A S-S-S-S composite panel with an extent of delamination of 0.4 and with an UDL at one end is examined assuming delamination has occurred at the middle of the plate. The plate thickness ratio ( $b/h$ ) is varied from 5 to 100 and studies are conducted for cross ply, angle ply and quasi isotropic ply orientations. It is seen from the Table 8 that plate with cross ply orientation possess highest stability and cross ply being least among the three. We can also infer that higher the thickness ratio higher the stability at any given condition.

### 4.3.6 Vibration Behavior of DLCP Under In-plane Uniform Loading for Different Ply Orientation

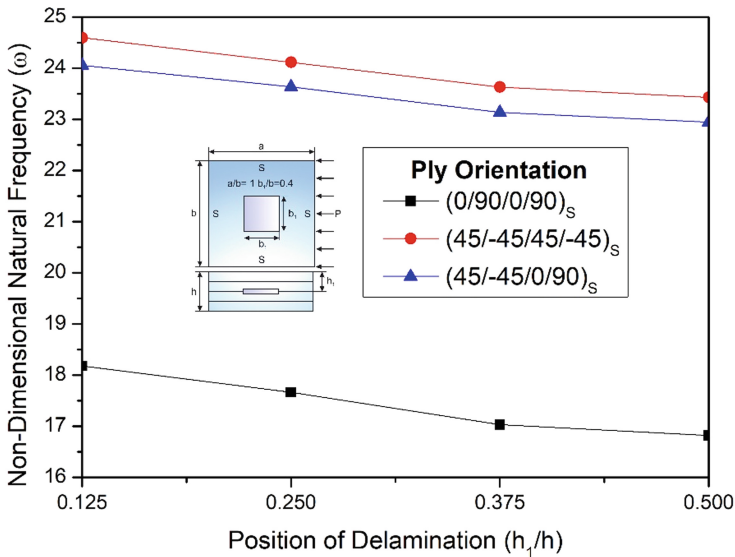


**Fig. 8.** Non Dimensional Natural frequency for various ply orientation with different delamination position.

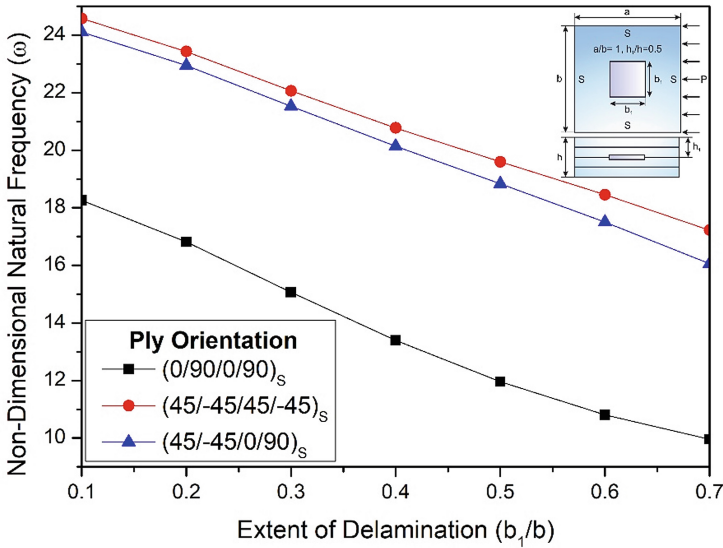


**Fig. 9.** Non Dimensional Natural frequency for various ply orientation under varying delamination.

A similar plate considered in buckling behavior under in-plane UDL for different ply orientation is taken and it is observed from the Fig. 8 and Fig. 9 that as the delamination of the plates moves deeper the non-dimensional natural frequency reduces. For and given case cross ply orientation has highest non-dimensional natural frequency, angle ply orientation has least non-dimensional natural frequency and Quasi isotropic ply orientation having the values in between both.

**4.3.7 Vibration Behavior of DLCP Under In-plane Uniform Loading for Different Thickness Ratios**

A S-S-S-S composite panel with an extent of delamination of 0.4 and with an UDL at one end is examined assuming delamination has occurred at the middle of the plate. The plate thickness ratio ( $b/h$ ) is varied from 5 to 100 and studies are conducted for cross ply, angle ply and quasi-isotropic ply orientations. It is seen from the Table 9 that plate with cross ply orientation have highest vibrating frequency and cross ply being least among the three. We can also infer that higher the thickness ratio higher the panel vibration increases at any given condition.

**Table 9.** Non-dimensional vibration frequency values for DLCP for simply supported for different thickness ratios.

Thickness ratio ( $b/h$ )	Non dimensional natural frequency ( $\omega$ )		
	(0/90) <sub>2S</sub>	(±45) <sub>4S</sub>	(±45/0/90) <sub>S</sub>
100	16.818	23.430	22.943
50	16.695	23.182	22.715
25	16.283	22.324	21.917
20	16.012	21.755	21.384
10	14.304	17.207	18.125
5	10.870	8.604	12.503

#### 4.3.8 Vibration Behavior of DLCP Under In-plane Uniform Loading for Different Extent of Delamination

Table 10 shows the result of vibrational behavior of a S-S-S-S DLCP of 1.0 aspect ratio loaded under an UDL. The plate is investigated for various ply angles and different extent of delamination from 0.1 to 0.7.

**Table 10.** Non-dimensional vibration frequency values for LCP for simply supported for under various extent of delamination for different ply angle

Extent of delamination ( $b_1/b$ )	Ply angle						
	(0/-0) <sub>2S</sub>	(15/-15) <sub>2S</sub>	(30/-30) <sub>2S</sub>	(45/-45) <sub>2S</sub>	(60/-60) <sub>2S</sub>	(75/-75) <sub>2S</sub>	(90/-90) <sub>2S</sub>
0.1	18.244	19.948	23.116	24.575	23.116	19.948	18.244
0.2	16.785	18.560	21.900	23.429	21.900	18.560	16.785
0.3	15.034	16.908	20.457	22.065	20.457	16.908	15.034
0.4	13.439	15.396	19.111	20.772	19.111	15.396	13.439
0.5	12.155	14.147	17.930	19.599	17.930	14.147	12.155
0.6	11.189	13.136	16.842	18.456	16.842	13.136	11.189
0.7	10.497	12.284	15.735	17.221	15.735	12.284	10.497

The delamination is assumed at the centre of the plate along xy plane and mid plane of the plate ( $h_1/h = 0.5$ ) in x-z and y-z plane. The results show that plate having (45/-45)<sub>2S</sub> ply angle has maximum vibrational frequencies and the ply with (90/-90)<sub>2S</sub> or (0/-0)<sub>2S</sub> has the least also, it can be observed that for any ply orientation as the delamination extents the vibrational frequency reduces.

## 5 Conclusion

In this paper an eight noded iso-parametric DLCP element was examined to analyze the buckling and vibration behavior under in-plane load. It was evident from the literature that buckling and vibration are very critical parameters for a structural member hence, its behavior need to be analyzed. However, it was also observed from many researchers

that the delamination plays a critical role while analyzing the composite plate therefore it was decided to analyze the buckling and vibration characteristics of composite plate by considering delamination at various positions, with different aspect ratios, thickness ratios and ply orientations.

1. For a given position of delamination, the buckling load reduces as the extent of delamination. The critical buckling load is inversely proportional to the increase in extent of delamination.
2. For any given dimension of delamination, the buckling strength further reduces as the position of the delamination changes from top layer to the centre of the plate.
3. The plate loaded under clamped condition will show better stability characteristics in comparison with simply supported BC and other combinations.
4. The composite plates with angle ply orientation i.e.  $(\pm 45)_{2S}$  shows greater stability as compared to other sequences considered in the study.
5. The severity in decreasing the buckling strength with respect to the delamination is found to be more significant as compared to that of thick plate.
6. The non-dimensional vibration frequency reduces for the given dimension of delamination, when it moves from top layer to the centre of the plate.
7. As the extent of delamination increases vibration frequency reduces and for any given condition.
8. The composite plates with angle ply orientation i.e.  $(\pm 45)$  has always shows higher natural frequency than any other ply combinations.

## References

- Akbarov, S.D., Yahnioğlu, N., Karatas, E.E.: Buckling delamination of a rectangular plate containing a rectangular crack and made from elastic and viscoelastic composite materials. *Int. J. Solids Struct.* **47**(25–26), 3426–3434 (2010)
- Anderson, R.G., Irons, B.M., Zienkiewicz, O.C.: Vibration and stability of plates using finite elements. *Int. J. Solids Struct.* **4**(10), 1031–1055 (1968)
- Arya, B., Rajanna, T.: Buckling behaviour of composite laminates of trapezoidal panel with cutout subjected to non-uniform in-plane edge loads. *Mater. Today Proc.* **45**, 21–26 (2020)
- Bert, C.W., Birman, V.: Dynamic instability of shear deformable antisymmetric angle-ply plates. *Int. J. Solids Struct.* **23**(7), 1053–1061 (1987)
- Chai, H., Babcock, C.D., Knauss, W.G.: One dimensional modelling of failure in laminated plates by delamination buckling. *Int. J. Solids Struct.* **17**(11), 1069–1083 (1981)
- Cook, R.D.: *Concepts and Applications of Finite Element Analysis*. Wiley, Hoboken (2007)
- Huang, C.S., Leissa, A.W., Chan, C.W.: Vibrations of rectangular plates with internal cracks or slits. *Int. J. Mech. Sci.* **53**(6), 436–445 (2011)
- Juhász, Z., Szekrényes, A.: The effect of delamination on the critical buckling force of composite plates: experiment and simulation. *Compos. Struct.* **168**, 456–464 (2017)
- Kim, H., Kedward, K.T.: A method for modeling the local and global buckling of delaminated composite plates. *Compos. Struct.* **44**(1), 43–53 (1999)
- Krawczuk, M., Ostachowicz, W., Zak, A.: Dynamics of cracked composite material structures. *Comput. Mech.* **20**(1–2), 79–83 (1997). <https://doi.org/10.1007/s004660050220>

- Kumar, L.R., Datta, P.K., Prabhakara, D.L.: Tension buckling and dynamic stability behaviour of laminated composite doubly curved panels subjected to partial edge loading. *Compos. Struct.* **60**(2), 171–181 (2003)
- Kumar, L.R., Datta, P.K., Prabhakara, D.L.: Dynamic instability characteristics of doubly curved panels subjected to partially distributed follower edge loading with damping. *Proc. Inst. Mech. Eng. C J. Mech. Eng. Sci.* **218**(1), 67–81 (2004)
- Kumar, L.R., Datta, P.K., Prabhakara, D.L.: Tension buckling and parametric instability characteristics of doubly curved panels with circular cutout subjected to nonuniform tensile edge loading. *Thin-Walled Struct.* **42**(7), 947–962 (2004)
- Lee, S.Y., Park, D.Y.: Buckling analysis of laminated composite plates containing delaminations using the enhanced assumed strain solid element. *Int. J. Solids Struct.* **44**(24), 8006–8027 (2007)
- Leissa, A.W.: The free vibration of rectangular plates. *J. Sound Vib.* **31**(3), 257–293 (1973)
- Mohanty, J., Sahu, S.K., Parhi, P.K.: Numerical and experimental study on free vibration of delaminated woven fiber glass/epoxy composite plates. *Int. J. Struct. Stab. Dyn.* **12**(02), 377–394 (2012)
- Mohanty, J., Sahu, S.K., Parhi, P.K.: Numerical and experimental study on buckling behaviour of multiple delaminated composite plates. *Int. J. Struct. Integrity* (2013)
- Mohanty, J., Sahu, S.K., Parhi, P.K.: Parametric instability of delaminated composite plates subjected to periodic in-plane loading. *J. Vib. Control* **21**(3), 419–434 (2015)
- Naganarayana, B.P., Atluri, S.N.: A computational model for analysing interactive buckling and delamination growth in composite structures. *Sadhana* **21**(5), 547–575 (1996)
- Prabhakara, D.L., Datta, P.K.: Static and dynamic elastic behaviour of damaged plates subjected to local inplane loads. *Mar. Struct.* **9**(8), 811–818 (1996)
- Prabhakara, D.L., Datta, P.K.: Vibration, buckling and parametric instability behaviour of plates with centrally located cutouts subjected to in-plane edge loading (tension or compression). *Thin-Walled Struct.* **27**(4), 287–310 (1997)
- Rajanna, T., Banerjee, S., Desai, Y.M., Prabhakara, D.L.: Vibration and buckling analyses of laminated panels with and without cutouts under compressive and tensile edge loads. *Steel Compos. Struct.* **21**(1), 37–55 (2016)
- Rajanna, T., Banerjee, S., Desai, Y.M., Prabhakara, D.L.: Effect of boundary conditions and non-uniform edge loads on buckling characteristics of laminated composite panels with and without cutout. *Int. J. Comput. Methods Eng. Sci. Mech.* **18**(1), 64–76 (2017)
- Ravi Kumar, L., Datta, P.K., Prabhakara, D.L.: Vibration and stability behavior of laminated composite curved panels with cutout under partial in-plane loads. *Int. J. Struct. Stab. Dyn.* **5**(01), 75–94 (2005)
- Reddy, J.N.: A simple higher-order theory for laminated composite plates (1984a)
- Reddy, J.N.: Exact solutions of moderately thick laminated shells. *J. Eng. Mech.* **110**(5), 794–809 (1984b)
- Reddy, J.N., Chao, W.C.: A comparison of closed-form and finite-element solutions of thick laminated anisotropic rectangular plates. *Nucl. Eng. Des.* **64**(2), 153–167 (1981)
- Reddy, J.N., Phan, N.D.: Stability and vibration of isotropic, orthotropic and laminated plates according to a higher-order shear deformation theory. *J. Sound Vib.* **98**(2), 157–170 (1985)
- Timoshenko, S.P., Gere, J.M.: *Theory of elastic stability*. Courier Corporation (2009)
- Timoshenko, S., Woinowsky-Krieger, S.: *Theory of plates and shells* (1959)



# Strengthening of Distressed Reinforced Concrete Structural Member by Use of FRP Composites: A Review

Nitesh Kumar and H. K. Sharma<sup>(✉)</sup>

Department of Civil Engineering, NIT Kurukshetra,  
Kurukshetra, Haryana 136119, India  
hksharmal010@nitkkr.ac.in

**Abstract.** In advance concrete technology Fiber Reinforced Polymer (FRP) is extensively used because of its good mechanical properties such as high stiffness, have good tensile strength, anti-corrosive, non-conducting etc. With passage of time Reinforced Concrete (RC) structural members would decrease its strength if adequate maintenance would not be provided, so these distressed RC structural member should require rehabilitation and proper maintenance or strengthening. Strengthening of these distressed RC members could be done either by the use of FRP either by Near surface mounted (NSM) technique or by Externally bonded (EB) technique. The gain of strength by application of FRP on a distressed RC member would depend upon type of FRP used like CFRP, GFRP, AFRP etc., also depends upon the orientation of FRP. This review focuses on the use of different type of FRP used for strengthening of a distressed RC member by enhancing its different strength parameters like flexural strength, axial load carrying capacity, shear strength, torsional strength, impact load and durability. This review also focuses on the rupture of FRP strengthened RC member.

**Keywords:** FRP · Strengthening · Durability · Failure mode

## 1 Introduction

In this running world, there is a one common thing present, that is structures which are generally made up of concrete. Everyone is living in the structures, which are mainly made up of concrete. With passage of time, anything one is using would decrease its efficiency. So, one has to go for maintenance from time to time for better use of the structure. So, coming to a civil engineering perspective, the most common thing that a civil engineer uses, is a concrete. So, with passage of time the physical, chemical, and mechanical properties of a concrete decrease. After some passage of time the component of structures like beam, column, slab, etc. would not perform their desired purpose because of several problems like occurrence of fine cracks, spalling of concrete, insufficient cover due to which corrosion of bars starts. So, for this problem, one solution is either to replace that part of structure with a new one or do retrofitting of that part. The first solution is very expensive for regular buildings which are present around us. But the second approach is very efficient as well as economical, so one prefers most



of the time is strengthening of the structures. So, best thing which are used for strengthening is the use of Fiber Reinforced Polymer (FRP). FRP is one of the most advanced concrete technology. FRP are made up of polymer layer's which have different fibers. Different types of FRP are Carbon Fiber Reinforced Polymer (CFRP), Glass Fiber Reinforced Polymer (GFRP), Aramid Fiber Reinforced Polymer (AFRP), Gudonis et al. (2014). These FRP composites are available in different form like in form of sheets, laminates, fibers, rods, which are bonded to concrete with the help of fasteners and adhesive. Reinforced Concrete (RC) structures are designed to carry the service loads, dead load, earthquake load, wind load as per the codes and they also provide protection against bending, shear, torsion, fatigue, vibration and impact as per the codes for specific condition. But due to some unforeseen condition's like exceed design loads concrete does not fulfill its desired purpose thus RC structures requires strengthening of structures to increase its durability and increases its load carrying capacity to meet the code requirement, Ghobarah et al. (2002). This review is based on the enhancement of different structural strength parameters of distressed structural members by the application of FRP. Basic methodology of strengthening is either global modification of structural members or local modification of structural components. Global modification refers to addition of a new members such as steel braces, structural wall etc. Local modification refers to determining the weak of deficit member and strengthening is done by steel jacketing, by use of FRP. The main properties of FRP over the steel plates are specific stiffness is high, strength is high, highly corrosion resistance, easy to handling and installation, non-corrosive, light weight and inflammable, high tenacity.

## 2 Function of FRP

Cracked beams or Uncracked beams which are wrapped or strengthened with FRP have been very popular nowadays because of their unique properties like strength-weight ratio, stiffness, high longitudinal tensile strength, non-corrosiveness, low thermal transmissibility, and facile installation, resistance against attack of insect and fungal, resistance against chemical attack. Distressed structural RC members which do not follow the values given in the specified codes, due to increase in static loading or occurrence of crack due to environmental degradation, earthquake, storms and corrosion of main reinforcement bars is repaired by the use of FRP composites which can rectify all the above problems Grace et al. (2012). FRP-strengthened Reinforced concrete structural members improves it's all strength parameters like flexural strength, torsion and shear capacity of the members, it also improves the ductility and durability of members which are wrapped with FRP. Past studies had made a considerable effort in developing new methods or technique for the strengthening of structural members with the help of FRP. These studies had established different-different guidelines for the application of FRP's under different loading as well as different critically environmental conditions. Selection of FRP for the strengthening is depend upon the many factors such as environment condition, extent of deterioration of component, cost indulged in the work, properties of material like for stiffness requirement one would go for CFRP as CFRP have high stiffness property than GFRP (Fig. 1).

### 3 Types of FRP

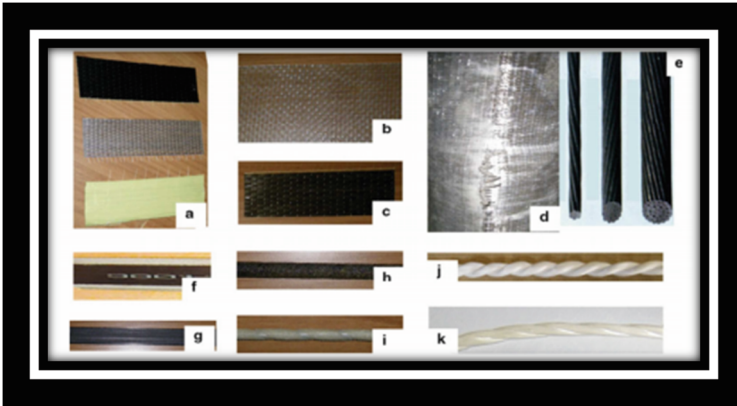


**Fig. 1.** Different Types of FRP (Ayesha et al. 2019).

Annotations used are:

(a) Carbon fiber reinforced polymer (CFRP), Glass fiber reinforced polymer (GFRP), Aramid fiber reinforced polymer (AFRP). (b) GFRP sheet, (c) Basalt fiber sheet, (d) Fractured confining GFRP jacket, (e) CFRP tendons, (f) CFRP Laminates, (g) NSM strips of CFRP, (h) Bars of CFRP, (i) Bars of GFRP, (j) Polypropylene fiber rope, (k) Vinylon rope.

## 4 Properties of Different FRP used for Retrofitting

### 4.1 Carbon Fibre Reinforced Polymer (CFRP)

The unit weight of CFRP lies between  $1500 \text{ kg/m}^3$  to  $1600 \text{ kg/m}^3$ . The weight of CFRP is very less than conventional steel i.e. it is lighter about 5 times than conventional steel, moreover the tensile strength is about 8–10 times more than conventional steel. CFRP have stiffness than GFRP and AFRP hence it is most widely used FRP for strengthening of distressed RC structural member. CFRP sheets having vertical fiber have more rupture strength than CFRP sheets having horizontal fiber.

### 4.2 Glass Fibre Reinforced Polymer (GFRP)

The unit weight of GFRP lies between  $1200 \text{ kg/m}^3$  to  $1500 \text{ kg/m}^3$ . The weight of GFRP is very less than conventional steel i.e. it is lighter about 5–8 times than conventional steel, moreover the tensile strength is about 3–6 times more than conventional steel. Where minor repair work is required GFRP is recommended because its cost is much less than CFRP. After peaking GFRP-strengthened beam have a residual strength therefore it would have a gradual failure whereas CFRP one reaching its ultimate strength it would fail immediately.

### 4.3 Aramid Fibre Reinforced Polymer (AFRP)

AFRP are non-conducting polymer used for strengthening of RC member and also used in aerospace engineering and also used for manufacturing of military application. These fibers have very high melting points. These fibers have good fabric integrity at elevated temperatures. These polymers have good resistance to organic solvents. These fibers have good mechanical properties such as high tenacity, low creep, high modulus of elasticity.

## 5 Method of Strengthening RC Members

- 5.1 Externally Bonded (EB) laminates
- 5.2 Near Surface Mounted (NSM) bars or strips
- 5.3 Mechanical anchorage system
- 5.4 Grooving method by using adhesive or by without adhesive

Externally Bonded laminates is used for strengthening of RC structural member by overlapping on the distressed structural member. The procedure for EB laminates is that the FRP is wrapped in number of layers which depends upon of the extent of deterioration of the RC member. In the case of the beam to increase the flexural strength the wrapping of FRP is done on the soffit of beams and to increase the shear capacity the wrapping is done on the side face of the beam. In NSM technique groove is cut on the tension face on the beam and strips is inserted in the groove and then the groove is covered with a cover which should have sufficient thickness.

## 6 Different Types of Adhesive Used for Bonding

For the perfect bonding of FRP composite with the surface of concrete, high quality adhesive resin should be used to ensure that proper regain of the strength. Resins are basically a polymer which may be found either in solid state or in liquid state which extremely viscous in nature. For perfect bonding with the other polymeric materials resins are used as adhesives which contains polyester, epoxy, or phenolic forms Ary and Kang (2012). Unit weight of epoxy resin varies from  $1.1 \text{ kg/m}^3$  to  $1.4 \text{ kg/m}^3$  and have approximately weight nearly equal to  $0.5 \text{ kg/m}^2$ . The tensile strength of epoxy resins varies from 30 MPa to 90 MPa, and at the time failure maximum elongation varies from 0.9% to 4.5%, and their elastic modulus varies from 1.1 GPa to 6 GPa. The curing period of epoxy resin varies from 3 days to 14 days having temperature varies from  $16^\circ\text{C}$  to  $23^\circ\text{C}$ .

## 7 Strength Enhancement by Use of FRP Composites

### 7.1 Axial Load Carrying Capacity of Compression Member

The eccentric loaded column had more significant effect of wrapping with CFRP than concentric loaded column because in eccentric column the gain of strength is more as

compared to concentric loaded column. With increase in number of layers of CFRP layer results in increase in load carrying capacity of column. With the CFRP wrapping the ductility of the column is also increased.

Jaya and Jessy (2012) studied that the load carrying capacity of column wrapped with 2, 4, 6 layers of GFRP leads to increase of 8%, 28%, 32% load carrying capacity respectively compared with the specimen which are unwrapped. The column which are wrapped with CFRP leads to increase the strength about an average of 98.3% compared to unwrapped column. Jaya and Jessy (2012) further compared the increase of load carrying capacity wrapped with CFRP and GFRP and they observed that CFRP wrapped gains 98.3% with single layer only but GFRP gains only 70% with 6 layers.

Rochette and Labossiere (2003) research on the square and rectangular column confined with carbon and aramid and then tested under compression. Author concluded that the confinement effect is directly related to the shape of cross section for a given numbers of wraps and a very sudden and destructive like a blast occur with an excessive confinement.

Chaalla et al. (2003) had done an experimental investigation by using CFRP wrap. The specimen had rectangular, square and circular cross section. They found that compressive strength increases more for rectangular or square section than circular section by the CFRP wrapping. They also found that with increase in number of layers of wrapping compressive strength increases drastically. Result also shows that the maximum gain of strength can be achieved for concrete column wrapped is approximately 90% as compared with controlled specimen.

## 7.2 Flexural Strengthening

Flexural strength is defined as the ability to resist the bend. Flexural strength of any structural element is the moment carrying capacity of that element against all the load (Dead load, imposed load, seismic load, wind load etc.) acting on it but due improper maintenance or due to improper workmanship at the time of casting the flexural strength of that element decreases, hence strengthening of that element would require, for this one would go for FRP wrapping which increases the flexural strength tremendously.

Philip et al. investigated RC beam which are under reinforced section and the externally bonded material are CFRP, GFRP, AFRP and these FRP are bonded on tension side of beam. Researchers found that stiffness is increasing between 17% to 99% and the flexural capacity of distressed beam increases from 40% to 97% when they use FRP plates.

Kachlakev and McCurry (2000) had done their investigation on an existing bridge, they replicated 4 beams and retrofitted with CFRP and GFRP they found with use of FRP the static load carrying capacity increases near about 150% compare with un-strengthened beam. The investigation suggested that the beams of the bridge which are retrofitted with GFRP and CFRP would easily carry the structural demand of the bridge i.e. static load of 658 KN and moment of 868 KN-m. They also concluded that the beam of the bridge which is retrofitted with GFRP have a failure under flexural at the midspan at an equivalent of 31% gain over control specimen, in this failure is caused due to the yielding of the tension failure. This study suggests that use of CFRP provides high stiffness and more durability when one uses CFRP than GFRP.

Zhuang et al. (2018) had done their investigation on damaged RC beams which are strengthened using CFRP composites. They had carried out their experimental analysis on an old distressed bridge, the beam specimen had a cross section of  $200 \times 250$  mm and length of 2300 mm on which they had applied four points load to carry out the flexure test. They had concluded that for a seriously damaged RC beams the best and effective way of strengthening is the application of externally bonded CFRP sheets. In their study, after strengthening with CFRP the yield growth increases from 5% to 36%.

Jamal and Abubakr (2020) had explained the use of CFRP and Galvanized Steel Mesh (GSM) both have some advantages and disadvantages, one of the major disadvantages is the CFRP and GSM bonded beam have lack of ductility so for overcoming this disadvantage Aluminum Alloys (AA) is used for overcoming the lack of ductility problem. For this they had performed an experimental investigation of 6 beam under flexure test. The result shows the flexural capacity and ductility is improving. The tested beams of AA with high density steel mesh (SMH) and AA with CFRP showed that the strain capacity in tested beams increases 6.52 and 4.55 times respectively compared to the beam bonded with GSM and CFRP alone. The flexural capacity increases around 28% due to strengthening of the beam with hybrid GSM and AA laminate.

Mashrei and Ali (2019) had performed an experimental analysis to examine the capacity gain of RC strengthened by groove-bonded CFRP using EBROG and EBRIG method as compared to beam which are not strengthened. In this 13 RC beam is strengthened by using different method. They had found the load carrying capacity of strengthened RC beams is increased. On application of a single layer of longitudinal CFRP sheet on grooves by EBRIG and EBROG has increased the load carrying capacity by 95% and 62% respectively and by the traditional strengthening with CFRP with application of one layer the increase in load carrying capacity is only 16.2% and with two layers of wrapping the increase in 77.5%.

### 7.3 Shear Strengthening

Shear strength of a concrete is the ability to counter or resist against sliding of surface. Shear strength depends upon the grade of concrete as well as the grade of reinforcing bar which is used in concrete. Sometimes, due to improper or inadequate cover to these bars, they get corroded or strength of these gets reduced, so strengthening is required for those concrete structures. The most effective way for shear strengthening is provide the FRP wrapping at an angle on the face of the concrete, this would increase the shear capacity of a distressed concrete member.

Bukhari et al. (2010) had experimentally investigated the amount of shear strength increases by the use of CFRP. In their research they had tested 7 continuous beam having rectangular cross section in which one is controlled specimen and remaining 6 is wrapped with CFRP. They come to a result that with the use of CFRP the shear strength increases drastically and they had also come to a conclusion the best angle suited for placing the FRP is  $45^\circ$ , at this orientation maximum gain of shear resistance is noted.

Thanasis (1998), his study aims to develop an analytical model which follows the code. Experimental analysis includes testing of 11 beam which are strengthened with CFRP and analytical part of the investigation deals with the developing a model which can shows the contribution of FRP in shear capacity of beam and this study also shows

the orientation of the FRP. This study concludes that this technique of strengthening with FRP is highly effective and the orientation of the FRP should be closer to the perpendicular to the diagonal crack this orientation increases the effectiveness of FRP.

Haya et al. (2019) had done an experimental analysis in which the distressed RC beam which have deficiency of shear resistance is strengthened with externally bonded CFRP sheets with different wrapping configuration i.e. U-wrapping and full wrapping. For this investigation a T-beam is used for the analysis, in which two different specimens of T-beam is also created in first the strengthening is done till web's height (WBR1) and in second strengthening is done for the full depth of beam. The study concludes that the beam which is strengthened with U-wrapped CFRP increased the shear strength of control specimen by 114.82%, and completely wrapped WBR1 and WBR2 gain shear strength by 69.28% and 201.63% respectively as compared to control specimen. This paper also concludes that complete wrapping would provide more ductility to the RC beam than the U-wrapping.

Kachlakev and McCurry (2000) had performed an experimental investigation by replicating the beam of an existing beam. The research shows that the GFRP (Glass Fiber Reinforced Polymer) added for shear was very much sufficient to nullify the lack of stirrups which makes the RC beam should fail by steel yielding (under reinforced section) at the mid span. By the addition of GFRP the allowable ultimate deflections to be 200% higher than the shear deficient control beam, which fails due to excessive diagonal crack.

#### 7.4 Torsional Strengthening

Torsional strength of a concrete structure is the ability to resist the twist or rotation. With the passage of the time, due to improper maintenance or heavy excessive load the torsional strength of the concrete decreases, so for restoring the strength, strengthening of this distressed member is done with the help of FRP wrapping.

Ghobarah et al. (2002) had performed an experimental analysis about the torsion strengthening, 8 beams having rectangular cross-section is casted which are wrapped with CFRP and GFRP with different configuration and 3 controlled specimens was casted. In this analysis a pure tension is applied to the RC beam and torsional capacity, angle of twist of the beam and strain is recorded. The torsional capacity increases about 72% to the controlled specimen. By performing several investigations, this study suggest that the full wrapped configuration is better than using strips only and study also suggest that the most effective angle of FRP is  $45^\circ$  because it improves ductility and torsional capacity of RC beam.

Vishnu et al. (2013) performed an experimental investigation, for this they had casted 14 beams for the analysis, they had used GFRP wrapping for strengthening and the test is done for combine bending and torsion. Their result shows that the torsional capacity of RC beam improves, and the study also shows that at the time of first crack the angle of twist is also increases, ductility is also improved by the use GFRP strengthening. Study also that the diagonal strips increases more torsional capacity than the vertical strips.

Punam and Vishal (2018) their study is to evaluate and compare, how much effective is epoxy bonded CFRP and GFRP with different configuration. For this study total of 30 rectangular cross section beam was used. The study concludes that the fatigue life is

more for CFRP than GFRP, GFRP is weaker as compared to CFRP in torsion resistance, in alkali environment CFRP is more durable than GFRP. Failure of CFRP strengthened RC beams is due to either by debonding of FRP or by crushing depending upon the slenderness ratio.

Shraddha and Vijaykumar (2015) performed a study for the torsional behavior of RC beam strengthened with CFRP and GFRP. For this analysis they had casted 39 rectangular specimen out of which 18 are wrapped with CFRP and 18 are wrapped with GFRP and 3 are controlled specimen. They had concluded that the torsional moment capacity wrapped with CFRP and GFRP increases 60.47% and 47.46% with respect to control specimen. Study also suggest that the maximum and minimum torsional capacity increases wrapped with CFRP is 101.8% and 40.02% respectively. And for GFRP maximum and minimum torsional capacity increases is 83.49% and 8.76%. along with torsional resistance the angle of twist and ductility also improves.

### 7.5 Impact Strength

Thong and Hong (2017) had done experimentally analysis of a FRP wrapped RC beam under impact loading, for this investigation total of 13 specimen was casted and 45° FRP U-wrapping was done and was tested under impact load and failure pattern was investigated, after performing the experiment they concluded that mode of failure of ductile flexure RC beam under static load was changed from brittle shear mode under impact load, they also observed that under the impact test the debonding strain of FRP was slightly lower than that in static tests, the experiment also shows that after FRP wrapping the stiffness of the wrapped RC beam was considerably increases.

Taiping et al. (2003) had performed an experimental investigation to study the effects of FRP wrapped RC beam under impact loads. For this they prepare 5 RC beam which are wrapped with Kevlar fiber and carbon fiber, the bonding of these polymer was done at the top and bottom faces of the beam, for creating the impact they dropped a steel cylinder from a particular height, after their investigation they found that the by the use of Kevlar and carbon fiber the impact resistance was increased very much, this increase in impact resistance vary with the thickness, weight, strength of the composites which we are using, they had also found that the carbon laminate produces very much stiffness.

### 7.6 Blast Resistance

Young et al. (2018) had study the effect of blast-induced local damage on the flexural strength of the specimen which are damaged due to the blast loading. For this study they had retrofitted the specimen which are damaged by blast loading by the steel fiber reinforced cementitious composite (SFRCC) and with CFRP. The result suggests that the use of high amount of steel stirrups does not improve the blast resistance however their study suggest that the use of small diameter bar with less spacing would increase the ductility but these are not adequate to prevent the local damages occurred due to the blast load. The SFRC would increase the ductility as well as the blast resistance. Use of CFRP as a retrofitting material also enhance the blast resistance, however the debonding failure between the CFRP and contact surface of RC member would occur when we use CFRP for retrofitting.



Elsanadedy et al. (2011) had performed an investigation on an existing RC circular column with the help of explosive charges, and the distressed RC column is wrapped by CFRP and a non-linear finite element analysis was done on LS-DYNA software. The result suggests that use of CFRP for the strengthening purpose is a best solution for the distressed column. The study also suggests that with the use of CFRP the lateral deflection was decreased exponentially as compared with unwrapped column.

## 7.7 Fatigue Life

Huang et al. (2017) investigated the fatigue behavior of post-tensioned prestressed CFRP which is externally bonded to RC beam. The main objective of this study was to predict the failure behavior of externally bonded CFRP wrapped RC beam and fatigue life. The researchers conclude that the failure mode due to fatigue is the rupture of main steel bar at the main cracked section. The fatigue life of bonded CFRP RC beam is far better than the controlled specimen.

Wu et al. (2010) had analysis of different FRP like CFRP, GFRP, poly-paraphenylenl benzobisoxazole (PBO) and basalt fibers wrapped RC member under cyclic loading. The result predicts that the fatigue behavior of PBO and basalt fibers are nearly same. Out of different FRP used best fatigue performance was shown by the CFRP and PBO. Tensile modulus improves by using FRP. Under the same load the hybrid FRP would lower the effect of the cyclic loading hence the fatigue life would improve (Table 1).

**Table 1.** Shows location of FRP and different failure modes

Sl	Reference	Technique of strengthening	Type of FRP used	Location of FRP	Mode of failure
1	Sabau et al. (2018)	NSM	CFRP	Side NSM strips	Concrete crushing due to intermediate crack induced due to debonding
2	Sabau et al. (2018)	NSM	CFRP	Bottom NSM strips	Separation of concrete cover
3	Teng et al. (2006)	NSM	CFRP	NSM strips are provided at mid span only	Concrete cover separation of concrete
4	Teng et al. (2006)	NSM	CFRP	Bottom NSM strips along 97% of span	Crushing of concrete along with separation of cover
5	Hawouldeh et al. (2006)	EB	CFRP	Along soffit of the beam	Yielding of steel along with debonding of FRP from the surface of RC member
6	Hawouldeh et al. (2006)	EB	CFRP	Along soffit	Locally debonding along with crushing of concrete

(continued)



**Table 1.** (continued)

Sl	Reference	Technique of strengthening	Type of FRP used	Location of FRP	Mode of failure
7	Hawouldeh et al. (2006)	EB	Hybrid	One layer of CFRP and one layer of GFRP	Flexural crack and crushing of concrete and locally debonding
8	Attari et al. (2012)	EB	CFRP	Parallel to the axis	Concrete crushing with rupture in FRP
9	Ebead and Saeed (2017)	EB	Hybrid	Pultruded GFRP and CFRP plate	Steel yielding with debonding
10	Ary and Kang (2012)	EB	CFRP	Fully wrapped strips which is located at a distance equal to half of depth	Rupture in FRP strips
11	Ary and Kang (2012)	EB	CFRP	U-wrapped strips which is located at a distance equal to half of depth	Debonding
12	Castilo et al. (2019)	EB	CFRP	U-wrapped strips with straight CFRP anchor	Rupture in FRP along with crushing of concrete
13	Adhikary and Mutsuyoshi (2004)	EB	CFRP	Two vertical sides wrapped with single layer of FRP which are spaced at a distance equal to half of depth	Separation of cover along with rupture in FRP in horizontal direction

## 8 Failure Of FRP-Strengthened Reinforced Concrete Beam

The failure would occur from the weak linkages, for this Camata et al. (2004) explained the potential failure zones from where an FRP wrapped RC beam would fail. Either debonding of FRP with the surface of RC member would occur or the steel yielding would occur or the concrete crushing would occur depending upon the weak link in the system. Failure of RC strengthened occurs due to several reasons like debonding of FRP, crushing of concrete, yielding of the main reinforcement, etc. (Figs. 2 and 3).

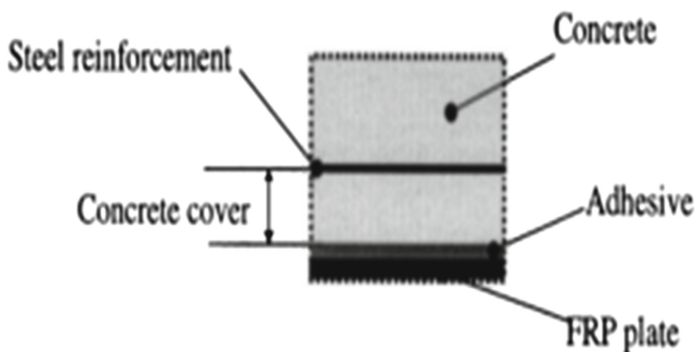


**Fig. 2.** Failure Zones in FRP-strengthened RC member Camata et al. (2004).

## 9 Failure Modes

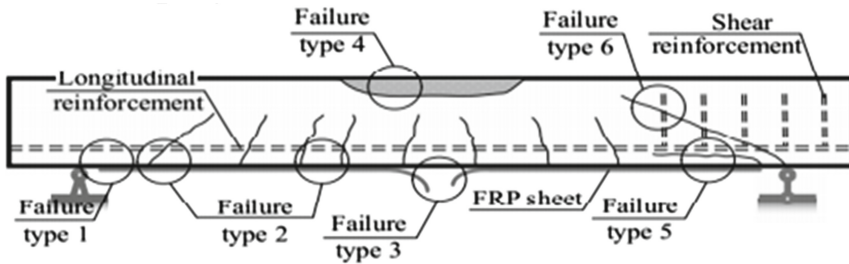


Fig. 3. Failure modes in an EB FRP RC Beam Gribniak et al. (2017).

## 10 Conclusion

1. FRP possess superior mechanical properties over the traditional steel therefore popularity of FRP is increasing day by day in modern concrete technology. This study concludes that:
2. For strengthening of a distressed RC member FRP is one of the most effective and efficient method because by applying FRP it can increase the strength approximately twice the strength of controlled RC member.
3. The eccentric loaded column had more significant effect of wrapping with CFRP than concentric loaded column because in eccentric column the gain of strength is more as compared to concentric loaded column.
4. With the increase in number of layers of FRP wrapping the strength changes drastically, some study found the strength increases about 90% as compared to controlled section.
5. Study suggests that by using FRP for strengthening purpose impact resistance, shear resistance, flexural resistance, stiffness, fatigue life, durability increase.
6. There are several techniques used for the application of FRP but, NSM technique is the most efficient than others because gain of strength is more, debonding failure is less.
7. Use of CFRP the shear strength increases drastically and they had also come to a conclusion the best angle suited for placing the FRP is  $45^\circ$ , at this orientation maximum gain of shear resistance is noted.
8. As compared between different FRP used the best one is CFRP because CFRP have high stiffness and strength as compared with GFRP and AFRP.
9. The failure mode depends upon the technique we used for strengthening, quality of material and loading condition. The failure mode would occur at the weak linkage. Various study suggests different mode of failure like crushing of concrete, debonding of FRP, yielding of main reinforcement.

## References

- Jamal, A.A., Hawouldeh, A.: Flexural strengthening of reinforced concrete beams with externally bonded hybrid systems. *Procedia Struct. Integ.* **28**(11), 282312–282319 (2018)
- Adhikary, B.B., Mutsuyoshi, H.: Behavior of concrete beams strengthened in shear with carbon-fiber sheets. *J. Compos. Construct.* **8**(3), 258–264 (2004)
- Ary, M.I., Kang, T.H.K.: Shear-strengthening of reinforced and prestressed concrete beams using FRP: part I—review of previous research. *Int. J. Compos. Construct. Mater.* **6**(28), 41–47 (2012)
- Attari, N., Amziane, S., Chemrouk, M.: Flexural strengthening of concrete beams using CFRP, GFRP and hybrid FRP sheets. *Construct. Build. Mater.* **37**, 37746–37757 (2012)
- Belarbi, A., Acun, B.: FRP systems in shear strengthening of reinforced concrete structures. *Procedia Eng.* **57**(10), 2–8 (2013)
- Bourmas, D.A., Pavese, A., Tizani, W.: Tensile capacity of FRP anchors in connecting FRP and TRM sheets to concrete. *Eng. Struct.* **82**(1), 72–81 (2015)
- Bukhari, I.A., Vollum, R.L., Ahmad, S., Sagaseta, J.: Shear strengthening of reinforced concrete beams with CFRP. *Magaz. Concrete Res.* **62**(1), 65–77 (2010)
- Camata, G., Spacone, E., Al-Mahaidi, R., Saouma, V.: Analysis of test specimens for cohesive near-bond failure of fiber-reinforced polymer-plated concrete. *J. Compos. Constr.* **8**, 528–538 (2004)
- del Rey, C.E., Griffith, M., Ingham, J.: Straight FRP anchors exhibiting fiber rupture failure mode. *Composite Struct.* **207**, 612–624 (2019)
- Omar, C., Mohsen, S., Munzer, H.: Confinement model for axially loaded short rectangular columns strengthened with carbon fiber reinforced polymer wrapping. *ACI Struct. J.* **100**(2), 215–221 (2003)
- Ebead, U., Saeed, H.: FRP stirrups interaction of shear-strengthened beams. *Mater. Struct.* **50**, 103 (2017)
- Elsanadedy, H.M., Almusallam, T.H., Abbas, H., Al-Salloum, Y.A., Alsayed, S.H.: Effect of blast loading on CFRP-Retrofitted RC columns a numerical study. *Latin Am. J. Solids Struct.* **8**, 55–81 (2011)
- Ghobarah, A., Ghorbel, M.N., Chidiac, S.E.: Upgrading torsional resistance of reinforced concrete beams using fiber-reinforced polymer. *J. Compos. Construct.* **6**(4), 257–263 (2002)
- Grace, C., Yang, Y., Sneed, L.: *Fracture Mechanics Approaches to Debonding Behavior of Reinforced Concrete Members With Externally-Bonded Fiber Reinforced Polymer Laminates*. American Concrete Institute, ACI Special Publications (2012)
- Gribniak, V., Tamulenas, V., Ng, P.L., Arnautov, A.K., Gudonis, E., Misiunaite, I.: Mechanical behavior of steel fiber-reinforced concrete beams bonded with external carbon fiber sheets. *Materials (Basel)* **10**(6), 666 (2017)
- Gudonis, E., Timinskas, E., Gribniak, V., Kaklauskas, G., Arnautov, A.K., Tamulėnas, V.: FRP reinforcement for concrete structures: state-of-the-art review of application and design. *Eng. Struct. Technol.* **5**, 147–158 (2014)
- Muhammad, N.S.H., Widiarsa, R., Bagus, I.: Axial and flexural performance of square RC columns wrapped with CFRP under eccentric loading. *Faculty of Engineering and Information Sciences - Papers: Part A*. vol. 8 (2012)
- Huang, H., Wang, W.-W., Dai, J.-G., John, C.B.: Fatigue behavior of reinforced concrete beams strengthened with externally bonded prestressed CFRP sheets. *J. Composites Construct.* **21**(3) (2017). (ASCE, ISSN 1090-0268)
- Huo, J., Li, Z., Zhao, L., Liu, J., Xiao, Y.: Dynamic behavior of CFRP-strengthened reinforced concrete beams without stirrups under impact loading. *ACI Struct. J.* **115**, 775–787 (2018)

- Vishnu, H.J., Paresh, V.P., Sharadkumar, P.P.: Strengthening of RC beams subjected to combined torsion and bending with GFRP composites, Chemical, Civil and Mechanical Engineering Tracks of 3rd Nirma University International Conference on Engineering (NUICONE 2012). *Procedia Eng.* **51**, 282–289 (2013)
- Jaya, K.P., Jessy, M.: Strengthening of RC column using GFRP and CFRP. In: World Conference on Earthquake Engineering (2012)
- Kachlakev, D., McCurry, D.D.: Behaviour of full-scale reinforced concrete beam retrofitted for shear and flexural with FRP laminates. *Composites: Part B* **31**, 445–452 (2000)
- Lee, J.-Y., Shin, H.-O., Min, K.-H., Yoon, Y.-S.: Flexural assessment of blast-damaged RC beams retrofitted with CFRP sheet and steel fiber. *Int. J. Polymer Sci.* **2018**, 1–9 Article ID 2036436 (2018)
- Haya, H.M., Hawouldehb, R.A., Jamal, A.A.: Shear strengthening of reinforced concrete beams using CFRP wraps. The 3rd International Conference on Structural Integrity, ICSI. *Procedia Struct. Integr.* **17**, 214–221 (2019)
- Mashrei, M.A., Sultan, A.: Flexural strengthening of reinforced concrete beams using carbon fiber reinforced polymer (CFRP) sheets with grooves. *Latin Am. J. Solids Struct.* **16** (2019)
- Zhuang, N., Dong, H., Chen, D., Ma, Y.: Experimental study of aged and seriously damaged rc beams strengthened using CFRP composites. *Adv. Mater. Sci. Eng.* **21**, Article ID 6260724, 9 (2018)
- Obaidat, Y.T., Heyden, S., Dahlblom, O.: The effect of CFRP and CFRP concrete interface models when modelling retrofitted RC beams with FEM. *Composites Struct.* **92**, 1391–1398 (2010)
- Osman, B.H., Wu, E., Ji, B., Abdulhameed, S.S.: Repair of pre-cracked reinforced concrete (RC) beams with openings strengthened using FRP sheets under sustained load. *Int. J. Composites Construct.* **11**, 171–183 (2017)
- Ou, Y., Zhu, D.: Tensile behavior of glass fiber reinforced composite at different strain rates and temperatures. *Construct. Build. Mater.* **96**, 648–656 (2015)
- Punam, P., Vishal, Y.: Comparative experimental study on torsional strengthening of RC beam using CFRP and GFRP fabric winding. *Int. Res. J. Eng. Technol.* **5**(4) (2018)
- Pham, T.M., Hao, H.: Impact behavior of FRP-strengthened RC beams without stirrups. *J. Compos. Constr.* **20**, 04016011 (2016)
- Remennikov, A., Goldston, M., Neaz, S.M.: Impact performance of concrete beams externally bonded with carbon FRP sheets. In: *Mechanics of Structures and Materials: Advancements and Challenges – Proceedings of the 24th Australasian Conference on the Mechanics of Structures and Materials. ACMSM*, vol. 24 (2017)
- Richtchie, P.A., Thamos, D.A., Le, L.W., Guy, C.: external reinforcement of concrete beams using fiber reinforced plastics. *ACI Struct. J.* **88**(4), 1991 (1991)
- Pierre, R., Pierre, L.: Axial testing of rectangular column models confined with composites. *J. Composites Construct. @ ASCE* **4**(3), 129–135 (2003)
- Sabau, C., Popescu, C., Sas, G., Schmidt, J.W., Blanksvärd, T., Täljsten, B.: Strengthening of RC beams using bottom and side NSM reinforcement. *Composites Part B Eng.* **149**(25), 82–91 (2018). (ISSN, 1359-8368)
- Siddika, A., Mamun, Md., Alyousef, R., Amran, M.: Strengthening of reinforced concrete beams by using fiber-reinforced polymer composites. *J. Build. Eng.* **25**, 100798 (2019)
- Sorrentino, L., Turchetta, S., Bellini, C.: In process monitoring of cutting temperature during the drilling of FRP laminate. *Composites Struct.* **168**, 549–561 (2017)
- Supian, A.B.M., Sapuan, S.M., Zuhri, M.Y.M., Zainudin, E.S., Ya, H.H.: Hybrid reinforced thermoset polymer composite in energy absorption tube application: a review. *Def. Technol.* **14**(4), 291–305 (2018)

- Taiping, T., Hamid, P.E.S., ASCE M.: Behavior of concrete beams strengthened with fiber-reinforced polymer laminates under impact loading. *J. Composites Construct.* **7**(3) (2003)
- Teng, J.G., De Lorenzis, L., Wang, B., Li, R., Wong, T.N., Lam, L.: Debonding failures of RC beams strengthened with near surface mounted CFRP strips. *J. Composites Construct.* **10**(2) (2006)
- Shraddha, B.T., Vijaykumar, R.R.: Comparative experimental study on torsional behavior of RC beam using CFRP and GFRP fabric wrapping. *International Conference on Emerging Trends in Engineering, Science and Technology (ICETEST), Procedia Technology* **24**, 140–147 (2015)
- Thanasis, C.T.: Shear strengthening of reinforced concrete beams using epoxy-Bonded FRP composites. *ACI Struct. J.* Title no. 95-S11 (1998)
- Wu, Z., Wang, X., Iwashita, K., Sasaki, T., Hamaguchi, Y.: Tensile fatigue behavior of FRP and hybrid FRP sheets. *Composites Part B* **41**(5), 396–402 (2010)



# Performance-Based Seismic Design: A Review

Shruti Chaudhary<sup>(✉)</sup> and Satyabrata Choudhury

Department of Civil Engineering, National Institute of Technology Silchar,  
Silchar, India

{shruti\_pg\_21, chou\_s}@civil.nits.ac.in

**Abstract.** This study presents an overview of the evolution of Performance-based seismic design. Owing to many limitations of force-based codal design, the Displacement-based design and Performance-based design have evolved. The aim of performance-based seismic design is to design structures for some pre-set design objectives under given hazard level. In this literature survey, the limitations of codal design, evolution of Displacement-based design, evolution of Performance-based design up to the Unified performance-based design have been highlighted.

**Keywords:** Force-based design · Performance-based design · Performance level · Unified performance-based design

## 1 Introduction

The philosophy and practice of seismic design has evolved significantly during the last 60 years. The journey was from Force-based design (FBD) to Displacement-based design (DBD) to Performance-based design (PBD). The goal of PBD is to design structures for some intended design objectives under some specified hazard level. The Codes do not address how the structure would cope in a major earthquake (Freeman et al. 2004).

Direct Displacement-based design (DDBD) is a DBD method in which the target design displacement is directly obtained by the applications of dynamic equations. DDBD can accommodate only drift as the target design criterion. Unified Performance-based design (UPBD) is an up gradation of DDBD method in which both drift and member performance level are accommodated in the design philosophy Choudhury (2008). DBD and PBD arose to overcome the limitations of FBD. The followings are some of the drawbacks of FBD approach:

1. Force is a poor predictor of damage potential; displacement (linear displacement, drift, plastic rotation, etc.) is a more accurate indicator of damage.
2. The response reduction factor is applied uniformly to all structures within a class. In reality it varies ductility and time period of the structure.
3. The response reduction factor is related to ductility, as assumed in the codes, is only valid for long period structures.
4. Stiffness is taken as independent of strength, which is not the case.
5. FBD is almost incapable of designing structure for intended objectives.

## 1.1 Performance-Based Design

To create the NEHRP Guidelines and Commentary for Seismic Rehabilitation of Buildings, FEMA worked with the BSSC and the Applied Technology Council (ATC) in the early to mid-1990s. In terms of performance-based seismic design methods, this was a watershed moment since it established several key earthquake-related ideas necessary for a PBD approach. In order to meet the performance target, the design hazard (seismic risks) had to be defined and an acceptable extent of the damage (performance level) had to be established when the design hazard occurred. The documents also introduced standard performance levels, which defined the degree of nonstructural and structural damage based on standard structural response parameters (FEMA 273/FEMA-356).

Drift, plastic rotation, crack width, along with other performance metrics are all target objectives. The design spectrum and its level represent the hazard level. A performance level (PL) is a damaged state as determined by plastic deformation. Performance Levels are classified into two categories: structural and nonstructural, as highlighted in Table 1 (Fig. 1).

**Table 1.** Performance levels designators

SI	Structural performance levels designators	Non-structural performance levels designators	Building performance levels designators
1	<b>S1:</b> Immediate Occupancy (IO) PL	<b>NA:</b> Operational PL	<b>S1-NA (1-A):</b> Operational Level (OL) building PL
2	<b>S2:</b> Damage Control performance range	<b>NB:</b> Immediate Occupancy PL	<b>S1-NB (1-B):</b> Immediate Occupancy (IO) building PL
3	<b>S3:</b> Life Safety (LS) PL	<b>NC:</b> Life Safety PL	<b>S3-NC (3-C):</b> Life Safety (LS) building PL
4	<b>S4:</b> Limited Safety performance range	<b>ND:</b> Hazard Reduced PL	<b>S5-NE (5-E):</b> Collapse Prevention (CP) building PL
5	<b>S5:</b> Collapse Prevention (CP) PL	<b>NE:</b> Not Considered	
6	<b>S6:</b> Not considered		

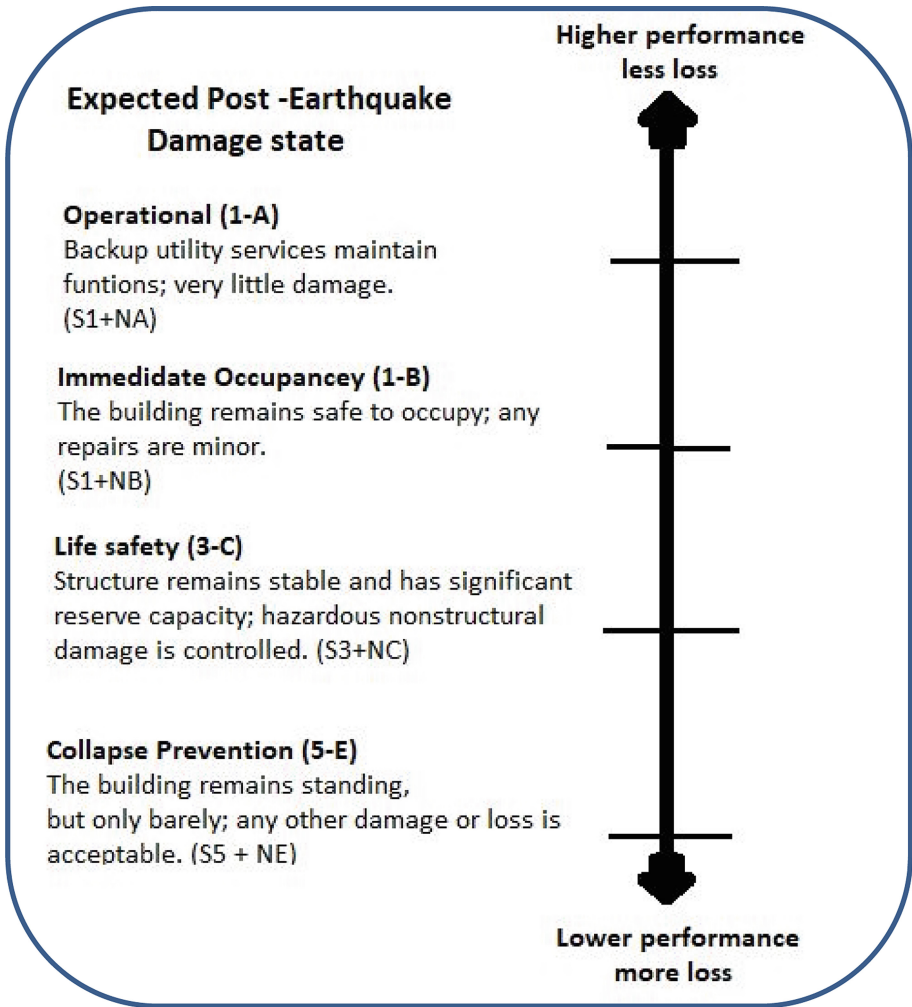


Fig. 1. Performance Ladder (after FEMA-273).

There were also four nonlinear and linear methods provided in the NEHRP Guidelines that could be used to calculate the predicted response parameter values for a specific degree of shaking and compare the expected performance of the building. Figure 2 depicts a hypothetical building's global force-displacement relationship overlaid with the qualitative performance standards laid forth in FEMA 274/273. The graphic shows the various degrees of damage in an easy-to-understand way. The damage to the structure and business interruption (downtime) associated with the three performance levels are summarized in Table 2.



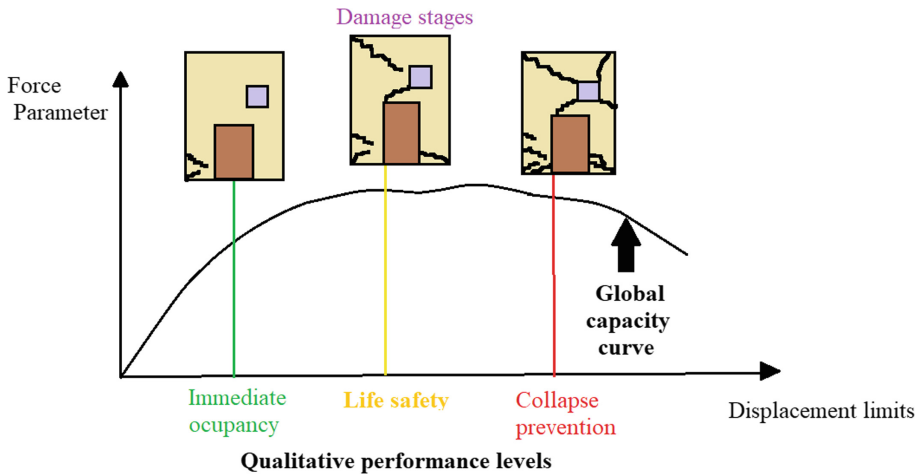
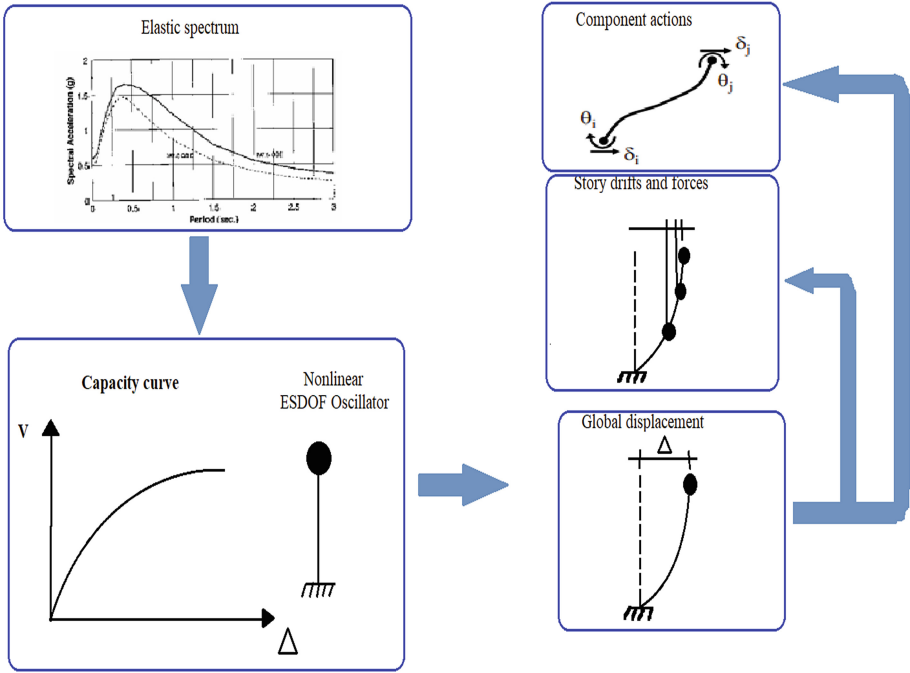


Fig. 2. Qualitative performance levels as per FEMA 273/356.

Figure 3 illustrates the FEMA 273 nonlinear static approach for performance evaluation. To begin, one or more elastic acceleration response spectra are used to quantify the seismic hazard. A nonlinear mathematical formulation of the structure is put under monotonically increasing loads or displacements to create the capacity curve shown in Fig. 3. There are several ways of displaying this curve, including: roofing displacement (abscissa) and base shear (ordinate). For each design spectrum, the ultimate roof displacement is determined using an equivalent SDOF nonlinear model of the building's structure. After establishing force actions and component deformation for performance evaluation, the nonlinear static analysis results are utilized to calculate component force actions and component deformation for a given roof movement. If component requirements do not surpass component capabilities, the building's performance objective is declared met. Figure 4 shows a performance flow chart.

Table 2. Building performance levels as per FEMA 273/356

Performance level	Damage description	Downtime
Immediate occupancy	Structural damage is negligible; critical systems remain working; total damage is minimal	24 h
Life safety	There is a possibility of structural damage; there is no collapse and there are few falling dangers	Possibility of complete loss
Collapse prevention	Structural damage is severe; imminent collapse; possible dangers of falling; possible restriction of access	Total loss is quite likely



**Fig. 3.** FEMA 356/273 performance evaluation method.

FEMA-273 established methods that were later improved and expanded by Vision-2000 (a framework for performance-based seismic design) and ATC-40 (a system for analyzing and upgrading concrete buildings). The American Society of Civil Engineers enhanced these technologies further by transforming the FEMA-273 research into the FEMA-356 Pre-standard for Building Seismic Rehabilitation. Collectively, the FEMA-356, Vision-2000 and ATC-40 publications describe the current state of performance-based seismic engineering design process.

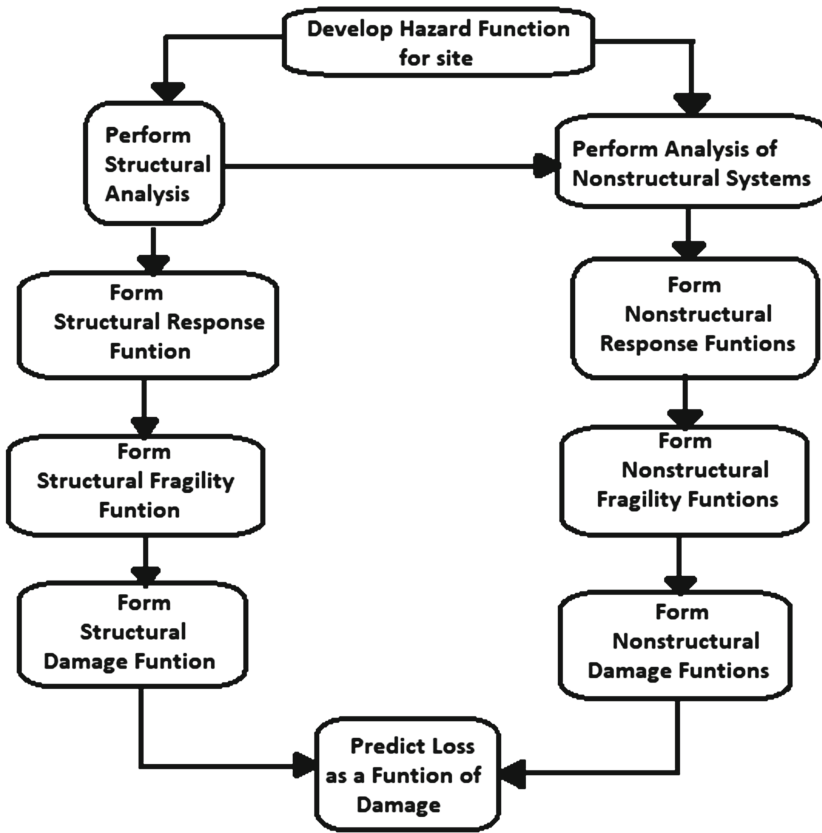


Fig. 4. ATC-58 performance prediction flowchart.

## 2 How the PBD Evolved

In practice, all design is performance-driven in some way, even if the engineers responsible for it are unaware. One goal of engineering is to have low failure rates under actual loads and loss of serviceability or little damage under normal loads, such as when designing for live and dead load resistance. This performance baseline is incorporated into the ultimate strength design (USD) and load and resistance factor design (LRFD) methods in both concrete and steel design standards (ACI 1999; AISC 1993). There are ways to make sure that factored loads don't go above capacity, but serviceability is confirmed by looking at deflections under actual (unfactored) design loads instead. The majority of loading conditions, including wind, snow, comparable loads, and ground pressure, are handled identically.

In two aspects, the design for earthquake resistance is distinctive. To begin, design standards did not require serviceability under projected earthquake loads; second, the design considers the risk of localized element failure under realistic stress while attempting to avoid overall collapse.

Freeman et al. (1975) established the concept of Performance-Based Design (PBD) in the 1970s as part of a pilot project at the Puget Sound Naval Shipyard to determine the seismic susceptibility of structures. The method is based on John Blume's reserve energy technique (Blume et al. 1961). Later, it was utilized to link seismic ground motion with measures of building performance (Freeman 1978). ATC-3-06 established the PBD as a measurable entity (1978).

ATC-40 introduced the capacity spectrum method (CSM) (1996). This approach finds the response point of the structure, which is the point at which the structure's capacity meets the reduced demand. Engineers benefit greatly from CSM's graphical approach to visualizing structural dynamics. ATC-40 specifies a combination of structural and nonstructural performance standards for buildings. Acceptance criteria for component performance levels are specified in terms of plastic rotations. In 1997, FEMA-273 was published in conjunction with NEHRP building repair requirements. This document, which coexisted with ATC-40, established building performance levels as well as approval requirements for member performance levels. The coefficient approach is given in this article for estimating the goal displacement while accounting for inelasticity, MDOF influence, and P-delta effect. This treatise also explored the Demand Capacity Ratio. For asymmetric structures, Kilar and Fajfar presented a pushover analysis (1997). Kim and Amore were the first to propose the pushover analysis (1999).

Another significant development in the PBD was the NEHRP 2000 (FEMA-368). It comprises a sizable number of variables associated with Response Reduction, Displacement Modification, and Overstrength. A re-evaluation of FEMA-273, FEMA-356 (2000) went one step further in setting performance thresholds and developing a methodology for evaluating existing or new structures. In the United States, Hamburger and Moehle (2000) conducted a state-of-the-art performance-based engineering review.

Chopra et al. (2001) built the Single Degree Freedom system's theoretical foundations using pushover analysis. Firescu and Fajfar (2002) asserted that the NSP and NLTHA provide comparable findings. Iwan and Guyader (2002) examined the accuracy of CSM and concluded that various dampers and time intervals might be used to improve the findings.

Matsumori and Shiohara (1999) examined the deformation requirement for earthquake members and discovered that ground motion characteristics had an effect on it. According to Bento et al. (2004), the nonlinear static approach with first mode proportional load is well suited for low-rise buildings.

FEMA-440 enhanced the coefficient method in 2004. FEMA-450 advocated for a bilinear approach and established seismic standards for new buildings and other structures. Pettinga and Priestley (2005) developed DDBD method for reinforced concrete frames frame buildings. Among the improvements proposed and validated were improved design displacement profiles and equal lateral force distributions.

To accommodate for higher-mode drifts in taller frames, a design drift reduction factor was added. For higher-mode amplification of the column bending moments, a simplified ductility-dependent equation was derived. This factor scales the capacity design equation for column moment design in the same way that previous force-based approaches did, but it does so in a way that is more consistent with time-history results.

Choudhury and Singh (2013) introduced the UPBD method for RC frame buildings. The proposed design method is designed to simultaneously fulfil performance level and target drift objectives. The first step is to determine a theoretically calculated beam size that meets performance requirements. The remainder of the design process is guided by Pettinga and Priestley. The recommended UPBD method was used to construct frame structures with two distinct designs and different heights for various drift and performance combinations. EC-8 spectra at a hazard level of 0.45 g were used to assess how well the structures performed using NLTHA and pushover analysis with five SCGM matches. It has been demonstrated that the suggested UPBD method is capable of creating frame structures with any drift and performance levels desired. The suggested approach always meets performance criteria, and the actual drift is well within the allowed range of the target drift.

Mayengbam and Choudhry (2014) developed a method for column size estimation in PBD. The authors also suggested a drift reduction formula. Das and Choudhury (2019) conducted research on the effect of gross stiffness, strength-based effective stiffness, and FEMA-specified effective stiffness. It was discovered that when gross stiffness is used in nonlinear analyses, the seismic response characteristics of the building are considerably underestimated. When structures generated at IO performance levels were assessed using gross stiffness, many of the structures remained elastic. Additionally, the maximum base shear stresses in the constructions with effective and gross stiffnesses are significantly different. It follows from this that including gross stiffness as an input in a nonlinear dynamic analysis will lead to the wrong results. Effective stiffness values (FEMA-356) have been found to be superior to gross stiffness values, as it produced better outcomes. They do not, however, correspond to the real structure. As a result, actual efficiency of systems during seismic activity must be determined using actual realistic stiffness based on strength. This aspect was established in genetic algorithm (Gandomi et al. 2021).

The PBD of frame buildings with fluid viscous dampers had been evolved and discussed (Sullivan and Lago 2012; Moradpour and Dehestani 2019; Malu and Choudhury 2020). The cost of dampers was estimated using the damping constant in its entirety (manufacturing cost). As damper nonlinearity grows, the overall damping constant falls. As the dampers' nonlinearity increases, the total damping constant decreases. When damping constants are compared, it is found that drift proportional and storey shear proportional damper designs have lower damping constant values, resulting in more economical construction (Malu and Choudhury 2020).

Banerjee and Choudhury (2020) developed UPND method for reinforced concrete (RC) bridge piers. A theoretical formula for pier size was developed to manage any combination of drift and PL under a specific risk threshold. The recommended UPBD approach was used to build a set of bridge piers. When comparing the goal and actual results, it was suggested that the wording for pier diameter be changed. Four bridges with piers were simulated using the improved pier diameter expression. SCGMs are Euro code compliant – The bridges were subjected to eight design spectrum tests at a seismic intensity of 0.6 g. Two bridges were built for IO PL with 0.5% drift, and two more bridges were built for LS PL with 1% drift. The achieved PL of the bridge piers was found to be equal to the planned PL, and the drift values were found to be within 20% of the desired drift. A designer may use the recommended UPBD technique to

design a bridge pier for two performance criteria (drift and PL) for a given hazard level without iterating. Bozorgnia and Bertero (2006) has compiled an edition on PBD. Table 3 depicts the evolution of PBD over time.

**Table 3.** Chronological development of PBD

Year	Development
1961	<b>Blume</b> suggested a reverse energy technique
1975	<b>Freeman et al.</b> as a technique for evaluating the seismic susceptibility of structures at the Puget Sound Naval Shipyard in a pilot project
1978	They were used as a procedure to correlate earthquake ground motion with observed building performance by <b>Freeman</b> . <b>ATC-3-06</b> put the design criteria on the footing of the first principle replacing old empirical concepts
1980	In <b>ATC-10</b> , It was utilised to establish a relationship between building performance and earthquake ground motion
1993	<b>DDBD</b> by Priestley (1993)
1995	<b>Vision 2000</b> document of SEAOC discussed rehabilitation of buildings
1996	<b>ATC-40</b> developed capacity spectrum method. Quantified performance levels
1997	<b>FEMA-273</b> gave coefficient method for target displacement
1999	SEAOC Blue Book published
2000	<b>FEMA-356</b> described guidelines for new buildings
2004	<b>FEMA-440</b> Gives equivalent bilinearization method. Adaptive pushover by Antoniou and Pinho (2004)
2004	<b>FEMA-450</b> gave seismic regulations for new buildings and other structures
2005	Pettinga and Priestley provided a <b>DDBD</b> of frame buildings
2006	<b>DDBD</b> of frame-wall buildings given by Sullivan et al. (2006a, b)
2008	<b>UPBD</b> method for Dual system by S. Choudhury
2013	Choudhury and Singh: <b>UPBD</b> method for RC frame buildings
2014	Mayenbam and Choudhury: Column size in <b>PBD</b>
2019	Das and Choudhury: <b>Effective Stiffness</b> was studied
2020	Malu and Choudhury: <b>DDBD</b> of a building incorporating viscous dampers
2020	Banerjee and Choudhury: <b>UPBD</b> of bridge piers
2021	Bhushanabeni Anil: <b>UPBD for Steel frame buildings</b> by Anil (2021)

### 3 PBD's Global Framework

Recent professional efforts have resulted in the development of many conceptual frameworks for PBEE (SEAOC Vision 2000, ATC-40, FEMA 273). They are distinct in their details but not in their conceptions. The global framework depicted in Fig. 5 outlines the ideas, processes, and critical concerns that must be addressed. Among the issues addressed are seismic, structural, geotechnical, MEP (nonstructural), and architectural concerns.

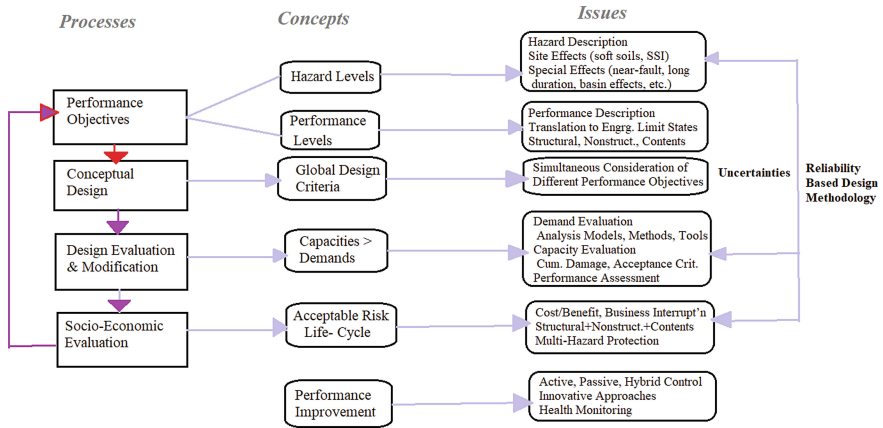


Fig. 5. Performance-based earthquake engineering global framework.

## 4 Conclusion

In this paper a brief outline of the evolution of PBD has been discussed. Force-based design had many limitations which led to the development of DBD, DDBD, PBD and UPBD. At present the designers have better control over design for target objectives under any given hazard level. PBD is a vast field, and it cannot be said that every aspect of PBD has been covered in this study.

## References

- ACI-318: Building Code Requirements for Structural Concrete. American Concrete Institute (1999)
- Anil, B.: Unified performance-based design of steel frame buildings. M.Tech. thesis under the supervision of S. Choudhury, Department of Civil Engineering, NIT Silchar (2021)
- Antoniou, S., Pinho, R.: Development of a displacement-based adaptive pushover procedure. *J. Earthquake Eng.* **8**(5), 643–664 (2004)
- Applied Technology Council: Methodology for Evaluation and Upgrade of Reinforced Concrete Buildings, Report No. ATC-40, California Seismic Safety Commission, Sacramento, California (1996)
- Applied Technology Council: NEHRP Guidelines for Seismic Rehabilitation of Buildings, Report No. FEMA-273, Federal Emergency Management Agency, Washington, D.C (1997)
- ATC-3-06: Tentative Provisions for the Development of Seismic Regulations of Buildings, Applied Geochronology Council (1978)
- ATC-40: Seismic Evaluation and Retrofit of Existing Concrete Buildings, Applied Geochronology Council (1996)
- AISC-360: Specification for Structural Steel Buildings. American Institute of Steel Construction (1993)

- Banerjee, S., Choudhury, S.: An introduction to unified performance-based design of bridge piers. In: 17th World Conference on Earthquake Engineering, 17WCEE Sendai, Japan, September (2020). 9e-0011
- Bento, R., Falcao, S., Rodrigues, F.: Nonlinear static procedures in performance based seismic design. In: 13th World Conference on Earthquake Engineering, Canada, 1-6 August 2004. Paper No. 2522
- Bozorgnia, Y., Bertero, V.V.: *Earthquake Engineering From Engineering Seismology to Performance-Based Engineering*. CRC Press, Boca Raton London New York Washington, D. C. (2006)
- Blume, J.A., Newmark, N.M., Coring, L.H.: *Design of Multistory Reinforced Concrete Buildings for Earthquake Motions*, Portland Cement Association, Chicago (1961)
- Chopra, A.K., Goel, R.K., Chintanapakdee, C.: Statistics of SDF-System Estimate of Roof Displacement for Pushover Analysis of Buildings. PEER Report No. 2001-16 (2001)
- Choudhury: Performance-based Seismic Design of Hospitals, Ph.D. thesis, Department of Earthquake Engineering, IIT Roorkee (2008)
- Choudhury, S., Singh, S.M.: A unified approach to performance-based design of RC frame buildings. *J. Inst. Eng.* **94**(2), 73–82 (2013). <https://doi.org/10.1007/s40030-013-0037-8>
- Das, S., Choudhury, S.: Influence of effective stiffness on the performance of RC frame buildings designed using displacement-based method and evaluation of column effective stiffness using ANN. *Eng. Struct.* **197**, 109354 (2019)
- FEMA-273: NEHRP Guidelines for the Seismic Rehabilitation of Buildings, US Federal Emergency Management Agency, Building Seismic Safety Council, Washington DC (1996)
- FEMA-356: Prestandard and Commentary for the Seismic Rehabilitation of Buildings, US Federal Emergency Management Agency (2000)
- FEMA-440: Improvement of Nonlinear Static Seismic Analysis Procedures, ATC-55 Project, Applied Technology Council and US Federal Emergency Management Agency (2004)
- FEMA-450: NEHRP Recommended Provisions for Seismic Regulations for New Buildings and other Structures, US Federal Emergency Management Agency (2004)
- Fireescu, D.J., Fajfar, P.: Comparison of Simplified Procedures for Nonlinear Analysis of Structures. Report No. PEER/2002/2, pp. 63-76 (2002)
- Freeman, S.A., Nicoletti, J.P., Tyrell, J.V.: Evaluation of existing buildings for seismic risk: a case study of puget sound naval shipyard, Bremerton, Washington. In: Proceedings of the US National Conference on Earthquake Engineers, EERI, Berkeley, California (1975)
- Freeman, S. A.: Prediction of response of concrete buildings to severe earthquake motion. In: McHenry D., (ed.) *International Symposium on Concrete and Concrete Structures*. Publication SP-55, American Concrete Institute, Detroit (1978)
- Freeman, S. A., Paret, T. F., Searer, G.R., Irfanoglu, A.: Musings on recent developments in performance-based seismic engineering. In: Structures Congress 2004. SEI, American Society of Civil Engineers, Nashville (2004, Submitted)
- Gandomi, A.H., Das, S., Mansouri, I., Choudhury, S., Hu, J.W.: A prediction model for the calculation of effective stiffness ratios of reinforced concrete columns. *Materials* **14**, 1792 (2021). <https://doi.org/10.3390/ma14071792>
- Iwan, W.D., Guyader, A.C.: A Study of the Accuracy of the Capacity Spectrum Method in Engineering Analysis. Report No. PEER/2002/2, pp. 135-146 (2002)
- Malu, A., Choudhury, S.: Direct displacement-based design of a building incorporating viscous dampers. *Proc. Int. Struct. Eng. Constr.* **7**(2) (2020). *Emerging Technologies and Sustainability Principles*. [https://doi.org/10.14455/ISEC.2020.7\(2\).STR-12](https://doi.org/10.14455/ISEC.2020.7(2).STR-12)
- Matsumori T., Otani, S., Shiohara, H.: Earthquake Member Deformation Demands in Reinforced Concrete Frame Structures. Report No. PEER/1999/10, pp. 79-94 (1999)



- Mayengbam, S.S., Choudhury, S.: Determination of column size for displacement-based design of reinforced concrete frame buildings. *J. Earthq. Eng. Struct. Dyn.* **43**(8), 1149–1172 (2014). Article first published online: 21 Nov 2013. <https://doi.org/10.1002/eqe.2391>
- Moradpour, S., Dehestani, M.: Optimal DDBD procedure for designing steel structures with nonlinear fluid viscous dampers. In: *Structures*, vol. 22, pp. 154–174. Elsevier (2019)
- Pettinga, J.D., Priestley, M.J.N.: Dynamic behaviour of reinforced concrete frames designed with direct displacement-based design. *J. Earthq. Eng.* **9**(2), 309–330 (2005)
- Priestley, M.J.N.: Myths and fallacies in earthquake engineering. *Bull. NZ National Soc. Earthq. Eng.* **26**(3), 329–341 (1993)
- SEAOC Blue Book: Recommended Lateral Force Requirement and Commentary, Structural Engineers Association of California (1999)
- Sullivan, T.J., Priestley, M.J.N., Calvi, G.M.: Direct displacement-based design of frame-wall structures. *J. Earthq. Eng.* **10**(1), 91–124 (2006a)
- Sullivan, T.J., Priestley, M.J.N., Calvi, G.M.: *Seismic Design of Frame-Wall Structures*, Research Report No. ROSE-2006/02 (2006b)
- Sullivan, T.J., Priestley, M.J.N., Calvi, G.M.: Direct displacement-based design of frames-wall structures. *J. Earthq. Eng.* **10**(1), 91–124 (2006)
- Sullivan, T. J., Lago, A.: Towards a simplified direct DBD procedure for the seismic design of moment resisting frames with viscous dampers. *Eng. Struct.* **35**, 140–148 (2012). Elsevier



# Evaluation of Role of Hybrid Damping System in Seismic Assessment

Ankita Thorat<sup>(✉)</sup> and Hanamant Magarpatil

School of Civil Engineering, MIT World Peace University, Pune, India  
{ankita.thorat, hanamant.magarpatil}@mitwpu.edu.in

**Abstract.** Energy dissipation capacity and seismic performance of steel moment resisting frame with hybrid damping system along with buckling restrained brace is investigated and an innovative approach of design of energy dissipating system is recommended. The nine storied structure is analyzed by nonlinear time history analyses using seven time histories and scaled to achieve a set of results and then compared the various possibilities. The multi-linear elastic and plastic links are used to model energy dissipating devices with the help of SAP 2000. The various results such as *story displacement*, *story drift*, *roof drift*, *base shear* and *roof acceleration* of steel moment resisting frame are compared with the system after installation of energy dissipaters in the same moment resisting frame that means a dual buckling restrained brace with steel moment resisting frame system and a dual hybrid damping system with steel moment resisting frame system. It was expected that the system will work in individual phases as earthquake intensity will go on increasing and in end results, the models have shown the same. It also has got depicted that the energy dissipation of the systems gets improved after installation of hybrid damping systems.

**Keywords:** Hybrid damping system · Steel moment resisting frame · Buckling restrained braces · Multi linear elastic and plastic links

## 1 Introduction

Structural Engineers are always considered responsible for a structure which should be economical, visually appealing and enough strong against all types of forces acting on it. Lateral forces such as wind or seismic cause the failure of structures. Members involved in structural columns such as column, when subjected to lateral forces, it fails in buckling or torsion (FEMA 2000). When these columns are of reinforced cement concrete, the possible failure pattern will be sudden and if those are of steel, failure will be ductile. Hence, steel structures are more ductile than reinforces cement concrete structures. Steel structures are stronger than RCC structures for lateral loads. But in India, RCC structures are more popular than steel structures. Steel structures are mainly used for industrial sheds and RCC structures for residential purpose (Rai and Wallace 1998; Sahoo and Rai 2007).

Open first story is the basic need for various purposes such as parking, open area for shop, etc. in high rise building. Parking floor has become an unavoidable feature for the most of urban multi-storied buildings (MagarPatil and Jangid 2012). Construction

of buildings with multiple stories having first few parking floors (soft storey) are more likely to get collapsed during a seismic event as the earthquake load distribution is spread along the wide area. According to recent observations, it is seen that usual practice is to design a structure without considering the reduction in stiffness at the bottom soft storey. It is important to consider that the stiffness of the building reduces drastically which may result in concentration of the process at that first floor level (MagarPatil and Jangid 2012). To avoid this concentration of forces, a few measures can be adopted such a gradual variation in cross section of the column, provision of walls at some locations in parking floor and provision of energy dissipating devices. The first two help in lateral drift demand reduction on the story columns. However, the latter is effective in reducing the drift as well as the strength demands on the columns. In order to establish a balance between strength, stiffness and damping, it is necessary to develop new systems to serve the purpose of improving seismic performance of the structure. For creating the necessary balance in stated three parameters, systems are to be carefully designed using base isolation or installation of control devices for energy dissipation. (MagarPatil and Jangid 2013). The system results in considerable extensive damage when it deforms in-elastically after it is designed with prescriptive approach. Re-examination of connection details was initiated after the damage caused by the 1994 Northridge, California earthquake. Therefore in order to make post-earthquake damage more predictable and to increase the efficiency of structural performance, provision of seismic protection system which are designed within the framework of performance based design are to be provided. The balance between strength, stiffness, ductility and damping can be achieved by careful design of base isolation, structural components and effective control devices to improve the seismic performance of the structure. Hence, development of effective structural system which will maintain the balance becomes more important. This balance can be achieved by energy dissipation through inelastic deformation of carefully detailed structural elements, base isolation, and a structural control device to dissipate energy and reduce deformations (Symans et al. 2008). It was necessary to study the connection details of the buildings in more details as the conventional methods of designs led to severe damages during 1994 Northridge, California and Hyogoken-Nanbu earthquake of January 17, 1995 (AIJ 1995; Marshall and Charney 2009). If the performance based assessment identifies any deficiency in some areas, then modification can be done locally for the isolated members or joints. If any deficiency is found throughout the structure then more detailed assessment is required to be done and accordingly modification can be recommended (Marshall and Charney 2012; MagarPatil and Jangid 2013). Numbers of techniques are available for strengthening of SMRF or its various members. Strengthening strategies are inter-related. Each strengthening strategy affects other. It means that no strengthening parameter can be changed without influencing the value of the other (MagarPatil and Jangid 2012). Hence, effect of the change in each item should be examined separately in order to investigate the effectiveness of each parameter. In this study an eleven storeyed frame is considered and the study mainly aims to analytical assessment of response of the building to a seismic event. Nonlinear time-history analysis and push over analysis of the lateral load resisting frame is carried out using SAP2000 to evaluate the performance in terms of drift limits, damage levels and lateral load capacity (CSI 2007; Marshall and Charney 2010). For the purpose of improving strength of the frame under

study, different techniques are implemented. The main objectives of strengthening are (i) reduction in open ground storey deformation (ii) improvement in lateral load carrying capacity and energy dissipation in the frame under study. It is necessary to investigate the influence of different stiffening measures analytically to make the structure perform in better manner during seismic event. Various analytical models were developed over the years based on the overall understanding of the physical behavior of an energy dissipater to simulate the actual behavior of frames.

Energy dissipation devices attached, uses the differential attachment point displacement to control the effects after an event. BRB are the devices which are performance wise rate independent or dependent on joint displacement. Energy dissipation does not take place till yielding of BRB is not started. As results of this, BRBs are proven to be vital energy dissipation devices only after yielding starts. Hybrid damper with high damping rubber damper and elastic springs with varying stiffness is used as damper. High damping rubber damper (HDRD) is a material with the combination of viscous and elastic properties (Marshall and Charney 2009). Performance of HDRD is dependent on rates that means it is velocity dependent device which dissipate energy on account of shear deformation. It was previously used in base isolator. Now a day, it is also used in damping systems (MagarPatil and Jangid 2013; Marshall and Charney 2010). It is modeled mathematically and used in this phased system. The springs are arranged and used with the strength capacities so that it can participate immediately after the high damping rubber damper losses its full strength. The mild steel section assembled after springs elements participate after springs gets displaced to a designed value. The phase system is developed in such a way that elements get sequentially engaged to resist seismic forces. Displacement and acceleration values are significantly reduced due to this phased system (Marshall and Charney 2012). Hybrid damping system is the combination of rate dependent or velocity dependent device along with rate independent or displacement dependent device (Marshall and Charney 2010). Rate dependent device or velocity dependent device dissipate energy when deformed. Rate-independent also called as displacement dependent devices provide both stiffness and energy dissipation. The increase in stiffness reduces displacement but base shear and acceleration will increase while yielding. Energy dissipation occurs while slip or yield force exceeds. Example for rate dependent device is HDRD whereas for rate independent device is BRB. Hence rate independent or displacement dependent devices are also called as added damping and stiffness (ADSS) devices (MagarPatil and Jangid 2013; Marshall and Charney 2010).

## 2 Analytical Formulation

A nine storied steel moment resisting frame is modeled and designed according to provisions in IS codes (IS 800:2007; IS 875: I, II, III; IS 1893, 2002). The frame has nine stories and five bays. Height of each storey is 4.5 m and bay width are 4 m. The control devices are placed in the bays which are at same distance from both sides of the frame to maintain economy. In previous research paper, the detailed analysis of the frame with respect to position of the energy dissipating device has been done (MagarPatil and Jangid 2013). Similarly, wall is modelled as diagonal strut as per

FEMA 356. The energy dissipaters are designed in such a way that the basic balance of strength, ductility, stiffness and damping is maintained.

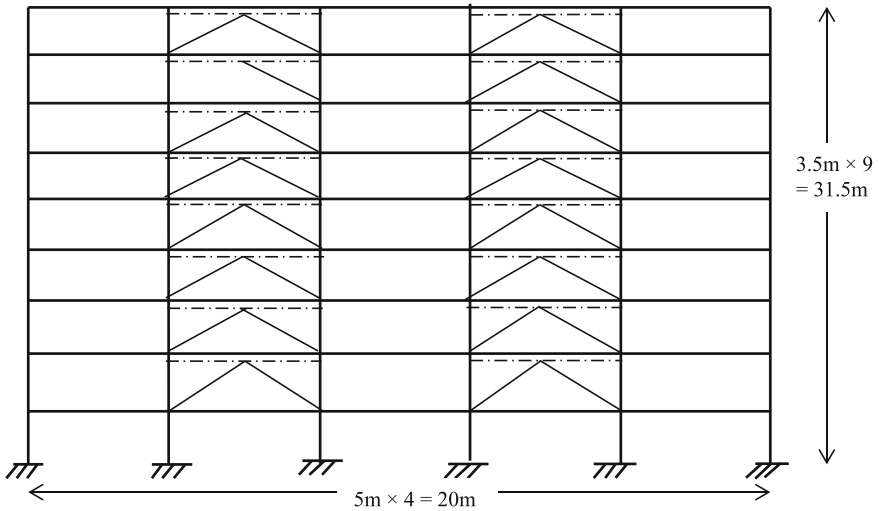


**Fig. 1.** Structural geometry.

Figure 1 depicts the installation location of energy dissipaters in the frame under study. The total stiffness of columns and beams of the modified frame are reduced to 13% and 10% respectively. Column cross-sections are kept larger as compared to beams so as to achieve the philosophy of strong columns and weak beams (MagarPatil and Jangid 2013; Marshall and Charney 2010). There is a partially restrained connection between columns and dampers which is located at a beam depth below the bottom surface of beam and oriented along the beam. The dampers are supported by chevron bracing system on other side as shown. Two different energy dissipating systems considered in this research work are as mentioned in Table 1.

**Table 1.** Energy dissipating systems

Sr. no.	Basic frame	Damping system
01	SMRF	No damping system
02	SMRF	BRB of Mild Steel on both sides of Chevron bracing
03	SMRF	HDS on both sides of Chevron bracing
04	SMRF	BRB of Mild Steel and HDS on both sides of Chevron Bracing

In previous research work, the possibility of use of aluminium dampers is also examined and concluded that they are economical but from results point of view such as story drift, story displacement, roof drift, roof acceleration, they resulted to be weak. The basic system considered is a bare SMRF with no energy dissipater, designed

according to IS codal provisions to sustain the loading as given in Sect. 3. The second system consists of Mild steel BRB as energy dissipater in SMRF. Section used is selected and designed according to Indian codal provisions and also as per availability in the Indian market. In third system, hybrid damping system is used as energy dissipater in steel moment resisting frame. Hybrid damping system is explained in Sect. 1 and is as shown in Fig. 2.

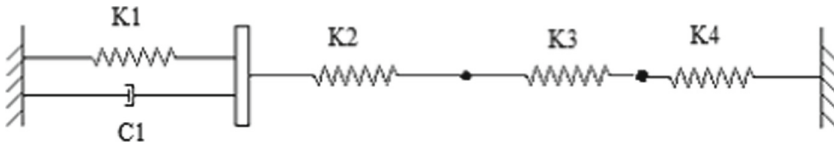


Fig. 2. Mathematical model for HDS.

Hybrid damping system is a phased system. It is designed to resist initial less intensity shocks and then moderate as well as heavy shocks sequentially. A combination of mild steel BRB and hybrid damping system is used in the fourth system. They are placed in parallel. The displacement of HDS and BRB will be same. Hence, in total, four systems are developed and analyzed. The braces used are of same sizes and same in number for all the structural frames and systems. Hybrid damping system is designed using link elements as discussed in Sect. 1.

The beam section used is as available in Indian market that means those are Indian standard sections but for columns, as strength demand was very high, British standard sections are used.

The systems as stated above are designed for condition of dynamic equilibrium as follows:

$$f_I + f_D + f_S = 0 \tag{1}$$

where,  $f_I$  is inertial force i.e.  $m\ddot{u}$ ,  $f_D$  is damping force i.e.  $c\dot{u}$  and  $f_S$  is stiffness of the system i.e.  $ku$ . The stiffness matrices will vary as far as structural members, their position, end conditions and loads to which they are subjected change, for all four cases. The stiffness is calculated by adding it for whole system that means addition of stiffnesses of columns, BRB, HDS along with stiffness of chevron braces by considering its effect when those are planned in parallel or in series as shown in Fig. 2. The total stiffness of hybrid damping system is calculated by addition of stiffnesses of the elements used in HDS that means stiffness of high damping rubber damper, springs of various stiffness and also that of mild steel BRB as those are placed in series.

Stiffness of hybrid damping system is the addition of stiffnesses of springs in series. Hence an expression for equivalent stiffness of the hybrid damping system is given as:

$$k_{eq(HDS)} = \frac{k_1 k_2 k_3}{k_1 k_2 + k_2 k_3 + k_1 k_3} \tag{2}$$

where,

- $k_1$  = Stiffness of first spring
- $k_2$  = Stiffness of second spring
- $k_3$  = Stiffness of buckling restrained brace

The hybrid damping system when used along with buckling restrained braces in parallel, equivalent stiffness will be,

$$k_{eq} = k(\text{Column}) + k_{eq}(\text{HDS}) + k_{eq}(\text{BRB}) + k_{eq}(\text{Bracing}) \tag{3}$$

Same size of dampers is used for all four cases. Details of the sizes and properties are depicted in Table 2.

**Table 2.** Damper properties for the structure

Structural system	1 <sup>st</sup> mode period	1 <sup>st</sup> mode frequency (rad/sec)	Damper size (L × Dia) mm (same for all floors)	Modal damping	Modal load participation ratio	
					Static percent	Dynamic percent
SMRF	0.317389	3.1507	–	0.05	100	100
SMRF + M.S. (BRB)	0.205904	4.8566	2000 × 150	0.05	100	100
SMRF + HDS	0.262681	3.8069	2000 × 150	0.05	100	100
SMRF + MS (BRB) + HDS	0.204418	4.8919	2000 × 150	0.05	100	100

### 3 Incremental Dynamic Analysis (IDA)

In earthquake engineering, in order to understand the performance of a structural model, a comprehensive computational dynamic analysis equivalent to Static Pushover Analysis is carried out, is known as Incremental Dynamic Analysis (IDA). It is to be performed in number of steps of non-linear dynamic analysis, when a structural model is subjected to a set of ground motion records scaled to multiple levels. Thus, the seismic response of the structure can be understood over wide range of earthquake intensities. The results of IDA are plotted in terms of graph of Scale factor or intensities versus various structural performance parameters. Output diagrams are known as IDA curves. In the present study, the said structural model is subjected to 7 different ground motion records (Table 3) scaled to various intensity levels for assessment of Dynamic response of the structure to the seismic events.

## 4 Details of Seismic Excitations

In this research, effect of wall is considered. First story is soft story. For load calculations, Gravity as well as seismic weight was considered. Along with that seven earthquake time history records are used in terms of base excitations while performing the analysis. The time history record of Chi Chi Taiwan (1999), Gazali USSR (1976), Irpina-Italy (1980), Imperial Valley (1940), Landers CA (1992), Loma Prieta (1989) and Northridge (1994) as shown in Table 3 are used in the nonlinear time history analysis (MagarPatil and Jangid 2013; Marshall and Charney 2010).

**Table 3.** Earthquake records

Earthquake records	Year	Earthquake record description
Chi-Chi, Taiwan	1999	CHY101, W (CWB)
Gazli, USSR	1976	GAZLI, KARAKYR, 000
Irpina, Italy-01	1980	IRPINIA EQ, STURNO, 000
Imperial Valley, CA	1940	IMPERIAL VALLEY, EL CENTRO ARRAY #9, 180 (USGS STATION 117)
Landers, CA	1992	LANDERS, LUCERNE, 000 (SCE STATION 24)
Loma Prieta, CA	1989	LOMA PRIETA, BRAN, 000 (UCSC STATION 13)
Northridge	1994	NORTHRIDGE AFTERSHOCK, ANAVERDE VALLEY - CITY RANCH,180

The scale factors were selected to bring the 5% damped elastic response spectrum of the original earthquake record close to code spectrum for the soil profile  $S_1$  specified for the dynamic lateral force procedures (Naeim et al. 2004). In dynamic incremental analysis, scale factor 1 is considered for Design Basis Earthquake and 1.5 for Maximum considered Earthquake. Parameters like story drift, story displacement, roof drift, base shear and roof acceleration are evaluated and assessed. For modal load participation ratio, full static and dynamic percentage is considered (Except bare SMRF). The hybrid damping system developed is assembled using mild steel pipe section. Modal damping is kept constant 5% for all cases.

## 5 Result Discussion

Bare frame with glass cladding is a popular concept for the commercial buildings from as it improves the elegance of the structure. But presence of wall matters a lot in structural behavior. The effects of bare frame are seen in our previous work. Here in this research work, effect of wall is also considered with first soft story. Soft story changes story stiffness tremendously. This sudden change in stiffness is harmful for the structure. Lateral forces increases story drift and story displacement also. Hence, it is



required to strengthen using energy dissipating system. The energy dissipators used here in this research work are buckling restrained braces and hybrid damping system. They are used alone or in combination to dissipate energy. BRB of mild steel reduces story displacement but the result found as shown in Fig. 3 for HDS alone are far better than MS BRB alone or when used in combination with HDS.

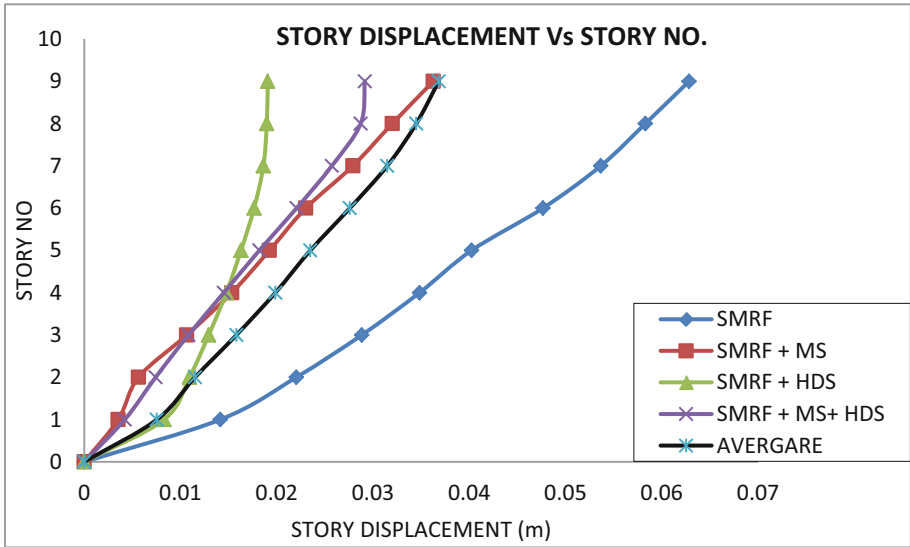


Fig. 3. IDA Results of displacement with respect to story number.

For first few stories, story displacement of the frame when MS BRB is used is less as compared with other systems. The sudden change in displacement profile can be found in this case. This sudden decrease in story displacement may result in opposite immediate force in columns in first few floors which develop cracks. Whereas, in case where HDS alone is used, story displacement of first few floors is more as compared with other two systems. But it is very less than SMRF without energy dissipating system. Here in case where, HDS alone is used, story displacement reduces slowly and at roof level it is much less as compared with all other cases. This slow reduction in story displacement is what targeted while modelling HDS. Story drift as shown in Fig. 4 clarifies the importance of use of energy dissipators.

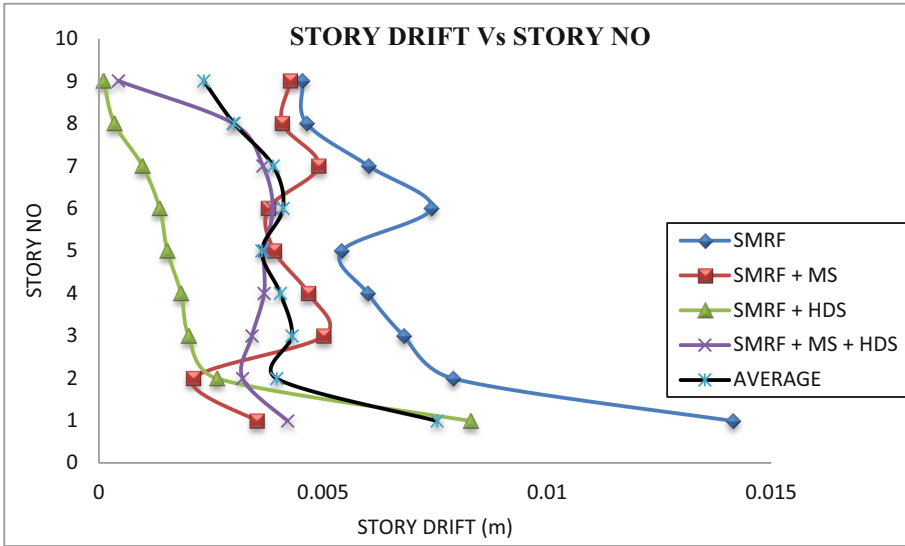


Fig. 4. IDA Results of story drift w.r.t. story number.

Story drift of all cases where energy dissipators are used is very less. Here in this graph again it can be seen that story drift in initial few stories is less for the case where MS BRB is used alone or in combination as compared with the case where HDS alone is used. But roof drift of the cases where HDS is used, is very less. Roof drift with respect to scale is as shown in the Fig. 5.

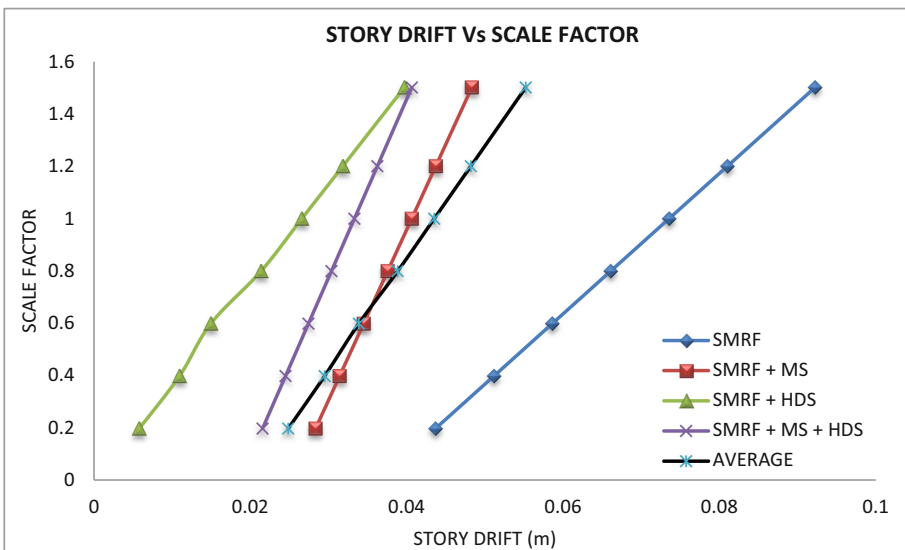
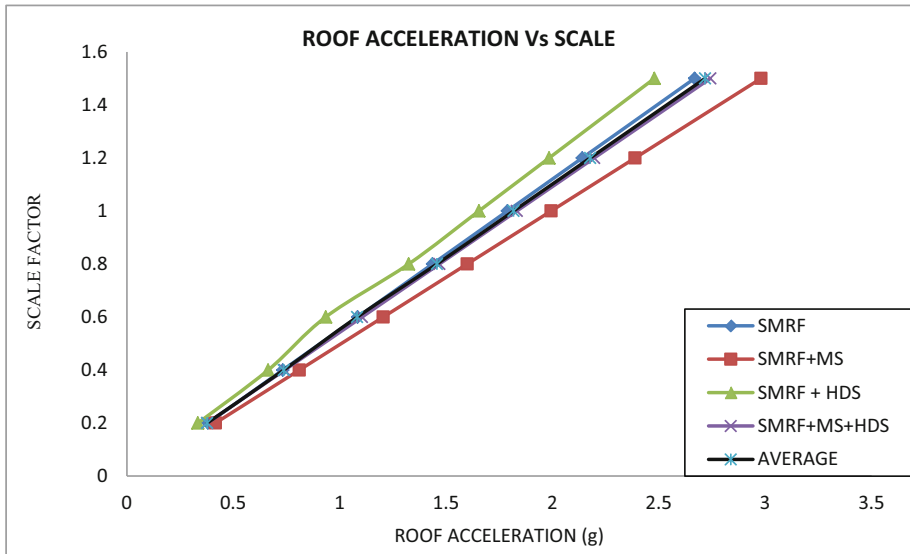


Fig. 5. IDA Results of story drift w.r.t. scale factor.

It is found that roof drift with scale increases linearly for all case. At lower scale HDS found to be very economical as compared to all other systems. HDS when used along with MS BRB results to be uneconomical at lower scales but as the scale is increased, it reduces story drift. Phased Behavior of HDS has performed well in reducing story drift and story displacement as well. It has performed well along with MS BRB in combination.



**Fig. 6.** IDA Results of Roof acceleration w.r.t. scale factor.

Figure 6 shows the comparison of roof acceleration with respect to scale. Roof acceleration for the case where HDS alone is used in SMRF, is less as compared to basic SMRF. But when it is used along with MS BRB, it results in increased roof acceleration for all scale factors. MS BRB is uneconomical for all scale factors as compared with all other cases. Hence, in case of roof acceleration also, HDS has proved its importance. Base Shear with respect to scale factor can be seen in Fig. 7.

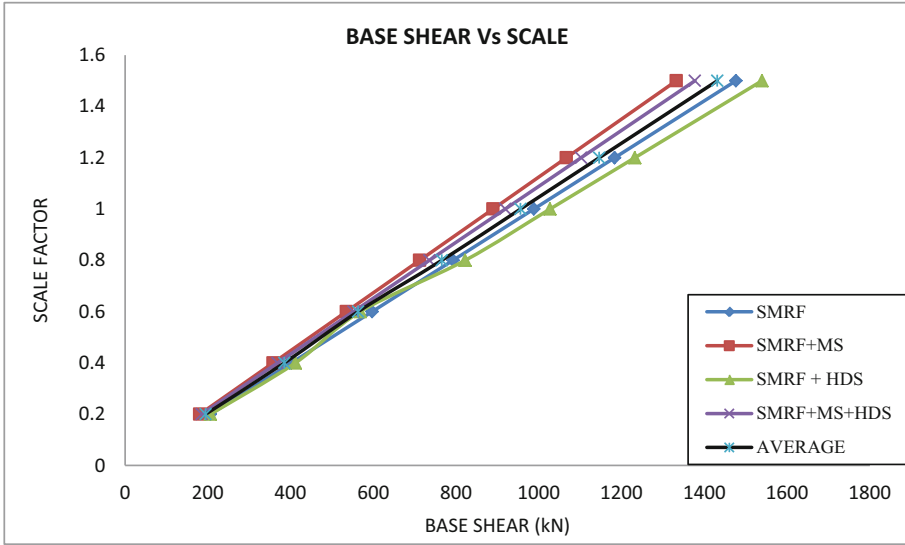


Fig. 7. IDA Results of Base Shear w.r.t. scale factor.

It is found that HDS alone when provided in SMRF proves to be uneconomical for all scales with respect to all energy dissipation systems. As compared with basic SMRF, base shear of the case where MS BRB alone or in combination with HDS is used, is less. MS BRB has performed well in respect of Base Shear for all scale factors. Here in this analysis, it is found that HDS has performed well in all respect except for base shear. The phased behavior of HDS and arrangement of high tensile springs in increasing order has played very important role. The combination of rate dependent and independent members showed their need in structural members. The pushover analysis done for all cases show results as in Fig. 8.

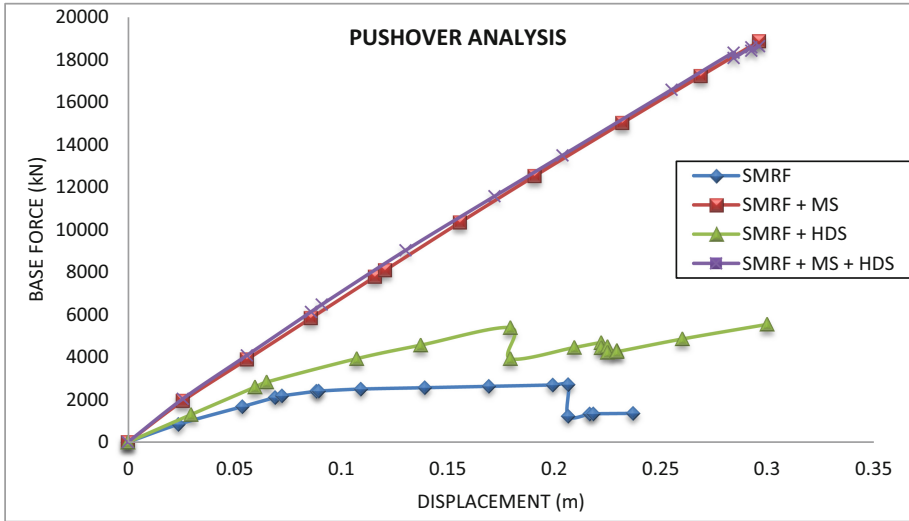


Fig. 8. IDA Results of Base Shear w.r.t. displacement.

The analysis show that base shear for displacement in case of MS BRB alone or when used in combination with HDS is more as compared with the case where HDS alone is used or of basic SMRF. The hybrid system phase changes can be seen in the plot. Once the full strength of the hybrid damping system is utilized, the stiffness of the model increases until the buckling restrained braces yield. Push over analysis show that performance point of all cases lies below collapse prevention case that means either immediate occupancy or life safety. At initial stage for the case where HDS is used in SMRF, base shear and roof displacement curve shows that large change in base shear causes large displacement but slowly this change in base shear is less for large change in roof displacement. But in systems where MS BRB is used alone or in combination with HDS, this change is almost linear.

## 6 Conclusions

Steel moment resisting frame with first soft story for parking purpose is unavoidable in Indian conditions. Basically, SMRF instead of RCC is a new concept in civil engineering industry. The energy dissipating system used in this research work has proved its importance in SMRF when subjected to seismic excitation. The hybrid damping system used in this research is developed according to formation of earthquake waves and behavior of structure and structural elements during a seismic event. Due to tremendous reduction in story displacement and drift, roof drift and roof acceleration, hybrid dampers have confirmed their need in SMRF with first few soft stories. When those are used along with buckling restrained braces of mild steel, the results are quite economical than MS BRB alone is used. The only benefit seen for MS BRB is decrease in base shear.

## References

- Chopra, A.K.: Dynamics of Structures: Theory and applications to Earthquake Engineering, 3rd edn. Pearson Prentice Hall, USA (2007). Multi degree shear building
- CSI 2007: CSI Analysis Reference Manual. Computers and Structures, Inc, Berkeley, CA
- Rai, D.C., Wallace, B.J.: Aluminium shear link for enhanced seismic resistance. *Earthq. Eng. Struct. Dyn.* **27**, 315–342 (1998)
- Sahoo, D.R., Rai, D.C.: Seismic Strengthening of RC Buildings using steel cage and Aluminium Shear Link. In: 8th Pacific Conference on Earthquake Engineering, Singapore 2007; Paper 117 (2007)
- Naeim, F., Alimoradi, A., Pezeshk, S.: Selection and scaling of ground motion time histories for structural design using genetic algorithm. *Earthq. Spectra* **20**(02), 413–426 (2004)
- FEMA 2000: State of the Art Report on Systems Performance of Steel Moment Frames Subject to Earthquake Ground Shaking (FEMA 355C), Federal Emergency Management Agency: Washington, D.C.
- IS: 800-2007: General Construction in Steel – Code of Practice
- IS: 875 (Part I,II,III)-1987, Code of Practice for Design Loads (Other than earthquake) for Buildings and Structures
- IS: 1893(Part I)-2002, Criteria for Earthquake Resistant Design of Structures
- Marshall, J.D., Charney, F.A.: Seismic response of steel frame structures with hybrid control systems. *Earthq. Eng. Struct. Dynam.* **41**(4), 715–733 (2012)
- Marshall, J.D., Charney, F.A.: Dynamic response of steel moment-frame structures with hybrid control systems. In: ATC and SEI 2009. Conference on Improving the Seismic Performance of Existing Buildings and Other Structures 2009, pp. 1022–1033 (2009)
- Mazza, F., Vulcano, A.: Control of the earthquake and wind dynamic response of steel framed buildings by using additional braces and/or viscoelastic dampers. *Earthquake Eng. Struct. Dynam.* **40**(2), 155–174 (2011)
- MagarPatil, H.R., Jangid, R.S.: Seismic assessment of steel moment resisting frame with and without masonry walls. In: Proceeding of International conference on Structural and Civil Engineering 2012, pp. 05–08 (2012)
- MagarPatil, H.R., Jangid, R.S.: Seismic vulnerability assessment of steel moment resisting frame due to infill masonry wall, variation in column size and horizontal buckling restrained braces. *Int. J. Civil Environ. Eng.* **2**(1), 20–27 (2013)
- Marshall, J.D., Charney, F.A.: A hybrid control device for steel structures: development and analysis. *J. Constr. Steel Res.* **66**(10), 1287–1294 (2010)
- Symans, M.D., et al.: Energy dissipation systems for seismic applications: current practice and recent developments. *J. Struct. Eng.* **134**, 13–21 (2008)

# Author Index

## A

Abdul Akbar, M., 79  
Adak, Dibyendu, 210  
Alam, Mehtab, 219  
Anandwala, Husain, 88  
Anas, S. M., 219

## B

Baruah, Kangkana K., 272  
Bhattacharjee, Bishwajit, 1  
Bhuvaneshwari, P., 102  
Billah, A. H. M. Muntasir, 43  
Biswas, Anupam Kumar, 344

## C

Chaudhary, Shruti, 404  
Choudhury, Satyabrata, 187, 239, 272, 282, 301, 364, 404

## D

Das, Sandeep, 210  
Datta, Alope Kumar, 344  
Dutta, Subhrajit, 210

## F

Fernandes, Thiago, 26  
Frederick, Franklin F. R., 257

## G

Gautam, Abhishek Kumar, 353  
Gupta, V. K., 257

## I

Iqbal, Sumbul, 200  
Islam, Nazrul, 200

## K

Kassim, Azeel P., 187  
Kontoni, Denise-Penelope N., 7  
Kumar, Abhishek, 177  
Kumar, Deepak, 153  
Kumar, Nitesh, 390  
Kumar, Vijay, 153  
Kumari, Sapna, 163

## M

Magarpatil, Hanamant, 88, 138, 416  
Magarpatil, Hanumant, 62  
Maiti, Pabitra Ranjan, 7, 177  
Majumdar, Shubhankar, 210  
Mandal, Sasankasekhar, 7, 163

## N

Narayana, Jinka Lakshmi, 102  
Nareshnayak, N., 250

## P

Pal, Manish, 301  
Pal, Shulanki, 239  
Patel, Vaibhav, 62  
Patil, Vedang, 138  
Prabhakara, D. L., 373  
Prakash, Boddu Venkata Sai, 102  
Prasanna, G., 325  
Priyadarsh, P. G., 336

**R**

Rajanna, T., 373  
Rakshith, H. S., 373  
Rana, Sahil, 79  
Rani, Neelam, 336  
Rao, B. N., 250  
Ravi Kumar, L., 373  
Regita, J. Jane, 118  
Roy, Bijan Kumar, 239  
Roy, N. Sarma, 282

**S**

Sengupta, Sanjay, 344  
Sharma, H. K., 390  
Sharma, Rachit, 79  
Sharma, U. K., 257  
Shendkar, Mangeshkumar R., 7  
Shukla, Anjani Kumar, 177

Singh, Ashish, 163  
Singh, Vinay Kumar, 353  
Sofi, A., 118  
Sudheer, Gaddam, 364  
Sumathi, A., 325

**T**

Thakur, Ankush, 79  
Thorat, Ankita, 138, 416  
Tiwari, R. P., 153  
Todorov, Borislav, 43  
Topdar, Pijush, 344

**U**

ul Ain, Qurat, 219

**V**

Vamsi, Gutti Nikhil, 102